Transactions of the ASME®

Journal of Fluids Engineering

Published Quarterly by The American Society of Mechanical Engineers

VOLUME 123 • NUMBER 2 • JUNE 2001

Transactions of the ASME, Journal of Fluids Engineering (ISSN 0098-2202) is published quarterly (Mar., June, Sept., Dec.) by The American Society of Mechanical Engineers, Three Park Avenue, New York, NY 10016. Periodicals postage paid at New York, NY and additional mailing offices.
POSTMASTER: Send address changes to Transactions of the ASME, Journal of Fluids Engineering, c/o THE AMERICAN SOCIETY OF MECHANICAL ENGINEERS, 22 Law Drive, Box 2300, Fairfield, NJ 07007-2300.
CHANGES OF ADDRESS must be received at Society headquarters seven weeks before they are to be effective. Please send old label and new address.
STATEMENT from By-Laws. The Society shall not be responsible for statements or opinions advanced in papers or ... printed in its publications (B7.1, Par. 3).

INDEXED by Applied Mechanics Reviews and Engineering Information, Inc. Canadian Goods & Services Tax Registration #126148048.

TECHNICAL PAPERS

(Contents continued on inside back cover)

This journal is printed on acid-free paper, which exceeds the ANSI Z39.48-1992 specification for permanence of paper and library materials. ♾™
♻ 85% recycled content, including 10% post-consumer fibers.

Journal of Fluids Engineering Volume 123, Number 2 JUNE 2001

TECHNICAL BRIEFS

ANNOUNCEMENTS

Fluid Flow Phenomena in Materials Processing—The 2000 Freeman Scholar Lecture

There has been an explosive growth in the development of new materials and processing techniques in recent years to meet the challenges posed by new applications arising in electronics, telecommunications, aerospace, transportation, and other new and traditional areas. Semiconductor and optical materials, composites, ceramics, biomaterials, advanced polymers, and specialized alloys are some of the materials that have seen intense interest and research activity over the last two decades. New approaches have been developed to improve product quality, reduce cost, and achieve essentially custom-made material properties. Current trends indicate continued research effort in materials processing as demand for specialized materials continues to increase. Fluid flow that arises in many materials processing applications is critical in the determination of the quality and characteristics of the final product and in the control, operation, and optimization of the system. This review is focused on the fluid flow phenomena underlying a wide variety of materials processing operations such as optical fiber manufacture, crystal growth for semiconductor fabrication, casting, thin film manufacture, and polymer processing. The review outlines the main aspects that must be considered in materials processing, the basic considerations that are common across fluid flow phenomena involved in different areas, the present state of the art in analytical, experimental and numerical techniques that may be employed to study the flow, and the effect of fluid flow on the process and the product. The main issues that distinguish flow in materials processing from that in other fields, as well as the similar aspects, are outlined. The complexities that are inherent in materials processing, such as large material property changes, complicated domains, multiple regions, combined mechanisms, and complex boundary conditions are discussed. The governing equations and boundary conditions for typical processes, along with important parameters, common simplifications and specialized methods employed to study these processes are outlined. The field is vast and it is not possible to consider all the different techniques employed for materials processing. Among the processes discussed in some detail are polymer extrusion, optical fiber drawing, casting, continuous processing, and chemical vapor deposition for the fabrication of thin films. Besides indicating the effect of fluid flow on the final product, these results illustrate the nature of the basic problems, solution strategies, and issues involved in the area. The review also discusses present trends in materials processing and suggests future research needs. Of particular importance are well-controlled and well-designed experiments that would provide inputs for model validation and for increased understanding of the underlying fluid flow mechanisms. Also, accurate material property data are very much needed to obtain accurate and repeatable results that can form the basis for design and optimization. There is need for the development of innovative numerical and experimental approaches to study the complex flows that commonly arise in materials processing. Materials processing techniques that are in particular need of further detailed work are listed. Finally, it is stessed that it is critical to understand the basic mechanisms that determine changes in the material, in addition to the fluid flow aspects, in order to impact on the overall field of materials processing. [DOI: 10.1115/1.1350563]

Yogesh Jaluria
Fellow ASME,
Department of Mechanical
and Aerospace Engineering,
Rutgers, the State University of New Jersey,
New Brunswick, NJ 08903
e-mail: jaluria@jove.rutgers.edu

Introduction

One of the most crucial and active areas of research in fluids engineering today is that of materials processing. With growing international competition, it is imperative that the present processing techniques and systems are optimized and the quality of the final product is improved. In addition, new materials and processing methods are needed to meet the growing demand for special material properties in new and emerging applications related to diverse fields such as environment, energy, bioengineering, transportation, communications, and computers.

Fluids engineering is extremely important in a wide variety of materials processing systems such as crystal growing, casting, chemical vapor deposition, soldering, welding, extrusion of plastics, food and other polymeric materials, injection molding, spray coating, glass fiber drawing, and composite materials fabrication. The flows that arise in the molten material in crystal growing, for instance, strongly affect the quality of the crystal and, thus, of the semiconductors fabricated from the crystal. Therefore, it is important to understand these flows and obtain methods to minimize or control their effects. Similarly, the flow of molten metal in welding and soldering is often determined mainly by surface tension effects. On the other hand, the profile in the neck-down region of glass in an optical fiber drawing process is largely governed by the viscous flow of molten glass and by gravity. The buoyancy-driven flows generated in the liquid melt in casting processes strongly influence the microstructure of the casting and the shape, movement and other characteristics of the solid-liquid interface.

Contributed by the Fluids Engineering Division for publication in the JOURNAL OF FLUIDS ENGINEERING. Manuscript received by the Fluids Engineering Division Dec. 18, 2000. Associate Editor: Joseph Katz.

In chemical vapor deposition, the flow is of paramount importance in determining the deposition rate and uniformity, which in turn affect the quality of the thin film produced. The flows in furnaces and ovens used for heat treatment and drying strongly influence the transport rates and the migration of impurities that affect quality. The formation of metal droplets and the flow in sprays are important in rapid fabrication using spray deposition. Therefore, it is important to determine the nature, magnitude and behavior of the flows that arise in these processes, their effect on the transport and the ultimate effect on the product quality and system performance.

Because of the importance of fluid flow in materials processing, extensive work is presently being directed at this area. But what is missing is the link between the diverse processing techniques and the basic mechanisms that govern the flow. Much of the effort is concerned with specific manufacturing systems, problems and circumstances. It is important to extract the main underlying features, with respect to fluids engineering, from these studies in order to expand the applicability of the techniques developed and the results obtained. It is also important to couple the microscale mechanisms that determine material characteristics with the fluid flow that occurs at the macroscale level. Another aspect that is lacking in the literature is quantitative information on the dependence of product quality, process control and optimization on the fluid flow. It is critical to determine how fluid flow affects, for instance, the growth of defects in an optical fiber or in a crystal. It is necessary to establish the present state of the art in fluid flow phenomena in materials processing. It is also important to determine the research needs in this area so that future efforts may be directed at critical issues. The coupling between practical engineering systems and the basic fluid mechanics is another very important aspect that should be considered, so that the current and future practice of fluids engineering have a strong impact in an area that is of particular importance today.

This review paper is directed at these important issues, focusing on the fluid flow that is involved with materials processing and linking it with the characteristics of the product and with the system for a wide variety of important practical processes. A range of processes are considered in order to determine the basic aspects that arise and their effect on the processed material. Interest lies mainly in the basic fluid phenomena, rather than in the complexities of the different processes. Because of the importance of this field today and in the future, a summary of the state of the art on this topic will make a very significant and timely contribution to the current and future efforts in materials processing, an area which encompasses a wide range of real problems of fluids-engineering interest.

The three main aspects that are considered in this paper are:

1 Basic fluid flow phenomena underlying materials processing, including non-Newtonian flows, free surface flows, surface tension driven flows, flows with phase change and chemical reactions, flow in sprays, flows under microgravity conditions, and other specialized flows that are of particular interest in this field.

2 Influence of fluid flow on the characteristics of the final product, in terms of consistency, uniformity, defect formation and concentration, and other relevant measures, as well as the rate of fabrication.

3 Coupling between fluid flow and the operation, design and optimization of the system, considering a range of practical and important processes for the fabrication of traditional and advanced materials.

Materials Processing

In the last two decades, there has been a tremendous growth in new materials with a wide variety of properties and characteristics. Such advanced and new materials include composites, ceramics, different types of polymers and glass, coatings, and many specialized alloys and semiconductor materials. By an appropriate combination and processing of materials, a very wide range of desired material characteristics can be obtained. The choice or, in many cases, design of an appropriate material for a given application has become a very important consideration in the design and optimization of processes and systems, as discussed by Jaluria [1]. Thus, new techniques have been developed and are used along with the classical techniques of materials processing, such as heat treatment, forming and casting, to obtain the desired properties in the chosen material. Consequently, a consideration of the processing of traditional, as well as advanced and emerging, materials involves both classical and new procedures, with a strong emphasis on the link between the resulting material properties and the process used.

Table 1 Different types of materials processing operations, along with examples of commonly used processes

1.	Processes With Phase Change casting, continuous casting, crystal growing, drying
2.	Heat Treatment annealing, hardening, tempering, surface treatment, curing, baking
3.	Forming Operations hot rolling, wire drawing, metal forming, extrusion, forging
4.	Cutting laser and gas cutting, fluid jet cutting, grinding, machining
5.	Bonding Processes soldering, welding, explosive bonding, chemical bonding
6.	Polymer Processing extrusion, injection molding, thermoforming
7.	Reactive Processing chemical vapor deposition, food processing
8.	Powder Processing powder metallurgy, sintering, sputtering
9.	Glass Processing optical fiber drawing, glass blowing, annealing
10.	Coating thermal spray coating, polymer coating
11.	Other Processes composite materials processing, microgravity materials processing

Fluid flow considerations are important in a wide variety of manufacturing processes. Some of the ways in which the flow affects the process are

1 Effect on the underlying transport mechanisms
2 Generation and distribution of impurities and defects
3 Mixing of different components in the material
4 Time spent by the material in the system
5 Process instability and feasibility
6 Shape of processed material
7 Properties and characteristics of the final product
8 Rate of fabrication
9 Product quality

A few important processes in which fluid flow plays a very important role are summarized in Table 1. Several manufacturing processes, in which the flow is of particular importance, are also sketched in Fig. 1. These include the optical glass fiber drawing process in which a specially fabricated glass preform is heated and drawn into a fiber, continuous casting which involves solidification of a liquid over an essentially stationary interface, mold casting in an enclosed region with time-dependent liquid-solid interface location, and screw extrusion in which materials such as plastics are melted and forced through an appropriate die to obtain specific dimensions and shape. Figure 2 shows a few common materials processing techniques used in the fabrication of electronic devices. The processes shown include Czochralski crystal growing in which molten material such as silicon is allowed to solidify across an interface as a seed crystal is withdrawn, the floating-zone method in which a molten zone is established between a polycrystalline charge rod and a crystalline rod, soldering to form solder coating or solder joints, and thin film fabrication by chemical vapor deposition (CVD). In all these processes, the quality and characteristics of the final product and the rate of fabrication are strong functions of the underlying fluid flow.

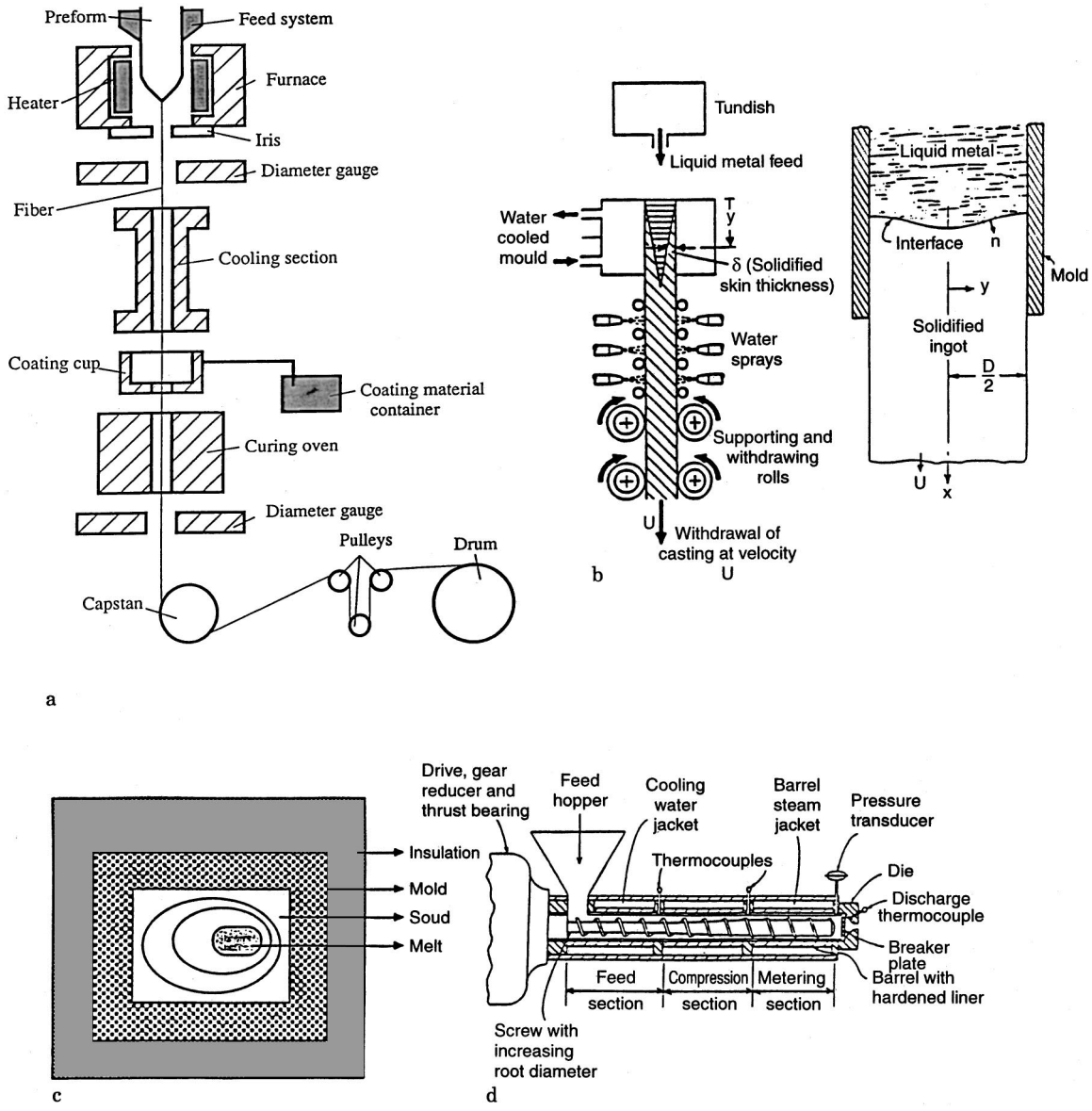

Fig. 1 Sketches of a few common manufacturing processes that involve the flow of the material being processed. (*a*) optical fiber drawing; (*b*) continuous casting; (*c*) mold casting; (*d*) plastic screw extrusion

Because of the importance of materials processing, considerable research effort has been directed in recent years at the transport phenomena in such processes. Many books concerned with the area of manufacturing and materials processing are available. However, most of these discuss important practical considerations and manufacturing systems relevant to the various processes, without considering in detail the underlying transport and fluid flow. See, for instance, the books by Doyle et al. [2], Schey [3] and Kalpakjian [4]. A few books have been directed at the fundamental transport mechanisms in materials processing, for instance, the books by Szekely [5] and by Ghosh and Mallik [6]. The former considers fluid flow in metals processing and presents both the fundamental and applied aspects in this area. Some other books consider specific manufacturing processes from a fundamental standpoint, see the books by Avitzur [7], Altan et al. [8], Fenner [9] and Easterling [10]. In addition, there are several review articles and symposia volumes on fluid flow and thermal transport in materials processing. Examples of these are the books edited by Hughel and Bolling [11], Kuhn and Lawley [12], Chen et al. [13], Li [14], and Poulikakos [15], and the review article by Viskanta [16].

Many important considerations arise when dealing with the mathematical and numerical modeling of the fluid flow and the associated transport in the processing of materials, as presented in Table 2. Many of the relevant processes are time-dependent, since the material must often undergo a given variation with time of the temperature, pressure, shear and other such variables in order to attain desired characteristics. Sometimes, a transformation of the variables in the problem can be used to convert a time-dependent problem to a steady one. Most manufacturing processes involve combined modes of transport. Conjugate conditions usually arise due to the coupling between transport in the solid material and-fluid flow. Thermal radiation is frequently important in these processes. The material properties are often strongly dependent on temperature, concentration, and pressure, giving rise to strong nonlinearity in the governing equations [17,18]. Also, the material

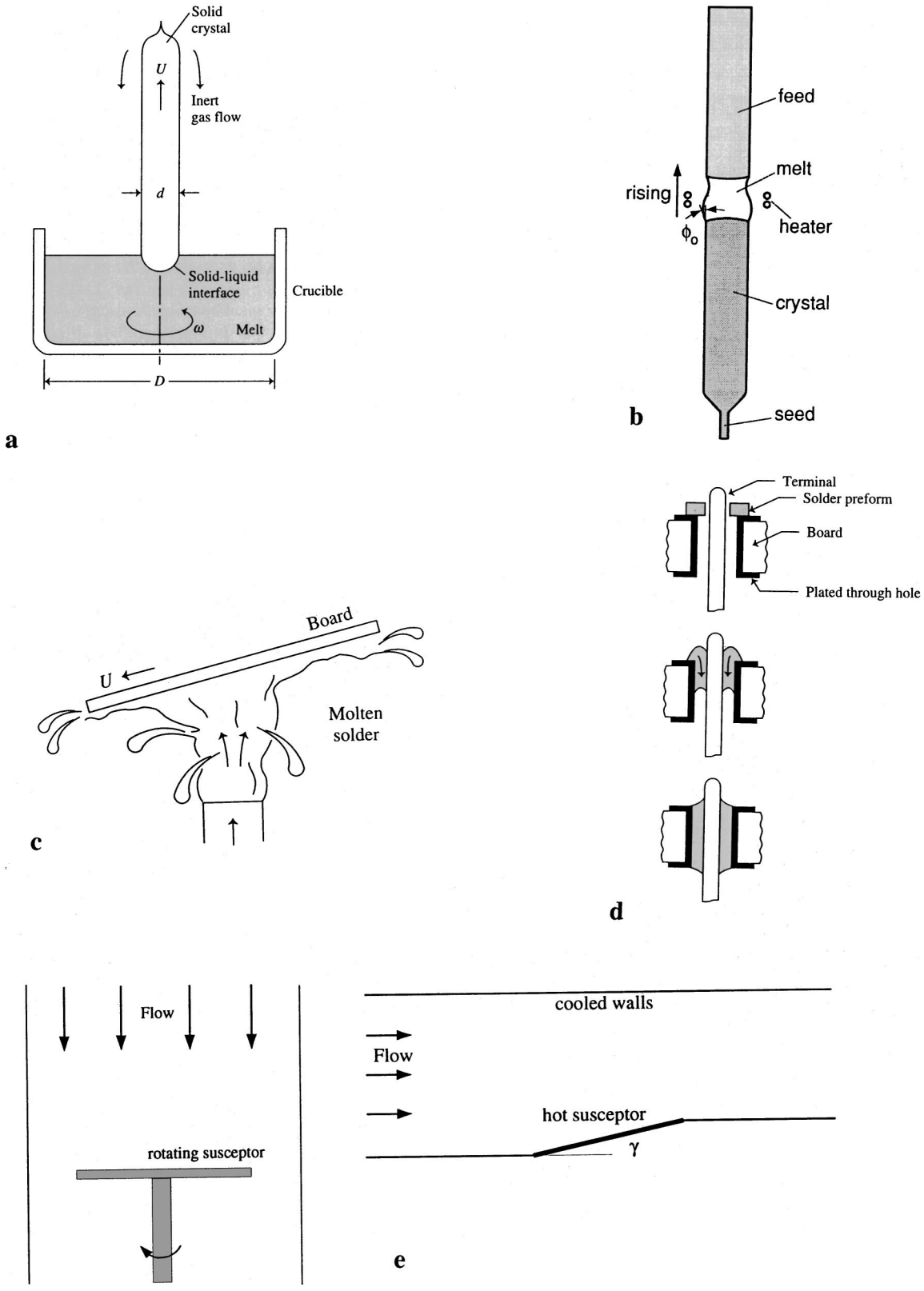

Fig. 2 Sketches of a few processes used for the manufacture of electronic devices. (*a*) Czochralski crystal growing; (*b*) floating-zone method for crystal growth; (*c*) wave soldering; (*d*) solder joint formation; (*e*) chemical vapor deposition

properties may depend on the shear rate, as is the case for polymeric materials which are generally non-Newtonian [9,19]. The material properties affect the transport processes and are, in turn, affected by the transport. This aspect often leads to considerable complexity in the mathematical modeling, as well as in the numerical simulation. The material undergoing the transport process may be moving, as in hot rolling or extrusion [20], or the energy or mass source itself may be moving, as in laser cutting or welding. Additional mechanisms such as surface tension and chemical reactions are important in many cases. Complex geometry and

Table 2 Some of the important considerations in fluid flow associated with materials processing

1.	**Coupling of Transport With Material Characteristics** different materials, properties, behavior, material structure
2.	**Variable Material Properties** strong variation with temperature, pressure and concentration
3.	**Complex Geometries** complicated domains, multiple regions
4.	**Complicated Boundary Conditions** conjugate conditions, combined modes
5.	**Interaction Between Different Mechanisms** surface tension, heat and mass transfer, chemical reactions, phase change
6.	**Micro-Macro Coupling** micro-structure changes, mechanisms operating at different length and time scales
7.	**Complex Flows** non-Newtonian flows, free surface flows, powder and particle transport
8.	**Inverse Problems** non-unique multiple solutions, iterative solution
9.	**Different Energy Sources** laser, chemical, electrical, gas, fluid jet, heat
10.	**System Optimization and Control** link between flow and system

boundary conditions are commonly encountered. Multiple, coupled, regions with different material properties arise in many cases. Frequently, an inverse problem is to be solved to obtain the conditions that result in a desired flow or temperature variation with time and space. Finally, the process is linked with the manufacturing system design, control, and optimization.

All these considerations make the mathematical and numerical modeling of materials processing very involved and challenging. Special procedures and techniques are often needed to satisfactorily simulate the relevant boundary conditions and material property variations. The results obtained are important and interesting, since these are generally not available in the existing fluid mechanics and heat and mass transfer literature. The results from the simulation provide appropriate inputs for the design and optimization of the relevant system. Experimental techniques and results are also closely linked with the mathematical modeling in order to simplify the experiments and obtain characteristic results in terms of important dimensionless parameters. Also, experimental results are of critical value in validating mathematical and numerical models, as well as in providing the physical insight needed for model development.

It must be noted that even though research on the fluid flow phenomena associated with materials processing can be used to provide important inputs to the area, it is necessary for researchers working in fluids engineering to thoroughly understand the concerns, intricacies and basic considerations that characterize materials processing in order to make a significant impact on the field. Otherwise, basic research serves only in a supporting capacity in this important field. The dependence of the characteristics of the final product on the flow must be properly understood and characterized so that analysis or experimentation can be used to design processes to achieve desired product characteristics and production rates. This is the only way research on fluid flow can stay at the cutting edge of technology in materials processing and significantly affect the future developments in this field.

This paper is concerned with fluid flow phenomena in materials processing. The basic flows that commonly arise in this area are first outlined. The main aspects that are common to many of these processes are outlined next, followed by a discussion of some of the major complexities, and common approaches to obtain the solution, using analytical, numerical and experimental methods. Typical results for several common processing methods for advanced and new materials, as well as for traditional materials, are then presented. These examples serve to indicate common features and considerations in different materials processing techniques. Experimental results are discussed at various stages as a means to validate the models, to provide insight into the underlying phenomena, and to provide inputs on material characteristics, properties and other aspects. Let us first consider the basic flows, followed by a discussion of the conservation principles and the appropriate governing equations for these processes.

Basic Flows

Materials processing involves a very wide range of problems in which fluids engineering is of particular interest. It is very important that a review of this area cover this diversity and extract the basic fluid flow phenomena that arise and affect the final product and the design of the relevant system. This is a fairly involved task because of different types of processes employed and the intrinsic complexity of each process. However, fluid flow mechanisms are similar in many cases and the basic techniques that apply in one case may be applied to another.

Some of the basic flows that arise in materials processing, along with the important considerations that are involved, are listed below:

1 Buoyancy-Driven Flows. This involves a consideration of the magnitude and nature of the buoyancy-induced flow, such as that in the melt regions sketched in Figs. 1(*c*) and 2(*a*). The dependence of this flow on the parameters of the problem such as material properties, boundary conditions and geometry must be determined. The effect of this flow on the rate of phase change, on the characteristics of the solid-liquid interface, and on the migration of impurities is important in casting and crystal growing. The modeling of the mushy (liquid-solid mixture) region is of interest for alloy and mixture solidification. Similarly, buoyancy effects arise in other materials processing techniques such as chemical vapor deposition, soldering, welding, and laser melting.

2 Non-Newtonian Flows. These flows, in which the viscosity of the fluid is dependent on the flow through the shear rate, are particularly important in the processing of plastics and other polymeric materials in processes such as extrusion, sketched in Fig. 1(*d*), and injection molding. Non-Newtonian behavior substantially complicates the solution for the flow. Additional complexities arise due to strong temperature dependence of properties, phase and structural changes, and viscous dissipation effects due to the typically large viscosities of these fluids. An important element in these processes is the nature of fluid mixing that arises due to shear and possible chaotic behavior of the flow.

3 Surface Tension Driven Flows. These flows are relevant to many materials processing techniques. The flow of molten metal in welding and soldering is largely driven by surface tension, see Fig. 2(*d*). Under microgravity conditions, such as those in space applications, surface tension effects become particularly important in processes such as crystal growing and solidification due to the reduction in the buoyancy force. Marangoni convection, that arises due to the variation of surface tension with temperature and concentration, is of particular interest in these circumstances. Materials processing in space is an important research area today because of the need to improve the quality of materials such as crystals by reducing the buoyancy-induced flow and its effects.

4 Particulate Flows. Many materials processing circumstances involve particle motion, for instance, spray coating and chemical vapor deposition, sketched in Fig. 2(*e*). Also, the characteristics of mixing and of impurity migration involve particle motion. The particles are driven by the flow and particle trajectories are obtained, often by the use of a Lagrangian approach, to characterize the process. An example of this consideration is the behavior of impurities in a solidifying material. Similarly, mixing in food extrusion is a very important consideration in the determination of the quality of the extruded product.

5 Flow of Powdery Materials. This is an important aspect in many materials processing applications, ranging from powder metallurgy to the processing of food and pharmaceutical materials. Powders are conveyed along channels in these processes with compaction arising due to the rise in pressure and heating due to friction. The flow of such materials and the compaction process are not very well understood at the present time, though some recent work has been directed at this problem due to its practical importance.

6 Flows With Combined Transport Mechanisms. In many cases, the flow is driven or influenced by combined effects of heat and mass transfer and this flow, in turn, affects the resulting transport rates. Reactive polymers involve chemical reactions, which affect the concentration and impart energy changes to the system. Similarly, moisture transport is very important in food processing since the moisture concentration substantially affects the properties of the fluid. Drying processes also involve combined transport mechanisms. The quality and productivity of thin films fabricated by chemical vapor deposition are determined by the interaction between the flow and the chemical reactions at the surface and in the gases. Therefore, such multi-species and multimode transport processes must be studied in order to understand the basic mechanisms involved and to determine the flow and transport in practical circumstances.

7 Fluid Flow in Coating Processes. An important materials processing technique is coating. Optical fibers are coated by polymers to impart strength to the fiber. Surfaces are commonly coated to increase their resistance to corrosive environments. A wide variety of materials, ranging from polymers to metals, are used for coating processes. The quality of the coating, particularly trapped bubbles and other imperfections, as well as its thickness are determined by the flow occurring in the coating die and applicator. It is important to understand the basic flow mechanisms involved in this process so that high quality coatings may be achieved at relatively large speeds of the coated material. The problem involves highly viscous flow in complicated channels, as well as menisci on either side of the coating region. Also important is spray coating, which involves droplet formation and the flow in sprays leading to deposition or etching.

8 Flows With Coupling of Micro/Macro Mechanisms. The characteristics and quality of the material being processed are often determined by the microscale transport processes occurring in the material, for instance at the solid-liquid interface in casting or at sites where defects are formed in an optical fiber. However, experiments, modeling and analysis usually consider the macroscale, with practical dimensions, typical physical geometries and appropriate boundaries. It is crucial to link the two approaches so that the appropriate boundary conditions for a desired microstructure can be imposed in a physically realistic system. A considerable interest exists today in this aspect of materials processing, particularly with respect to the underlying fluid mechanics.

9 Other Flows. Several other flows are of interest and importance in materials processing. These include flows with large property variations. This is a very important consideration since it applies to most problems of practical interest, such as those dealing with plastics, glass and ceramics. The temperature, pressure and concentration ranges are often large enough to affect the flow and transport processes very substantially due to strong property variations. Interfacial phenomena are important in continuous casting, crystal growing, among others. Similarly, free surface flows arise in material emerging from an extrusion process, wire and fiber drawing through a neck-down region, and use of fluid jets for cutting or heating. Another important area is that of radiation-correction coupled flows. Such flows arise, for instance, in furnaces and substantially affect the relevant processing techniques. Many of these flows are considered in greater detail in the following sections.

The preceding list indicates the wide range of flows that typically arise in materials processing. However, in most manufacturing processes, a combination of different flows is encountered making the analysis and simulation very complicated. This is illustrated by taking various examples of important practical manufacturing systems later in the review.

Basic Considerations and Governing Equations

General Equations. The governing equations for fluid flow and the associated heat transfer in materials processing are derived from the basic conservation principles for mass, momentum and energy. For a pure viscous fluid, these equations may be written as

$$\frac{D\rho}{Dt} + \rho \nabla . \bar{V} = 0 \tag{1}$$

$$\rho \frac{D\bar{V}}{Dt} = \bar{F} + \nabla . \underline{\tau} \tag{2}$$

$$\rho\, Cp \frac{DT}{Dt} = \nabla . (k \nabla T) + \dot{Q} + \beta T \frac{Dp}{Dt} + \mu \Phi \tag{3}$$

Here, D/Dt is the substantial or particle derivative, given in terms of the local derivatives in the flow field by $D/Dt = \partial/\partial t + \bar{V}.\nabla$. The other variables are defined in the Nomenclature.

For a solid, the energy equation is written as

$$\rho\, C \frac{DT}{Dt} = \frac{\partial T}{\partial t} + \bar{V}.\nabla T = \nabla . (k \nabla T) + \dot{Q} \tag{4}$$

where C is the specific heat of the solid material, the specific heat at constant pressure and at constant volume being essentially the same. For a stationary solid, the convection term drops out and the particle derivative is replaced by the transient term $\partial/\partial t$. In a deforming solid, as in wire drawing, extrusion or fiber drawing, the material is treated as a fluid, with an appropriate constitutive equation, and the additional terms due to pressure work and viscous heating are generally included. In the preceding equations, the material is taken as isotropic, with the properties assumed to be the same in all directions. For certain materials such as composites, the nonisotropic behavior must be taken into account.

The stress tensor in Eq. (2) can be written in terms of the velocity $\bar{V}$ if the material characteristics are known. For instance, if μ is taken as constant for a Newtonian fluid, the relationship between the shear stresses and the shear rates, given by Stokes, are employed to yield

$$\rho \frac{D\bar{V}}{Dt} = \bar{F} - \nabla p + \mu \nabla^2 \bar{V} + \frac{\mu}{3} \nabla (\nabla . \bar{V}) \tag{5}$$

Here, the bulk viscosity $K = \lambda + (2/3)\mu$ is taken as zero. For an incompressible fluid, ρ is constant, which gives $\nabla \cdot \bar{V} = 0$ from Eq. (1). Then, the last term in Eq. (5) drops out.

Buoyancy Effects. The body force $\bar{F}$ is also important in many manufacturing processes, such as crystal growing and casting where it gives rise to the thermal or solutal buoyancy term. The governing momentum equation is obtained from Eq. (5), when thermal buoyancy is included, as

$$\rho \frac{D\bar{V}}{Dt} = -\bar{e} g \rho \beta (T - T_a) - \nabla p_d + \mu \nabla^2 \bar{V} \tag{6}$$

where p_d is the dynamic pressure, obtained after subtracting out the hydrostatic pressure p_a. Therefore, p_d is the component due to fluid motion, as discussed by Jaluria [21] and Gebhart et al. [22]. Boussinesq approximations, that neglect the effect of the density variation in the continuity equation and assume a linear variation of density with temperature, are employed here. However, in many practical cases, these approximations cannot be

used and the solution is more involved. If the x coordinate axis is taken as vertical, the buoyancy term appears only in the x component of the momentum equation. The governing equations are coupled because of the buoyancy term in Eq. (6) and must be solved simultaneously. This differs from the forced convection problem with constant fluid properties, for which the flow is independent of the temperature and may be solved independently before solving the energy equation [23].

Viscous Dissipation. The viscous dissipation term $\mu\Phi$ in Eq. (3) represents the irreversible part of the energy transfer due to the stress. Therefore, viscous dissipation gives rise to a thermal source in the flow and is always positive. For a Cartesian coordinate system, Φ is given by the expression

$$\Phi = 2\left[\left(\frac{\partial u}{\partial x}\right)^2 + \left(\frac{\partial v}{\partial y}\right)^2 + \left(\frac{\partial w}{\partial z}\right)^2\right] + \left(\frac{\partial v}{\partial x} + \frac{\partial u}{\partial y}\right)^2 + \left(\frac{\partial w}{\partial y} + \frac{\partial v}{\partial z}\right)^2 + \left(\frac{\partial u}{\partial z} + \frac{\partial w}{\partial x}\right)^2 - \frac{2}{3}(\nabla . \overline{V})^2 \quad (7)$$

Similarly, expressions for other coordinate systems may be obtained. This term becomes important for very viscous fluids and at high speeds. The former circumstance is of particular interest in the processing of glass, plastics, food, and other polymeric materials.

Processes With Phase Change. Many material processing techniques involve a phase change. Examples of such processes are crystal growing, casting, and welding. For such problems, there are two main approaches for numerical simulation. The first one treats the two phases as separate, with their own properties and characteristics. The interface between the two phases must be determined so that conservation principles may be applied there and appropriate discretization of the two regions may be carried out [15,24]. This becomes fairly involved since the interface location and shape must be determined for each time step or iteration. The governing equations are the same as those given earlier for the solid and the liquid.

In the second approach, the conservation of energy is considered in terms of the enthalpy H, yielding the governing energy equation as

$$\rho \frac{DH}{Dt} = \rho \frac{\partial H}{\partial t} + \rho \overline{V} . \nabla H = \nabla . (k \nabla T) \quad (8)$$

where each of the phase enthalpies H_i is defined as

$$H_i = \int_0^T C_i dT + H_i^0 \quad (9)$$

C_i being the corresponding specific heat and H_i^0 the enthalpy at 0 K. Then, the solid and liquid enthalpies are given by, respectively,

$$H_s = C_s T \quad H_1 = C_1 T + [(C_s - C_1) T_m + L_h] \quad (10)$$

where L_h is the latent heat of fusion and T_m the melting point. The continuum enthalpy and thermal conductivity are given, respectively, as

$$H = H_s + f_1 (H_1 - H_s) \quad k = k_s + f_1 (k_1 - k_s) \quad (11)$$

where f_1 is the liquid mass fraction, obtained from equilibrium thermodynamic considerations. The dynamic viscosity μ is expressed as the harmonic mean of the phase viscosities, employing the limit $\mu_s \to \infty$, i.e., $\mu = \mu_1 / f_1$. This model smears out the discrete phase transition in a pure material. But the numerical modeling is much simpler since the same equations are employed over the entire computational domain and there is no need to keep track of the interface between the two phases [25–27]. In addition, impure materials, mixtures and alloys can be treated very easily by this approach. Figure 3 shows examples of the two approaches

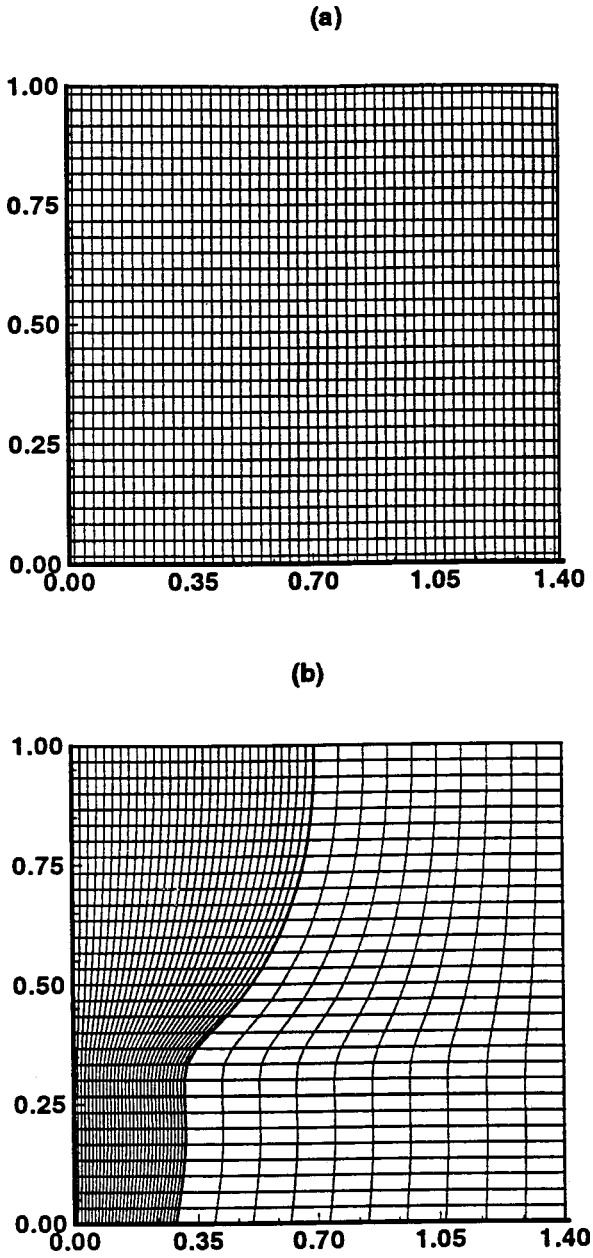

Fig. 3 Numerical grids used for the (*a*) enthalpy method (single region) and (*b*) the two-phase (two region) method

outlined here for numerical modeling, indicating a single domain for the enthalpy method and the interface between the two regions for the two-phase approach.

Chemically Reactive Flows. Combined thermal and mass transport mechanisms are important in many materials processing circumstances, such as chemical vapor deposition and processing of food, reactive polymers, and several other materials with multiple species. Extrusion is an important manufacturing technique for thermal processing of food materials, particularly snacks, cereals, pasta, and bread substitutes. Various starches, wheat, rice flour and other materials, along with a chosen amount of water, are fed into the hopper and cooked through the input of shear and heat to obtain different extruded products, see Harper [28] and Kokini et al. [29]. Chemical reactions occur in food materials and other chemically reactive materials to substantially alter the struc-

ture and characteristics of the product. Chemical reactions and conversion are also important in the curing of polymers, for example, in surface coating and chemical bonding.

A simple approach to model the chemical conversion process in reactive materials, such as food, in order to determine the nature and characteristics of the extruded material is outlined here. The governing equation for chemical conversion may be given as [30]

$$\frac{d}{dt}[(1-\tilde{X}]=-K(1-\tilde{X})^m \tag{12}$$

where $\tilde{X}$ is the degree of conversion, defined as,

$$\tilde{X}=\frac{M_i-M_t}{M_i-M_f} \tag{13}$$

Here M_i is the initial amount of unconverted material, taken as starch here, M_f is the final amount of unconverted starch and M_t is the amount of unconverted starch at time t. The order of the reaction is m and K is the reaction rate.

The order of the reaction m in Eq. (12) has been shown to be zero for starches and the rate of the reaction K given as a combination of thermal and shear driven convection as [30]

$$K=K_T+K_S \tag{14}$$

where

$$K_T=K_{T0}\exp(-E_T/RT) \quad K_S=K_{S0}\exp(-E_S/\tau\eta) \tag{15}$$

Here, E_τ and E_S are the corresponding activation energies, K_{T0} and K_{S0} are constants, τ is the shear stress, and η is a constant which is obtained experimentally for the material, along with other constants in the equation. A simple approximation may be applied to model the degree of conversion defined in Eq. (12), as given by [31,32]

$$w\frac{d\tilde{X}}{dZ}=K \tag{16}$$

Here, w is the velocity in the down-channel direction Z in an extruder. Thus, numerical results on conversion are obtained by integrating this equation.

Similarly, chemical kinetics play a critical role in the deposition of material from the gas phase in chemical vapor deposition systems [33,34]. The concentrations of the chemical species in the reactor affect the chemical kinetics, which in turn affect the deposition. In many cases, the process is chemical kinetics limited, implying that the transport processes are quite vigorous and the deposition is restricted largely by the kinetics. The chemical kinetics for several materials are available in the literature. For instance, the chemical kinetics for the deposition of Silicon from Silane (SiH_4) with Hydrogen as the carrier gas in a CVD reactor is given by the expression [35]

$$K=\frac{K_0 p_{\mathrm{SiH4}}}{1+K_1 p_{H2}+K_2 p_{\mathrm{SiH4}}} \tag{17}$$

where the surface reaction rate K is in mole of Si/m^2s, $K_0=A\exp(-E/RT)$, E being the activation energy, and A, K_1, and K_2 are constants which are obtained experimentally. The p's are the partial pressures of the two species in the reactor.

Material Property Considerations

Variable Properties. The properties of the material undergoing thermal processing play a very important role in the mathematical and numerical modeling of the process, as well as in the interpretation of experimental results. As mentioned earlier, the ranges of the process variables, such as pressure, concentration and temperature, are usually large enough to make it necessary to consider material property variations. The governing equations are Eqs. (1)–(4), which are written for variable properties. Usually, the dependence of the properties on temperature T is the most important effect. Numerical curve fitting may be employed to obtain a given material property as a function of T, as say, $k(T)=k_r[1+a(T-T_r)+b(T-T_r)^2]$, where T_r is a reference temperature at which $k=k_r$. Thus, a continuous function $k(T)$ replaces the discrete data on k at different temperatures [36]. This gives rise to nonlinearity since

$$\frac{\partial}{\partial x}\left[k(T)\frac{\partial T}{\partial x}\right]=\frac{\partial k}{\partial x}\frac{\partial T}{\partial x}+k\frac{\partial^2 T}{\partial x^2}=\frac{\partial k}{\partial T}\left(\frac{\partial T}{\partial x}\right)^2+k(T)\frac{\partial^2 T}{\partial x^2} \tag{18}$$

Similarly, the data for other material properties may be represented by appropriate curve fits. Because of the resulting additional nonlinearity, the solution of the equations and the interpretation of experimental results become more involved than for constant property circumstances. Iterative numerical procedures are often required to deal with such nonlinear problems, as discussed by Jaluria and Torrance [23]. Due to these complexities, average constant property values at different reference conditions are frequently employed to simplify the solution [37]. Similar approaches are used to interpret and characterize experimental data. However, such an approach is satisfactory only for small ranges of the process variables. Most manufacturing processes require the solution of the full variable-property problem for accurate predictions of the resulting transport.

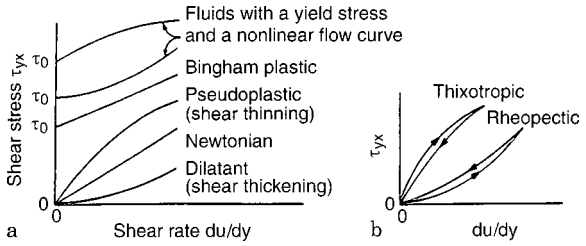

Fig. 4 Plots of shear stress versus shear rate for viscoinelastic non-Newtonian fluids. (*a*) Time-independent, and (*b*) time-dependent fluids.

Viscosity Variation. The variation of dynamic viscosity μ requires special consideration for materials such as plastics, polymers, food materials and several oils, that are of interest in a variety of manufacturing processes. Most of these materials are non-Newtonian in behavior, implying that the shear stress is not proportional to the shear rate. The viscosity μ is a function of the shear rate and, therefore, of the velocity field. Figure 4 shows the variation of the shear stress τ_{yx} with the shear rate du/dy for a shear flow such as the flow between two parallel plates with one plate moving at a given speed and the other held stationary. The viscosity is independent of the shear rate for Newtonian fluids like air and water, but increases or decreases with the shear rate for shear thickening or thinning fluids, respectively. These are viscoinelastic (purely viscous) fluids, which may be time-independent or time-dependent, the shear rate being a function of both the magnitude and the duration of shear in the latter case. Viscoelastic fluids show partial elastic recovery on the removal of a deforming shear stress. Food materials are often viscoelastic in nature.

Various models are employed to represent the viscous or rheological behavior of fluids of practical interest. Frequently, the fluid is treated as a Generalized Newtonian Fluid (GNF) with the non-Newtonian viscosity function given in terms of the shear rate which is related to the second invariant of the rate of strain tensor. For instance, time-independent viscoinelastic fluids without a yield stress are often represented by the power-law model, given by [38]

$$\tau_{yx}=K_c\left|\frac{du}{dy}\right|^{n-1}\frac{du}{dy} \tag{19}$$

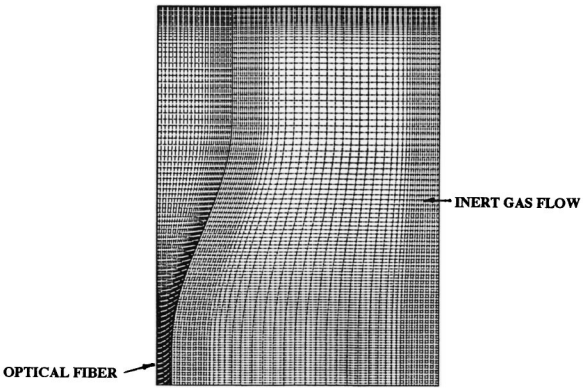

Fig. 5 Grid for the numerical modeling of the two regions, consisting of glass and inert gases, in optical fiber drawing

where K_c is the consistency index and n the power law fluid index. Note that $n=1$ represents a Newtonian fluid. For $n<1$, the behavior is pseudoplastic (shear thinning) and for $n>1$, it is dilatant (shear thickening). The viscosity variation may be written as [38]

$$\mu = \mu_0 \left(\frac{\dot{\gamma}}{\dot{\gamma}_0} \right)^{n-1} e^{-b(T-T_0)} \tag{20}$$

where

$$\dot{\gamma} = \left[\left(\frac{\partial u}{\partial y} \right)^2 + \left(\frac{\partial w}{\partial y} \right)^2 \right]^{1/2}, \quad \text{with} \quad \tau_{yx} = \mu \frac{\partial u}{\partial y}, \quad \tau_{yz} = \mu \frac{\partial w}{\partial y} \tag{21}$$

for a two-dimensional flow, with u and w varying only with y. Similarly, expressions for other two- and three-dimensional flows may be written. Here $\dot{\gamma}$ is the shear strain rate, the subscript o denotes reference conditions and b is the temperature coefficient of viscosity. Other expressions for the viscosity may be used to consider other reactive and non-reactive polymeric materials.

For food materials, the viscosity is also a strong function of the moisture concentration c_m and is often represented as

$$\mu = \mu_0 \left(\frac{\dot{x}}{\dot{\gamma}_0} \right)^{n-1} e^{-b(T-T_0)} e^{-b_m(c_m - c_{m0})} \tag{22}$$

The temperature dependence is also often represented more accurately by an Arrhenius type of variation, i.e.,

$$\mu = \mu_0 \left(\frac{\dot{\gamma}}{\dot{\gamma}_0} \right)^{n-1} e^{B/T} \tag{23}$$

In addition, chemical changes, that typically occur at the microscale level in the material, affect the viscosity and other properties. Other models, besides the power-law model, are also employed to represent different materials [19,38–40].

The non-Newtonian behavior of the material complicates the viscous terms in the momentum and the energy equations. For instance, the viscous dissipation term Φ_v for the two-dimensional flow considered earlier for Eq. (21) is

$$\Phi_v = \tau_{yx} \frac{\partial u}{\partial y} + \tau_{yz} \frac{\partial w}{\partial y} \tag{24}$$

where the variation of μ with $\dot{\gamma}$ and, therefore, with the velocity field is taken into account. Similarly, the viscous force term in the momentum equation yields $\partial(\tau_{yx})/\partial y$ in the x-direction, requiring the inclusion of the non-Newtonian behavior of the fluid [40]. Similarly, other flow circumstances may be considered for the flow of non-Newtonian fluids. Viscous dissipation effects are generally not negligible in these flows because of the large viscosity of the fluid.

Glass is another very important, though complicated, material. It is a supercooled liquid at room temperature. The viscosity varies almost exponentially with temperature. In optical fiber drawing, for instance, the viscosity changes through several orders of magnitude in a relatively short distance. This makes it necessary to employ very fine grids and specialized numerical techniques. Figure 5 shows the grid in glass, as well as in the inert gases flowing outside the fiber in a fiber-drawing furnace. Even a change of a few degrees in temperature in the vicinity of the softening point, which is around 1600°C for fused silica, can cause substantial changes in viscosity and thus in the flow field and the neck-down profile in optical fiber drawing. This can lead to a significant effect on defect generation in the fiber and thus on fiber quality [17,18,41].

Other Aspects. There are several other important considerations related to material properties. Constraints on the temperature level in the material, as well as on the spatial and temporal gradients, arise due to the characteristics of the material. In thermoforming, for instance, the material has to be raised to a given temperature level, above a minimum value $T_{\min}$, for material flow to occur in order for the process to be carried out. However, the maximum temperature $T_{\max}$ must not be exceeded to avoid damage to the material. In polymeric materials, $T_{\max} - T_{\min}$ is relatively small and the thermal conductivity k is also small, making it difficult to design a process which restricts the temperature to $T_{\max}$ while raising the entire material to above $T_{\min}$ for material flow to occur. An example of this process is the manufacturing of plastic-insulated wires, as considered by Jaluria [42]. Similarly, constraints on $\partial T/\partial t$, $\partial T/\partial x$, etc., arise due to thermal stresses in the material undergoing thermal processing. Such constraints are particularly critical for brittle materials such as glass and ceramics. The design of the manufacturing system is then governed by the material constraints.

In several circumstances, the material properties are not the same in all the directions because of the nature of the material or because of the configuration. For anisotropic materials, such as wood, asbestos, composite materials, cork, etc., the conduction flux vector $\bar{q}$ may be written as $\bar{q} = -\underline{\underline{k}} \nabla T$, where $\underline{\underline{k}}$ is the conductivity tensor, with nine components k_{ij}, obtained by varying i and j from 1 to 3 to represent the three directions. For orthotropic materials, the coordinate axes coincide with the principal axes of the conductivity tensor and the energy equation for a stationary material, in the Cartesian coordinate system, is

$$\rho C \frac{\partial T}{\partial t} = \frac{\partial}{\partial x} \left(k_x \frac{\partial T}{\partial x} \right) + \frac{\partial}{\partial y} \left(k_y \frac{\partial T}{\partial y} \right) + \frac{\partial}{\partial z} \left(k_z \frac{\partial T}{\partial z} \right) + \dot{Q} \tag{25}$$

Similarly, the equations for other coordinate systems may be written. In the annealing of coiled steel sheets, the thermal conductivity k_r in the radial direction is often much smaller than k_z in the axial direction, due to gaps within the coils and the governing conduction equation may be written taking this effect into account [43]. This affects the underlying fluid flow and the overall transport.

The preceding discussion brings out the importance of material properties in a satisfactory mathematical and numerical modeling of thermal manufacturing processes, as well as for accurate interpretation of experimental results. The properties of the material undergoing thermal processing must be known and appropriately modeled to accurately predict the resulting flow and transport, as well as the characteristics of the final product. However, this is an area in which there is acute lack of data and critical work is needed in the future.

Boundary Conditions and Simplifications

Many of the boundary and initial conditions are the usual no-slip conditions for velocity and the appropriate thermal or mass

transfer conditions at the boundaries. However, a few special considerations arise for the various processes considered earlier. Some of these are discussed here.

Free Surfaces and Openings. At a free surface, the shear stress is often specified as zero, yielding a Neumann condition of the form $\partial \overline{V}/\partial n = 0$, where n is normal to the surface, if negligible shear is applied on the surface. If the shear stress exerted by the ambient fluid is significant, it replaces the zero in this equation. Basically, a balance of all the forces acting at the surface is used to obtain the interface. As considered in detail by Roy Choudhury et al. [41] and as presented later, the free surface may be determined numerically by iterating from an initial profile and using the imbalance of the forces for correcting the profile at intermediate steps, finally yielding a converged profile such as the one shown in Fig. 5.

In a stationary ambient medium, far from the solid boundaries, the velocity and temperature may be given as $\overline{V} \rightarrow 0$, $T \rightarrow T_a$ as $n \rightarrow \infty$. However, frequently the condition $\partial \overline{V}/\partial n \rightarrow 0$ is used, instead, in order to allow for entrainment into the flow. The use of this gradient, or Neumann, condition generally allows the use of a much smaller computational domain, than that needed for a given value, or Dirichlet condition, imposed on the velocity $\overline{V}$ [20]. The gradient conditions allow the flow to adjust to ambient conditions more easily, without forcing it to take on the imposed values at a chosen boundary. This consideration is very important for simulating openings in enclosures, where gradient conditions at the opening allow the flow to adjust gradually to the conditions outside the enclosure. Such conditions are commonly encountered in furnaces and ovens with openings to allow material and gas flow.

Phase Change. If a change of phase occurs at the boundary, the energy absorbed or released due to the change of phase must be taken into account. Thus, the boundary conditions at the moving interface between the two phases (Fig. 1(c)) must be given if a two-zone model is being used. This is not needed in the enthalpy model given by Eqs. (8)–(11). For one-dimensional solidification, this boundary condition is given by the equation

$$k_s \frac{\partial T_s}{\partial y} - k_1 \frac{\partial T_1}{\partial y} = \rho L_h \frac{d\delta}{dt} \tag{26}$$

where $y = \delta$ is the location of the interface. This implies that the energy released due to solidification is conveyed by conduction in the two regions. Similarly, for two-dimensional solidification, the boundary condition is written as [24]

$$\left(k_s \frac{\partial T_s}{\partial y} - k_1 \frac{\partial T_1}{\partial y} \right) \left[1 + \left(\frac{\partial \delta}{\partial x} \right)^2 \right] = \rho L_h \frac{d\delta}{dt} \tag{27}$$

For a stationary interface, as shown in Fig. 1(b), the boundary condition is [44,45]

$$\left(-k \frac{\partial T}{\partial n} \right)_1 + \rho U L_h \frac{dy}{ds} = \left(-k \frac{\partial T}{\partial n} \right)_s \tag{28}$$

where ds is a differential distance along the interface and n is distance normal to it. Also, the temperature at the interface in all these cases is T_m.

Surface Tension Effects. Surface tension effects are important in many materials processing flows where a free surface arises. Examples include flows in welding, Czochralski and the floating-zone crystal growing methods, wave soldering, and continuous casting. Surface tension affects the force balance on a free surface and can affect, for instance, the equilibrium shape of a solder joint, such as the one shown in Fig. 2(d) [46]. Similarly, the profile of material emerging from a die or a roller can be affected by the surface tension, the relative significance of this effect being determined by other forces acting on the surface.

Surface tension can also have a significant effect on the flow near the free surface, which represents the interface between a liquid and a gas in many cases, and on the shape, stability and other characteristics of the interface. Large surface tension gradients can arise along the interface due to temperature T and concentration c_m gradients and the variation of surface tension σ with these variables. Such surface tension gradients can generate significant shear stresses and resulting flow along the interface. This flow, known as thermocapillary or Marangoni convection, is important in many material processing flows [47]. There has been growing interest in Marangoni convection in recent years because of materials processing under microgravity conditions in space where other more dominant effects, such as buoyancy, are considerably reduced, making thermocapillary convection particularly significant.

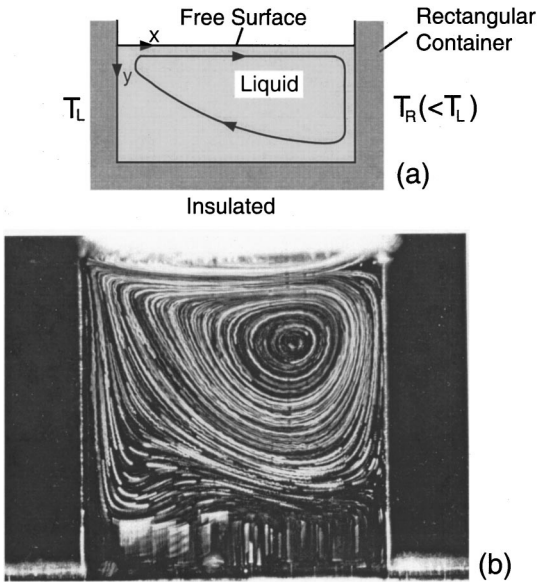

Fig. 6 Thermocapillary convection in a rectangular container: (*a*) schematic sketch and (*b*) flow in a $NaNO_3$ melt [47]

Consider a rectangular container with its left wall at temperature T_L and the right wall at a lower temperature T_R. The bottom is insulated, as shown in Fig. 6. Then the boundary condition at the free surface is

$$-\mu \frac{\partial u}{\partial y} = \frac{\partial \sigma}{\partial T} \frac{\partial T}{\partial x} + \frac{\partial \sigma}{\partial c_m} \frac{\partial c_m}{\partial x} \tag{29}$$

where u is the velocity component along the coordinate axis x. For most pure materials, σ decreases with T, i.e., $\partial \sigma/\partial T < 0$, and since $\partial T/\partial x < 0$ in this case, the fluid is pulled from the left to the right at the surface, resulting in a clockwise circulation, as shown. The flow pattern in a melt of $NaNO_3$ is also shown, indicating the dominance of thermocapillary convection and the vertical flow near the vertical wall due to thermal buoyancy. Similarly, boundary conditions may be written for other geometries.

Conjugate and Initial Conditions. Several other boundary conditions that typically arise in materials processing may be mentioned here. The normal gradients at an axis or plane of symmetry are zero, simplifying the problem by reducing the flow domain. The temperature and heat flux continuity must be maintained in going from one homogeneous region to another, such as the regions shown in Figs. 3 and 5. This results in the thermal conductivity at the interface being approximated numerically as the harmonic mean of the conductivities in the two adjacent regions for one-dimensional transport [23]. The conjugate conditions that arise at a solid surface in heat exchange with an adjacent fluid are

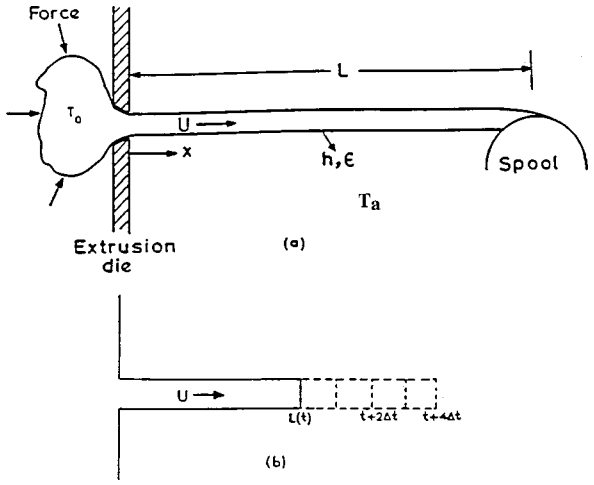

Fig. 7 (*a*) Sketch of the extrusion process for a heated material, (*b*) moving material at different time intervals

$$T_s = T_f; \quad \left(-k\frac{\partial T}{\partial n}\right)_s = \left(-k\frac{\partial T}{\partial n}\right)_f \tag{30}$$

where the subscripts s and f refer to the solid and the fluid, respectively.

The initial conditions are generally taken as the no-flow circumstance at the ambient temperature, representing the situation before the onset of the process. However, if a given process precedes another, the conditions obtained at the end of the first process are employed as the initial conditions for the next one. For periodic processes, the initial conditions are arbitrary.

Moving Material or Source. In the case of material flow in a moving cylindrical rod for extrusion or hot rolling, as sketched in Fig. 7, the temperature T is a function of time and location if a Lagrangian approach is used to follow a material element. However, by placing the coordinate system outside the moving material, a steady problem is obtained if the edge of the rod is far from the inlet, $x=0$, i.e., for large time, and if the boundary conditions are steady. Transient problems arise for small lengths of the rod, short times following onset of the process, and for boundary conditions varying with time [48,49]. For many practical cases, the temperature T may be taken as a function of time and only the downstream distance x, assuming it to be uniform at each cross-section. Such an assumption can be made if the Biot number Bi_R based on the radius R of the rod is small, i.e., $\mathrm{Bi}_R = hR/k \ll 1.0$, h being the convective heat transfer coefficient. Thus, for a thin rod of high thermal conductivity material, such an assumption would be valid. The governing energy equation is

$$\rho C\left(\frac{\partial T}{\partial t} + U\frac{\partial T}{\partial x}\right) = k\frac{\partial^2 T}{\partial x^2} - \frac{hP}{A}(T - T_a) \tag{31}$$

where P is the perimeter of the rod, A its area of cross-section and T_a the ambient temperature.

For a long, continuous, moving rod or plate, the problem may be considered as steady for many problems of practical interest. Then, the three-dimensional temperature distribution $T(x,y,z)$ in a moving plate is governed by the convection-conduction equation

$$\rho CU\frac{\partial T}{\partial x} = k\left(\frac{\partial^2 T}{\partial x^2} + \frac{\partial^2 T}{\partial y^2} + \frac{\partial^2 T}{\partial z^2}\right) \tag{32}$$

The boundary conditions in x may be taken as $T(0,y,z) = T_0$ and $T(\infty,y,z) = T_a$. For lumping in the y and z directions, an ordinary differential equation (ODE) is obtained from Eq. (31) by dropping the transient term. Similar considerations apply for the flow in such forming processes.

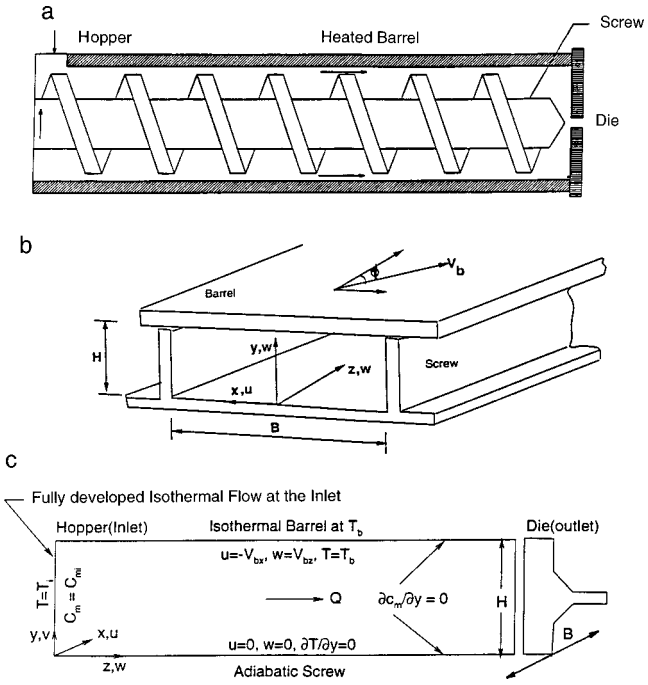

Fig. 8 Screw channel and simplified computational domain for a single-screw extruder

Similarly, coordinate transformations can be employed to convert transient problems to steady state ones in other circumstances. For instance, a moving thermal source at the surface of an extensive material gives rise to a transient circumstance if the coordinate system is fixed to the material. However, a steady state situation is obtained by fixing the origin of the coordinate system at the source. If x is measured in the direction of the source movement from a coordinate system fixed on the material surface and U is the location of the point source, the transformation used is $\xi = x - Ut$, which yields the governing equation

$$\frac{\partial^2 T}{\partial \xi^2} + \frac{\partial^2 T}{\partial y^2} + \frac{\partial^2 T}{\partial z^2} = -\frac{U}{\alpha}\frac{\partial T}{\partial \xi} \tag{33}$$

This transformation applies to processes such as welding and laser cutting. This equation is solved and the transformation is used to yield the time-dependent results.

In some manufacturing systems, the transient response of a particular component is much slower than the response of the others. The thermal behavior of this component may then be treated as quasi-steady, i.e., as a sequence of steady state circumstances. For instance, in a heat treatment furnace, the walls and the insulation are often relatively slow in their response to the transport processes, as compared to the flow. Consequently, these may be assumed to be at steady state at a given time, with different steady-states arising at different time intervals whose length is chosen on the basis of the transient response [43].

Very Viscous Flow. This circumstance usually gives rise to very small Reynolds numbers, for which the creeping flow approximation is often employed. For instance, the Reynolds number Re is generally much smaller than 1.0 for plastic and food flow in a single screw extruder and the inertia terms are usually dropped. Assuming the flow to be developed in the down-channel, z, direction and lumping across the flights, i.e., velocity varying only with distance y from the screw root towards the barrel, see Fig. 8, the governing momentum equations become [40]

$$\frac{\partial p}{\partial x} = \frac{\partial \tau_{yx}}{\partial y}, \quad \frac{\partial p}{\partial y} = 0, \quad \frac{\partial p}{\partial z} = \frac{\partial \tau_{yz}}{\partial y} \tag{34}$$

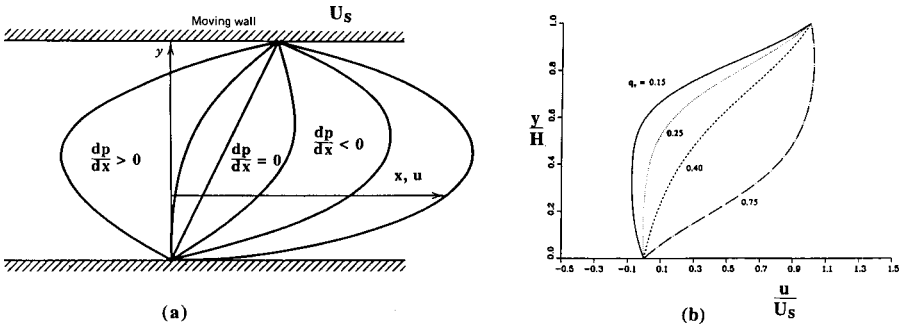

Fig. 9 Velocity profiles for developed flow in a channel of height H with combined shear due to a wall moving at velocity U_S and an imposed pressure gradient. (*a*) Newtonian fluid; (*b*) non-Newtonian fluid with n=0.5 at different q_v.

where the pressure terms balance the viscous forces. The coordinate system is generally fixed to the rotating screw and the channel straightened out mathematically, ignoring the effects of curvature. Then the complicated flow in the extruder is replaced by a pressure and shear driven channel flow, with shear arising due to the barrel moving at the pitch angle over a stationary screw, as shown in Fig. 8. This is similar to the shear and pressure driven channel flow available in the literature. Therefore, this approximation substantially simplifies the mathematical/numerical model.

Other Simplifications. The basic nature of the underlying physical processes and the simplifications that may be obtained under various circumstances can be best understood in terms of dimensionless variables that arise when the governing equations and the boundary conditions are nondimensionalized. The commonly encountered governing dimensionless parameters are the Strouhal number Sr, the Reynolds number Re, the Grashof number Gr, the Prandtl number Pr and the Eckert number Ec. These are defined as

$$\mathrm{Sr}=\frac{L}{V_c t_c},\quad \mathrm{Re}=\frac{V_c L}{\nu},\quad \mathrm{Gr}=\frac{g\beta(T_s-T_a)L^3}{\nu^2},\quad \mathrm{Pr}=\frac{\nu}{\alpha},$$

$$\mathrm{Ec}=\frac{V_c^2}{C_p(T_s-T_a)} \tag{35}$$

where V_c is a characteristic speed, L a characteristic dimension, and t_c a characteristic time. It is often convenient to apply different nondimensionalization to the solid and fluid regions.

The dimensionless equations may be used to determine the various regimes over which certain simplifications can be made. For instance, at small values of the Reynolds number Re, the convection terms are small, compared to the diffusion terms, and may be neglected. This approximation is applied to the flow of highly viscous fluids such as plastics and food materials, as mentioned earlier. At large Re, boundary layer approximations can be made to simplify the problem. At very small Prandtl number Pr, the thermal diffusion terms are relatively large and yield the conduction-dominated circumstance, which is often applied to the flow of liquid metals in casting, soldering and welding. A small value of $\mathrm{Gr}/\mathrm{Re}^2$ implies negligible buoyancy effects, for instance, in continuous casting where the effect of buoyancy on the transport in the melt region may be neglected. A small value of the Eckert number Ec similarly implies negligible pressure work effects and a small value of Ec/Re can be used to neglect viscous dissipation. Finally, a small value of the Strouhal number Sr indicates a very slow transient, which can be treated as a quasi-steady circumstance. Therefore, the expected range of the governing parameters such as Re, Gr, Pr, Sr, and Ec can be employed to determine the relative importance of various physical mechanisms underlying the transport process. This information can then be used to simplify the relevant governing equations and the corresponding modeling. Similarly, Marangoni number $\mathrm{Ma}=(\partial\sigma/\partial T)L\Delta T/\mu\alpha$, where ΔT is the total temperature difference, arises in thermocapillary flow, and Weber number $\mathrm{We}=\rho V_c^2 L/\sigma$ arises in flows with surface tension effects such as the one shown in Fig. 2(*d*).

Several other such simplifications and approximations are commonly made to reduce the computational effort in the numerical simulation of thermal manufacturing processes. For instance, dy/ds may be taken as unity in Eq. (28) for many continuous casting processes that use an insulated mold, which gives rise to a fairly planar interface. Also, for slow withdrawal rates, the heat transfer due to convection is small compared to that due to conduction within the moving material and may be neglected. If the extent of the material undergoing, say, thermal processing at the surface, is large, it may often be assumed to be semi-infinite, simplifying both the analysis and the numerical simulation [1]. Similarly, the boundaries are often approximated as planar to simplify the imposition of the boundary conditions there. Clearly, the preceding discussion is not exhaustive and presents only a few common approximations and simplifications.

Solution Techniques

Analytical. It is obvious from the complexity of the governing equations, boundary conditions, and the underlying mechanisms that analytical methods can be used to obtain the solution in very few practical circumstances. However, though numerical approaches are extensively used to obtain the flow and associated transport in most materials processing systems, analytical solutions are very valuable since they provide

1 Results that can be used for validating numerical models
2 Physical insight into the basic mechanisms and expected trends
3 Limiting or asymptotic conditions
4 Quantitative results for certain simple components

The validation of the numerical models, expected physical characteristics of the process, and limitations on important variables are all very important in the development of a numerical or experimental approach to study the process. Also, certain components or processes can be simplified and idealized to allow analytical solutions to be obtained.

A few examples of analytical solutions may be mentioned here. The complex flow in a screw extruder, such as the one shown in Fig. 1(*d*), was simplified to shear and pressure driven flow in a channel, as seen in Fig. 8(*c*). The simplest case is that of fully developed flow for which the velocity field is assumed to remain unchanged downstream. Analytical solutions can be obtained for such channel flows driven by pressure and shear, as shown in Fig. 9(*a*) for Newtonian fluids. When the pressure gradient is zero, the flow is only due to the viscous effect of the wall moving at ve-

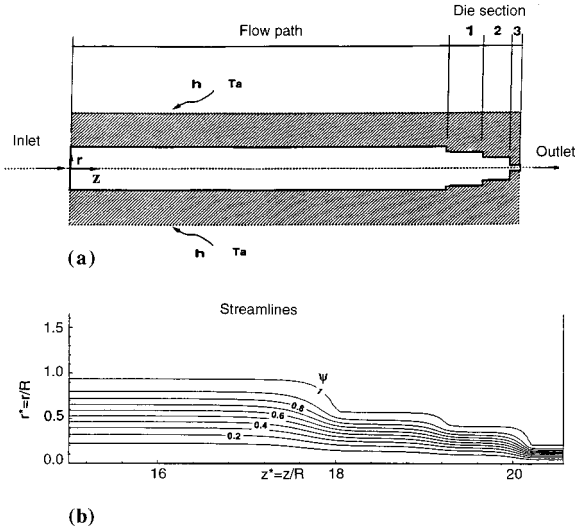

Fig. 10 Geometry of a practical extrusion die, with R as the inlet radius, along with the calculated streamlines for a non-Newtonian material for typical operating conditions

locity U_s and is termed drag flow. For Newtonian flow, the velocity profile is linear and the dimensionless flow rate, or throughput, q_v, which is the flow rate divided by the product of wall speed and cross-sectional area, is simply 0.5. For a favorable pressure gradient, the throughput exceeds 0.5 and for an adverse pressure gradient it is less. Similar trends are expected for non-Newtonian fluids though the profiles and the q_v value for drag flow would be different. Numerical results have confirmed this behavior and have used the analytical results to validate the model as well as to characterize different flow regimes, as shown in Fig. 9(*b*).

Another analytical solution that has been used to model the extrusion process is that of flow in a die. The relationship between the pressure drop Δp across a cylindrical region of length L and radius R, with mass flow rate $\dot{m}$ for a non-Newtonian fluid, was obtained by Kwon et al. [50] by assuming developed flow. The expression given is

$$\Delta p = \frac{2L}{R}\hat{C}(T)\left[\frac{3n+1}{4n}\frac{4\dot{m}}{\rho\pi R^3}\right]^n \tag{36}$$

where $\hat{C}(T)$ is a temperature dependent coefficient in the viscosity expression, which is given as $\mu = \hat{C}(T)(\dot{\gamma})^{1-n}$, $\dot{\gamma}$ being the shear rate, defined earlier. This expression would apply for the flat portions of a typical die, such as the one shown in Fig. 10. But the flow is not developed, as seen from the calculated streamlines shown in Fig. 10. However, the expression can be used without significant error for long cylindrical regions, such as the portion on the left of the die shown here [51]. Similarly, expressions for a conical die and for an orifice were given by Kwon et al. [50].

Numerical

The governing equations given earlier are the ones usually encountered in fluid flow and heat and mass transfer. Though additional complexities due to the geometry, boundary conditions, material property variations, combined mechanisms, etc., arise in materials processing, as mentioned earlier, the numerical solution of the governing equations is based on the extensive literature on computational fluid dynamics. Among the most commonly employed techniques for solving these equations is the SIMPLER algorithm, given by Patankar [52], and the several variations of this approach. This method employs the finite volume formulation with a staggered grid, so that the value of each scalar quantity, such as pressure, concentration and temperature, is associated with the grid node and the vector quantities like velocity are displaced in space relative to the scalar quantities and generally located on the faces of the control volume. This grid system has an advantage in solving the velocity field since the pressure gradients that drive the flow are easy to evaluate and the velocity components are conveniently located for the calculation of the convective fluxes. A pressure correction equation is used during the iteration or time marching to converge to the solution. Also, the pressure at any arbitrary point is chosen at a reference value and separate boundary conditions are not needed for pressure.

For two-dimensional and axisymmetric problems, the governing equations are often cast in terms of the vorticity and streamfunction by eliminating the pressure from the two components of the momentum equation and by defining a streamfunction to take care of the continuity equation [23]. This reduces the number of equations by one and pressure is eliminated as a variable, though it can be calculated after the solution is obtained. The solution yields the streamfunction, which is used for obtaining the velocity field and plotting streamlines, the temperature, which is used for plotting the isotherms and calculating heat transfer rates, and the vorticity. Because the streamfunction is specified on the boundaries, convergence of the streamfunction equation is usually quite fast. Thus, this approach is generally advantageous, as compared to the methods based on the primitive variables of velocity, pressure and temperature, for two-dimensional and axisymmetric flows. The latter approach is more appropriate for three-dimensional circumstances.

Both transient and steady state solutions are of interest, depending on the process under consideration. In the former case, time marching is used with convergence at each time step to obtain the time-dependent variation of the flow, temperature field, heat and mass transfer rates, chemical conversion, etc. For steady problems also, time marching may be used to obtain the desired results at large time. However, the problem can also be solved by iteration or by using false transients with large time steps [53]. Though central differences are desirable for all the approximations, numerical instability with the convection terms is often avoided by the use of upwind, exponential or power-law differencing schemes [52]. Because of the inaccuracy due to false diffusion, second-order upwind differencing and third-order QUICK schemes have become quite popular for discretizing the convection terms [54]. Under-relaxation is generally needed for convergence due to the strong nonlinearities that arise in these equations mainly due to property variations. Several methods are available to solve the vorticity transport and energy equations. The Alternating Direction Implicit (ADI) method of Peaceman and Rachford [55], as well as modifications of this time-splitting method, are particularly efficient for two-dimensional problems. Similarly, cyclic reduction, successive over relaxation and other standard methods may be used for the streamfunction or the pressure equation. Solution-adaptive methods have been developed in recent years to address many of the complexities that arise in heat transfer and fluid flow problems, as reviewed by Acharya [56].

As mentioned earlier, major difficulties arise in material processing simulations due to the complexity of the computational domain as well as that of the boundary conditions. Finite element and boundary element methods have been used advantageously to simulate a wide variety of material processing systems. Several of these cases are outlined later in the paper. Finite difference and finite volume methods have also been used with coordinate transformations employed to convert the complex domains into much simpler forms so that the discretization is simplified and accurate results are obtained. A few cases based on such transformations are also presented later.

Experimental

Experimental work is extremely important in a study of fluid phenomena in materials processing. The main contributions of experimental investigations are

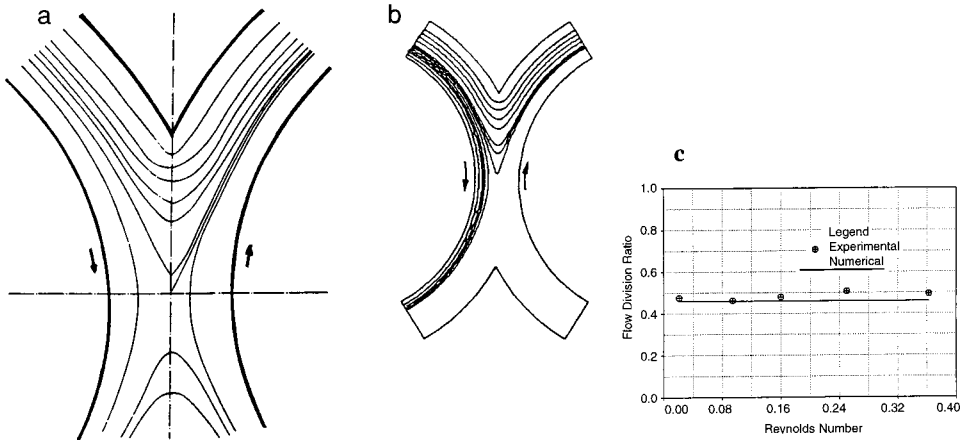

Fig. 11 Streamlines in the region between two rotating cylinders for CMC solution at 16 rpm. (*a*) Experimental results; (*b*) numerical predictions for flow entering the region over one cylinder; (*c*) comparison of flow division ratio x_f obtained from experimental and numerical results [57].

1 Enhancing the basic understanding of the flow and associated transport
2 Providing insight that can be used in the development of mathematical and numerical models, particularly for determining important aspects and variables
3 Providing results that can be used for validation of the models
4 Yielding quantitative results that can be used to characterize processes and components in the absence of accurate and dependable models

Though validation of models is often considered as the main reason for experimentation, there are many complex flows where experimental results guide the development of the model and also generate quantitative data that can be used as empirical inputs if accurate modeling is not available. Flow visualization is particularly important in studying the nature of the flow. However, many practical materials are opaque and must be substituted by simpler transparent materials for optical methods to visualize the flow. The same considerations apply for optical measurement techniques like laser Doppler anemometry and particle image velocimetry.

As an example, let us consider the fluid flow in the region between two rotating screws in mixers and extruders. This flow, as well as the nature of the resulting mixing process, are not very well understood. Sastrohartono et al. [57] carried out an experimental study of the flow in this region. Two rotating plexiglas cylinders were driven by a variable speed motor and the flow in the region between the two cylinders was observed. Corn syrup and carboxy-methyl-cellulose (CMC) solutions were used as the fluids, the former being Newtonian and the latter non-Newtonian. Air bubbles and dyes were used for visualization.

Figure 11 shows the experimentally obtained streamlines in the region between the two cylinders, along with the predictions from a numerical model. Clearly, good agreement is seen between the two. It is also seen that some of the fluid flowing adjacent the left cylinder continues to flow adjacent to it while the remaining goes to the other cylinder. This process is similar to the movement of fluid from one screw channel to the other in a tangential twin screw extruder. A flow division ratio x_f may be defined as the fraction of the mass flow that crosses over from one channel to the other. A dividing streamline that separates the two fluid streams was determined from the path lines and used to determine the flow division ratio. A comparison between experimental and numerical results is shown, indicating good agreement at small Reynolds numbers. A deviation between numerical and experimental results was observed for Reynolds numbers greater than around 1.0, mainly because of negligible inertia terms assumed in the mathematical model. These experiments indicate the basic features of the mixing process in the intermeshing region, even though only cylinders are considered. The flow division ratio may be taken as a measure of mixing.

Results for a Few Important Processes

The preceding sections have presented the basic considerations that arise in a study of fluid flow phenomena in materials processing. The important basic flows, governing equations and boundary conditions were outlined. The analytical, numerical and experimental approaches to investigate various types of flows were discussed. Several important processes were mentioned and briefly discussed. The common aspects that link different processes are seen in terms of the underlying mechanisms and governing equations and parameters. However, major differences exist between various materials processing techniques and demand specialized treatment. The desired results from numerical or experimental investigations are also usually quite different. It is not possible to discuss all the major aspects that characterize different processes and the available results in these areas. However, a few important processes are considered in greater detail in the following to illustrate the approaches used to obtain the desired solution as well as the characteristic results.

Polymer Extrusion. An important manufacturing process which has been mentioned in the preceding sections is plastic screw extrusion, sketched in Figs. 1(*d*) and 8. The viscosity expression and the governing equations for a relatively simple two-dimensional model were given earlier. This is a fairly complicated problem because of the strong shear rate and temperature dependence of the viscosity, complex geometry, large viscous dissipation, and the resulting coupling between the energy and momentum equations. Interest lies in control and prediction of the flow in order to improve mixing and modify physical and chemical changes undergone by the material.

Figure 12 shows typical computed velocity and temperature fields in an extruder channel. Large temperature differences are seen to arise across the channel height because of the relatively small thermal conductivity of plastics. The flow is well-layered, with little bulk mixing, due to the high viscosity of these fluids, the typical viscosity being more than a million times that of water at room temperature. Many approaches such as reverse screw elements and sudden changes in the screw have been used to disrupt the well-layered flow and promote mixing. Viscous dissipation causes the temperature to rise beyond the imposed barrel tempera-

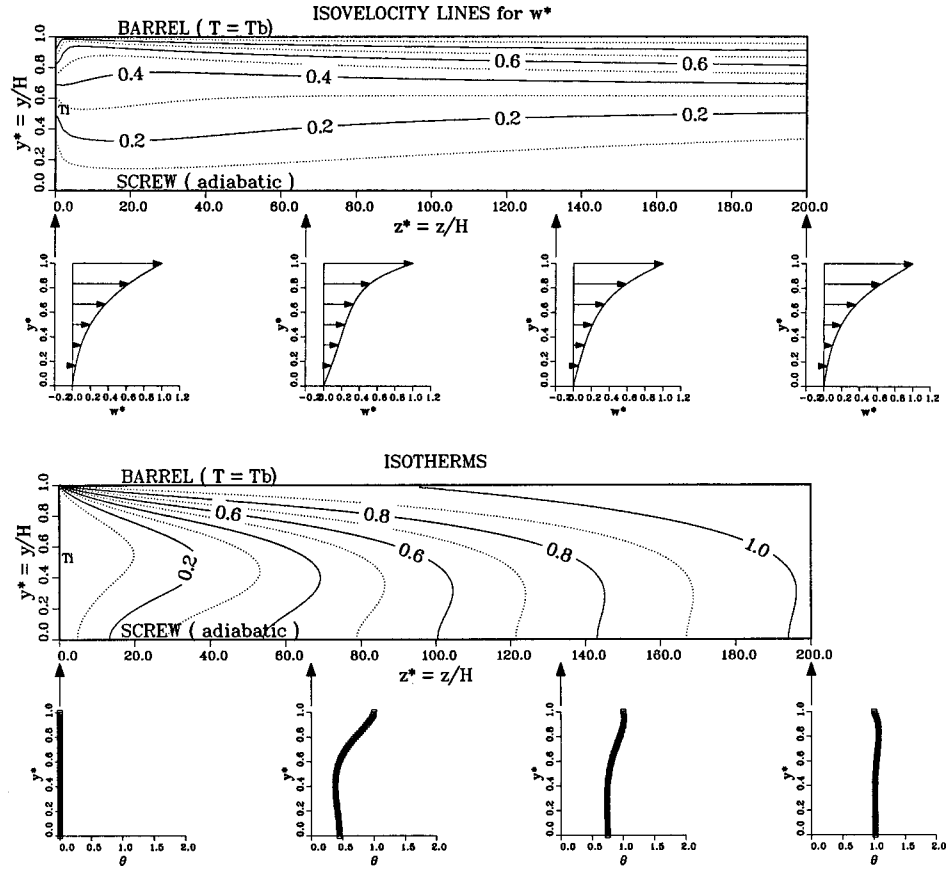

Fig. 12 Calculated velocity and temperature fields in the channel of a single screw extruder at n=0.5 and dimensionless throughput $q_v=0.3$, for typical operating conditions

ture. A lot of work has been done on this problem because of its importance to industry, as reviewed by Tadmor and Gogos [38] and Jaluria [19].

An important consideration in the extrusion process is the residence time distribution (RTD). The residence time is the amount of time spent by a fluid particle in the extruder from the hopper to the die. If the material spends an excessive amount of time, it may be over-processed, over-cooked, if it is food, or degraded. Similarly, too small a time may lead to under-processing. The final product is, therefore, strongly dependent on the residence time distribution since structural changes due to thermal processing and chemical reactions are usually time-dependent. The residence time distribution is largely a function of the flow field. It is experimentally obtained by releasing a fixed amount of color dye or tracer in the material at the hopper and measuring the flow rate of the dye material as it emerges from the extruder at the other end. The time it takes for the dye to first appear is the minimum residence time and relates to the fastest moving fluid. Similarly, an average residence time may be defined.

The experimental determination of residence time may be numerically simulated by considering the flow of a slab of a dye as it moves from the hopper to the die, as sketched in Fig. 13(*a*). If the velocity field is known from the solution of the governing equations, a fluid particle may be numerically traced by integrating the velocity over time. The axial component of the velocity is used to trace the particles. As expected, the particles near the barrel and the screw take a very long time to come out, as compared to the particles near the middle portion of the screw channel. This yields the amount of color dye emerging from the extruder as a function of time and may be used to obtain the minimum, average and the spatial distribution of the residence time. Figure 13(*b*) shows these results in terms of the dye flow rate, normalized by the total flow rate. Clearly, in this case, most of the dye emerges over a short time interval, with the extended regions representing fluid near the barrel and the screw root. The calculated cumulative function $F(t)$, which indicates the cumulative fraction of the total amount of dye emerging up to time t, is defined as

$$F(t)=\int_0^t f(t)dt \tag{37}$$

where $f(t)dt$ is the amount of material that has a residence time between t and $t+dt$. The average residence time $\bar{t}$ is given by V_e/Q_e, where V_e is the total internal volume of the extruder and Q_e the volume flow rate. $F(t)$ is plotted as a function of time in Fig. 13(*c*), along with the distributions for a few other flows. It is seen that, though the basic trends are similar, the RTD is affected by the nature of the fluid and the flow configuration. It is found to be only slightly affected by the barrel temperature. It is mainly affected by the flow rate, or throughput, which substantially influences the flow field. Results at different operating conditions have been obtained in the literature and used for selecting the appropriate conditions for a given material or thermal process.

Mixing. An important consideration is the fluid mixing inside the screw channel since it determines the homogeneity of the material being processed. A simple experiment as well as some results on mixing, as given by the flow division ratio for flow between two rotating cylinders, were discussed earlier. The flow undergone by the material particles as the fluid moves downstream may be considered for a better understanding of the mixing process. Based on the calculated three-dimensional velocity field, one can introduce particles inside the screw channel and follow

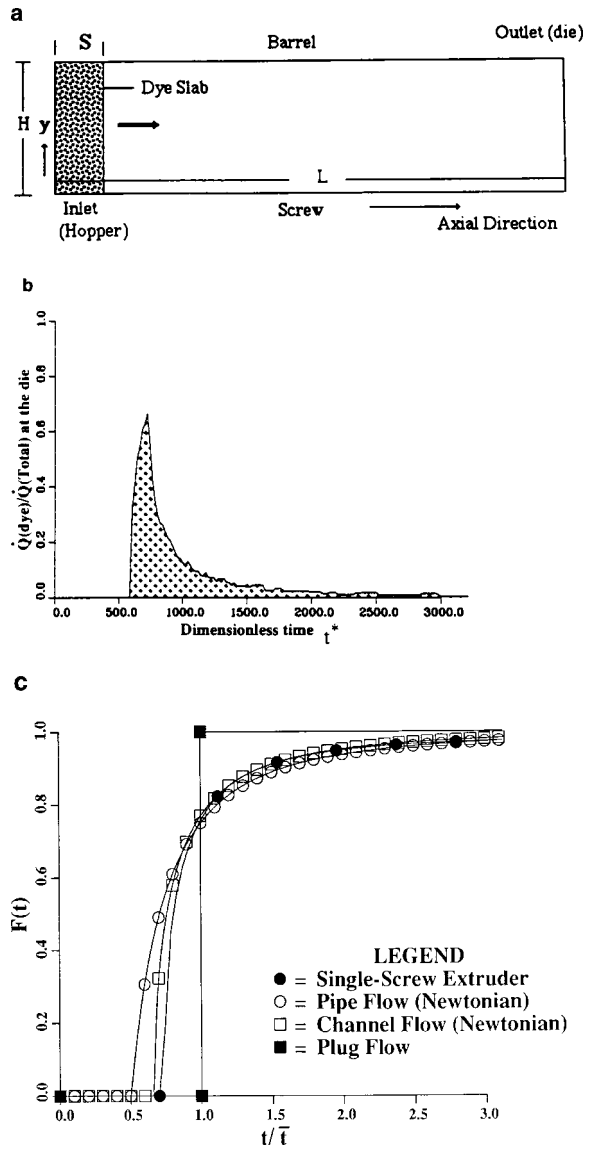

Fig. 13 Residence time distribution (RTD) calculations. (*a*) Schematic diagram showing the dye slab and the computational domain for RTD calculations; (*b*) variation of the dye flow rate, normalized by the total flow rate, with time for typical operating conditions; (*c*) variation of the cumulative distribution function F(t) for different flow configurations, with $\bar{t}$ as the average residence time.

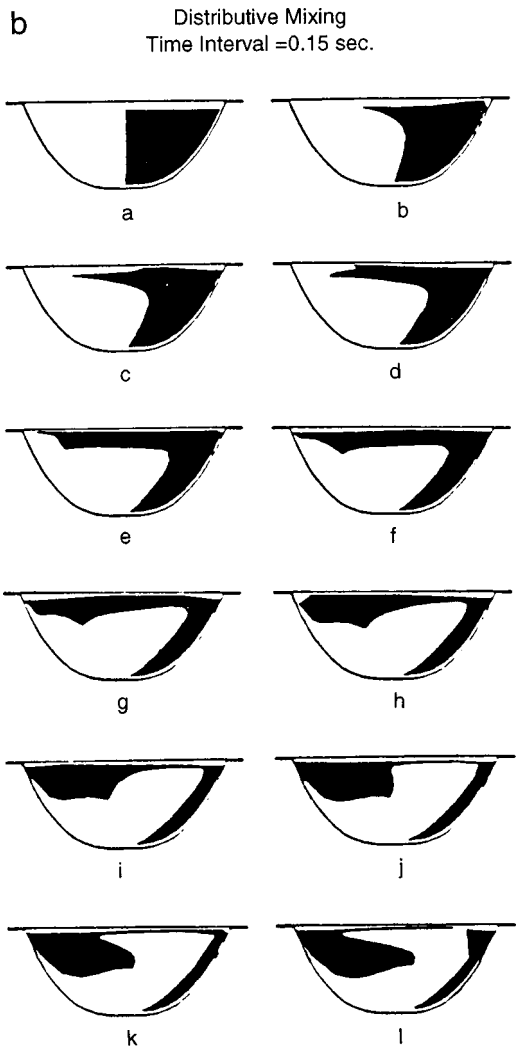

Fig. 14 Mixing characteristics in a single screw extruder channel shown in terms of time sequence of distributive mixing of two different materials inside the screw channel [58]

the movement of these particles along the channel [58]. The particles undergo spiral movements, except those near the barrel surface which go straight across the flight gap into the adjacent channel. The spiral movement of the particles inside the screw channel promotes mixing within the single screw extruder. This recirculating flow is not captured by the simpler two-dimensional model discussed earlier.

The distributive mixing inside the channel may be represented in terms of mixing between two different types of materials, shown as white and black portions in Fig. 14 with each initially occupying one half of the channel. These materials are followed with time as the fluid moves in the channel. Clearly, the process is a slow one, though the materials are eventually mixed with each other as time elapses. Several other measures of mixing have been considered in the literature. Kwon et al. [59] studied kinematics and deformation to characterize mixing. Substantial work has also been done on mixing in twin screw extruders, including the use of chaos introduced by changes in the geometry and the boundary conditions [60].

Experimental Results. Experimentation on fluid flow in the extruder channel is involved because of the complex domain and generally opaque nature of the typical materials. However, extensive experimental data on the overall characteristics of the extrusion process are available in the literature. Most of these concern the practical issues in extrusion such as temperature and pressure at the die, residence time distribution, total heat input, characteristics of the extrudate, total torque exerted on the screw, and flow rate. Much of this information is reviewed in books such as those by Tadmor and Gogos [38], Harper [28], and Rauwendaal [61]. However, very few studies have focused on the fluid flow in the channel. Over the last decade, Sernas and co-workers [62,63] have carried out well-designed, accurate, controlled and innovative experiments on single- and twin screw extruders. These results have been used for the validation of the analytical and numerical models presented here, as well as for providing a better understanding of the basic fluid flow and heat transfer processes associated with extrusion.

A specially designed single screw extruder is used for these experiments. A plexiglas window can be fitted at any one of the measuring ports to provide optical access to the flow to observe

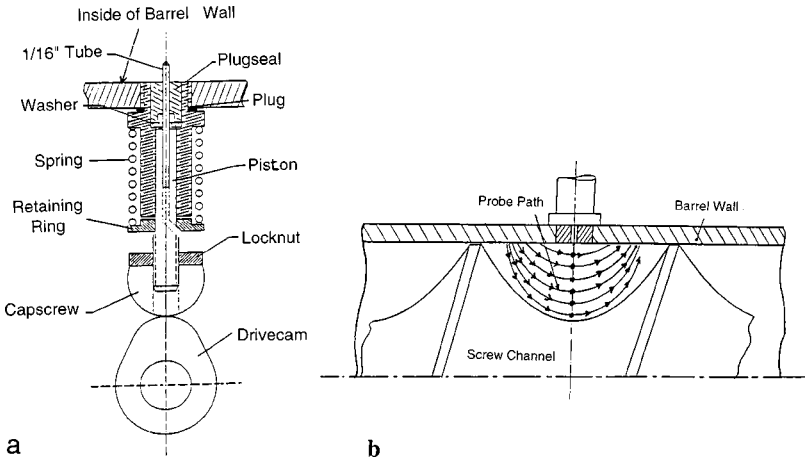

Fig. 15 (*a*) Cam-driven thermocouple for temperature measurements in the screw channel; (*b*) representation of the loci of points where temperature data are collected [62,63]

the extent of fill of the screw channel. The barrel is subdivided into three sections which can be maintained at different uniform temperatures by the use of circulating water jackets. The pressure and temperature are measured at various locations. The measurement of the temperature profile in the screw channel is complicated because of the rotating screw. A cam-driven thermocouple system, as shown in Fig. 15(*a*), is installed on the extruder to allow the thermocouple probe to travel in and out of the channel in a synchronized motion linked to the screw rotation. The probe moves into the channel to a preset distance while the flights traverse due to screw rotation. The loci of points where data are taken are sketched in Fig. 15(*b*). As expected, considerable amount of care is involved in extracting the appropriate data for the temperature profile [62,63].

Some characteristic experimental results for Viscasil-300M, which is a non-Newtonian fluid, are shown in Fig. 16, along with numerical results from two-dimensional finite difference and three-dimensional finite element calculations [40,64]. The effect of recirculation in the screw channel is seen in terms of the temperature near the screw root being closer to that near the barrel, than that predicted by the two-dimensional model. Clearly, a three-dimensional model is needed to capture this recirculation. It is interesting to note that these observations led to the development of the three-dimensional model for flow in the screw channel. A close agreement between the experimental and numerical results, in terms of pressure and temperature measured at the die, was also observed, providing strong support to the model. It was found that, for a given die, the die pressure rises with the flow rate which is increased by raising the screw speed. Also, as expected, the pressure increases as the fluid moves from the inlet towards the die.

Twin-Screw Extrusion. Twin screw extruders are used extensively in the processing of polymeric materials and in operations which include pumping, polymer blending, and distribution of pigments and reinforcing materials in molten polymers. The main advantages of twin-screw extruders, over single-screw extruders, are better stability, control and mixing characteristics. In twin screw extruders, two screws lie adjacent to each other in a barrel casing whose cross section is in a figure of eight pattern, see Fig. 17. Twin screw extruders are of many types, such as, intermeshing, non-intermeshing, co-rotating, counter-rotating, to name a few. When the screws rotate in the same direction they are called co-rotating and when they rotate in opposite directions, they are known as counter-rotating twin screw extruders. Depending upon the separation between the axes of the two screws, twin screw extruders are classified as intermeshing or non-intermeshing extruders. If the distance between the screw axes is less than the diameter at the tip of the screw flight, then one screw intermeshes with the other and thus yields an intermeshing twin screw extruder. Otherwise, it is known as a non-intermeshing twin screw extruder. When the distance between the screw axes is equal to twice the radius at the screw root and the flights of one screw wipe the root of the other screw, then the extruder is known as a fully intermeshing and self wiping twin screw extruder.

The flow domain of a twin-screw extruder is a complicated one and the simulation of the entire region is very involved and challenging [65]. In order to simplify the numerical simulation of the problem, the flow is divided into two regions: the translation, or T

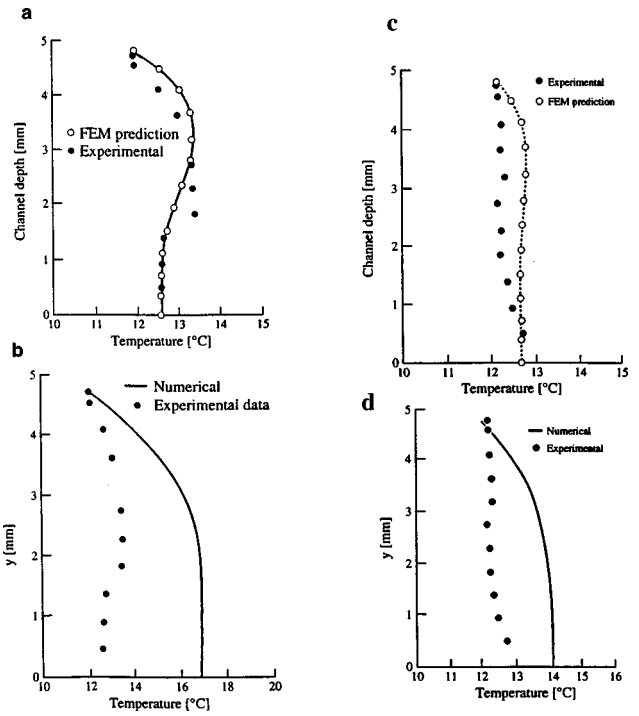

Fig. 16 Comparisons between numerical and experimental results on temperature profiles for Viscasil-300M, with (*a*) and (*c*) from the 3D (FEM) model and (*b*) and (*d*) from the 2D (FDM) model. For (*a*) and (*b*): $T_i=20.3°C$, $T_b=12.2°C$, $N=20$. For (*c*) and (*d*): $T_i=18.8°C$, $T_b=22.3°C$, $N=35$.

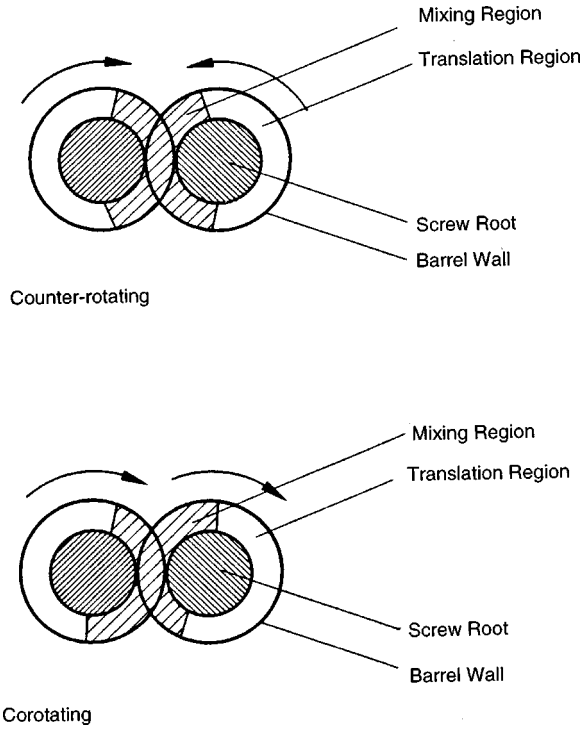

Fig. 17 Schematic diagram of the cross-section of a tangential twin screw extruder, showing the translation (T) and intermeshing, or mixing (M), regions

region, and the intermeshing, or *M* region, as sketched in Fig. 17. This figure schematically shows a section taken normal to the screw axis of a tangential co-rotating twin screw extruder and the two regions. The counter-rotating case is also shown. Due to the nature of the flow and geometric similarity, the flow in the translation region is analyzed in a manner identical to that for a single screw extruder. Therefore, this region is approximated by a channel flow. The intermeshing, or mixing, region is represented by the geometrically complex central portion of the extruder, between the two screws. The two regions are separated by a hypothetical boundary used for numerical calculations only. For further details on this model for the twin screw extruder and on the numerical scheme, see [60,65–67]. The finite-element method is particularly well suited to the complex domains that arise in twin-screw extruders. Figure 18 shows the finite element mesh used and some typical results on the transport in the mixing or nip region of the extruder. It is seen that large gradients in pressure, velocity and shear rate arise in the nip region, resulting in substantial fluid mixing, unlike the small recirculation in single-screw extruders.

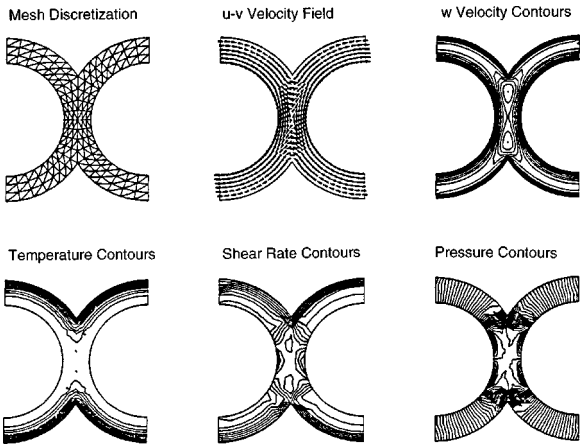

Fig. 18 Mesh discretization for the mixing region in a co-rotating tangential twin screw extruder, along with typical computed results for low density polyethylene (LDPE) at n=0.48, T_b=320°C, T_i=220°C, N=60 rpm, q_v=0.3

Chiruvella et al. [68] approximated the intermeshing region of a self-wiping co-rotating twin screw extruder to develop a control-volume based numerical scheme similar to the SIMPLER algorithm [52]. Figure 19(*a*) shows a cut-away view of the extruder considered. The flow in the intermeshing region is three-dimensional with the flow shifting by the flight width as it goes from one channel to the other. Solutions are obtained for the translation and intermeshing regions and linked at the interface, or overlapping region. The screw channels are assumed to be completely filled and leakage across the flights is neglected [68]. Figure 19(*b*) shows the pressure and temperature rise when the translation and intermeshing regions are coupled. A good agreement with earlier finite-element results is observed. Additional results at different operating conditions and materials were obtained [68,69]. Viscous dissipation was found to increase the temperature in the fluid above the barrel temperature for typical operating conditions. This model is much simpler than the finite element model, requiring much less storage space and computational time, thus making it attractive in modeling practical problems and in design for industrial applications.

Velocity measurements are quite involved because of the complex geometry and rotating screws. Karwe and Sernas [70] and Bakalis and Karwe [71] have carried out measurements of the fluid velocity field for heavy corn syrup which is transparent. A plexiglas window was used for visual access to the twin screws in the extruder. A two-component Laser Doppler Anemometer (LDA) in the back-scatter mode was used to measure the local velocities in the extruder, as shown in Fig. 20(*a*). As expected, the flow was found to be very complicated and three-dimensional. The flow field in the translation region could be compared with the numerical prediction and is shown in Fig. 20(*b*). A fairly good agreement is observed, lending support to the model and the experimental procedure. Tangential and axial velocity components were also measured in the intermeshing region and compared with numerical predictions, yielding good agreement. Leakage across the flights was found to be significant and the three-dimensional nature of the flow field was evident in the results.

Chemical Conversion. Typical results on the conversion of amioca, which is a pure form of starch, at constant screw speed and throughput, are presented in Fig. 21. The degree of conversion depends upon the velocity field and the reaction rate constant *K* which varies with the local temperature of the extrudate, as mentioned earlier. For smaller velocities, the degree of conversion up to a given axial location is higher. This is clear in the region near the screw root in all of the conversion contours. As the temperature increases along the down-channel direction, the degree of conversion increases, though the down-channel velocity does not change much. At a barrel temperature of 150°C, the local temperature is much higher than that at 115°C. Since the reaction rate constant is higher when the local temperature is higher, the material gets converted in a shorter distance than that in the case where the temperature is lower. Several other results were obtained under different temperature levels and throughputs [32]. This figure shows the typical trends observed. With increasing flow rate, the degree of conversion decreases since the residence time is smaller allowing less time for the chemical reactions to occur. A comparison with experimental results also showed good agreement. However, in these cases the screw is not filled with a rheological fluid throughout. Only a fraction of the channel length, as given in the figure, is completely filled, with the remaining portion either par-

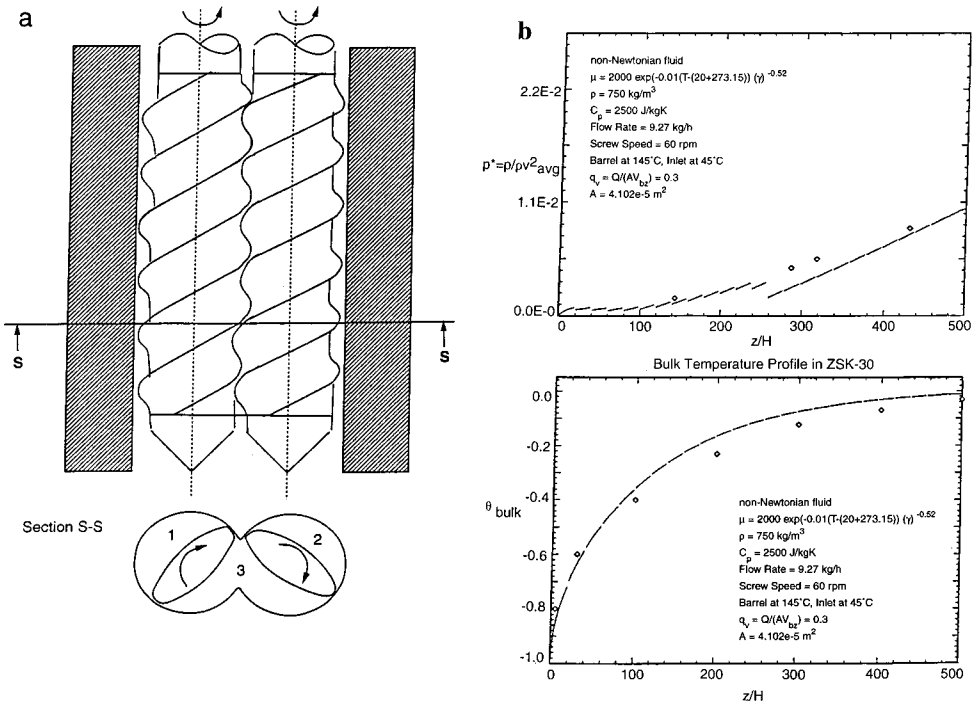

Fig. 19 (*a*) **A corotating twin screw extruder with a self-wiping screw profile;** (*b*) **comparison between the results obtained from finite volume and finite element approaches, the latter being shown as points, for a corotating, self-wiping, twin screw extruder**

tially full or containing powder which cannot be treated as a fluid. Further work is needed on chemical kinetics and on microstructural changes in such problems.

Powder Flow. In the processing of plastics and food, the material is generally fed into the extruder as solid pieces or as powder. This material is conveyed by the rotating screw, compacted and then melted or chemically converted due to the thermal and mechanical energy input. Figure 22(*a*) shows a schematic of the overall process for food extrusion. The solid conveying region is generally modeled as a plug flow with friction and slip at the boundaries, as sketched in Fig. 22(*b*). Friction factors have been measured for different materials and are available in the literature. The force balance yields the pressure variation in this region [38,72]. This material is compacted due to the increase in pressure downstream. For modeling the compaction process, information is needed on the variation of density or porosity of the material with pressure. Also, accurate friction factors are needed for the given powder and barrel and screw materials. Very little work has been done on powder flow and compaction, even though it is expected that this process will have a substantial effect on the flow, heat transfer and conversion processes downstream [72]. Clearly, further detailed work is needed on this problem.

Additional Aspects. The preceding presentation on polymer extrusion brings out the major concerns and complexities in this important area. However, there are many additional aspects that arise in practical circumstances. These include melting and solidification of the material, different screw configurations, leakage across screw flights, flow stability, process feasibility, and the conjugate transport due to conduction in the barrel. Transient effects are particularly important, both for the start-up of the process and for changes in the operating conditions. The feasibility of the process is determined largely by the pressure and temperature rise in the extruder and, therefore, by the flow. Many of these aspects have been considered in detail in the literature and the references given in this section may be used for additional information.

Summary. The processing of polymers and other similar materials like food, rubber and pharmaceutical materials is used extensively in a wide variety of industries. Extrusion also frequently precedes injection molding, another important processing method for plastics. Composite materials are also generally produced by reinforcing polymers with a variety of fibers made of metals, ceramics, glass, etc., to obtain the desired characteristics. Again, extrusion and injection molding are important processing techniques for such materials. The fluid flow strongly affects the mixing process, as well as the residence time, which influences the physical and chemical changes in the material. The flow also affects the thermal transport, which determines the temperature field, the fluid viscosity, and the pressure rise. These variables and the flow determine the characteristics of the final product.

Optical Fiber Drawing. Another important manufacturing process, which was considered in the preceding discussion and which has become critical for advancements in telecommunications and networking, is optical fiber drawing, sketched in Fig. 1(*a*). In this process, the viscosity of glass, which is a supercooled liquid at room temperature, is a very strong function of temperature. At its softening point, the viscosity is still very high, being of the same order as that of polymer melts considered in the previous subsection. Thus, viscous dissipation is important and the momentum and energy equations are coupled. The analytical/numerical treatment is thus similar to that described in the previous section. Even small temperature differences are important because of the effect on the viscosity and thus on the flow field. However, glass flow may be treated as Newtonian at typical draw speeds.

In optical fiber drawing, the diameter of the cylindrical rod, which is specially fabricated to obtain a desired refractive index variation and is known as a preform, changes substantially, from 2–10 cm to about 125 μm, in a distance of only a few centimeters. This places stringent demands on the grid, shown in Fig. 5, as well as on the numerical scheme because of the large change in the surface velocity. The radiative transport within the glass is

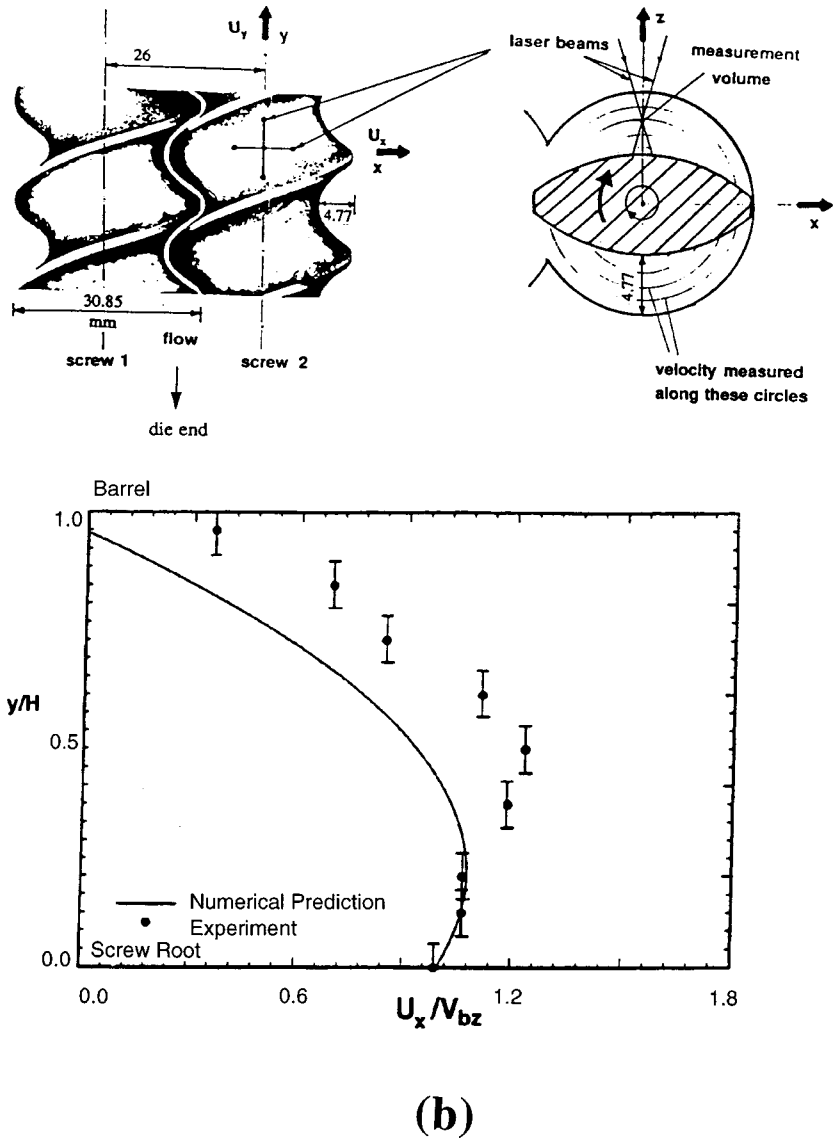

Fig. 20 (*a*) **Experimental arrangement for velocity measurements in the flow of corn syrup in a twin-screw extruder;** (*b*) **comparison between calculated and measured tangential velocity U_x profiles for isothermal heavy corn syrup at 26.5°C, with mass flow rate of 6 kg/h and screw speed of 30 rpm**

determined using the optically thick medium approximation or improved models such as the zonal method [73]. The main interest in this process lies in obtaining high quality optical fibers, as indicated by low concentration of process-induced defects, desired variation of refractive index, low tension, strength, and other important measures, at high draw speeds.

Typical computed results in the neck-down region, for a specified profile, are shown in Fig. 23, indicating the streamfunction, vorticity, viscous dissipation and temperature contours. The flow is smooth and well-layered because of the high viscosity. A typical temperature difference of 50–100°C arises across the fiber for preform diameters of around 2.0 cm. As mentioned earlier, even this small difference is an important factor in fiber quality and characteristics. Larger temperature differences obviously arise for larger preform diameters. Viscous dissipation, though relatively small, is mainly concentrated near the end of the neck-down, in the small diameter region, and plays an important role in maintaining the temperatures above the softening point. Further details on this problem may be obtained from [14,17,18,41,74].

Neck-Down. The simulation of the free surface is another difficult problem, as discussed earlier. Several studies in the literature have considered fiber formation from the melt, particularly for polymers, and jets and other free surface flows [75–78]. Optical fiber drawing involves modeling the free surface flow of glass under large temperature differences and large changes in viscosity and cross-sectional area. Several simple models have been employed to study the flow in this region, known as the neck-down region [74]. In a recent study, a combined analytical and numerical approach, based on the transport equations and surface force balance, was developed for the generation of the neck-down profile of an optical fiber during the drawing process [41]. An axisymmetric, laminar flow was assumed in the glass and in the circulating inert gases. The governing transport equations were solved employing a finite difference method. The radially lumped axial velocity, the normal force balance and the vertical momentum equations were used to obtain a correction scheme for the neck-down profile. After a new corrected profile is obtained, the full governing equations are solved for the flow and heat trans-

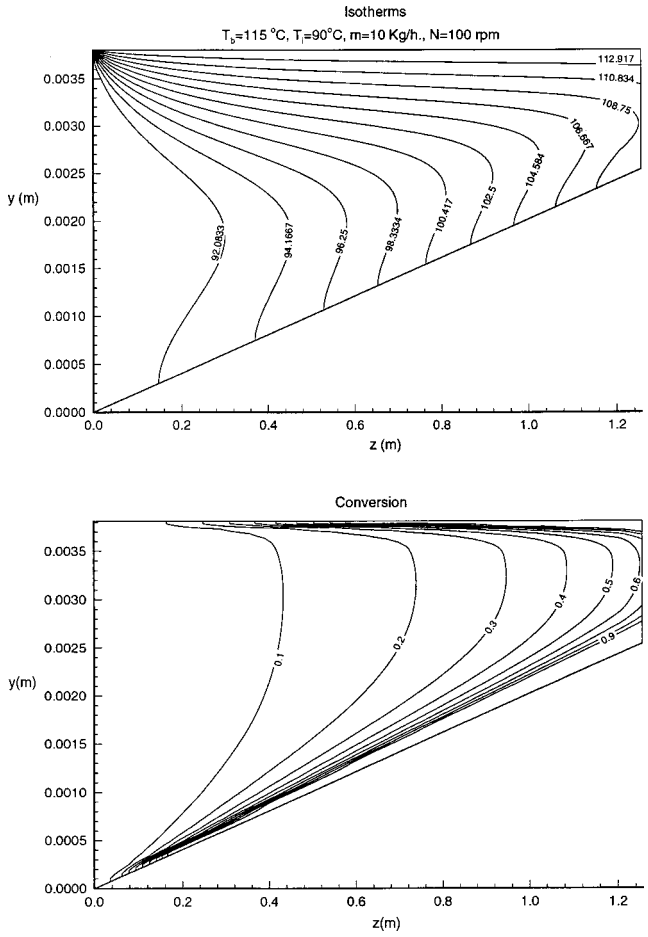

Fig. 21 Isotherms and conversion contours while extruding amioca in a tapered single screw extruder, with T_b=115°C, T_i=90°C, N=100 rpm, mass flow rate $\dot{m}$=10 kg/h, moisture =30 percent

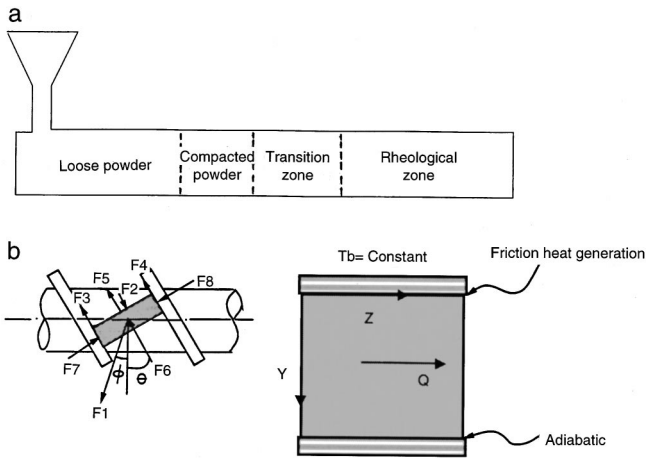

Fig. 22 (*a*) Schematic of the various regions in food extrusion; (*b*) modeling of powder flow in a single screw extruder

fer, considering both radiation and convection transport. This process is continued until the neck-down shape does not change from one iteration to the next. It was found that viscous and gravitational forces are dominant in the determination of the profile. Surface tension effects are small even though they are important in many other free boundary flows [79]. The external shear and inertial effects are small, as expected.

A typical example of the numerical generation of neck-down profile with a cosinusoidal starting profile is shown in Fig. 24(*a*). From the figure it is seen that during the first few iterations, the neck-down profile is quite unrealistic, with a flat region and an abrupt change in radius around where the starting polynomial profile ends. But after a few iterations the shape becomes smooth and monotonically decreasing, eventually reaching a steady, converged, profile, indicated by the invariance of the profile with further iterations. It must be mentioned here that the radius approaches the dimensionless fiber radius as the axial distance approaches the furnace exit. However, because of the small value of dimensionless fiber radius, the graphs seem to show that the value

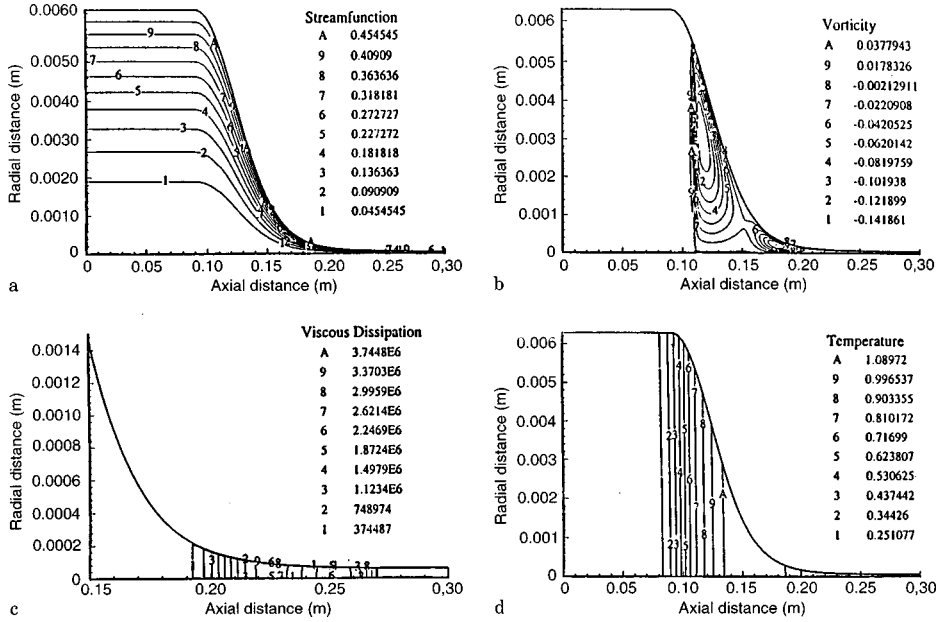

Fig. 23 Calculated (*a*) streamfunction, (*b*) vorticity, (*c*) viscous dissipation, and (*d*) temperature contours in the optical fiber drawing process for typical drawing conditions

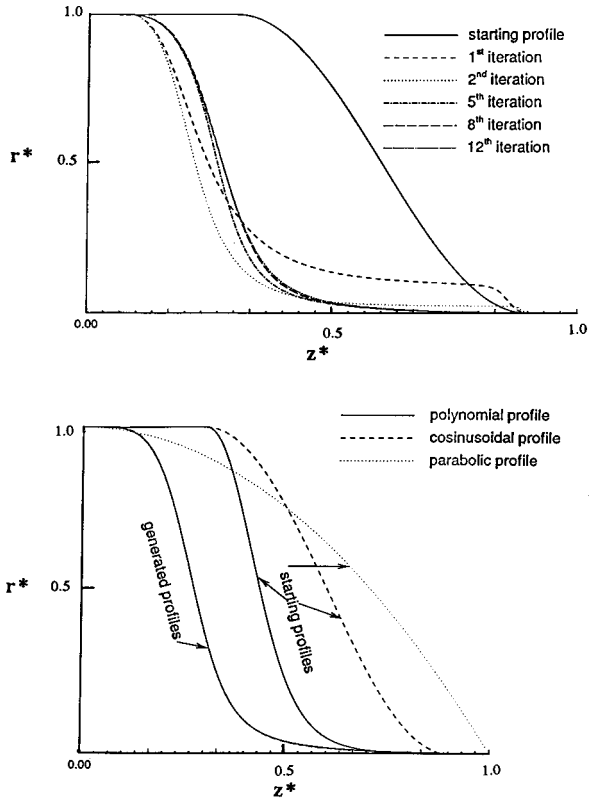

Fig. 24 Iterative convergence of the neck-down profile in optical fiber drawing. Here, r*=r/R and z*=z/L, where R is the preform radius and L the furnace length.

approached is zero. For convergent cases, perturbations to the initial profile and different starting shapes lead to the converged neck-down profile, as seen in Fig. 24(*b*), indicating the robustness of the scheme and the stability of the drawing process. The force balance conditions were also closely satisfied if the iterations converged. However, convergence does not occur in every case, leading to a feasible domain, as discussed below.

Feasible Domain. It was shown by Roy Choudhury et al. [41] that, for given fiber and preform diameters and for a given draw speed, the fiber cannot be drawn at any arbitrary furnace wall temperature distribution. If the furnace temperature is not high enough, the iterative radius correction shows that the fiber breaks due to lack of material flow, a phenomenon that is known as viscous rupture [80]. Similarly, it can be shown that for a particular furnace temperature and fiber speed, the fiber can be drawn only if it is above a certain diameter. It can also be shown that for a given preform and fiber size, and with a given furnace temperature, there is a limit on the speed beyond which no drawing is possible, as this leads to rupture. Figure 25(*a*) shows the different cases studied, including the cases where drawing was feasible and the cases when it was not. From this figure, a region can be identified beyond which drawing is not possible. For the region where drawing is feasible, the draw tension is calculated. The ''iso-tension'' contours are shown in Fig. 25(*b*). As expected, the draw tension is low at higher temperatures and lower speeds, which explains the positive slope of the iso-tension contours. For a realistic fiber-drawing operation, these results are very important, since the operating parameters (such as furnace temperature and draw-down speed) can be identified so that a fiber of desired diameter can be drawn at the applied tension [81,82]. It must be pointed out that only a combination of fiber speed and furnace temperature has been considered here. It is possible to obtain similar results for different combination of other physical and process variables such as the external gas, flow velocity, flow configuration, furnace temperature profile, furnace size, etc. Thus, feasibility of the process is determined largely by fluid flow, as was the case in polymer processing.

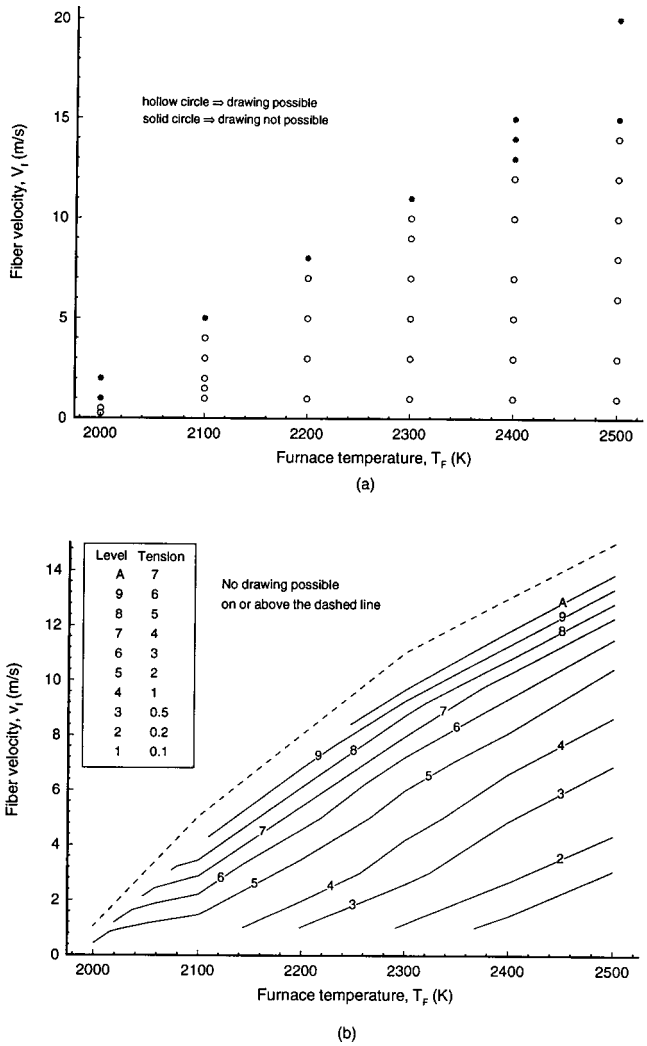

Fig. 25 Results obtained from a feasibility study of the fiber drawing process: (*a*) different cases studied, showing both feasible and infeasible combinations of parameters and (*b*) ''iso-tension'' contours for the feasible range of fiber drawing

Experiments. Experimental work on the flow and thermal transport in the optical fiber drawing is very complicated because of the high temperatures, high draw speeds and difficult accessibility into the furnace [74]. Most measurements have focused on the characteristics of the fiber for different operating conditions such as furnace wall temperature, draw speed and applied tension. Relatively few results are available that may be used for comparisons with numerical predictions. A comparison with the profile experimentally obtained by Paek and Runk [83] has been carried out. For the heat transfer coefficient distribution given by Paek and Runk, a parabolic furnace temperature profile has been used by Lee and Jaluria [17,18] to predict the maximum temperature in the preform/fiber and its location. The same parabolic furnace temperature profile, with a maximum temperature of 3000 K and minimum temperature of 2300 K, was used for obtaining the neck-down profiles [41]. From the analytical results obtained by Paek et al. [84], the draw tension plotted on a logarithmic scale is expected to vary linearly with the inverse of the furnace temperature. A comparison of the computed results with the experimental

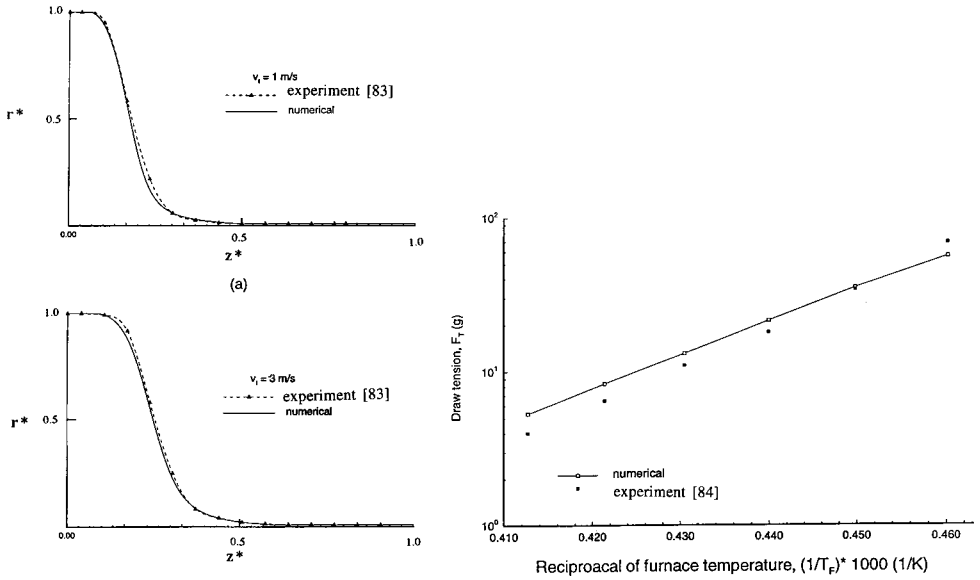

Fig. 26 Comparison of the numerical predictions of neck-down profile and draw tension with experimental results

data show good agreement, as seen in Fig. 26. The quantitative trend is reasonably good, even though the furnace temperature profile, except for the maximum value, is guessed, and all properties for fused silica are taken from the literature. These comparisons with experimental results lend strong support to the approach outlined here for determining the neck-down profile.

A study of the flow and thermal transport associated with the draw furnace require accurate knowledge of the furnace wall temperature distribution. An experimental procedure involving mounting rods of different materials and diameters and feeding them axially within the furnace cavity was employed for this purpose, see Fig. 27(*a*). Each rod was instrumented with thermocouples inserted through an axial hole along the centerline. The temperature measurements were used along with a numerical model for the flow and heat transfer in the furnace in order to obtain the furnace wall temperature profile [85]. This is an inverse problem since the centerline temperature in the rod is known whereas the furnace thermal conditions are not known. The results obtained using the graphite rods suggest that the furnace temperature is not affected by rod size. Figure 27(*b*) shows the computed temperature distribution along the graphite heating element. The dashed lines represent the water cooled portion of the furnace cavity. The convergence of the optimization method used for deriving the heating element temperature distribution is demonstrated by the agreement between the predicted and measured rod temperatures. The computed maximum element temperatures were in good agreement with the furnace sensor temperature at the hot zone centerline, lending support to the model for the flow and thermal transport in the furnace. The small difference between the computed element temperatures for the two rod sizes is in support of the previous statement that there was a small influence of rod size on the furnace temperature distribution. However, the effect of larger than the presently used rod sizes on furnace temperature needs further investigation. Similar results were obtained for the other furnace temperatures and for other materials, including silica glass [86].

Coating. As shown in the schematic diagram of the typical fiber drawing process in Fig. 1(*a*), the fiber is cooled as it moves toward the coating section where it is coated with a jacketing material for protection against abrasion, to reduce stress induced microbending losses, and for increased strength. The upper temperature at the coating section is limited by the properties of the coating material used. For commercial curable acrylates, this tem-

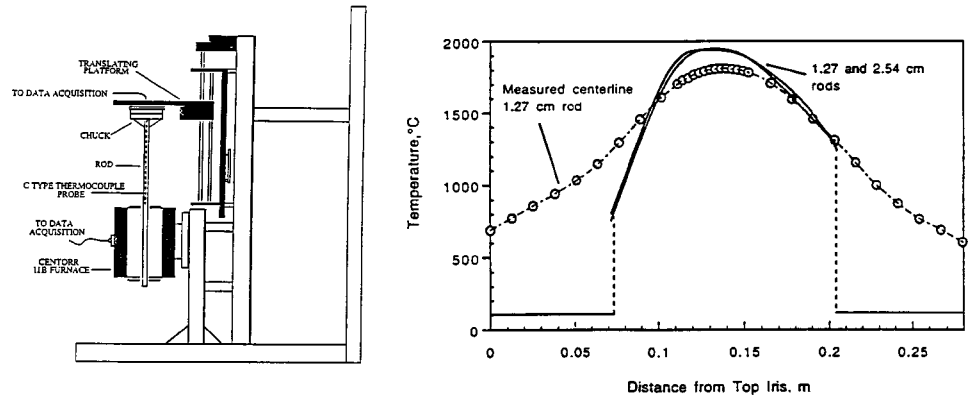

Fig. 27 (*a*) Schematic of an experimental system for measuring the temperature distribution in a rod located in an optical fiber drawing furnace; (*b*) computed furnace temperature distributions (solid line) from graphite rod data. Experimental points are from the 1.27 cm diameter rod.

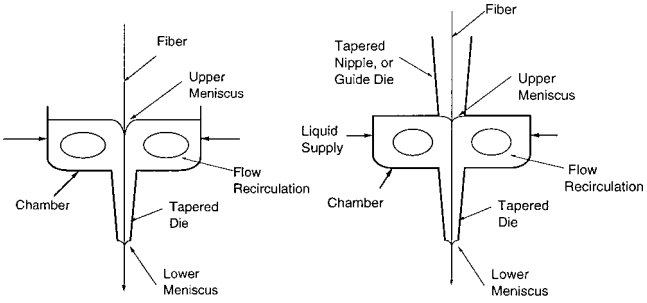

Fig. 28 Sketch of the flow in the chamber and the die for (*a*) an open cup, and (*b*) a pressurized coating applicator, showing the upper and lower menisci

perature generally cannot exceed 150°C. The wet coating is then cured by ultra-violet radiation as it passes through the curing station, and finally the fiber is spooled around a takeup drum at the base of the tower.

The basic coating process involves drawing the fiber through a reservoir of coating fluid from where it is passed through a die that may be used to control the thickness and the concentricity of the coating layer. Coating thickness may also be controlled by ''metering'' the flow rate, while a flexible exit die may be used for centering the fiber. This is immediately followed by a curing process that results in solidification of the coating material around the fiber. Figure 28 shows schematic diagrams of typical coating applicator and die systems. Viscous shear due to the moving fiber results in a circulatory fluid motion within the fluid. This problem is very similar to polymer flow in a channel or die, as discussed earlier. A balance between surface tension, viscous, gravitational, and pressure forces results in an upstream meniscus at the cup entrance [87–90]. This consideration is similar to that employed for determining the neck-down profile in fiber drawing and a similar approach may be used in this case too. A downstream meniscus at the die exit results primarily from a balance between viscous and inertia forces, the surface tension being a relatively small effect. Centering forces within the tapered die contribute to the positioning of the fiber at the die exit center. Successful coatings are concentric, of uniform thickness, and free of particle inclusions or bubbles. Excellent reviews of much of the earlier investigations on fiber coatings have been presented by Blyler et al. [91], Li [14], and Paek [92].

The use of high draw rates requires consideration of alternate pressurized applicator designs, where pressure induced motion of the coating material is used to reduce the shear at the fiber surface and probably results in the establishment of a stable free surface flow, though this aspect needs further investigation. An additional benefit resulting with such pressurized dies has been the incorporation of gas bubble reducing, or bubble stripping, designs which have resulted in minimizing gas bubbles entrained at the coating cup entrance and then trapped within the coating layer. The physical and rheological properties of coating materials and their temperature dependence are particularly important for the flow within the applicator. However, accurate property data are generally not available. Coating layer thicknesses range between 30 and 300 μm.

Several investigators have focused their attention on air entrapment by the moving fiber and the resulting deterioration of the coating. The characteristics of the meniscus, particularly its stability, have been studied in detail. Ejection of air bubbles by tip streaming from interface cusps near the fiber was investigated [93]. The dynamic meniscus in pressurized and unpressurized fiber coating applicators was studied in detail, experimentally and numerically, by Ravinutala et al. [94], following an experimental study by Abraham and Polymeropoulos [95]. Figure 29 shows images of the meniscus formed with the fiber moving into an unpressurized open cup applicator, as well as inside a micropipette tube with a pressurized applicator. The fiber speed was 20 m/min. In both cases, the dynamic contact angle was near 180 deg. Figure 29 A clearly shows the breakdown of the meniscus into saw tooth patterns and tip streaming as previously observed. On the other hand, the pressurized applicator meniscus image, Fig. 29 B, appears to be smooth, suggesting suppression of large scale breakdown at the same fiber speed. Figures 29 C and D are low magnification images clearly demonstrating that the unpressurized meniscus generates a large number of relatively large air bubbles compared to the pressurized meniscus in Fig. 29 D where air bubbles are probably too small to be detected. Comparison of the shape of the menisci in Figs. 29 A and 29 B shows that the effects of pressure and geometry are to flatten the meniscus and to increase the slope of the liquid-air interface near the fiber compared to those for an unpressurized meniscus. This probably results in a smaller air volume available for entrainment accounting for the difference between Figs. 29 C and 29 D. Numerical modeling results were found to agree closely with the experimental observations on the flow and pressure distributions. However, further investigation is clearly needed to understand the effect of pressure on air entrainment and to design applicators and dies to obtain high-quality fiber coatings.

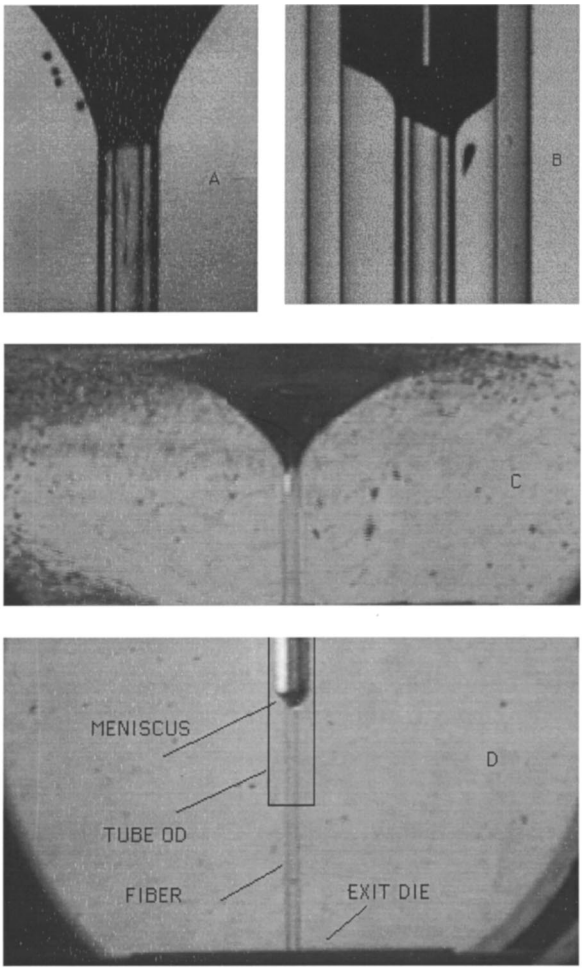

Fig. 29 (A, C) Unpressurized test section; (B, D) Meniscus in 630 μm diameter tube, test section pressurized. Fiber speed = 20 m/min.

Additional Aspects. The main considerations that arise in the drawing of optical fibers are outlined in this section. The problem is an extremely complex one, though it is also a very important material processing technique because of the tremendous worldwide demand for optical fibers. This has led to increasing draw

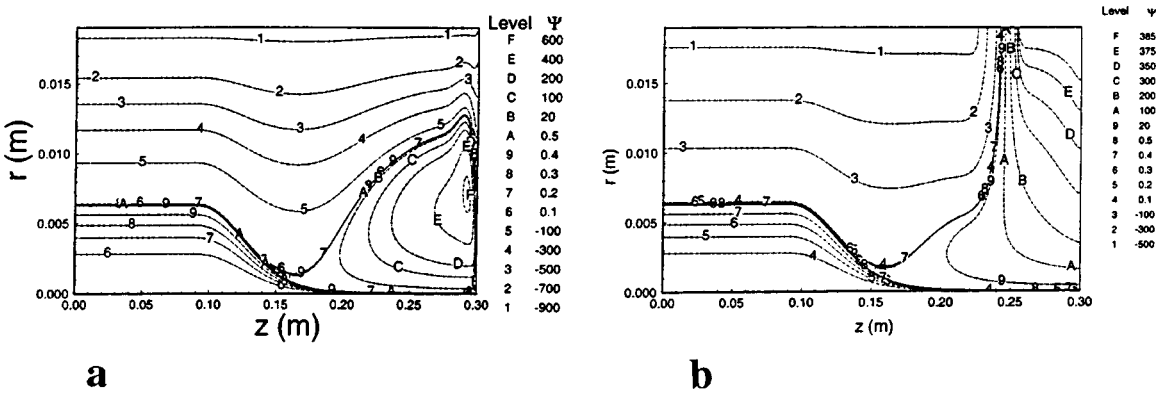

Fig. 30 Inert gas flow field in the optical fiber drawing furnace for two geometrical configurations: inlet flow in opposite direction to fiber motion and side entry

speeds and preform diameters, resulting in stringent requirements being applied to both the process and to its modeling. The fiber has to be cooled rapidly in order to reach appropriate temperature levels before coating is applied. Substantial work has been done on the flow in the forced cooling process, considering laminar and turbulent flow in the cooling section [74,96]. This is similar to the continuous processing problem, considered later in this paper.

The flow of inert gases in the draw furnace plays a very important role in the transport processes within the furnace and thus in the flow and heat transfer in the glass. However, the flow is a strong function of the geometry, particularly the locations of the inlet/outlet channels, and of the flow rate. The flow can affect local transport rates and thus cause local hot or cold spots. Figure 30 shows the calculated flows for two different configurations. The side inlet, though more convenient to design and operate [81], directs the cold fluid at the fiber, causing possible local cooling and breakage. Similarly, flows that aid or oppose fiber motion respectively increase or decrease the heat transfer, significantly affecting the process.

Defects are another important consideration, because these affect the quality of transmission in the fiber and the distance one could go without enhancing the signal. Many defects are generated by the thermal field and the flow, and enhanced cooling could affect the distribution and retention of these defects. The glass flow also affects the distribution of these defects, as well as of dopants put into the preform to obtain specialized fibers. Several studies have considered the kinetics of thermally induced defects [97,98]. Yin and Jaluria [82] used the equation for the kinetics of these defects to obtain their concentrations as functions of location and operating conditions. The approach is similar to that for the inclusion of chemical kinetics in other materials processing cases, such as in food and reactive polymer extrusion considered earlier.

Summary. The flow of glass and inert gases in the furnace affect the heating up of the glass preform and the neck-down profile, which in turn affect the temperature field, the generation of defects, the tension in the fiber, and the distribution of impurities and dopants. Similarly, the flow in the coating process affects the menisci, which determine the entrapment of bubbles and the uniformity, thickness and concentricity of the coating. Thus, the flow strongly affects fiber quality as well as the stability and feasibility of the process.

Casting. Solidification and melting processes have been studied extensively because of their importance in a wide variety of processes such as casting, crystal growing, welding, and polymer injection molding, considering pure materials as well as mixtures such as alloys [99–103]. As mentioned earlier, the natural convection flow in the liquid or melt region is solved and coupled with the transport in the solid. The location of the moving boundary is not known and must be obtained from the solution, as is the case for mold casting shown in Fig. 1(*c*). A coordinate transformation, such as the Landau transformation, which was also used for the neck-down region in optical fiber drawing, may be employed to make the computational domains rectangular or cylindrical, from the complicated ones shown [24,104,105]. This considerably simplifies the numerical procedure by allowing a regular rectangular or cylindrical mesh to be used. Several other techniques have been developed to treat such moving boundary problems and the complicated domains that arise. For the continuous casting problem of Fig. 1(*b*), the interface between the solid and the liquid is not known at the onset and an iterative procedure may be adopted to determine its shape and location. Again, body fitted coordinates may be employed to approximate the irregular shaped computational domains. Of course, if the enthalpy model is employed, the entire region is treated as one, considerably simplifying the computational procedure. Interest lies in obtaining high quality castings, with few voids and defects, good grain structure and low stresses, at high production rates.

Figure 31 shows the numerical results for melting in an enclosed region using the enthalpy model. Streamlines and isotherms are shown for four different times during the melting of pure Gallium. This is a benchmark problem in which melting is initiated by a step change in the temperatures at the left and right boundaries, the left being at temperature higher than the melting point and the right lower. The streamlines indicate the effect of thermal buoyancy which causes the interface between the solid and the liquid to bend, rather than remain parallel to the vertical boundaries. The amount of material melted increases with time till it reaches a steady state for this problem. The recirculation in the liquid is clearly seen. These results are found to agree well with experimental results available in the literature [16]. The two-region approach can also be used for modeling this problem. For pure metals, the two-phase, two-region, approach leads to more accurate results, whereas the enthalpy method is more useful for alloys and mixtures. A lot of work has been done on such melting and solidification problems, as reviewed by Viskanta [16,100].

Conjugate transport is also important in these problems, as was also the case in polymer extrusion and optical fiber drawing. Figure 32 shows typical numerical results when conduction in the mold is coupled with heat transfer in the liquid and the solid [106]. With increasing time, the liquid region shrinks due to solidification, whereas the solidified region increases. The effect of the imposed conditions at the outer surface of the mold on the solidification process can be investigated by solving this conjugate problem, which yields the temperature field in the mold along with that in the solid and the liquid, as shown. Banaszek et al. [107] carried out experiments and numerical simulations to demonstrate the importance of conduction in the wall, as shown in Fig. 33. Such numerical and experimental studies can be used to

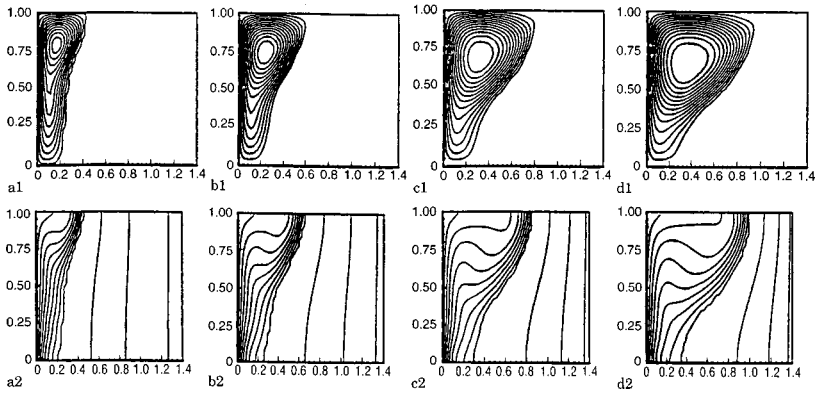

Fig. 31 Streamlines (1) and isotherms (2) for melting of Gallium in an enclosed region, with the left vertical boundary at a temperature higher than melting point, the right vertical boundary at a temperature lower than melting point and the remaining two boundaries insulated. The enthalpy method is used and results are shown at different dimensionless time t following the onset of melting. (*a*) t=0.5248, (*b*) t=1.0416, (*c*) t=1.5622, (*d*) t=1.9789.

determine the progression of the solidification front and thus monitor the generation of voids and other defects in the casting.

Experimental studies have been relatively few because of the complexity of the process arising from a moving interface and time-dependent flow [108,109]. However, detailed experimental results are needed to critically evaluate the various models employed for simulation as well as to provide information on the characteristics of the interface for development of microscale models. Figure 34 shows typical experimental results, along with numerical predictions, for the melting and solidification of pure tin [110,111]. The comparisons are fairly good, though the differences at small time indicate the need to improve the model to more closely approximate the experimental conditions.

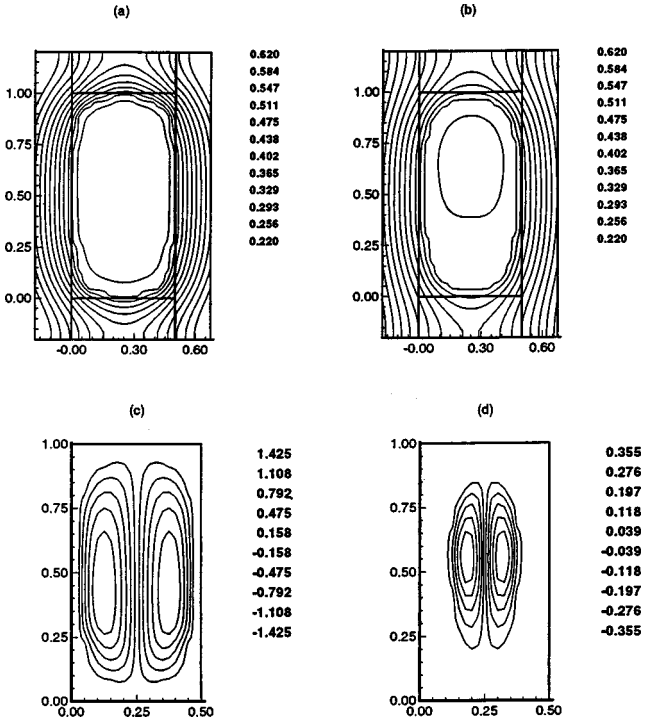

Fig. 32 Isotherms (*a,b*) and streamlines (*c,d*) for solidification in a cavity with conjugate transport to the mold. (*a, c*) t=0.05, and, (*b, d*) t=0.1.

Alloys. There has been a growing interest in the basic characteristics of solidification for mixtures, particularly alloys, as reviewed by Prescott and Incropera [103]. Combined heat and mass transfer processes arise in this case and significantly affect the flow. Figure 35 shows a schematic of the double-diffusive convective flow that arises and increases in intensity with time. The left wall is heated and solidification occurs on the right wall. As the salt-enriched liquid is ejected from the mushy zone, it forms a layer at the bottom and subsequently additional layers arise, with recirculation in each layer driven by horizontal temperature gradients. Lower heat transfer at the bottom results in larger mushy region thickness [112]. Many interesting experiments on the solidification of aqueous NH_4Cl solutions and other such fluids have been carried out to study the flow structure [101–103]. Similarly, interest lies in understanding microscopic phenomena associated with solidification. This is an area of intense current research work. The solidification front can be divided into various morphological forms such as planar, cellular and dendritic. Various mod-

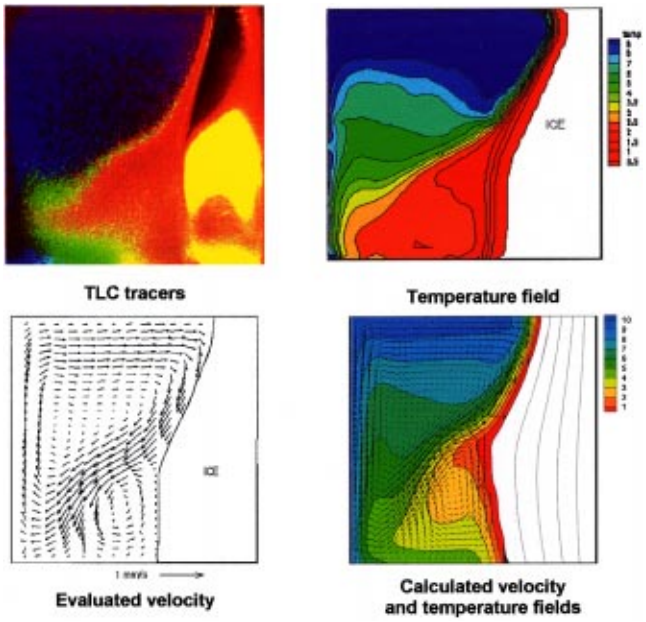

Fig. 33 Experimental and numerical results for water solidification driven by convection and conduction

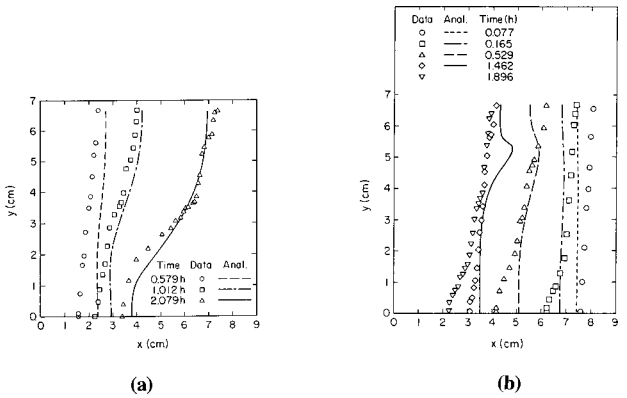

Fig. 34 Comparison between measured and predicted interface locations during (*a*) melting, and (*b*) solidification of pure tin from a vertical surface [110,111]

els have been proposed and experiments carried out to characterize such structures and growth [113,114]. For instance, Fig. 36 shows equiaxed and columnar denritic crystals. Averaging volumes and dendrite envelopes that may be used for modeling of the microscopic phenomena are shown.

The numerical results for continuous casting are shown in terms of isotherms in Fig. 37, again using the enthalpy method [115]. The material is *n*-octadecane which starts as a liquid at the top and solidifies as it flows through a mold. The buoyancy effects in the flow are found to be small in this case. The shaded region indicates the demarcation between pure liquid and pure solid. Therefore, the liquid fraction f_1 is 1.0 at the top of the shaded region and zero at the bottom of this region. A value of 0.5 may be taken to represent the liquid-solid interface, but the enthalpy method yields a finite region over which solidification is predicted to occur. It is seen that the material solidifies over a shorter distance at a larger value of the heat transfer rate, indicated by the Biot number, as expected.

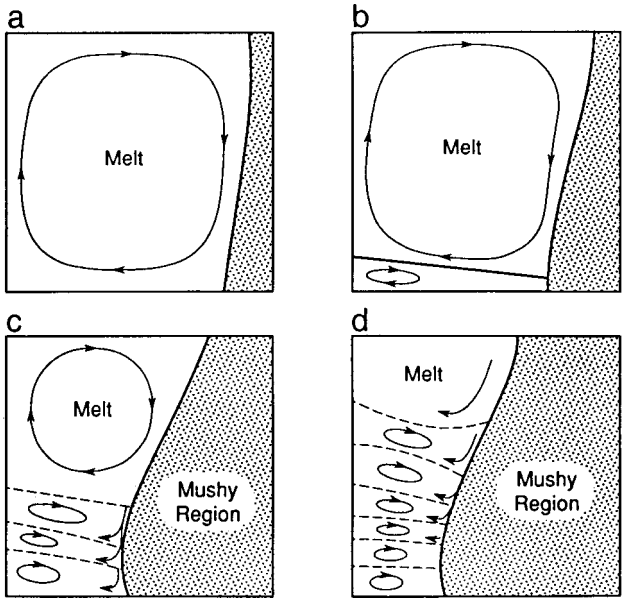

Fig. 35 Schematic of double-diffusive convection during solidification of aqueous Na_2CO_3 solution at various times following start of the solidification process. (*a*) 10 min; (*b*) 30 min; (*c*) 75 min, and (*d*) 150 min [112].

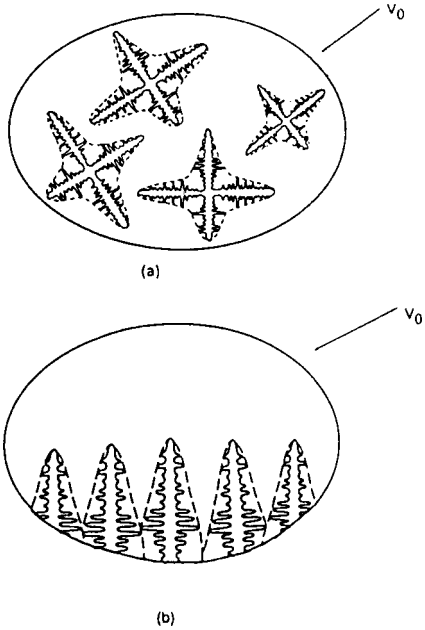

Fig. 36 Schematic illustration of the averaging volume and the dendrite envelopes for (*a*) equiaxed growth and (*b*) columnar growth [113]

Polymer Melting and Solidification. In many polymer processing applications, the melting and solidification of the material is an important consideration. In injection molding, for instance, the molten polymer is injected under pressure in a mold and, after the mold is filled, the material is allowed to cool and thus solidify. Solidification in extrusion dies and in channels leading to a mold is not desirable since it affects the flow and the pressure due to the resulting blockage. The basic flow configuration is shown in Fig. 38(*a*), indicating a solidified layer near the boundaries and flow in the central core. Work has been done on this problem using the enthalpy approach discussed earlier. The interface between the solid and melt regions, and the velocity and temperature distributions are computed [116]. Some typical results are shown in Figs.

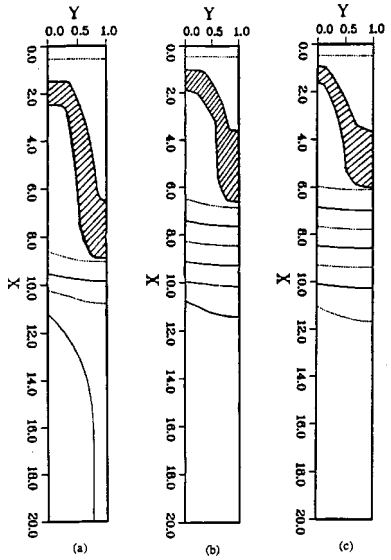

Fig. 37 Effect of cooling rate at the mold in terms of the Biot number Bi on the solidification in vertical continuous casting of n-octadecane, using the enthalpy method. (*a*) Bi=0.05, (*b*) Bi=0.1, (*c*) Bi=0.15.

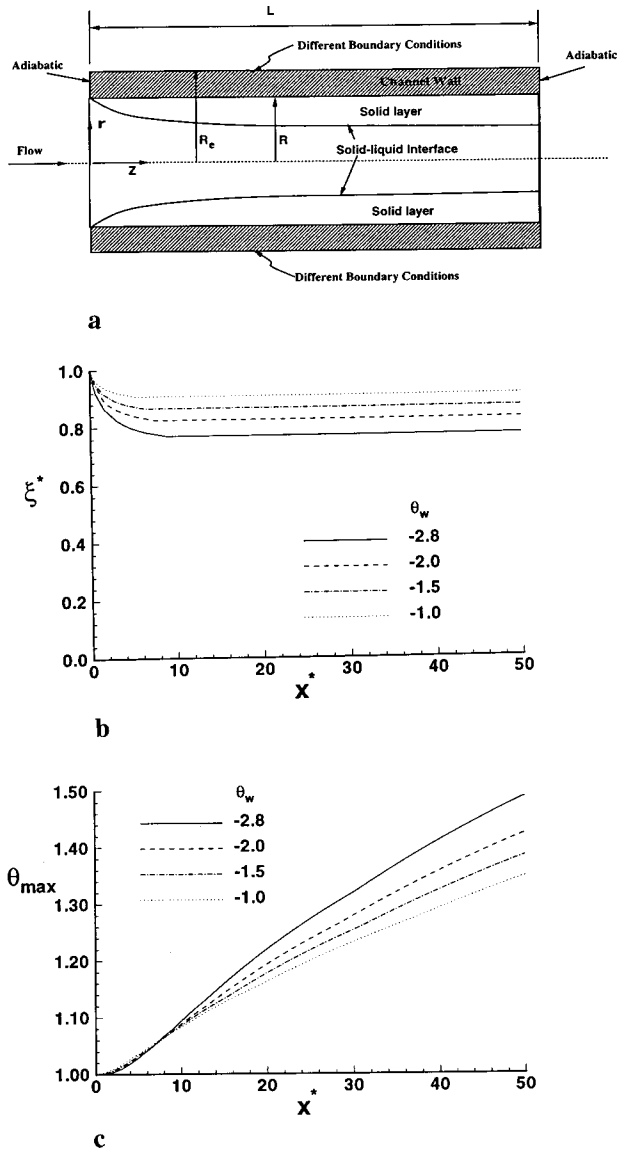

Fig. 38 (*a*) Schematic of polymer solidification in a channel; (*b*) dimensionless solid-liquid interface ξ^*; and (*c*) maximum temperature θ_{max} in the melt, for different outer wall temperatures θ_w

38(*b*) and (*c*). It is interesting to note that as the temperature at the boundary is decreased, the thickness of the solidified layer increases, resulting in greater blockage to the flow. This, in turn, causes increased viscous dissipation, which heats up the fluid flowing in the central region. Thus, lowering the wall temperature ends up increasing the fluid temperature over the parametric ranges considered here. Complete blockage is not found to occur because of increased viscous dissipation effects with greater blockage.

Summary. The preceding discussion outlines only a few important aspects in the modeling of material processing techniques based on phase change. More work is clearly needed on coupling microscale phenomena with the overall macro-model of the process and the system. However, recent studies have led to a much better understanding of the solidification process than what was available before. The flow affects the heat and mass transfer processes, which in turn influence the characteristics of the melt-solid interface and the rate of melting/solidification. The flow also affects the quality of the product because of undesirable oscillations, generation of voids, and distribution of impurities.

Continuous Processing. A continuously moving material undergoing processing results in another important complication in the numerical simulation and experimentation of manufacturing processes. The cooling of the moving optical fiber before coating is an example of such processing. If the location of the moving surface is known, as is the case for the circumstance of Fig. 7(*b*), the continuous movement of the boundary may be replaced by steps, so that the length L is held constant over a time increment Δt and the transient conduction problem is solved over this interval. The length L is then taken at the increased value for the next time interval, with the additional finite region adjacent to the base taken at temperature T_0, and the computation is carried out for this interval. The procedure is carried out until results are obtained over a given time interval or until the steady state circumstance is obtained [20]. The corresponding initial and boundary conditions are

$$t=0:\ L(t)=0$$

$$t>0: \text{at } x=0,\ T=T_0;\ \text{at } x=L(t), -k\frac{\partial T}{\partial x}=h_L(T-Ta) \tag{38}$$

where h_L is the heat transfer coefficient at the end of the moving rod. The problem may be solved analytically [49] or numerically, with the latter approach more appropriate for two- and three-dimensional problems. As time increases, the length of the rod L increases and the temperature at the end decreases. At large time, a steady-state distribution arises over the rod and the temperature at the moving end reaches the ambient temperature. The problem may then be solved as a steady, continuously moving, infinite rod case.

Conjugate conditions are very frequently encountered in manufacturing processes like hot rolling, extrusion, metal forming and fiber drawing, which was discussed earlier. Conjugate conditions arise at the surface and the convective transport in the fluid must be solved in conjunction with conduction in the moving solid [117]. The region near the point of emergence of the material has large axial gradients and require the solution of the full equations. However, far downstream, the axial diffusion terms are small and a parabolic, marching, scheme may be adopted. This reduces the computational time, as compared to the solution of the elliptic problem over the entire computational domain. In continuous processing, interest lies in controlling the local and global processing of the material to obtain uniformity, high productivity, and desired product characteristics.

Figure 39 shows the typical streamlines for a plate moving in a quiescent medium. The ambient fluid is drawn toward the moving surface. Large pressure gradients directed towards the origin give rise to a small reverse flow in this region. Farther downstream, this effect dies down and the flow approaches the characteristics of a boundary-layer flow, with its thickness growing in the direction of motion. The inclusion of buoyancy effects due to a heated plate increases the maximum velocity in the boundary layer, beyond the plate speed U_s, if the buoyancy and the plate motion are both directed upward, as shown in the figure. This, in turn, increases the heat transfer from the plate. Similarly, other orientations have been investigated.

The time-dependent flow that arises at the initial stages of the process is also important. Figure 40 shows the numerical results for an aluminum plate moving vertically upward in water. A long plate is assumed to start moving at time $t=0$, when the upstream temperature is also raised to a temperature T_0 which is higher than the ambient temperature T_a. The flow is seen to start near the moving boundary due to the no-slip conditions. A recirculating flow region appears near the heated end, gradually moves downstream, and is finally swept away by the flow. The boundary layer thickness grows along the direction of motion. The heat transfer

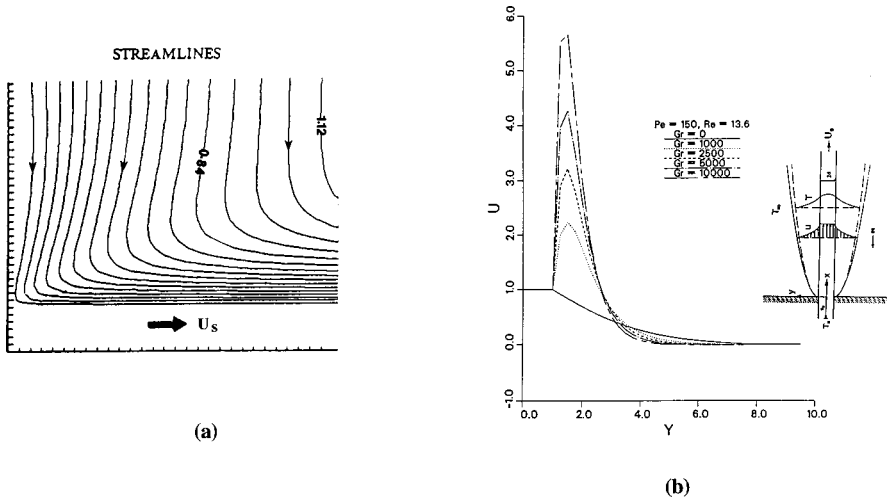

Fig. 39 (*a*) **Flow in the ambient fluid due to a continuously moving material;** (*b*) **dimensionless velocity** (u/U_s) **distribution in the fluid due to a vertically moving heated plate with aiding buoyancy effects**

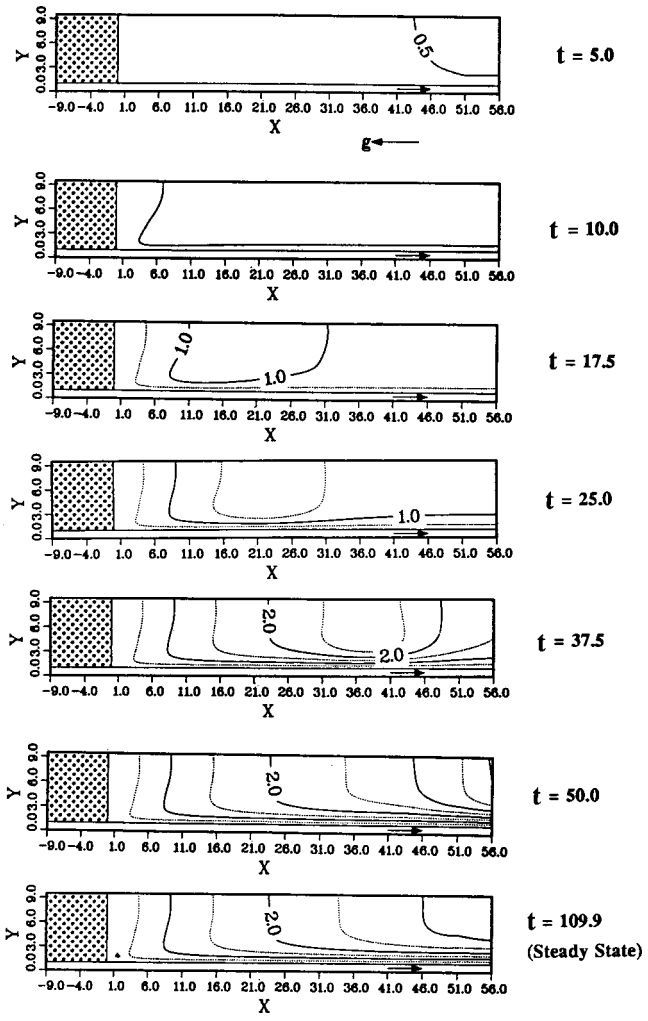

Fig. 40 Calculated time-dependent streamlines for a heated aluminum plate moving vertically in water at Pr=7.0, Re=25, and Gr=1000

coefficient from the plate was found to reach a minimum near the recirculation region. Local hot spots can thus arise in this region. Buoyancy effects were found to increase with time as the fluid temperature rises. Therefore, the transient flow and the heat transfer rates can be substantially different from steady state conditions which are eventually reached and which agree well with experimental results. Many different fluids, materials, and flow condi-

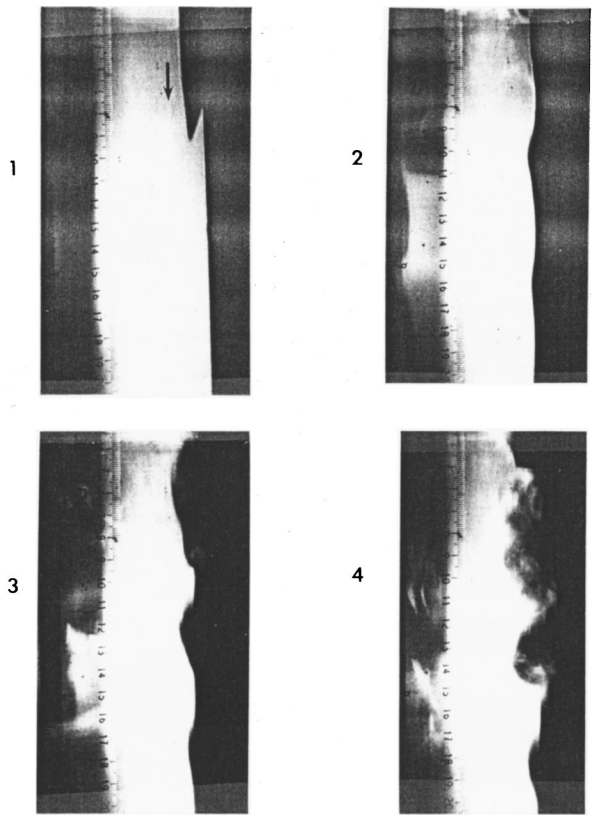

Fig. 41 Sequence of shadowgraph photographs showing the flow near the surface of an aluminum plate moving vertically downward in water at a speed of 3.7 cm/s, at Re=140.36 and $Gr/Re^2=0.45$

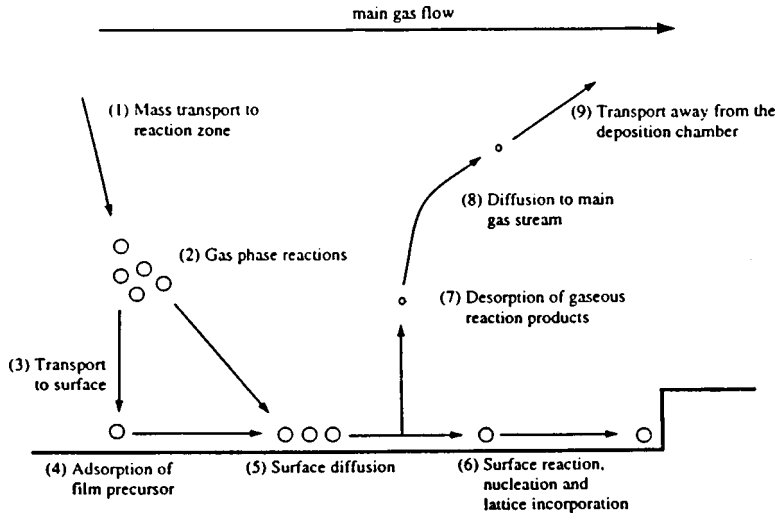

Fig. 42 Schematic of steps in a chemical vapor deposition process [34]

tions, including channel flows and the effect of buoyancy, have been considered for a wide variety of applications in materials processing [20].

A few experimental investigations have also been carried out on this problem and provide the results that can be used for the validation of the mathematical/numerical model [118–120]. Generally, good agreement has been obtained between numerical and analytical predictions and experimental results for a wide range of materials, geometries and speeds. However, the occurrence of instability, transition and turbulence at large speeds or at large temperature differences has been found to increase the difference between numerical and experimental results, indicating the need for better modeling of these flows. Figure 41 shows a sequence of shadowgraph photographs of the flow near the surface of an aluminum plate moving vertically downward. As time increases, a large disturbance leading to flow separation is seen to arise. The flow under consideration is an opposing buoyancy circumstance, which could lead to flow separation downstream [22]. The disturbance was found to remain largely at one location and not move downstream, indicating that the observed phenomenon is due to opposing buoyancy and not transient effects. The effect is governed by the local mixed convection parameter $\mathrm{Gr}_x/\mathrm{Re}_x^2 = g\beta\Delta Tx/\nu^2$, and the effect was found to be larger at larger values of this parameter. Such disturbances in the flow affect the local transport at the surface and thus the local characteristics of the product. It is important to understand and control these effects for better consistency in the processed material.

Summary. The flow is driven by forced flow mechanisms, due to the moving surface and external pressure field, as well as by buoyancy effects. Thus orientation and geometry are often important considerations in determining the flow. The flow field influences the thermal transport that can affect the local and average processing undergone by the material. Transient effects are important at the initial stages of the process and also if changes occur in the operating conditions.

Chemical Vapor Deposition. The deposition of thin films on- to a solid substrate has become an important technique for materials processing and is of interest in a wide variety of applications such as those involved with the fabrication of microelectronic circuits, optical and magnetic devices, high performance cutting and grinding tools, and solar cells. Though a relatively new method for materials processing, thin film deposition has attracted the interest of many researchers because of its relevance to many important areas, high quality of material generated, good control of the process and overall efficiency of the process.

Thin films are generally deposited from a gas phase onto a solid surface. A chemical reaction takes place during the deposition process and this is referred to as chemical vapor deposition (CVD). The products of the reactions form a solid crystalline or amorphous layer on the substrate. The activation energy needed for the numerous chemical reactions is provided by an external heat source. After material deposition on the surface, the byproducts of the reactions are removed by carrier gases [34]. The sequence of events involved in a CVD process are shown schematically in Fig. 42. Film thicknesses range from a few nanometers to tens of microns. The quality of the film deposited is characterized in terms of its purity, composition, thickness, adhesion, surface morphology and crystalline structure. The level of quality needed depends on the intended application, with electronic and optical materials imposing the most stringent demands. In order to improve the quality of the film deposited, it is necessary to understand the basic mechanisms that govern the access of the appropriate chemical species to the substrate. This in turn depends on the flow, the associated heat and mass transfer in the flow region and at the surface, and chemical reactions that arise. Large area

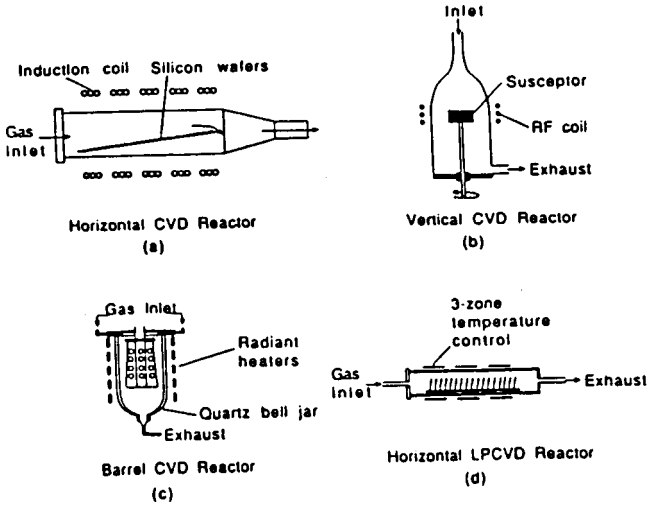

Fig. 43 Practical CVD reactor configurations: (*a*) horizontal reactor, (*b*) vertical reactor, (*c*) barrel reactor, (*d*) conventional multiple-wafer-in-tube low-pressure reactor [33]

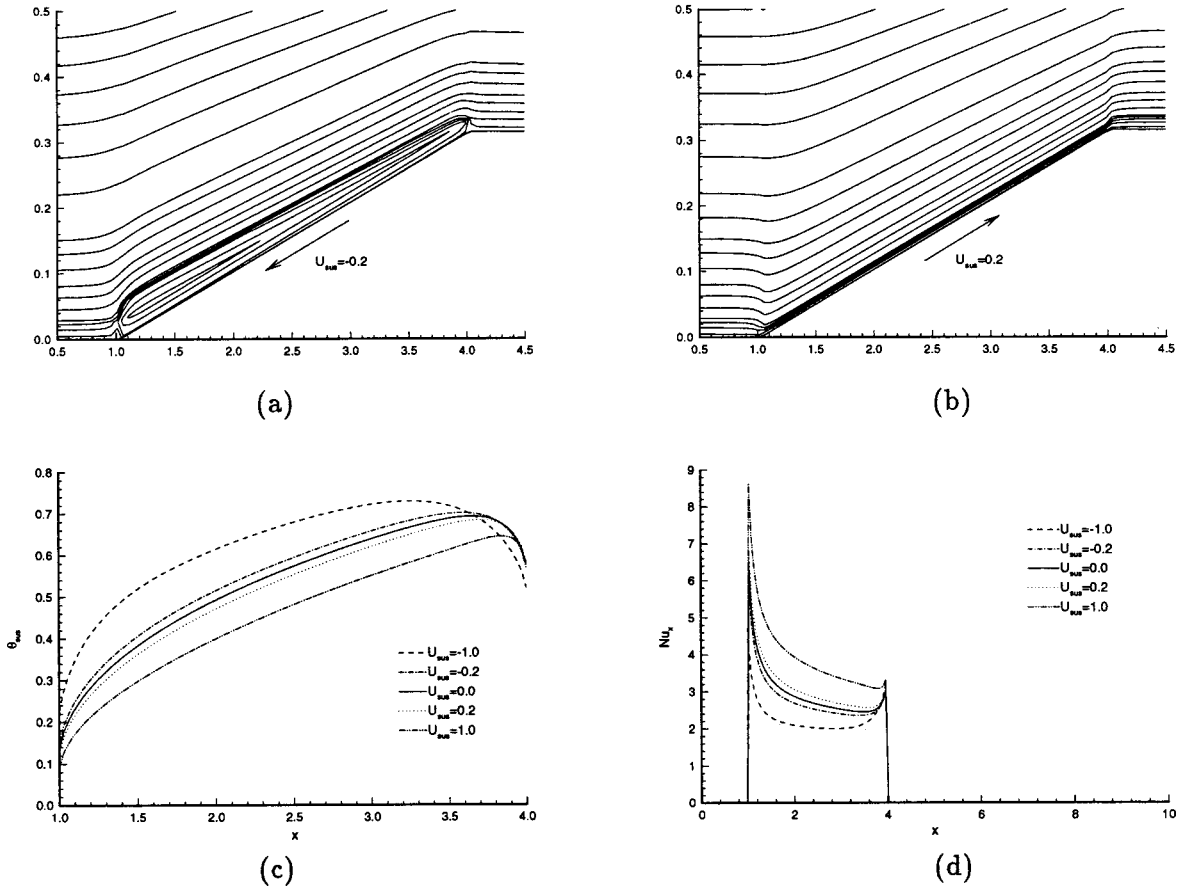

Fig. 44 Computed streamlines, temperature distribution, and Nusselt number for different values of dimensionless susceptor velocity U_{sus}

film thickness and composition uniformity are achieved by proper control of the governing transport processes [33,34].

Many different types of CVD reactors have been developed and applied for different applications. Most reactor configurations can be classified into two general classes; the horizontal and the vertical reactor. In the horizontal reactor, the heated susceptor on which deposition is to be obtained is placed at an angle to the incoming horizontal flow. The vertical flow reactor has the susceptor positioned perpendicular to the downward flow. Both types of reactors are commonly used. A few practical CVD reactor configurations are shown in Fig. 43. In most cases, a batch process is used, with the susceptor stationary or rotating, and after the process is completed the susceptor is removed and a new charge undertaken. Though much of the initial effort was directed at silicon deposition because of its relevance to the semiconductor industry, much of the recent interest is directed at the deposition of materials such as titanium nitride, silicon carbide, diamond, and metals like titanium, tungsten, aluminum, and copper.

The quality, uniformity, and rate of deposition are dependent on the fluid flow in a CVD reactor, on the heat and mass transfer, and on the chemical reactions that are themselves strongly influenced by temperature and concentration levels. Mahajan [34] has presented an excellent review on CVD for materials processing. The flow and heat transfer in CVD reactors were investigated by Evans and Greif [121], Fotiadis et al. [122] and Karki et al. [123]. These studies used numerical models based on parabolic governing equations along with experimental data to verify numerical predictions. Analytical models using similarity variables had been used in earlier work, followed by numerical models using boundary layer approximations. One and two dimensional studies were carried out by Fotiadis et al. [122] using finite element methods (FEM). This is appropriate for complex geometries encountered in some CVD processing systems. Rotating susceptor, three dimensional flow, and experimental measurements have also been considered in various investigations.

Figure 44 shows some typical results obtained with a moving susceptor by Chiu and Jaluria [124]. Both analysis and experimen-

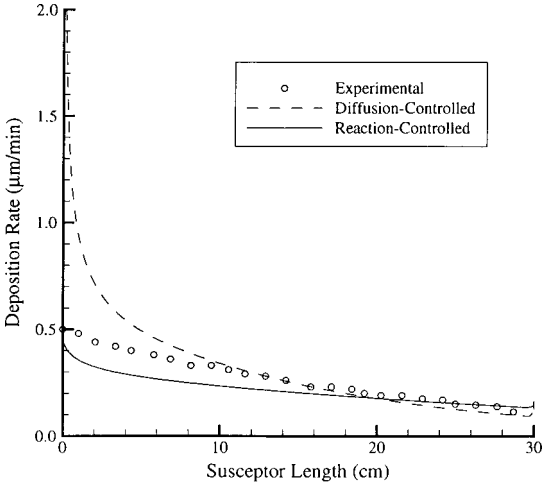

Fig. 45 Comparison between numerical predictions, using the diffusion-controlled approximation and the reaction-controlled chemical modeling, and experimental results of Eversteyn et al. [125]

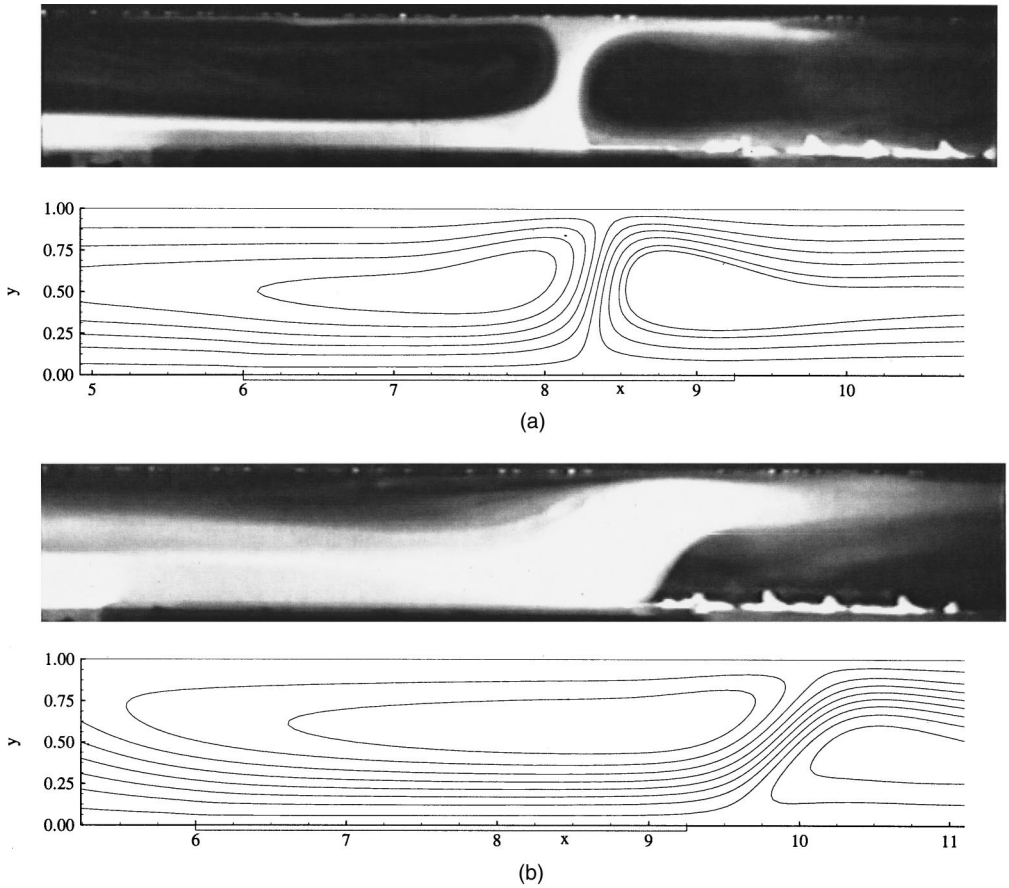

Fig. 46 Comparison between experimental observations and numerical predictions of streamlines at Re=9.48 and Re=29.7 for a ceramic susceptor

tal studies have indicated the feasibility of such continuous motion. Clearly, continuous processing is a very desirable feature since it will impact positively on production rates of the processed materials. It is seen that, at small susceptor speeds, the effect on the flow and the temperature field is relatively small, making it possible to use a continuous process. Also, the speed and direction of motion may be used advantageously to affect the film quality. Conjugate transport at the heated surface is also an important consideration, since in actual practice thermal energy is supplied to the susceptor, often at a constant rate, and the temperature distribution at the surface depends on the transport processes that arise. An isothermal condition is an idealization and is rarely obtained.

Experimental Results. Figure 45 shows a comparison between the silicon deposition rate computed using the chemical kinetics expression given by Eq. (17) with the measurements of Eversteyn et al. [125]. A fairly good agreement is observed. This model assumes chemical kinetics limited deposition. Similarly, a diffusion limited case was considered where the deposition is largely restricted by the transport process. A large discrepancy is seen near the susceptor's leading edge in this case. The reaction-controlled deposition model thus yields much better agreement with experimental results. The reaction-controlled deposition model accounts for the deposition rate dependence on temperature and species concentration at the deposition surface. Depending on the materials involved, the deposition characteristics may be taken as diffusion or kinetics limited. Of course, the problem is fairly complicated and the transport processes as well as the chemical reactions must be considered at the surface and in the gas phase to satisfactorily model the overall deposition process. Even though kinetics results are available for common materials like silicon, lack of accurate data for deposition of metals and other materials is a major problem in accurate prediction of the deposition rate.

Experimental studies have also been carried out on the flow in channels, such as those shown in Fig. 2(*e*), for CVD applications [33,126,127]. Predicted streamlines are compared to experimental observations in Fig. 46 for flow of air in a straight horizontal channel over a susceptor heated by a uniform heat flux source, for two flow rates. As the gas travels over the heated susceptor, gas heating gives rise to buoyancy effects. In the case of the lower Re, a plume develops above the susceptor. This flow pattern generates two transverse rolls, with their axis of rotation perpendicular to the flow direction. The upstream roll produces a recirculation region, while the downstream roll entrains flow from outside. These

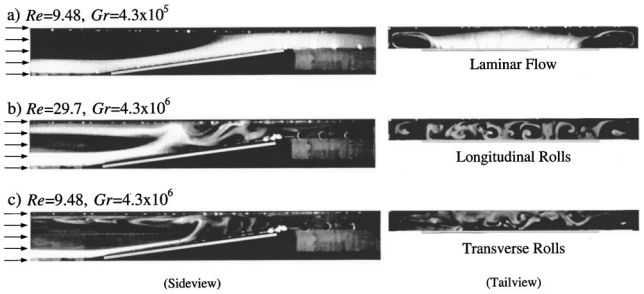

Fig. 47 Side view and tail view of the flow pattern in a converging channel with 8 deg tilt. Tail views are located at the end of the heated section with a light sheet oriented perpendicular to the main flow.

rolls can have significant effect on the deposition rate and film uniformity due to the convective displacement of reactants and effect on heat transfer rates. As Re is increased, the plume shifts downstream due to greater bulk gas flow. Consequently, the two transverse rolls become smaller and flow entrainment from the outside is reduced. The appearances of oscillatory flow, turbulent flow, transverse and longitudinal rolls are found to be dependent on the channel cross-sectional aspect ratio, flow rate and heating rate.

Significantly different flow regimes are observed when the same parametric space is examined for a converging channel with an 8 deg tilted heating section. The flow remains steady and laminar over a larger range of conditions, as compared to a straight channel, since the reduction in channel height increases the local gas velocity and diminishes the relative effect of the buoyancy force. When the flow rate and heating rate are increased, the transition to a new flow regime, composed of longitudinal rolls with the axis of rotation parallel to the main flow, occurs. The side view of this regime shows oscillatory flow. The tail view reveals the presence of rolls along the heated plate. These rolls are unsteady in nature and their presence promotes mixing within the channel. Buoyancy effects increase as Re is decreased or as Gr is increased, and a thermal plume appears above the heated plate, as shown in Fig. 47. The corresponding side view shows the breakup of longitudinal roll structures. When this condition occurs, the flow shifts to a regime dominated by transverse rolls. The plume generated above the heated plate creates an upstream transverse roll which is observed to be two-dimensional near the center of the channel. Near the exit, the flow structure breaks up into turbulent flow. The transition from longitudinal rolls to transverse rolls is defined by fitting a curve across the transition zone, yielding a critical mixed convection parameter of $Gr/Re^2=6000$. The effect on the temperature field and on the heat transfer is also studied. In the design of CVD reactors, entrainment at the exit and transverse rolls are undesirable. Flow entrainment introduces byproducts and other forms of contaminants onto the deposition surface, thereby lowering product quality. Rolls may act like stagnation zones, preventing the desired species from migrating to the deposition surface. These issues must be considered in detail when CVD reactors are designed.

Summary. The flow in the CVD reactor affects the temperature and concentration fields, which determine the local and average deposition rates. Instability and oscillations in the flow can affect the film quality, particularly its uniformity. The flow depends on the geometry, operating conditions like flow rate, temperature, and inlet species concentration, and the fluids involved. Detailed investigations are needed on the chemical kinetics, the associated flow and the resulting deposition for a variety of new and emerging materials.

Additional Flows. The preceding discussion has presented several important materials processing techniques and outlined the present state of the art in analysis, numerical simulation and experimentation of the fluid flows associated with these. However, as mentioned earlier, materials processing is a vast field and it is not possible to cover all the different techniques and systems used for fabricating new, advanced or traditional materials. The preceding discussion presents just a few important processes. There are many more processes in which fluid flow is of critical importance and which have seen intense research activity in recent years. Three such processes are outlined below to bring out some additional concerns and to link these with the flows considered earlier.

Crystal Growing. This is a very important area since most semiconductor devices are fabricated from single crystals grown from the vapor phase or from the melt. The former generally involves sublimation and chemical transport in a sealed enclosure [128]. The latter was mentioned earlier and sketches of two important techniques, Czochralski and floating zone, were shown in Fig. 2. Several other crystal growth techniques, such as Bridgman

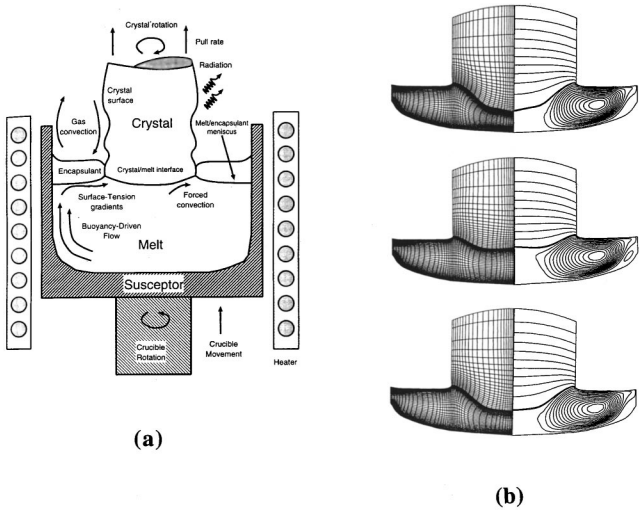

Fig. 48 (*a*) Schematic of the high-pressure liquid-encapsulated Czochralski crystal growing system; (*b*) grid distribution, flow field and melt-crystal interface at three instants of time showing strong oscillatory behavior which damps out at large time [130]

crystal growth in which the furnace has an upper zone at temperature above the melting point and a lower zone at temperature below the melting point, have been developed [47,129]. The Czochralski method has dominated the production of single crystals for microelectronics and has been the subject of considerable research interest [129,130]. The fluid flow phenomena involves buoyancy-driven convection due to temperature and concentration gradients, forced and mixed convection because of moving surfaces and materials, thermocapillary flows because of surface tension gradients, phase change, and thermal and mass transport processes. The main concerns are very similar to those in casting and other phase-change processes. The flow affects the quality of the crystal through oscillations, instability, effect on local and average transport rates, and distribution of impurities.

Though Silicon crystals have been of particular interest in the fabrication of electronic devices, there has been growing interest in GaAs, InP and other such compounds because of their use in various electro-optic applications. An encapsulant layer of a very viscous melt such as boric oxide is placed over the melt to curb escape of volatiles in these cases. Figure 48(*a*) shows a schematic of the high pressure liquid-encapsulated Czochralski process, indicating various mechanisms that arise [130, 131]. The flow in the melt arises under the combined effects of buoyancy, surface tension and rotation. Similar mechanisms arise for the process shown in Fig. 2(*a*). Several studies have considered these mechanisms separately, as well as together, to determine the dominant ones and to develop methods to control undesirable flow-induced effects. The flow due to the combined effects of these mechanisms is shown in Fig. 48(*b*), indicating oscillatory behavior of the flow and of the melt-crystal interface. Oscillations damp out at large time. However, at higher rotational speeds, the oscillatory behavior increases and the process is difficult to simulate due to thin boundary layers. An applied magnetic field has been found to suppress oscillations and result in a flat interface [130]. Various other aspects, such as three-dimensional effects, continuous growth system, thermal boundary conditions, and convection in high-pressure liquid-encapsulated Czochralski crystal growth, have been investigated.

Microgravity Materials Processing. Over the past two decades, there has been considerable interest in materials processing under microgravity conditions. Such an environment would be obtained, for instance, in laboratories orbiting in space and would

allow the processing of materials to be carried out with reduced effects of the terrestrial gravitational field. As discussed earlier, buoyancy-driven flows in the melt of a crystal growing system affect the quality and characteristics of the crystal by impacting on the solidification process, local transport rates and the nature of the liquid-solid interface. Similarly, gravity plays an important role in the shape of the meniscus in the fiber coating process and in the neck-down profile in optical fiber drawing. Thus, by controlling the gravitational force, we could influence the resulting flow and thus the process and the final product [132,133]. Consequently, substantial research effort is being directed in this area by NASA, the European Space Agency, and other space organizations.

The gravitational force is reduced to much smaller amounts in space. However, it is not zero and buoyancy-driven flows, though substantially reduced, are still present. Similarly, other effects due to gravity are present in reduced form. Also, several other effects and mechanisms that are relatively small on the Earth become much more important. These include thermocapillarity, orbital rotation which gives rise to the Coriolis force, disturbances and fluctuations. Detailed investigations have been carried out on thermocapillarity since this is often the dominant mechanism for flow under microgravity conditions. Attention has been directed at the resulting steady flows that would affect the solidification process and the solid-liquid interface. Since instabilities and oscillations are not desirable for a uniform, defect-free, crystal of high purity, extensive work has been done on the onset of instability, nature of oscillatory flows that arise and the different flow regimes that result for various governing parameters such as Prandtl, Marangoni, and Biot numbers [134–137]. The nature of flow under specified conditions, the critical Marangoni numbers, and the stability diagrams have been determined. Both numerical and experimental studies have been carried out, including experiments under microgravity. Many papers have focused their attention on crystal growing processes like floating zone and Czochralski methods. Many other aspects of materials processing under microgravity, such as bubble migration, film deposition and deforming interfaces, have also been investigated [138,139]. Such efforts continue and are expected to lead to a much better understanding of the fluid flow for materials processing under microgravity conditions.

Thermal Sprays. This is another area which has received considerable attention as a viable process for manufacturing near-net shape structured materials. Sprays containing droplets of the desired deposition material are directed at a chosen substrate and deposited by rapid solidification. The process is fast since many processing steps are eliminated and rapid solidification eliminates macro-segregation which weakens traditionally cast materials [140]. Superior properties associated with fine-grained microstructures and non-equilibrium phases are usually obtained. A wide variety of materials, such as aluminum, tin, and various alloys have been employed in the droplet-based manufacturing process. This process involves generating the droplets, the convective flow in the spraying process, droplet impact and deformation, and rapid solidification [140–144]. Plasma spraying is used for fabricating ceramics, particularly nanostructured ceramics, and various other materials [145,146].

Much of the effort in these and other papers has focused on rapid solidification because the properties of the final product are strongly dependent on this process. Various models have been developed and carefully conducted experimental data have been used for validating and improving the models. The impact of the droplet on the surface, its deformation and spread, and the solidification time are determined. The velocity field inside the spreading droplet is computed and the free surface is tracked. The solidification process is then treated with multi-dimensional models to determine pores, cavities and other defects. The stagnation-flow problem is investigated to model the spray and its impingement on a substrate, involving solidification of liquid in motion. In-flight behavior of droplets, particularly with respect to nucleation and solidification, are also considered. The overall problem is obviously very complicated since it involves complex flows with free boundaries, moving surfaces, phase change, and rapid changes with time. However, because of the advantages it offers in material fabrication, in terms of speed and quality, substantial research effort is directed at the thermal spray process at present.

System Simulation, Design and Optimization. Another important aspect that must be mentioned here is the numerical simulation of the overall system, since the process undergone by the material is a consequence of the flow and energy exchange with the various components of the system. The numerical simulation of the system refers to the use of the numerical model to obtain a quantitative representation of the physical system and to characterize its behavior for a given design or set of operating conditions and for variations in these. Consider, for instance, a typical electrical furnace, which consists of the heater, walls, insulation, inert gas environment and the material undergoing heat treatment. The transport mechanisms in all these components are coupled through the boundary conditions. The gas flow is driven by an externally imposed pressure difference, such as that due to a fan or a blower, by moving materials in continuous processing, and by buoyancy. Each individual component may first be numerically simulated as uncoupled from the others, by employing prescribed boundary conditions. Then, these individual simulations are combined, employing the appropriate coupling through the boundary conditions. This procedure provides a systematic approach to the numerical simulation of the system, which may be a simple one or a complicated practical one [23,43]. Once the simulation of the system is achieved, with satisfactory experimental validation, the design and optimization of the process as well as of the system may be undertaken. The results obtained from the simulation provide the necessary inputs for improving existing designs and developing new ones for improving the productivity and the product quality for a given manufacturing process [1].

Present State-of-the-Art

It is obvious from the preceding review that the fluid flow phenomena associated with a wide variety of materials processing techniques have been investigated in detail. Mathematical models of various complex circumstances that arise in materials processing have been developed and applied to practical systems and processes. Some of the common situations are:

1 Moving and free boundaries
2 Combined transport mechanisms
3 Conjugate conditions that couple different regions
4 Mechanisms occurring at different length and time scales
5 Flows with phase change and chemical reactions
6 Large material property changes
7 Non-Newtonian flows
8 Particulate flows

Though numerical approaches have been most extensively used to solve the governing equations, analytical solutions have also been obtained for certain simplified and idealized cases. These have been mainly used for validating numerical models and for providing physical insight into underlying mechanisms. Experimental results have also been obtained in a limited number of flows in order to validate the numerical models and to provide guidelines for model development by increasing the basic understanding of the process.

Much of the effort in this area has been directed at the numerical modeling and simulation of processing. Using advances in computational fluid dynamics, many specialized techniques have been developed to simulate the complexities that typically arise in materials processing. These include

1 Coordinate transformations for grid generation in complex domains
2 Coupling of different regions and mechanisms
3 Finite difference, finite element and other approaches
4 Simulation of deforming materials
5 Solution of inverse problems
6 Modeling complicated boundary conditions
7 Solution of time-dependent problems
8 Other complications mentioned earlier

Advantage has been taken of advances in computational hardware and software for visualization, improving accuracy, and for reducing computational storage and time. Similarly, experimental work has relied heavily on the techniques developed for flow visualization and measurement, such as laser Doppler anemometry, particle image velocimetry, infra-red, laser and video imaging, high-speed photography, as well as traditional methods of measuring flow, temperature, pressure and other variables. Specialized techniques for measuring, for instance, temperature and velocity in a rotating screw extruder, have been developed to investigate flow phenomena in materials processing. The preceding review has presented several analytical, numerical and experimental methods that have been employed to investigate these flows.

Future Research Needs

Our understanding of flow phenomena in materials processing has grown significantly over the last three decades. However, there are still many areas that need detailed and concentrated further investigation. These are considered in terms of separate categories in the following.

Critical Areas. The three main areas that are in critical need of further study are:

1. *Material properties*. In many of the simulations and experiments, the material properties available in the literature have been used. Frequently, data are available only under standard conditions, even though the processes occur at much higher temperature and pressure. Equations for chemical kinetics are often not available or only a few data points are available. Therefore, the measurement and availability of accurate material properties are crucial to a study in this area.

2. *Experimentation*. It has been mentioned that experimental results are very sparse because of the time and effort needed for accurate data. However, experiments are strongly needed for validation of models and for providing inputs and insight for future model development.

3. *Coupling of micro/macro scales*. It is very important to satisfactorily link the transport mechanisms at the microscale where material processing generally occurs with those at the macro or engineering scale where the appropriate boundary conditions are imposed. A few studies have considered this aspect, as mentioned earlier. But much more needs to be done in order to link material quality with the operating and design conditions.

Additional Topics. Besides these three major areas that need further investigation, work is needed on several other topics. Some of the main ones are:

1 New and innovative experimental techniques for realistic materials which are often opaque and for measurements under high temperature and pressure.

2 Numerical techniques for very large material property changes and for coupling the transport equations with the chemical kinetics which may involve several different reactions, with different reaction rates, activation energy, and other constants.

3 Flow circumstances involving complex materials such as powders, particulates, granules, and highly porous materials.

4 Accurate numerical modeling of combined mechanisms, multiple domains, multiphase flows, and conjugate conditions.

5 Instability of the process due to underlying flow instability mechanisms. Effect of these instabilities on process feasibility.

6 Characteristics of free surfaces and interfaces.

7 Effect of flow on product characteristics and thus on the operation and optimization of the process and system.

8 Development of new products, processes and systems on the basis of underlying fluid phenomena.

Important Processes for Future Study. Several important materials processing techniques and systems have been considered in this review and their future reseach needs have been outlined. However, there are many others that need careful detailed investigation because of their growing importance. Some of the important processes that are expected to be important in the future and that should be targeted for research are:

1 Chemical reaction based processing
2 Biological systems and biomaterials
3 Droplet-based manufacturing: rapid solidification, thermal and plasma sprays
4 Advanced polymers and composites
5 Crystal growth
6 Space-based materials processing
7 High speed coating
8 Processing of ceramics, glass, nanostructured ceramics
9 Laser processing
10 Solidification of alloys and mixtures
11 Power processing

Concluding Remark

Finally, It must be stressed that fluids engineering research can impact on the growing and important field of materials processing only if significant effort is also directed at understanding the basic mechanisms and processes that govern changes in the material. It is not enough to use available kinetics or information on material behavior to model the relevant fluid flow phenomena. One must understand how the observed phenomena affect the material properties, structure and characteristics. This makes the study of fluid flow phenomena in materials processing challenging, interesting and useful.

Acknowledgments

This review was made possible by the Freeman Scholar Program in Fluids Engineering of ASME. The author is grateful to the Program and the Standing Committee of C. T. Crowe (Chair), R. A. Bajura and M. L. Billet for providing him this opportunity. The support of the National Science Foundation, of the industry, and of the New Jersey Commission on Science and Technology through various Centers for much of the work reported here and for the preparation of this paper is gratefully acknowledged. The author also acknowledges the work done by several students, as referenced here, that made it possible to present this review. Figure 6 was provided by Prof. S. Kou and is gratefully acknowledged.

Nomenclature

b, b_m, B = constants, Eqs. (20), (22), and (23)
Bi = Biot number, $\mathrm{Bi} = hL/k_s$
c_m = species concentration
C = specific heat
C_p = specific heat at constant pressure
$\underline{e}$ = unit vector in the direction of gravitational force
E = activation energy
Ec = Eckert number, Eq. (35)
f_1 = liquid mass fraction
$F(t)$ = cumulative residence time function, Eq. (37)
$\underline{F}$ = body force vector
g = magnitude of gravitational acceleration
Gr = Grashof number, Eq. (35)
h = convective heat transfer coefficient
H = enthalpy

H^o = enthalpy at 0 K
$\underline{i}$ = unit vector in x-direction
k = thermal conductivity
K = bulk viscosity, reaction rate
K_c = consistency index for non-Newtonian fluid, Eq. (19)
L = characteristic length
L_h = latent heat of fusion
$\dot{m}$ = mass flow rate
Ma = Marangoni number
n = power-law fluid index
N = speed in revolutions/min (rpm)
p = local pressure
p_a = hydrostatic pressure
p_d = dynamic pressure due to fluid motion
Pr = Prandtl number, Eq. (35)
q = heat flux
q_v = dimensionless volume flow rate in an extruder
Q = volumetric source
R = universal gas constant, radius
Re = Reynolds number, Eq. (35)
Sr = Strouhal number, Eq. (35)
t = time
T = temperature
u,v,w = velocity components in x, y, and z directions, respectively
U, $\underline{U_S}$ = speed of a moving solid or source
V = velocity vector
We = Weber number
$\tilde{x}$ = position vector
x, y, z = coordinate distances
X,Y,Z = dimensionless coordinate distances

Greek Symbols

α = thermal diffusivity
β = coefficient of thermal expansion
$\dot{\gamma}$ = strain rate
δ = location of interface between solid and liquid
ε = surface emissivity
λ = second viscosity coefficient
μ = dynamic viscosity of fluid
ν = kinematic viscosity
Φ = viscous dissipation function
ρ = density
σ = surface tension
θ = dimensionless temperature
τ = shear stress

Subscripts

a = ambient
b = barrel, wall
i = initial, inlet
l = liquid
m = melting point
o = reference
s = solid, surface

References

[1] Jaluria, Y., 1998, *Design and Optimization of Thermal Systems*, McGraw-Hill, New York.
[2] Doyle, L. E., Keyser, C. A., Leach, J. L., Scharder, G. F., and Singer, M. B., 1987, *Manufacturing Processes and Materials for Engineers*, Prentice-Hall, Englewood Cliffs, NJ.
[3] Schey, J. A., 1987, *Introduction to Manufacturing Processes*, 2nd Ed., McGraw-Hill, New York.
[4] Kalpakjian, S., 1989, *Manufacturing Engineering and Technology*, Addison-Wesley, Reading, MA.
[5] Szekely, J., 1979, *Fluid Flow Phenomena in Metals Processing*, Academic Press, New York.
[6] Ghosh, A., and Mallik, A. K., 1986, *Manufacturing Science*, Ellis Horwood, Chichester, U.K.
[7] Avitzur, B., 1968, *Metal Forming: Processes and Analysis*, McGraw-Hill, New York.
[8] Altan, T., Oh, S. I., and Gegel, H. L., 1971, *Metal Forming: Fundamentals and Applications*, Amer. Soc. Metals, Metals Park, OH.
[9] Fenner, R. T., 1979, *Principles of Polymer Processing*, Chemical Publishing, New York.
[10] Easterling, K., 1983, *Introduction to Physical Metallurgy of Welding*, Butterworths, London, U.K.
[11] Hughel, T. J., and Bolling, G. F., eds., 1971, *Solidification*, Amer. Soc. Metals, Metals Park, OH.
[12] Kuhn, H. A., and Lawley, A., eds., 1978, *Powder Metallurgy Processing, New Techniques and Analysis*, Academic Press, New York.
[13] Chen, M. M., Mazumder, J., and Tucker, C. L., eds., 1983, ''*Transport Phenomena in Materials Processing*,'' HTD Vol. 29, Amer. Soc. Mech. Engrs., New York.
[14] Li, T., ed., 1985, *Optical Fiber Communications, Vol. 1: Fiber Fabrication*, Academic Press, New York.
[15] Poulikakos, D., ed., 1996, *Transport Phenomena in Materials Processing*, Adv. Heat Transfer, Academic Press, San Diego, CA **18**.
[16] Viskanta, R., 1988, ''Heat Transfer During Melting and Solidification of Metals,'' ASME J. Heat Transfer, **110**, pp. 1205–1219.
[17] Lee, S. H.-K., and Jaluria, Y., 1996, ''Effect of Variable Properties and Viscous Dissipation During Optical Fiber Drawing,'' ASME J. Heat Transfer, **118**, pp. 350–358.
[18] Lee, S. H.-K., and Jaluria, Y., 1996, ''Simulation of the Transport Processes in the Neck-Down Region of the Furnace Drawn Optical Fiber,'' Int. J. Heat Mass Transf., **40**, pp. 843–856.
[19] Jaluria, Y., 1996, ''Heat and Mass Transfer in the Extrusion of Non-Newtonian Materials,'' Adv. Heat Transfer, **28**, pp. 145–230.
[20] Jaluria, Y., 1992, ''Transport from Continuously Moving Materials Undergoing Thermal Processing,'' Annu. Rev. Heat Transfer, **4**, pp. 187–245.
[21] Jaluria, Y., 1980, *Natural Convection Heat and Mass Transfer*, Pergamon Press, Oxford, UK.
[22] Gebhart, B., Jaluria, Y., Mahajan, R. L., and Sammakia, B., 1988, *Buoyancy-Induced Flows and Transport*, Taylor and Francis, Philadelphia, PA.
[23] Jaluria, Y., and Torrance, K. E., 1986, *Computational Heat Transfer*, Taylor and Francis, Philadelphia, PA.
[24] Ramachandran, N., Gupta, J. P., and Jaluria, Y., 1982, ''Thermal and Fluid Flow Effects During Solidification in a Rectangular Enclosure,'' Int. J. Heat Mass Transf., **25**, pp. 187–194.
[25] Bennon, W. D., and Incropera, F. P., 1988, ''Developing Laminar Mixed Convection with Solidification in a Vertical Channel,'' ASME J. Heat Transfer, **110**, pp. 410–415.
[26] Viswanath, R., and Jaluria, Y., 1993, ''A Comparison of Different Solution Methodologies for Melting and Solidification Problems in Enclosures,'' Numer. Heat Transfer, Part B, **24B**, pp. 77–105.
[27] Prescott, P. J., and Incropera, F. P., 1996, ''Convection Heat and Mass Transfer in Alloy Solidification,'' Adv. Heat Transfer, **28**, pp. 231–338.
[28] Harper, J. M., 1981, *Extrusion of Foods: Volume I*, CRC Press, Boca Raton, FL.
[29] Kokini, J. L., Ho, C.-T., and Karwe, M. V., eds., 1992, *Food Extrusion Science and Technology*, Marcel Dekker, New York.
[30] Wang, S. S., Chiang, C. C., Yeh, A. I., Zhao, B., and Kim, I. H., 1989, ''Kinetics of Phase Transition of Waxy Corn Starch at Extrusion Temperatures and Moisture Contents,'' J. Food. Sci., **54**, pp. 1298–1301.
[31] Abib, A. H., Jaluria, Y., and Chiruvella, R. V., 1993, ''Thermal Processing of Food Materials in a Single Screw Extruder,'' *Heat Transfer in Food Processing*, ASME Heat Transfer Div., Vol. 254, ASME, New York, pp. 57–67.
[32] Chiruvella, R. V., Jaluria, Y., and Karwe, M. V., 1996, ''Numerical Simulation of Extrusion Cooking of Starchy Materials,'' J. Food. Eng., **30**, pp. 449–467.
[33] Jensen, K. F., Einset, E. O., and Fotiadis, D. I., 1991, ''Flow Phenomena in Chemical Vapor Deposition of Thin Films,'' Annu. Rev. Fluid Mech., **23**, pp. 197–232.
[34] Mahajan, R. L., 1996, ''Transport Phenomena in Chemical Vapor-Deposition Systems,'' Adv. Heat Transfer, **28**, pp. 339–425.
[35] Jensen, K. F., and Graves, D. B., 1983, ''Modeling and Analysis of Low Pressure CVD Reactors,'' J. Electrochem. Soc., **130**, pp. 1950–1957.
[36] Jaluria, Y., 1996, *Computer Methods for Engineering*, Taylor and Francis, Washington, DC.
[37] Chiu, W. K.-S., Jaluria, Y., and Glumac, N. C., 2000, ''Numerical Simulation of Chemical Vapor Deposition Processes Under Variable and Constant Property Approximations,'' Numer. Heat Transfer, **37**, pp. 113–132.
[38] Tadmor, Z., and Gogos, C., 1979, *Principles of Polymer Processing*, Wiley, New York.
[39] Pearson, J. R. A., and Richardson, S. M., eds., 1983, *Computational Analysis of Polymer Processing*, Appl. Sci. Pub., London, UK.
[40] Karwe, M. V., and Jaluria, Y., 1990, ''Numerical Simulation of Fluid Flow and Heat Transfer in a Single-Screw Extruder for Non-Newtonian Fluids,'' Numer. Heat Transfer, **17**, pp. 167–190.
[41] Choudhury, S. Roy, Jaluria, Y., and Lee, S. H.-K., 1999, ''Generation of neck-down profile for furnace drawing of optical fiber,'' Numer. Heat Transfer, **35**, pp. 1–24.
[42] Jaluria, Y., 1976, ''Temperature Regulation of a Plastic-Insulated Wire in Radiant Heating,'' ASME J. Heat Transfer, **98**, pp. 678–680.
[43] Jaluria, Y., 1988, ''Numerical Simulation of the Transport Processes in a Heat Treatment Furnace,'' Int. J. Numer. Methods Eng., **25**, pp. 387–399.
[44] Siegel, R., 1978, ''Shape of Two-Dimensional Solidification Interface During

Directional Solidification by Continuous Casting,'' ASME J. Heat Transfer, **100**, pp. 3–10.
[45] Siegel, R., 1984, ''Two-Region Analysis of Interface Shape in Continuous Casting with Superheated Liquid,'' ASME J. Heat Transfer, **106**, pp. 506–511.
[46] Chu, T. Y., 1975, ''A Hydrostatic Model of Solder Fillets,'' The Western Electric Engineer, **19**, No. 2, pp. 31–42.
[47] Kou, S., 1996, *Transport Phenomena and Materials Processing*, Wiley, New York.
[48] Jaluria, Y., and Singh, A. P., 1983, ''Temperature Distribution in a Moving Material Subjected to Surface Energy Transfer,'' Comput. Methods Appl. Mech. Eng., **41**, pp. 145–157.
[49] Choudhury, S. Roy, and Jaluria, Y., 1994, ''Analytical Solution for the Transient Temperature Distribution in a Moving Rod or Plate of Finite Length with Surface Heat Transfer,'' Int. J. Heat Mass Transf., **37**, pp. 1193–1205.
[50] Kwon, T. H., Shen, S. F., and Wang, K. K., 1986, ''Pressure Drop of Polymeric Melts in Conical Converging Flow: Experiments and Predictions'' Polym. Eng. Sci., **28**, pp. 214–224.
[51] Lin, P., and Jaluria, Y., 1997, ''Conjugate Transport in Polymer Melt Flow Through Extrusion Dies,'' Polym. Eng. Sci., **37**, pp. 1582–1596.
[52] Patankar, S. V., 1980, *Numerical Heat Transfer and Fluid Flow*, Taylor and Francis, Philadelphia, PA.
[53] Mallinson, G. D., and de Vahl Davis, G., 1973, ''The Method of False Transient for the Solution of Coupled Elliptic Equations,'' J. Comput. Phys., **12**, pp. 435–461.
[54] Leonard, B. P., 1997, ''Bounded Higher-Order Upwind Multidimensional Finite-Volume Convection-Diffusion Algorithms,'' *Advances in Numerical Heat Transfer*, Minkowycz, W. J. and Sparrow, E. M., eds., Vol. 1, Taylor and Francis, Philadelphia, PA, pp. 1–57.
[55] Peaceman, D. W., and Rachford, H. H., 1955, ''Numerical Solution of Parabolic and Elliptic Differential Equations,'' J. Soc. Ind. Appl. Math., **3**, pp. 28–41.
[56] Acharya, S., 1994, ''Solution-Adaptive Techniques in Computational Heat Transfer and Fluid Flow,'' Springer, Heidelberg, Germany **14**, pp. 447–467.
[57] Sastrohartono, T., Esseghir, M., Kwon, T. H., and Sernas, V., 1990, ''Numerical and Experimental Studies of the Flow in the Nip Region of a Partially Intermeshing Co-Rotating Twin Screw Extruder,'' Polym. Eng. Sci., **30**, pp. 1382–1398.
[58] Sastrohartono, T., and Kwon, T. H., 1990, ''Finite Element Analysis of Mixing Phenomena in Tangential Twin Screw Extruders for Non-Newtonian Fluids,'' Int. J. Numer. Methods Eng., **30**, pp. 1369–1383.
[59] Kwon, T. H., Joo, J. W., and Kim, S. J., 1994, ''Kinematics and Deformation Characteristics as a Mixing Measure in the Screw Extrusion Process,'' Polym. Eng. Sci., **34**, pp. 174–189.
[60] Kalyon, D. M., Gotsis, A. D., Yilmazer, U., Gogos, C., Sangani, H., Aral, B., and Tsenoglou, C., 1988, ''Development of Experimental Techniques and Simulation Methods to Analyze Mixing in Co-Rotating Twin Screw Extrusion,'' Adv. Polym. Technol., **8**, pp. 337–353.
[61] Rauwendaal, C., 1986, *Polymer Extrusion*, Hanser Pub., New York.
[62] Esseghir, M., and Sernas, V., 1991, ''A Cam-Driven Probe for Measurement of the Temperature Distribution in an Extruder Channel,'' *SPE ANTEC Tech. Papers*, Vol. 37, pp. 54–57.
[63] Esseghir, M., and Sernas, V., 1992, ''Experiments on a Single Screw Extruder with a Deep and Highly Curved Screw Channel,'' *Food Extrusion Science and Technology*, J. L. Kokini, C. T. Ho, and M. V. Karwe, eds., Marcel Dekker, New York, pp. 21–40.
[64] Sastrohartono, T., Jaluria, Y., Esseghir, M., and Sernas, V., 1995, ''A Numerical and Experimental Study of Three-Dimensional Transport in the Channel of an Extruder for Polymeric Materials,'' Int. J. Heat Mass Transf., **38**, pp. 1957–1973.
[65] Wang, Y., and White, J. L., 1989, ''Non-Newtonian Flow Modeling in the Screw Region of an Intermeshing Co-rotating Twin Screw Extruder,'' J. Non-Newtonian Fluid Mech., **32**, pp. 19–38.
[66] Kwon, G. H., Jaluria, Y., Karwe, M. V., and Sastrohartono, T., 1991, ''Numerical Simulation of the Transport Processes in a Twin screw Polymer Extruder,'' *Prog. Modeling Polymer Processing*, A. I. Isayev, ed., Ch. 4, Hanser Pub., New York, pp. 77–115.
[67] Sastrohartono, T., Jaluria, Y., and Karwe, M. V., 1994, ''Numerical Coupling of Multiple Region Simulations to Study Transport in a Twin Screw Extruder,'' Numer. Heat Transfer, **25**, pp. 541–557.
[68] Chiruvella, R. V., Jaluria, Y., Karwe, M. V., and Sernas, V., 1996, ''Transport in a Twin-Screw Extruder for the Processing of Polymers,'' Polym. Eng. Sci., **36**, pp. 1531–1540.
[69] Zhu, W., and Jaluria, Y., 2001, ''Transport Processes and Feasible Operating Domain in a Twin-Screw Polymer Extruder,'' Polym. Eng. Sci., **41**, pp. 107–117.
[70] Karwe, M. V., and Sernas, V., 1996, ''Application of Laser Doppler Anemometry to Measure Velocity Distribution Inside the Screw Channel of a Twin Screw Extruder,'' Journal of Food Process Engineering, **19**, pp. 135–152.
[71] Bakalis, S., and Karwe, M. V., 1997, ''Velocity Field in a Twin Screw Extruder'' Int. J. Food Sci. Technol., **32**, pp. 241–253.
[72] Jaluria, Y., Liu, Y., and Chiruvella, R. V., 1999, ''Modeling and Simulation of the Solids Conveying and Unfilled Regions in Polymer Extrusion,'' J. Reinf. Plast. Compos., **18**, pp. 15–26.
[73] Yin, Z., and Jaluria, Y., 1997, ''Zonal Method to Model Radiative Transport in an Optical Fiber Drawing Furnace,'' ASME J. Heat Transfer, **119**, pp. 597–603.
[74] Paek, U. C., 1999, ''Free Drawing and Polymer Coating of Silica Glass Optical Fibers,'' ASME J. Heat Transfer, **121**, pp. 775–788.
[75] Goren, S. L., and Wronski, S., 1966, ''The Shape of Low-Speed Jets of Newtonian Liquids,'' J. Fluid Mech., **25**, pp. 185–198.
[76] Nickell, R. E., Tanner, R. I., and Caswell, B., 1974, ''The Solution of Viscous Incompressible Jet and Free-Surface Flows using Finite-Element Methods,'' J. Fluid Mech., **65**, pp. 189–206.
[77] Lewis, J. A., 1977, ''The Collapse of a Viscous Tube,'' J. Fluid Mech., **81**, pp. 129–135.
[78] Gifford, W. A., 1982, ''A Finite Element Analysis of Isothermal Fiber Formation,'' Phys. Fluids, **25**, pp. 219–225.
[79] Levich, V. G., and Krylov, V. S., 1969, ''Surface-Tension Driven Phenomena,'' Annu. Rev. Fluid Mech., **1**, pp. 293–316.
[80] Dianov, E. M., Kashin, V. V., Perminov, S. M., Perminova, V. N., Rusanov, S. Y., and Sysoev, V. K., 1988, ''The Effect of Different Conditions on the Drawing of Fibers from Preforms,'' Glass Technol., **29**, No. 6, pp. 258–262.
[81] Choudhury, S. Roy, and Jaluria, Y., 1998, ''Practical Aspects in the Thermal Transport During Optical Fiber Drawing,'' J. Mater. Res., **13**, pp. 483–493.
[82] Yin, Z., and Jaluria, Y., 2000, ''Neck Down and Thermally Induced Defects in High Speed Optical Fiber Drawing,'' ASME J. Heat Transfer, **122**, pp. 351–362.
[83] Paek, U. C., and Runk, R. B., 1978, ''Physical Behavior of the Neck-down Region during Furnace Drawing of Silica Fibers,'' J. Appl. Phys., **49**, pp. 4417–4422.
[84] Paek, U. C., Schroeder, C. M., and Kurkjian, C. R., 1988, ''Determination of the Viscosity of High Silica Glasses During Fibre Drawing,'' Glass Technol., **29**, No. 6, pp. 263–266.
[85] Issa, J., Yin, Z., Polymeropoulos, C. E., and Jaluria, Y., 1996, ''Temperature Distribution in an Optical Fiber Draw Tower Furnace,'' J. Mater. Process. Manuf. Sci., **4**, pp. 221–232.
[86] Liu, Y., and Polymeropoulos, C. E., 1998, ''Measurement and Prediction of Thermocouple Probe Temperatures Within Glass Rods Subjected to Radiative Heating,'' *Proc. 11th Int. Heat Transfer Conf.*, Kyongju, Korea, Taylor and Francis, Philadelphia, Vol. 4, pp. 27–32.
[87] Christodoulou, K. N., and Scriven, L. E., 1989, ''The Fluid Mechanics of Slide Coating,'' J. Fluid Mech., **208**, pp. 321–354.
[88] Dussan, E. B., Rame, E., and Garoff, S., 1991, ''On Identifying the Appropriate Boundary Conditions at a Moving Contact Line: an Experimental Investigation,'' J. Fluid Mech., **230**, pp. 97–116.
[89] Chen, Q., Rame, E., and Garoff, S., 1997, ''The Velocity Field Near Moving Contact Lines,'' J. Fluid Mech., **337**, pp. 49–66.
[90] Quere, D., 1999, ''Fluid Coating on a Fiber,'' Annu. Rev. Fluid Mech., **31**, pp. 347–384.
[91] Blyler, L. L., and DiMarcello, F. V., 1980, ''Fiber Drawing, Coating and Jacketing,'' *Proc. IEEE*, **68**, pp. 1194–1198.
[92] Paek, U. C., 1986, ''High Speed High Strength Fiber Coating,'' J. Lightwave Technol., **LT-4**, pp. 1048–1059.
[93] Simpkins, P., and Kuck, V., 2000, ''Air Entrapment in Coatings Via Tip Streaming Meniscus,'' Nature (London), **403**, pp. 641–643.
[94] Ravinutala, S., Rattan, K., Polymeropoulos, C., and Jaluria, Y., 2000, ''Dynamic Menisci in a Pressurized Fiber Applicator,'' *Proc. 49th Int. Wire Cable Symp.*, Atlantic City, NJ.
[95] Abraham, A., and Polymeropoulos, C. E., 1999, ''Dynamic Menisci on Moving Fibers,'' *Proc. 48th Int. Wire Cable Symp.*, Atlantic City, NJ.
[96] Vaskopulos, T., Polymeropoulos, C. E., and Zebib, A., 1995, ''Cooling of Optical Fibers in Aiding and Opposing Forced Gas Flow,'' Int. J. Heat Mass Transf., **18**, pp. 1933–1944.
[97] Hanafusa, H., Hibino, Y., and Yamamoto, F., 1985, ''Formation Mechanism of Drawing-Induced E' Centers in Silica Optical Fibers,'' J. Appl. Phys., **58**, No. 3, pp. 1356–1361.
[98] Hibino, Y., Hanafusa, H., and Sakaguchi, S., 1985, ''Formation of Drawing-Induced E' Centers in Silica Optical Fibers,'' Jpn. J. Appl. Phys., **24**, No. 9, pp. 1117–1121.
[99] Flemings, M. C., 1974, *Solidification Processing*, McGraw-Hill, New York.
[100] Viskanta, R., 1985, ''Natural Convection in Melting and Solidification,'' *Natural Convection: Fundamentals and Applications*, S. Kakac, W. Aung, and R. Viskanta, eds., Hemisphere Pub. Co., Washington, DC, pp. 845–877.
[101] Huppert, H. E., 1990, ''The Fluid Mechanics of Solidification,'' J. Fluid Mech., **212**, pp. 209–240.
[102] Davis, S. H., 1990, ''Hydrodynamic Interactions in Directional Solidification,'' J. Fluid Mech., **212**, pp. 241–262.
[103] Prescott, P. J., and Incropera, F. P., 1996, ''Convection Heat and Mass Transfer in Alloy Solidification,'' Adv. Heat Transfer, **28**, pp. 231–338.
[104] Sparrow, E. M., Patankar, S. V., and Ramadhyani, S., 1977, ''Analysis of Melting in the Presence of Natural Convection in the Melt Region,'' ASME J. Heat Transfer, **99**, pp. 520–526.
[105] Voller, V. R., 1997, ''An Overview of Numerical Methods for Solving Phase Change Problems,'' *Advances in Numerical Heat Transfer*, Minkowycz, W. J., and Sparrow, E. M., eds., Vol. 1, Taylor and Francis, Philadelphia, PA, pp. 341–380.
[106] Viswanath, R., and Jaluria, Y., 1995, ''Numerical Study of Conjugate Transient Solidification in an Enclosed Region,'' Numer. Heat Transfer, **27**, pp. 519–536.
[107] Banaszek, J., Jaluria, Y., Kowalewski, T. A., and Rebow, M., 1999, ''Semi-implicit FEM Analysis of Natural Convection in Freezing Water,'' Numer. Heat Transfer, **36**, pp. 449–472.
[108] Bathelt, A. G., Viskanta, R., and Leidenfrost, W., 1979, ''An Experimental

Investigation of Natural Convection in the Melted Region Around a Heated Horizontal Cylinder,'' J. Fluid Mech., **90**, pp. 227–240.
[109] Gau, C., and Viskanta, R., 1986, ''Melting and Solidification of a Pure Metal on a Vertical Wall,'' ASME J. Heat Transfer, **108**, pp. 174–181.
[110] Wolff, F., and Viskanta, R., 1987, ''Melting of a Pure Metal from a Vertical Wall,'' Exp. Heat Transfer, **1**, pp. 17–30.
[111] Wolff, F., and Viskanta, R., 1988, ''Solidification of a Pure Metal at a Vertical Wall in the Presence of Liquid Superheat,'' Int. J. Heat Mass Transf., **31**, pp. 1735–1744.
[112] Thompson, M. E., and Szekely, J., 1988, ''Mathematical and Physical Modeling of Double-Diffusive Convection of Aqueous Solutions Crystallizing at a Vertical Wall,'' J. Fluid Mech., **187**, pp. 409–433.
[113] Beckermann, C., and Wang, C. Y., 1995, ''Multiphase/-Scale Modeling of Alloy Solidification,'' Annu. Rev. Heat Transfer, **6**, pp. 115–198.
[114] Wang, C. Y., and Beckermann, C., 1993, ''A Unified Solute Diffusion Model for Columnar and Equiaxed Dendritic Alloy Solidification,'' Mater. Sci. Eng., **A171**, pp. 199–211.
[115] Kang, B. H., and Jaluria, Y., 1993, ''Thermal Modeling of the Continuous Casting Process,'' J. Thermophys. Heat Transfer, **7**, pp. 139–147.
[116] Lin, P., and Jaluria, Y., 1997, ''Heat Transfer and Solidification of Polymer Melt Flow in a Channel,'' Polym. Eng. Sci., **37**, pp. 1247–1258.
[117] Kang, B. H., Jaluria, Y., and Karwe, M. V., 1991, ''Numerical Simulation of Conjugate Transport from a Continuous Moving Plate in Materials Processing,'' Numer. Heat Transfer, **19**, pp. 151–176.
[118] Arridge, R. G. C., and Prior, K., 1964, ''Cooling Time of Silica Fibers,'' Nature (London), **203**, pp. 386–387.
[119] Tsou, F. K., Sparrow, E. M., and Godstein, R. J., 1967 ''Flow and Heat Transfer in the Boundary Layer on a Continuous Moving Surface,'' Int. J. Heat Mass Transf., **10**, pp. 219–235.
[120] Karwe, M. V., and Jaluria, Y., 1992, ''Experimental Investigation of Thermal Transport from a Heated Moving Plate,'' Int. J. Heat Mass Transf., **35**, pp. 493–511.
[121] Evans, G., and Greif, R., 1987, ''A Numerical Model of the Flow and Heat Transfer in a Rotating Disk Chemical Vapor Deposition Reactor,'' ASME J. Heat Transfer, **109**, pp. 928–935.
[122] Fotiadis, D. I., Boekholt, M., Jensen, K. F., and Richter, W., 1990, ''Flow and Heat Transfer in CVD Reactors: Comparison of Raman Temperature Measurements and Finite Element Model Predictions,'' J. Cryst. Growth, **100**, pp. 577–599.
[123] Karki, K. C., Sathyamurthy, P. S., and Patankar, S. V., 1993, ''Three-Dimensional Mixed Convection in a Chemical Vapor Deposition Reactor,'' ASME J. Heat Transfer, **115**, pp. 803–806.
[124] Chiu, W. K. S., and Jaluria, Y., 2000, ''Continuous Chemical Vapor Deposition Processing with a Moving Finite Thickness Susceptor,'' J. Mater. Res., **15**, pp. 317–328.
[125] Eversteyn, F. C., Severin, P. J. W., Brekel, C. H. J., and Peek, H. L., 1970, ''A Stagnant Layer Model for the Epitaxial Growth of Silicon from Silane in a Horizontal Reactor,'' J. Electrochem. Soc., **117**, pp. 925–931.
[126] Chiu, W. K.-S., Richards, C. J., and Jaluria, Y., 2000, ''Flow Structure and Heat Transfer in a Horizontal Converging Channel Heated From Below,'' Phys. Fluids, **12**, pp. 2128–2136.
[127] Chiu, W. K. S., and Jaluria, Y., 1997, ''Heat Transfer in Horizontal and Vertical CVD Reactors,'' *ASME Heat Transfer Div.*, Vol. 347, Amer. Soc. Mech. Engrs., New York, pp. 293–311.
[128] Rosenberger, F., 1980, ''Fluid Dynamics in Crystal Growth from Vapors,'' PhysicoChem. Hydrodyn., **1**, pp. 3–26.
[129] Ostrach, S., 1983, ''Fluid Mechanics in Crystal Growth—The 1982 Freeman Scholar Lecture,'' ASME J. Fluids Eng., **105**, pp. 5–20.
[130] Prasad, V., Zhang, H., and Anselmo, A. P., 1997, ''Transport Phenomena in Czochralski Crystal Growth Processes,'' Adv. Heat Transfer, **30**, pp. 313–435.
[131] Brown, R. A., 1988, ''Theory of Transport Processes in Single Crystal Growth from the Melt,'' AIChE J., **43**, pp. 881–911.
[132] Ostrach, S., 1982, ''Low-Gravity Fluid Flows,'' Annu. Rev. Fluid Mech., **14**, pp. 313–345.
[133] Guyene, T. D., and Hunt, J., eds., 1983, ''Materials Sciences Under Microgravity,'' *European Space Agency*, Rep. ESA-SP-191.
[134] Kamotani, Y., Ostrach, S., and Pline, A., 1994, ''Analysis of Velocity Data Taken in Surface Tension Driven Convection Experiment in Microgravity,'' Phys. Fluids, **6**, pp. 3601–3609.
[135] Xu, J., and Zebib, A., 1998, ''Oscillatory Two- and Three-Dimensional Thermocapillary Convection,'' J. Fluid Mech., **364**, pp. 187–209.
[136] Le Cunff, C., and Zebib, A., 1999, ''Thermocapillary-Coriolis Instabilities in Liquid Bridges,'' J. Phys. Fluids, **11**, pp. 2539–2545.
[137] Schwabe, D., 1999, ''Microgravity Experiments on Thermocapillary Flow Phenomena: Examples and Perspectives,'' Journal of Japanese Society of Microgravity Applications, **16**, pp. 1–6.
[138] Balasubramaniam, R., and Lavery, J. E., 1989, ''Numerical Simulation of Thermocapillary Bubble Migration Under Microgravity for Large Reynolds and Marangoni Numbers,'' Numer. Heat Transfer, **16**, pp. 175–187.
[139] Mundrane, M., Xu, J., and Zebib, A., 1995, ''Thermocapillary Convection in a Rectangular Cavity with a Deformable Interface,'' Adv. Space Res., **16**, pp. 41–53.
[140] Wang, G. X., and Prasad, V., 2000, ''Rapid Solidification: Fundamentals and Modeling,'' Annu. Rev. Heat Transfer, **11**, pp. 207–297.
[141] Bian, X., and Rangel, R. H., 1996, ''The Viscous Stagnation-Flow Solidification Problem,'' Int. J. Heat Mass Transf., **39**, pp. 3581–3594.
[142] Delplanque, J. P., and Rangel, R. H., 1998, ''A Comparison of Models, Numerical Simulation, and Experimental Results in Droplet Deposition Processes,'' Acta Mater., **46**, pp. 4925–4933.
[143] Bussmann, M., Mostaghimi, J., and Chandra, S., 1999, ''On a Three-Dimensional Volume Tracking Method of Droplet Impact,'' Phys. Fluids, **11**, pp. 1406–1417.
[144] Pasandideh-Fard, M., Bhola, R., Chandra, S., and Mostaghimi, J., 1998, ''Deposition of Tin Droplets on a Steel Plate: Simulations and Experiments,'' Int. J. Heat Mass Transf., **41**, pp. 2929–2945.
[145] Delplanque, J. P., Cal, W. D., Rangel, R. H., and Lavernia, E. J., 1997, ''Spray Atomization and Deposition of Tantalum Alloys,'' Acta Mater., **45**, pp. 5233–5243.
[146] Ahmed, I., and Bergman, T. L., 1999, ''Thermal Modeling of Plasma Spray Deposition of Nanostructured Ceramics,'' Journal of Thermal Spray Technology, **8**, pp. 315–322.

Effects of Guide-Vane Number in a Three-Dimensional 60-Deg Curved Side-Dump Combustor Inlet

Tong-Miin Liou
Professor,
Fellow ASME

Hsin-Li Lee
Ph.D. Candidate

Department of Power Mechanical Engineering,
National Tsing Hua University, Hsinchu,
Taiwan 30043, Republic of China

Chin-Chun Liao
Thermofluids Analysis Assistant Manager,
Design Department,
First International Computer, Inc.,
Portable Computing Group, Taiwan

Three-dimensional flowfields in a 60-deg curved combustor inlet duct of rectangular cross-section with and without guide vanes were measured using Laser-Doppler velocimetry for the longitudinal, radial, and spanwise velocity components. The Reynolds number based on the bulk mean velocity and hydraulic diameter was 2.53×10^4. The main parameters examined were the guide-vane number and Reynolds number. The results show that to completely eliminate flow separation in the curved combustor inlet three guide vanes should be installed. The critical Reynolds number for the absence of the flow separation is found to decrease with increasing product of radius and aspect ratios. In addition, it is found that in most regions the maximum radial mean velocity, difference between radial and spanwise normal stress, and the turbulent kinetic energy decrease with increasing guide-vane number. A rationale for the absence of flow separation in the one-vane case predicted by previous researchers is also provided.
[DOI: 10.1115/1.1358843]

1 Introduction

In a curved duct the imbalance between the centrifugal force and the radial pressure gradient drives the secondary flow perpendicular to the main direction of flow. A full account of the generation of the secondary flow can be found in Ward-Smith [1]. The secondary flow makes the flow structure complicated and causes a larger pressure loss than in a straight duct. The flow characteristics in the combustor inlets, which are curved, have a direct effect on the performance of the succeeding combustor. Accordingly, for improved engineering design further efforts are needed for a clear understanding of the detailed fluid dynamics and the role of the secondary flow in curved ducts.

In an early flow visualization experiment, Eustice [2] demonstrated the existence of a secondary flow by injecting ink into water flowing through a coiled pipe. Recent development of the laser-Doppler velocimetry (LDV) has provided more accurate and detailed velocity measurements in the curved duct. Agrawal et al. [3] measured the two-dimensional (2-D) laminar water flow in a 180-deg curved circular pipe and both Humphrey et al. [4,5] and Taylor et al. [6] measured the laminar ($Re_h=790$) and turbulent ($Re_h=4\times10^4$) water flows in 90-deg curved square ducts. They found that the boundary layer thickness at bend entry influenced the flow development and strength of the secondary flow. Secondary flows were more pronounced in the laminar flow than in the turbulent case. This was attributed mainly to the thicker boundary layer at the bend inlet for the laminar case. Chang et al. [7] measured the 2-D turbulent water flow in a strongly curved U-bend and downstream tangent of square cross-sections. Their results suggested that anisotropy, stabilizing and destabilizing curvature, and complex fluid-wall interactions were among the effects requiring modeling in the bend and that quick reduction of secondary motions required modeling in the downstream tangent. In the airflow measurement, Holt et al. [8] studied the developing turbulent flow in a 2-D 90-degree curved square duct. Moreover, Liou et al. [9,10] investigated the effects of the Reynolds number and aspect ratio (b/a) on the flowfield characteristics in a 2-D 90-deg curved square duct. They demonstrated that as the aspect ratio was increased, the strength of the main secondary flow decreased.

The brief survey presented above reveals the lack of three-dimensional (3-D) turbulent flow measurements in curved ducts. Among the above-mentioned papers, only Taylor et al. [6] measured the velocity component in the spanwise direction of a 90-deg curved square duct. However, their measurements of the spanwise velocity component were only performed in the downstream tangent; none of the data were taken in the bend. There is thus a need to measure both radial and spanwise velocity components in a curved duct. In addition, there are relatively few works on curved ducts installed with various number of guide vanes. Kotb et al. [11] have numerically studied the laminar and turbulent flows in a two-dimensional bend with and without a guide vane, and Liou and Liao [12] have performed preliminary 3-D LDV measurements of flows in a curved combustor inlet with and without a guide vane. The purpose of the present work is therefore to characterize the three-dimensional developing turbulent flow in a 60-deg rectangular inlet duct with various numbers of guide vanes located upstream of a side-dump combustor through LDV measurements of longitudinal, radial and spanwise velocity components. In particular, emphasis is placed on studying the effects of the number of guide vanes on the flow characteristics in the curved combuster inlet, which is absent in open literature. It is hoped that the measured results can aid in a better understanding of the complex and highly anisotropic flow structure and provide a useful data base for this type of flow. Moreover, the 2-D numerical results of Kotb et al. [11] are examined in the context of the present measured data.

2 Experimental Apparatus and Conditions

2.1 LDV System. The two curved inlet ducts of a side dump combustor and the LDV setup are shown schematically in Fig. 1 where a partial view of the second curved inlet duct is shown for space limitation. Air was drawn into two curved side inlets through two settling chambers and two 10:1 bell-mouth-like contractions by a blower at the downstream end. The settling chamber contained a flow straightener and six screens. The air then flowed into the curved inlet ducts, the combustion chamber, a

Contributed by the Fluids Engineering Division for publication in the JOURNAL OF FLUIDS ENGINEERING. Revised manuscript received by the Fluids Engineering Division May 5, 2000; final manuscript received December 20, 2000. Associate Editor: P. W. Bearman.

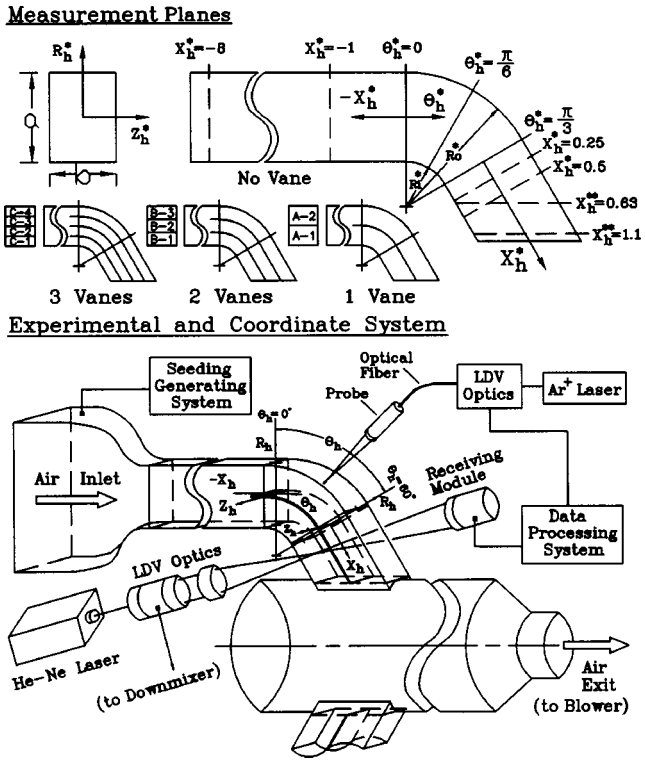

Fig. 1 Sketch of experimental and coordinate system, and measurement planes of curved inlet duct models

flow straightener, a flowmeter, a bellows, and was exhausted by the blower. A conventional dual beam LDV system was set up in a forward or off-axis scattering configuration. A 300-mw helium-neon laser with a 632.8 nm (red) line provided the coherent light source. The approximate probe-volume dimensions ($1/e^2$ light intensity) in a forward scattering configuration were 0.57 mm in length and 0.18 mm in diameter. The LDV system mentioned above was utilized to measure the longitudinal and radial velocity components from the side wall of the curved inlet duct. The spanwise velocity component was measured from the outer wall of the curved duct, using a one-component fiber-optic probe LDV system whose light source was a linearly polarized 300-mw argon ion laser (514.5 nm wavelength) and probe-volume dimensions were approximately 0.12 mm$\times$1.56 mm. The detailed optical arrangements of the He-Ne laser and Ar^+ laser LDV systems were described in Liou and Wu [13] and Tsai and Liou [14], respectively. The entire conventional LDV system and the fiber-optic probe were mounted on a milling machine with four vibration isolation mounts, allowing the probe volume to be positioned with 0.01 mm resolution. The light scattered from salt particles with a nominal diameter of 0.8 μm was collected into a photomultiplier and subsequently downmixed to the appropriate frequency shift of 2–5 MHz. A counter processor with 1-ns resolution was used to process the Doppler signal. The Doppler signal was monitored on an oscilloscope, and the digital output of the counter processor was fed directly to a microcomputer for storage and analysis.

2.2 Curved Duct Model. The configuration of the curved inlet duct model and coordinate system for the one-vane case are sketched in Fig. 1. The inlet duct consists of an upstream tangent, a 60-deg bend of mean radius (R_m) 47 mm, and a downstream tangent. Please refer to the Nomenclature and our preliminary work (Liou and Liao [12]) for the detailed dimensions of the curved duct model. The internal dimensions of the cross-section are 47 mm$\times$35 mm (a$\times$b), the corresponding hydraulic diameter (D_h) is 40 mm, and the radius ratio (R_m/D_h) is 1.2. Figure 1 shows that four types of the curved inlet duct, viz., no-vane, 1-vane, 2-vane, and 3-vane, are investigated. With the same geometry, they are distinctive in the number of the guide vanes. The shape of the guide vane is a circular-arc, from the bend entry plane to the bend-exit plane. In addition, the guide vane has a straight upstream extension of 0.25 D_h at the leading edge and a downstream extension to the dump plane ($X_h^{**}=1.1$) at the trailing edge. The shape of the leading edge of the vanes is a semicircle with a radius of 0.0125 D_h. The guide vane with a thickness of 0.025 D_h divides the curved duct into equal segments. Each segment is given a label, as shown in the upper half of Fig. 1. The two rectangular inlet ducts intersect the combustor at an inlet angle of 60 deg. The centerlines of both inlet ducts intersect the combustor at the same axial station and are located circumferentially at 180 deg to each other. The internal dimensions of the dump plane are 35 mm$\times$54.2 mm. To facilitate data presentation, three coordinate systems are adopted in the present work; each for a given zone: two separate Cartesian systems, one each for the straight ducts (negative X_h^* for the upstream tangent and positive X_h^* for the downstream tangent) and a cylindrical system for the bend.

2.3 Experimental Conditions. The measurement planes along the longitudinal direction are shown in the upper half of Fig. 1. There were four longitudinal stations, $\theta_h=30$ deg, $\theta_h=60$ deg, $X_h^*=0.25$, and $X_h^*=0.5$, and five spanwise stations, $Z_h^*=0.89$, 0.69, 0.46, 0.23, and 0, where all three components were measured. Note that the $X_h^{**}=0.63$ and $X_h^{**}=1.1$ stations were respectively located at 0.5 D_h and 0.1 D_h above the combustor inlet port and were chosen to be parallel with the combustor side walls instead of being perpendicular to the duct walls to provide appropriate inlet boundary conditions for combustor flowfield computations. The measuring positions were chosen to give a clear pattern of the flow field. The bulk mean velocity, 9.9 m/s, was used as a reference (U_{ref}) to nondimensionalize the results. The Reynolds number based on the bulk mean velocity and hydraulic diameter was 2.53×10^4, the corresponding Dean number ($\text{Re}(D_h/2R_m)^{0.5}$) was 1.65×10^4.

3 Results and Discussion

The present study is part of a series of systematic experimental investigations of the flow field in simulated ramjet combustors and inlets. A much more detailed data description is included in the Ph.D. thesis of Liao [15]. Only some typical results are presented below.

3.1 Uncertainty Estimate. The mean velocity and turbulence intensity components were calculated from the probability density function of the measurements (Liou and Kao [16]). Typically, 2000$\sim$4000 realizations were averaged at each measuring location. The corresponding statistical errors were between 0.1 and 1.8 percent in the mean-velocity component and between 2.0 and 3.1 percent in the turbulence intensity component for the 95 percent confidence level. The well-known weighting method of McLaughlin and Tiederman and the constant time-interval sampling mode were used to correct velocity bias for regions where local turbulence intensity was below and above 25 percent, respectively (Drain [17]). The difference between corrected and uncorrected data sets was found to be below 2.4 percent. Verification of the spanwise symmetry of the mean velocity and turbulence intensity for three components was performed for various streamwise stations. For instance, the deviations from symmetry of the mean velocity and turbulence intensity for three components were found to be within 2.8 and 1.5 percent of U_{ref}, respectively, for the one-vane case. Accordingly, in each of the measuring planes data were collected only in the symmetrical half. To check the conservation of the mass flow rate, the mean longitudinal velocities were integrated over each measure cross section and the integrated values were compared. The integrated results were also

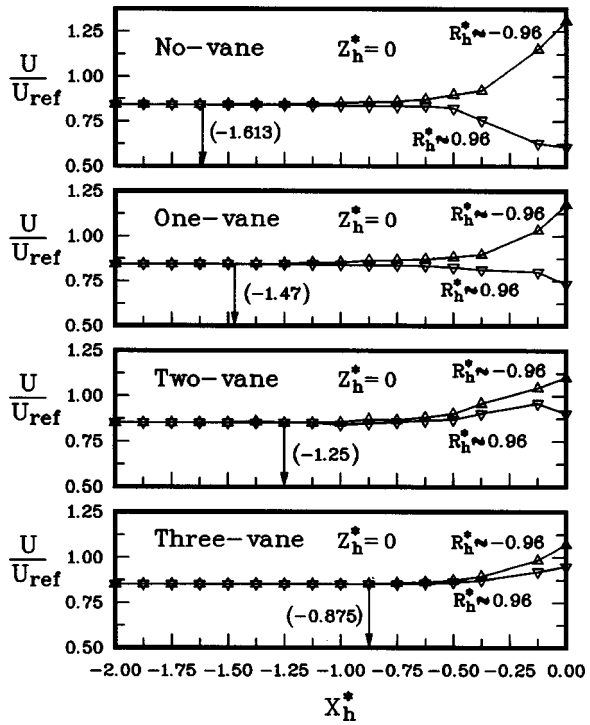

Fig. 2 Distributions of longitudinal mean velocity along $R_h^*\approx0.96$ and -0.96 (Uncertainty in U/U_{ref}: less than ±2.8 percent)

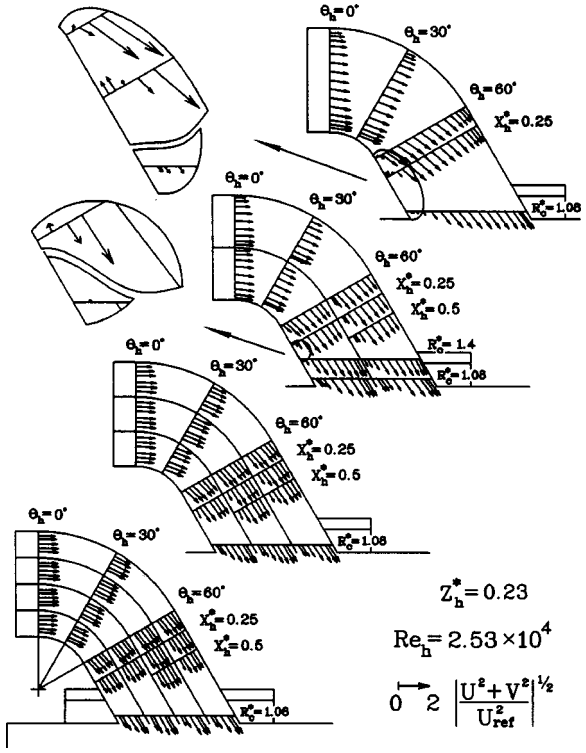

Fig. 3 Streamwise mean flow pattern in terms of resultant velocity vectors at $Z_h^*=0.23$ for four cases (Uncertainty in $(U^2+V^2)^{1/2}/U_{ref}$: less than ±2.8 percent)

compared with the readings of flow meter located downstream of the test section. These comparisons showed that the continuity errors of all the cross-sectional planes for the four cases investigated were within 4 percent. The uncertainty in evaluating the streamwise vorticity by numerical differentiation is given in the caption of Fig. 4 and was doubly checked by numerical integration based on circulation.

3.2 Upstream Tangent. The typical distributions of the longitudinal mean velocity and turbulence intensity at $X_h^*=-8$ and $X_h^*=-1$ in the upstream tangent for the one-vane case are top-hat shape (Liou and Liao [12]). As the flow proceeds from $X_h^*=-8$ to $X_h^*=-1$, the region of core fluid is narrowed from 84 percent–53 percent of the cross-stream plane, which indicates that the fluid flowing into the bend entry plane is a hydrodynamically developing flow. The streamwise mean velocity profiles in the boundary layers near the outer, inner, and side walls are close to the one-seventh-power law profile at $X_h^*=-1$ and the boundary layer thickness, defined as 95 percent of the centerline mean velocity, are $\delta/D_h=0.15$, 0.16, and 0.16, respectively. In fact, the ratio of the measured displacement to momentum thickness, i.e., the shape factor, is approximately 1.5, whereas the shape factors of the laminar and turbulent flat-plate flows are 2.6 and 1.3, respectively. Moreover, the corresponding turbulence intensity at $X_h^*=-1$ is 1.8 percent of U_{ref} in average, except near the walls. These results suggest that the boundary layer at $X_h^*=-1$ is turbulent.

The near uniform subsonic inflow from the upstream tangent is affected by the bend to some extent, as can be examined from Fig. 2. Figure 2 displays the distributions of longitudinal mean velocity at a distance of 1 mm from the outer ($R_h^*=1$) and inner wall ($R_h^*=-1$), respectively, in the $Z_h^*=0$ plane for the four cases investigated. It can be seen that for a given number of vanes the difference in the U/U_{ref} distribution between $R_h^*\approx0.96$ and $R_h^*\approx-0.96$ decreases with increasing upstream extent ($-X_h^*$). The U/U_{ref} distributions of $R_h^*\approx0.96$ and $R_h^*\approx-0.96$ converge after a certain upstream extent (indicated by the arrow in Fig. 2). The upstream extent or the distance between the position labeled by the arrow and the entry of the bend ($X_h^*=0$) is found to decrease with increasing number of vanes and is about 1.62, 1.47, 1.25, and 0.88 D_h for the no-vane, one-vane, two-vane, and three-vane cases, respectively. In other words, the effect of the bend on the flow pattern in the upstream tangent decreases with increasing guide-vane number.

3.3 Bend and Downstream Tangent. The streamwise evolution of the longitudinal and radial mean velocity components along the $Z_h^*=0.23$ plane for the four cases examined are depicted in Fig. 3 in terms of the resultant vector plots. At $\theta_h=0$ deg the near uniform flow from the upstream tangent has been affected by the curvature. The streamwise mean velocity displays an acceleration near the inner wall and a deceleration near the outer wall for the front part of the bend, but for the latter part of the bend it is reversed. The aforementioned phenomenon results from the influence of the longitudinal pressure gradient and has been discussed in detail in Liou and Liao [12]. Apart from flow distortion encountered in all four cases, flow separation adjacent to the inner wall of the inner passage in the downstream tangent for the no-vane and one-vane cases is clearly visible. Note that the separated recirculation zone in the one-vane case is smaller than that in the no-vane case. By installing a single guide vane in the curve inlet duct, the size of the separated flow region along the inner wall is narrowed to about 25 percent of the size observed for the case without a guide vane. It should be mentioned here that in the numerical study of Kotb et al. [11], there is, however, no flow separation in the two-dimensional 90-deg bend installed with one guide vane at $Re_h=1\times10^5$. The difference between their computational and our measured results for the one-vane case is attributed to the differences in dimension (2-D versus 3-D), bend angle (90-deg versus 60-deg), Re_h, and, to some extent, to the numerical scheme and turbulence models adopted by them. A further identification of the

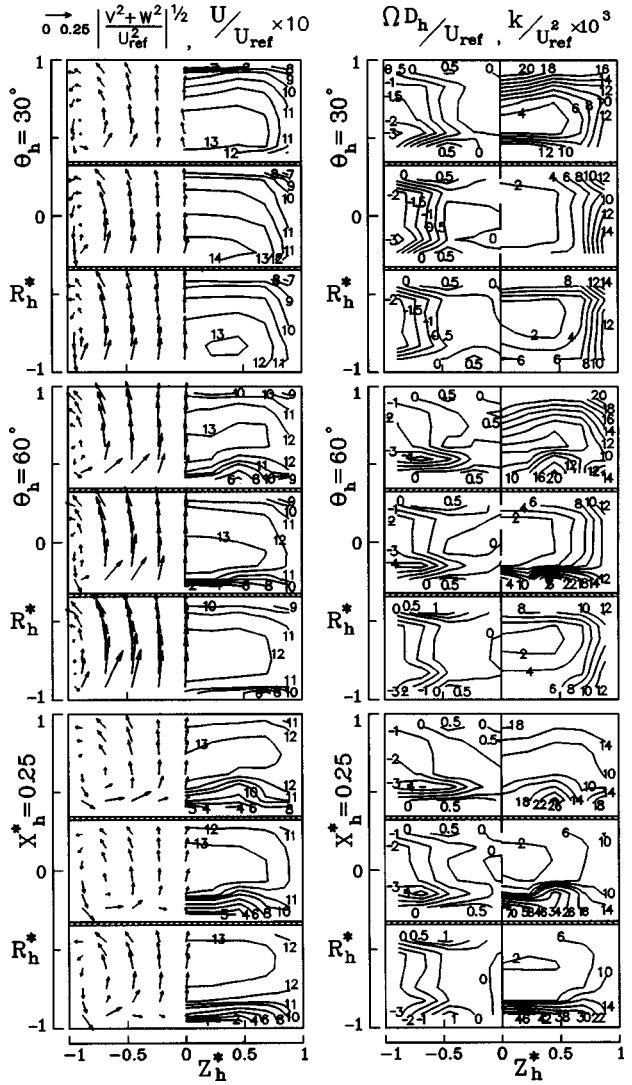

Fig. 4 Secondary mean flow pattern in terms of resultant velocity vectors and U, Ω, and k contours at three selected cross-sectional planes for two-vane case (Uncertainty in $(V^2+W^2)^{1/2}/U_{ref}$: less than ±2.8 percent, in $\Omega D_h/U_{ref}$: less than ±8.6 percent, in k/U_{ref}^2: less than ±7.4 percent)

possible rationale for the difference will be supplemented in a later section. For $Re_h=2.53\times10^4$ in the present work, the separated flow region along the inner wall is further eliminated by installing two or more guide vanes. Why does an increase in vane number suppress separation? Its physical explanation is provided in a later section. A further discussion of Re_h effect on removing flow separation is also given in the later text. It is important to extract such information from the measured results since the size of the separated flow region in the curved inlet duct affects the size of the dome recirculation zone and, in turn, the fluid mixing and the flame stability inside the combustor (Shahaf et al. [18]; Liou et al. [19]).

The secondary-flow mean velocity vectors and longitudinal mean velocity contours at $\theta_h=30$ deg, $\theta_h=60$ deg, and $X_h^*=0.25$ for the two-vane case are shown in Fig. 4 as a typical case. A pair of counter rotating vortices is generated in the cross-sectional plane by the imbalance between the centrifugal force and the inward force resulting from the radial pressure gradient. The secondary flow motion displaces high-speed fluid towards the outer wall along the region containing the central plane, and low-speed fluid towards the inner wall along the side wall. These main secondary flow vortices are narrow and prevail near the side walls. It should be mentioned that a second vortex pair having a sense of rotation opposite of that of the main vortex pair develops within the bend and near the central outer wall for the case of no vane, as have been identified by smoke visualization of laser light sheet at $\theta_h=30$ and $\theta_h=60$ deg (not shown). Similar observations have also been made in pipe bends of circular cross-section (Rowe [20]). However, this second vortex pair is rather unstable, it appears and disappears alternately. Further downstream in the downstream tangent for the no-vane case, a more stable third vortex pair having a sense of rotation opposite of that of the main vortex pair appears near the central inner wall. Note that these additional vortex pairs developing in the no-vane case are absent in the two-vane case. The positive radial mean velocities at $\theta_h=60$ deg are greater than those at $\theta_h=30$ deg and $X_h^*=0.25$ because the centrifugal force generated by the curvature vanishes in the downstream tangent. Quantitatively, the radial mean velocity reaches a value as high as 0.68, 0.43, 0.39, and $0.31U_{ref}$ for the no-vane, one-vane, two-vane, and three-vane cases, respectively. As a reference, the maximum positive radial mean velocity of the turbulent flow in a straight rectangular duct with $Re_h=4.2\times10^4$ only reaches a value of $0.12U_{ref}$ (Melling and Whitelaw [21]) due to the lack of curvature effect. Also, Taylor et al. [6] reported a maximum positive radial mean velocity of $0.4U_{ref}$ for their 90-deg curved square duct $b/a=1$ with $R_m/D_h=2.3$ and $Re_h=4\times10^4$. This value is smaller than $0.68U_{ref}$ measured for our no-vane case with a duct cross-sectional aspect ratio $b/a=0.74$, $R_m/D_h=1.2$ and $Re_h=2.53\times10^4$, as a result of duct aspect ratio effect (Liou et al. [19]), Reynolds number effect (Taylor et al. [6]), mentioned in the Introduction, and radius ratio effect. All these three effects indicate that the strength of the main secondary flow decreases when any one of them is increased. The maximum negative radial mean velocities at $X_h^*=0.25$ are about 0.147, 0.22, 0.146, and $0.13U_{ref}$ for the no-vane, one-vane, two-vane, and three-vane cases, respectively. The maximum spanwise mean velocities at $X_h^*=0.25$ are about 0.1, 0.16, 0.18, and $0.15U_{ref}$ for the no-vane, one-vane, two-vane, and three-vane cases, respectively. Due to convective transport of the low-momentum fluid by the side-wall secondary flow from the outer wall to the inner wall and the influences of flow separation, the core flow and the position where the maximum longitudinal mean velocity occurs are displaced progressively from the regions near the inner walls towards the center of the passage as the fluid proceeds downstream from $\theta_h=30$ deg to $X_h^*=0.25$ or $X_h^*=0.5$. The distributions of the streamwise mean vorticity, $\Omega=\partial W/\partial R_h-\partial V/\partial Z_h$, are also plotted in Fig. 4 in terms of contours for the two-vane case. It can be seen that the negative vorticity contours mainly prevailing near the side walls reveal the presence of the counterrotating main secondary flow vortices. This observation is consistent with the previous discussion of the secondary flow mean velocity. The streamwise mean vorticity of this work is about one order of magnitude larger than that obtained by Yokosawa et al. [22] in the smooth and rough square duct using hot-wire anemometry. Further discussion about the variation of Ω with the guide-vane number is given in a later section.

Due to the secondary flow motion, the interchange of the turbulent kinetic energy between the outer and inner walls is responsible for the occurrence of high levels of turbulence near the side walls. Figure 4 also provides the contour maps of the turbulent kinetic energy at $\theta_h=30$ deg, $\theta_h=60$ deg, and $X_h^*=0.25$ for the two-vane case as a typical example to illustrate the aforementioned result. The turbulence levels are higher near the outer wall than near the inner wall in the first part of the bend ($\theta_h=30$ deg); this trend is reversed in the latter part of the bend ($\theta_h=60$ deg) and the downstream tangent ($X_h^*=0.25$). In addition, the maximum turbulence levels increase with increasing streamwise distance. At $X_h^*=0.25$,

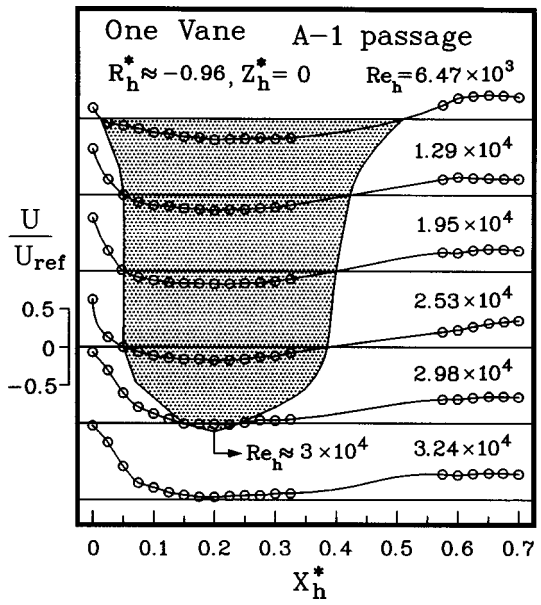

Fig. 5 Streamwise variation of longitudinal mean velocity along $R_h^* \approx -0.96$ in A-1 passage at various Reynolds numbers (Uncertainty: see Fig. 2 caption)

$$\sqrt{\overline{u^2}}_{\max}, \quad \sqrt{\overline{v^2}}_{\max}\sqrt{\overline{w^2}}_{\max}, \quad \text{and} \quad k_{\max}$$

are ($0.41U_{\text{ref}}$, $0.19U_{\text{ref}}$, $0.25U_{\text{ref}}$, $0.13U_{\text{ref}}^2$), ($0.34U_{\text{ref}}$, $0.16U_{\text{ref}}$, $0.2U_{\text{ref}}$, $0.08U_{\text{ref}}^2$), ($0.32U_{\text{ref}}$, $0.14U_{\text{ref}}$, $0.16U_{\text{ref}}$, $0.075U_{\text{ref}}^2$), and ($0.2U_{\text{ref}}$, $0.13U_{\text{ref}}$, $0.12U_{\text{ref}}$, $0.03U_{\text{ref}}^2$), for the no-vane, one-vane, two-vane, and three-vane case, respectively. It is found that all three turbulence intensity components and the turbulent kinetic energy decrease with increasing guide-vane number. In a turbulent rectangular duct with $Re_h = 4.2\times10^4$ (Melling and Whitelaw [21]), $\sqrt{\overline{u^2}}_{\max}$, $\sqrt{\overline{v^2}}_{\max}\sqrt{\overline{w^2}}_{\max}$, and $k_{\max}$ are about $0.1U_{\text{ref}}$, $0.074U_{\text{ref}}$, $0.074U_{\text{ref}}$, and $0.01U_{\text{ref}}^2$, respectively. The maximum turbulence levels in the present curved duct with various guide-vane numbers are greater than those in the straight rectangular duct due to the presence of curvature effect.

3.4 Influence of Guide-Vanes Number and Reynolds Number. The streamwise variation of the longitudinal mean velocity along $R_h^* \approx -0.96$ in the A-1 passage (Fig. 1) at various Reynolds numbers are shown in Fig. 5. The region of negative longitudinal mean velocity reduces with increasing Reynolds number since the loss of mean-flow energy as a result of wall friction decreases with increasing Reynolds number. It should be recalled that the friction loss in a straight pipe flow also decreases with increasing Reynolds number, as supported by the Moody chart for the range of Reynolds number examined in Fig. 5. Accordingly, a critical Reynolds number of $Re_h = 3\times10^4$ can be extrapolated for the absence of longitudinal flow reversal. Similar observations can be made for the no-vane, A-2, B-1, and B-2 passages (Fig. 1) to obtain the corresponding critical Reynolds numbers. It should be pointed out that there is no separation in the curved inlet duct with three guide vanes. Thus, the separation length $X_{h,\text{sep}}$, defined as the longitudinal distance where the longitudinal mean velocity is negative along $R_h^* \approx -0.96$ (i.e., 1 mm from the inner wall), decreases with increasing Reynolds number Re_h, as depicted in Fig. 6(*a*). The aforementioned critical Reynolds numbers (solid symbols) are also included in Fig. 6(*a*) where $X_{h,\text{sep}} = 0$. It is interesting to apply Fig. 6(*a*) to identify the possible reason for the difference mentioned in 3.3 section regarding the presence or absence of flow separation in curved ducts installed with a single guide vane. The prediction of Kotb et al. [11] was performed at

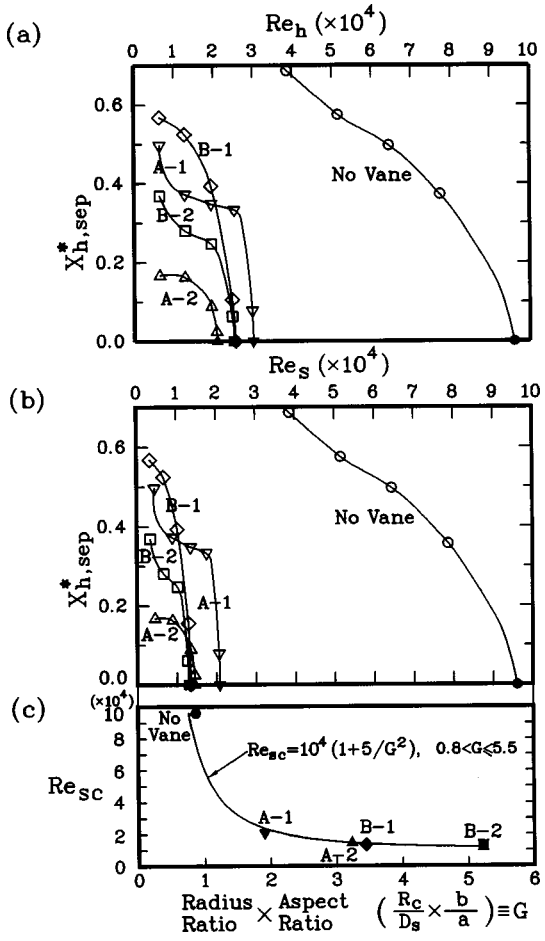

Fig. 6 Variations of separation length with Re_h and Re_s, and variation of Re_{sc} with product of radius ratio and aspect ratio (Uncertainty in $X_{h,\text{sep}}^*$: less than ±5.2 percent)

$Re_h = 1\times10^5$ which is well beyond the critical Reynolds number determined from Fig. 6(*a*). Their computation showed the absence of flow separation, a result justified by Fig. 6(*a*). On the other hand, our measurements show the presence of flow separation for the one-vane case since the data were taken at Reynolds number ($Re_h = 2.53\times10^4$) lower than the critical Re_h depicted in Fig. 6(*a*).

If the Reynolds number Re_s, whose characteristic length is the hydraulic diameter of each sub-passage, is used, the corresponding results are shown in Fig. 6(*b*). From Figs. 6(*a*) and (*b*), one can see that the values of the critical Re_h are different from those of the critical Re_s (Re_{sc}). It should be pointed out that curved ducts with the same radius ratio may have different aspect ratios. Nevertheless, all the previous researchers in their studies on curved duct flows only correlated their results with either aspect ratio or radius ratio. Hence, to extend the application range, Fig. 6(*c*) shows the variation of the Re_{sc} with the product of the radius ratio and aspect ratio for each sub-passage in which the flow separation is present. It can be seen that the Re_{sc}, above which no separation occurs in the passage, decreases with increasing product of the radius ratio and aspect ration (G). The correlation between the Re_{sc} and G can be obtained by the least squares method as following:

$$Re_{sc} = 10^4(1+5G^{-2}), \quad (0.8 < G \leqslant 5.5),$$

The deviations of the above correlated values from the respective experimental data are within 3.5 percent. There is no separation in the B-3 passage and sub-passages for the 3-vane case whose products of radius and aspect ratios are all greater than 5.5.

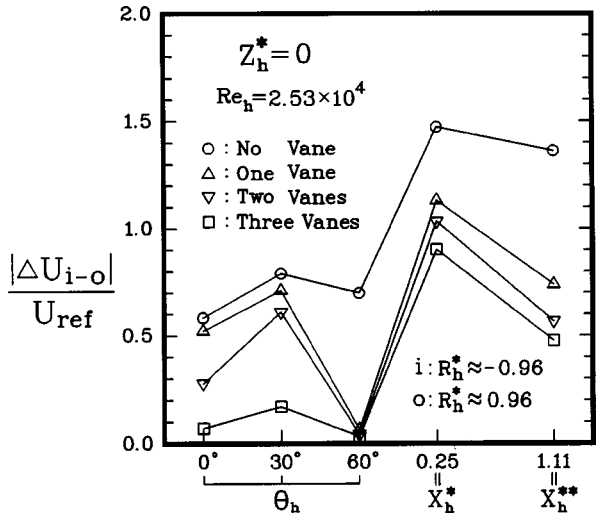

Fig. 7 Absolute longitudinal mean velocity differences between inner and outer walls for the four cases examined (Uncertainty in $|\Delta U_{i\text{-}0}|/U_{ref}$: less than ±3.2 percent, in normalized longitudinal position ±0.6 percent)

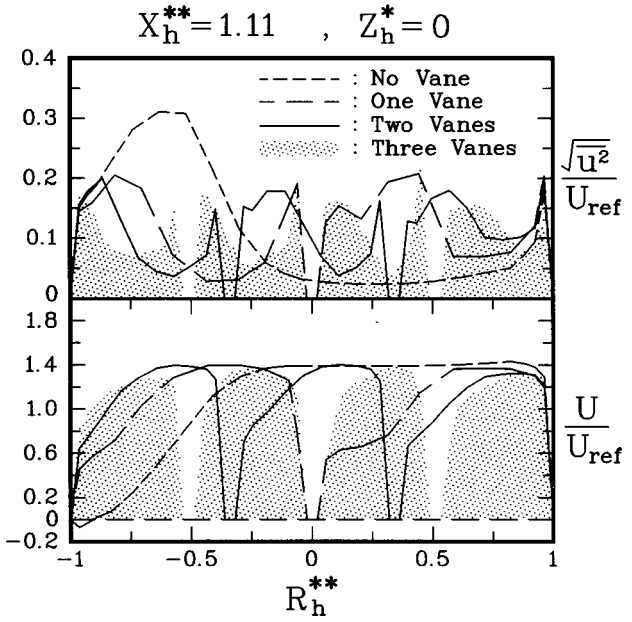

Fig. 8 Profiles of central-plane ($Z_h^*=0$) longitudinal mean velocity and turbulence intensity at $X_h^{**}=1.11$ for the four cases examined (Uncertainty in $\sqrt{\overline{u^2}}/U_{ref}$: less than ±3.8 percent, in U/U_{ref}: see Fig. 2 caption)

The absolute differences between the longitudinal mean velocities at a distance of 1 mm from the inner and outer walls, respectively, are shown in Fig. 7. The velocity differences increase before $\theta_h=30$ deg and then decrease until $\theta_h=60$ deg. At the exit of the bend, the longitudinal mean velocities at $R_h^*\approx-0.96$ and 0.96 are almost equal, except for the case of the inlet duct without a guide vane. The velocity differences increase again in the downstream tangent and then restore to smaller values for all four cases. Note that the differences between the longitudinal mean velocities near the inner and outer wall in the curved inlet duct decrease with increasing guide-vane number.

The profiles of the longitudinal mean velocity and turbulence intensity in the $Z_h^*=0$ plane at $X_h^{**}=1.11$ station, located at a stage of 0.0875 D_h above the dump plane, for the four cases are shown in Fig. 8. For the no-vane case, a higher turbulence intensity level appears at the proximity of the inner wall as a result of the flow separation adjacent to the inner wall. However, the flow separation near the inner wall at the $X_h^{**}=1.11$ station for the no-vane case is eliminated by installing guide vanes into the curved duct, resulting in lower turbulence levels for the curved duct with guide vanes. The presence of the guide vanes makes the longitudinal mean velocity distributions across the sub-passages of the curved duct more uniform even though the no-slip condition at the guide vanes produces velocity deficits around the guide vanes. From Figs. 7 and 8, a consequence of introducing more guide vanes into the curved duct is a reduction of the velocity differences between the inner and outer walls and, hence, a more uniform distribution of the velocity across the sub-passages near the exit of the curved duct. It is worth pointing out that the main concern here is how to eliminate flow separation inside the downstream tangent of the curved inlet duct using guide vanes. The presence of flow separation and reattachment (Figs. 3, 5, 6) tends to make the flow unstable at the dump plane of the combustor, which, in turn, results in an oscillatory impingement flow inside the combustor, therefore, unstable flame holding recirculating zone (combustion instability) in the dome region of the dump combustor. Among the guide-vane number examined, only the case of three guide vanes makes the flow separation disappeared in the downstream tangent of the curved inlet duct for the range of Reynolds number tested, thus providing the most uniform velocity distribution near the dump plane of the combustor. Measurements inside the combustor needs to be performed in the future study to understand the detailed effect of the level of flow uniformity on the succeeding combustion process.

There is one more point worth being addressed. Information of wall-friction loss in the curved duct with guide vanes is also important to a complete design optimization as far as the curved duct itself is considered. Measurements of wall static pressure loss between a reference station ($X_h^*=-0.5$) located in upstream tangent and the combustor dump plane $X_h^{**}=1.1$ indicate a significant drop of friction factor f from a value of $f=0.51$ for the no-vane case to $f=0.42$ of one vane case due to a large reduction in the size of flow separation bubble. When the number of guide vanes is increased, the value of f is increased again from $f=0.45$ for the two-vane case up to $f=0.54$ for the three-vane case due to the slight decrease in the size of separation bubble but the large increase in the friction surface area with increasing guide-vane number. Note that the three-vane case only causes a wall-friction loss slightly larger than the no-vane case, which suggests that the friction loss resulting from flow separation for the no-vane case is significantly and nearly the same as the friction loss associated with increasing friction surface area of three vanes.

Figure 9 shows the variations of Ω_{max}, V_{max}, $(\overline{v^2}-\overline{w^2})_{max}$, and k_{max} with the streamwise distance for the four cases examined. The comparison of Ω_{max} shown in Fig. 9 reveals that the strongest main secondary flow vortex is developed within the downstream tangent of the curved duct with three guide vanes. In general, the maximum secondary-flow vortex, $\Omega_{max}D_s/U_{ref}$, becomes stronger as the number of guide vanes is increased. In other words, the ability of the secondary motion to convect the high velocity fluid across the main flow increases with increasing guide-vane number or aspect ratio of the sub-passage. The trend of $\Omega_{max}D_s/U_{ref}$ shown in Fig. 9 explains the reduction of the separation bubble with increase in guide-vane number. It is worth mentioning that the computational results of Kotb et al. [11] for turbulent flows in a 2-D 90-deg bend with or without a guide vane also indicates the reduction of the recirculating zone when a guide vane is arranged in the bend. In fact, that $|\Delta U_{i-0}|/U_{ref}$ decreases with increasing guide-vane number, as shown previously in Fig. 7, also suggests

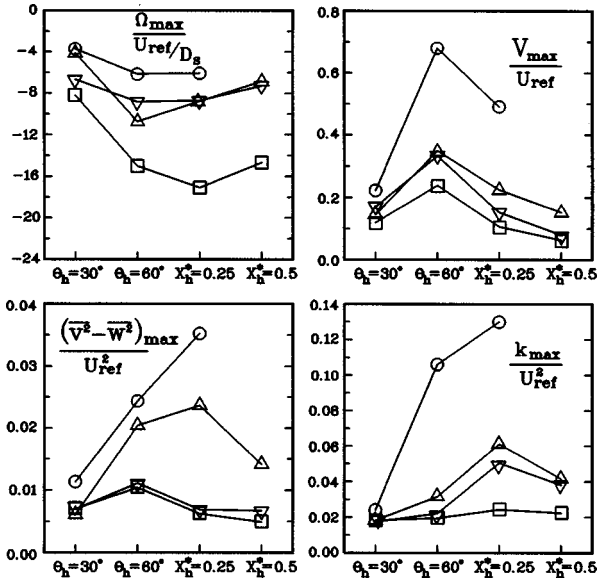

Fig. 9 Variations of Ω_{max}, V_{max}, $(\overline{v^2}-\overline{w^2})_{max}$, and k_{max} with streamwise distance for the four cases examined (symbols: see Fig. 7; Uncertainty in Ω_{max}: see Fig. 4 caption, in V_{max}: less than ±2.8 percent, in $(\overline{v^2}-\overline{w^2})_{max}/U_{ref}^2$: less than 9.6 percent, in k_{max}: see Figs. 4 caption)

an amelioration in the adverse pressure gradient along the inner wall in the downstream tangent, and, in turn, a reduction in the size of separation as the guide-vane number is increased. It may be appropriate here to explain why the no-vane case shown in Fig. 6 deviates significantly from the configurations that involve guide vanes. Because the relative thickness of the boundary layers at a curved-duct entrance is known to significantly affect the flow development within the duct or sub-passages, Fig. 10 depicts the variations of various boundary layer thickness at $\theta_h=0$ deg and $Z_h^*=0$ with guide vane number (Fig. 10(*a*)) and radial distance (Fig. 10(*b*)). As one can see that for the no-vane case, a relative thick and thin boundary layers have developed on the outer ($R_h^*=1$) and inner ($R_h^*=-1$) duct walls, respectively, due to the deceleration and acceleration of fluid flow along the outer and inner duct walls, respectively, in the front half of the curved duct. The large difference between the boundary layer thickness of outer and inner walls is markedly reduced as one guide-vane is installed in the curved duct and then gradually reduced to nearly zero (uniform mean velocity distribution) when the guide-vane number is increased from 1–3. Thus, the trend depicted in Fig. 10(*a*) correlates well with that depicted in Fig. 6(*a*). The reduction of the above difference in boundary layer thickness between outer and inner walls is attributed to the increase in the aspect ratio of the sub-passage and, in turn, augmentation of the ability of the secondary motion to convert the high velocity fluid across the main flow, as precedingly mentioned. Figure 10(*b*) further depicts the radial variation of inlet boundary layer thickness of sub-passage. The large difference in δ/D_h on the $R_h^*=1$ wall between the no-vane case and the configurations involving guide vanes again correlates with that shown in Fig. 6(*a*). Note that the small difference in δ/D_h among the curved duct with different guide-vane numbers for $-1<R_h^*<1$ is because that the boundary layer on the inner or outer wall of sub-passages all stars to develop at the guide-vane leading edge.

Figure 9 also shows that the maximum radial mean velocities at $\theta_h=60$ deg are greater than those at other longitudinal stations for all four cases since the centrifugal force generated by the curvature is maximum near the outer wall. In most regions, V_{max} decreases with increasing guide-vane number. This is attributed to

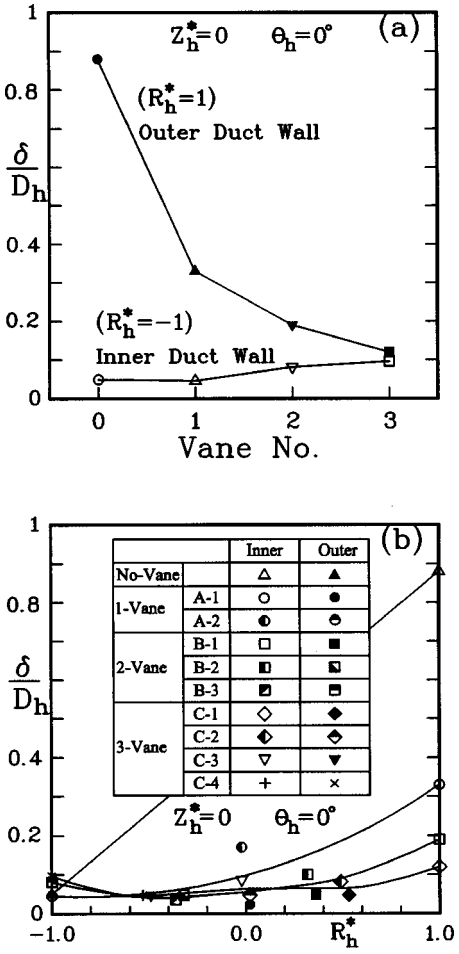

Fig. 10 Variations of various boundary layer thickness at $\theta_h=0$ deg and $Z_h^*=0$ with guide-vane number and radial distance (Uncertainty in δ/D_h: less than 3.6 percent)

that the fluids flowing toward the outer wall along the central plane are restricted by the guide vanes. In a similar trend $(\overline{v^2}-\overline{w^2})_{max}$ decreases with increasing guide-vane number. Note that $\overline{v^2}-\overline{w^2}$ is one of the driving forces for generating secondary flow of the second kind in the streamwise vorticity transport equation. All cases show that the turbulent kinetic energy increases with increasing streamwise distance until $X_h^*=0.25$ and then restores to a smaller value at $X_h^*=0.5$. In addition, the turbulent kinetic energy decreases with increasing guide-vane number for most regions. The maximum turbulence level is approximately constant within the side-inlet curved duct with three guide vanes.

4 Summary and Conclusions

The following conclusions are drawn from the data presented:

1 The effect of the bend on the fluid flow in the upstream tangent decreases with increasing guide-vane number.

2 The separated flow region along the inner wall decreases with increasing guide-vane number. There is no flow separation in the curved combustor inlet installed with three guide vanes.

3 The critical Reynolds number (Re_{sc}) for the absence of flow separation decreases with increasing product of radius ratio and aspect ratio (G). The correlation between the Re_{sc} and G is obtained for the first time and has the form

$$Re_{sc}=10^4(1+5G^{-2}), \quad (0.8<G\leqslant 5.5),$$

$$G\geqslant 5.5, \text{ no separation.}$$

4 For the guide-vane numbers examined, the most uniform mean velocity distribution near the dump plane of the combustor can be obtained by installing three guide vanes. The three-vane case results in a friction loss nearly as large as the no-vane case.

5 All three turbulence intensity components and the turbulent kinetic energy increase with increasing streamwise distance in the bend and then restore to smaller values at $X_h^* = 0.5$.

6 In most regions the maximum radial mean velocity, difference between radial and spanwise normal stress, and the turbulent kinetic energy decrease with increasing guide-vane number. In addition, the maximum turbulence level is approximately constant within the curved combustor inlet with three guide vanes.

Acknowledgment

Support for this work was partially provided by the National Science Council of the Republic of China under contract NSC-82-0424-E007-034.

Nomenclature

a = radial height of channel cross-section, 47 mm
b = spanwise width of channel cross section, 35 mm
D_h = channel hydraulic diameter, 40 mm
D_s = sub-passage hydraulic diameter, mm
f = friction factor, $\equiv(\Delta P/\Delta X)(D_h/0.5\rho U_{\text{ref}}^2)$
k = turbulent kinetic energy, $\equiv 1/2(\overline{u^2}+\overline{v^2}+\overline{w^2})$, m^2/s^2
P = wall static pressure, kg/m^3
R_c = mean radius of curved passage, mm
Re_h = Reynolds number, $\equiv D_h U_{\text{ref}}/\nu$
Re_s = subpassage Reynolds number, $\equiv D_s U_{\text{ref}}/\nu$
R_h, Z_h = radial, spanwise coordinate, mm
R_h^* = normalized radial coordinate (measurement planes parallel to the longitudinal direction), $R_h^* = R_h/(R_0 - R_i)/2 = R_h/a/2$
R_h^{**} = normalized radial coordinate (measurement planes parallel to the dump plane), $R_h^{**} = R_h/(R_0 - R_i)/2\cos(30\text{ deg})$
R_i, R_0, R_m = inner, outer, and mean radius of curved duct ($R_i = 23.5$, $R_0 = 70.5$, $R_m = 47$), mm
U, V, W = longitudinal, radial, and spanwise mean velocity, m/s
U_c = core-flow mean velocity, m/s
U_{ref} = longitudinal bulk mean velocity for curved combustor inlet, 9.9 m/s
u, v, w = longitudinal, radial, and spanwise fluctuating velocity, m/s
$\overline{v^2} - \overline{w^2}$ = difference between radial and spanwise normal stress, m^2/s^2
X_h, θ_h = longitudinal coordinate, mm, deg
X_h^* = normalized longitudinal coordinate (measurement planes perpendicular to the longitudinal direction), $X_h^* = X_h/D_h$
X_h^{**} = normalized longitudinal coordinate (measurement planes parallel to the dump plane), $X_h^{**} = X_h/D_h$
Z_h^* = normalized spanwise coordinate, $Z_h^* = Z_h/(b/2)$
ν = kinematic viscosity, m^2/s
δ = boundary layer thickness, mm
ρ = air density, kg/m^3
Ω = streamwise vorticity, s^{-1}

References

[1] Ward-Smith, A. J., 1980, *Internal Fluid Flow: The Fluid Dynamics of Flow in Pipes and Ducts*, Oxford University Press, Oxford.
[2] Eustice, J., 1911, ''Experiments on Stream-Line Motion in Curved Pipes,'' Proc. R. Soc. London, **85**, pp. 119–131.
[3] Agrawal, Y., Talbot, L., and Gong, K., 1978, ''Laser Anemometer Study of Flow Development in Curved Circular Pipes,'' J. Fluid Mech., **85**, pp. 497–518.
[4] Humphrey, J. A. C., Taylor, A. M. K. P., and Whitelaw, J. H., 1977, ''Laminar Flow in a Square Duct of Strong Curvature,'' J. Fluid Mech., **83**, pp. 509–527.
[5] Humphrey, J. A. C., Whitelaw, J. H., and Yee, G., 1981, ''Turbulent Flow in a Square Duct with Strong Curvature,'' J. Fluid Mech., **103**, pp. 443–463.
[6] Taylor, A. M. K. P., Whitelaw, J. H., and Yianneskis, M., 1982, ''Curved Ducts with Strong Secondary Motion: Velocity Measurements of Developing Laminar and Turbulent Flow,'' ASME J. Fluids Eng., **104**, pp. 350–359.
[7] Chang, S. M., Humphrey, J. A. C., and Modavi, A., 1983, ''Turbulent Flow in a Strongly Curved U-Bend and Downstream Tangent of Square Cross-Sections,'' Physico-Chemical Hydrodynamics, **4**, pp. 243–269.
[8] Holt, M., Flores, J., and Turi, P. J., 1982, ''Measurements of Air Flow in a Curved Pipe Using Laser-Doppler Velocimetry,'' 1st International Symposium on Application of LDA to Fluid Mechanics, Lisbon, Portugal.
[9] Liou, T. M., and Liu, C. H., 1986, ''An Investigation of Pressure Loss and Mean Velocity Field in a Curved Square Duct with Different Reynolds Numbers,'' Journal of the Chinese Society of Mechanical Engineers, **7**, No. 4, pp. 243–251.
[10] Liou, T. M., and Wu, S. M., 1987, ''The Effect of Aspect Ratio on the Air Flow in Curved 90 Ducts with Uniform Inlet Condition,'' Journal of the Chinese Institute of Engineers, **10**, pp. 147–156.
[11] Kotb, N. A. E., Mokhtarzadeh-Dehghan, M. R., and Ward-Smith, A. J., 1988, ''A Numerical Study of Laminar and Turbulent Flows in a Two-Dimensional Bend with or without a Guide Vane,'' Int. J. Numer. Methods Eng., **26**, pp. 245–262.
[12] Liou, T. M., and Liao, C. C., 1995, ''Flows in a Curved Combustor Inlet with and Without a Guide Vane,'' J. Propul. Power, **11**, No. 3, pp. 464–472.
[13] Liou, T. M., and Wu, S. M., 1988, ''Flowfield in a Dual-Inlet Side-Dump Combustor,'' J. Propul. Power, **4**, No. 1, pp. 53–60.
[14] Tsai, M. K., and Liou, T. M., 1991, ''Study of Flow Induced by Nonuniform Lateral Injection,'' J. Propul. Power, **7**, No. 5, pp. 668–677.
[15] Liao, C. C., 1997, ''A Study of Curved Duct Flows Associated with Side-Dump Combustor and Artery Disease,'' Ph.D. thesis, Department of Power Mechanical Engineering, National Tsing Hua University, Hsin-Chu, Taiwain.
[16] Liou, T. M., and Kao, C. F., 1988, ''Symmetric and Asymmetric Turbulent Flows in a Rectangular Duct with a Pair of Ribs,'' ASME J. Fluids Eng., **110**, pp. 373–379.
[17] Drain, L. E., 1980, *The Laser Doppler Technique*, Wiley, New York, NY, pp. 136–145.
[18] Shahaf, M., Goldman, Y., and Greenberg, J. B., 1980, ''An Investigation of Impinging Jets in Flow with Sudden Expansion,'' Proceedings of the 22nd Israel Annual Conference on Aviation and Astronautics, pp. 100–106.
[19] Liou, T. M., Hwang, Y. H., and Wu, S. M., 1990, ''The Three-Dimensional Jet-Jet Impingement Flow in a Closed-End Cylindrical Duct,'' ASME J. Fluids Eng., **112**, pp. 171–178.
[20] Rowe, M., 1970, ''Measurements and computations of flow in pipe bends,'' J. Fluid Mech., **43**, Part 4, pp. 771–783.
[21] Melling, A., and Whitelaw, J. H., 1976, ''Turbulent Flow in a Rectangular Duct,'' J. Fluid Mech., **78**, pp. 289–315.
[22] Yokosawa, H., Fujita, H., Hirota, M., and Iwata, S., 1989, ''Measurement of Turbulent Flow in a Square Duct with Roughened Wall on Two Opposite Sides,'' Int. J. Heat Fluid Flow, **10**, pp. 125–130.

LDA Measurements of Feed Annulus Effects on Combustor Liner Port Flows[1]

Adrian Spencer

James J. McGuirk

Department of Aeronautical and Automotive Engineering, Loughborough University, Leicestershire, LE11 3TU United Kingdom
e-mail: A.Spencer@lboro.ac.uk

A detailed LDA experimental study is reported on the effect of variations in feed annulus conditions on port flow jet characteristics. The data are relevant to primary and dilution jet flows as found in gas-turbine combustor liners. Alteration of jet velocity ratios and associated bleed flows past the jet ports for a typical annulus height/port diameter configuration was observed to produce significant variations in separation regions in the annulus, distortions in downstream annulus profiles, and jet exit conditions. Profiles of jet exit velocity, flow angle, and turbulent kinetic energy distribution have been provided which should prove invaluable as boundary conditions for related CFD studies. For the first time the influence of swirl in the approach annulus was examined, at a level consistent with residual swirl passing down the annulus from compressor exit conditions. Noticeable deviations in jet characteristics were again observed, reducing jet entry angles by some 20 deg over the rear half of the port. [DOI: 10.1115/1.1365932]

Introduction

Mass flow splits between the principle air admission ports to a combustor (see Fig. 1) need to be finely balanced in order to produce the internal mixing which is crucial to achieving a desirable combustor exit temperature pattern. Slight deviations from design flow splits, or in the inflowing jet injection angles, can lead to hot spots in the combustor exit plane with inevitable consequences on turbine life. Moreover, smoke production and NO_x formation can rise rapidly to unacceptable levels if inadequate mixing is achieved in the combustor primary zone. One aspect which can affect jet properties and flow splits, beyond the obvious first-order influences of port size and combustor liner pressure drop, is the supply flow history, i.e., the details of the supply flow along the inner and outer feed annuli. This aspect has only received scant attention in published work to date. Typical feed annuli arrangements of a modern aero gas turbine combustor can be seen in Fig. 1.

Design of the combustor to give a particular flow split between the several air admission ports is often performed using a 1D analysis. Such analyses are often carried out using flow network software (Stuttaford and Rubini [1]) which combine (i) geometrical information on the available flow area along the several flow paths from compressor exit to combustor exit with (ii) empirical airflow correlations obtained from experimental studies (for example Adkins and Gueroui [2]) in terms of discharge coefficient/pressure drop variations for the various entry ports. Such methods provide only limited detail on jet characteristics (e.g., no information on jet velocity profiles, entry angle profiles and turbulence conditions is obtained). It is also well known (Hay and Spencer [3]) that small geometric variations of port shape can bring about large changes in its C_d. In addition, under certain geometry conditions, it has been observed that undesirable flow features can occur (e.g., vortices within the ports, Baker and McGuirk [4], Doerr et al. [5]). Finally, all existing correlations take no account of any swirl in the approach annulus flow. It is conceivable, however, that under some circumstances, small levels of residual swirl at compressor exit could turn into perhaps 15 deg of swirl in the inner annulus duct, due to spin-up of the flow angular momentum due to the change of radius as the flow enters the inner annulus, Carrotte and Bailey [6].

For these reasons, the present study was designed to create an experimental facility which would allow detailed measurements of annulus approach flows to be made, and be flexible enough to create a range of supply conditions simulating both combustor primary zone and dilution zone ports. The data also capture the consequences of these variations on jet entry conditions, since this information may then be used to improve existing empirical correlations and also validate CFD studies of these flows. Particular care had to be taken to enable accurate measurement of these port exit profiles, as described below. The rest of the paper is divided into sections which provide a detailed description of the experimental facility and instrumentation used and results obtained in the present experimental study.

Experimental Facility

The experimental facility to be described was designed and built especially for this study. It is an isothermal, vertically flowing, constant head, water flow rig. Significant effort in the initial design stage was concentrated on maximizing flow controllability, optical access, and ease of maintenance. The following focuses

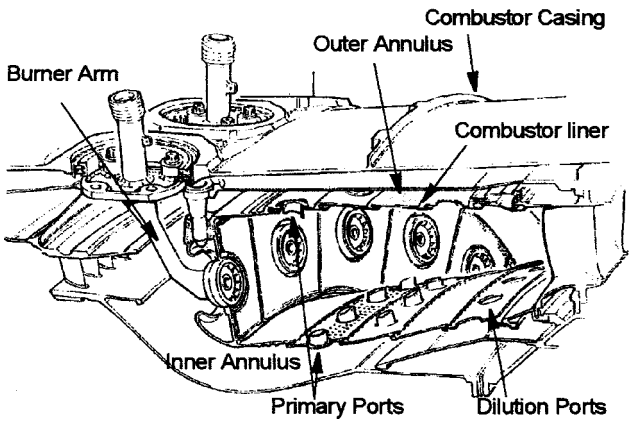

Fig. 1 Typical combustor arrangement

[1]"© British Crown copyright 2000. Published with the permission of the Defense Evaluation and Research Agency on behalf of the Controller of HMSO"

Contributed by the Fluids Engineering Division for publication in the JOURNAL OF FLUIDS ENGINEERING. Manuscript received by the Fluids Engineering Division January 28, 2000; revised manuscript received December 22, 2000. Associate Editor: P. W. Bearman.

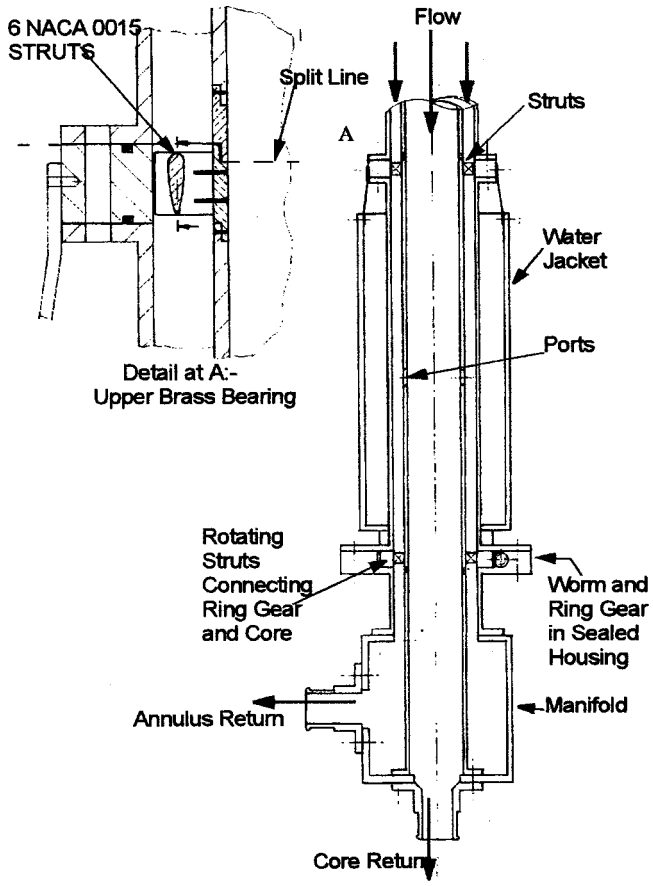

Fig. 2 Cross section of the test section

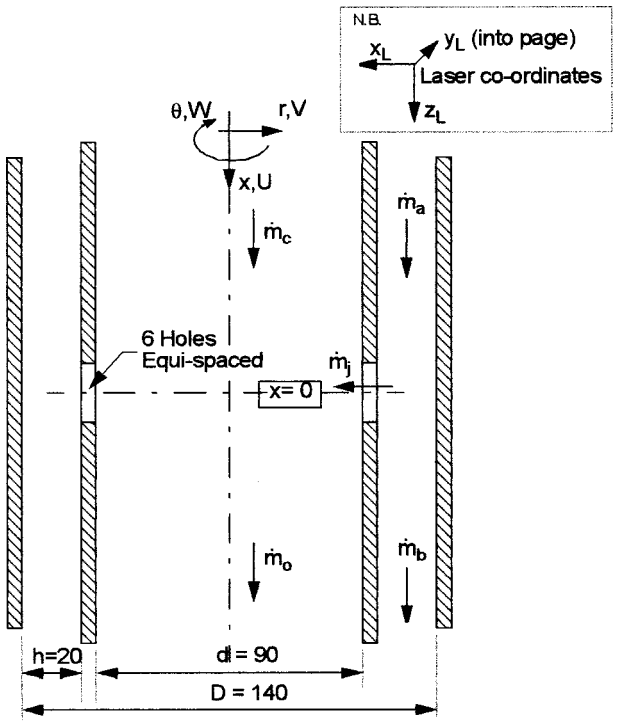

Fig. 3 Coordinate system used for the test section (dimensions in mm)

attention on the test section but a fuller description of the entire experimental facility may be found in Spencer [7].

The approach velocities in the annulus of a combustor are typically of order 30 m/s and up to 150 m/s through the principle air admission ports. At typical compressor exit temperatures of around 800°C this converts to flow Mach numbers of below 0.3 implying the effects of compressibility are minimal. Given this, water has often been chosen as the working fluid for external aerodynamic combustor studies to facilitate measurements. Coupland and Priddin [8] have also provided CFD predictions which support the use of a water analogy facility as a useful tool in understanding combustor flow. Examples of combustor studies using water are Baker [9], Koutmos and McGuirk [10], and Stull et al. [11]. Water was hence chosen as the working medium for this study, allowing the effects of combustor aerodynamics to be considered in isolation. Employing water as the working fluid has additional advantages. First, domestic water has a naturally high particulate concentration suitable for laser doppler anemometer (LDA) measurements, the primary measurement method for this study. Thus the use of additional ''seeding'' material can be avoided. This high seeding concentration results in favorable signal to noise ratios, increasing the validated data rate of the system, see Turner [12]. Second, water allows gravity to be used as a stable driving force. Fluctuations in pump delivery rates are eliminated by the use of a constant head tank with an overflow branch, with the result that the mass flow through the working section can be kept constant over very long periods of time. Finally, with practical considerations in mind, low speed flows in geometry of manageable scale can be used to create Reynolds numbers high enough to simulate those found within combustors.

The working section of the current rig is shown in cross section in Fig. 2. It comprises of two circular pipes 600 mm long, the inner one being held concentric with the outer at each end via a set of NACA 0015 struts. The inner pipe contains six 20 mm diameter, sharp edged ports approximately half way along its length. A square acrylic jacket filled with water surrounds the whole of the working section to reduce refraction effects at the air-acrylic interface. This is standard practice, Bicen [13], ensuring that the optical axis is perpendicular to the outer wall of the jacket. Unique to this rig is the ability to rotate the inner pipe. This ability allows the exploration of more of the flow field than possible on previous annulus/port flow rigs such as that used by Baker [9]. The lower struts connect a ring gear situated in a sealed flange to the bottom of the inner pipe. By turning a worm gear, this allows the inner pipe of the test section, along with the upper and lower support struts, to be rotated. This removes the need to be able to rotate the laser about the axis of the two pipes to measure velocities on different azimuthal planes. Instead, the inner pipe is rotated, hence offering a different azimuthal plane to the optical axis of the laser.

To ensure that the flow field rotated with the inner pipe a stringent test was devised to highlight the strongest effect of inner pipe rotation. First, a flow feature most sensitive to flow condition was identified. This was found to be the onset of a recirculation bubble on the outer annulus wall above each port which formed as the bleed fraction was reduced from 70 percent to around 60 percent (at bleeds of 70 percent or greater the axial velocity near the outer annulus wall was always positive). At the rig condition which just created the recirculation bubbles the minimum axial velocity ($U_{\min}$) 3 mm from the outer annulus wall over each port was located and recorded, this occurred at $(x,r)=(15,67)$ mm and $\theta=0,60,\ldots,300$ deg. The variation in $U_{\min}$ from port to port was found to be $0.07U_a$ with the inner pipe stationary. While this variation in $U_{\min}$ may seem high it must be reminded that this represents the worst case scenario that was found. Away from the bleed conditions for separation onset and away from this region of the flow field the port sector to sector variation was much better, typically with $<0.02\ U_a$ variations in velocity magnitude. However, the variation of $U_{\min}$ for any one port as the inner pipe was rotated was found to be $0.04\ U_a$, close to half of that of the port

sector to sector variation. For typical test conditions it is thought that rotation of the inner pipe may result in typically up to 2 percent change in velocity magnitude. It was thus concluded that the effect of inner pipe rotation was small when compared to sector to sector variations and it is thus a valid procedure to measure the axial and circumferential velocity components on the diameter aligned with the optical axis, then rotate the core pipe through 90 deg to measure the radial velocity on the diameter perpendicular to the optical axis.

One further feature of the rig geometry reported here was the ability to introduce swirl in the annulus by replacing the upper support struts with a set of swirl vanes. Fifteen NACA 65-8 10 (thickened) vanes were used to produce approximately 12 deg of swirl.

The coordinate systems and nomenclature adopted in the experimental work are depicted in Fig. 3. Cylindrical polar coordinates were used for referencing the control volume position, (x,r,θ), and velocity vector, (U,V,W), as shown. Five mass flows have been included to allow a complete description of the flow scenarios studied below: **c**—core inlet, **a**—annulus inlet, **j**—jet, **o**—core outlet and **b**—annulus bleed. Where these letters are used as subscripts they imply area averaged values at each of these stations.

Instrumentation

A one-dimensional LDA system was used as the main, nonintrusive interrogation method. The system could be used in either differential forward scatter or back scatter mode. Forward scatter mode was adequate for most measurements, offering high data rates. However, in certain situations back scatter mode was more convenient. The advantage of backscatter mode is that the receiving optics do not need altering once they have been setup since they are common with the transmitting optics. Therefore, when traversing the laser through regions of substantial refraction, constant re-alignment of the receiving optics is not required. The disadvantage of this method though is that additional seeding material was required in the form of latex spheres or TiO_2. Even with the additional seeding, data rates were still found to be an order of magnitude less than when operating in forward scatter (data rates of 2 kHz compared with 20 kHz). The only back scatter measurements reported here are shown in Fig. 16.

An optical bench with rigid support for the laser and photo multiplier was secured to the top of a milling table traverse mechanism to give three axes of movement, (x_L,y_L,z_L). To remove possible errors due to backlash in the gearing, two digital position indicators were used. These were fixed to the milling table to display the laser location with an accuracy of ± 0.01 mm. The traverse origin $(x_L,y_L,z_L)=(0,0,0)$ was chosen to be colocated with the control volume set at the rig coordinate system origin, $(x,r,\theta)=(0,0,0)$ see Fig. 3.

To help set the control volume to the origin of the rig coordinates a light sensitive diode was used. The photo-multiplier was replaced by the diode so that as the control volume passed through a perspex/water interface the light flare produced would be indicated by the meter. An accuracy of around 0.2 mm was then achievable in locating the perspex tube walls, depending on the local surface quality.

A Uniphase 10 mW He-Ne laser was used, along with a Dantec 55X optical unit. The photomultiplier had a pre-amplifier built in which allowed it to be used in both forward and back-scatter modes. The characteristics of the optical system are given in Table 1.

The error introduced because of statistical uncertainty in calculating the mean velocity, U, from N randomly sampled data is given by Yanta and Smith [14] as:

$$\text{error}=\frac{1.96}{\sqrt{N}}\frac{\sqrt{u^2}}{U}$$

Table 1 Laser characteristics

Property	Value
Power output	10 mW
Wavelength	632.8 nm
Diameter of beam at $1/e^2$	0.68 mm
Half angle of beam intersection (in air)	5.53°
Transmitting lens focal length	310 mm
Minor axis of control volume	0.30 mm
Major axis of control volume	3.12 mm
Fringe spacing	3.28 μm
No. fringes	46

where u is the fluctuating component about the mean and the factor 1.96 implies a 95 percent confidence level on the measured mean. Enough samples were taken to keep the error below 4 percent. However, with high levels of turbulence and possible flow unsteadiness occurring, it was also often necessary to ensure the data was collected over a time period significantly greater than any period of unsteady oscillation, in order to capture all of the frequencies associated with the flow. This was done by accepting a predetermined number, N, of samples at a given rate, rather than accepting the first N samples measured. Typically 40 K samples were taken at 2 kHz (some larger sets were necessary, i.e., near jet impingement). Applying the same statistical analysis to the normal stress measurements (for details see Castro [15]), the error in the measured variance relative to the true value, with 95 percent confidence was 6 percent.

The other errors associated with making LDA measurements had a negligible effect on the error compared to that produced by the statistical uncertainty. For example, consider broadening of the probability distribution function due to mean velocity gradients. By using the methodology of Durst et al. [16] broadening was found to introduce a maximum of 0.1 percent error to the mean velocity measurements for the expected flow field. This small error is possible by ensuring the minor axis of the control volume was perpendicular to any strong velocity gradients and is consistent with the findings of Durst et al. where it was seen that these errors were only significant in the near wall viscous sub layer of a turbulent pipe flow. Corrections for broadening of the probability distribution function were therefore not used for this study.

Estimates of the data rate density according to Edwards [17] for the current measurements give values of $N_2T=10$ which are in the high data density band, and shown by Edwards to be effectively free from velocity bias and filter bias for the current set-up using a sample and hold processor (IFA550). Directional ambiguity was also avoided by using a frequency shift of 0.4 MHz typically. Fringe bias was avoided by not taking measurements in regions where the ray tracing algorithm (described in the next section) predicted significant distortion or skewing of the control volume.

Data Reduction

Optical Corrections to LDA Measurements. When using LDA to measure the flow inside an acrylic test rig the laser beams are refracted as they pass through the fluid/acrylic interfaces. It is necessary to make corrections to account for this. The physics of refraction at interfaces where there is a change in refractive index is well known and described by Snell's law. Equations have been derived (see, e.g., Bicen [13] and Boadway and Karahan [18]) to allow position and velocity magnitude corrections to be made to LDA measurements taken inside a single cylinder. A set of twelve equations is presented in Bicen [13] which describe three correction factors for four recommended orientations of the laser. Two of the corrections evaluate the positional shift of the control volume in the radial and circumferential directions, and the final one is a velocity correction factor. The four orientations of the laser suggested correspond to traversing the control volume along diameters of the test section coincident or perpendicular to the op-

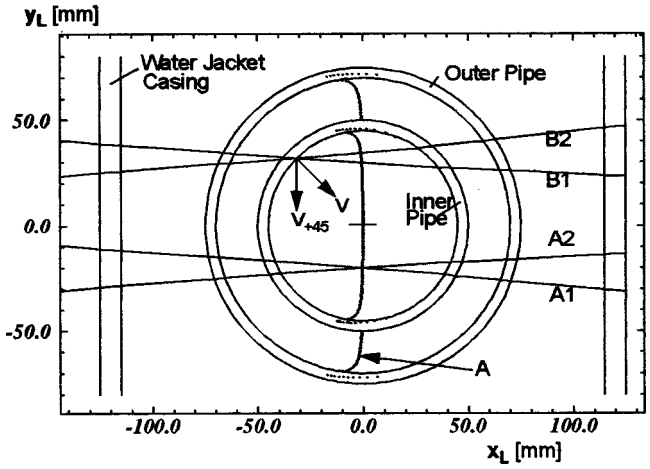

Fig. 4 Calculation of measurement volume location

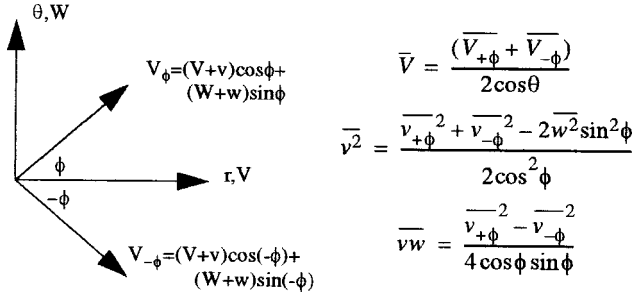

Fig. 5 Evaluation of radial velocity component

tical axis with the laser beams either vertical or horizontal. In the present study, when measuring inside the core region (through two cylindrical walls) or in the far annulus when the laser needs to pass fully through the core pipe (through three cylindrical walls) these equations do not apply. Moreover, it is possible in certain orientations that one beam passes through the wall of the inner pipe but the other passes through a port. In order to correct for the optical effects of all the possible scenarios of having two concentric tubes, a simple ray tracing program was written. The program uses three-dimensional vector analysis to trace both beams through the specified geometry. To verify the program, a comparison with Bicen's formulas was performed and showed perfect agreement.

An advantage of using a general computational method is that it can calculate the correction factors required when the control volume is not on the optical axis or on the diameter perpendicular to it, impossible to do with the trigonometric equations described in Bicen [13]. A further benefit of this approach is that it allows the traverse system coordinates (x_L, y_L, z_L) to be found which will locate the laser measuring volume at any arbitrary rig coordinates (x, r, θ). This is done by applying the algorithm in an iterative process, by specifying the required laser beam intersection point then repeatedly optimizing the laser coordinates until the measuring volume is calculated to be at the required rig location.

Two example calculations using the ray tracing algorithm are shown in Fig. 4. First, the curved line ''A'' is the locus of beam intersections when the laser is orientated to measure the radial velocity component, V, on a diameter perpendicular to the optical axis. The beams A1 and A2 are one example point on this locus when the laser is moved to $y_L = -20$ mm, keeping x_L and z_L fixed. High levels of refraction are seen as the beams approach concave walls of the pipes and it is unlikely that sensible measurements could be made in such regions, due to fringe bias. Second, the beams B1 and B2 are those required to measure the velocity component at 45 deg to the radial direction at the exit plane of a port. The laser movement (x_L, y_L) is thus found to locate the measuring volume at a certain (r, θ) location in the rig.

Port Exit Velocity Profile. Due to the large refractions as described above the port exit radial velocity could not be measured directly. However, by measuring the mean and r.m.s. velocities at $\pm\phi$ deg to the radial component, $V_{+\phi}$, $v_{+\phi}$, $V_{-\phi}$ and $v_{-\phi}$, and the circumferential velocities, W and w at the same point, the radial velocity, V, the radial normal stress, vv, and the radial-circumferential shear stress, vw, can be evaluated from the relationships given in Fig. 5 where the overbars denote time averaged values. For a derivation of these relationships see Durst et al. [19]. In order to measure V_ϕ and $V_{-\phi}$ the axis of the port under investigation was rotated until it was at angles of either 45 or -45 deg (the value chosen for ϕ) to the optical axis. W, as usual, was measured with the port axis in line with the optical axis, i.e., $\theta = 0$. The (x_L, y_L) positions of the laser to make each of these three measurements was calculated by the method described in the previous section. At each of these positions the laser was traversed across the vertical diameter of the port ($-10 < z_L < 10$ mm) to enable the construction of the exit velocity profile to be carried out.

Construction of Velocity Vectors and Turbulence Field. Since only a 1D LDA system was available, each of the three velocity components was measured on separate traverses through the test section. Because the correction factors for optical shifting of the measuring volume were different in each case, the three velocity components were generally measured at slightly different locations along each traverse. Indeed, the test section had to be rotated through 90 deg such that the radial velocity could be measured on the diameter perpendicular to the optical axis. A method was therefore required to allow each velocity component to be transposed onto a common, regular data presentation grid. A true 3D velocity vector could then be constructed and defined at each point in this data presentation grid.

The method adopted was to fit a cubic spline (Press et al. [20]) to the data set of each 1D traverse. Boundary conditions had to be given for the ends of each curve in order to calculate the cubic spline. A zero gradient constraint was used when the end point was taken at a plane of assumed symmetry, at the center line for example. Otherwise a zero value was added to the end of the profile to represent a wall velocity. This is in effect an extrapolation of the data, since no measurements were made closer than 3 mm to a concave wall or 1.5 mm from a convex wall. These boundary condition values have been included to complete the field plots.

Measurement grids were such that typically all three velocity components could be measured during one session without altering the rig operating condition, as is the case with the measurements reported here. However, repeatability tests showed that variations in velocity measurements were less than 3 percent of the local value.

By stacking up a series of consecutive parallel traverses of all of the measured velocity components a full 3D vector field could be constructed on a 2D rectangular data presentation mesh. Furthermore, the turbulent kinetic energy, k, could then be calculated; $k = 1/2(u^2 + v^2 + w^2)$, (u, v, and w being the r.m.s. value of the fluctuating part of U, V, and W), for each point in the grid.

Evaluation of Inlet Mass Flow Rates. Inlet velocity distributions were assumed to be axisymmetric and integration of the measured inlet velocity profile allowed the mass flow to be obtained from,

$$\dot{m} = \int_{\text{Area}} \rho U.dA = 2\pi\rho \int_0^{D/2} Ur.dr$$

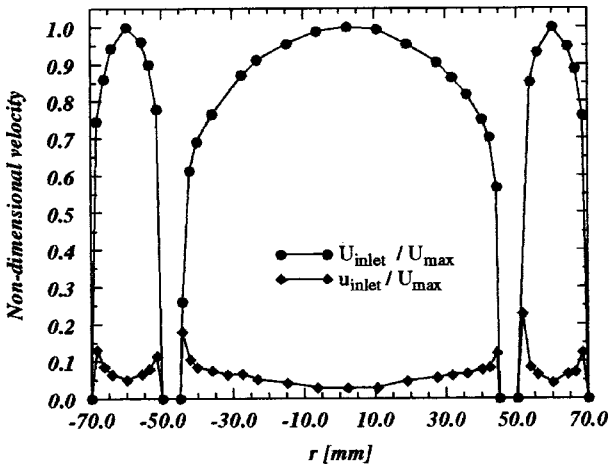

Fig. 6 Inlet axial velocity profiles

This process was repeated for two radial traverses displaced circumferentially by 180 deg and averaged (see Fig. 6). The assumption of axisymmetry was perfectly acceptable for the core flow, however, for the annulus flow, due to the presence of the 6 strut wakes a small correction (2 percent) was necessary.

Evaluation of Exit Mass Flow Rates. Mass flow rates exiting the core and annulus were measured using standard BS1042 orifice plates. The pressure drop across each plate was monitored via inverted water manometers. Agreement of better than 3 percent was obtained for the difference in measured inlet and outlet mass flows for all tests.

Test Section Inlet Conditions. Figure 6 shows a graph of the mean axial velocity and r.m.s. component at inlet (taken at $x = -150$ mm). Acceptable turbulence intensities of 4 and 5 percent are seen at the center of the core and annulus passages, with the expected distributions, increasing toward the walls of the pipes. Measurements close to the walls were not possible with the current setup since the control volume was 3.12 mm along its major axis, and the minor axis could not be brought close to the concave walls because in this orientation high levels of refraction occur (see Fig. 4). Very similar profiles were measured across the diameter perpendicular to the optical axis and with the inner pipe rotated to various positions indicating a good level of symmetry. Care had to be taken, however, when measuring in the annulus due to the presence of the six strut wakes causing a maximum velocity deficit of 6 percent. For this reason, the wakes were always arranged to be mid-way between port centres. Whilst the core flow is not expected to be fully developed with only 18 pipe diameters from pipe entry to working section, the annulus profile would be expected to be developed, having a length equivalent to 53 annulus heights to ensure so. The level of secondary velocity components (swirl and radial velocity) at inlet were less than 1 percent of the mean axial velocity, small enough to be comparable to the error involved in measuring the axial velocity with the LDA system.

Results

Two principle flow scenarios will be reported in detail. These were chosen to be representative of the flow conditions for primary ports and dilution (or secondary) ports. The bulk flow conditions chosen to correspond to these typical situations are given in Table 2. (N. B. subscripts as given in Fig. 3 and indicate bulk average quantities at each station).

With the exception of W_a/U_a (which is calculated from only LDA measurements) these quantities can only be determined using both orifice plate and LDA measurements. For example V_j is calculated from the difference between the core inlet mass flow rate (LDA) and the core exit mass flow rate (orifice) divided by ρA_j. The principle changes affecting the annulus flow between these two port flow scenarios are the different velocity ratios, *R*, and the change in bleed ratio, *B*. Since primary jets are required to penetrate much stronger than dilution jets, the corresponding radial to axial velocity ratio is twice as high. The decrease in bleed fraction from primary to dilution ports occurs because the bleed flow past primary ports is required to feed the downstream dilution ports and any bleed past them. To investigate the effect of swirl in the annulus the dilution configuration was also studied with a swirl velocity component introduced (equivalent to 12 deg) into the annulus flow. For all tests the jet Reynolds number was kept above 2.4×10^4 to eliminate any Reynolds number dependence, see Margason [21].

Table 2 Flow conditions

Annulus flow:	No swirl		Swirl
Flow parameter	Primary	Dilution	Dilution
$R(V_j/U_c)$	5.0	2.0	2.0
$B(\dot{m}_b/\dot{m}_a)$	50%	20%	20%
Re_j	>24000	>24000	>24000
W_a/U_a (Swirl)	0.0	0.0	0.215

Dilution Port Flow Configuration. Results in this section will focus on the $\theta=0$ deg plane, i.e., an *x*-*r* plane passing through the centerline of a port. The velocity field in the annulus representative of a dilution port scenario is shown in Fig. 7. Shading in this figure indicates that the axial velocity component (*x*-direction) is negative.

At inlet ($x=-100$ mm) a fully developed turbulent profile is seen. This profile becomes noticably biased toward the inner wall as the front edge of the port is approached. Sitting principally behind the port centerline ($x=0$) is a large region of reverse flow (shaded), with the separation point of the flow from the outer wall clearly upstream of the port centerline. This region of reverse flow, which must be fed from out of plane, appears to have two significant effects. First, the port is fed near to perpendicular at its center line and the axial velocity components at the front and rear of the port are comparable in magnitude but have opposite direction. The net effect of this is that the bulk average flow direction in this plane will be close to radial, with only a slightly positive axial component. This will impact, of course, on the jet entry angle variation across the port (see below). The second effect is that the velocity profile downstream of the port is heavily biased toward the inner wall on this particular plane ($\theta=0$ deg). Flow conditions approaching any subsequent row of air admission ports would therefore be far from uniform. However, the next figure shows that the levels of turbulence in this region allow the skewness of the velocity distribution to be quickly mixed out. It is worth noting that this skewness will vary circumferentially and problems could arise due to uneven feed of near-by film cooling rings.

Figure 8 shows the corresponding normal stresses and turbulent kinetic energy distribution for the dilution flow scenario. The bulk average velocity at inlet to the annulus has been used to nondimensionalize the values and the contour level increments are the

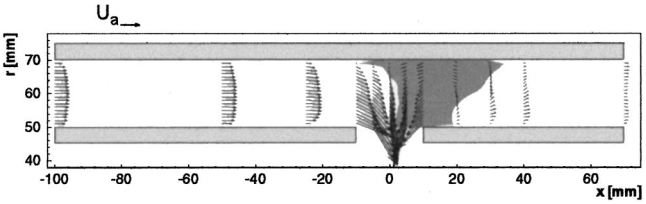

Fig. 7 Velocity vectors-dilution port flow

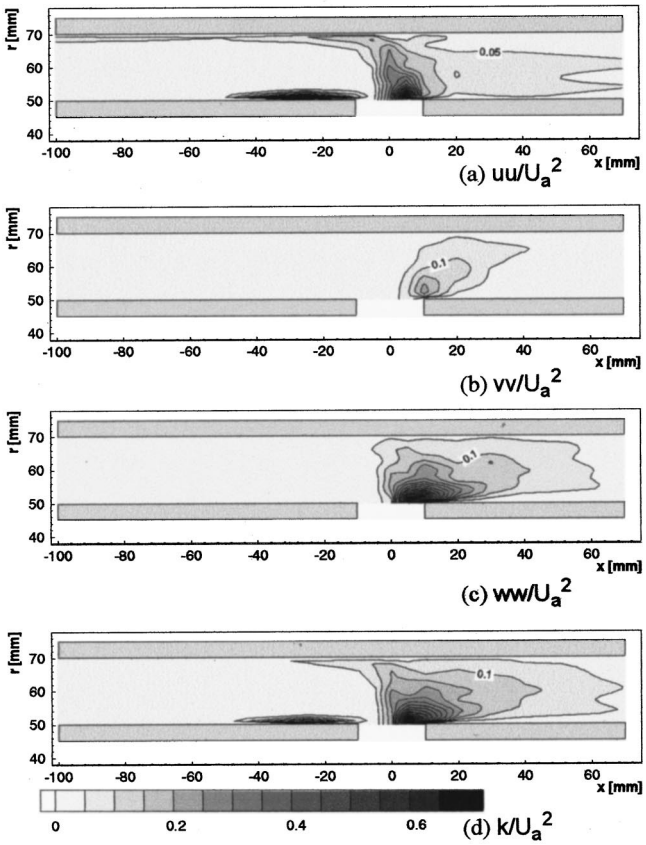

Fig. 8 Annulus turbulence field-dilution port flow

same for each of the four plots (0.05). Axial and circumferential normal stresses are similar in magnitude and distribution, with the highest levels coincident with the area of reverse flow. However, the radial normal stresses indicate significant anisotropy with levels of around one quarter of the other two components. Close to the separation point from the outer wall high levels of *uu* are seen, suggesting some unsteadiness associated with the separation. This phenomenon could conceivably create oscillations in the resulting jet trajectory, though a spatial cross-correlation would be required to confirm this. Highest levels of normal stresses occur over the rear half, and just behind, the port. This could be attributed to the flow history, though it will be seen later that an unsteady radial vortex is likely to be a significant contribution, particularly to the axial and circumferential components.

In Fig. 8(*d*) the normal stresses are combined to produce the turbulent kinetic energy field. It is clear from this figure that a uniform turbulence distribution would not be expected for the resulting jet, with higher levels clearly biased toward the downstream edge of the port. In addition, the level of turbulence intensity is higher than perhaps expected corresponding to an intensity level of 40–50 percent. There was evidence from flow visualisation that some contribution to these high ''turbulence'' levels, as obtained here from long time-averaged measurements, arise from through port vortex flow oscillations associated with the outer wall separation in the annulus mentioned above. However, no attempt was made to estimate the quantitative contribution as the measurements made here are intended to help validate time-averaged RANS CFD predictions. Correlations used for producing boundary conditions for predictions of internal combustor flow fields do not provide any information on the jet turbulence levels, let alone distribution. To introduce realistic boundary conditions to CFD predictions of combustor flows, the present experimental data provides very useful information.

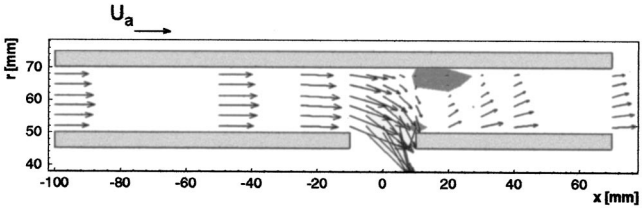

Fig. 9 Velocity vectors-primary port flow

Primary Port Flow Configuration. Increasing the bleed ratio to 50 percent (and the jet to core flow velocity ratio to 5) produces the primary port-like flow configuration. The change in velocity field (measured at a lower spatial resolution) can be seen by comparing Fig. 9 with Fig. 7.

Several distinct differences can be seen. The flow entering the port has much more axial momentum, the region of reverse flow is greatly reduced and the skewness created in the velocity distribution downstream of the port is still evident at $x=70$ mm. Note of these differences should be made as each will be examined in more detail below.

As bleed flow is increased the annulus flow will return quicker to an undisturbed developed annulus velocity profile. It would follow from this simple idea that levels of turbulence would decrease with increasing bleed. This is evident in Fig. 10, where the maximum value of k for the primary-like-port is around one third of that for the dilution configuration. Despite this difference in absolute levels of k the distribution is quite similar (as is the nature of the anisotropy which is not shown for brevity). The highest level of turbulent kinetic energy is found where the radially inflowing fluid impinges on the inner annulus wall just downstream of the port, producing what may be described as a wall jet when examining the velocity field in the given $\theta=0$ deg plane. The distribution of k around the maxima appears to be dominated by the shear layer driving the separation bubble on the outer annulus wall. The impingement process and reduced turbulence levels are perhaps responsible for the much more radial inward bias of the velocity profile at the most downstream station ($x=70$ mm) when compared to the dilution configuration. The effects of this skewed velocity profile on the quality of feed air to the downstream air-admission ports is largely unknown.

Circumferential variations in the axial velocity distribution are shown in Fig. 11 on an $x=10$ mm plane, i.e., a plane tangent to the most downstream edge of the port. Unshaded regions indicate reverse flow and a constant contour increment of $U/U_a=0.2$ is used.

In Fig. 11(*a*) the fact that much of the port feed comes from the downstream annulus is reemphasised (Fig. 7), with the reverse flow region being of very similar width to the diameter of the (just) upstream port. The increase in this width when very close to the outer wall suggests that the annulus flow is close to separation around the whole of the annulus. For the primary port Figure 11(*b*) it is clear the outer separation is indeed a localized bubble, circumferentially aligned with the port, though just downstream as

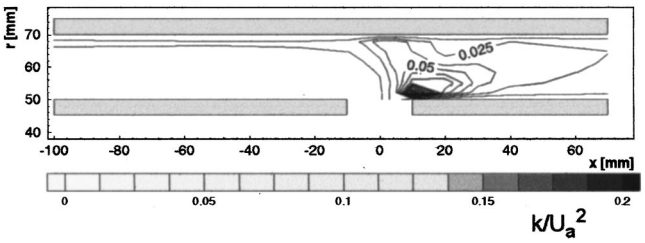

Fig. 10 Turbulent kinetic energy-primary port flow

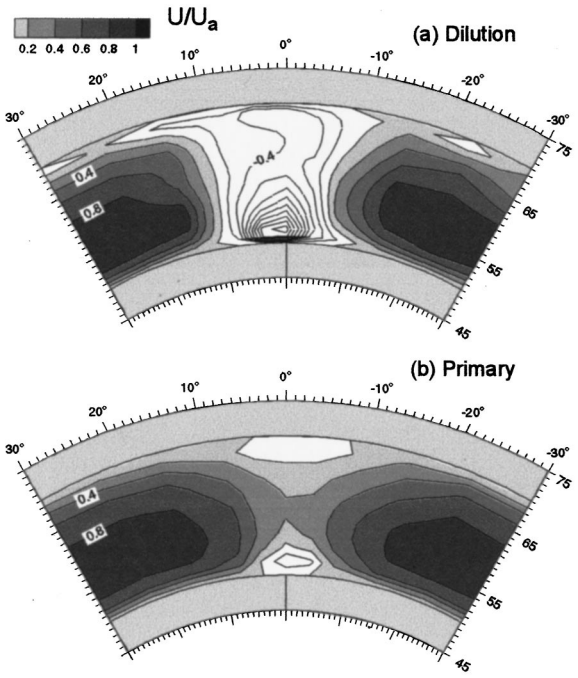

Fig. 11 Axial velocity distribution $x=10$ mm

shown in Fig. 9. The negative velocity next to the inner wall is the flow from impingement entering the very rear edge of the port. It is clear from Fig. 11(*a*) and (*b*) that any subsequent, downstream, ports will be fed by annulus flow which has a very distorted profile, both radially and circumferentially.

A further insight into the three-dimensional nature of the annulus flow is shown in Fig. 12. Here the secondary velocity components (U and W) are shown on a plane of constant radius, 3 mm above the inner annulus wall. A clear idea of the fraction of port fed by the highly turbulent downstream annulus flow is obtained. This time-averaged velocity field does mask an unsteadiness in this flow. The near-symmetrical recirculations of the fluid into the rear of the port have a tendency to behave in a similar fashion to a vortex street behind a cylinder. One will tend to dominate producing a bath-plug-like through-port vortex. With no distinct frequency this will be shed and convected downstream while the opposite side will grow and become dominant. This unsteady aspect is currently being investigated further.

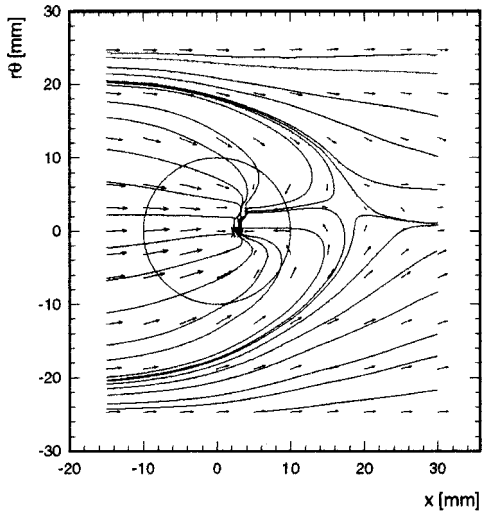

Fig. 12 Particle paths of flow entering hole-dilution port conditions

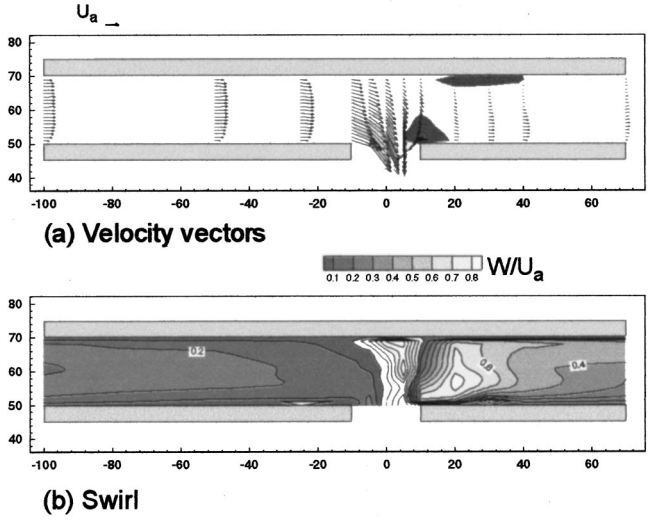

Fig. 13 Velocity field in annulus-dilution port conditions with swirl

Annulus Swirl. The next three figures indicate the effect of introducing swirl to the annulus for the dilution port. With careful thought, the velocity fields given on the $\theta=0$ deg, $x=10$ mm and $r=53$ mm planes allow a reasonably complete picture of the flow topology to be imagined. Several interesting features are noted.

Figure 13 shows the velocity field on the $\theta=0$ deg plane with the through plane velocity, W, indicated using contours where unshaded regions indicate a negative component. Moderate inlet swirl of 12 deg to axial ($W/U_a=0.215$) appears to be amplified by the presence of the port. Downstream of the port—where bulk average velocities are reduced by 80 percent—the swirl component is seen to increase by a factor of 2 or 3, indicating high flow angles relative to the axial direction in this plane. Furthermore, the considerably high negative W indicates the presence of a strong through port vortex which can be seen to originate on the outer annulus wall (by following the $W=0$ contour at $x=8$ mm).

The swirl produces a skewing of the axial velocity profile downstream of the port, as shown in Fig. 14, with the skew in the circumferential direction increasing with radius. The size of the recirculation region is slightly reduced, but the strength is increased close to the inner and outer annulus walls. The marginal separation close to much of the outer wall in Fig. 11(*a*) is not seen here, possibly due to the help of a radial acceleration of the fluid produced by the high swirl components present.

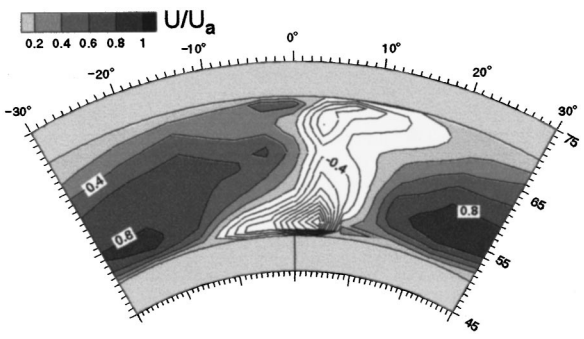

Fig. 14 Axial velocity distribution $x=10$ mm (looking downstream)

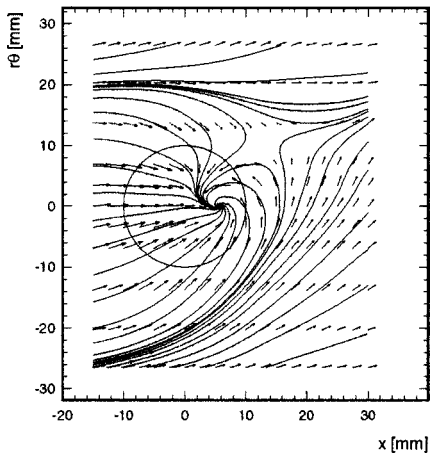

Fig. 15 Particle paths of flow entering hole-dilution port conditions with swirl

The strong through port vortex is evident in Fig. 15. It appears a quite dramatic effect in secondary velocity components has been brought about downstream of the port by the moderate 12 deg of swirl introduced upstream. This time-averaged flow field is perhaps not too dissimilar to an equivalent instantaneous flow field in the otherwise identical case but with no annulus swirl (Fig. 12). However, the comparable instant being an extreme when one of the recirculations passing in to the rear of the port is most dominant and vortex-like. Flow visualization evidence shows that the presence of swirl has a stabilizing effect on this flow structure and the swirl induced vortex is a much more stable flow structure than that for the same dilution port with no annulus swirl. PIV techniques will be an invaluable tool for investigation of these unstable vortex structures.

Jet Characteristics. The above discussion would not be complete without comment on the resultant effects on the jet characteristics. Figure 16 shows both the velocity magnitude and flow angles issuing from the port exit plane for the three flow scenarios considered. The given profiles have been measured on the port diameter coincident with the $\theta=0$ deg plane. Considering V_j is double U_a for the primary port configuration (Dilution: $V_j = 3.2U_a$) and applying an error band of $\pm 0.04U_a$ it is possible to determine that the maximum error in the values of α and β presented is ± 1.5 deg.

The dilution port configuration with and without swirl have a noticable peak of velocity magnitude toward the rear of the port, coincident with the region fed by the downstream annulus which may contain strong vorticity. Separation of the flow from the upstream edge of the port results in a low velocity close to the upstream edge ($x/r<0.8$) for all cases. Due to recirculation in the flow at this point a discontinuity is also seen in the flow angle profiles. Between these two areas a plateau region of constant velocity is present across the core of each of the jets.

Despite the constant velocity magnitude in the core of the jet, considerable variation in jet trajectory is noted in the distribution of α-generally becoming more vertical toward the rear of the port. For the dilution port configuration the rear of the jet actually has negative axial momentum due to the strong reverse flow in the downstream feed annulus. This effect is not seen for the case with annulus swirl because the fraction of the port fed by flow with the strongest negative axial velocities is skewed out of the measurement plane by the swirl (see Fig. 15).

The variation of β is only shown for the flow scenario with swirl ($\beta=90$ deg for the other two cases). For the core of the jet a deviation of a fraction of a degree is observed. However, toward the rear of the port the effect of the through port vortex (shown close to port entry in Fig. 15) is clearly apparent as a change in β from greater than 90° to less than 90° (due to a change in sign of W).

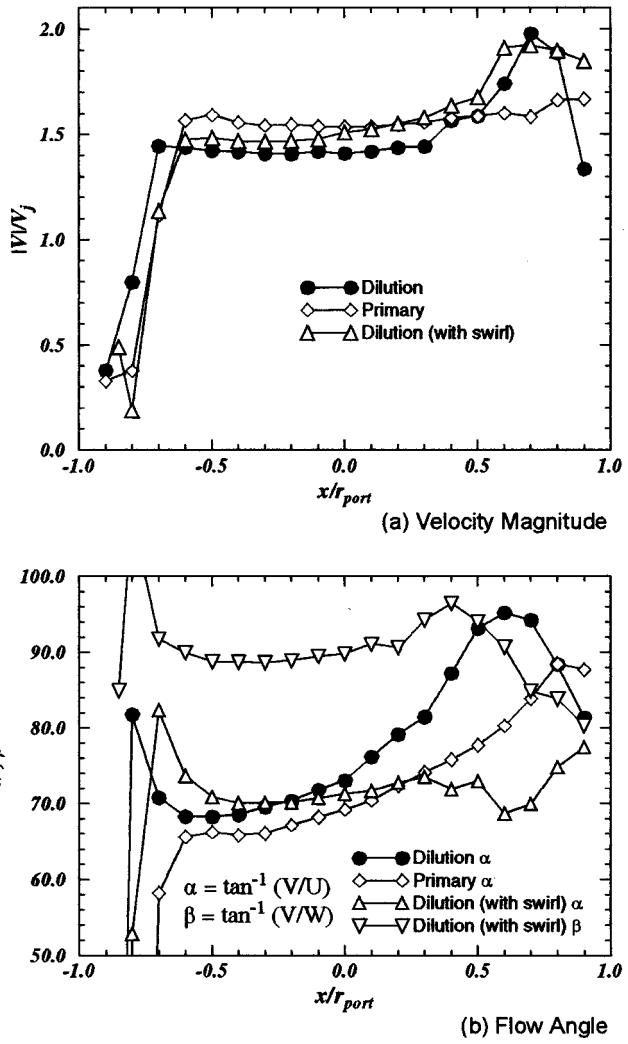

Fig. 16 Profile characteristics of jet flow through ports for primary and dilution cases

1D representation (a single value of U, V, and W over the whole port) of these characteristics is evidently going to provide a poor estimate of the actual jet. The use of 1D correlations as jet boundary conditions to internal only combustor calculations is widespread and has been found to have significant effect on subsequent calculations of the internal flow. This effect is described in significant detail in McGuirk and Spencer [22]. In this related work, the measurements presented here are compared to the exit plane velocity contours as predicted by high resolution RANS CFD calculations of the port flow which help to further emphasise the non-uniformity of the jet across the port exit plane.

Conclusions

- Experimental facility designed and successfully used to explore detailed flow structures in annulus supply ducts feeding combustor liner ports.
- LDA data gathered for mean velocity and turbulence field for both primary zone port conditions (high jet to core flow velocity ratio, R, and high bleed flow past hole, B) and for dilution zone conditions (reduced R and B).
- Significant flow structure observed in feed annulus in immediate vicinity of ports. Large levels of turbulence and anisotropy were documented.

• Differences between primary and dilution configurations were partly attributed to different separation patterns in the annulus flow, leading to larger axial velocity components in the primary port and larger and longer lasting disturbances of annulus flow passed downstream to bleed flow.

• Profiles of radial velocity component and jet angle which result for both annulus conditions were documented. These provide important information to add to 1D empirical correlations and aid specification of CFD boundary conditions.

• Swirl in the annulus was found to produce noticable disturbances in jet exit characteristics and alter vortex position observed in port.

Acknowledgments

This work has been carried out within the University Technology Center in Combustion Aerodynamics at Loughborough University. The authors would like to acknowledge funding, support, and useful discussions with colleagues at Loughborough, Rolls-Royce plc. and DERA (Pyestock).

Nomenclature

A = area
B = bleed ratio
C_d = discharge coefficient
D, d = diameter of core/port
h = annulus height
J = momentum flux ratio
k = turbulent kinetic energy
$\dot{m}$ = mass flow rate
U, V, W = mean velocity components
x, y, z = rectangular cartesian coordinates
x, r, θ = cylindrical polar coordinates
α = jet injection angle
β = jet skew angle

Subscripts

a = annulus inlet
b = annulus bleed
c = core inlet
h = hole, port
j = jet
L = laser coordinates
o = core outlet

References

[1] Stuttaford, P. J., and Rubini, P. A., 1997, ''Preliminary gas turbine combustor design using a network approach,'' ASME J. Eng. Gas Turbines Power, **119**, No. 3, July, pp. 546–552.
[2] Adkins, R. C., and Gueroui, D., 1986, ''An Improved Method For Accurate Prediction Of Mass Flows Through Combustor Liner Holes,'' ASME Paper 86-GT-149.
[3] Hay, N., and Spencer, A., 1992, ''Discharge Coefficients Of Cooling Holes With Radiused and Chamfered Inlets,'' ASME J. Turbomach., **114**, pp. 701–706.
[4] Baker, S., and McGuirk, J. J., 1992, ''Multi-Jet Annulus/Core-Flow Mixing—Experiments and Calculations,'' ASME Paper 92-GT-111.
[5] Doerr, Th., Blomeyer, M., and Hennecke, 1995, ''Optimization of Multiple Jets Mixing With a Confined Crossflow,'' ASME Paper 95-GT-313.
[6] Carrotte, J. F., and Bailey, D. W., 1995, ''Detailed Measurements On A Modern Dump Diffuser System,'' ASME J. Eng. Gas Turbines Power, **117**, pp. 678–685.
[7] Spencer, A., 1998, ''Gas Turbine Combustor Port Flows,'' Ph.D. thesis, Loughborough University.
[8] Coupland, J., and Priddin, C. H., 1986, ''Modelling the Flow and Combustion In A Production Gas Turbine Combustor,'' Turbulent Shear Flows 5, F. Durst et al. eds., Springer-Verlag.
[9] Baker, S. J., 1992, ''Combined Combustor/Annulus Flows: Isothermal Experiments and Predictions,'' Ph.D. thesis, Imperial College of Science.
[10] Koutmos, P., and McGuirk, J. J., 1989, ''Isothermal Modeling of Gas Turbine Combustors: Computational Study,'' J. Propulsion, **7**, No. 6, pp. 1064–1071.
[11] Stull, F. D., Craig, R. R., Streby, G. D., and Vanka, S. P., 1985, ''Investigation of a Dual Inlet Side Dump Combustor,'' J. Propul. Power, **1**, No. 1, Jan., pp. 83–88.
[12] Turner, J. T., 1990, ''Application of LDA in Liquid Flows,'' LDA Short Course Lecture Notes, UMIST.
[13] Bicen, A. F., 1981, ''Refraction Correction For LDA Measurements in Flows With Curved Optical Boundaries,'' Imperial College, Fluids Section, Report FS/81/17.
[14] Yanta, W. J., and Smith, R. A., 1973, ''Measurements of Turbulence Transport Properties with a Laser Doppler Velocimeter,'' AIAA Paper 73-169.
[15] Castro, I. P., 1989, *An Introduction to the Digital Analysis of Stationary Signals*, Adam Hilger, Bristol, England.
[16] Durst, F., Jovanovic, J., and Sender, J., 1993, ''Detailed Measurements of the Near Wall Region of Turbulent Pipe Flows,'' Proc. Ninth Symposium on Turbulent Shear Flows, pp. 2.2-1 to 2.2-6, Kyoto, Japan.
[17] Edwards, R. J., 1987, ''Report of the Special Panel on Statistical Particle Bias Problems in Laser Anemometry,'' ASME J. Fluids Eng., **109**, pp. 89–93.
[18] Boadway, J. D., and Karahan, E., 1981, ''Correction of Laser Doppler Anemometer Readings for Refraction at Cylindrical Interfaces,'' DISA Information, No. 26, pp. 4–6.
[19] Durst, F., Melling, A., and Whitelaw, J. H., 1976, *Principles and Practice of Laser Doppler Anemometry*, Academic Press, NY.
[20] Press, W. H., Teukolsky, S. A., Vetterling, W. T., and Flannery, B. P., 1992, ''Numerical Recipes in FORTRAN The Art of Scientific Computing,'' Cambridge University Press, 2nd Ed., U.K.
[21] Margason, R. J., 1993, ''Fifty Years of Jet in Cross Flow Research,'' AGARD-CP-534, pp. 1-1–1-41.
[22] McGuirk, J. J., and Spencer, A., 2000, ''Coupled and Uncoupled CFD Prediction of the Characteristics of Jets From Combustor Air Admission Ports,'' ASME paper 2000-GT-0125.

Francois Schmitt
e-mail: francois@stro.vub.ac.be

Birinchi K. Hazarika

Charles Hirsch

Department of Fluid Mechanics,
Vrije Universiteit Brussel,
Pleinlaan 2, B-1050 Brussels, Belgium

LDV Measurements of the Flow Field in the Nozzle Region of a Confined Double Annular Burner

A database for the complex turbulent flow of a confined double annular burner in cold conditions is presented here. In the region close to the exit of the annular nozzles LDV measurements at 5515 grid points in the meridional plane were conducted. At each measurement position, validated data for 3000–16,000 particles were recorded, and the mean axial and radial velocities, axial and radial turbulence intensity and Reynolds stresses were computed. The resulting mean flow field is axisymmetric within an uncertainty of 2 percent. The contour plots of turbulent quantities on the fine grid, as well as the streamlines based on the mean flow field, are presented for the flow.
[DOI: 10.1115/1.1366681]

1 Introduction

Industrial devices in fluid engineering often involve complex turbulent flows. Turbine engines, industrial furnaces, combustors, and burners are a few examples of such devices. A better understanding of the flows associated to these devices is essential in the context of energy savings, and for environmental concerns, linked to pollution and global warming. Unfortunately, these flows are still inadequately modeled and therefore need further experimental studies to fully understand them (see Wilcox [1] and Piquet [2] for recent reviews on turbulence modeling). One area where special effort is needed is turbulence modeling and its coupling with chemistry, involving scalar mixing.

For the design of new turbulence models and for the validation and parameter tuning of available ones, either Direct Numerical Simulation (DNS) or experimental data are needed. Even with the tremendous improvements in computer technology, DNS is possible only at low Reynolds numbers; therefore, experimental data are still the only practical solution for the data needed for complex turbulent flows. The generation of experimental databases is thus essential, but complete databases are still rare for complex flow configurations. In this project, contribution is made to this task by generating a database for a burner representative of industrial situations. The data will be freely available through Internet (http://stro9.vub.ac.be/expdata); the content and format of the files are described below.

Industrial burners are designed to generate stationary combustion in a confined chamber, with desired values of velocity, temperature and species concentrations at the exit of the combustion chamber [3]. Burners are often installed to destroy pollutant gases resulting from industrial activities, before releasing them to the atmosphere. Since international norms in the matter of pollution are getting more and more restrictive, modification of burner and correct prediction of flow in order to minimize emission has become essential. To achieve this goal, it is necessary to understand the behavior of the flow field and the combustion process associated with burners. Since the turbulent diffusion of species is faster than the combustion process, the first step is to study the behavior of the various jets and their interaction with the surrounding flows in cold conditions. However, one cannot ignore the possibility that chemical reactions occurring in a reacting burner modify the flow, so that a cold flow could be unrepresentative of a reacting flow through the same geometry, as is argued in [4] for a swirling flow. Nevertheless, it is clear that research on steady turbulent flow in axisymmetric geometries under nonreacting conditions is of primary importance for combustion modeling, since it is a necessary first step before introducing combustion in the computational models.

The burner to be investigated in this project consists of 2 coaxial annular orifices, leading the confined co-annular jets to discharge into a sudden expansion, the combustion chamber (see Fig. 1). In hot flow conditions there is a central pipe which supplies the fuel, while the annular jets supply the air. Since in hot conditions the velocity of the central jet providing the fuel is very low compared to the air velocity, the central jet has been ignored for the present study. This geometry provides a recirculation zone, together with several vortices, which help to stabilize the flame.

The final measurements of the flow field in the nozzle region of a model burner are described here. This region is also named the initial region and the near wake region by various investigators. The model burner is built twice the scale (to increase precision) of a prototype 100 kW burner. From the exit plane of the burner to a distance of 1.5 diameter 5515 measurements were made on 36 sections using a two-dimensional laser Doppler Anemometry (2D LDA) system. At each section measurements were taken either at 101 or at 201 measurement positions. This gives a precise and complete description of the flow in the region of interest. The experimental arrangement and the measurement procedure are described in the following sections, and finally the results are presented. The results include the estimation of mean values of first and second moments and the errors in axisymmetry.

2 Experimental Arrangement

2.1 The Burner. The cross section, in the meridional plane, of the burner and the experimental setup is shown in Fig. 1. Figure 2(*a*) shows a photograph of the entrance of the burner and Fig. 2(*b*) shows a photograph of the exit. The entry to the burner is shaped to avoid any separation bubbles that appear in ordinary entrance regions. The dimensions of the different parts of the test facility are given in Figs. 1, 3, and 4. The burner model is built around the central steel cylinder 85 mm in diameter. Two ducts, whose dimensions are given in Fig. 4, produce the primary and secondary flows. At the exit of the nozzle, 2 annular pieces acting as contracting nozzles (pieces I and J in Fig. 4) are fixed on plastic tubes. At the nozzle end the concentricity of the 3 units is maintained by 2 sets of 3 airfoils each. These airfoils are placed inside the streams and occupy the axial length between 60 mm and 80 mm upstream of the burner face, with the maximum thickness of the airfoil sections being 1 mm. They locally perturb the flow, but

Contributed by the Fluids Engineering Division for publication in the JOURNAL OF FLUIDS ENGINEERING. Manuscript received by the Fluids Engineering Division November 20, 2000; revised manuscript received February 6, 2001. Associate Editor: K. Zaman.

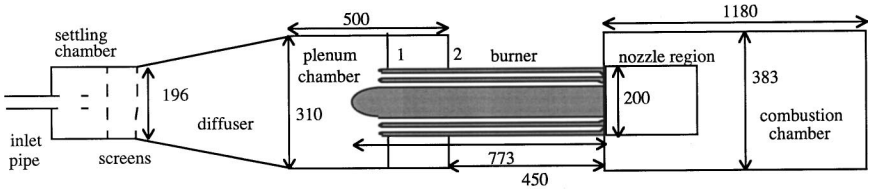

Fig. 1 An overall display of the facility. Inlet arrangement, a cut on the burner, and the combustion chamber are shown. The nozzle region corresponding to the measurements is indicated. The burner is made of 5 PVC tubes: two tubes are used for the exterior boundary, two for the boundary between the two ducts, and one for the central boundary. The tubes stay together using threaded rods. Two supports (denoted 1 and 2) support the burner. Dimensions in mm.

maintaining accurate axisymmetry is considered most important in this case. The concentricity at the entrance of the burner is maintained with a crosspiece that is fixed with screws on the aluminum intake rings and the central tube. The portions of this crosspiece, which is exposed to the flow, are also given the airfoil shape with 3-mm maximum thickness and 20 mm chord.

The model burner gives a secondary to primary velocity ratio of close to unity (experimentally 0.97). To change the velocity ratio it is necessary to introduce low solidity screens in the flow passages where reduction velocity is needed. The present experiment corresponds to a configuration with a velocity ratio of 1.

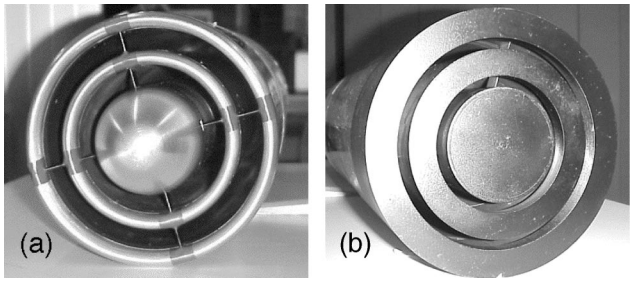

Fig. 2 (a) Picture of the entrance of the burner, showing the aluminum rings; (b) picture of the exit of the burner, showing the nozzles producing the primary and secondary flows

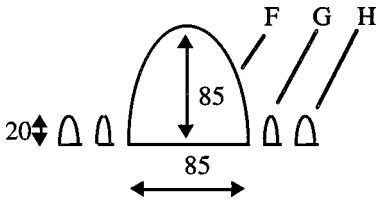

Fig. 3 The entrance of the burner: there are 3 elements in this region to facilitate smooth entry, denoted F, G, and H. The entrance of the central tube is covered with a bullet of ellipsoid shape (F). The two streams are separated by an annular boundary, whose entrance is covered with an aluminum ring (G), of elliptic cross section, with axial length of 20 mm. The exterior boundary has an entrance covered with an aluminum ring (H).

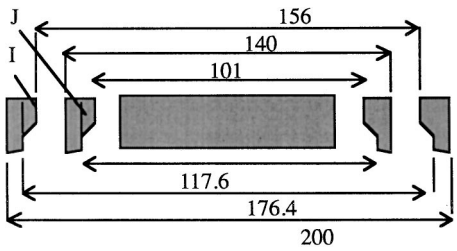

Fig. 4 The exit of the burner, indicating the dimensions of different diameters and showing contracting nozzle pieces I and J. Piece J and I produce area contraction ratio of 2.2:1 and 2.4:1, respectively.

2.2 Inlet Conditions and Combustion Chamber. A compressor provides the air which flows through a settling chamber, diffuser and plenum chamber, then through the burner to the combustion chamber (see Fig. 1). A brief description of the complete set up is given below.

An incremental shaft encoder precisely measures the rotation speed of the compressor. A speed controller allows to choose a speed between 0–150 percent of the nominal speed of 3000 rpm. The air then passes through an inlet pipe, which brings the air into the entrance of the settling chamber. The air flows axially through two wire mesh screens, to a conical diffuser, and then a plenum chamber. The burner is inserted into the plenum chamber, and is maintained by 2 supports to ensure a precise alignment of the axis of the burner and the plenum chamber. The settling chamber and plenum chamber are not described in detail since the contraction ratio from the plenum to the burner inlet is larger than 20. In addition, the ratio of the length to the diameter of the channels inside the burner is sufficiently large for the fully developed flow to be well established, and influences from the inlet disturbances are negligible.

A mild steel tube frame supports the burner and the cold chamber. The assembly is clamped to a table after setting the axis of the chamber and burner assembly horizontal. The cold chamber is constructed from a PVC tube. At the entrance of the chamber, a portion 285 mm along the axis and 350 mm along the circumference has been removed from the tube to have optical access to the flow. A window made of transparencies is glued to the tube to cover the opening, giving a relatively stiff clear wall 0.9 mm thick. At the exit of the cold chamber, four circular holes are made on the wall to evacuate the flow. The air with smoke is evacuated with a ventilator. With this arrangement, the flow in the cold chamber is completely isolated from the laboratory, and cannot be perturbed by it.

2.3 Technical Specifications of the LDA System. The laser rays for the 2D LDA system is provided by an Argon Ion Laser with rated output of 4 watts. Of this, 1.7 watt is emitted in the green color at the wavelength 514.5 nm and 1.3 watt is emitted in the blue color at the wavelength 488.0 nm. The beams are split and given 40 MHz frequency shift with a bragg cell for detection of flow direction. The LDA system used for the purpose is based on fiber optics with backscatter method, and has processors based on spectrum analysis of the back scattered signals. This gives the processor the ability to process signals with very low signal to noise ratio. The measurements are conducted using data acquisition software.

The intersection of the two blue and the two green beams generates an ellipsoidal probe volume approximately 0.12 mm diameter and 0.9 mm long. The measurement point can be chosen and the probe volume moved using a 3D traverse system. The green and blue beams belong to 2 planes whose intersection, called the

LDA probe axis, was always kept horizontal. In general the probe axis is normal to the cold chamber axis. The measurements close to the nozzle of the burner (between 0 and 25 mm) needed a slight rotation of angle $\alpha = 6$ deg of the probe axis from the normal to the chamber axis. For each particle, velocity, transit time across the probe volume, and arrival time, are recorded.

3 Results

3.1 Errors of the Measurements

Data Processing. The data acquisition software includes some automatic filters in order to retain the record of only those considered valid among the detected particles. Raw valid data are recorded for each position: velocity, transit time and arrival time. After the acquisition, data can be processed. The first transformation is to take into account the orientation of the laser probe relative to the burner. The measured velocity components are processed to give axial and radial components (u,v) of the velocity in the laboratory coordinate system.

For each position, all the valid data have been stored. Several statistical quantities have also been estimated for each position: $U=\overline{u}$, $V=\overline{v}$, $\tau_{uu}=\overline{(U-u)^2}$, $\tau_{vv}=\overline{(V-v)^2}$ and $\tau_{uv}=\overline{uv}-UV$. The cross-moment τ_{uv} is estimated taking into account only the pair of data belonging to a coincidence window of duration 50 ms. This condition reduces the number of valid points taken into account to estimate this statistical quantity.

Estimation of the Error. The sources leading to the error in the mean quantities and non-axisymmetry are discussed and an estimation of these errors is given in this section. These errors can come from several independent origins:

(a) Errors in the mean velocity of the inlet flow: This corresponds to errors of the rotation speed of the compressor. This can be controlled using the incremental shaft encoder recording the rotation speed of the compressor with a precision of 0.1 rpm. For these measurements rotation speed of 2000 rpm is used. Due to fluctuations in the electrical power supply, or to mechanical defaults, the compressor rotation speed presents some unavoidable fluctuations. Using a very sensitive potentiometer, this rotation speed was maintained inside the interval (1990, 2010), which corresponds to an error of .5 percent.

(b) Errors in the estimation of the instantaneous velocities by the LDA system: This velocity is proportional to the Doppler frequency shift, which is estimated through a Fourier transform. Since this law is linear and the proportionality factor is fixed, the LDA apparatus does not need any calibration. The burst spectrum analyzer used to process the Doppler signal received from the probe volume has high resolution. This provides at the output a very low error, depending on the record length. In the present experiment, the record length for the first beam (axial velocity) is 16 and 64 for the second (radial velocity), giving (according to the manufacturer's specifications) errors of 0.025 percent and 0.006 percent for axial and radial velocity respectively. This is an infinitesimal source of error compared to the other sources.

(c) Statistical error in the mean values: Since the in-flow conditions are stationary with good precision, it can be stated that when taking N measurements, the mean of these N values converges toward the true average, when the measurements are taken during a time larger than the correlation time. With a Reynolds number of about 3.10^4, the flow is fully turbulent, and presents an energy cascade which introduces correlations (see e.g., Frisch [5] for a recent overview). These correlations are characterized by the largest eddy in the system, given by the dimension of the outer jet, of diameter 0.16 m. With a mean velocity in this region of about 4 m/s, the largest time scale of correlation at a given position is of the order of 40 ms. Depending on the zone of the flow considered, the detection of several thousands particles took between 10 s and 2 minutes, which is much larger than the correlation time. This confirms that the mean of N values should converge toward the true mean value.

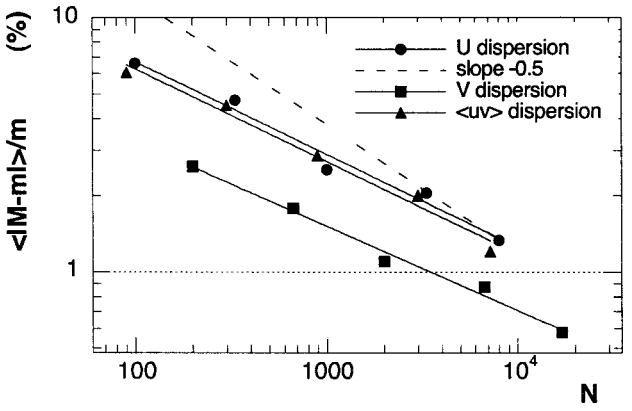

Fig. 5 Decrease of the error in the estimate of mean values, with the number of particles considered

The convergence of the statistics depends on the number of events that are chosen. A direct test can be applied. Let $m=\overline{X}$ be the mean value (time average) of a random variable X, and M the mean average of N successive realizations X_i of this random variable:

$$M=\frac{1}{N}\sum_{i=1}^{N} X_i \tag{1}$$

Denoting $\langle\cdot\rangle$ ensemble average, the normalized dispersion $\langle|M-m|\rangle/m$ gives the percentage of statistical error in the estimate of mean quantities, which can be written as:

$$\text{Stat. Error}=\frac{\langle|M-m|\rangle}{m}=\frac{A}{N^a} \tag{2}$$

where A is a constant and $a>0$. When successive measurements are independent random variables, the classical result for the second moment gives $a=1/2$ due to the central-limit theorem [6]. Figure 5 shows an example, where the procedure has been tested for several values of N and for 3 time series records: axial velocity, radial velocity and stress. The graph shows a slower decrease than this $-1/2$ law, which could be explained by some dependency in close successive values. When generalized for other locations, Fig. 5 also indicates that to reach an error of less than 2 percent, $N=3000$ is sufficient for axial velocity and stress, whereas $N=800$ is sufficient for radial velocity. For better accuracy in the measured quantities, at each grid point several thousands data (between 3000 and 16,000 depending on the location) have been recorded. This will provide statistical errors that are below, or of the same order of magnitude as the geometry errors.

(d) Geometrical errors in building the burner leading to a non-axisymmetry: When all other sources of errors are minimized, a superposition of different traverse provides a direct estimate of the geometry error. With careful construction this error is kept to a minimum, since, in order to provide comparisons between measurements and CFD codes, very good axisymmetry of the measurements is needed. This error has been checked for three different traverse positions close to the nozzle exit. Figure 6 shows a superposition of six axial and radial velocity profiles at the exit of the nozzle, taken at different angles of the burner. The maximum axial velocity recorded at the nozzle exit is $U_m=6.3$ m/s, which is used to normalize all mean velocities. The second moments are normalized by U_m^2. The radius of the outer jet, which is 78 mm, is used to normalize the lengths. The excellent superposition (within 1 percent) of the measured quantities from different angular positions shows that at the exit the axisymmetry is of high quality. Symmetric measurements for axial and radial velocity, turbulent

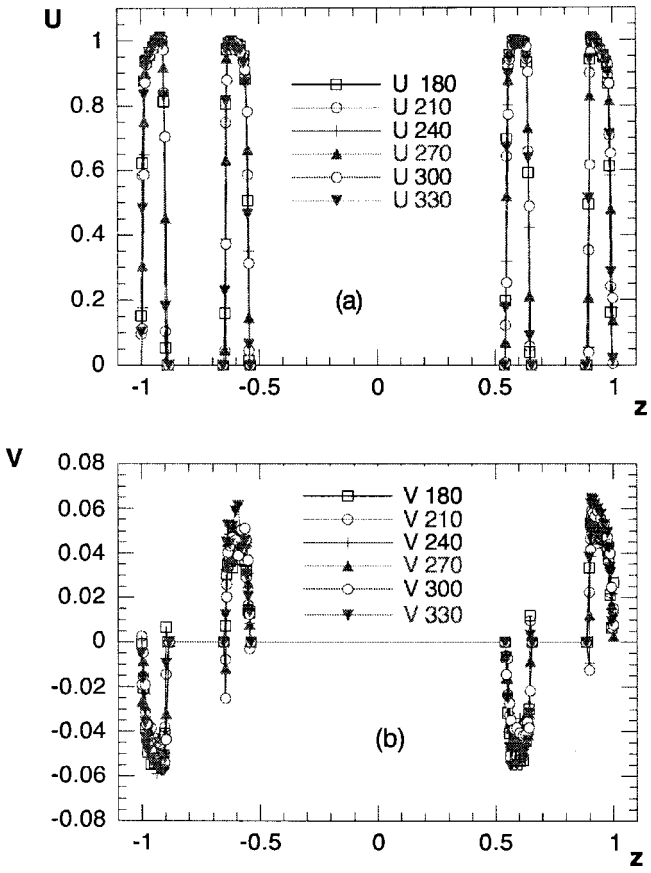

Fig. 6 Superposition of axial velocity profiles, and of radial velocity, at the exit of the nozzle, for different angles of the burner

kinetic energy and stress for $x=0.19$ and $x=0.38$ (x and z are the normalized axial and radial distances, respectively) are shown in Figs. 7 and 8. For the radial velocity and the stress, the values on one side of the axis are compared with the opposite of the values on the other side, since the fields are skew-symmetric. These figures also show very good superposition: globally, the average error (relative to U_m) is below 2 percent for mean values and for second moments (relative to the maximum kinetic energy, $k_m=0.18$); the average error in the quantities U, V, τ_{uu}, τ_{vv} and τ_{uv} for the nozzle region are given in Table 1.

3.2 Physical Characteristics of the Flow

Reynolds Number. The Reynolds number associated with the flow is calculated by taking the outer diameter of the outer jet, 156 mm, as the length scale. The velocity used for the calculation is the average velocity of the flow if the total volume of the air is flowing through this circular area of the jet uniformly, which is estimated to be 2 m/s. The corresponding Reynolds number is estimated by using these scales, giving $R_e \cong 3.10^4$.

Craya-Curtet Number. Annular burners develop coaxial jets in extremely high temperature gradient. When having informations in isothermal conditions, it would be useful to be able to predict the flow in the combustion case. When the fuel and oxidizer jets enter the combustion chamber, the jets mix with each other as well as with the surrounding recirculating fluid. The temperature of the jet rapidly increases and chemical reactions occur, changing the viscosity and density of the fluid. These changes of the properties of the fluid have severe effects on the flow field. Therefore, it is useful to link the isothermal and nonisothermal flows with a similitude number, the Craya-Curtet number, which characterizes the recirculation of confined jet flows [3]. This number was first obtained empirically by Thring and Newby [7], and then by solving the axisymmetric equations governing the flow field in an isothermal confined jet [8,9]. Later it was shown by experimental studies in hot and cold conditions [10,11], that the flow and mixing properties of the classical axisymmetric confined jet depends only on the Craya-Curtet number. This experimental study is missing in the case of our double annular burner; it is

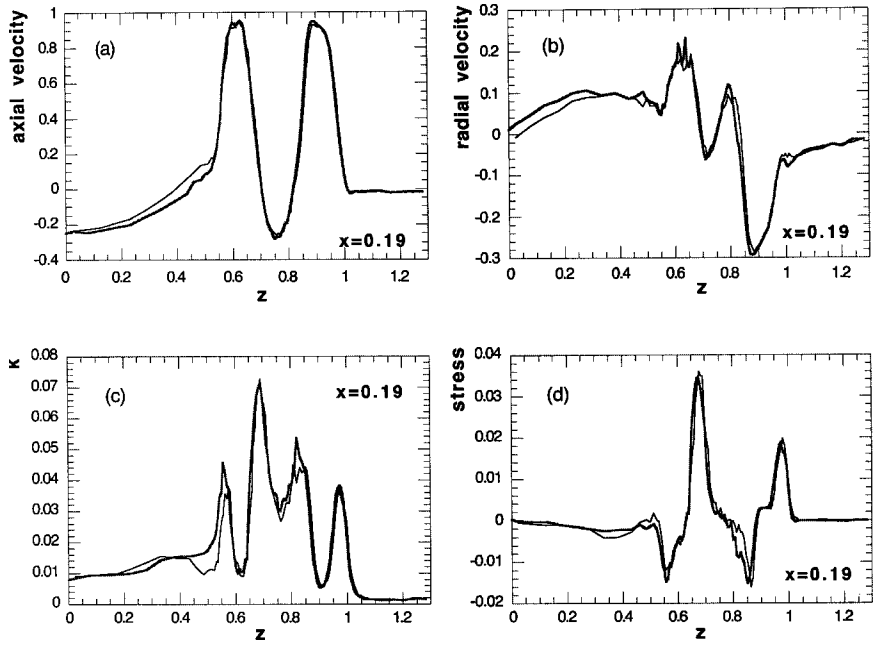

Fig. 7 Superposition of axial velocity, radial velocity, kinetic energy *k* and stress, for x=0.19. This traverse goes through all the vortices, big central and small lateral.

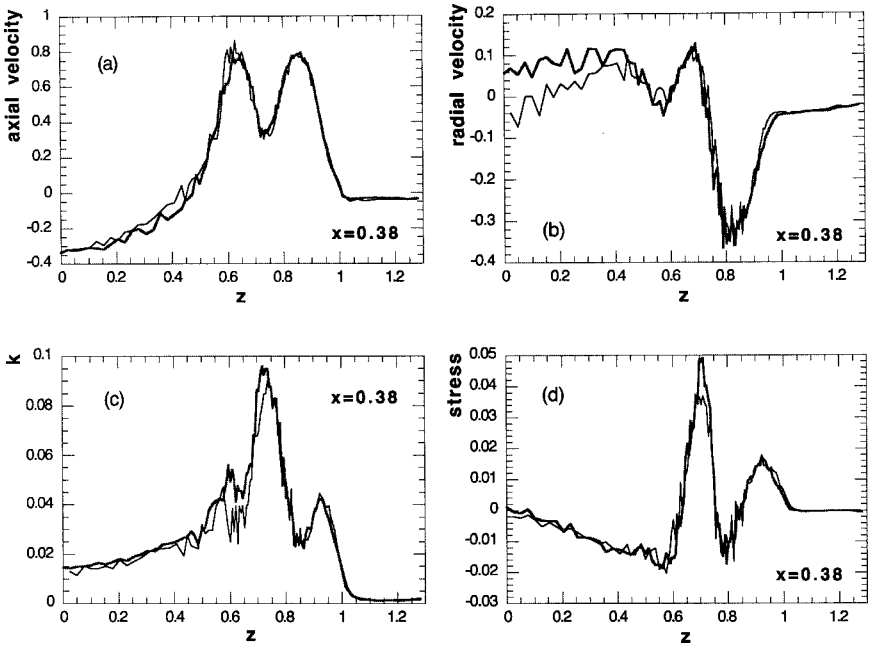

Fig. 8 Superposition of axial velocity, radial velocity, kinetic energy *k* and stress τ_{uv}, for x=0.38. This traverse goes only through the big central vortex.

assumed that a single related number also gives its qualitative properties. Adapting a presentation of the classical central jet case done in Guruz et al. [12], the Craya-Curtet number is defined here using stagnation pressure loss:

$$\frac{g(P_e^* - P_i^*)}{u_e^2 \rho} = \frac{1}{C_t^2} \tag{3}$$

Where, $P_e^* - P_i^*$ is the stagnation pressure loss in the system (the difference between exit and entrance stagnation pressure), u_e is the bulk-averaged velocity of the exit stream far from the nozzle, after the attachment, ρ is the density and C_t the nondimensional Craya-Curtet number. Using mass flow balance and overall force balance equations, this gives:

$$C_t = \left(\frac{A_1}{A_e}\right)^{1/2} \frac{1+\beta}{(1+\alpha^2\beta)^{1/2}} \tag{4}$$

where a constant density flow is considered and involves large area ratio geometry $A_e/A_1 \gg 1$, and $A_e/A_2 \gg 1$ of exit to primary and secondary nozzle areas. It is also considered that the nozzles are thin: $A_1 = 2\pi r_1 dr$ and $A_2 = 2\pi r_2 dr$ where r_1 and r_2 are the respective radii. α is the ratio of secondary to primary bulk-averaged velocity, and $\beta = r_2/r_1$. For these measurements, the velocity ratio is $\alpha = 0.97$, radius ratio is $\beta = 70/50.5 = 1.55$, and an exit area to primary area ratio is $A_e/A_1 = 45.5$, which gives a Craya-Curtet number of $C_t = 0.24$; a small value corresponding to large static pressure loss, indicating recirculation.

Table 1 Average axisymmetric error estimated for the whole nozzle region for the 5 basic quantities experimentally estimated. The error is relative to U_m for first moments, and relative to the maximum kinetic energy $k_m = 0.18$ for second moments.

Quantity	Average error (%)
U	1.6
V	1.1
τ_{uu}	1.3
τ_{vv}	1.3
τ_{uv}	.7

3.3 Structure of the Flow. Traversing stations on the flow, taken at different distances from the exit of the burner, help to identify several zones, exhibiting different flow properties. The nozzle region can be divided into four zones (denoted A–D). The different zones are illustrated in Fig. 9, giving the axial mean velocity obtained on traverse lines at different distances x from the exit of the burner. Depending on this distance, the profile shows different physical situations. The different zones are:

- For $0 \leqslant x < 0.32$ (zone A): there are two recirculation regions, one around the axis, and the other annular, between the two streams.
- For $0.32 \leqslant x < 0.70$ (zone B): there is one recirculation region, around the axis, with a complex annular jet around it, with a local minimum of its velocity.
- For $0.70 \leqslant x < 1.02$ (zone C): there is one recirculation region, around the axis, with an annular jet around it. This axisymmetric jet behaves as if there was only one stream.
- For $1.02 \leqslant x < 3.2$ (zone D): there is one axisymmetric jet, with a complex shape possessing a local minimum at the center.
- For $x > 3.2$, we are outside the nozzle region, and the burner behaves as if there were only a simple axisymmetric jet.

The inside-out reverse flow region surrounds the complete region, A–D, described above.

3.4 Streamlines and Contour Maps. The burner along with the test-rig was installed horizontally where the axis of the chamber Ox is in the mean flow direction. All measurements were taken by traversing the probe volume from the point $(x,0,-1.3)$ to $(x,0,1.3)$ vertically upwards passing through the point $(x,0,0)$. These traverse were made at 36 different stations, starting from $x=0$ to $x=3.2$. The distribution of these traverse stations was such that several traverse stations were located in each zone of the flow. This covers the complete nozzle region of the flow. For the positions below $x=1.22$ (included), 201 measurement points were chosen for each traverse (except $x=0$), whereas for other posi-

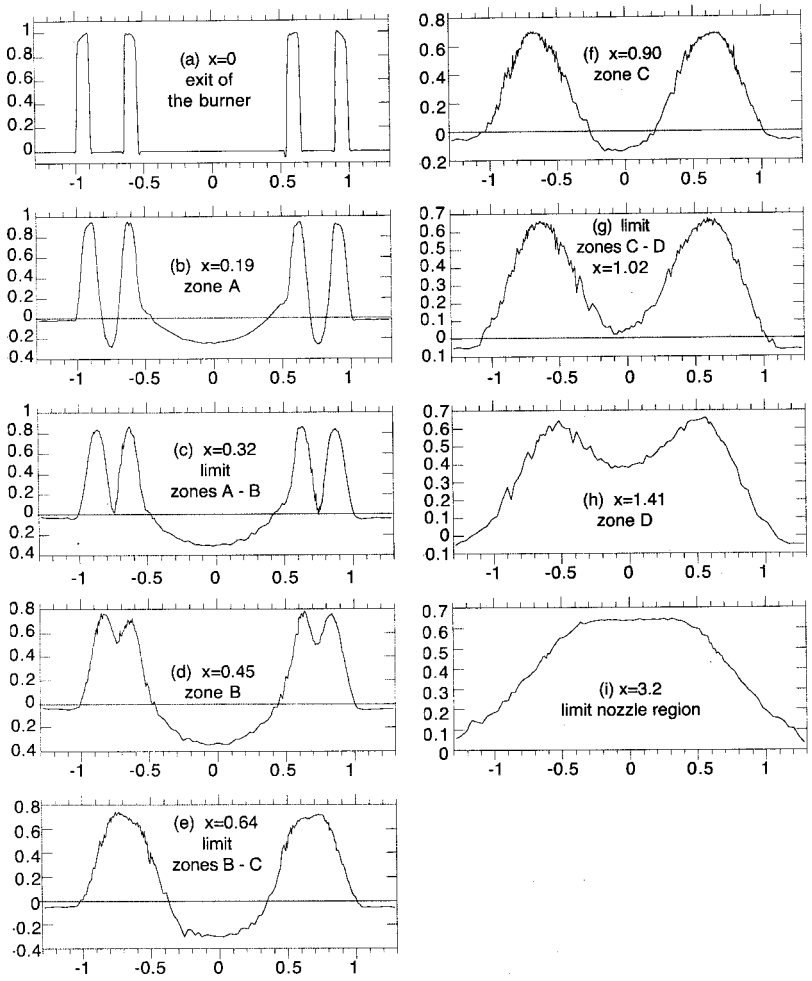

Fig. 9 From top to bottom, left to right: evolution of the axial velocity profile, with the distance from the burner exit. Different zones are found, possessing recirculation and merging of the different streams. Zone A corresponds to primary and secondary vortices, and possesses 3 recirculation regions. Zone B corresponds to an annular jet, with 2 recirculation regions. Zone C corresponds to a central jet, with 1 recirculation region.

tions, there were 101 measurement points. It is clear that the zones where the jets join and mix are more interesting than other regions; they also need more precision in measurements. The measurement positions were then unevenly chosen along the traverses: in calm zones, the space between consecutive measurements was 2 mm–4 mm, whereas for more turbulent zones, this space was 0.5 mm. These different measuring positions generate a grid, which was chosen through a rather empirical method, and it is shown in Fig. 10. When the flow field was plotted from these measurements, it could be seen that the grid chosen was not optimal, since the grid size is sometimes too rough in interesting regions. This in fact could not be guessed before taking the measurements, and it is considered that the grid chosen is nevertheless very dense for an experimental database.

The streamlines and contour maps of different quantities that characterize the flow are presented in this paper. The original data set is first interpolated on a finer and more regular (along Oz axis) grid, keeping all the original traverse positions, and interpolating raw data along each traverse, on a grid of size 0.5-mm in the z direction. This produces a smoother behavior of the particle traces. This new data set is symmetrized: for a given value of x, where the average values at position $(x,0,z)$ and $(x,0,-z)$ is set as the values at these two points. For all experimental values, this gives a perfectly axisymmetric field. An error field is also re-

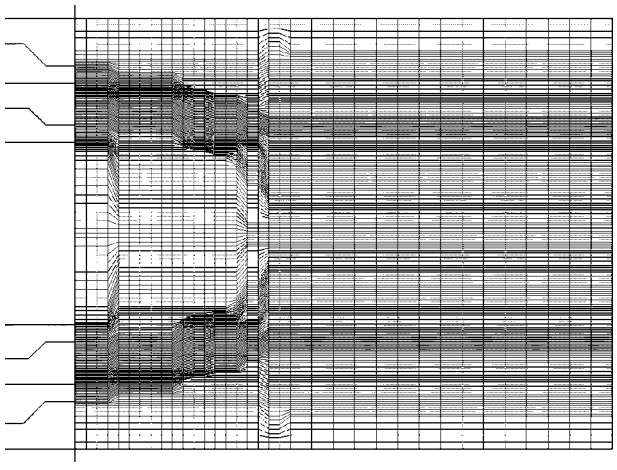

Fig. 10 Experimental grid chosen for the measurements. Darker zones correspond to one measurement every 0.5-mm along the vertical.

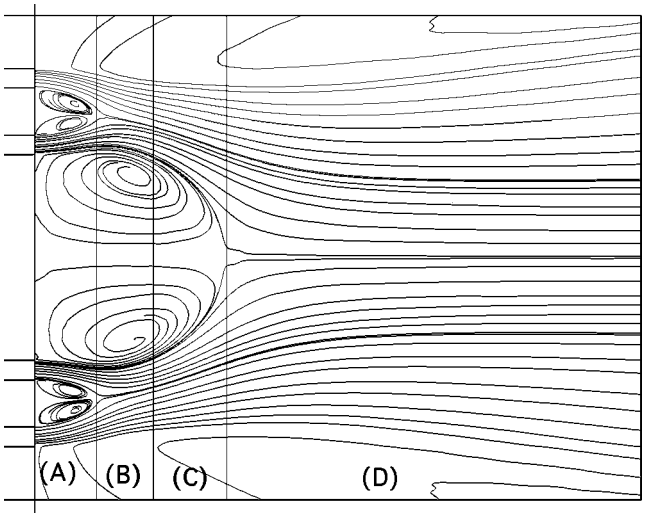

Fig. 11 Streamlines of the flow. This shows the direct and recirculating flows, the central vortex and double-toroidal vortices. The different zones identified with traverse sections in Fig. 9 are indicated.

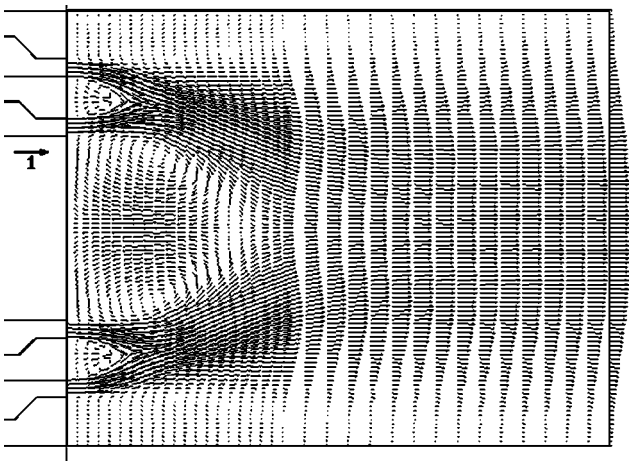

Fig. 12 Vector plot of the velocity field on some grid points

corded: this represents the axisymmetric errors, and corresponds to the raw data minus the averaged data. It gives a map showing the percentage of error in axisymmetry. The data available through internet will be organized as follows: they will be given as 36 text files, one for each traverse (unequally spaced between $x=0$ and $x=3.2$), containing experimental data corresponding to each of the 401 data points along the radial direction. Each file will provide the 5 basic quantities and their axisymmetry errors, i.e. the following values: z, $U(z)$, $V(z)$, $\tau_{uu}(z)$, $\tau_{vv}(z)$, $\tau_{uv}(z)$, $\delta U(z)$, $\delta V(z)$, $\delta\tau_{uu}(z)$, $\delta\tau_{vv}(z)$, $\delta\tau_{uv}(z)$ for 401 values of z equally space between -1.28 and 1.28.

The plots obtained from the first moments of the data are presented here. Figure 11 shows the streamlines of the axisymmetric velocity field and Fig. 12 the vector field. This helps to identify the structure of the flow: first the primary and secondary streams merge, creating a vortex bubble between them. This bubble corresponds to a pair of contrarotating toroidal vortices. Then the annular jet transforms into a central jet, creating a big central vortex bubble. This central vortex is less stable than the toroidal one; a recent study with the same geometry has shown that, for high enough Reynolds numbers, instantaneous shots (with a PIV technique for example) may not show this central vortex, whereas the toroidal one is much more stable [13]. Nevertheless, the surrounding high velocity primary stream maintains the overall shape of the central vortex. Inside this vortex, instantaneous shots reveal irregular vortices of various sizes, but in the average velocity field, the contra-rotating cells are clearly visible, and the vortex here has a nearly spherical shape, due to the velocity ratio of 1. Figure 13 shows a map and contour plot of the axial velocity. This indicates clearly the main flow, and the recirculation regions and the different vortices. The combustion chamber influences the flow, at least at the vicinity of the secondary jet, since it introduces an outer recirculation due to confinement. This recirculation is more visible in Fig. 13 (dark zones correspond to recirculation) than in Fig. 12 since the recirculation velocity is very low.

We represent also the second moments. The tangential turbulence $\overline{w'^2}$ is not measured, but it is natural to assume, due to isotropy of fluctuations around the axis, that $\overline{v'^2}=\overline{w'^2}$; then $k=1/2(\overline{u'^2}+2\overline{v'^2})$. This is shown in Fig. 14: the kinetic energy is maximal on the boundaries of the flows, especially at the edges of the vortices. It keeps also larger values in the wake of the

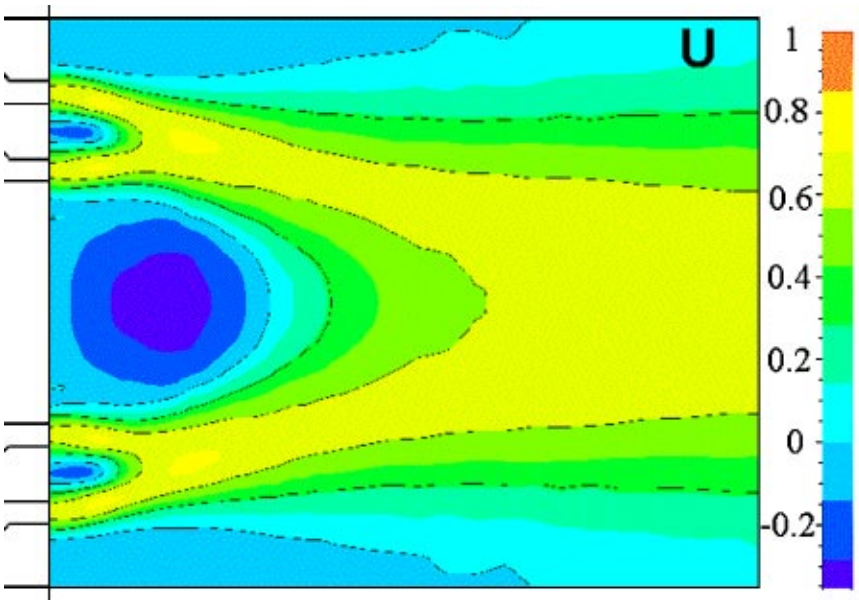

Fig. 13 Axial velocity: gray levels and isolines 0, 0.3, and 0.57. Isoline 0 surrounds 5 recirculation regions

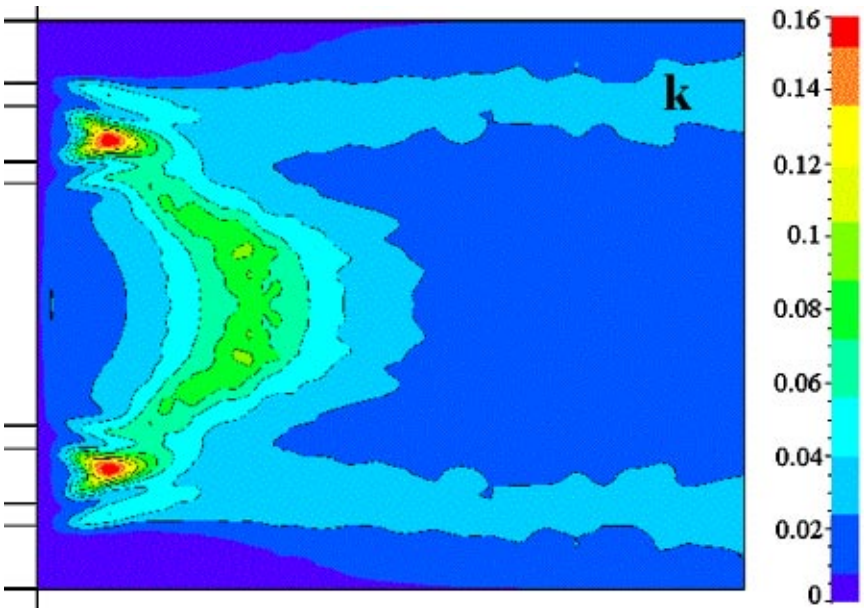

Fig. 14 Isolines and display of the kinetic energy *k*. The values of the isolines are the following: .024, .04, .056, .072, .088, .104, .12.

secondary stream. Figure 15 shows the Reynolds stress $\tau_{uv}=\overline{uv}-UV$. It has also larger values in the wake of the secondary stream, and close to the boundaries of the vortices. It has large intensity values in localized positions at the edges of the vortices.

4 Conclusion and Developments

The cold flow properties of a double annular burner were studied using 2D LDV measurements. The main challenge for this type of study is to obtain a good axisymmetry in the measurements, for validation of numerical models. Complete descriptions of first and second moments of the velocity field, on a precise experimental grid were obtained in this study. The overall axisymmetry is excellent, on the average below 2 percent for all quantities. The double annular geometry creates a complex flow, which is precisely identified here, possessing recirculation regions, several toroidal vortices, and stagnation point and stagnation lines. The vector plots, streamlines of the flow and several color maps representing the kinetic energy *k*, and the Reynolds stress are presented here. In order to minimize the error due to a lack of convergence of the statistics, the signal from more than 3000 particles at each measurement points were considered. A quantitative analysis of experimental results, showing the degree of axisymmetry along some traverse for mean velocity and second moments were performed and presented here.

The experimental results obtained have a more general impact than simply the knowledge of a particular burner, since this database can be used for comparison with the output of turbulence models (for turbulence models applied to a similar configuration

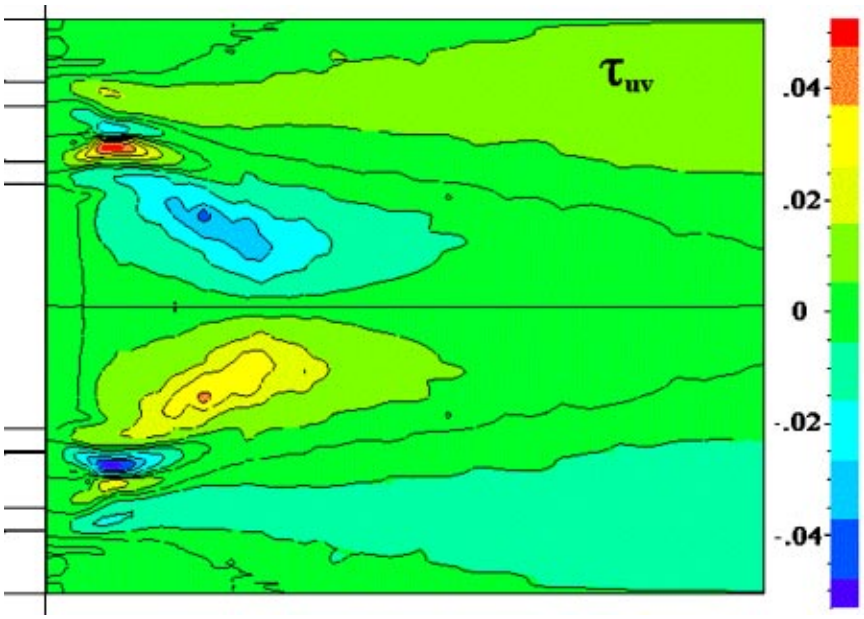

Fig. 15 Isolines and display of the stress $\tau_{uv}=\overline{uv}-UV$. The values of the isolines are the following: −.037, −.026, −.015, −.005, 0., .005, .015, .026, .037.

see [14]). Due to the fine grid used for the measurements, it is also possible to estimate the velocity gradient tensors and several invariants of the flow. Boussinesq's hypothesis, which is at the heart of the classical k-ϵ turbulence type models [15], can then be tested by experimentally estimating the alignment of the strain and (traceless) stress tensors, and nonlinear generalizations [16,17] of the constitutive relation can be checked. The result of this post-processing technique applied to experimental database presented here are developed and presented by Schmitt and Hirsch [18].

Acknowledgments

This work is supported by a grant from the Fonds voor Wetenschappelijk Onderzoek-Vlaanderen (FWO) #G028396N.

Nomenclature

A = constant
a = exponent
A_1 = area of the primary nozzle
A_2 = area of the secondary nozzle
A_e = area of the exit section
α = a dimensional number
β = a dimensional number
C_t = a dimensional Craya-Curtet number
δx = error in the measurement of the quantity x
k = kinetic energy
k_m = maximum kinetic energy
m = $\overline{X}$ mean value of a random variable
M = random variable
N = number of measurement samples
P_e^* = stagnation pressure at the exit of the burner
P_i = pressure at the entrance of the burner
r = ratio
r_1, r_2 = radii of primary and secondary streams
$\mathrm{R_e}$ = Reynolds number
ρ = density of the gas
σ_x^2 = variance of X
$\tau_{uu'}$ = axial normal stress
τ_{vv} = radial normal stress
τ_{uv} = $\overline{uv} - UV$ Reynolds stress
u = axial component of the velocity
u_e = bulk-averaged velocity of the exit stream
U = $\overline{u}$ time average of the axial velocity
U_m = maximum velocity
v = radial component of the velocity
V = $\overline{v}$ time average of the radial velocity
x = a dimensional distance from the nozzle (axial coordinate)
X = random variable
X_i = a realization of X
z = a dimensional distance from the axis (radial coordinate)
$-$ = time average
$\langle \cdot \rangle$ = ensemble average

References

[1] Wilcox, D. C., 1998, *Turbulence Modeling for CFD*, DCW Industries.
[2] Piquet, J., 1999, *Turbulent Flows, Models and Physics*, Springer-Verlag, Berlin.
[3] Beér, J. M., and Chigier, N. A., 1983, *Combustion Aerodynamics*, Robert E. Krieger Publi. Comp., Malabar.
[4] Escudier, M. P., and Keller, J. J., 1985, ''Recirculation in Swirling Flow: A Manifestation of Vortex Breakdown,'' AIAA Journal, **23**, p. 111.
[5] Frisch, U., 1995, *Turbulence, The Legacy of A. N. Kolmogorov*, Cambridge University Press, Cambridge.
[6] Gnedenko, B. V. and Kolmogorov, A. N., 1954, *Limit Distributions for Sums of Independent Random Variables*, Addison-Wesley.
[7] Thring, M. W., and Newby, M. P., 1953, ''Combustion Length of Enclosed Turbulent Jet Flames,'' Fourth Symposium on Combustion, Williams and Wilkins, pp. 789–796.
[8] Craya, A. and Curtet, R., 1955, ''Sur l'évolution d'un jet en espace confine,'' C. R. Acad. Sci., Paris, 241, p. 621.
[9] Curtet, R., 1958, ''Confined Jets and Recirculation Phenomena with Cold Air,'' Combust. Flame, **2**, p. 383.
[10] Becker, H. A., 1961, ''Concentration Fluctuation in Ducted Jet-Mixing,'' Sc. D. thesis in Chem. Engg., MIT, Cambridge, Mass.
[11] Becker, H. A., Hottel, H. C., and Williams, G. C., 1963, ''Mixing and Flow in Ducted Turbulent Jets,'' Ninth Symposium on Combustion, Academic Press, pp. 7–20.
[12] Guruz, A. G., et al., 1975, ''Aerodynamics of a Confined Burning Jet,'' Combust. Sci. Technol., **9**, p. 103.
[13] Hazarika, B. K., Vucinic, D., Schmitt, F., and Hirsch, Ch., 2001, ''Analysis of Toroidal Vortex Unsteadiness and Turbulence in a Confined Double Annular Jet,'' AIAA paper 2001-0146, 39th AIAA Aerospace Sciences Meeting & Exhibit, Reno, January 2001.
[14] Zhu, J., and Shih, T.-H., 1994, ''Computation of Confined Coflow Jets with Three Turbulence Models,'' Int. J. Numerical Meth. Fluids, **19**, p. 939.
[15] Launder, B. E., and Spalding, D. B., 1974, ''The Numerical Computation of Turbulent Flows,'' Comput. Methods Appl. Mech. Eng., **3**, pp. 269–289.
[16] Gatski, T. B., and Speziale, C. G., 1993, ''On Explicit Algebraic Stress Models for Complex Turbulent Flows,'' J. Fluid Mech., **254**, p. 59
[17] Shih, T.-H., and Lumley, J. L., 1993, ''Remarks on Turbulent Constitutive Relations,'' Math. Comput. Modell., **18**, p. 9.
[18] Schmitt, F., and Hirsch, Ch., 2000, ''Experimental Study of the Constitutive Equation for an Axisymmetric Complex Turbulent Flow,'' Z. Angew. Math. Mech., **80**, pp. 815–825.

Kyoung-Su Im
Research Associate

Ming-Chia Lai
Professor

Yi Liu
Researcher

Mechanical Engineering Department,
Wayne State University,
5050 Anthony Wayne Dr.,
Detroit, MI 48202

Nasy Sankagiri
Researcher,
MSX International,
Detroit, MI

Thomas Loch
Sr. Tech. Specialist

Hossein Nivi
Manager

AMTD, Ford Motor Company,
Detroit, MI

Visualization and Measurement of Automotive Electrostatic Rotary-Bell Paint Spray Transfer Processes

In order to improve the transfer efficiency and finish quality in automotive spray painting, a better understanding of the paint spray structure and transfer processes of the electrostatic rotary bell applicators is needed. This paper briefly reviews the current technological challenges and research issues, and then describes the spray atomization, visualization, droplet size, and velocity measurement results of a water-borne paint spray system under various operating parameters. The optical techniques used are copper vapor laser light sheet visualizations and the phase Doppler particle analyzer. Four main operating parameters are varied in this study: liquid flow rate (100 ml/min to 250 ml/min), shaping airflow rate (120 l/min to 180 l/min), bell rotational speed (20,000 rpm to 50,000 rpm), and high voltage setting (60 kV to 90 kV, and 0 V for comparison). For simplicity, water is used as the paint surrogate, and a flat metallic panel is used as the target surface. The results show that bell speed dominates the atomization, but high voltage and flow rate settings significantly modify the spray transport. The results of this study also provide detailed information on the paint spray structure and transfer processes, which can be used on model development and validation in future. Also, the microscopic visualization images provide qualitative information on the atomization mechanism.
[DOI: 10.1115/1.1359210]

Introduction

Two challenges facing the automotive finishing industry are to increase the paint transfer efficiency and to reduce volatile emissions without sacrificing the surface quality and line speed. The automotive paint-shop is an expensive manufacturing facility to maintain within an automotive company; even one percent improvement in transfer efficiency can save significant money in bulk material costs. Higher transfer efficiency also has a corresponding reduction in the amount of volatile organic compounds (VOC) emitted, paint sludge production, and the associated after treatment costs. The reduced overspray allows a reduction in the booth downdraft and other compressed air flow usage, creating significant energy efficiency and cost reduction.

The optimal transfer efficiency for electrostatic rotary bell (ESRB) applicators is higher than 90 percent, under ideal operating conditions. Most parameters known to influence transfer efficiency are related to application settings. However, booth airflow management (Tong et al. [1]), line-speed, and the shape of the surface being painted also affect the transfer efficiency.

Surface quality requires continuous improvement and reformulation, especially for metallic paints, to satisfy consumer demands. In addition to color and brightness, aspects such as film-build consistency and reduction of application defects must be maintained. Therefore, the solution to these challenges may require a combination of new paint formulations, operation optimization, and new applicator designs.

The trend of the current automotive finishing industry is to use more ESRB applicators because of their higher transfer efficiency. However, there is an observed trade-off relationship between the increase of transfer efficiency and the surface quality, especially for metallic paints. Compared with the pneumatic spray gun, the ESRB produces darker and duller appearance but much higher transfer efficiency. It is well known that the application of an electric charge will change the apparent color of some metallic paints to varying degrees. However, the mechanisms are not well defined. It was formerly thought that the discoloration was due to improper flake orientation during fluid transportation for the following reasons: 1) the shearing deformation of the ESRB processes; 2) the electrical fields in flight (which has been discredited by Inkpen and Melcher [2]); 3) the film during the curing stage; 4) the splashing deformation upon impact (Fukuta et al. [3]). But recent results also suggested that the difference of the flake content in the deposited paint is the cause of the color shift (Inkpen and Melcher [2]; Elmoursi and Lee [4]; Tachi and Okuda [5]). Nevertheless, the optimal operating conditions at which the droplet size and flake content are most uniform at the target surface depend on the entire paint transfer process, which also changes with the properties of the paint and the target surface.

Previous Research Works

The use of a rotating cup in burners for domestic heating has been well known in Europe since the 1930s. Marshall [6], Matsumoto et al. [7], and Lefebvre [8] summarize the earlier research results on the atomization. Hinze and Milborn [9] were among the first to document the atomization process of a rotating cup. They identified three different types of disintegration: (a) direct drop formation at low speed and feed rate; (b) ligament breakup; and (c) film breakup. They observed that the transition from regime (a) into (b), or from (b) into (c), is promoted by an increased liquid feed rate, an increased angular speed, a decreased diameter of the cup, an increased density, increased viscosity, and a decreased surface tension of the liquid. They also measured the drop size in the ligament breakup regime using sooted glass impingement technique and correlated with relevant dimensionless groups. Dombrowski and Lloyd [10] also visualized the atomization process using photography and measured the drop size using

Contributed by the Fluids Engineering Division for publication in the JOURNAL OF FLUIDS ENGINEERING. Manuscript received by the Fluids Engineering Division October 30, 1998; revised manuscript received December 6, 2000. Associate Editor: P. W. Bearman.

a light absorption technique. However, these earlier studies mostly use smooth rotating cups, i.e., without serration, which rotate at much lower speeds compared with today's turbine-driven applicators, and without electrostatics and shaping air control.

In addition to automotive applications, electrostatic atomization is widely applied in agriculture spraying, office furniture refinishing, ink jet printing, and others. Actually, experiments of electrostatic atomization, particle charging, and deposition have existed before the well-known interests of Benjamin Franklin. Kelly [11] found applications of electrostatic atomization as far back as 1754 AD. He also suggested that the mean drop diameter of Newtonian liquid larger than one micron is not dependent on all fluid and device related to the properties but solely a function of fluid charging levels, which is directly proportional to droplet diameter. However, the detailed role that electrostatics plays in the ESRB atomization is still unclear.

Compared with pneumatic spray guns, which are easier to set up and operate (e.g., Kowk and Liu [12]; Domnick et al. [13]), there are only a few research articles available on the ESRB processes. Bell and Hochberg [14] should be credited as the first major contributors. They summarized their results on the ESRB spray using many experimental techniques, including light scattering, Doppler method, high-speed video, and charge/mass ratio measurement. The experimental data was correlated against the application conditions and paint properties. The measured charge/mass ratios were only about 4 percent–25 percent of the Rayleigh limit for their test cases. Using photography, Bailey and Balachandran [15] also observed that the number of ligaments increased with increasing high voltage.

Corbeels et al. [16] used a laser diffraction instrumentation and photography to study the influence of fluid properties and operational parameters on the atomization characteristics of a high-speed rotary bell with serration, but without electrostatics and shaping air control. They found that the high viscosity fluid filmed the bell evenly and produced long regular ligaments, whereas the low viscosity fluid filmed incompletely and produced very irregular ligaments that disintegrated near the bell edge. Their particle size data, which were limited at one location (35 mm from the bell edge), were found to be insensitive to large changes in flow rate and viscosity at a bell speed higher than 20,000 rpm.

Bauckhage et al. [17] used a short spark photography, and diffraction spectrometry to study the ESRB atomization of water based metallic paint. The small dispersion of the drop size distribution suggests that the ESRB works in the ligament atomization mode, which is confirmed by the photograph near the nozzle. They also used a laser light sheet for visualization; the unpublished video results suggested two axial zones and a radial zone of recirculations, which are influenced by the shaping air. Later, they also used a phase Doppler particle analyzer to study the effect of electrostatics and found that the drop size with higher voltage is smaller but the visualized spray cone is wider (Bauckhage et al. [18]).

While the operating parameters of an ESRB are closely related to transfer efficiency and surface quality, most of the previous studies used old applicators that do not have a control unit of a wide range of operation parameters. They only concentrated on the atomization aspects having very limited drop size data at one location and the visualization to the vicinity at the edge of the bell cup.

The challenges facing the automotive finishing industry warrant a better understanding of the ESRB paint spray transfer fundamentals in order to improve the bell sprayer performance and to screen new sprayer designs in an actual painting environment. Few research papers have been published on the subject, although there are some performance data in trade journals. For example, Fukuta et al. [3] developed a new metallic bell by changing the shaping air nozzles in the bell to increase the droplet speed and thus improve the atomization and finishing quality. In spite of the extensive use of the ESRB in the automotive finishing industry, there is still insufficient information available to the performance characteristics to be predicted with confidence over a wide range of operation conditions.

Detailed characterization of the processes, including the initial atomization at the spray applicator, the interaction with the electrostatics and shaping airflow, and the boundary layer formation and deposition at automotive body surfaces are needed to validate physical models of the automotive ESRB operations. Currently, other than some trial-and-error approaches and empirical databases, there is very little research on the simulation of automotive paint spray transfer processes.

The purpose of this study is to give a better understanding of the paint transfer fundamental and provide the data for the further model development by conducting the visualization of the transfer process and the drop size measurement of the ESRB spray using laser-based optical diagnostics.

Experimental Setup

A research paint booth completed with a digital controller for ESRB is used for the investigation. The bell assembly and a detail of the bell cup are illustrated in Fig. 1. The optical techniques used are laser light sheet visualizations by copper-vapor and a phase Doppler particle analyzer (PDPA) (Fig. 2). Four main operating parameters are varied in this study: liquid flow rate, shaping airflow rate, bell rotational speed, and high voltage setting. Deionized water was used as a paint surrogate for simplicity. A flat metallic panel (4 ft $\times$ 3 ft, electrically grounded) is used as the target surface, and the downdraft air is turned off. The test conditions are summarized in Table 1.

A production ESRB (Behr Eco-bell 55 mm diameter, serrated edge, designated 55S) for waterborne paint was chosen for the study. The major difference between solventborne base painting and waterborne base painting is in the electrical charging system and supplying component of the paint. In solventborne base painting, the charging electrode can be built into the applicator and provide a reliable electric field by conduction, induction, and corona current, due to the low conductivity of the solvent. However, waterborne painting requires the external charging component or isolation of the entire circulation system or isolation via a voltage block. Figure 3 clearly shows two different spray atomizers. The ESRB used in this study utilize external space charging in order to apply corona charging to the spray by corona discharge.

This applicator has a range of operation conditions; the following nominal conditions were selected as the baseline in this parametric study: liquid flow rate at 200 ml/min, shaping air flow rate at 160 l/min, bell speed at 40,000 rpm, and high voltage setting at 90 kV. This baseline set of conditions is underlined and boldfaced in Table 1. In order to discern the effect of changing main operating parameters, only one parameter was changed at a time, while the other three were maintained at the reference condition.

A schematic diagram of the experimental setup is shown in Fig. 1. The bell disk consists of four parts, as shown in the upper left corner. The paint flow is supplied to the atomizer ring by the ring gap and moves toward the bell edge due to the centrifugal and Coriolis forces created by the rotating bell. Many of the available bell disk variants have similar means for paint flow division; 80 percent of the paint quantity is supplied to the atomizer rim by the ring gap. The remaining 20 percent of the volume flow passes through the central drilled hole on the front side of the distributor ring to effect a permanent rinsing of the bell disk surface and to prevent paint deposits on the distributor ring. Small wedges, which are called serration or circumferential knurls (see Fig. 4), can be machined along the edge of the bell disk. They permit the paint film flowing over the surface of the bell disk to be divided into defined individual flows and ligaments that eventually break

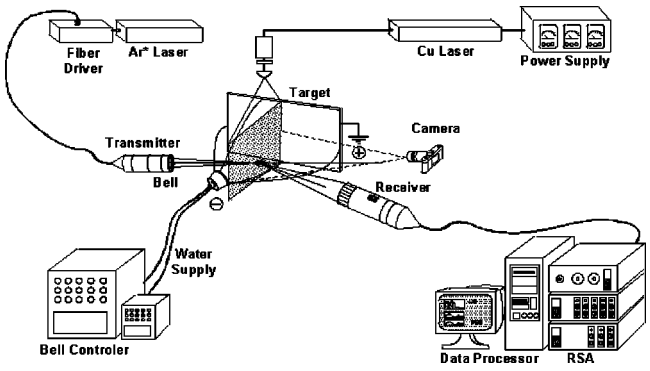

Fig. 1 Schematic diagram for experimental setup

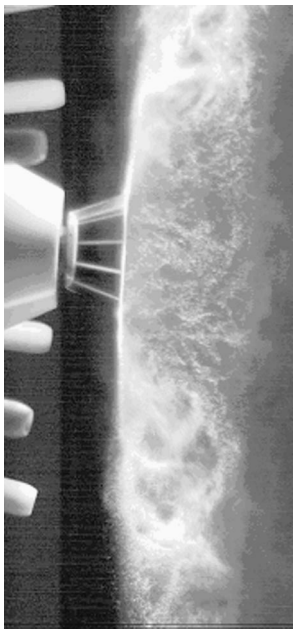

Fig. 2 Near field light-sheet spray visualization at 0 kV condition

Table 1 Test conditions

Liquid Flow rate (ml/min)	100	150	**200**	250
Shaping air flow rate (l/min)	120	140	**160**	180
Bell rotation speed (rpm)	20,000	30,000	**40,000**	50,000
Voltage setting (kV)	0	60	70	80 **90**
Downdraft air flow rate (m/s)	0			
Booth condition	Normal ambient - 21±3°C			
Liquid properties (water)	surface tension = 76mN/m viscosity = 1.0 mNs/m^2			

up into droplets. The bell diameter is 55 mm, with option for either a straight-serrated edge or a smooth edge. This paper presents only the serrated edge data.

A turbine housing protects the drive unit of the high-speed rotary atomizer, which is driven by compressed air. Behind the rotary cup, shaping air exits from 40 holes annularly arranged on the stationary housing. Shaping air is used primarily to support the transport of paint droplets, to stabilize the flow conditions around the atomizer, and to permit a precise alignment of the spray pattern by limiting the atomizing cone. The high voltage from the six external electrodes, which are negatively polarized and located at

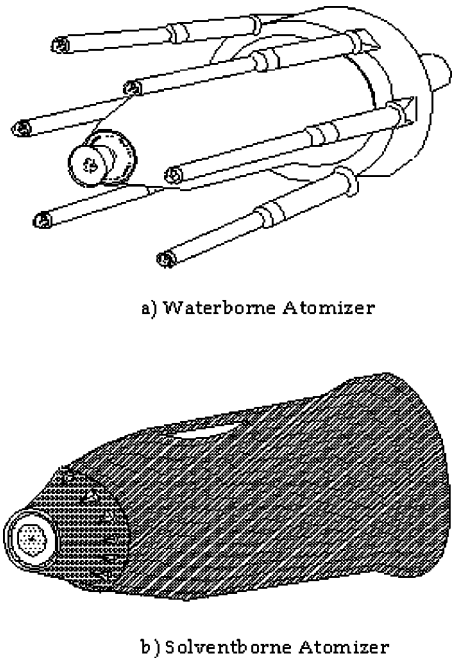

Fig. 3 Typical paint spray atomizers

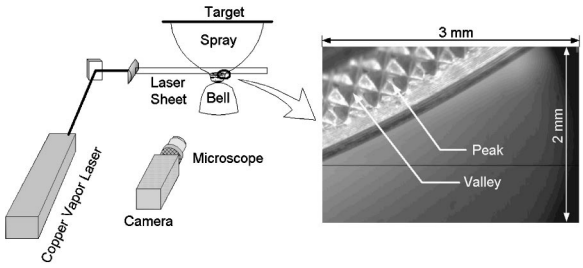

Fig. 4 Schematic of liquid breakup visualization on the bell-cup edge

75 mm from the cup, charge and propel the atomized droplets to the grounded work piece. The target plane is located at 254 mm away from the edge of the rotary cup.

Visualization Results

Microview. Microscopic visualization was carried out to study liquid break up near the bell edge. A schematic of the visualization facility is shown in Fig. 4. The sampling area, 3×2 mm on the bell cup edge, is illuminated by 15W OXFORD copper-vapor laser (Model Cu-15A). Megaplus CCD Camera (Kodak ES 1.0) with a special long distance microscopic lens is used to obtain magnified images (at ~ 100×) at the bell edge.

A few sample images are shown in Fig. 5 and Fig. 6 for different operating conditions. Some qualitative observations can be made from these images. At 50 ml/min and 20,000 rpm, the ligaments emanated from the serrations on the bell edge (Fig. 5(*a*)). The ligaments are uniformly spaced, coinciding with spacing of serrations, and are uniform in diameter. At 30,000 rpm, the uniform spacing is still preserved, but the ligaments are relatively longer and thinner (Fig. 5(*b*)). At 40,000 rpm, the formation of multiple ligaments is observed between serrations, and consequently, the ligament diameter decreased further (Fig. 5(*c*)). This trend indicates that drop size decreases with increase in bell speed. When the liquid flow rate is increased holding bell speed constant, the filaments are formed in increasing numbers with irregular spacing and nonuniform ligament diameters; the liga-

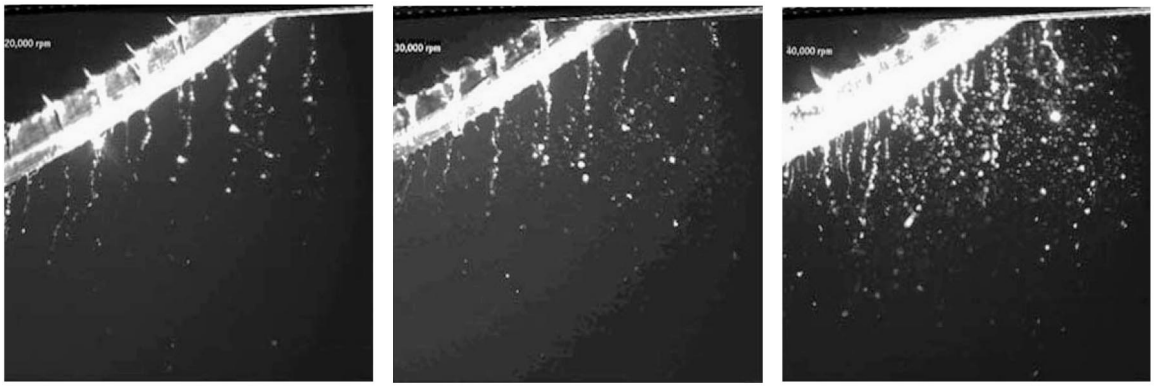

a) 20,000 rpm b) 30,000 rpm c) 40,000 rpm

Fig. 5 Microscopic visualization on the bell speed at the liquid flow rate = 50 cc/min (magnification=100×)

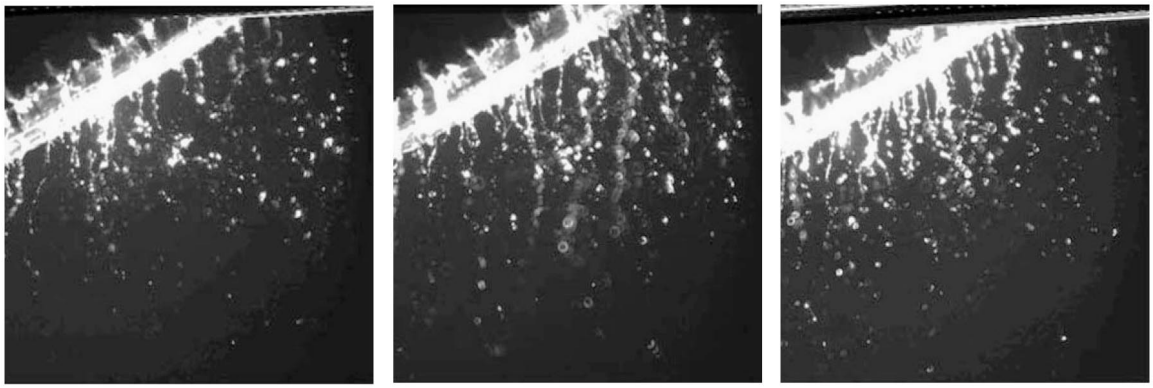

a) 150 cc/min b) 250 cc/min c) 350 cc/min

Fig. 6 Microscopic visualization on the liquid flow rate at the bell speed = 20,000 rpm (magnification=100×)

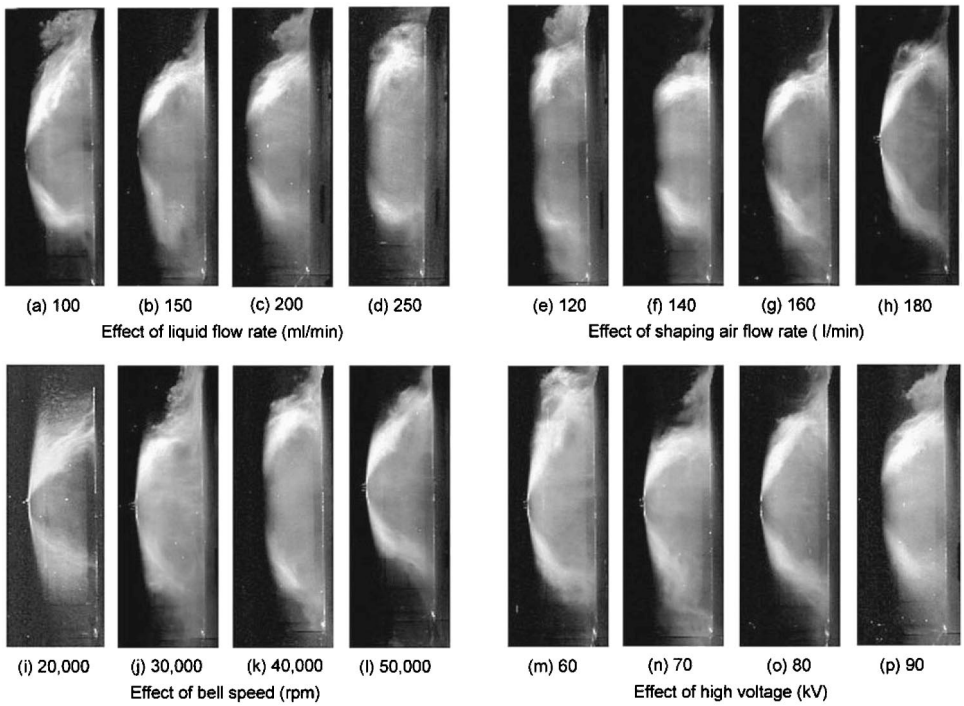

Fig. 7 Parametric effects of operation conditions on axial spray cross section

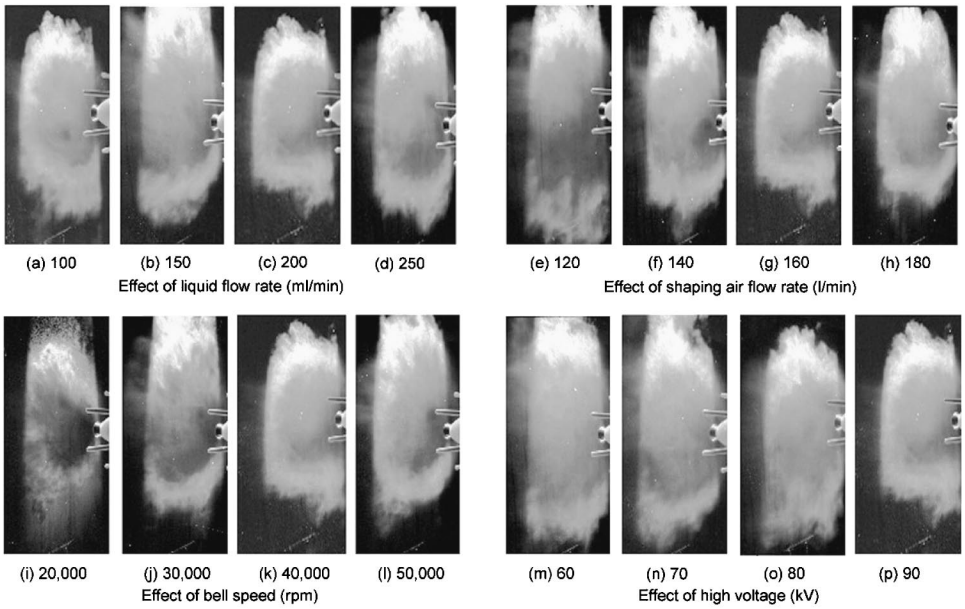

Fig. 8 Parametric effects of operation conditions on radial spray cross section

ments are seen to interact with each other before breakup. In general, the nonuniformity of ligament formation increased with increasing flow rate. A liquid sheet is seen to link the ligaments at the bell cup edge for flow rate greater than 250 ml/min.

Overall. Spray visualization is also carried out using a light sheet generated by the same copper-vapor laser operated at 10 kHz. The light sheet generation optics is connected to the laser through a fiber-optic cable to provide lighting for either the axial or radial cross sections. The laser sheet was expanded to penetrate the entire spray vertically to illuminate the center vertical plane. The camera was positioned normal to the plane of light sheet to acquire images of spray structure. The radial cross section was taken with the light sheet in between the bell and the target plane (i.e., at 12.7 cm from the target), and the camera located sideways at a 50 deg oblique angle from the spray centerline axis. Either a digital Kodak Megaplus camera or a Nikon 35-mm SLR camera loaded with ISO-400 color film is used for taking the photograph. This setup enables more detailed future study using particle image velocimetry.

Figure 2 shows the light-sheet spray visualization near the applicator taken by the Kodak camera with an exposure time of 3.3 ms. The applicator is operated at the baseline condition but with the high voltage turned off. Dense spray at the edge of cup shows a large-eddy structure. These large eddies result in an inherently unsteady turbulent spray cross-section, which changes from one instant to the next. At the center, a recirculation zone loaded with sparse droplets is also visible.

Figures 7 and 8 show the effects of operation parameters on the overall axial spray shape, which were photographed with the SLR camera with an exposure time of 33.3 ms. The short exposure time does not allow enough time averaging; however, sufficient information can be obtained from the image. The spray cone angle θ, taken to be the angle between the spray trajectories from the edge of the bell cup to that of the ESRB centerline, was also measured directly from the photograph and plotted in Fig. 9. The error percent of the spray angle, which is measured 10 times for each image from five different snapshots, is ranged from 1.1 percent–2.5 percent for the standard mean values.

The results show that an increase in liquid flow rate from 100 ml/min–250 ml/min [Fig. 7(*a*) to 7(*d*)], while keeping the other three parameters at reference condition, tends to widen the spray shape slightly. This is due to a higher spray swirl momentum associated with the increased spray mass and possibly larger drop-size.

Figure 7(*e*)–(*h*) and Fig. 8(*e*)–(*h*) demonstrate the effects of shaping air. At higher flow rate of shaping air, the spray cone is generally narrower. This is particularly obvious when comparing Fig. 7(*e*) (120 l/min) and 7(*f*) (140 l/min). This indicates that the shaping air should operate higher than 120 l/min. The shaping air permits precise adjustment of the spray pattern by limiting the spray cone angle; it also increases impinging energy at the target.

The influence of bell speed on the overall spray pattern is shown in Fig. 7(*i*)–(*l*) and Fig. 8(*i*)–(*l*). At the low bell speed of 20,000 rpm, where the centrifugal force is the smallest, large droplets are clearly observed outside of the denser and finer spray region, unaffected by the shaping air. These large droplets suggest that the atomization mode is not well developed. Therefore, the ESRB should be operated at a speed higher than 20,000 rpm. At higher bell speed, when centrifugal force is larger, the spray cone decreases due to more consistent and finer atomization. The spray also tends to concentrate more inside the spray cone as a greater number of smaller particles find themselves into the recirculating zones (Fig. 9).

The influence of the high voltages on spray shape is shown in Fig. 7(*m*)–(*p*) and Fig. 8(*m*)–(*p*). Insufficient high voltage exerts only small forces on the droplets, resulting in wider spray and poorer transfer efficiency. At the highest voltage, the spray also becomes denser and more uniform at the core region.

The radial cross-sectional visualization also shows very high swirling velocity induced by the rotary bell. The center of the rotation is observed to move around in a precession, but with a much slower precessional speed and with a counter-rotational direction compared to those of the bell itself.

PDPA Results

Two-channel PDPA system (Aerometrics) with a 300-mW Argon-ion Laser was used for detailed measurements of the drop size distribution. The focusing lenses of both the transmitter and receiver have a long focal length of 750 mm to avoid interfering with the spray. The optics is integrated with fiber optics cables and is mounted on a heavy-duty computer controlled traversing stand. Measurement data were taken along the axial direction at

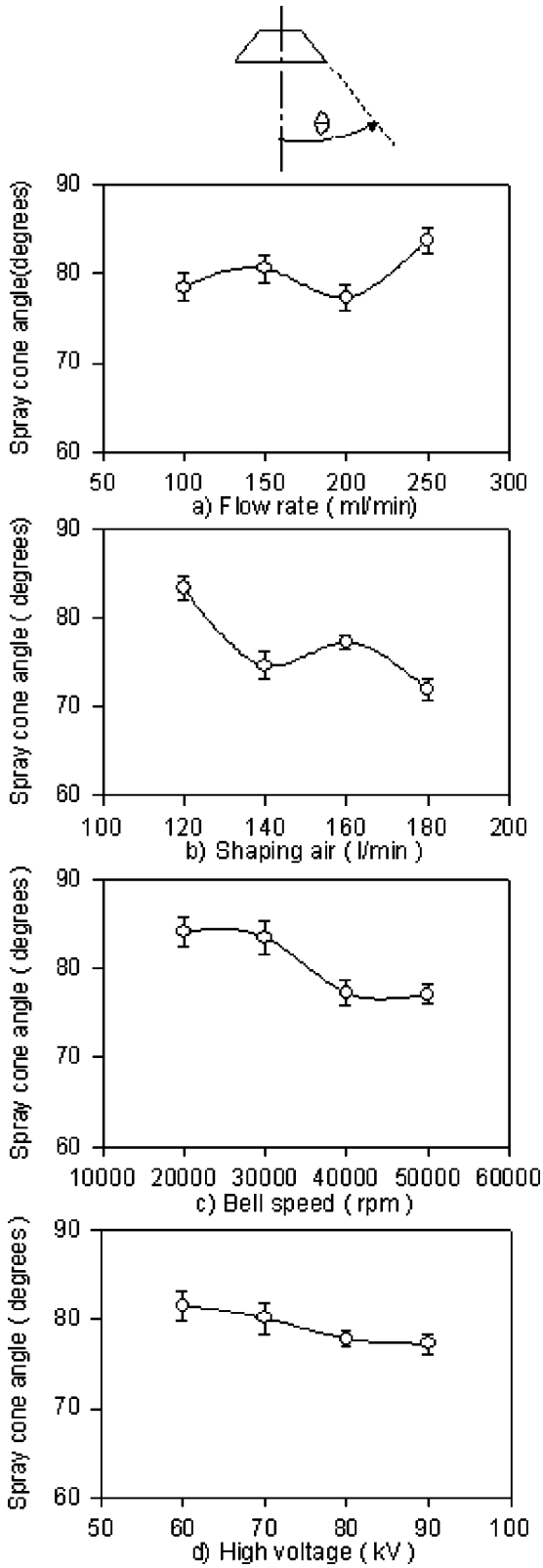

Fig. 9 Sensitivity of bell operation parameter on spray cone angle

x=2.5, 10.2, 17.8, and 24.1 cm from the bell cup edge, and at the radial locations of r=0, 10.2, 20.3, 30.5 and 40.6 cm. Statistics at each point are averaged over 20,000 data points. The radial profiles at x=17.8 cm are presented here for comparison in the parametric study.

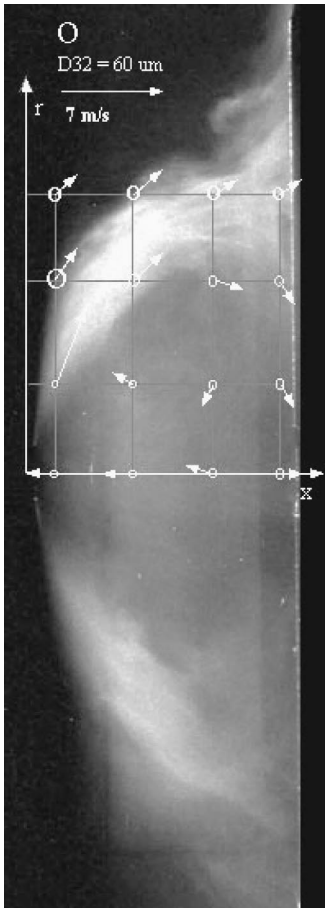

Fig. 10 PDPA results at the reference condition

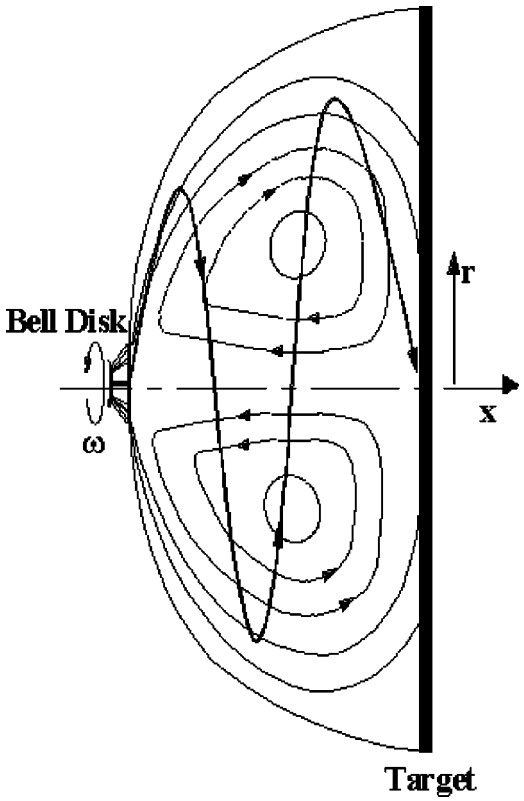

Fig. 11 Streamline of the ESRB spray

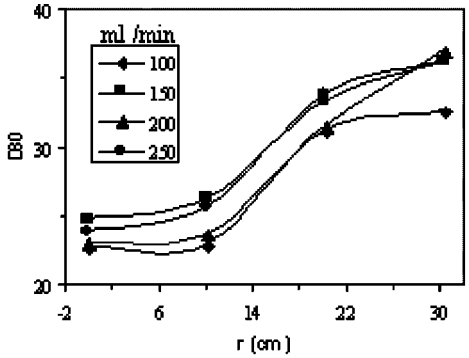

a)Effects of liquid flow rate

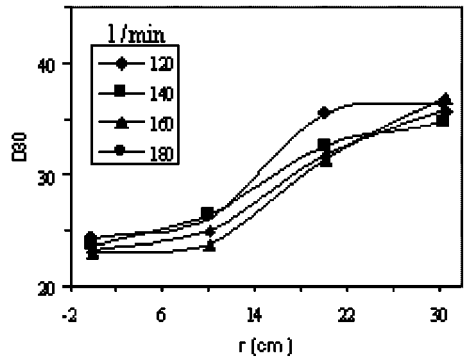

b)Effects of shaping air

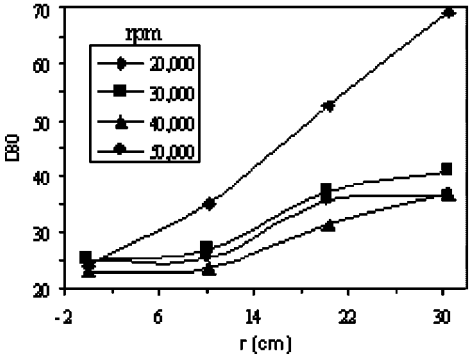

c)Effects of bell speed

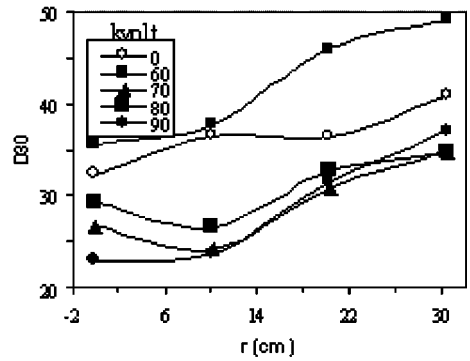

d)Effects of high voltage

Fig. 12 The effects of bell operation parameters on the drop size profile measured at 7.62 cm from the target

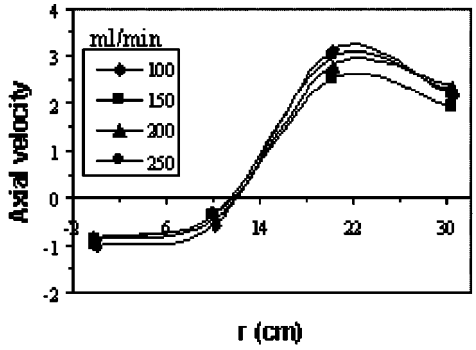

a)Effects of liquid flow rate

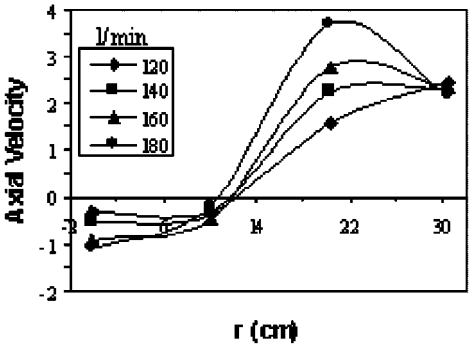

b)Effects of shaping air

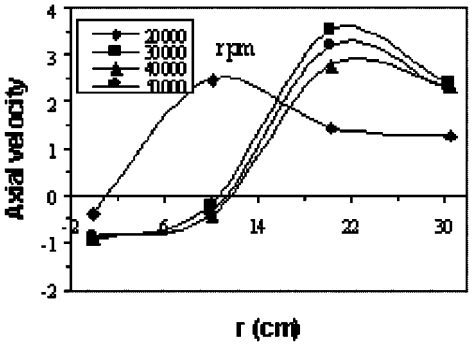

c)Effects of bell speed

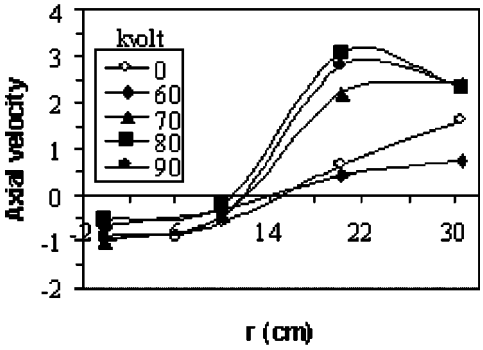

d)Effects of high voltage

Fig. 13 Sensitivity of bell operation parameters on drop size measurement at 7.62 cm from the target

Figure 10 shows the PDPA results at the reference condition superimposed on the spray light sheet photograph. The measured sauter mean diameter (SMD) is proportional to the size of circle plotted at each measuring position; the measured two directional velocities are also plotted as a vector. The vector plots clearly show a toroidal vortex induced by the strong swirling spray, and contained between the bell cup and the target plane. At the target plane, the paint spray tends to concentrate on an annular stagnation zone.

In spite of the high circumferential velocity at the edge of the

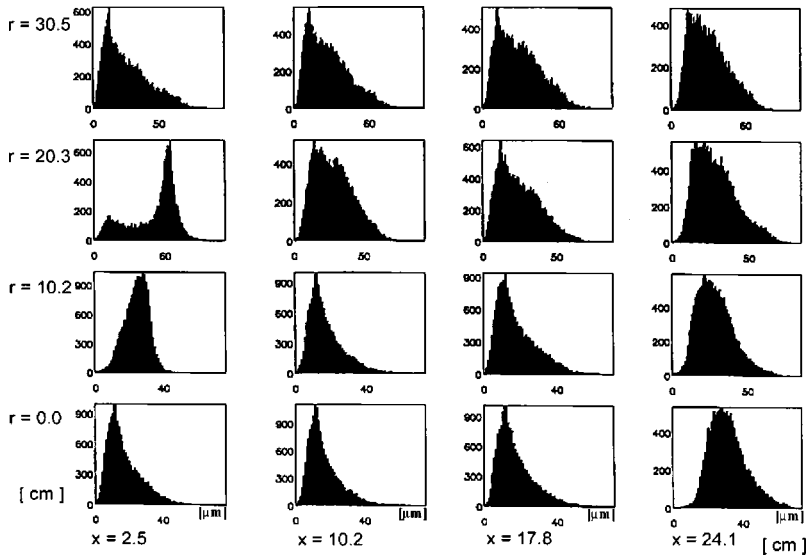

Fig. 14 Spatial distributions of the drop size histograms at reference condition

rotary bell (115 m/s at the reference condition), the velocity in the axial plane flow field is quite small, with the mean deposition velocity on the order of 1-2 m/s at the target plane. The largest velocity and mean drop size were measured along the trajectory of the spray near the edge of the spray, shown in Fig. 10 at $x=2.5$ cm and $r=30.5$ cm. This is expected since the centrifugal force throws the liquid out at high speed, but the drag force reduces the velocity rapidly. From this point, Fig. 10 also shows that the drop size decreases at a significant fast rate as it moves away from the bell cup, suggesting that the breakup process is not complete at this location. The vector plot in Fig. 10, combined with the visualization results, gives rise to the conceptual streamline plot in Fig. 11, which is similar to the one proposed by Bauckhage et al. [17]). Figure 10 also shows that larger droplets stay on the outside of the spray, while smaller droplets are more easily entrained into the toroidal vortex zone (Figs. 12 and 13). As the penetration length increases, the radial diameter profile becomes more uniform.

The histogram data of the reference condition are shown in Fig. 14, corresponding to the measurements shown in Fig. 10. There is a notably bimodal distribution at the maximum dropsize/velocity point. This bimodal distribution is also observed in the low-speed regime (in Fig. 15) and at low voltage condition (in Fig. 16), all taken at 7.6 cm from the target plane. The reason for this inter-

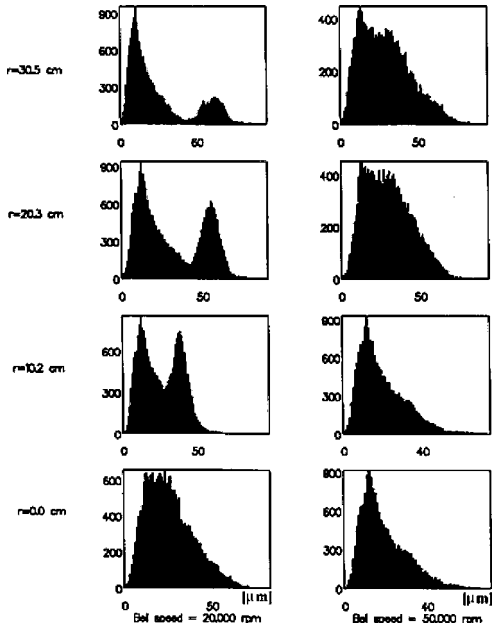

Fig. 15 Drop size histogram variation with bell rotational speed at 7.62 cm from the target plane

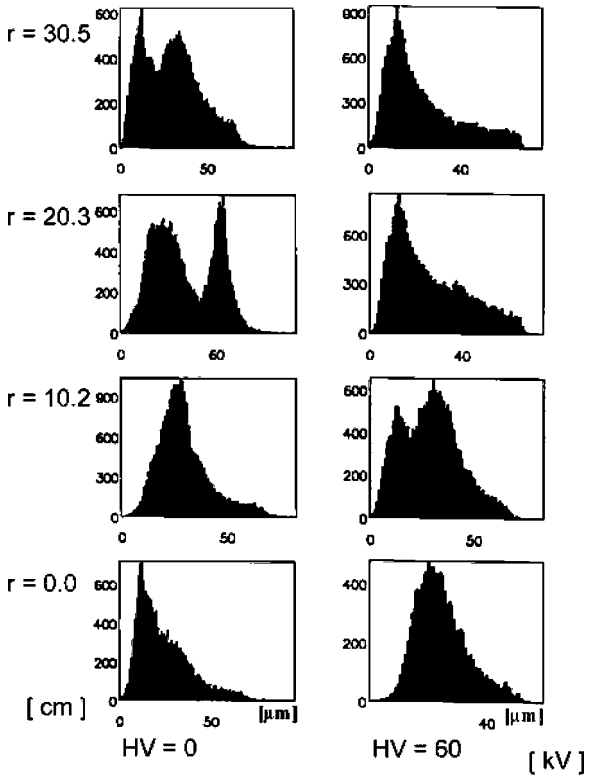

Fig. 16 Drop size histogram variation with high voltage setting at 7.62 cm from the target plane

esting bimodal distribution is unclear. It may be due to a dual-mode operation of the ESRB atomization, where both the ligament and the film breakup mode coexist. But it could also be due to a secondary breakup process where much distinctly smaller satellite drops are formed. The swirling and recirculation flow field will also differentiate and transport the droplets according to their size and drag. Therefore, more study is required to solve this puzzle.

Conclusions

A parametric study was carried out using copper vapor laser light sheet visualizations and a phase Doppler particle analyzer to gain a better understanding of the paint spray structure and transfer processes of the automotive electrostatic rotary bell applicators. The results show that bell speed dominates the atomization, but high voltage and flow rate settings significantly modify the spray transport. The results of this study also provide detailed information on the paint spray structure and transfer processes, which can be used in future model development and validation.

Acknowledgments

This research is supported by grants from Ford University Research Foundation and the WSU Institute of Manufacturing Research. The beneficial discussions with Mr. Ernest Tong of Ford AMTD, Dr. Jacob Braslaw of Ford Scientific Research Laboratory, Dr. K. C. Kwok of ITW, and Dr. Richard Miller of Dupont are very much appreciated. We also acknowledge the engineering support from Mr. Jim Dominiak, and thank Behr Company for the Bell.

References

[1] Tong, E., Chmielewski, G., and Nivi, H., 1995, ''Paint Spray Airflow Management,'' Proceedings of International Body Engineering Conference & Exposition (IBEC '95), pp. 39–49, Oct. 31–Nov. 2, 1995, Detroit, MI.

[2] Inkpen, S., and Melcher, J. R., 1987, ''Dominant Mechanisms for Color Differences in the Mechanical and the Electrostatic Spraying of Metallic Paints,'' Industrial Engineering Chemistry Research, **26**, pp. 1645–1653.

[3] Fukuta, K., Murate, M., Ohhashi, Y., and Toda, K., 1993, ''New Electrostic Rotary Bell for Metallic Paint,'' Met. Finish., pp. 39-42.

[4] Elmoursi, A. A., and Lee, H. Y., 1989, ''Droplet and Flake Size Distribution in the Electrostatic Spraying of Metallic Paint,'' SAE paper 890354.

[5] Tachi, K., and Okuda, C., 1992, ''Color Variation of Automotive Metallic Finishes,'' J. Coat. Technol., **64**, No. 811, pp. 64-77.

[6] Marshall, W. R., 1954, ''Performance Characteristics of Spinning-Disk Atomizers,'' *Atomization and Spray Drying*, Chapter 3, Republished by Johansen Crosby & Assoc., Inc., Madison, WI, 1986.

[7] Matsumoto, S., Belcher, D. W., and Crosby, E. J., 1985, ''Rotary Atomizers: Performance Understanding and Prediction,'' Proceedings of ICLASS-85, Madison, WI, pp. 1A/1/1-21.

[8] Lefebvre, A. H. 1989, *Atomization and Sprays*, Taylor and Francis, Bristol, PA.

[9] Hinze, J. O., and Milborn, H., 1950, ''Atomization of Liquids by Means of a Rotating Cup,'' ASME J. of Appl. Mech., **17**, pp. 145-153.

[10] Dombrowski, N., and Lloyd, T. L., 1974, ''Atomization of Liquids by Spinning Cups,'' Chem. Eng. J., **8**, pp. 63–81.

[11] Kelly, A. J., 1994, ''On the Statistical Quantum and Practical Mechanics of Electrostatic Atomization,'' Journal of Aerosol Science, **25**, pp. 1159–1177.

[12] Kwok, K. C., and Liu, B. Y. H., 1991, ''New Research Approach to Air Spray Painting,'' Proceedings of ICLASS-91, Gaithersburg, MD, pp. 105–112.

[13] Domnick, J., Lindenthal, A., Tropea, C., and Xu, T. H., 1994, ''Measurement in Paint Sprays Using a Phase-Doppler Anemometer,'' Atomization Sprays, **4**, pp. 437–450.

[14] Bell, G. C., and Hochberg, J., 1981, ''Mechanisms of Electrostatic Atomization, Transport, and Deposition of Coatings,'' Proceedings of Seventh International Conference in Organic Science and Technology, Athens, Greece.

[15] Bailey, A. G., and Balachandran, W., 1984, ''The Dispersion of Liquids using Centrifugal and Electrostatic Forces,'' IEEE Trans. Ind. Appl. IA-20, **3**, pp. 682–686.

[16] Corbeels, P. L., Senser, D. W., and Lefebvre, A. H., 1992, ''Atomization Characteristics of a High Speed Rotary Bell Paint Applicator,'' Atomization Sprays, **2**, pp. 87–99.

[17] Bauckhage, K., Scholz, T., and Schulte, G., 1994, ''Atomization of Water-based Metallic Paints by means of Electrostatic Rotary Atomizers,'' Proceedings of ICLASS-94, pp. 1010–1019, July 18–22, 1994, Rouen, France.

[18] Bauckhage, K., Scholz, T., and Schulte, G., 1995, ''The Influence of Applied High-Voltage on the Atomization Characteristic of a Commercial High-Speed Rotary Atomizer,'' 4th International Congress Optical Particle Sizing, Nürnberg, Germany, 21–23 March 1995, pp. 337–346.

Yang Jian
Associate Professor,
Mechanical Engineering Department,
Sha Zhou Engineering College,
Zhang Jiagang City, Jiangsu Province,
People's Republic of China
e-mail: yang2580@pub.sz.jsinfo.net

Sun Jiajun
Professor,
Mechanical Engineering Department,
China University of Mining and Technology,
Xuzhou City, Jiangsu Province,
People's Republic of China

The Development of the Water Jet Scalpel With Air Pressure

The development of a new kind of air-pressurized water jet scalpel is discussed, including its design, assembly, and adjustment, the choice of optimum parameters, results of animal experiments, and clinical applications. The water jet scalpel is known for its compact structure and safe operation. The air pressure to drive the water jet scalpel varies from 1.0–1.5 MPa, and the quantity of normal saline used is 3×10^{-3} to 4×10^{-3} m^3 per operation. The results of preliminary clinical applications have shown that the water jet scalpel has many advantages over the conventional scalpel in operations requiring liver cutting. [DOI: 10.1115/1.1359211]

1 Introduction

In the last fifteen years, the water jet technique has become increasingly popular in a variety of applications in the medical field. In 1982, it was reported that a new method for stone destruction in the common bile duct [1] was developed by Frankfort University and Hanover University in Germany, and the pulse jet with a maximum pressure of 100 MPa was adopted as the means of stone destruction. In 1986, the researchers at Frankfort University and Hanover University introduced a method of cracking ureter calculi by high-speed water jet pulses and this pulse jet also had a maximum pressure of 50 MPa [2]. After a few years of their efforts in conducting experimental research on animals and in autopsy, they accumulated a great deal of experimental data and prepared for clinical applications.

The experiment and applications of the continuous water jet scalpel have been conducted in the medical field for a long time and remarkable progress has been made, especially in the last fifteen years. The practical applications involve dentistry, wound cleaning, and other surgical operations [3,4]. Since 1960, dental calculus has been cleaned with water jets at a pressure of 0.6 MPa, and many kinds of water irrigating devices have been widely adopted in dental operation. Large-area wounds are also cleaned effectively with water jets after the pressure is increased to 0.9 MPa. Furthermore, amputations on patients and animals have been performed with continuous water jets at pressures between 138 and 172 MPa. Although some operations are successful, some are not and experimental research still goes on [3].

The water jet scalpel belongs to the applied scope of continuous water jets. As far as cutting ability is concerned, any parts and tissue of human and animal bodies can be cut with a water jet scalpel, if the appropriate pressure is used. Through years of experimental research the operations involving the cutting of liver and pancreas with water jet scalpel have been very successful. In 1986, a water jet scalpel made in Sweden [5] for the purpose of cutting liver was exhibited at The World Congress on Surgery in Lunde City, Sweden. Its pressure range is 0.5–1.5 MPa. Patients lose less blood during the operation with the water jet scalpel and recover more quickly after the operation. Isotonic pressure normal saline or glucose is used as the liquid of water jet scalpel. Animal experiments and clinical applications also provided referenced data for the choice of the pressure and flow rate of water [4,6]. At present, a new kind of the water jet dissector has been developed and used for laparoscopic surgery on a patient with chronic cholecystitis by the researchers at Kitasato University School of Medicine, Japan. Satisfactory results have been obtained in clinical applications [7].

Contributed by the Fluids Engineering Division for publication in the JOURNAL OF FLUIDS ENGINEERING. Manuscript received by the Fluids Engineering Division June 23, 2000; revised manuscript received January 10, 2001. Associate Editor: D. R. Williams.

Yet as a new type of surgical device, the water jet scalpel still has some problems to be solved.

1 The water jet scalpel needs to be disinfected before the operation.
2 The noise levels must be reduced while the device is working.
3 The accumulation and splashing of blood and liquid from the device must be eliminated during the operation.

Our research on the water jet scalpel is aimed at solving these problems. Through many animal experiments and the clinical applications of human liver cutting, the water jet scalpel safety has increased and blood loss during the operation was decreased. Furthermore, it is lighter in weight, creates no noise during the operation, and is simple to disinfect.

2 Component Parts and Working Principle of the Water Jet Scalpel With Air Pressure

As shown in Fig. 1, the input pressure to the device comes from carbon dioxide pressurized at 10–15 MPa. A bottle of carbon dioxide with an initial pressure at 15 MPa was sufficient for 150 patients' operations according to the present experimental results.

The main components and their functions in the air pressurized water jet scalpel are as follows: a normal saline bottle with air pressure transforms air pressure into normal saline pressure with a maximum pressure of 80 MPa. A pressure regulating valve is used to provide stable pressure for the jet. The on/off value can be controlled by hand or foot. (In Fig. 1, it is controlled by foot.) The water jet scalpel itself consists of a stainless-steel rod and a ruby nozzle whose diameter is from 0.15×10^{-3}–0.2×10^{-3} m. Connecting pipes and couplings are used to connect the pressure bottle, normal saline bottle, pressure regulating valve, on/off valve, and scalpel.

The water jet scalpel with air pressure consisting of the abovementioned five components is compact in structure and light in weight. The aspirator, which is used as an auxiliary component for preventing the back spray, and the pressure bottle can be chosen according to the conditions of the hospital.

3 The Nozzle Design and the Relationships Between Pressure, Nozzle Diameter, and the Flow Rate of Saline Solution

The nozzle is an important part of water jets. The function of it is not only to transform the static pressure of fluid into dynamic pressure, but also to assure that it has a good flow quality and dynamic performance.

The flow rate coefficient of the nozzle is given as [8]

$$\psi = 1 - \frac{4\delta}{d_1} \tag{1}$$

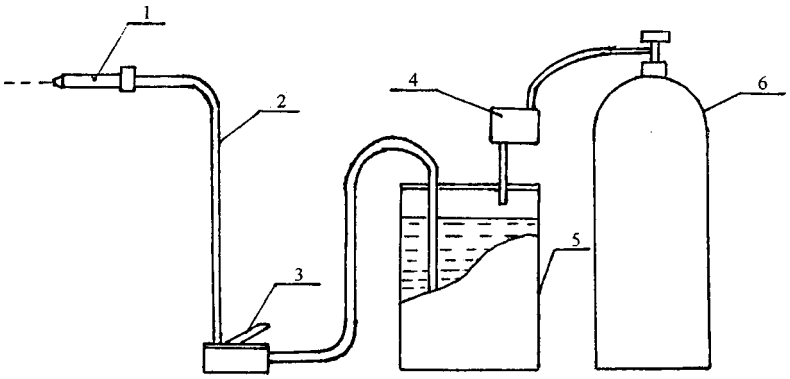

Fig. 1 Device of water jet scalpel with air pressure. 1. Air pressure water jet scalpel, 2. hose, 3. on/off valve, 4. pressure regulating valve, 5. normal saline bottle with air pressure, 6. pressure bottle.

where d_1 is the diameter of the nozzle and δ is the thickness of boundary layer $(4\times10^{-6}-10\times10^{-6})m$. As shown in Fig. 2, the geometric parameters of the nozzle mainly include the contraction angle α, diameter d_1, cylindrical length l, nozzle's length L, and the roughness of internal surface of the nozzle. In general, diameter d_1 depends on the flow rate of jets and is an important parameter for nozzle design. Typically, $l=(2.5–3.0)d_1$, $\alpha=13.5°$; however, the optimum parameters are determined by experiments.

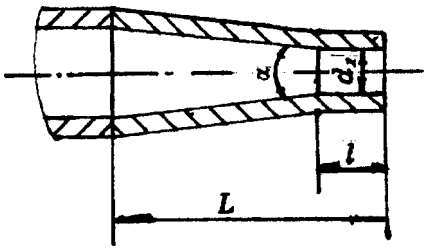

Fig. 2 Geometrical shape of nozzle

Table 1 The relationships between nozzle diameter and flow rate of normal saline at the pressure of 1.0 MPa

$d_1\times10^{-3}$ (m)	0.10	0.15	0.20	0.25
$Q\times10^{-6}$ (m^3/s)	0.35	0.78	1.39	1.70

Table 2 The relationships between nozzle diameter and flow rate of normal saline at the pressure of 1.5 MPa

$d_1\times10^{-3}$ (m)	0.10	0.15	0.20	0.25
$Q\times10^{-6}$ (m^3/s)	0.43	0.96	1.70	2.66

Table 3 The relationships between nozzle diameter and flow rate of normal saline at the pressure of 2.0 MPa

$d_1\times10^{-3}$ (m)	0.10	0.15	0.20	0.25
$Q\times10^{-6}$ (m^3/s)	0.49	1.11	1.96	3.06

Table 4 The relationships between nozzle diameter and flow rate of normal saline at the pressure of 2.5 MPa

$d_1\times10^{-3}$ (m)	0.10	0.15	0.20	0.25
$Q\times10^{-6}$ (m^3/s)	0.55	1.24	2.19	3.43

The relationships between pressure, nozzle diameter, and the flow rate of saline solution are given as [8]:

$$Q=\psi\frac{1}{4}\pi d_1^2\sqrt{\frac{2p}{\rho}} \tag{2}$$

where p is the working pressure, Q the flow rate of the saline solution, and ρ the density of the saline solution ($\rho=1000\ kg/m^3$, at the temperature of 20°C). The nozzle design and the experimental data are based on the above information.

The liquid used in the scalpel is normal saline solution. The relationships between pressure, nozzle diameter, and flow rate of normal saline are shown in Tables 1, 2, 3, and 4, according to the experiments and the calculations. Therefore, if the nozzle diameter of 0.2×10^{-3} m is used and the pressure is at 1.5 MPa, the quantity of normal saline is at $2\times10^{-3}\ m^3$ for one operation including liver cutting.

4 The Experiments With Animals

In this paper, an example of liver cutting is used to show the overall operating process with the water jet scalpel. First of all, the normal saline pressure is regulated by a pressure-regulating valve, then the on/off valve is turned on and the static pressure of normal saline is changed into kinetic pressure. High-speed water jets cut the necessary tissue to be removed like a sharp knife. Generally speaking, the liver contains bile ducts, blood vessels, and hepatocytes and so on. The blood vessels and bile ducts contain microscopic structures, which enable them to bear a certain pressure without being damaged. Therefore during the operation the appropriate pressure is chosen in which the jets can cut the viral tissue from the liver without cutting off the blood vessels and bile ducts. This reduces the blood loss of the patients to a minimum. Obviously the success or failure of the operation depends on the pressure selected above, and the appropriate pressure is determined by the experiments shown in Table 5 [6].

The data for liver cutting in Table 5 show that a heavier hog requires the higher pressure. But is it a general rule? Additional data need to be accumulated by experiments and clinical applications before the question can be answered.

The experimental process and results are described below for dogs. There were five hybrid dogs whose weights range from 15–20 kilograms. First of all, the dog is anaesthetized with 3 percent of amyl barbital and the liver film is cut with the usual scalpel. After the abdominal incision, the liver is incised with the water jet scalpel. The appropriate pressure for cutting dog livers is 0.8 MPa, and the depth of the dog's liver cutting is 5×10^{-2} m. At the same time, the blood vessels and bile ducts are incised and ligated, so that the haemorrhage quantity is decreased. All the dogs began to eat during the first day after their operations and

Table 5 Comparison data of liver cutting of hogs

No.	Sample	Weight of hog (kg)	Removals of liver cutting $\times 10^{-3}$ (kg)	Appropriate pressure (MPa)	Nozzle diameter $\times 10^{-3}$ (m)
1	Hog	17.0	65.0	1.0–1.5	0.15
2	Hog	18.5	120.0	0.7–1.0	0.15
3	Hog	22.0	44.0	0.7–1.0	0.15
4	Hog	15.0	66.0	1.0–1.3	0.15
5	Hog	15.0	30.0	0.7–0.8	0.15
6	Hog	15.0	45.0	0.7–0.8	0.15
7	Hog	14.0	30.0	0.5–0.7	0.15
8	Hog	12.5	20.0	0.5–1.0	0.15
9	Hog	23.5	14.5	0.7–2.0	0.15
10	Hog	17.0	34.0	0.5–1.0	0.15

survived. The wounds on their livers recovered well. They were then subject to euthanasia and autopsied one to two weeks after their operations. Dead tissue zones and haemorrhages on the livers were not found. Experiments show that the water jet scalpel has been effectively applied to the surgery operations in a hospital in China.

5 Clinical Applications

Based on the experiments described above, operations were performed on four patients (2 males, 2 females, aged 34–52) with a water jet scalpel for the liver cutting. Two patients suffered from liver cancer, the others had liver calculus. One of the two patients with liver cancer had accompanying cirrhosis. Half-hepatic sinister lobe was removed for one patient, external hepatic sinister lobe for two patients and part of the front hepatic dexter lobe for one patient. The four patients recovered quickly after the operation. During the operations the usual homeostatic devices were not used and yet the haemorrhage quantity was greatly decreased. After the operations, blood transfusion was not necessary, and the livers of all four patients worked well as shown by the hepatoscopy.

During the above clinical applications, the liver of the patients could not be incised at 0.8 MPa. The appropriate pressure was found to be from 1.8–3.0 MPa. For the cirrhosis patients, the pressure required was 3.0 MPa.

6 Summary Discussions

It is well known that the liver is an organ of blood circulation and is delicate in structure. The flow rate of blood feeding into the liver should not exceed 1×10^{-3} cubic meter per minute. Because the blood in the liver vein flows backward during the liver cutting operation, it may be difficult to control the hemorrhage of liver. So the success of the operation of liver cutting mainly depends on homeostasis. At present, for the purpose of homeostasis, there are new medical devices available during the surgical operation of liver cutting, such as the laser coagulator, microwave coagulator, cavity ultrasonic surgical aspirator, and the water jet scalpel. The principle of the operation of laser coagulator and microwave coagulator is to change light and electrical energy into thermal energy, thus leading to the vaporization and carbonation of liver tissue to attain the purpose of liver removal. Meanwhile, the bile ducts and blood vessels of operational parts are coagulated for homeostasis. However, because of the high temperature, healthy liver tissue is agglomerated or burned by a laser or microwave coagulator during the operation. Therefore there is a wider dead tissue zone on the surface of residual liver after the operation. This is the main disadvantage of laser or microwave coagulator.

The cavity ultrasonic surgical aspirator is an energy accumulating ultrasonic wave with the frequency of 23,000 Hz injected by a cavity detecting head made of titanium. The device selectively cracks liver tissue without cracking the liver ducts. As to the principle of liver cutting, it is equivalent to the water jet scalpel. Since the ultrasonic aspirator is quite expensive, it has not been widely used in China.

The power source for the water jet scalpel is the pressure bottle. The pressure of the water jet scalpel comes directly from the saline solution bottle under air pressure. Without a motor the jets themselves make little noise at lower pressure. Therefore, with the small flow rate of the water jet scalpel, the device makes no noise during the operation.

7 Preliminary Conclusions

Through the experiments on animals and clinical applications of the air pressurized water jet scalpel, we conclude the following:

1 The appropriate pressure of water jet is from 1.8–3.0 MPa for liver incisions of the patients.

2 The water jet scalpel with air pressure can precisely remove the viral tissue of liver without cutting off the bile ducts and blood vessels, so that the blood loss of the patients is reduced to a minimum during the operation. The liver of the patient recovers well after the operation.

3 The water jet scalpel device is easy to disinfect and it makes no noise, but the problem of the back spray of blood and liquid during the operation has not been solved.

4 From the effects of the liver cutting, the water jet scalpel gains an advantage over laser and microwave coagulator and is equivalent to the ultrasonic aspirator. But the cost of an ultrasonic aspirator greatly exceeds the water jet scalpel. Therefore, if the problem of the back spray of water jet scalpel is solved successfully, no doubt, its future for clinical applications in the liver surgery field will be very bright.

References

[1] Jessen, K., Philipp, J., Classen, M., Schikorr, W., and Louis, H., 1982, ''Endoscopic jet cutting—A new method for stone destruction in the common bile duct,'' *6th International Symposium on Jet Cutting Technology*, BHRA, England, pp. 39–52.

[2] Aeikens, B., Decker, B., Haferkamp, H., and Louis, H., 1986, ''Cracking of ureter calculi by high speed water jet pulses,'' *8th International Symposium on Jet Cutting Technology*, BHRA, England, pp. 157–166.

[3] Vijay, M. M., 1989, ''A critical examination of the use of water jets for medical applications,'' *Proc. 5th U.S. Water Jet Conference*, Toronto, Canada, pp. 425–448.

[4] Nishisaka, T., and Yonekawa, M., 1984, ''Development of the water jet scalpel,'' *Proc. International Symposium on Water Jet Technology*, Tokyo, Japan, pp. 49–61.

[5] Summers, D. A. and Viebrock, J., 1988, ''The impact of water jet on human flesh,'' *Proc. 9th International Symposium on Jet Cutting Technology*, BHRA, England, pp. 423–433.

[6] Uchino, J., Une, Y., Horie, T., Yonekawa, M., Kakita, A., and Sano, F., 1988, ''Surgical cutting of the liver by water jet,'' *Proc. 9th International Symposium on Jet Cutting Technology*, BHRA, England pp. 641–650.

[7] Muneki YOSHIDA and Akira KAKITA, 1999, ''The Usefulness of the Water Jet Dissector for Laparoscopic Surgery in the Patient with Chronic Cholecystitis,'' *Proc. Pacific Water Jet Conference*, Ishinomaki, Japan, pp. 461–465.

[8] Sun Jiajun, 1992, *Technology of Water Jet Cutting*, Press of China University of Mining and Technology, Xuzhou, pp. 90–98.

Charles N. McKinnon[1]
Boeing North American, Downey, CA

Danamichele Brennen[1]
McGettigan Partners, Philadelphia, PA

Christopher E. Brennen
California Institute of Technology
Pasadena, CA 91125

Hydraulic Analysis of a Reversible Fluid Coupling

This paper presents a hydraulic analysis of a fluid coupling which is designed to operate either in a forward or reverse mode when a set of turning vanes are respectively withdrawn or inserted into the flow between the driving and driven rotors. The flow path is subdivided into a set of streamtubes and an iterative method is used to adjust the cross-sectional areas of these streamtubes in order to satisfy radial equilibrium. Though the analysis requires the estimation of a number of loss coefficients, it predicts coupling performance data which are in good agreement with that measured in NAVSSES tests of a large reversible coupling intended for use in a ship drive train.
[DOI: 10.1115/1.1350819]

1 Introduction

Fluid couplings and torque converters are now commonly used in a wide variety of applications requiring smooth torque transmission, most notably in automobiles. They usually consist of an input shaft that drives a pump impeller which is closely coupled to a turbine impeller that transmits the torque of an output shaft coaxial with the input shaft. The fluid is usually hydraulic oil and the device is normally equipped with a cooling system to dissipate the heat generated. In a typical fluid coupling used, for example, in a ship propulsion system, the pump and turbine are mounted back to back with little separation between the leading and trailing edges of the two impellers. It is common to use simple radial blades and a higher solidity (the present pump rotor has 30 vanes) than would be utilized in most conventional pumps or turbines (Stepanoff [1], Brennen [2]). A torque converter as used in automotive transmission systems has an added set of stator vanes mounted between the turbine discharge and the pump inlet.

In the present paper, we present a hydraulic analysis of another variant in this class of fluid transmission devices, namely a reversible fluid coupling. This device was developed and built by Franco Tosi in Italy in conjunction with SSS Gears Ltd. in the U.K. and is described in detail in Fortunato and Clements [3], Clements and Fortunato [4] and Clements [5]. Tests on the device conducted by the US Navy (NSWC Philadelphia) are documented in Nufrio et al. [6] (see also, Zekas and Schultz [7]). This paper presents a method of analysis of the performance of such devices and uses one of the Franco Tosi designs tested by NSWC as an example. As shown diagrammatically in Fig. 1, the reversible fluid coupling has an added feature, namely a set of guide- vanes. With the vanes retracted the device operates as a conventional fluid coupling and the direction of rotation of the output shaft is the same as the input shaft. When the vanes are inserted, the direction of rotation of the output shaft is reversed. In traditional terms, the reversible fluid coupling can, in theory, operate over a range of slip values from $S=0$ to $S=2$. In the present paper, we utilize overall coupling performance data obtained by NSWC and several investigations of flow details carried out by WesTech Gear Corporation.

A number of recent papers have demonstrated how complex and unsteady the flow is in torque converters (see, for example, By and Lakshminarayana [8], Brun et al. [9], Gruver et al. [10]). Due, in part, to the need to operate the machines over a wide range of slip values, the incidence angles on the impeller blades tend to be very large thus generating substantial flow separation at the leading edges as well as much unsteadiness and high turbulence levels. To accommodate these violent flows and to force the flow to follow the vanes at impeller discharge, the solidity of the impellers is usually much larger than would be optimal in other turbomachines.

Though several efforts have been made to compute these flows from first principles (By et al. [11], Schulz et al. [12]), such complex, unsteady and turbulent flows with intense secondary flows are very difficult to calculate because of the lack of understanding of unsteady turbulent flows. In the present paper we begin with a simple one-dimensional analysis of the flow in a reversible fluid coupling. This one-dimensional analysis may be used as a first-order estimate of the coupling performance. Alternatively, it can be applied to a series of streamtubes into which the coupling flow is divided. Such a multiple streamtube (or two-dimensional flow) analysis allows accommodation of the large variations in flow velocity and inclination which occur between the core and the shell of the machine.

In the multiple streamtube analysis the flow is subdivided into streamtubes as shown in Fig. 2; all the data presented here used ten streamtubes of roughly similar cross-sectional area. The flow in each streamtube is characterized by meridional and tangential components of fluid velocity, u_i and v_i, at each of the transition stations, $i=1,2,3$, between the turbine and the pump ($i=1$), between the pump and the turning vanes ($i=2$) and between the turning vanes and the turbine ($i=3$). A typical velocity triangle, in this case for the transition station $i=1$, is included in Fig. 3; the velocity triangles for the other transition stations are similar.

Later we will present measured performance data for the reversible coupling whose basic geometry is listed in Table 1.

In the multiple streamtube analysis, the mean radius of the jth streamtube (the numbering of the streamtubes is shown in Fig. 2) at each of the locations $i=1,2,3$ is defined by $\overline{r}_{j,i}$. Since the distribution of velocity will change from one station to the other, only one of these three sets of streamtube radii can be selected *a priori*. We chose to select the series $\overline{r}_{j,1}$ at the turbine/pump transition. It follows that $\overline{r}_{j,2}$ and $\overline{r}_{j,3}$, the streamtube radii at the pump discharge and at the turning vane discharge must then be calculated as a part of the solution. Discussion of how this is accomplished is postponed until the solution methodology is described in Section 3.

2 Basic Equations

The process of power transmission through the coupling (operating under steady state conditions) will now be delineated. In the process, several loss mechanisms will be identified and quantified so that a realistic model for the actual interactions between the mechanical and fluid-mechanical aspects of coupling results.

[1]Formerly with WesTech Gear Corporation, now part of Philadelphia Gear.

Contributed by the Fluids Engineering Division for publication in the JOURNAL OF FLUIDS ENGINEERING. Manuscript received by the Fluids Engineering Division, August 4, 2000; revised manuscript received December 5, 2000. Associate Editor: Y. Tsujimoto.

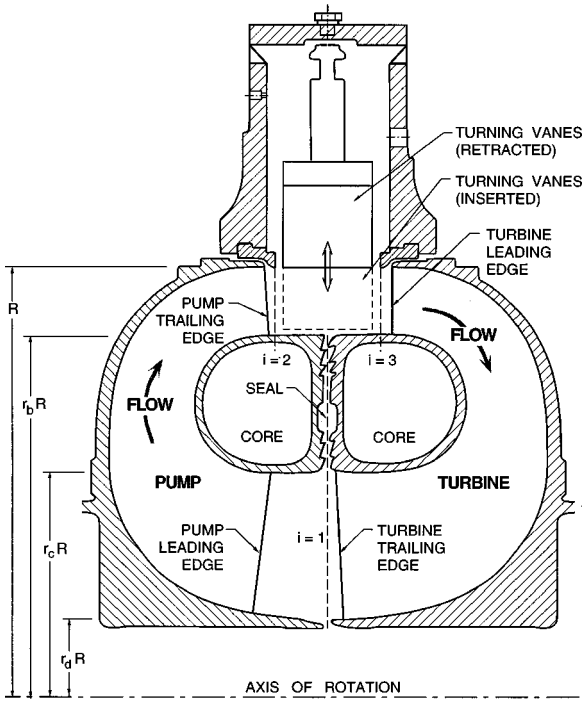

Fig. 1 Cross section of reversible fluid coupling showing key locations in the fluid cavity

2.1 Pump. The power input to the pump shaft is clearly $N_p T_p$. Some of this is consumed by windage losses in the fluid annulus between the pump shell and the stationery housing. This is denoted by a pump windage torque, T_{pw}, which will be proportional to N_p^2. Included in this loss will be the shaft seal loss as it has the same functional dependence on pump speed. It is convenient to denote this combined windage and seal torque, T_{pw}, by a dimensionless coefficient, C_{pw}, where $T_{pw}=C_{pw}\rho R^5 N_p^2$. Appropriate values of C_{pw} can be obtained, for example, from Balje [13] who indicates values of the order of 0.005.

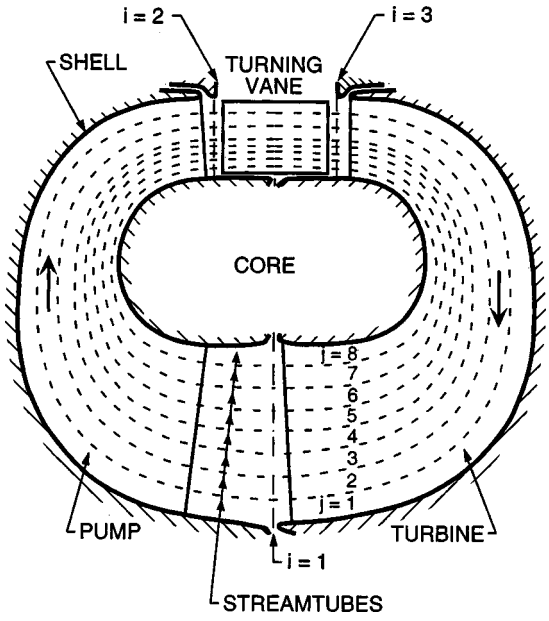

Fig. 2 Sketch showing the subdivision of the flow into streamtubes

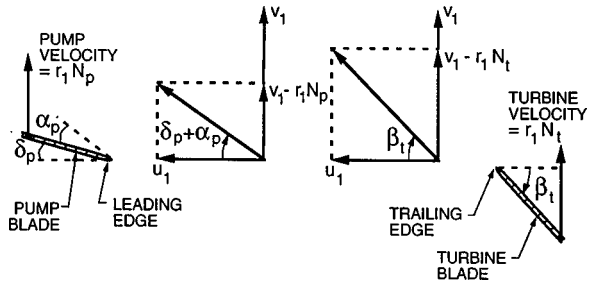

Fig. 3 Velocity triangle at the turbine/pump transition station, $i=1$. Flow is from the right to left, the direction of rotation is upward and the angles are shown as they are when they are positive.

Furthermore, the labyrinth seal in the core between the pump and turbine rotors causes direct transmission of torque from the pump shaft to the turbine shaft. This torque, which is proportional to $(N_p-N_t)^2$, will be denoted by T_s and is represented by a seal windage torque coefficient, C_{sw}, defined as

$$T_s=C_{sw}\rho R^3(r_b^2-r_c^2)(N_p-N_t)^2 \tag{1}$$

A comparison with the experimental data (Section 4) suggests a value of C_{sw} of about 0.014. In referring to this labyrinth seal, we should also observe that the leakage through this seal has been neglected in the present analysis.

It follows that the power available for transmission to the main flow through the pump is $N_p(T_p-T_{pw}-T_s)$ and this manifests itself as an increase in the total pressure of the flow as it passes through the pump. For simplicity, the present discussion will employ a two-dimensional representation of the fluid flow in which the flow is characterized at any point in the circuit by a single meridional velocity, u_i, and a single tangential velocity, v_i, at the appropriate rms radius. In practice, these quantities will vary over the cross section of the flow and this variation is considered later. At this stage it is not necessary to introduce this complexity. The power balance between the mechanical input, the losses and the ideal fluid power applied to the pump, then yields

$$N_p(T_p-T_w-T_s)=QH_{pi} \tag{2}$$

where, from the application of angular momentum considerations in the steady flow between pump inlet ($i=1$) and pump outlet ($i=2$), the pump head rise, H_{pi}, is given by

$$H_{pi}=\rho N_p(r_2 v_2-r_1 v_1) \tag{3}$$

More specifically, H_{pi} will be referred to as the ideal pump total pressure rise in the absence of fluid viscosity when the pump would be 100 percent efficient. However, in a real, viscous flow, the actual total pressure rise produced, H_p, is less than H_{pi}; the deficit is denoted by H_{pl} where

$$H_p=H_{pi}-H_{pl} \tag{4}$$

Table 1 Basic geometric data for the reversible coupling

Pump discharge vane angle, β_p, at shell	0 deg
Pump discharge vane angle, β_p, at core	0 deg
Turbine discharge vane angle, β_t, at shell	31.5 deg
Turbine discharge vane angle, β_t, at core	44 deg
Turning vane discharge angle, β_v	−55 deg
Pump inlet vane angle, δ_p, at shell	−17 deg
Pump inlet vane angle, δ_p, at core	−10 deg
Turbine inlet vane angle, δ_t, at shell	0 deg
Turbine inlet vane angle, δ_t, at core	0 deg
Turning vane inlet angle, δ_v	55 deg
Outer core radius/Outer shell radius, r_b	0.861
Inner core radius/Outer shell radius, r_c	0.592
Inner shell radius/Outer shell radius, r_d	0.29

This total pressure loss, H_{pl}, is difficult to evaluate accurately and is a function, among other things, of the angle of attack on the leading edges of the vanes. Note that the angle of attack, α_p, on the pump blades is given by

$$\alpha_p = \tan^{-1}\left\{\frac{v_1 - r_1 N_p}{u_1}\right\} - \delta_p \tag{5}$$

In the present context the total pressure loss, H_{pl}, is ascribed to two coefficients, C_{pa}, and C_{pb}. The first coefficient, C_{pa}, describes a loss which is a fraction of the dynamic pressure based on the component of relative velocity parallel to the blades at the pump inlet. The second coefficient, C_{pb}, describes a loss which is a fraction of the dynamic pressure based on the component of the pump inlet relative velocity perpendicular to the blades. Thus

$$H_{pl} = \frac{\rho}{2}[u_1^2 + (v_1 - r_1 N_p)^2][C_{pa} + (C_{pb} - C_{pa})\sin^2\alpha_p] \tag{6}$$

The coefficients C_{pa} and C_{pb} can be estimated using previous experience in pumps. Though there are many possible representations of the pump total pressure loss, the above form has several advantages. First, at a given flow rate, the loss is appropriately a minimum when α_p is zero, a condition which would correspond to the design point in a conventional pump. And this minimum loss is a function only of C_{pa}. On the other hand, at shut-off (zero flow rate) the loss is a function only of C_{pb}. These relations permit fairly ready evaluation of C_{pa} and C_{pb} in conventional pumps given the head rise and efficiency as a function of flow rate. Typical values of C_{pa} and C_{pb} are of the order of unity; but the value of C_{pa} must be less than the value of C_{pb}, the difference representing the effect of the inlet vane angle on the losses in the pump.

The hydraulic efficiency of the pump, η_p, is $1 - H_{pl}/H_{pi}$. In a conventional centrifugal pump for which $v_1 = 0$, the maximum design point efficiency, η_p, is expected to be about 0.85. With the kind of uneven inlet flow to be expected in the present flow a lower value of the order of 0.80 is more realistic. This value provides one relation for C_{pa} and C_{pb}.

2.2 Turbine. We now jump to the turbine output shaft and work back from there. The power delivered to the turbine shaft is $N_t T_t$. As in the pump there are windage losses, $N_t T_{tw}$, where the windage torque, T_{tw}, is described by a dimensionless coefficient, $C_{tw} = T_{tw}/\rho N_t^2$. Then the power delivered to the turbine rotor, $N_t(T_t + T_{tw} - T_s)$, by the main flow through the turbine is related to the ideal total pressure drop through the turbine, H_{ti}, by

$$N_t(T_t + T_{tw} - T_s) = QH_{ti} \tag{7}$$

where, again, from angular momentum considerations

$$H_{ti} = N_t(r_2 v_3 - r_1 v_1) \tag{8}$$

With an inviscid fluid, H_{ti} would be the actual total pressure drop across the turbine. But in a real turbine the actual total pressure drop is greater by an amount, H_{tl}, which represents the total pressure loss in the turbine, and hence

$$H_t = H_{ti} + H_{tl} \tag{9}$$

In a manner analogous to that in the pump, the total pressure loss in the turbine, H_{tl}, is ascribed to two coefficients C_{ta} and C_{tb}. The first coefficient, C_{ta}, describes a loss which is a fraction of the dynamic pressure based on the component of relative velocity parallel to the blades at the turbine inlet. This coefficient essentially determines the minimum loss at the design point where the angle of attack, α_t, is zero. The second coefficient, C_{tb}, describes a loss which is a fraction of the dynamic pressure based on the component of the turbine inlet velocity perpendicular to the blades. Thus

$$H_{tl} = \frac{\rho}{2}[u_3^2 + (v_3 - r_3 N_t)^2][C_{ta} + (C_{tb} - C_{ta})\sin^2\alpha_t] \tag{10}$$

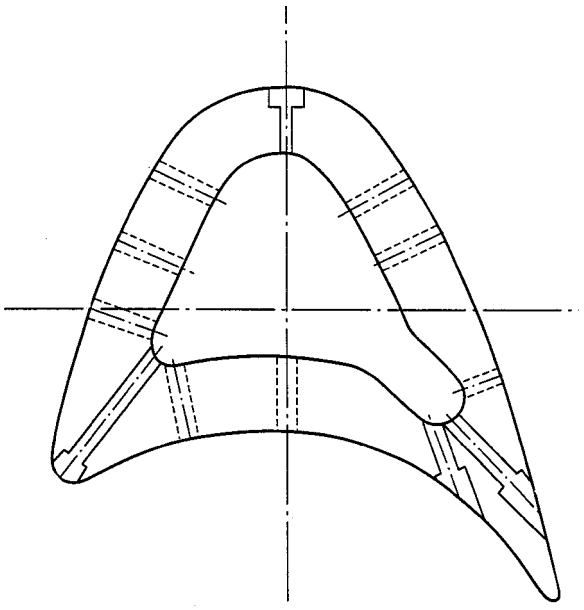

Fig. 4 Cross section of a turning vane

where the angle of attack, α_t, on the turbine blades is given by

$$\alpha_t = \tan^{-1}\left\{\frac{v_3 - r_2 N_t}{u_3}\right\} - \delta_t \tag{11}$$

As in the case of the pump, appropriate values of C_{ta} and C_{tb} are of the order of unity and should be such as to yield a stand-alone turbine efficiency, H_{ti}/H_t of the order of 0.85. However, C_{tb} must be greater than C_{ta} to reflect the appropriate effect of the inlet vane angles on the hydraulic losses.

2.3 Turning Vanes. The geometry of a turning vane used in the coupling discussed here is shown in Fig. 4.

The total pressure rise produced by the pump, H_p, is equal to the total pressure drop across the turbine, H_t, plus the total pressure drop across the turning vanes, H_v, so that

$$H_p = H_t + H_v \quad \text{with the turning vanes inserted} \tag{12}$$

$$H_v = 0 \quad \text{with the turning vanes retracted} \tag{13}$$

It is this balance which essentially determines the flow rate, Q, and the meridional velocities, u_i. The total pressure drop across the vanes, H_v, is described a loss coefficient defined by

$$C_v = 2H_v/\rho(v_3^2 + u_3^2) \tag{14}$$

Though both H_v and C_v will vary with the angle of attack of the flow on the turning vanes, α_v, we have not exercised that option here since there is no independent information on the turning vane performance. Estimates from experience suggest that C_v should lie somewhere between about 0.3 and 1.0.

2.4 Turbine Partial Admission Effect. Due to the large blockage effects of the turning vanes, the flow discharging from the vanes consists of an array of jets interspersed with relatively stagnant vane wakes. This means that during reverse operation the turbine experiences inlet conditions similar to those in a partial admission turbine. In the hydraulic analysis we can approximately account for these partial admission effects by taking note of the following property of partial admission. Consider and compare the flux of angular momentum in the flow into the turbine, first, for full admission and, second, for partial admission. Under uniform, full admission conditions, u_3 and v_3 are independent of circumferential position and the flux of angular momentum entering the turbine is proportional to $u_3 v_3$. If the swirl angle were

defined by the turning vane discharge angle then this reduces to $u_3^2 \tan \beta_v$. On the other hand, a partial admission flow consisting of jets with velocity components u_3^*, v_3^* alternating with stagnant wakes of zero velocity would have a flux of angular momentum equal to $k u_3^* v_3^*$ where k is the fraction of the cross-sectional area occupied by the jets ($0<k<1$). But if the total flow rate is the same in both cases then $u_3^* = u_3/k$ and if the jets are parallel with the turning vane discharge angle then $v_3^* = u_3^* \tan \beta_v$. Hence the flux of angular momentum becomes $u_3^2 \tan \beta_v / k$. In other words, the blockage which creates the jets and wakes also leads to an *increase* in the flux of angular momentum by the factor, $1/k$.

To account for this in the flow analysis, the appropriate angular momentum flux (which is essential to the basic principles of the pump or turbine) can be maintained by inputting an *effective* turning vane discharge angle denoted by β_v^*. Comparing the above expressions the effective turning vane discharge angle is given by

$$\tan \beta_v^* = \tan \beta_v / k \tag{15}$$

Hence by inputting a somewhat larger than actual turning vane discharge angle we can account for these partial admission effects.

The problem therefore reduces to estimating an appropriate value for k from the experimental measurements. For this purpose, we develop the relation between k and the loss coefficient for the turning vanes, C_v. If the total head of the jets is assumed to be equal to the upstream total head (at location $i=2$), then it is readily shown that the *mean* total head of the discharge (including the wakes) implies the following relation between k and C_v:

$$k = \left\{ \frac{1 - C_v \tan^2 \beta_v}{1 + C_v} \right\}^{1/2} \tag{16}$$

The value of $C_v = 0.36$ which is deployed later along with the appropriate $\beta_v = -55$ deg yield $\beta_v^* = -72.8$ deg and a blockage ratio (or partial emission factor) of $k = 0.44$ which seems reasonable given the geometry of the turning vane cascade.

3 Solution of the Flow

3.1 Solution for an Individual Streamtube. Consider first the solution of the flow in an individual streamtube where it is assumed that the velocity at any location in the circular path (Fig. 2) can be characterized by a single meridional and a single tangential velocity. Assume for the moment that the radial positions of the streamtube are known; then the inlet and discharge angles encountered by that particular streamtube at those radial positions at each of the transition stations can be determined. Then for a given slip, $S = 1 - N_t/N_p$, the first step is to solve the flow equation (12) or more specifically:

$$H_{pi} - H_{pl} = H_{ti} + H_{tl} + H_v \tag{17}$$

to obtain the flow rate and velocities. The procedure used starts with a trial value of u_1. Values of u_2, u_3 follow from continuity knowing the areas A_i:

$$u_i = u_1 A_1 / A_i, \quad i = 2,3 \tag{18}$$

Furthermore, it is assumed that the relative velocity of the flow discharging from the pump, the turning vanes or the turbine is parallel with the blades of the respective device (or the effective angle in the case of the turning vanes). Given the high solidity of the pump and turbine, this is an accurate assumption. This allows evaluation of the tangential velocities:

$$v_1 = r_1 N_t + u_1 \tan \beta_t \tag{19}$$

$$v_2 = r_2 N_p + v_2 \tan \beta_p \tag{20}$$

where r_1 and r_2 are rms channel radii at each location and $v_3 = v_2$ for the turning vanes retracted and $v_3 = u_3 \tan \beta_v$ for the turning vanes inserted. These relations can then be substituted into the definitions (3), (8), (6), (10), and (14) to allow evaluation of all the terms in Eq. (17). That equation is not necessarily satisfied by the initial trial value for u_1. Hence an iteration loop is executed to find that value of u_1 which does satisfy Eq. (17). The velocities and flow rate are thus determined for a given value of the slip.

Table 2 Power transmission losses

Pump shaft power	$= N_p T_p$
Power lost in pump windage	$= N_p T_{pw}$
Power to turbine through seal	$= N_p T_s$
Power to main pump flow	$= Q H_{pi}$
	$= N_p (T_p - T_{pw} - T_s)$
Power in main flow out of pump	$= Q(H_{pi} - H_{pl})$
Power lost in turning vanes	$= Q H_v$
Power in flow entering turbine	$= Q(H_{pi} - H_{pl} - H_v)$
	$= Q(H_{ti} + H_{tl})$
Power to turbine rotor by flow	$= Q H_{ti}$
	$= N_t (T_t + T_{tw} - T_s)$
Power to turbine through seal	$= N_t T_s$
Power lost in turbine windage	$= N_t T_{tw}$
Turbine shaft power	$= N_t T_t$

3.2 Multiple Streamtube Solution. As described in the last section, the multiple streamtube analysis begins with a set of guessed values for the streamtube locations at the transition stations, $i=2$ and $i=3$. It also begins with an assumed value for the flowrate in each streamtube (more specifically an assumed value of $u_1 = 1$). Then the method of the last section is used to solve for the flow and allows evaluation of the total pressure changes and losses in each streamtube. Then, the degree to which Eq. (17) is satisfied is assessed. This leads to an improved value of u_1 and the process is repeated to convergence (only three or four cycles are necessary). By doing this for each streamtube we obtain the total pressure and the static pressure differences between all three locations for each streamtube.

The principle by which the streamtube geometry is adjusted is that the flows in each of the three locations should be in radial equilibrium. This implies that, at each of the locations $i=1,2,3$, the flow must satisfy

$$\left(\frac{\partial P}{\partial r} \right)_i = \frac{\rho v_i^2}{r_i} \tag{21}$$

where P is the static pressure. Application of this condition at the turbine/pump transition station ($i=1$) establishes the static pressure difference between each streamtube. Then using the information from the flow solution on the static pressure differences between transition stations we can establish the pressure distribution between the streamtubes at transition stations $i=2$ and $i=3$. Then using Eq. (21) we examine whether the flows in these locations are in radial equilibrium. Given the initial trial values of $\overline{r}_{j,2}$ and $\overline{r}_{j,3}$, this will not, in general, be true. The method adjusts the values of $\overline{r}_{j,2}$ and $\overline{r}_{j,3}$ and then repeats the entire process until radial equilibrium is indeed achieved at transition stations $i=2$ and $i=3$. This requires as many as 30 iterations.

3.3 Power Transmission Summary. This completes the description of the power transmission through the coupling which is summarized in Table 2. The overall efficiency of the coupling, η, is given by

$$\eta = \frac{N_t T_t}{N_p T_p} = \frac{Q H_{ti} - N_t T_{tw} + N_p T_s}{Q H_{pi} + N_p T_{pw} + N_p T_s} \tag{22}$$

or substituting from Eqs. (4) and (9):

$$\eta = \frac{N_t (r_2 v_3 - r_1 v_1) - (N_t T_{tw} + N_t T_s)/Q}{N_p (r_2 v_2 - r_1 v_1) + (N_p T_{pw} + N_p T_s)/Q} \tag{23}$$

This expression demonstrates an important feature of the reversible coupling. In the forward mode with the vanes removed, $v_2 = v_3$, the quantities in first parentheses in the numerator and denominator are identical. Therefore, if the windage torques, T_{tw} and T_{pw}, are small as is normally the case and if Q is not close to zero (as can only happen close to $S=0$) then the coupling efficiency is close to $N_t/N_p = 1-S$. Thus, in the forward mode, only the windage losses cause the efficiency to deviate from $1-S$. On the other hand, no such simple relation exists in the reverse mode.

Apart from the overall efficiency, η, two other coupling characteristics will be presented, namely the pump torque coefficient, C_p, and the turbine torque coefficient, C_t. Note the choice of N_p in the denominator for C_t.

4 Comparison With Experiments

4.1 Experimental Data. The efficiency, torque coefficients and fluid velocities measured during tests of the coupling conducted by NAVSSES (using an oil of density 849 kg/m^3) at a input (or pump) speed of 1000 rpm will be compared to the results of the present analytical model. Note that although three graphs for η, C_p and C_t are presented, these only represent two independent sets of data since $\eta = C_t(1-S)/C_p$.

4.2 Performance. A typical set of results for the performance of the coupling are presented in Figs. 5 and 6. The coefficients C_{pa}, C_{pb}, C_{ta}, C_{tb}, and C_{va} (and, to a lesser extent, C_w and C_{sw}) were chosen to match the experimental data by proceeding as follows. First note that C_w and C_{sw} have little effect *except* close to $S=0$. In fact, the peak in η near $S=0$ is almost entirely determined by C_w and values of $C_w = 0.02$ were found to fit the data near $S=0$ quite well. This value is also consistent with previous experience on windage coefficients (Balje [13]). Similarly past experience would suggest a value of 0.005 for the seal windage coefficient, C_{sw}.

Turning to the pump, turbine and turning vane loss coefficients, it is clear that the turning vanes have no effect on forward performance ($S<1$). Hence the pump and turbine loss coefficients were chosen to match this data. In this regard the efficiency is of little value since the forward efficiency is always close to $(1-S)$. Values of $C_{pa}=C_{ta}=0.7$ and $C_{pb}=C_{tb}=1.0$ seemed to match the forward torque coefficients well. These could be supported by the argument that all the dynamic head normal to the vanes at inlet will likely be lost (thus $C_{pb}=C_{tb}=1.0$) and a high fraction of that parallel with the vanes is also likely to be lost (thus $C_{pa}=C_{ta}=0.7$). Note that the results presented are not very sensitive to the precise values used for these loss coefficients. It should also be noted that these loss coefficients yield sensible peak efficiencies for the pump or turbine when these are evaluated for stand-alone performance (respectively 79 percent and 86 percent).

Finally, then, we turn to the reverse performance ($S>1$) with only one loss coefficient left to determine, namely the loss due to the turning vanes, C_{va}. In the example shown a value of C_{va} of 0.36 yields values of the efficiency which are consistent with the experimental results.

Note that if the coefficients described above were used with the actual turning vane discharge angle, there would be substantial discrepancies between the observed and calculated results; this helps to confirm the analysis of section and the use of the effective turning vane discharge angle, $\beta_v^* = -72.8$ deg.

4.3 Velocity Distributions. The multiple streamtube approach also provides information on the distributions of flow, angles of attack, etc. within the coupling and demonstrates how these change with slip. Examination of the results revealed several ubiquitous nonuniformities and one example, presented in Fig. 7, will suffice to illustrate these. At low slip values in forward operation the meridional velocity profiles are very nonuniform. This nonuniformity consists of much higher meridional velocities near

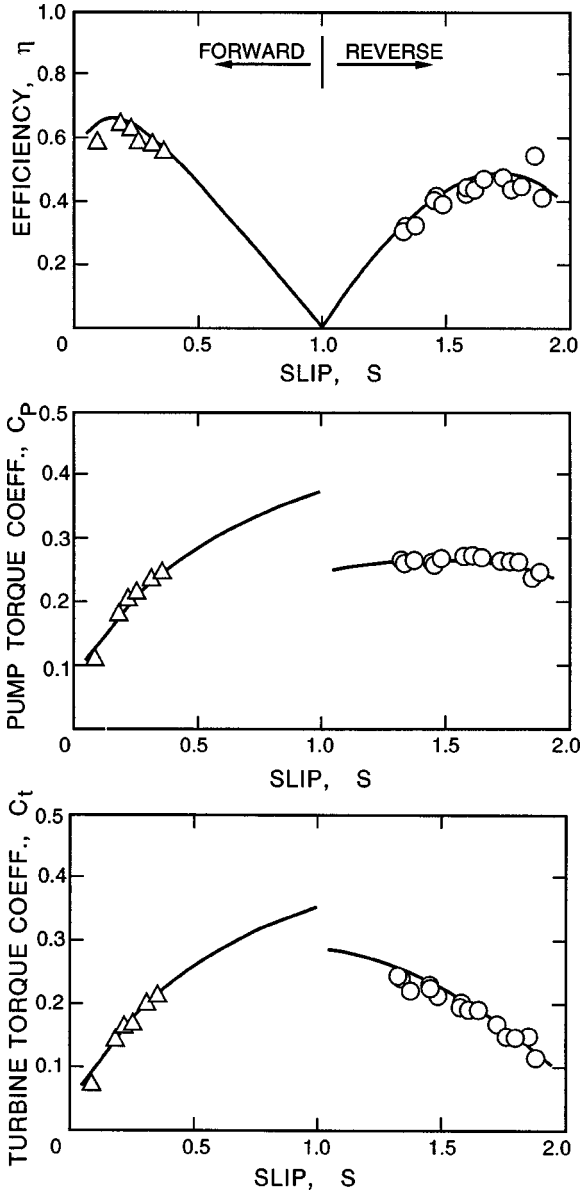

Fig. 5 Efficiency and torque coefficients for the reversible coupling using $C_{pa}=C_{ta}=0.7$, $C_{pb}=C_{tb}=1.0$, $C_v=0.36$, $C_{sw}=0.02$, $C_w=0.005$ and an effective turning vane discharge angle of -72.8 deg

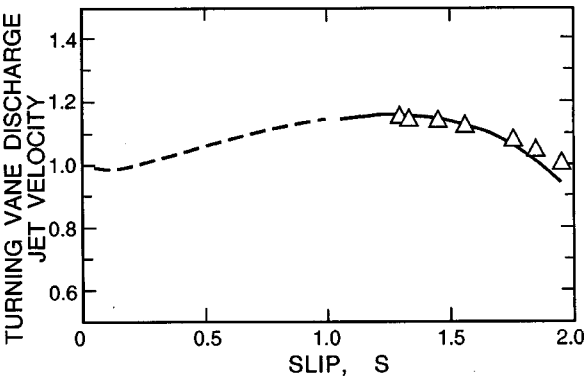

Fig. 6 Velocity of turning vane discharge jets for the same conditions as listed in Fig. 5

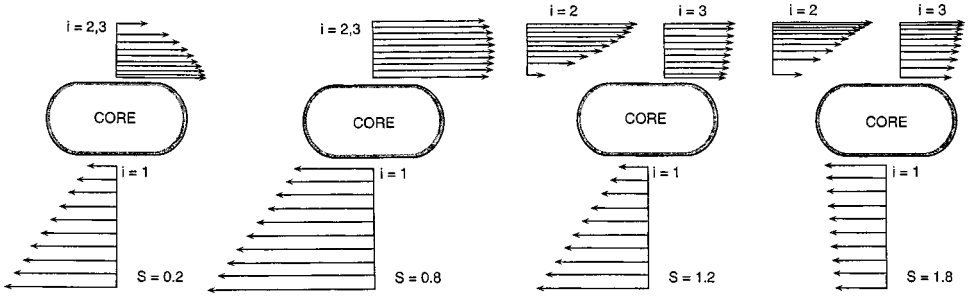

Fig. 7 Meridional velocity distributions at the transition stations for four different slip values

the axis in the turbine-to-pump transition and at the outer radius in all the transitions. As the slip increases in forward operation this nonuniformity decreases; near $S=1$ it has disappeared at the pump-to-turbine transition but remains at the turbine-to-pump transition. When the turning vanes are inserted, the velocity profiles show a highly nonuniform character in the pump-to-turning-vane transition but this is almost completely evened out by the turning vanes. The turbine-to-pump nonuniformity near $S=1$ is not too dissimilar to that in forward operation near $S=1$. However, it is interesting to note that this nonuniformity is reversed as $S=2$ is approached. These changing nonuniformities are important because they imply corresponding changes in the distribution of the angles of attack on the pump, turning vanes, and turbine. Consequently, the optimal vane inclination distributions (which would have as their objective uniform angles of attack) are different for forward and reverse operation.

5 Conclusions

This paper presents a hydraulic analysis of a reversible fluid coupling operating over a range of slip values in both forward ($0<S<1$) and reverse ($1<S<2$) operation. The analysis employs estimated loss coefficients for the pump, turbine, turning vanes, windage, and core seal. It splits the flow into an array of streamtubes with pressure balancing adjustment across those streamtubes and solves to find the fluid velocities, flow rate, and static pressures at each of the transition stations for each streamtube. This information then allows evaluation of the overall performance characteristics including the efficiency and the pump and turbine torque coefficients. Comparison with data from the full scale testing (conducted by the U.S. Navy) of a reversible fluid coupling made by Franco-Tosi demonstrates good agreement between the analysis and the experiments. While the analysis involves the selection and identification of a number of hydraulic loss coefficients, the values of the coefficients do appear to be valid over a wide range of operating points, slip values, and speeds. Moreover, though these coefficients are necessarily specific to the particular coupling studied, they nevertheless provide benchmark guidance for this general class of machine.

When the coupling is operated in the forward mode, the flow rates are small and hence the hydraulic losses are quite minor. Thus the efficiency is close to the ideal. However, as the slip increases, the flow rates become larger and the hydraulic losses (which increase like the square of the flowrate) become substantial. Under these conditions the device behaves much more like an interconnected pump and turbine than a conventional fluid coupling and the overall efficiency is similar to that one would expect from a device which links drive trains through a combination of a pump and a turbine. Even under the best of circumstances the analysis suggests that the efficiency of this generic type of coupling could not be expected to exceed 60 percent in the reverse mode.

The analysis presented here also demonstrates that, since it is used over a wide range of slip values, a reversible fluid coupling must operate over a wide range of angles of attack of the flows entering the pump and turbine rotors. With fixed geometry rotors, this inevitably results in substantial hydraulic losses, particularly in the reverse mode. Choosing the inlet blade angles in order to minimize those losses is not simple and it is not clear how the fixed geometry should be chosen in order to achieve that end.

Acknowledgments

The analyses described were performed for WesTech Gear Corporation, now part of Philadelphia Gear, and the authors are very grateful to both organizations for their concurrence in the publication of this paper. We are also very appreciative of the help and advice of Tom Gugliuzza of WesTech Gear.

Nomenclature

A_i = cross-sectional area of flow at $i=1,2,3$
C_p = pump torque coefficient, $C_p=T_p/\rho R^5 N_p^2$
C_t = turbine torque coefficient, $C_t=T_t/\rho R^5 N_p^2$
C_{pw}, C_{tw} = pump and turbine windage loss coefficients
C_{sw} = seal windage torque coefficient
C_{pa}, C_{pb} = pump hydraulic loss coefficients
C_{ta}, C_{tb} = turbine hydraulic loss coefficients
C_v = loss coefficient for the turning vanes
H_p, H_{pi} = actual, ideal total pressure rise across pump
H_t, H_{ti} = actual, ideal total pressure drop across turbine
H_{pl}, H_{tl}, H_v = total pressure losses in pump, turbine, turning vanes (nondimensionalized by $\rho R^2 N_p^2$)
k = turning vane discharge blockage ratio
N_p, N_t = angular velocities of the pump, turbine (rad/s)
P_i = fluid pressure at locations $i=1,2,3$
Q = volume flow rate of fluid
R = outer shell radius (0.5 m)
r_i = radial position in the flow (m)
r_b = outer core radius/R
r_c = inner core radius/R
r_d = inner shell radius/R
$\overline{r}_{j,i}$ = mean radius of jth streamtube/R
S = slip$=1-N_t/N_p$
T_p, T_t = shaft torques for the pump, turbine
T_s = torque in seal between pump+turbine rotors
T_{pw}, T_{tw} = windage torques for the pump, turbine
u_i = meridional component of fluid velocity at stations $i=1,2,3 (=Q/A_i)$
v_i = tangential fluid velocity at $i=1,2,3$
$\alpha_p, \alpha_t, \alpha_v$ = angles of attack of flow on pump, turbine, turning vanes (relative to axial plane)
$\beta_p, \beta_t, \beta_v$ = discharge vane angles for pump, turbine, turning vanes (relative to axial plane)
β_v^* = effective discharge angle for turning vanes
$\delta_p, \delta_t, \delta_v$ = inlet vane angles at pump, turbine, turning vanes (relative to axial plane)
η = overall coupling efficiency, $\eta=N_t T_t/N_p T_p$
ρ = fluid density

References

[1] Stepanoff, A. J., 1957, *Centrifugal and Axial Flow Pumps*, Wiley, New York.
[2] Brennen, C. E., 1994, *Hydrodynamics of Pumps*, Oxford University Press and Concepts ETI, Inc.
[3] Fortunato, E., and Clements, H. A., 1979, ''Marine reversing gear incorporating single reversing hydraulic coupling and direct-drive clutch for each turbine,'' ASME Paper No. 79-GT-61.
[4] Clements, H. A., and Fortunato, E., 1982, ''An advance in reversing transmissions for ship propulsion,'' ASME Paper No. 82-GT-313.
[5] Clements, H. A., 1989, ''Stopping and reversing high power ships,'' ASME Paper No. 89-GT-231.
[6] Nufrio, R., Schultz, A. N., and McKinnon, C. N., 1987, ''Final report—reverse reduction gear/reversible converter coupling test and evaluation,'' PM-1500B.
[7] Zekas, B. M., and Schultz, A. N., 1997, ''Unique reverse and maneuvering features of the AOE-6 reverse reduction gear,'' ASME Paper No. 97-GT-515.
[8] By, R. R. and Lakshminarayana, B., 1995, ''Measurement and analysis of static pressure field in a torque converter pump,'' ASME J. Fluids Eng., **117**, pp. 109–115.
[9] Brun, K., Flack, R. D., and Gruver, J. K., 1996, ''Laser velocimeter measurements in the pump of an automotive torque converter. Part II—Unsteady measurements,'' ASME J. Fluids Eng., **118**, pp. 570–577.
[10] Gruver, J. K., Flack, R. D., and Brun, K., 1996, ''Laser velocimeter measurements in the pump of an automotive torque converter. Part I—Average measurements,'' ASME J. Fluids Eng., **118**, pp. 562–569.
[11] By, R. R., Kunz, R., and Lakshminarayana, B., 1995, ''Navier-Stokes analysis of the pump flow field of an automotive torque converter,'' ASME J. Fluids Eng., **117**, pp. 116–122.
[12] Schulz, H., Greim, R., and Volgmann, W., 1996, ''Calculation of three-dimensional viscous flow in hydrodynamic torque converters,'' ASME J. Fluids Eng., **118**, pp. 578–589.
[13] Balje, O. E., 1981, *Turbomachines. A Guide to Design, Selection and Theory*, Wiley, New York.

Hydraulic Performance of a Mixed-Flow Pump: Unsteady Inviscid Computations and Loss Models

B. P. M. van Esch
Assistant Professor,
Department of Mechanical Engineering,
Eindhoven University of Technology,
P.O. Box 513,
5600 MB Eindhoven,
The Netherlands

N. P. Kruyt
Assistant Professor,
Department of Mechanical Engineering,
University of Twente,
P.O. Box 217,
7500 AE Enschede,
The Netherlands

The hydraulic performance of an industrial mixed-flow pump is analyzed using a three-dimensional potential flow model to compute the unsteady flow through the entire pump configuration. Subsequently, several additional models that use the potential flow results are employed to assess the losses. Computed head agrees well with experiments in the range 70 percent–130 percent BEP flow rate. Although the boundary layer displacement in the volute is substantial, its effect on global characteristics is negligible. Computations show that a truly unsteady analysis of the complete impeller and volute is necessary to compute even global performance characteristics; an analysis of an isolated impeller channel and volute with an averaging procedure at the interface is inadequate.
[DOI: 10.1115/1.1365121]

1 Introduction

Over the past few years, there is a tendency toward the development of numerical methods based on the Navier-Stokes equations with turbulence models, in order to account for viscous effects like wakes, boundary layers, secondary flow and separation. However, current methods are of limited suitability as part of a design tool given their extreme requirements in terms of computer resources. In addition, other open problems in such computations are (see Gülich [1]): (i) accurate modeling of boundary layer transition and separation (Muggli et al. [2]); (ii) the choice of an appropriate turbulence model that accounts for the effects of three-dimensional boundary layers, curvature and rotation (Rodi [3]; Speziale [4], Lakshminarayana [5], Schilling [6]); (iii) interaction between impeller and diffuser (Gülich and Egger [7]); and (iv) influence of mesh size near solid walls on prediction of losses (Gülich et al., [8]).

For most pumps operating near design conditions, the influence of viscosity is restricted to thin boundary layers and wake areas. The core of the flow is governed by the influence of centrifugal and Coriolis forces due to rotation and curvature, and can thus be predicted fairly accurately by means of three-dimensional inviscid methods. If one further assumes the incoming flow to be irrotational (e.g., a uniform pipe flow), the core of the flow in hydraulic pumps can be modeled as an incompressible potential flow.

In this paper, we evaluate the use of a potential flow method capable of computing the three-dimensional unsteady flow in a complete mixed-flow pump. All impeller channels, as well as the casing of the pump, are treated simultaneously, thus allowing the instantaneous impeller flow to be different from one channel to the other. Also, the interaction between the flow in the impeller and the pump casing (e.g., backflow from the volute into the impeller) can be simulated by this method. The method is extended with additional standard models to account for viscous losses. Input of these models is supplied by the inviscid computation. A scale model of an industrial mixed-flow pump is analyzed for which measurements of the overall performance characteristics head and efficiency are available. The necessity of performing unsteady whole-pump computations even for global performance characteristics will be shown.

Contributed by the Fluids Engineering Division for publication in the JOURNAL OF FLUIDS ENGINEERING. Manuscript received by the Fluids Engineering Division June 15, 1999; revised manuscript received January 31, 2001. Associate Editor: B. Schiavello.

2 Computational Method

2.1 Unsteady 3D Potential Flow Model. Many investigators have presented numerical methods for computing the steady potential flow inside an impeller channel in two or three dimensions, or the unsteady potential flow in complete impeller-volute configurations in two dimensions (e.g., Daiguji [9,10], Maiti et al. [11], Chen and Sue [12], Badie et al. [13]).

A very efficient numerical method has been developed for solving the unsteady three-dimensional potential flow through entire pump configurations (van Esch [14], Kruyt et al. [15]). With this method, the instantaneous flow through each of the impeller channels, which in general differs from one channel to the other, and the casing can be calculated simultaneously. By introducing a sliding interface in the computational domain between the impeller and the casing of the pump, the rotating motion of the impeller relative to the volute is simulated. Leakage flows are not addressed directly in these computations. Instead, the effect of leakage is computed using an additional model (Section 2.6).

Although, strictly speaking, secondary flows cannot be simulated with an inviscid method since no boundary layers are considered, the resulting flow through the impeller is by no means homogeneous. After all, a potential model truly accounts for centrifugal- and Coriolis forces due to rotation and curvature. As a result, the typical flow relative to the impeller channels shows a vortical structure near the hub, counterrotating with respect to the shaft direction of rotation, and a similar vortex in the meridional plane near the pressure surface of the blades, rotating in a direction from hub to shroud at the leading edge and from the shroud back to the hub near the trailing edge. These vortices tend to be more pronounced at low flow rates.

The potential flow model is implemented as a multi-block finite element method, employing the superelement approach (Zienkiewicz and Taylor [16]). Systems of equations are solved by a direct method. By employing linear elements in combination with the SPR-technique for velocity (Zienkiewicz and Zhu [17]), second-order accuracy for potential, velocity and pressure was found (van Esch [14]). To determine the blade loading, the Kutta condition is imposed at all nodes located on the trailing edges of the impeller blades. As the loading of the blades is nonuniform

(along the blades' span) as well as time-dependent, unsteady wakes emanate from the blades' trailing edges. The unsteadiness of the wakes is simulated by vortices which are shed downstream with the local mean velocity along a sheet of zero thickness. The strength of a vortex is equal to the change of the local blade circulation over the timestep considered.

2.2 Boundary Layer Model. Quantities like boundary layer displacement thickness and momentum thickness are computed using a steady one-dimensional thin shear layer (TSL) method in integral formulation. A method like this can be applied at isolated streamlines along solid surfaces. The method of Thwaites [18] is employed for the laminar part of the boundary layer, while Green's ''lag entrainment method'' (Green et al. [19]) is used for the turbulent part. Thwaites' criterion is employed to predict laminar separation (Thwaites [18]):

$$\delta_2^2\left(\frac{\partial v_e}{\partial s}\right)\Big/\ \nu \leqslant -0.082 \tag{1}$$

where δ_2 denotes the momentum thickness, v_e the velocity outside of the boundary layer, ν the viscosity, and s the local coordinate along the streamline. According to Mayle [20], the free-stream turbulence intensity in many turbomachinery applications is high enough to be responsible for transition of the boundary layer (bypass-transition). He showed that a correlation of experiments indicates the following criterion for bypass transition

$$\mathrm{Re}_{\delta_2,t} = 400\ \mathrm{Tu}^{-5/8} \tag{2}$$

where $\mathrm{Re}_{\delta_2,t}$ is the Reynolds number based on momentum thickness at transition, and Tu denotes the turbulence intensity (percents). This simple criterion appears to be valid for zero-pressure gradient flows ($0.2<\mathrm{Tu}<10$), as well as for flows encountering adverse and favorable pressure gradients where Tu is larger than 3 percent. For turbulence levels exceeding 1 percent, this transition criterion is not influenced by convex or (mild) concave curvature (see Mayle [20], for a discussion). Relaminarization (or reverse transition) of a turbulent boundary layer is expected to occur if the acceleration parameter, defined as $K=\nu(\partial v_e/\partial s)/v_e^2$, exceeds the value of $3(10)^{-6}$. Also, transition from a laminar to a turbulent state is suppressed at these levels of acceleration.

Streamline curvature and rotation induce additional centrifugal and Coriolis accelerations in the boundary layer equations. However, for mild curvature and rotation, these extra accelerations need not be considered in the TSL approximation (Bradshaw [21]). The following conditions should hold for this approximation

$$\frac{\delta}{R} \ll 1 \quad \text{and} \quad \frac{\Omega\delta}{v_e} \ll 1 \tag{3}$$

where R is the radius of streamline curvature, δ the boundary layer thickness, Ω the rotational speed, and v_e the velocity outside of the boundary layer. In the current application δ/R typically has values between 0 and 0.02 at the blade suction side and between 0 and 0.05 at the pressure side, while $\Omega\delta/v_e$ ranges between 0 and 0.03 at the suction side and between 0 and 0.05 at the pressure side. Still, rotation and curvature do have an influence on the level of Reynolds stress in the turbulent boundary layer. It is accounted for by a correction of the mixing length, that is present in the lag entrainment method, with a factor $1/F$, where

$$F = 1 + \beta_c \mathrm{Ri}_c + \beta_\Omega \mathrm{Ri}_\Omega \tag{4}$$

with $\mathrm{Ri}_c = 2(v_e/R)/(\partial v/\partial n)$ and $\mathrm{Ri}_\Omega = -2\Omega/(\partial v/\partial n)$ the Richardson numbers for curvature and rotation, respectively, v the velocity in the boundary layer and n the direction normal to the surface. β_c and β_Ω are empirically determined constants: β_c equals 7 for convex walls and 4.5 for concave walls (Bradshaw [22]), and β_Ω has an approximate value of 6 (Johnston and Eide [23]).

The criteria for separation of turbulent boundary layers to occur, as indicated in the literature, vary considerably; values for the shape factor $H_{12}=\delta_1/\delta_2$ are in the range 2.0–4.0 (Schlichting [24]). Here it is assumed that a turbulent boundary layer is prone to separation if H_{12} exceeds the value of 2.8.

2.3 Head, Power Loss, and Efficiency. The power P_{sh} which is applied at the shaft of the pump is only partly converted into net power P_{net}, used to increase the total pressure of the fluid between inlet and outlet of the pump. A sometimes substantial part of the shaft power is used to overcome losses in the pump

$$P_{\mathrm{sh}} = P_{\mathrm{net}} + \Delta P \tag{5}$$

where ΔP denotes the overall loss, for example by mechanical losses in bearings and seals, dissipation in boundary layers and mixing areas, disk friction at the impeller external surfaces, and leakage flows through the wear ring. The shaft power is related to the shaft torque M_{sh} and the angular velocity Ω by

$$P_{\mathrm{sh}} = \Omega M_{\mathrm{sh}} \tag{6}$$

while the net power relates to the pump's head H as

$$P_{\mathrm{net}} = \rho g Q H \tag{7}$$

with ρ the density, g the gravitational acceleration and Q the flow rate.

The overall efficiency η of the pump is simply defined as the ratio of net power and shaft power

$$\eta = \frac{P_{\mathrm{net}}}{P_{\mathrm{sh}}} \tag{8}$$

The shaft power can be written as

$$P_{\mathrm{sh}} = P_{\mathrm{fluid}} + \Delta P_{df} + \Delta P_{\mathrm{mech}} \tag{9}$$

with P_{fluid} the power imparted by the impeller to the fluid by pressure and shear forces, ΔP_{df} the power loss due to shear stress at the impeller external surfaces (disk friction) and ΔP_{mech} the power loss due to friction in bearings and seals.

The power P_{fluid} transferred to the internal fluid relates to the inviscid head H_{inv} as

$$P_{\mathrm{fluid}} = \rho g (Q + Q_{\mathrm{leak}}) H_{\mathrm{inv}}. \tag{10}$$

Note that the larger flow rate through the impeller as a result of leakage flow Q_{leak} has been taken into account. The actual head delivered by the impeller is lower by $\Delta H_{\mathrm{hydr},i}$ as a result of hydraulic losses in the impeller

$$H_i = H_{\mathrm{inv}} - \Delta H_{\mathrm{hydr},i} \tag{11}$$

in which H_i is the head measured between stations located just up- and downstream of the impeller. P_{fluid} can now be written as

$$P_{\mathrm{fluid}} = \rho g Q H_i + \Delta P_{\mathrm{hydr},i} + \Delta P_{\mathrm{leak}} \tag{12}$$

in which the hydraulic power loss in the impeller is given by

$$\Delta P_{\mathrm{hydr},i} = \rho g (Q + Q_{\mathrm{leak}}) \Delta H_{\mathrm{hydr},i} \tag{13}$$

and the leakage loss by

$$\begin{aligned}\Delta P_{\mathrm{leak}} &= \rho g Q_{\mathrm{leak}} H_i \\ &= \rho g Q_{\mathrm{leak}} (H_{\mathrm{inv}} - \dot{\Delta} H_{\mathrm{hydr}})\end{aligned} \tag{14}$$

On passing through the volute of the pump the head H_i is further reduced by hydraulic losses in the volute to its final value H

$$H = H_i - \Delta H_{\mathrm{hydr},v} \tag{15}$$

with $\Delta H_{\mathrm{hydr},v}$ the head loss in the volute.
Combining Eqs. (7), (12), and (15) gives

$$P_{\mathrm{fluid}} = P_{\mathrm{net}} + \Delta P_{\mathrm{hydr},i} + \Delta P_{\mathrm{hydr},v} + \Delta P_{\mathrm{leak}} \tag{16}$$

where the power loss in the volute is given by

$$\Delta P_{\text{hydr},v} = \rho g Q \Delta H_{\text{hydr},v} \tag{17}$$

Equations (5), (9), and (16) give the overall power loss ΔP in its components

$$\Delta P = \Delta P_{\text{hydr},i} + \Delta P_{\text{hydr},v} + \Delta P_{\text{leak}} + \Delta P_{df} + \Delta P_{\text{mech}} \tag{18}$$

2.4 Computation of P_{fluid}. Conservation of angular momentum in integral form states that

$$\Sigma M_A = \frac{\partial}{\partial t} \int_V \rho (r \times v) dV + \int_A \rho (r \times v)(v.n) dA \tag{19}$$

where V is a control volume, A its boundary, n the outward unit normal vector, v the absolute velocity vector, and r the position vector. The left-hand side of Eq. (19) denotes the sum of all moments acting at the boundary of the control volume. The throughflow areas A_1 and A_2 immediately up- and downstream of the impeller can be taken as the boundaries of the control volume V. If the shear forces at boundaries A_1 and A_2 are neglected, the sum of all moments M_A equals M_{fluid}, which is the moment exerted by the impeller on the internal fluid by both shear and pressure forces and relates to P_{fluid} as

$$P_{\text{fluid}} = \Omega M_{\text{fluid}} \tag{20}$$

with Ω the angular velocity. Equation (19) can now be written as

$$M_{\text{fluid}} = \rho \int_{A_1 + A_2} r v_\theta (v.n) dA \tag{21}$$

As the instantaneous flow field is different from one impeller blade channel to the other, as well as dependent on impeller position with respect to the volute, the integration in Eq. (21) should include the entire impeller and its value should be averaged in time. In this expression the time-derivative of Eq. (19) is omitted, since it does not contribute to the time-average of a periodic quantity.

Even if the flow in the suction pipe is free of angular momentum, the integral over the inlet surface A_1 is in general nonzero. The reason is that the returning leakage flow will carry angular momentum. From conservation of angular momentum it follows that the contribution to the integral over A_1 is equal to the angular momentum M_{leak} of the leakage flow upon re-entrance, which is

$$M_{\text{leak}} = \rho r_s v_{\theta,\text{leak}} Q_{\text{leak}} \tag{22}$$

with r_s the radius of the seal or wear ring exit and $v_{\theta,\text{leak}}$ the averaged circumferential velocity of the leakage flow.

Since in practice the slip for prerotation is very small (Visser et al. [25]) the integral over the outlet surface A_2 in Eq. (21) may be determined without leakage flow prerotation.

2.5 Hydraulic Power Losses. Irreversible pressure losses in the internal flow itself are called hydraulic losses. The most important sources of hydraulic loss a re energy dissipation in boundary layers along walls, losses through mixing processes, and losses due to sudden expansions and contractions in through-flow area. The various losses may be added to obtain the total hydraulic loss, since the influence of viscosity is relatively small and confined to local areas.

Dissipation Loss in Boundary Layers. The dissipation loss in attached boundary layers can be quantified using a fairly simple method based on the dissipation coefficient c_D (Schlichting [24]). The dissipation loss can be written as

$$\Delta P_{\text{diss}} = \frac{1}{2} \rho \int c_D w^3 dA \tag{23}$$

where A denotes the wall surface and w is the velocity of an inviscid flow tangential to the wall. According to Denton [26] the dissipation coefficient for turbulent boundary layers is relatively insensitive to the detailed state of the boundary layer (accelerating or decelerating). Denton suggests an average value of 0.0038 for turbulent boundary layers with Re_{δ_2} (Reynolds number based on boundary layer momentum thickness δ_2) of order 1000, but it should be stressed that actual values vary between 0.002 for accelerating flows and 0.005 for flows encountering an adverse pressure gradient. The loss in a laminar boundary layer is also not very sensitive to its state but it does very much depend on its thickness (Truckenbrodt [27]). As a first estimate boundary layers, both in the impeller and in the volute, are assumed to be turbulent, with $c_D = 0.0038$.

Mixing Losses. Two types of mixing are important in pumps:
-mixing of the returning leakage flow with the undisturbed entrance flow, and
-mixing of shed vortices from the trailing edges of impeller blades with the ambient flow.
The power loss $\Delta P_{\text{mix,leak}}$ associated with the first type of mixing can be quantified as follows. Assume that the flow in the suction pipe upstream of the mixing area is uniform and free of rotation. Assume further that the leakage flow enters the main flow at right angles and that downstream of the mixing area the axial flow component is uniform while the circumferential velocity component has a profile which can be written as

$$v_\theta = \alpha r^n \tag{24}$$

with α and n constant and positive. Applying conservation of angular momentum (neglecting wall shear) gives the following expression for the circumferential velocity component v_θ after mixing

$$\alpha = \frac{n+3}{2} v_{\theta,\text{leak}} \frac{\varepsilon}{1+\varepsilon} \left(\frac{1}{r_s} \right)^n \tag{25}$$

with $v_{\theta,\text{leak}}$ the circumferential velocity component of the leakage flow, r_s the radius of the seal or wear ring exit, and ε defined as

$$\varepsilon = \frac{Q_{\text{leak}}}{Q} \tag{26}$$

Given that the throughflow areas up- and downstream are equal, conservation of axial momentum (again neglecting wall shear stresses) states that

$$p + \rho v_a^2 = \text{const} \tag{27}$$

with p the static pressure and v_a the axial velocity component. Using expressions (24), (25), and (27), the change in total pressure p_0 of the main flow over the mixing area can be written as (analogous to Denton [26])

$$\Delta p_0 = \frac{1}{2} \rho v_a^2 \frac{(2\varepsilon + \varepsilon^2)}{(1+\varepsilon)^2} - \frac{(n+3)^2}{8} \rho v_{\theta,\text{leak}}^2 \left(\frac{\varepsilon}{1+\varepsilon} \right)^2 \left(\frac{r}{r_s} \right)^{2n} \tag{28}$$

with v_a the axial velocity component after mixing. The first term on the right-hand side is in excellent agreement with values obtained by experiments for pipe flow T-junctions with negligible branch area and zero circumferential velocity (e.g., Miller [28]). The power loss through mixing, which is defined as the product of total flow rate $Q + Q_{\text{leak}}$ and the mass averaged total pressure loss, can now be expressed as

$$\Delta P_{\text{mix,leak}} = \frac{1}{2} \rho v_a^2 Q_{\text{leak}} \left(\frac{2+\varepsilon}{1+\varepsilon} \right) - \frac{(n+3)^2}{8(n+1)} \rho v_{\theta,\text{leak}}^2 Q_{\text{leak}} \left(\frac{\varepsilon}{1+\varepsilon} \right) \tag{29}$$

The value of $(n+3)^2/8(n+1)$ is taken as unity, which is approximately true for moderate values of n (between 0 and 4). The way to compute $v_{\theta,\text{leak}}$ is described in Section 2.6.

The second type of mixing loss $\Delta P_{\text{mix,wake}}$ occurs in wakes behind blunt trailing edges of impeller (or stator) blades. According to Denton [26] this loss can be quantified by

$$\Delta P_{\text{mix,wake}} = \frac{1}{2}\rho w_{\text{ref}}^2 (Q + Q_{\text{leak}}) \cdot \left[-\frac{C_{pb} b}{W} + \frac{2\delta_2}{W} + \left(\frac{\delta_1 + b}{W} \right)^2 \right] \tag{30}$$

with b the blade thickness and W the blade tangential pitch, both at the trailing edge. The sum of the boundary layer displacement thicknesses at pressure and suction side, at a station near the trailing edge, is given by δ_1. The same applies to δ_2, the sum of the momentum thicknesses. The base pressure coefficient C_{pb} is defined by

$$C_{pb} = 2(p_b - p_{\text{ref}})/(\rho w_{\text{ref}}^2) \tag{31}$$

with p_b the static pressure just behind the trailing edge and p_{ref} and w_{ref} the pressure and velocity at a reference position just before the trailing edge. In general the value of C_{pb} will be negative, with typical values close to -0.15. The boundary layer displacement and momentum thickness at the blade trailing edge are computed by the one-dimensional integral boundary layer method (Section 2.2).

Expansion and Contraction Losses. Abrupt changes in throughflow area result in so-called expansion and contraction losses. For turbulent flow, the loss of total pressure Δp_0 as a result of a sudden expansion can be derived from conservation of momentum as

$$\Delta p_{0,\text{exp}} = \left(\frac{1}{\beta} - 1 \right)^2 \frac{1}{2}\rho v^2 \tag{32}$$

while the equivalent for a sudden contraction is found from experiments to be

$$\Delta p_{0,\text{contr}} = 0.45(1 - \beta)\frac{1}{2}\rho v^2 \tag{33}$$

(see e.g., Bird et al. [29]). In both expressions β denotes the ratio of the smaller to the larger cross sectional area, and v is the velocity downstream of the expansion or contraction. The power loss is subsequently obtained by multiplying the loss of total pressure by the flow rate Q.

2.6 Leakage Loss. In pumps equipped with shrouded impellers, volumetric loss results from leakage flow through the cavity between the shroud of the impeller and the pump housing. It flows from the pressurized impeller outlet region back to the impeller inlet. Wear rings are used to minimize this leakage flow. The circumferential velocity of the leakage flow is subject to two driving mechanisms. The first is the inviscid effect of a larger circumferential velocity at smaller radii, like in a free vortex. The second effect results from the wall shear stress. It tends to force the circumferential velocity toward half the velocity of the rotating wall. When modeling the leakage flow, the cavity region cannot be neglected as it influences the circumferential velocity distribution and is responsible for a considerable pressure drop. For this pump the height of the leakage area is sufficiently small for the flow to be modeled as a thin lubricant film (Hirs [30]). A method similar to that of Childs [31] was implemented to solve the equations of motion for the bulk-flow through arbitrary combinations of cavities and wear rings. It uses Moody's [32] expressions for the shear stress components (see also Nelson and Nguyen [33]) and it accounts for the loss (or gain) in static pressure at the entrance, the exit, and at any intermediate abrupt expansion or contraction. On passing these changes in through-flow area, the circumferential velocity component v_θ may be taken constant (Denton [26]). Results for annular seals are in agreement with the empirical model of Yamada [34].

Input values for the leakage flow model are the static pressure difference between entrance and exit of the cavity and the circumferential velocity near the cavity entrance, all circumferentially averaged. These input values are supplied by the unsteady potential flow computations without leakage. Once the leakage flow rate Q_{leak} and the circumferential velocity component upon reentrance, $v_{\theta,\text{leak}}$, are obtained, the leakage loss can be computed. It consists of four contributions, two of which are inviscid effects: the larger flow rate through the impeller and the angular momentum of the returning leakage flow (Eq. (22)), both causing a decrease in head. The remaining two contributions are viscous losses: the larger hydraulic losses in the impeller caused by the larger flow rate, and the mixing loss $\Delta P_{\text{mix,leak}}$ (Eq. (29)).

As a byproduct one obtains the values of the shear stress τ at the external surface of the impeller shroud. It is used to compute the disc friction loss (Eq. (35)).

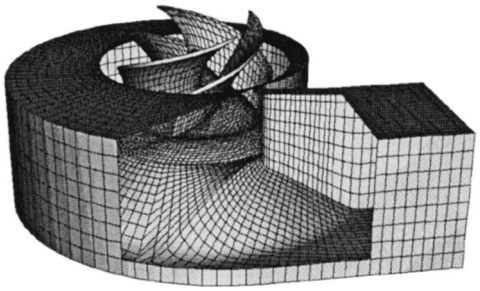

Fig. 1 Surface mesh for the test mixed-flow pump. The shroud of the impeller and part of the volute wall is removed to offer a better view.

2.7 Disk-Friction Loss. The power loss ΔP_{df} originates from the frictional torque M_{df} exerted by the fluid on the external surfaces of the impeller

$$\Delta P_{df} = \Omega M_{df} \tag{34}$$

where

$$M_{df} = \int_A \tau r dA \tag{35}$$

with τ the wall shear stress in circumferential direction and r the radius. If the shear stress values are not given by a method like the one presented in Section 2.6 for the leakage flow area, and throughflow is negligible, empirical values obtained by Daily and Nece [35] can be used instead.

3 Test Setup and Pump Specifications

The pump is a scale model (1:3–1:7) of a single suction industrial mixed-flow pump, used for cooling water supply in power stations. Experiments are performed at the test facility of Flowserve in Hengelo (The Netherlands). The model (Fig. 1) contains a shrouded mixed-flow impeller, with four blades which are forward leaned. It has a specific speed n_ω of 1.6, where specific speed is defined as

$$n_\omega = \Omega Q_{\text{BEP}}^{1/2}/(gH_{\text{BEP}})^{3/4} \tag{36}$$

with $Q_{\text{BEP}} = 0.24\ \text{m}^3/\text{s}$ and $H_{\text{BEP}} = 10.9\ \text{m}$ the flow rate and head at best efficiency point (BEP) for a shaft speed of 990 rpm. The outer diameter D of the scale model is 0.35 m. Thus, BEP operating conditions are at flow coefficient $\Phi = Q/(\Omega R^3) = 0.448$, head coefficient $\Psi = gH/(\Omega R)^2 = 0.328$, and Reynolds number $\text{Re} = \Omega D^2/\nu = 1.1 \cdot 10^7$, with R the radius of the model impeller and ν the kinematic viscosity of water at 15°C.

The volute is unvaned with a trapezoidal cross-section and is designed according to the method of constant mean velocity (Stepanoff [36]). The model pump is mounted in a closed circuit.

Delivered head is derived from averaged static pressure measurements at the inlet and outlet of the pump and the assumption of uniform velocity at inflow and outflow stations. The measured shaft power is corrected for losses in bearings and seals by calibrations. Uncertainties are ± 1 percent for head, flow rate, and

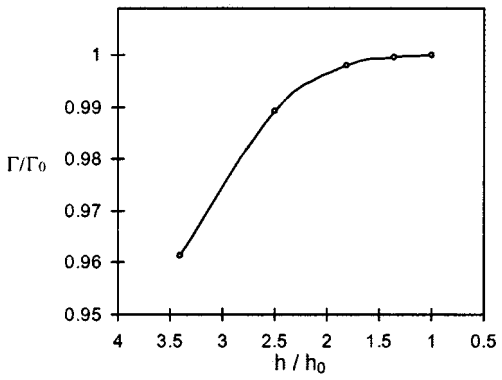

Fig. 2 Average blade circulation Γ as a function of mesh size h. Circulation at finest mesh size h_0 is Γ_0.

shaft torque and ±1 rpm for shaft speed, according to DIN-1944 class 1 and ISO-5198 class A. The attained accuracy for efficiency is ±3 percent. Head and efficiency values are measured for flow rates ranging from 50 percent–150 percent BEP flow rate.

4 Computational Aspects

In Fig. 1 the computational mesh is shown. The domain is divided into 8 blocks in the rotor and 8 blocks in the volute, with a total number of 81,000 nodes and 380,000 tetrahedral elements. Each full shaft revolution is divided into 120 time steps. Depending on flow rate, it takes 5–6 full shaft revolutions before a periodic solution is obtained. Computing time per flow rate is 20 hours on a conventional PC with a 200 MHz Pentium processor. Maximum internal memory required is 80 MBytes.

To assess the dependency on mesh size, computations on a number of meshes of different mesh refinement are performed. In Fig. 2, the results for the average value of the blade circulation Γ is given as a function of mesh size *h*. It can be concluded that the error in blade circulation for the finest mesh is well below 1 percent. This mesh is used for all subsequent computations.

5 Results

In this section, computed values for head, efficiency, and shaft power are compared with values obtained from experiments. In Fig. 3 (left) the result for the computed inviscid head coefficient is given. The inviscid result is not yet corrected for leakage flow rate. It clearly shows that inviscid computations overpredict the pump's head considerably. In the following, the losses in the impeller and volute will be quantified.

5.1 Leakage Flow. The model of Section 2.6 is used to compute the leakage flow; boundary conditions are taken uniform by a circumferential and time averaging. The friction factors of Moody are used with a surface roughness of 7 μm for the cavity and 2 μm for the wear ring. The ratios Q_{leak}/Q are found to be quite high, varying from 1.7 percent at high flow rate ($Q/Q_{\text{BEP}}=1.4$) up to 6.4 percent at the lowest flow rate considered ($Q/Q_{\text{BEP}}=0.6$). This is a result of the rather large wear ring clearance of 0.9 mm (in radius) in the test set-up. The power loss by leakage is given in Fig. 4.

For mixed-flow impellers the ratio of outer to inner radius of the impeller shroud is limited. As a consequence the wall shear forces are dominant over the ''free-vortex mechanism.'' This leads to a circumferential velocity which tends to become equal to half the rotational speed of the impeller upon leaving the wear ring. Only for very low flow rates (i.e., large leakage flow rates) circumferential velocities are computed with somewhat higher values.

5.2 Euler Head. In Fig. 3 the inviscid head before and after correction for leakage flow is shown. The latter corresponds to H_{inv} in Eq. (10). The head reduction is caused by the higher flow rate through the impeller (QH-curve shifts to the left), and by the angular momentum of the leakage flow (Eq. (22)). The relative contribution of the former ranges from 30 percent at the lowest flow rate, up to 50 percent at the highest flow rate considered. The head is calculated at individual time steps and subsequently averaged.

5.3 Hydraulic Losses. In Fig. 4 several types of hydraulic losses are plotted against flow rate. The models as presented in Section 2.5 are used for this purpose. Obviously, boundary layer dissipation in the impeller region of the pump is the most important source of hydraulic loss for this mixed-flow pump, followed by boundary layer dissipation loss in the volute. The energy dissipation coefficient c_D of Eq. (23) is taken 0.0038, a constant value for all surfaces and for all flow rates. Although losses along the impeller blades will possibly be much larger at 60 percent Q_{BEP} due to boundary layer separation, this is believed to be an acceptable first estimate.

The flow experiences a sudden expansion in radial direction as it leaves the impeller and enters the (much wider) volute. A fraction of the kinetic energy of the radial velocity is dissipated in the process, according to Eq. (32).

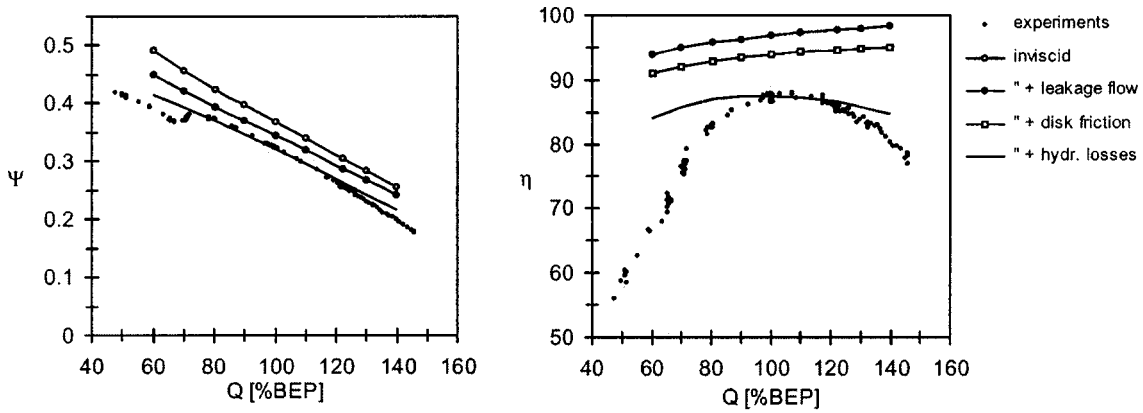

Fig. 3 Head coefficient Ψ and efficiency η, as a function of flow rate *Q*. The left figure shows the influence of leakage flow and hydraulic losses on head coefficient. The right figure gives the effects of leakage flow, hydraulic losses and disc friction loss on efficiency.

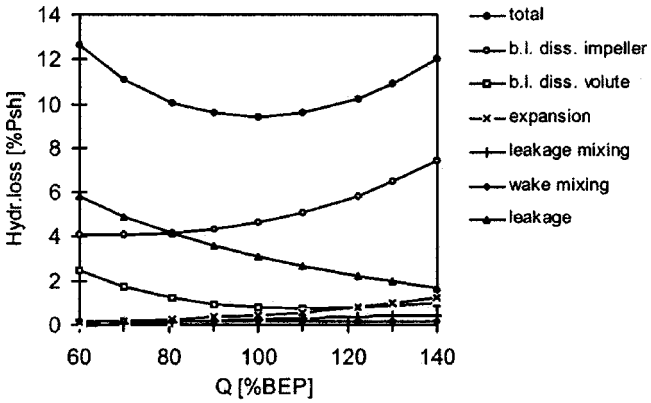

Fig. 4 Various types of hydraulic losses and leakage loss plotted against flow rate Q. Loss is expressed in percentage of calculated shaft power P_{sh}

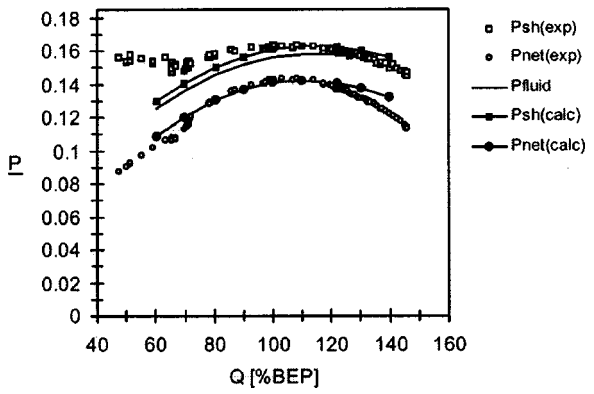

Fig. 5 Experimental and computed values for the power coefficient $\underline{P}$, defined as $P/(\rho\Omega^3 R^5)$

Both boundary layer dissipation loss in the impeller and expansion loss are based on the larger flow rate due to leakage.

The total internal loss is obtained by adding the leakage loss to the sum of all hydraulic losses. It is a convex function of flow rate, with a minimum at Q_{BEP}.

5.4 Boundary Layers in the Impeller. The method as described in Section 2.2 is used to compute the boundary layers at three streamlines along the pressure and suction sides of the blades; starting at the leading edge near the hub, at half span, and near the shroud of the impeller. Time-averaged velocities are used. This is done for several flow rates in the range $0.4 \leqslant Q/Q_{BEP} \leqslant 1.4$. Although the actual level of turbulence intensity in the set-up is unknown, a free-stream turbulence intensity of 5 percent is assumed. For most of the streamlines and flow rates considered, transition is predicted shortly after the leading edge (within 5 percent of the blade length) and no separation, either laminar or turbulent, is obtained. There are however some exceptions. At the pressure side, near the hub, reverse flow exists for flow rates $Q/Q_{BEP} \leqslant 1.2$. The area over which the reverse flow extends changes with flow rate: from covering the whole blade length for $Q/Q_{BEP}=0.4$ down to an area between 25 percent and 50 percent of the blade length for $Q/Q_{BEP}=1.2$. In this area, the boundary layer appears to be separated, although in fact it is a potential flow effect. After this region the flow will attach to the wall and the strong acceleration over the second half of the pressure side (near the hub) will lead to a laminar state of the boundary layer. The most important phenomenon which is predicted is laminar separation at the suction side between mid-span and the hub, immediately after the leading edge, for flow rates $Q/Q_{BEP} \leqslant 0.6$. Whether this leads to separation bubbles of a finite length or to massive separation (stall) remains unknown. Even if the separated flow manages to reattach beyond this point, high losses will inevitably be the result.

In general, the effect of a high turbulence level is that transition tends to precede separation of the laminar boundary layer (see also Murawaski and Vafai [37]). At lower turbulence intensity (Tu$\sim$1percent) laminar separation at the pressure side occurs shortly after the leading edge near the hub for flow rates $Q/Q_{BEP} \geqslant 1.2$ and at mid-span for lower flows. For extremely low turbulence intensity (Tu$\sim$0.03 percent) and flow rates exceeding Q_{BEP}, the boundary layer at the suction side even remains laminar over the first half until laminar separation occurs at the second half.

For backward curved blades, streamline curvature and rotation generally have counteracting effects on the stability of the boundary layer on both the pressure and the suction side. For this particular case, however, it prevents the turbulent boundary layer at the pressure side from separating near the shroud for low flow rate ($Q/Q_{BEP}=0.4$) and near the hub for large flow rate ($Q/Q_{BEP}=1.4$). The combined effect of curvature and rotation on boundary layer displacement thickness and momentum thickness at the trailing edge is, however, very small.

5.5 Disk Friction Losses. The empirical expressions of Daily and Nece [35] for disk friction with zero leakage flow are used for the cavity between the lower hub surface and the pump casing. For the leakage area between the shroud and the pump casing the more advanced leakage flow method (discussed in Section 2.6) is used. The disk friction losses vary with the main flow rate due to a varying leakage flow rate and a change in circumferential velocity of the incoming fluid. Typical for impellers with backward curved blades, the circumferential velocity at the cavity entrance is below half the value of the rotor tip speed. As a consequence, disk friction is larger than predicted by the model of Daily and Nece. The power loss through disk friction (computed using the leakage flow model of Section 2.6) increases with flow rate; over the range considered it varied with more than 30 percent. Yet, the fraction of shaft power lost by friction at the impeller outer walls is roughly constant, at a value of 3 percent.

5.6 Shaft Power, Head, and Efficiency. In Fig. 3 the computed head and efficiency are compared with experiments. The effects of leakage, hydraulic losses and disk friction are indicated. The computed head characteristic appears to be in very good agreement with measurements, although deviations tend to increase at the lowest and highest flow rates considered. As was discussed in Section 5.4, the large deviation at flow rates below $Q/Q_{BEP}=0.8$ might be related to the predicted laminar separation near the leading edge, at the suction side of the blades. The comparison between computed and measured values for the efficiency shows a larger deviation at off-design conditions. Still, at flow rates between 85 percent–135 percent Q_{BEP} computed values are within the experimental uncertainty of ± 3 percent. The question arises whether deviations at off-design conditions should be attributed to an incorrect computation of viscous losses or to the inviscid computations to begin with, or possibly to both.

For this question to be answered, a comparison of in- and output power coefficients is made in Fig. 5. Experimental values for the shaft power $P_{sh,exp}$, corrected for mechanical losses, and the net power $P_{net,exp}$, based on delivered head, are plotted. Computed values for P_{fluid}, the power which is transferred by the impeller to the internal fluid, and the shaft power $P_{sh,calc}$ are given as well, the difference being the disk friction losses at the external surfaces of the impeller. The net power $P_{net,calc}$ is computed by correcting P_{fluid} for leakage flow and hydraulic losses (Eq. (16)). It appears that for flow rates below best efficiency point the shaft power is underestimated considerably. A likely explanation for this power loss is inlet recirculation. The general view is that inlet recirculation tends to also increase the head due to a deflection of streamlines in the impeller inlet towards smaller radii. It was also

Table 1 Comparison of relative power losses (in percentage shaft power) at BEP flow rate for a mixed-flow pump with specific speed $n_\omega = 1.6$

Mixed-flow pump	Computed	Stepanoff
Impeller loss	4.8	2.3
Volute loss	1.2	3.5
Leakage loss	3.4	1.0
Disc friction loss	3.0	2.2

noted in the literature that this effect is much smaller in cases where inlet guidevanes or inlet swirl brakes are absent. In these cases the effect is (at least partly) counterbalanced by the higher inlet swirl. Our computations show that the head value is even overpredicted by an inviscid-based method. It supports the view of Kurokawa et al. [38] who argue that the dip in the QH-curve, as seen in mixed-flow and axial flow pumps, should be considered as a sudden drop in head below its theoretical value due to the swirl of reverse flow at the impeller inlet. At flow rates larger than Q_{BEP} the shaft power is predicted very well. Hydraulic loss is in the correct range, although at highest flow rate, it appears to be somewhat underestimated.

5.7 Evaluation of Loss Models. For the mixed-flow pump operating at best efficiency point, the power loss resulting from hydraulic losses, leakage flow and disk friction can be compared with correlations given by e.g., Stepanoff [36] for a pump with a similar specific speed. Results are depicted in Table 1. Hydraulic losses are divided into losses in the impeller and losses in the volute. Leakage loss includes the effect of the higher flow rate through the impeller, as well as the inlet swirl velocity and the mixing loss at the impeller entrance. Wake mixing loss is attributed to impeller hydraulic losses, expansion losses to volute hydraulic losses. Several conclusions can be drawn referring to the correlations of Stepanoff. It appears that the total hydraulic losses agree well, although the distribution over impeller and volute is quite different. It should be noted that Stepanoff (quite arbitrarily) assumed a constant impeller hydraulic loss of 2.25 percent (for all specific speeds) and attributed the remaining loss to the volute. The wear ring clearance is quite large, resulting in a relatively high loss.

The power loss as a function of flow rate can be found in Fig. 4. In accordance with e.g., Stepanoff, leakage loss decreases with flow rate, and hydraulic losses show a parabolic-like dependence on flow rate with a minimum value near best efficiency point. Stepanoff states that disk friction decreases with flow rate. Computations, however, show values which tend to increase with flow rate. The reason is that a lower capacity leads to a larger leakage flow rate and a higher circumferential velocity at the impeller discharge. Both effects result in a larger overall circumferential velocity within the clearance region, which in turn leads to a lower disk friction at the impeller outer surface. Reference is made to the work of Schubert [39], who found from experiments that shear forces decrease with leakage flow rate.

6 Boundary Layer Displacement Effect

In the impeller, the computed displacement of the flow due to the presence of boundary layers is generally very small; typically 0.7 mm at the suction side and 0.2 mm at the pressure side at BEP flow rate. It leads to a total area blockage at the impeller exit of roughly 1.5 percent. The influence of this on produced head and losses is not considered. For the volute, however, a boundary layer analysis shows that the displacement thickness of boundary layers can become quite substantial. To study the effect of the displacement thickness of boundary layers can become quite substantial. To study the effect of the displacement on quantities like head and efficiency, an iterative procedure of (1) computing the inviscid main flow, (2) a boundary layer analysis at the volute wall, and (3) the adjustment of the volute wall according to the displacement thickness is performed until convergence is obtained. In this analysis, a streamline at the outer wall of the volute (at half-height) is taken as representative for the flow in the volute. In order to estimate the displacement thickness at the upper and lower volute wall, a rather crude assumption of a free vortex velocity distribution is made. The implication on the geometry for three flow rates is depicted in Fig. 6. Total area blockage in the throat of the volute is 2 percent at 120 percent Q_{BEP}, 6 percent at Q_{BEP}, and even 12 percent at 80 percent Q_{BEP}. The influence of these rather high displacements on the computed head and efficiency is however very small; 0.06 percent at 120 percent Q_{BEP} up to 0.5 percent at 80 percent Q_{BEP} for both head and efficiency. The effect can hardly be distinguished in Figs. 3 and 5.

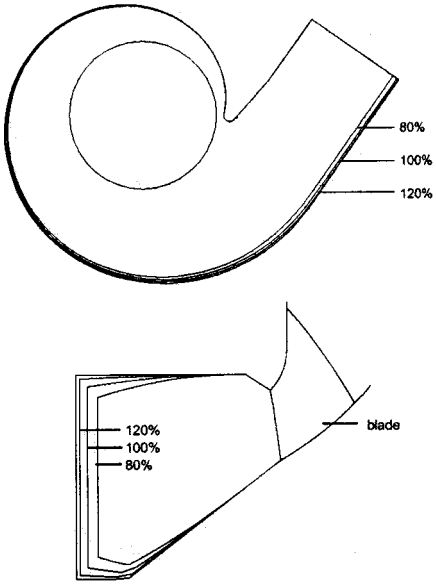

Fig. 6 Two-dimensional views of volute shape after boundary layer displacement correction, for three different flow rates (showing percentages of nominal flow rate)

7 Unsteady versus Quasi-Steady Computations

In most present-day flow solvers so-called ''complete pump computations'' are actually quasi-steady; the flow in one impeller channel and the flow in the volute are computed by means of an

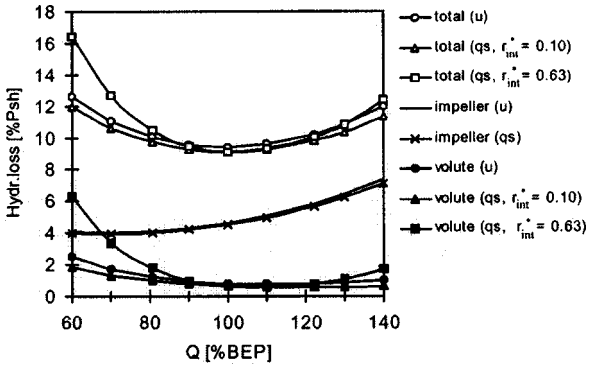

Fig. 7 Boundary layer dissipation loss in impeller and volute and total loss for unsteady (u) and quasi-steady (qs) computations

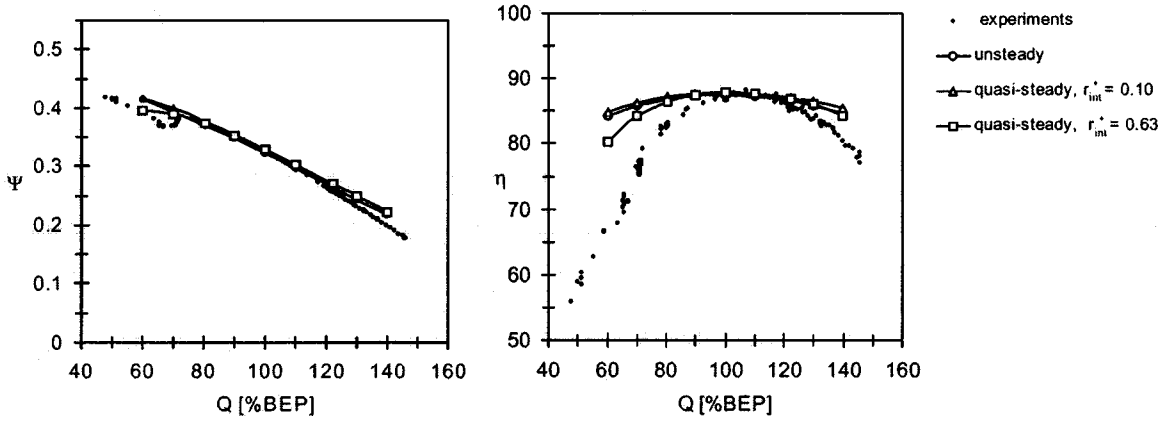

Fig. 8 Head coefficient Ψ and efficiency η, as a function of flow rate Q; for unsteady and quasi-steady computations

averaging procedure at the interface between both parts. The flow in the impeller is assumed to be symmetric; i.e., identical for all impeller channels. Furthermore, the boundary conditions at the interface are taken axially symmetric. In such methods, truly unsteady phenomena, like asymmetric flow in the impeller, and thus asymmetric inflow into the volute, or backflow from the volute into impeller channels near the tongue, are not captured.

To get an indication of the effect of an approach like this, a similar procedure is carried out with the current method; both the flow in one channel of a free impeller and the flow in the isolated volute are computed for each flow rate, where conditions at the location of the interface are averaged and serve as boundary condition for the volute computation. It appears that the result depends strongly on the location of the interface between impeller and volute. Two cases are considered; $r^*_{\text{int}}=0.10$ and $r^*_{\text{int}}=0.63$, where r^*_{int} denotes the normalized radial location of the interface defined as

$$r^*_{\text{int}}=\frac{r_{\text{int}}-r_{2i}}{r_{\text{tongue}}-r_{2i}} \tag{37}$$

with r_{int} the radius of the interface, r_{2i} the outer radius of the impeller, and r_{tongue} the radius of the tongue. The inviscid head, as computed for a free impeller, is slightly higher than that obtained by an unsteady computation. The largest difference, however, is the boundary layer dissipation loss in the volute. In Fig. 7 it is shown that this loss depends strongly on r^*_{int} at off-design conditions. The effect on head and efficiency curves is shown in Fig. 8. Although the result of the quasi-steady computation with $r^*_{\text{int}}=0.63$ appears to be better, it is actually incorrect. The influence of r^*_{int} on results can be explained as follows. Losses in the volute at off-design conditions are dominated by flow distortions near the tongue due to a shift of the stagnation point at the tongue into the volute scroll (for high flow rate) or into the discharge pipe (for low flow rate). In reality, the inflow or backflow spreads over the region between the tongue and the impeller outlet. It sometimes even reaches into nearby impeller channels (backflow). In the quasi-steady computations, however, since no backflow across the interface is allowed, the fluid is forced to flow through the gap between the tongue and the interface, leading to larger computed boundary layer dissipation losses as the gap size decreases (r^*_{int} increases).

8 Conclusions

The hydraulic performance of a mixed-flow pump is analyzed using a three-dimensional potential flow model to compute the unsteady flow through the entire pump configuration and a subsequent analysis of losses using several additional models. For flow rates in the range 70 percent–130 percent Q_{BEP}, the computed head characteristic is in good agreement with measurements. Leakage loss is found to be considerable, due to a rather large wear ring clearance. Shaft power is predicted well at design flow rate and higher. For low flow rate, the shaft power is underpredicted, possibly as a result of inlet recirculation. Hydraulic losses at flow rates exceeding 120 percent Q_{BEP} are probably underestimated. Efficiency is predicted correctly between 85 percent and 130 percent Q_{BEP}. Outside of this range, large deviations from measurements are observed, due to the underprediction of hydraulic losses (at high flow rates) and shaft power (at low flow rates).

Although the computed overall hydraulic loss at Q_{BEP} is in agreement with correlations given by Stepanoff, the distribution over impeller and volute is quite different for this mixed-flow pump. Stepanoff estimated that 60 percent of the hydraulic losses occur in the volute, whereas this investigation indicates that only 20 percent should be attributed to the volute.

According to computations, boundary layer displacement in the volute, which is quite substantial at low flow rate, has a negligible effect on global characteristics.

Computations show that a truly unsteady analysis of the complete impeller and volute is necessary to compute even global performance characteristics; an analysis of an isolated impeller channel and volute with an averaging procedure at the interface is inadequate.

Acknowledgment

The authors like to thank Flowserve Hengelo (P.O. Box 55, 7550 AB Hengelo, The Netherlands), and ing. J. G. H. op de Woerd in particular, for providing the data on the geometry and the permission to perform measurements on the Flowserve mixed-flow pump.

Nomenclature

A = surface area [m^2]
D = diameter at shroud [m]
g = gravitational acceleration [m/s^2]
H = head [m]
M = torque [Nm]
n_ω = $\Omega Q^{1/2}/(gH)^{3/4}$, specific speed [−]
p = static pressure [Pa]
p_0 = total pressure [Pa]
P = power [Nm/s]
Q = flow rate [m^3/s]
r = radius [m]
R = radius; radius of streamline curvature [m]
Tu = turbulence intensity [percent]
v = absolute velocity [m/s]

w = relative velocity [m/s]
δ_1 = displacement thickness [m]
δ_2 = momentum thickness [m]
η = efficiency [percent]
Φ = $Q/(\Omega R^3)$, flow coefficient [−]
Ψ = $gH/(\Omega R)^2$, head coefficient [−]
Ω = angular velocity [rad/s]

Subscripts

BEP = Best efficiency point
e = outside boundary layer
df = disk friction
i = impeller
inv = inviscid
s = seal
sh = shaft
t = transition
v = volute
θ = circumferential

References

[1] Gülich, J. F., 1999, *Kreiselpumpen-Ein Handbuch für Entwicklung, Anlageplanung und Betrieb*, Springer, Berlin.
[2] Muggli, F. A., Eisele, K., Casey, M. V., Gülich, J., and Schachenmann, A., 1997, ''Flow analysis in a pump diffuser. Part 2: Validation and limitations of CFD for diffuser flows,'' ASME J. Fluids Eng., **119**, pp. 978–984.
[3] Rodi, W., 1986, ''Turbulence modelling for incompressible flows,'' Phys. Chem. Hydrodyn., **7**, pp. 297–324.
[4] Speziale, C. G., 1989, ''Turbulence modelling in noninertial frames of reference,'' Theor. Comput. Fluid Dyn., **1**, pp. 3–19.
[5] Lakshminarayana, B., 1991, ''An assessment of computational fluid dynamic techniques in the analysis of turbomachinery,'' ASME J. Fluids Eng., **113**, pp. 315–352.
[6] Schilling, R., 1994, ''A critical review of numerical models predicting the flow through hydraulic machinery bladings,'' 17th IAHR Symp., Beijing, GL2.
[7] Gülich, J. F., and Egger, R., 1992, ''Part load flow and hydraulic stability of centrifugal pumps,'' EPRI Report TR-100219, Mar.
[8] Gülich, J. F., Favre, J. N., and Denus, K., 1997, ''An assessment of pump impeller performance predictions by 3D-Navier Stokes calculations,'' ASME FED Summer Meeting, Vancouver, Canada.
[9] Daiguji, H., 1983, ''Numerical analysis of three-dimensional potential flow in axial flow turbomachines,'' Bull. JSME, **26**, pp. 763–769.
[10] Daiguji, H., 1983, ''Numerical analysis of three-dimensional potential flow in centrifugal turbomachines,'' Bull. JSME, **26**, pp. 1495–1501.
[11] Maiti, B., Seshadri, V., and Malhotra, R. C., 1989, ''Analysis of flow through centrifugal pump impellers by finite element method,'' Appl. Sci. Res., **46**, pp. 105–126.
[12] Chen, K. S., and Sue, M. C., 1993, ''Finite element analysis of steady three-dimensional potential flow in the blade passage of a centrifugal turbomachine,'' Comput. Struct., **46**, pp. 625–632.
[13] Badie, R., Jonker, J. B., and Braembussche, R. A. van den, 1994, ''Finite element calculations and experimental verification of unsteady potential flow in a centrifugal pump,'' Int. J. Numer. Methods Fluids, **19**, pp. 1083–1102.
[14] Esch, B. P. M. van, 1997, ''Simulation of three-dimensional unsteady flow in hydraulic pumps,'' Ph.D. dissertation, Department of Mechanical Engineering, University of Twente, Enschede, The Netherlands.
[15] Kruyt, N. P., Esch, B. P. M. van, and Jonker, J. B., 1999, ''A superelement-based method for computing unsteady three-dimensional potential flows in hydraulic turbomachines,'' Communications in Numerical Methods in Engineering, **15**, pp. 381–397.
[16] Zienkiewicz, O. C., and Taylor, R. L., 1989, *The finite element method*, McGraw-Hill, Maidenhead, UK.
[17] Zienkiewicz, O. C., and Zhu, J. Z., 1992, ''The superconvergent patch recovery and a posteriori error estimates Part I: the recovery technique,'' Int. J. Numer. Methods Eng., **33**, pp. 1331–1364.
[18] Thwaites, B., 1949, ''Approximate calculation of the laminar boundary layer,'' Aeronaut. Q., **1**, pp. 245–280.
[19] Green, J. E., Weeks, D. J., and Brooman, J. W. F., 1972, ''Prediction of turbulent boundary layers and wakes in compressible flow by a lag-entrainment method,'' RAE Technical Report 72231, pp. 49–53.
[20] Mayle, R. E., 1991, ''The role of laminar-turbulent transition in gas turbine engines,'' ASME J. Turbomach., **113**, pp. 509–537.
[21] Bradshaw, P., 1975, ''Complex turbulent flows,'' ASME J. Fluids Eng., **97**, pp. 146–154.
[22] Bradshaw, P., 1969, ''The analogy between streamline curvature and buoyancy in turbulent shear flow,'' J. Fluid Mech., **36**, pp. 177–191.
[23] Johnston, J. P., and Eide, S. A., 1976, ''Turbulent boundary layers on centrifugal compressor blades: Prediction of the effects of surface curvature and rotation,'' ASME J. Fluids Eng., **98**, Sept., pp. 374–381.
[24] Schlichting, H., 1979, *Boundary Layer Theory*, McGraw-Hill, NY.
[25] Visser, F. C., Brouwers, J. J. H., and Badie, R., 1994, ''Theoretical analysis of inertially irrotational and solenoidal flow in two-dimensional radial-flow pump and turbine impellers with equiangular blades,'' J. Fluid Mech., **269**, pp. 107–141.
[26] Denton, J. D., 1993, ''Loss mechanisms in turbomachines,'' ASME J. Turbomach., **115**, pp. 621–656.
[27] Truckenbrodt, E., 1952, ''A method of quadrature for the calculation of laminar and turbulent boundary layers in plane and rotational symmetric flow,'' NACA TM 1379.
[28] Miller, D. S., 1978, ''Internal flow systems,'' British Hydromechanics Research Association (BHRA) Fluid Engineering Series, Vol. 5.
[29] Bird, R. B., Steward, W. E., and Lightfoot, E. N., 1960, *Transport Phenomena*, Wiley, NY., pp. 217–220.
[30] Hirs, G. G., 1973, ''A bulk-flow theory for turbulence in lubricant films,'' ASME J. Lubr. Technol., **95**, Apr., pp. 137–146.
[31] Childs, D. W., 1989, ''Fluid-structure interaction forces at pump-impeller-shroud surfaces for rotor-dynamic calculations,'' ASME J. Vibration, Acoustics, Stress, and Reliability in Design, **111**, pp. 217–225.
[32] Moody, L. F., 1994, ''Friction factors in pipe flow,'' Trans. ASME, **66**, pp. 671–684.
[33] Nelson, C. C., and Nguyen, D. T., 1987, ''Comparison of Hirs' equation with Moody's equation for determining rotordynamic coefficients of annular pressure seals,'' ASME J. Tribol., **109**, pp. 144–148.
[34] Yamada, Y., 1962, ''Resistance of a flow through an annulus with an inner rotating cylinder,'' Bull. JSME, **5**, No. 18, pp. 302–310.
[35] Daily, J. W., and Nece, R. E., 1960, ''Chamber dimension effects on induced flow and friction resistance of enclosed rotating disks,'' ASME J. Basic Eng., **82**, pp. 217–232.
[36] Stepanoff, A. J., 1957, *Centrifugal and axial flow pumps-Theory, design, and application*, 2nd edition, Wiley, NY.
[37] Murawaski, C. G., and Vafai, K., 2000, ''An experimental investigation of the effect of freestream turbulence on the wake of a separated low-pressure turbine blade at low Reynolds numbers,'' ASME J. Fluids Eng., **122**, pp. 431–433.
[38] Kurokawa, J., Kitahora, T., and Jiang, J., 1994, ''Performance prediction of mixed-flow pumps using inlet reverse flow model,'' Proceedings 17th IAHR symp., Beijing, Vol. 1, pp. 177–188.
[39] Schubert, F., 1988, ''Untersuchungen der Druck- und Geschwindigkeitsverteilung in Radseitenräumen radialer Strömungsmaschinen,'' Dissertation, Technische Universität Braunsweig.

Unsteady Flow Pattern Characteristics Downstream of a Forward-Curved Blades Centrifugal Fan

Sandra Velarde-Suárez
Associate Professor

Rafael Ballesteros-Tajadura
Associate Professor

Carlos Santolaria-Morros
Professor

José González-Pérez
Assistant Professor

Universidad de Oviedo,
Área de Mecánica de Fluidos,
Campus de Viesques,
33271 Gijón Asturias, Spain

The results of an experimental investigation of the flow at two exit radial locations of a forward-curved blades centrifugal fan are presented. Hot wire techniques were used to obtain steady velocity components and velocity unsteadiness levels (rms value of the components of velocity fluctuation) for different operating conditions. Globally speaking, the data reveal a strong flow asymmetry, with considerable changes in both magnitude and direction along the different circumferential positions. Particularly, big differences appear between the circumferential positions closer to the volute tongue and the other ones. The periodic character of the velocity signals due to the passing of the blades, clearly observed around the impeller, is missed in the vicinity of the volute tongue, where the main contribution to the velocity fluctuations appears to be random. Based on the measured velocity signals, velocity unsteadiness of the flow is determined analyzing the main contributions as a function of the flow rate and the measurement position. High levels of velocity unsteadiness were observed near the volute tongue, mainly at low flow rates. [DOI: 10.1115/1.1351175]

Introduction

Forward-curved blades centrifugal fans usually exhibit instability phenomena, which reduce their operating range. A basic feature of such impellers is the deficient flow guiding, as a result of the short radial length of the blades and their high chamber. This effect is counterbalanced by a greater number of blades. Such an arrangement can cause the flow to stall, even at design conditions. A perturbation at the inlet or at the outlet planes can be amplified, giving rise to flow instabilities, noise and vibrations both in the fan and in the system. Cau et al. [1] show in their work that the poor design of the flow channel in these fans causes a severely distorted primary flow, with early flow separation on the suction side at both low and design flow rates. They ascribed the inefficiencies of these machines to the sharp axial to radial bend, to the large inlet gap between inlet cone and impeller shroud and to the poor matching between impeller outlet and volute.

On the other hand, the unsteady flow field at the outlet of the impeller is not axisymmetric due to the effect of the volute. Many authors have demonstrated that the primary sources of noise in centrifugal turbomachines are associated with the interaction of the unsteady nonuniform outflow from the impeller with the volute tongue (see for example Chu [2,3]).

There has been extensive research carried out on flow unsteadiness generated in axial compressors (e.g., Goto [4], Moore et al. [5], and Liu et al. [6]) and centrifugal pumps (e.g., Pinarbasi et al. [7] and Ubaldi et al. [8,9]).

In this paper, the results of a detailed experimental investigation of the unsteady flow at two exit planes of a forward-curved centrifugal fan are presented. Based on the measured velocity signals, the unsteady characteristics of the flow are determined analyzing the main contributions depending on the flow rate and the measurement location. These experimental results can lead to a better knowledge of the aerodynamic noise generation mechanisms in centrifugal fans, in order to design quieter and more efficient machines.

Contributed by the Fluids Engineering Division for publication in the JOURNAL OF FLUIDS ENGINEERING. Manuscript received by the Fluids Engineering Division August 12, 1999; revised manuscript received December 11, 2000. Associate Editor: B. Schiavello.

Performance Testing

The tests were made on a single-intake centrifugal fan with forward-curved blades. The shrouded rotor has an inlet diameter of 328 mm, an outlet diameter of 400 mm, and a width of 170 mm. It has 38 forward-curved blades and is driven by an AC 9.2 kW motor. The impeller rotates at 1480 rpm with a fluctuation level lower than 0.5% for the whole range of the analyzed flow rates. The volute has a width of 248 mm.

Figure 1 shows a sketch of the fan with the main dimensions expressed in mm. The minimum radial distance between the fan impeller outer diameter and the volute is 50 mm at the tongue (base circle diameter 500 mm). The inlet blade angle is 0 degrees with respect to the radial direction; the incidence angle between the relative velocity and the blade direction at the leading edge at the design flow rate is 68.83 degrees, thus flow separation occurs for all flow conditions. Blade chord angle is 44 degrees with respect to the radial direction; the blade chord i 45 mm, and the blade solidity, obtained as the ratio of the blade chord to the inlet-to-outlet average pitch is 1.5. The outlet blade angle is 16 deg relative to the tangential direction. The fan sucks air from the atmosphere through a suction nozzle.

A test facility was designed and built following the British Standard BS 848: Part 1 [10] and the BS 848: Part 2 [11]. With such arrangement, the same facility could be used to measure the fan performance curves and the fan acoustic behavior. Figure 2 shows a sketch of the test facility with its main elements. After the fan, the air passes through a straightener in order to remove the existing swirl at the fan discharge. The straightener consists of eight radial vanes equally spaced. At the end of the facility, an anechoic termination removes undesired noise reflections and the regulation cone permits to modify the fan operating point. The procedure indicated in the Standard to obtain the performance curves works as follows. The total pressure rise of the fan is obtained adding to the static pressure measured in section A, the velocity head at section A and the loss allowances for standard-

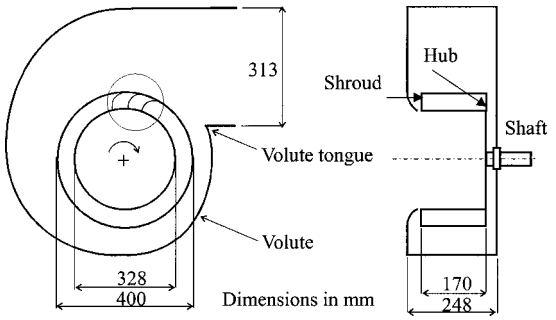

Fig. 1 Test fan

ized airways between the fan outlet and section A. Static pressure was measured using a differential manometer with one side connected to four wall tappings evenly distributed at Section A and the other side open to the atmospheric pressure in the laboratory. Velocity head was deduced from the flow rate and the duct cross section. The flow rate was measured with a Pitot-static tube, placed at section B, using a traversing method. The shaft power was determined measuring the electrical power and taking into account the electrical motor efficiency.

In order to obtain the fan sound power level (SWL), the Standard specifies the measurement of the sound pressure level in one third of octave band, at three different radial positions ($2R/D = 0.5, 0.65, 0.8$) inside the discharge duct at Section B (Fig. 2). The sound pressure level (SPL) measurements were taken using a 1/2 in. microphone fully immerged in the test medium with a nose cone anti-wind protector connected to a Brüel & Kjaer real time frequency analyzer. These values were averaged in the radial direction and modified with some correction factors: frequency response microphone correction, noise cone anti-wind correction, modal correction and wind turbulence correction. Finally, the sound power level is obtained with the following formula:

$$\mathrm{SWL} = \mathrm{SPL} + 10 \log_{10} \frac{A}{A_0}$$

where A is the cross section of the measurement duct and A_0 is a reference section (1 m^2). Measurements were made for each third of octave band, and the global value of SWL was calculated by adding the values for each band.

The following uncertainties were obtained for the measured and calculated magnitudes:

— Differential total pressure: ±1.4% (±21 Pa).
— Flow rate: ±2% (±0.06 m^3/s).
— Shaft power: ±2% (±0.19 kW).
— Sound power level: ranges between ±1.6 dB and ±4 dB depending upon the frequency band considered:

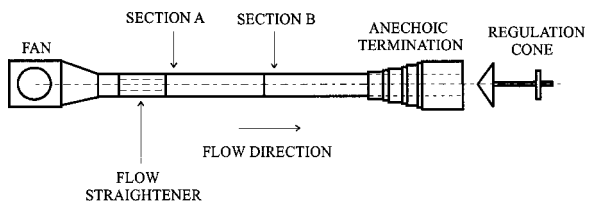

Fig. 2 Test facility

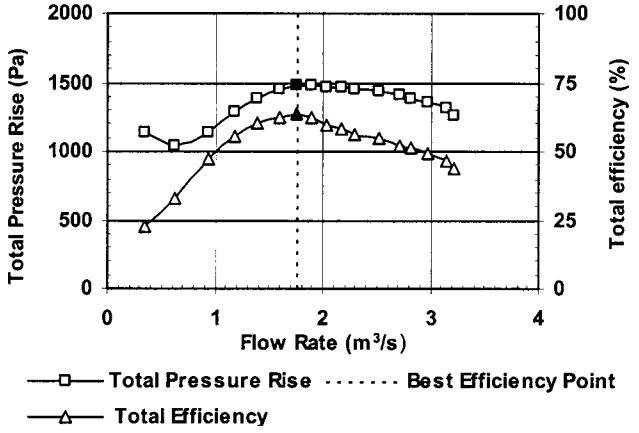

Fig. 3 Total differential pressure and efficiency versus flow rate

Frequency (Hz)	Uncertainty (dB)
50	3.5
63	3.0
80	2.5
100	2.5
125	2.0
160–2500	1.6
3150–4000	2.0
5000	2.5
6300–8000	2.5
10,000	4.0

Figure 3 shows total pressure rise and efficiency against the flow rate. The subscript ''o'' identifies the design operatives point corresponding to $Qo = 1.7$ m^3/s and $Efo = 0.63$. On the total pressure curve a wide zone with positive slope, in which some aerodynamic unstable phenomena may appear, can be observed. Furthermore, the design point, corresponding to the highest efficiency is at the beginning of that zone, revealing a marginal fan design. Some references [12] report the following aerodynamic instability phenomena which are responsible for the increase in noise generation and level of mechanical vibrations and the decrease in aerodynamic performance: flow separation in the blade channels, reverse flow, and prerotation at fan suction.

Figure 4 shows shaft power and sound power level (SWL) against flow rate. The shaft power curve increases with the flow rate, thus causing a drive overload when working at high flow rates during long periods of time. In the SWL curve, higher levels were measured for the lower flow rates. The lowest value corresponds to the highest value of efficiency, and beyond that point, its value increases slightly for increasing flow rate.

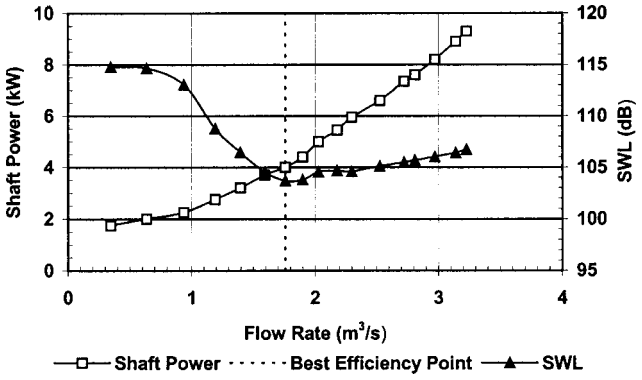

Fig. 4 Shaft power and SWL versus flow rate

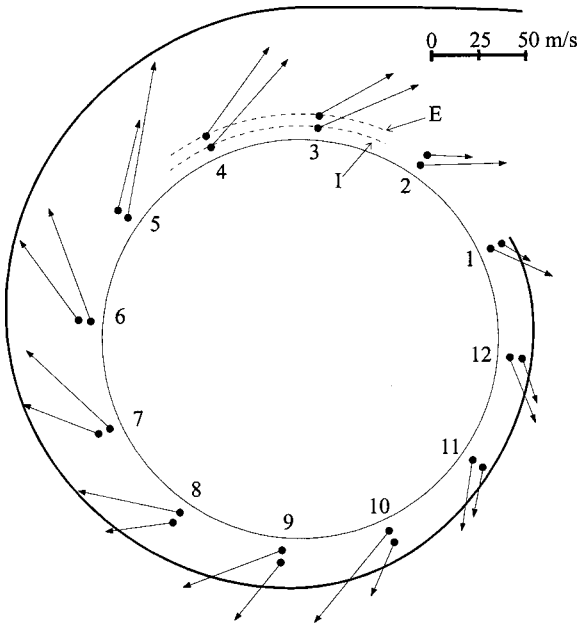

Fig. 5 Measurements points and absolute velocity at impeller outlet, 0.7× *Q*o

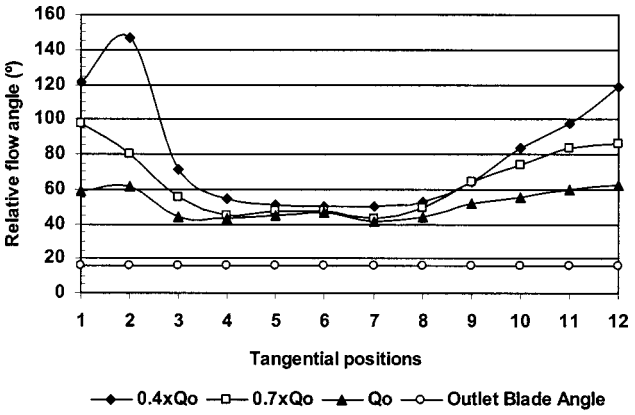

Fig. 6 Mean relative flow angle closer to impeller outlet (with respect to the tangential direction; radial location $R_I = 1.05\ R_2$)

Aerodynamic Testing

The flow field at the impeller exit plane was measured for three operating conditions in the positive slope zone of the characteristic curve: the design flow rate Qo, $0.4\times Q$o, and $0.7\times Q$o. For that purpose, hot wire velocity signals were measured on 12 circumferential points evenly distributed at two radial locations (Fig. 5). The inner location is named I and the outer location is named E, and the respective radius are 210 mm and 240 mm, i.e., 5% and 20% of the impeller outlet diameter. These velocity measurements were made at mid-blade width. In addition, the spanwise variation of the flow field was obtained by taking velocity measurements in different axial positions for several circumferential locations. The main conclusion of the spanwise investigation of the velocity pattern indicated an almost constant tangential component over the blade span, while the radial component decreased clearly at both blade hub and blade shroud.

To measure the radial and the tangential components of the absolute velocity at the impeller exit, a two-wire probe was used. Hot wire anemometry is able to get the two-dimensional character of the flow with a high temporal resolution (Comte-Bellot [13]). A direct calibration procedure of the probe was chosen. In that way, it is possible to derive two calibration coefficients to represent flow angle and velocity magnitude changes. The variation of these coefficients is established through an angular calibration and the resulting curves were used instead of the response equations of the wires. Full details of the calibration procedures and the methodology used can be found in Blanco-Marigorta et al. [14] and Velarde-Suárez [15]. For the two-wire probe, the maximum angular and velocity uncertainties were estimated to be 2° and 2%, respectively. The probe support has a diameter of 4 mm. The wires are in a plane perpendicular to the axis of the support and they form an angle of 120 deg. The length of the wires is 2 mm and their diameter 5 μm; therefore, their aspect ratio is 400. The minimum distance between the wires is 1 mm. These dimensions can be compared to the impeller blade pitch: 33 mm, and the distance between the impeller and the volute tongue: 50 mm.

The signals coming from the probe wires were introduced in the anemometer IFA-100 of TSI Inc. The filtering frequency was set to 5 kHz per channel to avoid aliasing. The output voltages from the anemometer for each location and operating condition were registered with the digital recorder STOREPLEX DELTA of RACAL Recorders Ltd. Apart from the wires signals, a one pulse per revolution trigger signal was also recorded. This signal helps to determine the impeller revolutions in the wires signals. The acquisition process was made in two steps. In the first step, the signals were recorded on magnetic tapes (S-VHS) at a frequency of 11.4 kHz per channel, which was imposed by the tape recorder. In the second step, the recorded data were transferred to a personal computer using an analog-to-digital card DAS16/330i of ComputerBoards Inc. with acquisition frequency of 9373.3 Hz per channel (380 points per revolution) to obtain a good resolution. Afterwards, data were stored in files and transformed according to the calibration charts of the probe to obtain the flow velocity and the flow angle. A code was developed in order to calculate the rms value of the components of velocity fluctuation, or velocity unsteadiness.

Figure 5 shows the average absolute velocity field for $0.7\times Q$o, at the radial locations I and E. Each vector was obtained by averaging all the values recorded in each measurement position (about 20 impeller rotations). Basically, the vector represented is the value which would be measured by using a low response pressure probe. Smaller values of the absolute velocity are obtained near the volute tongue than in the rest of the volute, due to the induced blockage. The behavior of the vector at the location 5E can not be easily explained and might be an incorrect measurement.

The mean absolute flow velocity at the impeller outlet was split up into the peripheral velocity at the test radial position I ($R = 210$ mm), i.e., $U_I = 32.1$ m/s, and the mean relative flow velocity, thus obtaining the mean relative flow angle at test radial section I. This angle is compared in Fig. 6 with the outlet blade angle, both measured with respect to the tangential direction, for all the circumferential positions. Large differences can be appreciated among those angles particularly in the vicinity of the volute tongue, these differences increasing with decreasing flow rates.

Figures 7 and 8 show the circumferential distribution of the velocity unsteadiness for three different operating conditions, around the inner radial location I. The radial component was normalized using the mean value V_{rm} of that component for all the measurement locations. The tangential component was normalized using the impeller outlet peripheral velocity, $U_2 = 30.6$ m/s. As stated by Goto [4], the velocity unsteadiness contains real turbulence, flow perturbations generated by the rotor wake velocity deficit, unsteadiness due to vortex shedding, sawing movements of leakage vortices, fluttering of the separated flows and unsteadiness of separation points. This combined unsteadiness of the velocity field at the impeller discharge and its interaction with the volute tongue generate pressure fluctuations, which will produce noise and vibrations both in the fan and system.

Particularly, in Fig. 7, a strong velocity unsteadiness in the

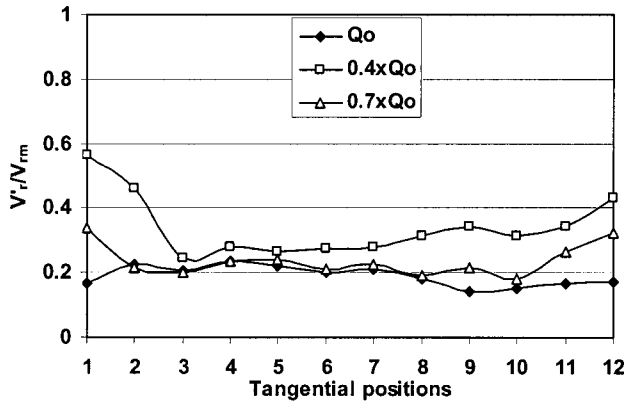

Fig. 7 Circumferential distribution of velocity unsteadiness in the radial direction (radical location $R_I=1.05\,R_2$)

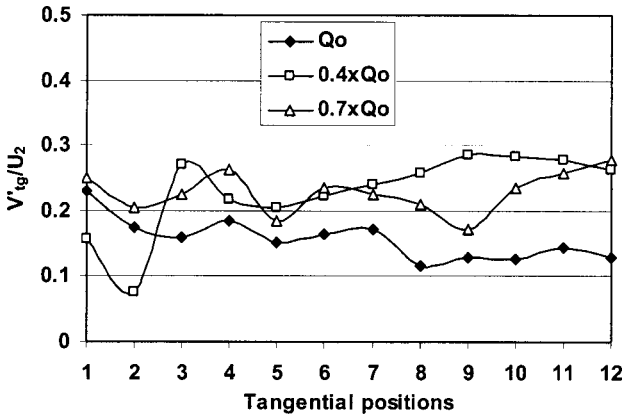

Fig. 10 Circumferential distribution of velocity unsteadiness in the tangential direction (radial location $R_E=1.2\,R_2$)

radial direction is observed near the volute tongue. A larger zone with high levels of velocity unsteadiness both in level and extension appears for decreasing flow rates. The velocity unsteadiness in the tangential direction, shown in Fig. 8, presents a similar behavior.

Figures 9 and 10 show the velocity unsteadiness circumferential distribution around the outer radial location E. Figure 9 shows the same trend as Fig. 7, but with a higher velocity unsteadiness in the former near the volute tongue. In most positions of the volute, velocity unsteadiness increases when the flow rate decreases. That trend can also be extended to the velocity unsteadiness of the tangential component (Fig. 10).

Figures 11–14 compare the blade-to-blade distributions of the components of velocity and velocity unsteadiness for three differ-

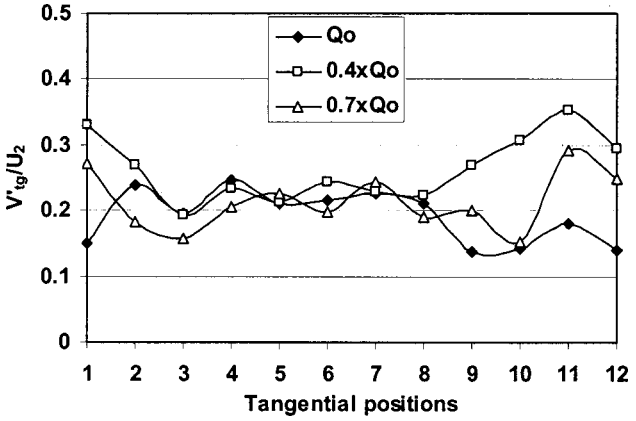

Fig. 8 Circumferential distribution of velocity unsteadiness in the tangential direction (radial location $R_I=1.05\,R_2$)

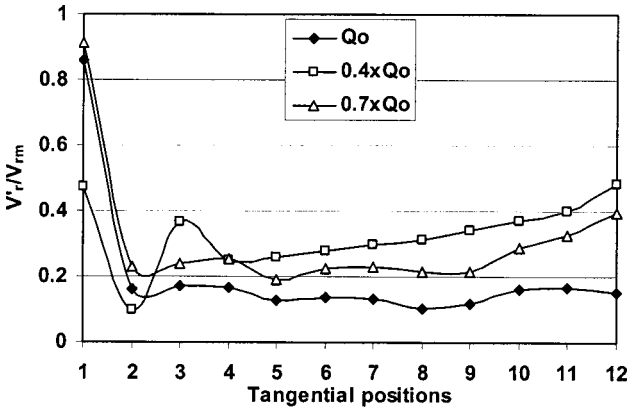

Fig. 9 Circumferential distribution of velocity unsteadiness in the radial direction (radial location $R_E=1.2\,R_2$)

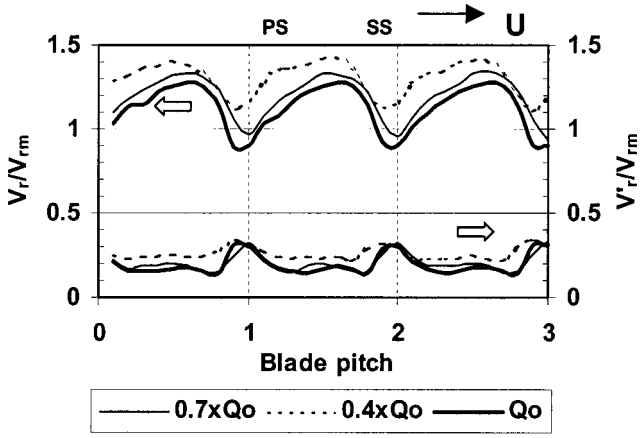

Fig. 11 Blade-to-blade distribution of mean radial component of velocity and velocity unsteadiness in the radial direction at the position 6 I

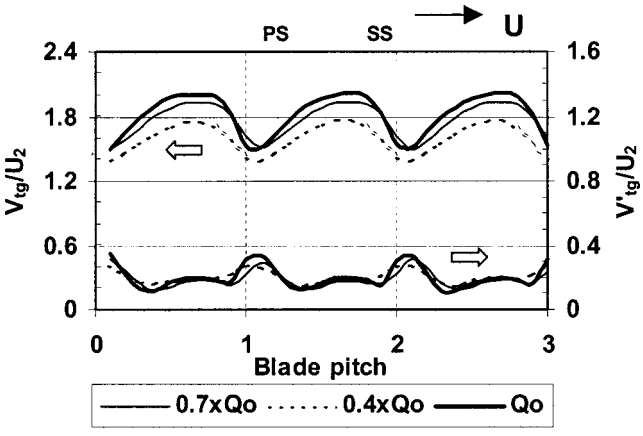

Fig. 12 Blade-to-blade distribution of mean tangential component of velocity and velocity unsteadiness in the tangential direction at the position 6 I

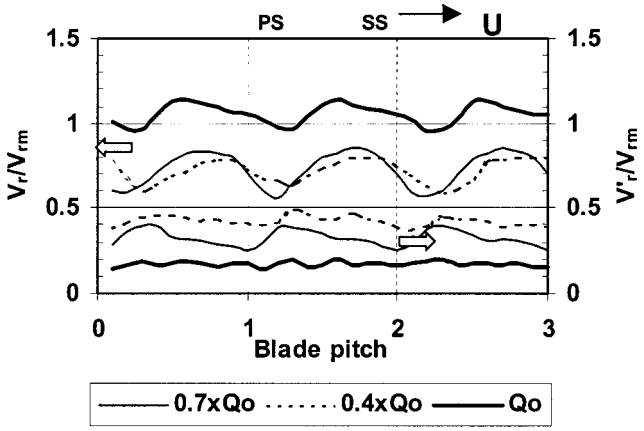

Fig. 13 Blade-to-blade distribution of mean radial component of velocity and velocity unsteadiness in the radial direction at the position 12 I

ent operating conditions and at two measurement positions: one opposite (position 6 I) and one close to the volute tongue (position 12 I).

Figures 11 and 12 (which correspond to position 6 I, 150 deg away from volute tongue) show a jet-wake pattern for all the measured flow rates, with high levels of velocity unsteadiness at the blades wakes. However, Figs. 13 and 14 (which correspond to position 12 I, 30 deg away from volute tongue) show that the jet-wake pattern is still present in the velocity components (more clearly in the radial component than in the tangential) but not so clear in the velocity unsteadiness. The velocity unsteadiness increases for decreasing flow rate and the high levels of velocity unsteadiness for $0.4\times Qo$ remain almost invariable for the whole blade pitch, not only at the blades wakes.

Figures 15 and 16 show the proper spectra of the velocity fluctuation in the tangential direction for the flow rate $0.4\times Qo$ at the positions 6 I and 12 I. The peaks corresponding to the blade passing frequency (924 Hz) and its harmonics are clearly present in the spectrum of the position 6 I, thus confirming that the main contribution to the velocity unsteadiness around that point is due to the blade wake. Also high broad band levels were encountered at low frequencies. On the other hand, in the spectrum of the position 12 I, only the blade passing frequency is barely noticeable and the other harmonics are masked by broad band levels. Levels at lower frequencies than the blade passing frequency are comparable to the peak level corresponding to the blade passing

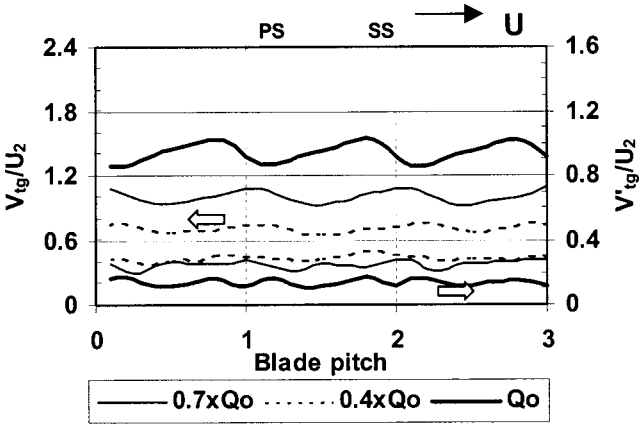

Fig. 14 Blade-to-blade distribution of mean tangential component of velocity and velocity unsteadiness in the tangential direction at the position 12 I

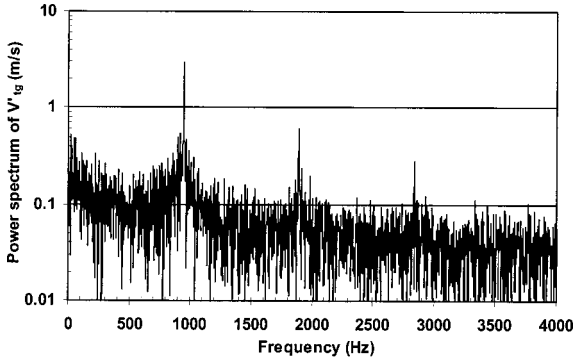

Fig. 15 Power spectrum of velocity fluctuation in the tangential direction at the position 6 I, $0.4\times Qo$

frequency, whose highest value is found at the position 6 I. In fact, around the volute tongue (position 12 I), the velocity unsteadiness has low frequency components with a random behavior. This might be due to large flow separation inside the impeller channel which crosses the volute tongue. The flow separation tends to replace the well-structured jet-wake pattern with a turbulent vortex inside the full blade channel producing broad range-low frequency velocity fluctuations. Figures 17 and 18 show the power spectra of the velocity fluctuation in the tangential direction for the flow rate $0.4\times Qo$ at the positions 6 E and 12 E. In this case, only the peak corresponding to the blade passing frequency (924 Hz) is clearly present at the position 6 E. The spectrum corresponding to the position 12 E reveals the same behavior observed at position 12 I, and even the blade passing frequency is hardly appreciated.

These experimental results can explain some of the spectral characteristics of the noise generated by the fan, analyzed in a

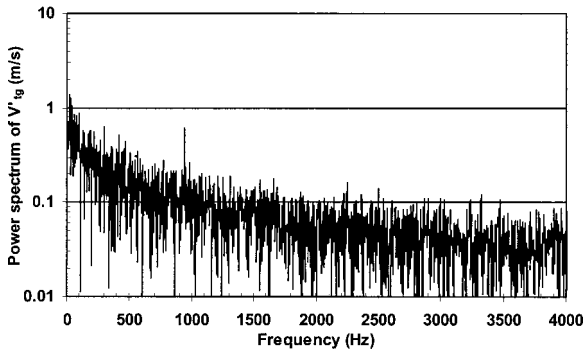

Fig. 16 Power spectrum of velocity fluctuation in the tangential direction at the position 12 I, $0.4\times Qo$

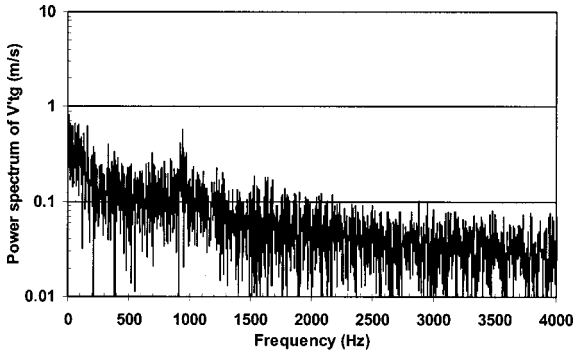

Fig. 17 Power spectrum of velocity fluctuation in the tangential direction at the position 6 E, $0.4\times Qo$

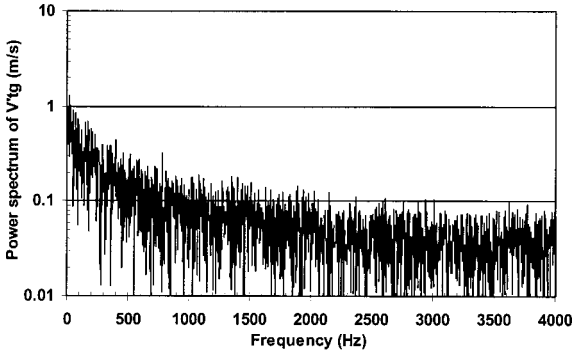

Fig. 18 Power spectrum of velocity fluctuation in the tangential direction at the position 12 E, 0.4× *Q*o

previous paper (Velarde-Suárez et al. [16]). That work showed how the main contributions to the fan noise spectra were predominant at low frequencies, especially when the flow rate was reduced. Tonal aerodynamic noise corresponding to the blade passing frequency and its harmonics were found to be a lower contribution to the noise spectra.

Conclusions

An experimental characterization of the flow field in a forward-curved blades centrifugal fan with unstable performance curve was carried out. The velocity field measurements allow the study of the aerodynamic noise generated by the fan, which can be related to the unsteady character of the flow at two impeller exit radial locations.

The test performance curves revealed the unstable characteristic of the fan over a wide flow rate range, where even the best efficiency point is included. This behavior is related to the poor design of the blades, which have an inlet blade angle of 0 degrees and operate with high positive incidence angle at design flow rate.

Regarding the velocity field at the two impeller exit radial locations considered, a great asymmetry is found, with considerable changes in both magnitude and direction among the differential circumferential positions. In particular, big differences appear between the circumferential positions closer to the volute tongue and the other ones.

Velocity unsteadiness distributions and velocity components power spectra exhibit a similar behavior: high levels at low flow rates in the vicinity of the volute tongue, which apparently are not caused by the blades wakes, but produced at low frequencies and with random behavior, probably because of a large flow separation turbulent eddy. However, in the rest of the volute, the velocity unsteadiness levels are not so high: in fact, they decrease when the flow rate decreases and exhibit their higher levels at the blades wakes with a clear periodic behavior. These results contribute to explain the spectral characteristics of the noise generated by the fan.

Acknowledgments

This work was supported by the Research Project ''Modelado del comportamiento del flujo no estacionario subsónico en la interacción entre haces fijos y móviles de turbomáquinas axiales,'' Ref. DPI2000-0702-C02-01, CICYT, Spain.

Nomenclature

A = cross section
A_0 = reference section (1 m^2)
D = duct diameter at Section B (Fig. 2)
Ef = Efficiency
Efo = Maxoimum efficiency
Q = flow rate
Qo = design flow rate (best efficiency point)
R = radius
SWL = sound power level
SPL = Sound pressure level
V_r = steady radial component of the absolute velocity
V_{rm} = pitch average radial component of the absolute velocity
V_r' = Rms value of velocity fluctuations in the radial direction
V_{tg} = steady tangential component of the absolute velocity
V_{tg}' = Rms value of velocity fluctuations in the tangential direction
U = peripheral velocity

Subscripts

1 = impeller inlet
2 = impeller outlet
I = internal radial test location
E = external radial test location
o = design operating conditions

References

[1] Cau, G., Mandas, N., Manfrida, N., and Nurzia, F., 1987, ''Measurements of Primary and Secondary Flows in an Industrial Forward-Curved Centrifugal Fan,'' ASME J. Fluids Eng., **109**, pp. 353–358.
[2] Chu, S., Dong, R., and Katz, J., 1995, ''Relationship Between Unsteady Flow, Pressure Fluctuations, and Noise in a Centrifugal Pump-Part A: Use of PDV Data to Compute the Pressure Field,'' ASME J. Fluids Eng., **117**, pp. 24–29.
[3] Chu, S., Dong, R., and Katz, J., 1995, ''Relationship Between Unsteady Flow, Pressure Fluctuations, and Noise in a Centrifugal Pump-Part B: Effects of Blade-Tongue Interactions,'' ASME J. Fluids Eng., **117**, pp. 30–35.
[4] Goto, A., 1992, ''Three-Dimensional Flow and Mixing in an Axial Flow Compressor with Different Rotor Tip Clearances,'' ASME J. Turbomach., **114**, pp. 675–685.
[5] Liu, B., Moore, J. G., and Moore, J., 1998, ''Total Unsteadiness Downstream of an Axial Compressor Rotor,'' AIAA Paper No. 98-0967.
[6] Moore, J., and Moore, J. G., 1998, ''Turbulence energy and spectra downstream of an Axial Compressor Rotor,'' AIAA Paper No. 98-2550.
[7] Pinarbasi, A., and Johnson, M. W., 1994, ''Detailed Flow Measurements in a Centrifugal Compressor Vaneless Diffuser,'' ASME J. Fluids Eng., **116**, pp. 453–461.
[8] Ubaldi, M., Zunino, M., and Cattanei, A., 1993, ''Relative Flow and Turbulence Measurements Downstream of a Backward Centrifugal Impeller,'' ASME J. Turbomach., **115**, pp. 543–551.
[9] Ubaldi, M., Zunino, M., Barigozzi, G., and Cattanei, A., 1996, ''An Experimental Investigation of Stator Induced Unsteadiness on Centrifugal Impeller Outflow,'' ASME J. Turbomach., **118**, pp. 41–54.
[10] British Standard BS-848, 1980, ''Fans for General Purposes. Part 1. Methods of Testing Performance.''
[11] British Standard BS-848, 1985, ''Fans for General Purposes. Part 2. Methods of Noise Testing.''
[12] Neise, W., 1992, ''Review of Fan Noise Generations Mechanisms and Control Methods,'' *Proceedings of the SFA Symposium on Fan Noise*, Senlis, France.
[13] Comte-Bellot, G., 1975, ''Hot-Wire Anemometry,'' Annu. Rev. Fluid Mech., **8**, pp. 209–231.
[14] Blanco, E., Ballesteros, R., and Santolaria, C., 1998, ''Angular Range and Uncertainty Analysis of Non-Orthogonal Crossed Hot Wire Probes,'' ASME J. Fluids Eng., **120**, pp. 90–94.
[15] Velarde-Suárez, S., 1997, ''Comportamiento Aeroacústico de Ventiladores Inestables,'' Ph.D. Thesis (in Spanish), Universidad de Oviedo, Spain.
[16] Velarde-Suárez, S., Santolaria-Morros, C., and Ballesteros-Tajadura, R., 1999, ''Experimental Study on the Aeroacoustic Behavior of a Forward-Curved Centrifugal Fan,'' ASME J. Fluids Eng., **121**, pp. 276–281.

B. K. Gandhi
Senior Lecturer,
Mechanical Engineering Department,
SGSITS, Indore (MP) 452 003,
India

S. N. Singh
Professor

V. Seshadri
Professor

Department of Applied Mechanics,
I.I.T. Delhi 110 016,
India

Performance Characteristics of Centrifugal Slurry Pumps

The performance of two centrifugal slurry pumps has been reported for three solid materials having different particle size distribution (PSD) in terms of head, capacity, and power characteristics. The results have shown that the values of head and efficiency ratios are not only dependent on solid concentration but are also affected by PSD of the solids and properties of the slurry. The addition of fine particles in the slurry of coarser material leads to reduction in the additional losses that occur in the pumps due to the presence of solids. It is also observed that with the increase in the pump size, the additional losses due to presence of solids reduce. [DOI: 10.1115/1.1366322]

Introduction

Centrifugal slurry pumps are being used extensively for pipeline transportation systems because of their capabilities to economically convey large size abrasive solids in bulk. These pumps have been developed by suitably modifying the design of conventional centrifugal pumps to ensure proper flow of solid-liquid mixtures and to minimize erosive wear. The head and the efficiency of these pumps with slurries are, in general, lower for traditional designs in comparison to water due to the presence of suspended solids. Stepanoff [1] had previously concluded that the solid particles do not absorb, store, or transmit pressure energy, but still it was difficult to establish the effect of solids on the pump performance.

Researchers over the years (Fairbank [2], Wiedenroth [3], Vocadlo et al. [4], Burgess and Riezes [5], Sellgren [6], Walker and Goulas [7], Sellgren and Vappling, [8], Sellgren et al. [9], Wilson et al. [10], Gahlot et al. [11] Kazim et al. [12], and Ni et al. [13]) have observed that the performance of the pump decreases for increased solid concentration, particle size, and specific gravity. On the other hand, Chand et al. [14] have reported that the head and efficiency of the pump increases due to addition of solid particles. Fairbank [2] found that the head developed by the pump for water decreases with increase in either concentration or median particle size of sand/ clay and has attributed this to the difference in the velocity of the liquid and the solid particles leaving the impeller. This phenomenon has also been reported for the pump handling coarse solids by Wiedenroth [3], who has attributed the head reduction to the additional friction losses in the flow passages due to the suspended solids. Vocadlo et al. [4] have reported higher reduction in the head and efficiency of the rubber-lined slurry pumps compared to the metallic pumps. Experiments conducted by Bugress and Riezes [5] have shown higher drop in the head compared to the efficiency. Sellgren [6] has reported that the decrease in the head is a function of solid concentration, specific gravity and the particle drag coefficient. Walker and Goulas [7] observed that the drop in the head and the efficiency of the pump handling non-Newtonian slurries depend on the rheological properties of the slurry and the pump Reynolds number. Sellgren and Vappling [8] observed higher reduction in the efficiency compared to the head developed by rubber-lined pump for solid concentrations higher then 20 percent by volume. Sellgren et al. [9] have attempted to correlate the experimental data for different pumps available in the literature and their own experimental data with weighted mean particle size of the solid material, and normalized impeller diameter and width. The effect of solids on the pump performance has also been critically reviewed in the book by Wilson et al. [10]. They have produced generalized diagrams for estimation of the performance of the pump handling slurries. Gahlot et al. [11] observed higher drop in the head compared to that in the efficiency, whereas, subsequently, Kazim et al. [12] have reported higher drop in the efficiency compared to that in the head. Ni et al. [13] observed that the drop in the head and efficiency of the pump handling slurries of narrow sized sand particles increases with increase in the particle size. Many of these investigators (Fairbank, [2], Wiedenroth [3], Vocadlo et al. [4], Burgess and Riezes [5], Sellgren [6], Sellgren et al. [9], Gahlot et al. [11], and Kazim et al. [12]) have proposed empirical/semi-empirical correlations based on their experimental observations to estimate the effect of suspended solids on the water performance of the pump. These correlations are generally expressed in terms of head ratio (HR) and efficiency ratio (ER), which are defined as

$$\mathrm{HR} = \frac{\text{head developed with slurry (m of slurry column) at any flowrate}}{\text{head developed with water (m of water column) at the same flowrate}} \tag{1}$$

and

$$\mathrm{ER} = \frac{\text{efficiency of the pump for slurry at any flowrate}}{\text{efficiency of the pump for water at the same flowrate}} \tag{2}$$

These correlations are dependent on pump size and the properties of slurries and solid particles, and hence are not universally applicable. Additionally, the flow in the pump could also be homogeneous or heterogeneous depending on the particle size and flow conditions. In commercial applications, the particle sizes vary over a wide range (very often by few microns to as high as 2 to 3 millimetres). In such case, the finer particles are homogeneously distributed in the solid-liquid mixture, where as larger particles are heterogeneously distributed (Wilson et al. [10]). The present state of knowledge on additional hydraulic losses due to such type of flows in the pump is at best incomplete. Thus, for

Contributed by the Fluids Engineering Division for publication in JOURNAL OF FLUIDS ENGINEERING. Manuscript received by the Fluids Engineering Division September 7, 1999; revised manuscript received January 31, 2001. Associate Editor: B. Schiavello.

designing or selecting a centrifugal slurry pump, extensive database is required for accurate estimation of the deviation from the water performance of the pump while handling slurries.

In the present paper, the effect of particle size distribution (PSD) and slurry properties on the pump performance has been discussed. Extensive tests have been carried out on two different size centrifugal slurry pumps handling the mixtures of different solid materials, namely, fly ash, bed ash, and zinc tailings. Measurements have been made in the operating range of the pumps for a wide range of solid concentrations. The head, discharge capacity, and input power of the smaller pump have been measured whereas for the bigger pump, only head developed at various discharge capacities has been measured. Based on these measurements, an attempt has been made to establish the effect of multisized concentrated slurries on the performance of the pumps tested.

Experimental Setup and Measurement Uncertainties

Figure 1 shows the schematic diagram of the experimental setup used in the present work to evaluate the performance of two centrifugal slurry pumps. The setup comprises of two separate pipe loops, one for each pump, both connected to the common mixing tank and the measuring tank. The 50 mm pipe loop is a bypass test loop of short length and is connected with ''50K WILFLEY'' pump (pump A). The 100 mm test loop is a recirculatory loop having a total pipe length of 60 m and is connected with ''100K WILFLEY'' pump (pump B). The slurry for the tests was prepared in the hopper shaped mixing tank having a suitable stirring arrangement for keeping the slurry always in a well-mixed state during experimentation. The slurry is drawn from the mixing tank by any one of the pumps and returned after circulation through the test loops either directly to the mixing tank or to the measuring tank. The rate of flow is ascertained by monitoring the rise of the slurry level in the measuring tank collected over a known interval of time. Flowrate by this method was evaluated within an error of ± 0.5 percent. Measuring tank was also used to calibrate the electro-magnetic flowmeters which were installed in the vertical pipe section of each test loop for continuous monitoring of the flowrate. Each test loop was also provided with an efflux sampling tube fitted with a plug valve, in the vertical pipe section for collection of the slurry sample to monitor solid concentration. The errors in the individual measurement of solid concentration were in the range of ± 2 percent. Pressure taps were provided in the suction and delivery lines of the pump to measure the total head developed by the pump. The suction and delivery heads were measured through separation chambers by using a U-tube mercury manometer and a Bourdon tube type pressure gauge, respectively. The U-tube manometer was inclined at 30 deg angle to the horizontal to have higher sensitivity. The pressure gauges have an uncertainty of ± 1 percent and were calibrated using a deadweight pressure gauge tester at regular intervals during experimentation. All measurements were made in accordance with the requirements specified in relevant pump test codes [IS-5120 [15] and BS-5316 [16]].

V-belt pulley drives were used to run the pump A by a 22 kW, 415 V, 40 amp induction motor and to run the pump B by a 37 kW, 415V, 63 amp induction motor. The pump speed was measured by an optical digital electronic tachometer having resolution of ± 1 rpm. The pump input power was measured indirectly from the measurement of the input power to the precalibrated 22 kW motor and its efficiency, allowing 3 percent power loss for V-belt drive system IS-5120 [15]. For measurement of the motor input power, two-Wattmeter method was used by maintaining constant voltage supply through a voltage regulator. Both the calibrated Wattmeters (Class 0.5 AE make) were connected to the input supply via current transformers. This arrangement allowed measurement of the input power of the motor within an error of ± 1 percent and a maximum error of ± 3 percent in estimation of the pump efficiency, besides the V-belt efficiency assumption.

The measurement of important dimensions of both the metal pumps (WILFLEY model, Make: Hindustan Dorr-Oliver Ltd.) used in the present investigation and their performance at the test speed as given by the manufacturer are given in Table 1. The impellers of both the pumps are of closed type having 5 vanes (pump A) and 7 vanes (pump B). The overall dimensions of pump B are larger than that of pump A. The volute casings of both the pumps are of single type with larger throat area for pump B. The performance characteristics supplied by the manufacturer for the test speed show higher values of head and discharge at BEP for pump B compared to pump A, in spite of having lower pump speed. The efficiency of pump B is also significantly higher (Table 1). This shows that the overall size of pump B is much larger compared to pump A. The dimensionless specific speeds (Ω_s) of these pumps were determined using the expression

$$\Omega_s = \frac{\omega\sqrt{q}}{(gH)^{3/4}} \tag{3}$$

given by Fox and McDonald [17]. In this expression, ω is the operating speed in radians per second, q is the capacity in m^3/s, g is the acceleration due to gravity in m/s^2, and H is the head developed by the pump in mwc (meters of water column). The specific speed (N_s) is also expressed as

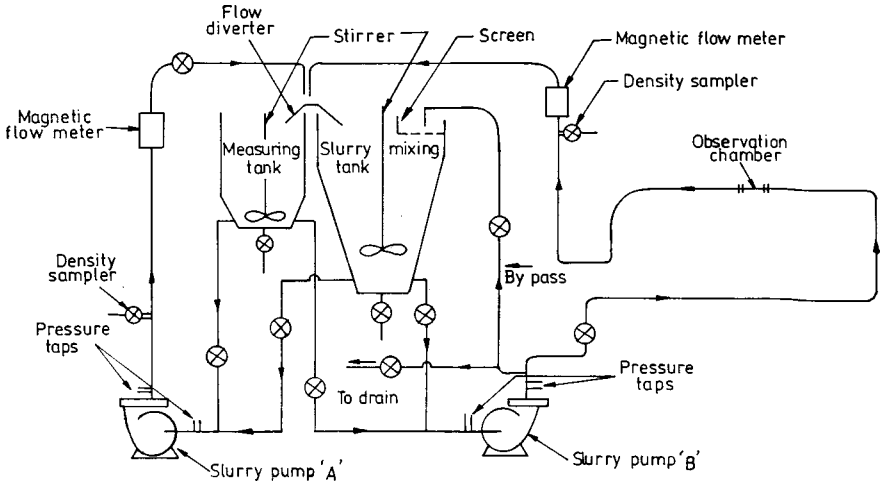

Fig. 1 Schematic diagram of the experimental setup used for pump performance investigation

Table 1 Measured dimensions and performance parameters (as per manufacturer) of the pumps used for the investigation

Sl. No.	Specification	Pump A	Pump B
1	Impeller		
	(a) Type	Closed	Closed
	(b) Material	Ni-hard	Ni-hard
	(c) No. of vanes	5	7
	(d) Impeller eye diameter (mm)	114	190
	(e) Impeller width at eye (mm)	32.5	60
	(f) Impeller inlet vane angle (degree)	23	25
	(g) Impeller outlet diameter (mm)	264	400
	(h) Impeller width at outlet (mm)	22.7	40
	(i) Impeller outlet vane angle(degree)	25	34
2	Casing		
	(a)Type	Single volute	Single volute
	(b) Material	Ni-hard	Ni-hard
	(c)Throat area (mm^2)	4700	8000
3	Suction flange size (mm)	100	150
4	Delivery flange size (mm)	50	100
5	Operating speed (rpm)	1450	1250
6	Manufacturer's data at operating speed		
	(i) Shut-off head (mwc)	20.3	34.7
	(ii) Best Efficiency Point (BEP)		
	(a) Total head (mwc)	14.5	27.1
	(b) Discharge capacity (l/s)	16.0	58.1
	(c) Pump efficiency (percent)	46.0	58.0
	(d) Pump input power (kW)	4.94	26.62
	(iii) Dimensionless specific speed (Ω_s)	0.466	0.479
	(iv) Specific speed (N_s)	1480	1521

$$N_s = \frac{n\sqrt{Q}}{(H)^{3/4}} \tag{4}$$

where n is in revolutions/min., Q is in m^3/hr and H is in mwc. This specific speed is related to the dimensionless specific speed as

$$N_s = 3176\,\Omega_s \tag{5}$$

The dimensionless specific speed of the two pumps evaluated using the manufacturer's data was observed to be nearly the same, depicting similar design. These pumps are commercially available and are being used in various industries for slurry handling duties.

Properties of Material Used. The following three materials have been used for preparing slurry for the present study:

1 Fly ash collected from a thermal power plant
2 Zinc tailings obtained from a processing plant, and
3 Bed ash collected from a coal fluidized bed combustion boiler

The comparison of physical properties of the three solid materials and their slurries is given in Table 2 and Table 3. Additionally, their particle size distribution (PSD) and settling characteristics are compared graphically in Figs. 2 and 3, respectively. Table 2 shows that the specific gravity of these materials varies in the

Table 2 Physical properties of solid materials and slurries

S. No.	Property	Fly ash	Bed ash	Zinc tailings
1	Specific Gravity	2.08	2.44	2.82
2	Representative particle size			
	(a) Weighted mean (μm)	59	209	202
	(b) Median (μm)	42	135	145
3	Final static settled concentration of slurry, % by weight	67.6	64.7	62.0
4	pH value of slurry	7–7.30 up to Cw=60%	7–7.74 up to Cw=50%	7–7.30 up to Cw=60%

Table 3 Comparison of rheological properties of slurries

Sl. No.	Rheological parameters in terms of relative viscosity and yield stress						
		Fly ash slurry		Bed ash slurry		Zinc tailings slurry	
	Cw (% by weight)	τ_y*	η_R	τ_y*	η_R	τ_y*	η_R
1	0	0	1.000	0	1.000	0	1.000
2	10	0	1.129	0	1.010	0	1.174
3	20	0	1.318	0	1.088	0	1.348
4	30	0	1.866	0	1.296	0	1.504
5	40	0.0021	4.109	0	1.636	0.0006	1.645
6	50	0.0140	16.326	0	2.762	0.0100	2.236
7	60	0.0600	48.590	-	-	-	-

*$\tau_y = 0$ corresponds to Newtonian fluid behavior otherwise the fluid behavior is Bingham.

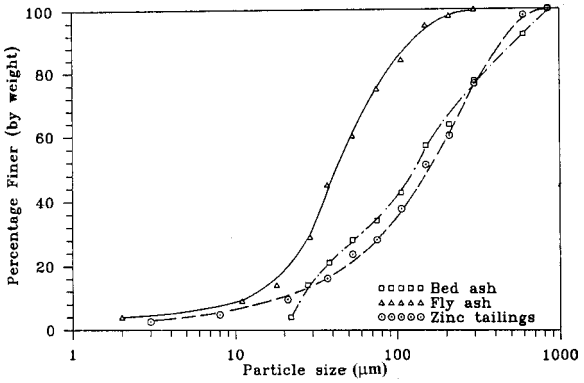

Fig. 2 Particle size distribution of different solid materials

range of 2.08–2.82. The representative particle sizes in terms of weighted mean and median diameter show the variation in the range of 59–209 μm and 42–145 μm, respectively. The final static settled concentration value for all the three materials was above 60 percent by weight. All the slurries have pH value in the range of 7–7.8 representing chemically nonreactive nature. The particle size distribution, shown graphically in Fig. 2, depicts a larger amount of finer particles in fly ash (approximately 75 percent particles are finer than 75 μm) compared to the other two materials. The zinc tailings and bed ash show nearly similar particle size distribution except that the bed ash samples did not contain particles finer than 18 μm size. Figure 3 shows that the settling rate of zinc tailings and fly ash slurries, which follow a similar pattern, whereas the bed ash slurry settles at a much faster rate. This is due to the absence of very fine particles in the bed ash, which would slow down the settling rate of bigger particles. Hence, the rheological properties of bed ash slurries were determined after preparing fresh slurry samples by removing particles bigger than 300 μm size to minimize the artifacts due to settling.

The rheological behavior of the suspensions of the three materials was determined using Weissenberg rheogoniometer at different solid concentrations and is given in Table 3. The nonzero value of yield stress for the slurry is indicative of Bingham fluid characteristics. The rheological equation for Bingham fluids is given by

$$\tau = \tau_y + \eta(du/dy) \tag{6}$$

where τ is the shear stress, τ_y is the yield stress and η is the coefficient of rigidity. Relative viscosity is defined as the ratio of Bingham's coefficient of rigidity or Newtonian dynamic viscosity of the slurry to the viscosity of water under identical conditions. Table 3 shows that the bed ash slurry follows Newtonian fluid characteristics for the tested range of solid concentration (i.e., $Cw = 50$ percent) whereas the slurries of the other two materials (zinc tailings and fly ash) follow Newtonian fluid characteristics only up to $Cw = 30$ percent, beyond which they follow Bingham fluid characteristics. At $Cw = 50$ percent, the relative viscosity of coarser slurries, namely zinc tailings and bed ash, reaches a value of 2.3 /2.75 whereas it attains a value of 16.3 for fly ash slurry. This effect could be attributed to the presence of larger amount of fine particles in the fly ash slurry. For $Cw = 60$ percent, the relative viscosity of fly ash slurry reaches a value of 48.6. It is observed that the rate of increase of yield stress for zinc tailings slurry is much smaller compared to fly ash slurry.

The comparison of the properties of the three materials shows that in spite of only small variation in the specific gravity values, their slurries exhibit quite different behavior. These materials are a good representative of the characteristics of different types of fine and coarser sized slurries generally transported through pipelines in industry and hence represent a wide variation to establish the effect of solids on the pump performance.

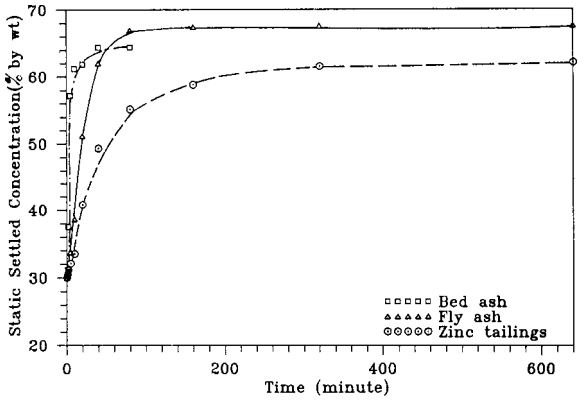

Fig. 3 Static settling characteristics of different materials

Experimental Procedure and Range of Parameters Studied

The performance of both the pumps was determined with clear water before, as well as periodically during, actual experiments so as to eliminate the possible effects of erosion of different pump components. After evaluating the performance characteristics of the pumps with water, the performance of the pumps was evaluated with the three solid materials at different solid concentrations (by weight). Care was taken to ensure that the solids were properly mixed in the mixing tank and fully suspended before taking measurements for the pump performance. The performance of pump A is evaluated at the rated speed of 1450 rpm in the range of $Cw = 13.3–60.5$ percent for fly ash, $Cw = 15.1–45.0$ percent for zinc tailings and $Cw = 12.1–52.1$ percent for bed ash. To confirm the findings on pump A and to investigate the effect of pump size on the performance, the head-capacity characteristics of a bigger sized pump (pump B) is also evaluated at the rated speed of 1250 rpm with clear water and slurries of bed ash and fly ash. During each test, two efflux samples were collected to monitor the concentration. The efflux samples collected were further analyzed for particle size distribution to detect any attrition of solid particles. The particle size distribution did not show any significant change during the tests.

Experimental Results.

(a) Performance Characteristics of Pump A. The experimental observations on pump A with water and different solid-liquid mixtures at the operating speed of 1450 rpm are presented in Figs. 4–6.

The performance characteristics of the pump with water are presented graphically in Fig. 4. It is seen that the maximum pump efficiency is about 44.5 percent. The corresponding values of head, discharge capacity, and input power are 14.46 mwc, 16.22 l/s, and 5.17 kW, respectively. These data show reasonable agreement with the data given by the manufacturer for best efficiency point (BEP) (see Table 1). The maximum flowrate that could be obtained in the test setup was around 5 percent higher than the BEP capacity quoted by the manufacturer. This restricted the operation of the pump over the entire characteristic. Evaluation of the pump performance with water was always repeated after conducting any series of experiments with the solid-liquid mixture. No significant change in the pump performance with water was seen during this experimental work.

(i) Overall Performance. Figure 4(*a*)–(*c*) gives the pump performance with bed ash slurry at five concentrations. The head-capacity curves shown in Fig. 4(*a*) depict drooping nature similar to water data. The head developed decreases with increase in concentration, the change in the head beyond 33 percent concentra-

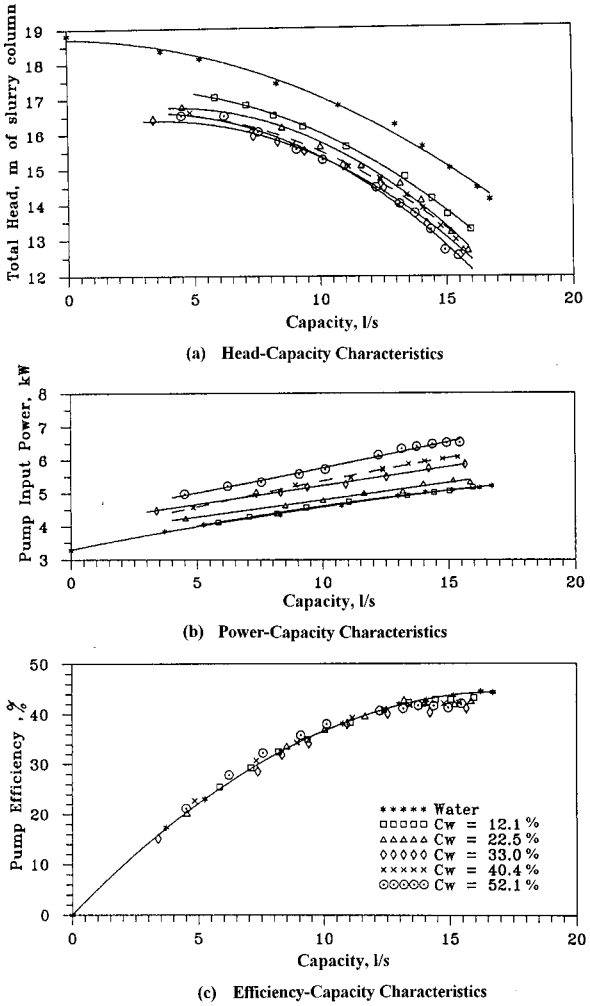

Fig. 4 Performance characteristics of pump "A" with bed ash slurry at 1450 rpm

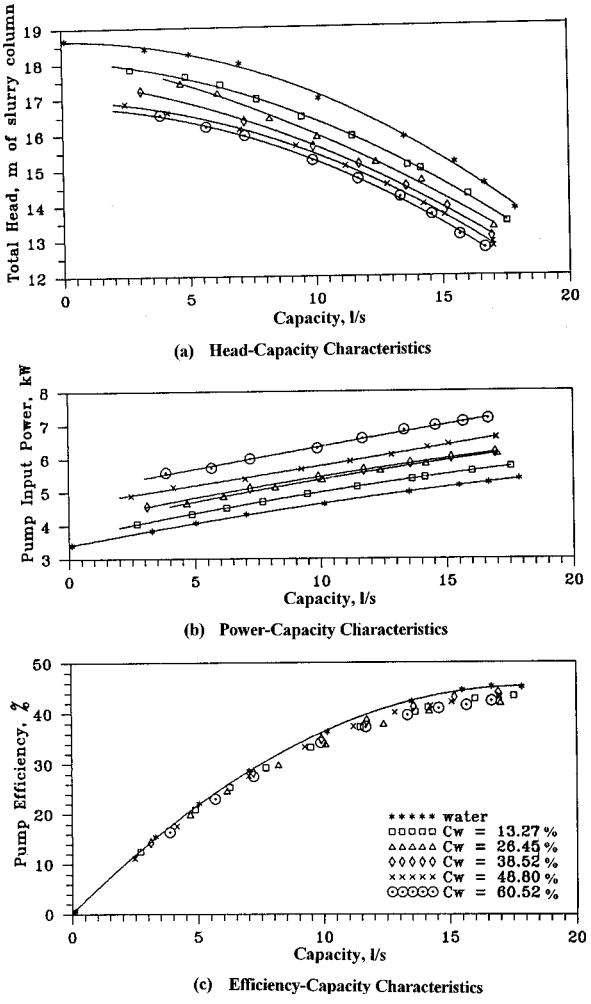

Fig. 5 Performance characteristics of pump "A" with fly ash slurry at 1450 rpm

tion is only marginal. This behavior is in line with the conclusion drawn by Stepanoff [1], based on the observations of Mano [18] for carbide slurry. The total head developed at BEP reduces with increase in concentration with the maximum drop of 2.4 m (16.6 percent relative to water) being observed at 52.1 percent solid concentration (by weight). Figure 4(*b*) shows the variation of the input power with flowrate for the same slurry. The input power is not affected significantly for $Cw=12.1$ percent, whereas the specific gravity of the mixture increases by 7.6 percent compared to water. With further increase in solid concentration, the input power increases at a rate that is lower compared to the rate of increase of mixture specific gravity. For example, at $Cw=40.4$ percent the specific gravity of the mixture increases by 31.2 percent relative to water whereas the increase in the input power relative to water performance is around 19 percent. This implies that the increase in pump power required for pumping bed ash slurries at any concentrations does not increase in the same proportion as the increase in specific gravity of the mixture. At BEP capacity (Fig. 4(*b*)), it is seen that input power increases with increase in concentration, the increase being 1.4 kW at $Cw=52.1$ percent, which is an increase of 27 percent. Figure 4(*c*) depicts the variation of efficiency with discharge rate. It is seen that there is no significant effect in the efficiency of the pump for all the tested concentrations and the variations observed are with in the measurement uncertainties. The maximum drop in head and efficiency of the pump at BEP capacity is around 2.4 m and 3.2 percent, respectively, for 52.1 percent solid concentration (by weight)in comparison to water data. Also, at the highest solid concentration tested (i.e., $Cw=52.1$ percent), the maximum efficiency point for the pump is observed at a lower flowrate compared to that of water. Similar observations have also been reported by Gahlot [19] for nearly similar type of solid material.

Figure 5(*a*)–(*c*) presents the pump performance with water and fly ash slurries at different concentrations. The head-capacity characteristics of the pump have the same drooping nature as observed for bed ash slurry (Fig. 5(*a*)). The drop in head at BEP capacity (Fig. 5(*a*)) is about 1.8 m (12.4 percent relative to water) for $Cw=60.5$ percent and nearly the same drop is seen close to the shut-off head. The variation in the power input (Fig. 5(*b*)) shows that the increase in the power required for pumping fly ash slurries is almost equal to the increase in specific gravity of the mixture at low concentrations ($Cw\leqslant 26.5$ percent by weight), whereas the increased values of power input are lower than the increase in mixture specific gravity at higher solid concentrations. This also implies that power required for pumping fly ash slurries at higher concentrations does not increase in the same proportion as the increase in specific gravity of the mixture. This same phenomenon could be attributed to the change in rheological properties of the slurry which shows Newtonian fluid behavior up to 30 percent solid concentration (by weight) and Bingham fluid behavior for higher concentrations (Table 3). At BEP capacity, the maximum increase in the input power is 1.9 kW at $Cw=60.5$ percent and corresponding absolute drop in the pump efficiency is around 2.8 percent (Fig. 5(*c*)). The pump efficiency

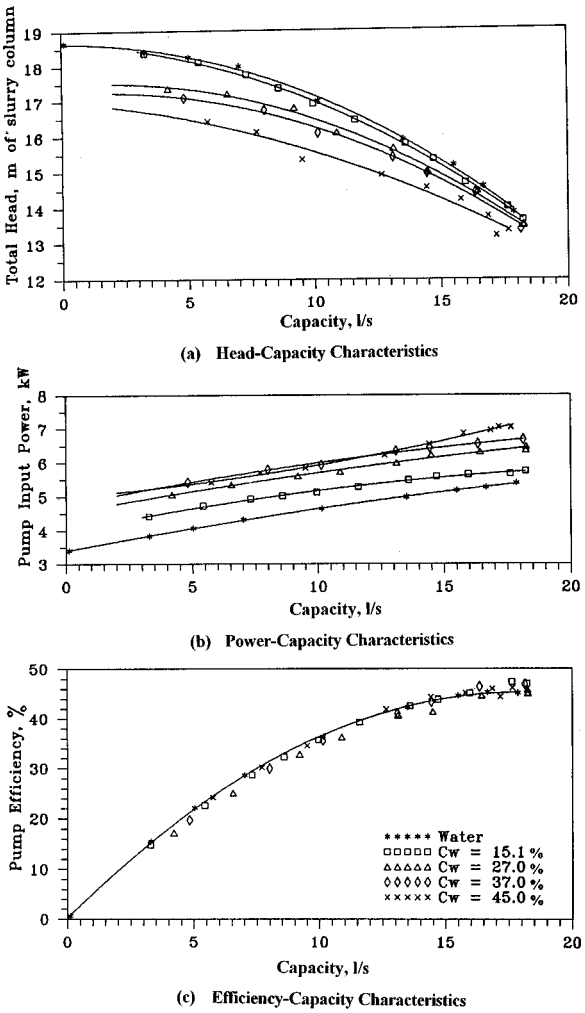

Fig. 6 Performance characteristics of pump "A" with zinc tailings slurry at 1450 rpm

variation (Fig. 5(*c*)) also shows that the pump efficiency is lower than that for water when handling slurries. The variation in the maximum efficiency for BEP capacity is within the measurement uncertainties. No shift in BEP is observed with increase in solid concentration for fly ash slurry. Similar feature has also been reported by Gahlot [19] for coal-water slurries.

Pump performance tests conducted with zinc tailings slurries up to 45 percent solid concentration (by weight) are presented graphically in Fig. 6(*a*)–(*c*). The head-capacity characteristics for zinc tailings slurry have nearly identical nature to those of bed ash slurry and fly ash slurry (Figs. 4(*a*) and 5(*a*)). However, the fall in head at low discharge rates is more than that at other discharge rates. This deviation may be attributed to the flow behavior of the mixture within the pump. Zinc tailings material contains around 28 percent particles finer than 75 μm (by weight) and around 23.5 percent particles are bigger than 300 μm size (Fig. 2). This composition of particles may be forcing the solid particles to be homogeneously distributed at higher velocities/flowrates. At low flowrates, the settling behavior of bigger particles may be causing additional head losses resulting in higher fall in head. The maximum drop in head at BEP is approximately 0.75 m (5.2 percent relative to water) and is around one third of the drop near shut-off condition. The variation in power curve at different solid concentration depicted in Fig. 6(*b*) is similar to the variation seen for fly ash slurries. The power input to the pump at BEP capacity increases with increase in solid concentration and is 1.7 kW at $Cw=45$ percent. The increase in the input power values with increase in specific gravity of the slurry at BEP capacity for different solid concentrations is found nearly as that for fly ash slurries. Figure 6(*c*) shows that the variation of absolute values of efficiency with solid concentration is within the limit of measurement uncertainties. For this slurry also, no shift in BEP is observed as in the case of fly ash slurry.

(ii) Comparison of the Performance of Pump A for Different Slurries. The pump performance evaluated for the three different types of slurries has been compared for BEP capacity. Among the three slurries, bed ash slurry has PSD representative typically of coarse slurry (without fines), zinc tailings is more representative of a commercial slurry having continuous distribution of particles from coarse to very fine size PSD and fly ash is very finely dispersed multiphase mixture, making it to behave like a single fluid for head generation and losses. The weighted mean particle diameter for bed ash and zinc tailings is nearly the same, whereas for fly ash it is less than one third of the other two materials (Table 2).

Comparison of the pump performance for absolute deviations (drop) at BEP with three materials at the rated speed of 1450 rpm has shown the following features:

(i) At the highest concentrations tested, the drop in head at BEP for coarser bed ash slurry (34 percent particles finer than 75 μm but no particles less than 18 μm) is 2.4 m, 1.7 m for fly ash slurry (75 percent particles finer than 75 μm and 14 percent particles finer than 18 μm) and 0.8 m for zinc tailings slurry having continuous particle size distribution (28 percent particles finer than 75 μm and 9 percent particles finer than 18 μm). The performance was evaluated up to a maximum $Cw=45$ percent for Zinc tailings slurry, which is the lowest among all the values of highest concentration tested for the three materials. To bring out the effect of different slurries, the head drop at BEP capacity for $Cw=45$ percent is evaluated for bed ash and fly ash slurries, also by interpolation from the measurements taken at neighboring concentrations and are evaluated as 2.35 m (16.3 percent relative to water) and 1.35 m (9.3 percent relative to water), respectively. These drops in head are significantly higher than that for the zinc tailings. This phenomenon can be explained from the differences in the rheological behavior of the slurries and the particle motion. For coarser slurry like bed ash slurry (with rapid settling characteristics), the head loss is more due to the extra energy required to keep coarser particles in motion. For the commercial slurry like zinc tailings slurry (with slow settling tendency though containing coarser particles), the head loss is minimum as the finer particles help in suspending the larger particles and hence the energy spent is lower. The increase in zinc tailings slurry viscosity is comparatively less pronounced. For fine particulate slurry like fly ash slurry (slow settling tendency), less energy is required for suspen-

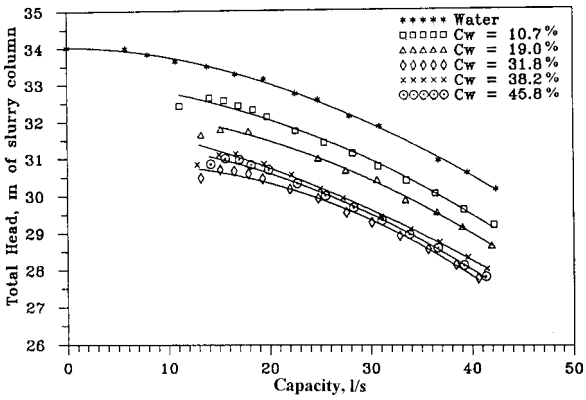

Fig. 7 Performance characteristics of pump "B" with bed ash slurry at 1250 rpm

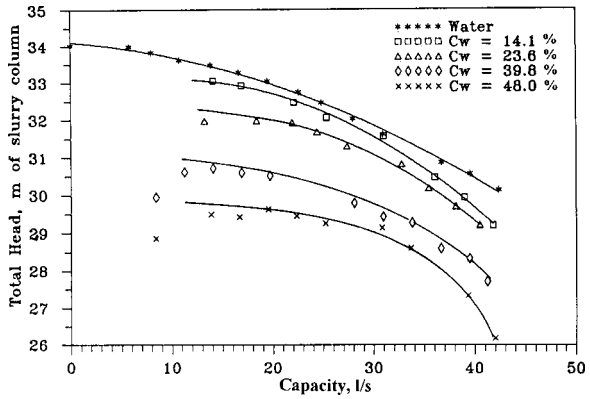

Fig. 8 Performance characteristics of pump "B" with fly ash slurry at 1250 rpm

sion of fine particles but the additional energy required to overcome the frictional losses is reasonably high due to marked increase in slurry viscosity.

(ii) Similar variation is seen in pump input power for the three materials at BEP and can be explained on the same lines as for head.

(iii) The fall in pump efficiency is higher for bed ash and fly ash slurries whereas for zinc tailing slurry it is randomly distributed over the efficiency characteristics with water. However, it is difficult to draw any conclusion from this variation as it is within measurement uncertainties.

(b) Head-Capacity Characteristics of Pump B. The head-capacity characteristics of pump B is investigated at 1250 rpm with water and two slurries namely, bed ash and fly ash to observe the effect of pump size on the characteristics. The experimental data is presented graphically in Figs. 7 and 8. Similar to pump A, the head-capacity curve has a drooping nature without any cavitation inception and unstable region of operation (Fig. 7). The experimental observations with water show the shut-off head as 34.1 mwc. The maximum discharge capacity of the pump obtained in the pilot plant test loop was 42.34 l/s at a total head of 30.1 mwc, which is only 73 percent of the BEP capacity declared by the manufacturer (Table 1). Thus the test loop has limited the flowrate range for evaluating the pump performance with water and slurries.

The head-capacity characteristics of the pump with bed ash slurry at various solid concentrations presented graphically in Fig. 7 show that the head developed decreases with increase in discharge capacity at any solid concentration following same behavior as observed with water. The head developed reduces with increase in concentration at any given discharge capacity for all concentrations except around 32 percent concentration beyond which the characteristics show basically no further drop. The relative drop in head with increase in solid concentration for higher concentrations is within experimental measurement uncertainties in head and discharge capacity of the pump. These observations are similar to pump A for the same slurry. For this pump, the performance could not be evaluated at very low flowrates due to settling of solids in the suction pipeline.

The head-capacity curves of the pump with fly ash slurry are shown in Fig. 8 which depicts similar trends as seen for pump A with the same slurry. However, the drop in head observed for this pump is not the same as seen for fly ash slurry for pump A.

Discussion

To bring out the relative pump performance with the three solid materials over the entire range, the measured data is expressed in terms of head ratio, power ratio and efficiency ratio. The power ratio (PR) is defined in this paper as under,

$$\mathrm{PR} = \frac{\text{input power drawn by the pump for slurry at any flowrate}}{\text{input power drawn by the pump for water at the same flowrate}} \tag{7}$$

To calculate these ratios accurately, at any desired discharge capacity, the head and efficiency of the pump with water and slurry are expressed as second-order polynomials, treating discharge capacity as the variable. It allows calculation of the pump head, input power and efficiency with water and slurry at any discharge capacity with an accuracy of ± 1 percent, ± 2 percent and ± 3 percent, respectively, provided measurement of flowrate is taken as accurate. This method is used to calculate HR, PR, and ER at the specified discharge capacities. It is observed that HR, PR, and ER do not vary significantly with discharge and the variation is within ± 6 percent at any concentration tested. Hence, it has been assumed that these ratios are reasonably independent of discharge. Similar results have been reported by Stepanoff [1], Kazim et al. [12], and Wilson et al. [10]

The slurry pumps are operated for large number of applications either at BEP flowrate or slightly lower than that at BEP (Want [20]) although whole operating range and appropriate design may be required for many other services. With reference to the first group, the variation in HR, PR, and ER with solid concentration are graphically presented at two flowrates corresponding to BEP and 75 percent of BEP flowrate (Figs. 9–12).

(i) Variation of HR, PR and ER for Pump A. Figure 9(*a*) shows the variation in HR for pump A for all the three materials at BEP flowrate. It is seen that the values of HR for bed ash slurry drop significantly with concentration up to $Cw = 30$ percent beyond which the drop is only marginal. For fly ash, the HR drops rapidly with concentration up to $Cw = 15$ percent but this drop is significantly lower than the drop for bed ash slurry. Beyond 15 percent concentration, the drop in HR with concentration for fly ash slurry is nearly linear. The drop in head ratio for zinc tailings with concentration is nearly linear for the concentration range tested but is very less in comparison to the other two materials. This phenomenon has also been observed by Gahlot [19] for similar pump handling zinc tailings slurry and Ni et al. [13] for a centrifugal slurry pump handling narrow sized medium sand (median diameter $= 372\ \mu$m). The comparison of the trends of variation of head ratio for different slurries shows that the value of head ratio for zinc tailings slurry is within 0.96–1.0 for all the concentrations tested indicating smaller deviations from water characteristics. The values of HR for Zinc tailings slurry are always significantly higher than that for the other two slurries. Similar variation of the head ratio for different materials is seen at 75 percent of BEP flowrate (Fig. 9(*b*)). This phenomenon again can be explained on the basis of the performance at the BEP. The weighted mean particle diameter of bed ash and zinc tailings materials is approximately the same. Hence, the above phenomenon in the pump is primarily related to the PSD and settling behavior of the slurry and their effect on the additional losses. The bed ash slurry is coarser and has nearly no fine particles to provide support to the larger particles for suspension at low velocities. Therefore,

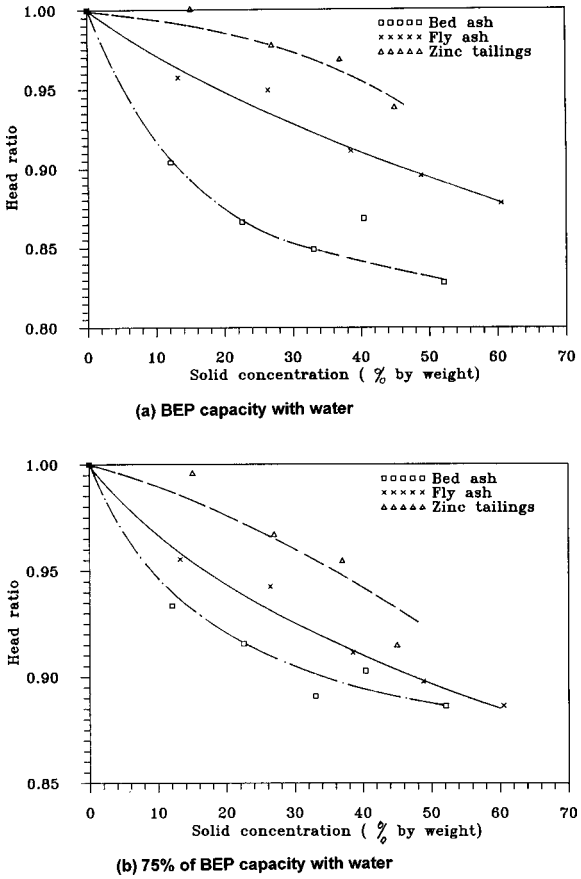

Fig. 9 Variation of head ratio with solid concentration for different solid materials at 1450 rpm (pump "A")

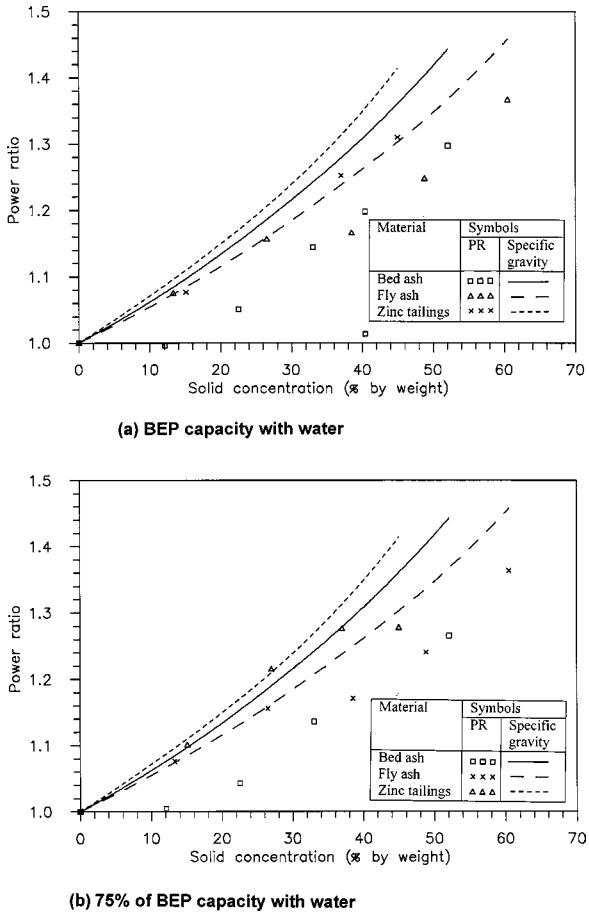

Fig. 10 Variation of power ratio with solid concentration for different solid materials at 1450 rpm (pump "A")

the head loss for coarser slurry is greater as higher energy is required to push the coarse slurry across the pump. For zinc tailings slurry, the presence of finer particles ($\leqslant 18\ \mu$m) provides support to the coarse particles and hence the additional losses are low. For this reason, the head ratio values for zinc tailings slurry are always higher than those for bed ash slurry. Wilson et al. [10] have also reported higher HR values for the rubber-lined pump handling slurry having large amount of finer particles in comparison to that for the slurry having less amount of fine particles but both having same median particle diameter. The marginal reduction in HR value for bed ash beyond 30 percent concentration (by weight) could be attributed to improved distribution (reduction in heterogeneity) of particles at higher concentrations, observed in horizontal pipelines by Mishra [21]. However, this trend has not been observed in the case of slurries of zinc tailings. The head ratio values of fly ash slurry lie in between the values of head ratios of bed ash slurry and fly ash slurry. This could be attributed to the smaller representative particle size of the fly ash and higher relative viscosity of the slurries compared to the other two slurries which is in agreement with the results available in the literature (Fairbank [2], Wiedenroth [3], Vocadlo et al. [4], Burgess and Riezes [5], Sellgren [6], Walker and Goulas et al. [7], Sellgren and Vappling, [8], Wilson et al. [10], Gahlot et al. [11], Kazim et al. [12], and Ni et al. [13]). The finer particles of fly ash are homogeneously distributed in the slurry and hence require less energy for transportation leading to higher head ratio values compared to coarser slurry of bed ash. The HR values for fly ash slurry compared to zinc tailings slurry are lower and can be attributed to the increased frictional losses due to higher viscosity (Table 3) even when it flows almost homogeneously at all solid concentrations and flowrates. The variation of HR with solid concentration for all the three materials does not show an exact linear variation with solid concentration but depends on PSD, rheological behavior of the mixture and the percentage of finer particles present.

Figure 10(*a*)–(*b*) shows the variation of PR for pump A with solid concentrations at the two flowrates. The PR increases with increase in solid concentration. However the increase in the PR is not the same as the increase in the specific gravity of the mixture. Figure 10(*a*) shows that the PR for all the three slurries is always lower than the corresponding values of the mixture specific gravity. Similar variation in PR is also observed at 75 percent of BEP capacity. This is in line with the results of Gahlot et al. [19] but do not agree fully with the findings of Ni et al. [13]. Ni et al. [13] observed variation of PR with concentration to be nearly the same as that seen in the specific gravity, for the narrow sized mixture for median particle diameters up to 372 μm but for higher particle size, PR value was always higher than the values of mixture specific gravity.

Figure 11(*a*) shows the variation in efficiency ratio at BEP capacity (Table 1) of the pump A with solid concentration for all the three slurries. It is seen that the efficiency ratio for zinc tailings slurry is randomly distributed around 1.0 at different solid concentration. The efficiency ratio for bed ash and fly ash slurries is also randomly distributed around 0.94. At 75 percent of the BEP flowrate, Fig. 11(*b*) shows that the variation in efficiency ratio for all the three slurries is in the range of 0.93–1.0 and is within the range of measurement uncertainties. Hence it is not very appropriate to draw any conclusion for the trend of variation of ER with concentration from these data.

The above experimental results show that the head, power, and efficiency of the pump are affected by the presence of suspended

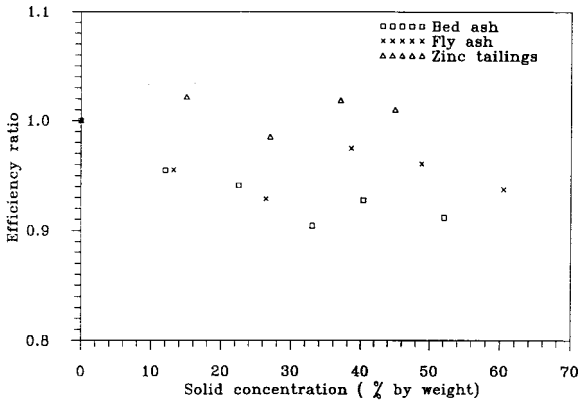

Fig. 11 Variation of efficiency ratio with solid concentration for different solid materials at 1450 rpm (pump "A")

solid particles in the carrier liquid. Comparison of the three ratios shows that the values of ER are always higher than the corresponding HR values by about 2–10 percent for all the three solid materials depending upon the concentration and properties of the solid material. Vocadlo et al. [4] have suggested that the values of head ratio and the efficiency ratio at any concentration are nearly equal for fly ash, sand, and gravel mixtures. Sellgren [6] found nearly equal values of the head and efficiency ratios at solid concentrations below 20–25 percent (by volume) for industrial minerals and ores whereas at higher concentrations the values of efficiency ratios are found to be lower than those of the head ratios.

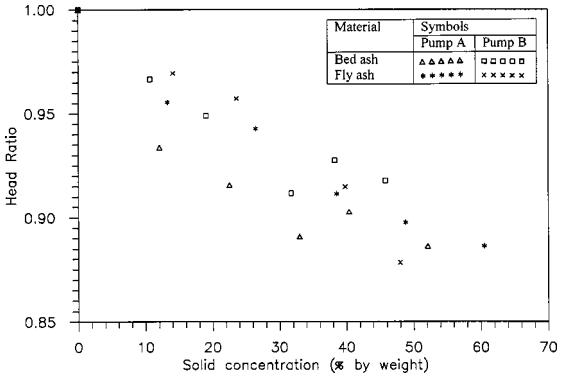

Fig. 12 Comparison of head ratio for two solid materials at 73 percent of BEP capacity of pump "B" (1250 rpm) and 75 percent of BEP capacity of pump "A" (1450 rpm)

Similar results have also been reported by Sellgren and Vappling [8] for the rubber-lined pump handling perlite material and copper tailings and by Ni et al. [13] for the pump handling narrow sized sand slurries. Kazim et al. [12] have reported that the ER is within 5 percent of the HR values on lower side for coal, zinc, iron and different Sand samples. However, Gahlot et al. [11] have shown that the efficiency ratio is always higher than the corresponding head ratio by approximately 2–9 percent at all concentrations for zinc tailings and coal slurries. The present findings are in agreement with the findings of Gahlot et al. [11]. The present findings, and those reported in the literature, suggest that the pump performance is sensitive to the changes in properties of the slurry and the pump geometry. There is a need to establish the dependence of head ratio and efficiency ratio on the above variables.

(ii) Variation of HR for Pump B. Evaluation of head ratio for pump B shows no variation with flowrate for all concentrations tested except at higher concentrations of fly ash slurry. The head ratio values calculated at 73 percent of BEP flowrate are presented graphically in Fig. 12. The head ratio values for bed ash slurry in comparison to fly ash slurry, for solid concentrations up to 37 percent by weight are lower. The rate of reduction in head ratio value is greater for bed ash slurry compared to fly ash slurry up to 32 percent concentration (by weight). Further increase in the concentration does not affect the head ratio. For fly ash slurry, the head ratio continuously decreases with increase in concentration and beyond 40 percent concentration, the values of head ratio are lower for fly ash slurry compared to that for Bed ash slurry.

(iii) Comparison of HR of Pump A and Pump B. The HR values of the two pumps for slurries of bed ash and fly ash are compared at capacity corresponding to nearly similar fraction of their BEP capacity with water in Fig 12. The comparison shows that the HR values for bed ash slurry (in the tested range of concentration) and for fly ash slurry (up to $Cw=40$ percent) are tendentiously lower for pump A. This suggests that the additional head loss for the slurry flow decreases with increase in pump size. Such tendency is more evident in the literature, as observed by Wiedenroth [3], Sellgren [6], and Wilson et al. [10]. They have attributed this phenomenon to increased flow passages in larger pumps.

Conclusions

From the present experimental investigations on the pump characteristics with different slurries, following broad conclusions can be drawn:

1 The head and efficiency of the pump decrease with increase in solid concentration, particle size, and slurry viscosity, the decrease in the head being 2–10 percent higher than that of the efficiency. The presence of finer particles ($<18\,\mu$m) in coarser slurries substantially attenuate the loss of performance of the pump in terms of head and efficiency.

2 At low solid concentrations (<30 percent by weight), the increase in the pump input power is directly proportional to the specific gravity of slurry whereas the same relationship is not applicable at higher concentrations. The variation of the efficiency ratio is within the measurement uncertainties.

3 The study on the pumps has basically confirmed that the additional head loss for slurries decrease with increase in the pump size.

Acknowledgment

This study was supported by funds from Fly Ash Mission, Department of Science and Technology, Govt. of India. Dr. B. K. Gandhi was deputed to Indian Institute of Technology, Delhi under QIP scheme of All India Council of Technical Education, Ministry of Human Resource Development, Govt. of India.

Nomenclature

HR = head ratio
PR = power ratio
ER = efficiency ratio
Cw = solid concentration by weight (percent)
η_R = relative viscosity
τ_y = yield stress (N/m^2)
Ω_s = dimensionless specific speed (rad/s, m^3/s, m)
N_s = specific speed (rpm, m^3/hr, m)

References

[1] Stepanoff, A.J., 1965, *Pumps and Blowers, Two Phase Flow - Flow and Pumping of Solids in Suspension and Fluid Mixtures*, J. Wiley, NY.
[2] Fairbank, L. C., 1942, ''Effect on the Characteristics of Centrifugal Pumps,'' in ''Solids in Suspension Symposium,'' Trans. ASME, **107**, pp. 1564–1575.
[3] Wiedenroth, W., 1970, ''The Influence of Sand and Gravel on the Characteristics of Centrifugal Pumps, Some Aspects of Wear in Hydraulic Transportation Installations,'' Hydrotransport 1, BHRA Fluid Engg., Warwick, Paper E1.
[4] Vocadlo, J.J., Koo, J.K., and Prang, A.J., 1974, ''Performance of Centrifugal Pumps in Slurry Service,'' Hydrotransport 3, BHRA Fluid Engg., Colorado, Paper J2.
[5] Burgess, K.E., and Riezes, S.A., 1976, ''The Effect of Sizing, Specific Gravity and Concentration on the Performance of Centrifugal Slurry Pumps,'' Proc. Inst. Mech. Eng., **190**, No. 36/76, pp. 391–399.
[6] Sellgren, A., 1979, ''Performance of a Centrifugal Pump when Pumping Ores and Industrial Minerals,'' Hydrotransport 6, BHRA Fluid Engg., Canterbury U.K., Paper G1.
[7] Walker, C.I., and Goulas, A., 1984, ''Performance Characteristics of Centrifugal Pumps when Handling Non-Newtonian Homogeneous Slurries,'' Proc. Inst. Mech. Eng., **198A**, No. 1, pp. 41–49.
[8] Sellgren, A., and Vappling, L., 1986, ''Effects of Highly Concentrated Slurries on the Performance of Centrifugal Pumps,'' Proc. International Symposium on Slurry Flows, FED, ASME, USA, Vol. 38, pp. 143–148.
[9] Sellgren, A., Turner, T.M., and Addie, G.R., 1990, ''Determination of the Effect of Solids on Centrifugal Slurry Pumps,'' Fifth Annual AIME Regional Phosphate Conference, Lokeland, Florida.
[10] Wilson, K.C., Addie, G.R., and Clift, R., 1992, *Slurry Transport using Centrifugal Pumps*, Elsevier, New York.
[11] Gahlot, V.K., Seshadri, V., and Malhotra, R.C., 1992, ''Effect of Density, Size Distribution, and Concentration of Solid on the Characteristics of Centrifugal Pumps,'' ASME J. Fluids Eng., **114**, pp. 386–389.
[12] Kazim, K.A., Maiti, B., and Chand, P., 1997, ''A Correlation to Predict the Performance Characteristics of Centrifugal Pumps handling Slurries,'' Proc. Inst. Mech. Eng., **211**, Part A, pp. 147–157.
[13] Ni, F, Vlasblom, W. J., and Zwartbol, A. 1999, ''Effect of High Solid Concentration on Characteristics of a Slurry Pump,'' Hydrotransport 14, BHRA Fluid Engg., Maastricht, The Neatherland, pp. 141–149.
[14] Chand, P., Adinarayana, B., and Singh, R. P., 1985, ''Effect of Drag Reducing Polymers on Slurry Pump Characteristics,'' Bulk Solids Handling, **5**, No. 4, pp. 807–811.
[15] IS : 5120 1990, ''Technical Requirements for Rotodynamic Special Purpose Pumps,'' First Revision, Bureau of Indian Standards, New Delhi.
[16] BS 5316 : Part 1, 1976, ''Acceptance Tests for Centrifugal, Mixed Flow and Axial Pumps - Part 1. Class C Tests,'' Gr 8, British Standards Institution, London.
[17] Fox, R. W., and McDonald, A. T., 1995, *Introduction to Fluid Mechanics*, Fourth edition, J. Wiley, New York.
[18] Mano, 1955, ''Conveyance of Carbide Slurry,'' Journal of JSME, **62**, No. 485, pp. 927–933 (in Japanese).
[19] Gahlot, V.K., 1987, ''Studies on the Effect of Particle Size Distribution and Material Properties on the Rheological Parameters of Slurries and the Performance of Slurry Pumps,'' Ph.D. thesis, Indian Institute of Technology, Delhi.
[20] Want, F.M., 1980, ''Centrifugal Slurry Pump Wear-Plant Experience,'' Hydrotransport 7, BHRA Fluid Engg., Sendai, Japan, Paper H1.
[21] Mishra, Rakesh, 1996, ''A Study on the Flow of Multi-sized Particulate Solid-Liquid Mixtures in Horizontal Pipelines,'' Ph.D. thesis, I.I.T. Delhi.

Flow Control of Rotating Stall in a Radial Vaneless Diffuser

Hiromu Tsurusaki
Professor

Takahiro Kinoshita
Former Graduate Student

Department of Mechanical Engineering,
Fukuyama University,
Fukuyama, Hiroshima 729-0292 Japan
e-mail: htsu@fume.fukuyama-u.ac.jp

The instabilities of a backflow layer on a diffuser wall and the main flow with vorticity have already been shown theoretically to cause the occurrence of rotating stall in a vaneless diffuser. These instabilities, however, have not yet been proven to exist experimentally. This study was carried out to examine the factors contributing to the occurrence of rotating stall using a jet installed in a diffuser. Rotating stall was completely suppressed by a jet that was set in the direction opposite to the vector of the impeller peripheral velocity, and amplified by the jet set in the same direction as that vector. The effects of the jets were confirmed by the experiment using the jets installed at positions other than the neighborhood of the diffuser wall. The results suggest that the instability of the main flow contributes to the onset of rotating stall. The factors contributing to the onset of rotating stall and the effect of the jet on the performance of the impeller-diffuser combination are discussed. [DOI: 10.1115/1.1351174]

Introduction

It is well known that rotating stall occurs in the vaneless diffuser of a centrifugal fan/compressor. The fluid oscillation due to rotating stall in many cases limits the stable operation range of the turbomachine. Many of the studies that were carried out on rotating stall in vaneless diffusers dealt with the flow patterns present during rotating stall (Tsurusaki et al. [1]), the methods for predicting the initiation flow rate and rotational speed of stall cells based on experimental results (Kinoshita and Senoo [2], Tsurusaki et al. [3]), and passive/active control methods (Abdelhamid [4], Yoshida et al. [5], Kurokawa et al. [6]). The instabilities that occur between the backflow layer on the diffuser wall and the main flow with vorticity were identified as factors contributing to the occurrence of rotating stall by theoretical analyses (Jansen [7], Abdelhamid [8]). The unsteady interaction between the inviscid main flow and the boundary layers was studied as a theoretical model of rotating stall (Frigne and Van den Braembussche [9]). At the critical flow rate for the onset of rotating stall, the flow angles were measured near the diffuser wall along the radius of the diffuser (Imaichi and Tsurusaki [10]). In the experiment, the radial extent of the backflow layer at the critical flow rate was estimated to be about 15 percent of the diffuser radial length. For convenience, the flow rate when the backflow layer develops on the diffuser wall can be considered the initiation flow rate of rotating stall. However, the process of the transition of the backflow layer to rotating stall, and the instability of the main flow itself remain to be clarified. The mechanism of the occurrence of rotating stall remains unknown.

The main objective of this study is to examine experimentally the factors contributing to the occurrence of rotating stall. To this end, a jet was introduced into the flow to control rotating stall. The jet was directed parallel to the diffuser wall. The effect of the jet on the performance of the impeller-diffuser combination is also discussed.

Experimental Apparatus

The experimental apparatus is shown in Fig. 1. Air pressurized in the booster blower was piped into a flow meter, the suction pipe, the two-dimensional centrifugal impeller, and the parallel walled vaneless diffuser, and finally emitted to the atmosphere. The impeller was driven by a motor at a rotational speed of 2100 rpm. The specifications of the impeller and the vaneless diffuser are shown in Table 1.

The jet used in the experiment was constructed as follows. Air pressurized in the blower was introduced into the flow meter, the flow distributer, the vinyl tubes and nozzles, and then flowed out from nozzle-holes 1 mm in diameter (Fig. 2) in the direction parallel to the diffuser wall. The velocity of the jet was 61 m/s. Eight nozzles were arranged at the same azimuthal intervals on a circle with $r/r_2 = 1.06$. The flow direction of the jet was set by a protractor attached to the nozzle. All of the vinyl tubes had the same length so that the flow rates through each of the jets were the same. The total flow rate of the eight jets was 23 (l/min), which was equivalent to 3% of the flow coefficient $\phi = 0.074$ when rotating stall was fully developed. This value was fixed regardless of the flow direction of the jet.

Measurement Method

A semiconductor-type pressure transducer was mounted at the position $r/r_2 = 1.06$ on the wall, in the neighborhood of the diffuser inlet. The frequency spectra of the pressure fluctuations were measured using a FFT analyzer. A frequency spectrum was obtained from the ensemble average of 128 spectra by using an averaging function of the FFT analyzer. The measurement system is shown in Fig. 3(*a*). The pressure measurement point and the nozzle position were located at different azimuthal locations. It was confirmed that the influence of the jet on the measured value of the pressure fluctuation was negligible. The stall cell number λ was obtained from the equation $\lambda = \delta/\gamma$, by using the phase difference δ (degree) of the pressure fluctuations measured at two points located apart γ (degree) on the circle with $r/r_2 = 1.06$. The

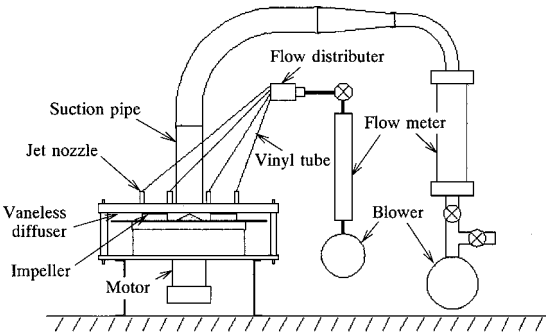

Fig. 1 Experimental apparatus

Contributed by the Fluids Engineering Division for publication in the JOURNAL OF FLUIDS ENGINEERING. Manuscript received by the Fluids Engineering Division September 21, 1999; revised manuscript received December 1, 2000. Associate Editor: D. Williams.

Table 1 Specifications of impeller and vaneless diffuser

Impeller		Vaneless diffuser	
Inlet diameter	80 mm	Inlet dimeter	171 mm
Outside diameter	171 mm	Outside diameter	340 mm
Blade height	17 mm	Width	17.5 mm
Inlet angle	25.5°		
Discharge angle	22.5°		
Number of blades	8		

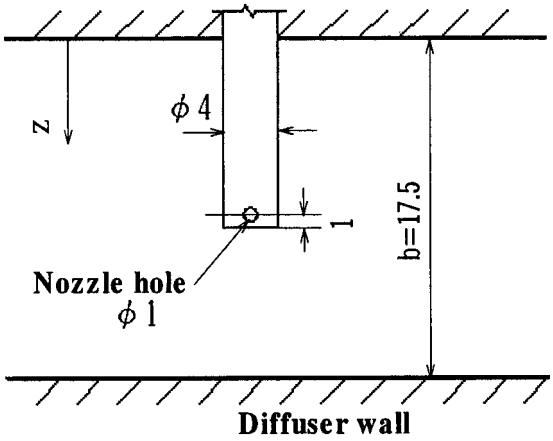

Fig. 2 Jet nozzle inserted in diffuser

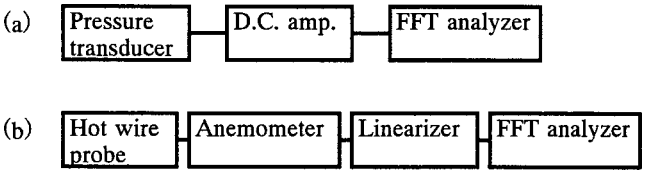

Fig. 3 Measurement systems of pressure fluctuation (*a*) and of velocity fluctuation (*b*)

phase difference was obtained from the phase of the cross spectrum between the two points. The rotational speed, f_r, of the stall cell was determined from $f_r = f/\lambda$, by using the fundamental frequency, *f*, of rotating stall and the cell number λ.

An I-type hot wire probe was inserted vertically into the diffuser at the position $r/r_2 = 1.52$, and the frequency spectra of the velocity fluctuations were measured at several points located along the diffuser depth. In the measurements, the wire of the probe was aligned with the radial direction of the diffuser. The measurement system is shown in Fig. 3(*b*).

The performance of the impeller-diffuser combination was obtained by the measurement of the pressure difference between the diffuser exit and the impeller inlet.

Experimental Results and Discussion

Conditions of Rotating Stall. Figure 4 shows the frequency spectra of the pressure fluctuation measured at $r/r_2 = 1.06$. The flow coefficient ϕ of the impeller was varied between 0.116 and zero. Three groups of discrete frequencies due to rotating stall of the vaneless diffuser are observed. The stall cell number of each group is 1, 2, and 3 from the left in the figure.

Figures 5(*a*) and 5(*b*) show the variation of nondimensional amplitude of the fundamental component of the pressure fluctuation with the flow coefficient ϕ, and that of nondimensional rotational speed of the stall cell, respectively. The points shown as zeros indicate that rotating stall was not observed in the measurement. The flow coefficient for the shock-free entry of the tested

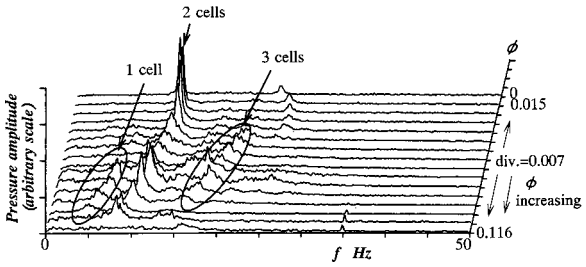

Fig. 4 Frequency spectra of pressure fluctuation. Uncertainty of data: *f*: ±0.125 Hz, ϕ: ±0.001, pressure amplitude: ±6%.

impeller is 0.104, which means that rotating stall of the vaneless diffuser was initiated at a flow rate slightly higher than that. By comparing the rotational speed of the stall cell with that measured previously (Tsurusaki et al. [3]), it was judged that the fluctuation measured here was due to rotating stall of the vaneless diffuser.

When $0.03 < \phi < 0.10$, the 1-, 2-, and 3-cell components appear at the same flow rate, but they have different rotational speeds. As the flow rate decreases to the region of $0 < \phi < 0.05$, the amplitude of 2-cell component becomes large, while other components become small and finally disappear.

Dependence of Control Effect on the Flow Angle of Jet. The variation of the pressure fluctuation (nondimensional amplitude of the fundamental component) with the flow angle θ of the

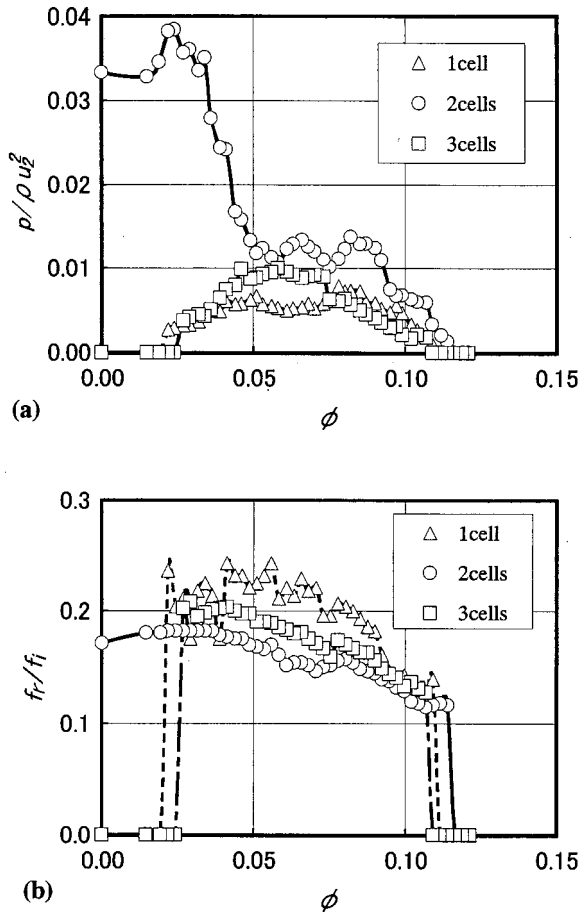

Fig. 5 (*a*) Nondimensional pressure amplitude and (*b*) rotational speed ratio of cells. Uncertainty of data: ϕ: ±0.001, $p/\rho u_2^2$: ±6%, f_r/f_i: ±0.004 (1 cell), ±0.002 (2 cells), ±0.001 (3 cells).

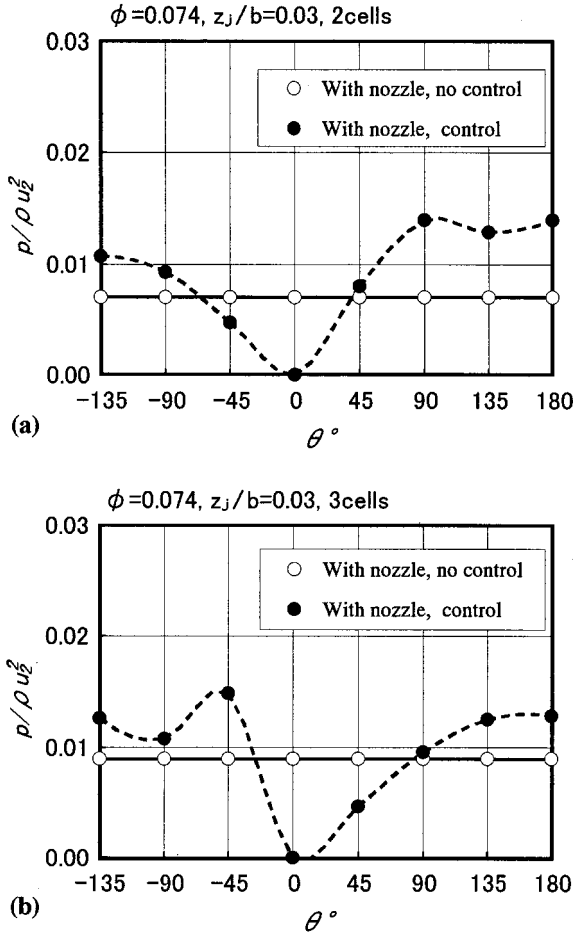

Fig. 6 Dependence of control effect on jet direction (*a*) 2-cell component and (*b*) 3-cell component. Uncertainty of data: θ: ±1 deg, $p/\rho u_2^2$: ±6%.

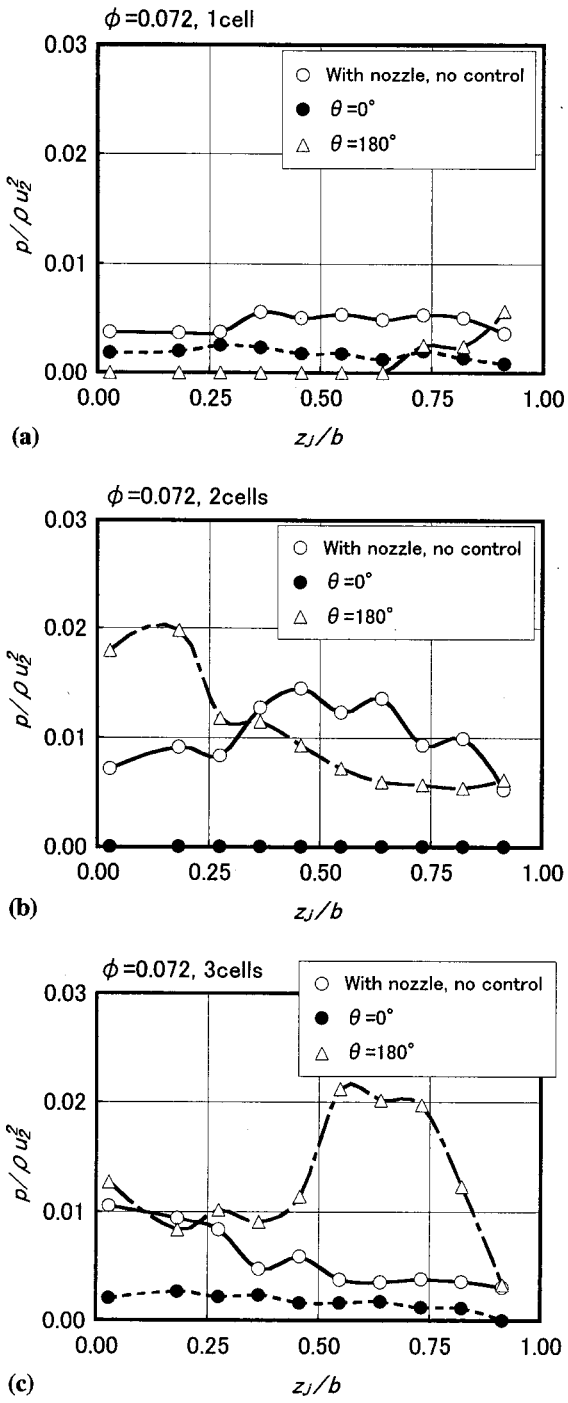

Fig. 7 Dependence of control effect on jet position (*a*) 1-cell component, (*b*) 2-cell component, and (*c*) 3-cell component. Uncertainty of data: z_j/b: ±0.03, $p/\rho u_2^2$: ±6%.

jet installed at $z_j/b=0.03$ is shown in Figs. 6(*a*) and 6(*b*). Solid and open circles represent the cases with and without the jet, respectively. $\theta=0$ designates the direction which is opposite to the vector of the impeller peripheral velocity, $\theta=90$, the diffuser outlet direction, and $\theta=180$, the direction of the impeller peripheral velocity vector. At $\phi=0.074$, rotating stall cells (2 and 3 cells) were completely controlled by the jet in the $\theta=0$ direction, and amplified by the jet oriented in the $\theta=180$ direction. However, at $\phi=0$, rotating stall was not amplified by the jet oriented in the $\theta=180$ direction, although it was suppressed by the jet over a wide range of θ. The same experiments were carried out with the jet positioned at $z_j/b=0.46$ and 0.91, at $\phi=0.074$ and $\phi=0$. In those experiments, the suppression was achieved over a wide range of θ regardless of the cell number; however, no amplification was observed.

Dependence of Control Effect on the Location of Jet. As the dependence of the control effect on the flow angle of the jet was clarified, the location of the jet was changed along the diffuser depth direction for two cases of $\theta=0$ and 180. Figures 7(*a*)–7(*c*) show the results at $\phi=0.072$, where the abscissa designates the location of the jet. Open circles represent the case where the jet was not activated, although the nozzles were inserted into the diffuser. Solid circles and triangles represent the case of $\theta=0$ (suppression) and $\theta=180$ (amplification), respectively. At this flow rate, the 1-, 2-, and 3-cell components coexist under the condition without control. In the case of $\theta=0$, all components were controlled regardless of the jet location, and especially the 2-cell component disappeared completely. However, the effect of amplification in the case of $\theta=180$ varies according to the jet location. The 2-cell component was amplified by the jet near $z_j/b=0$. The 3-cell component was amplified by the jet between $z_j/b=0.5$ and 0.8, and at the same time the 2-cell component was suppressed. The 1-cell component was suppressed even in the case of $\theta=180$ except in the neighborhood of $z_j/b=1.0$.

Figure 8 shows the results measured at $\phi=0$. The 2-cell component was amplified by the jet in the $\theta=180$ direction near $z_j/b=0.5$, but it was suppressed near $z_j/b=0$.

It became clear that rotating stall was amplified or suppressed by the jet even when it was installed at positions other than the

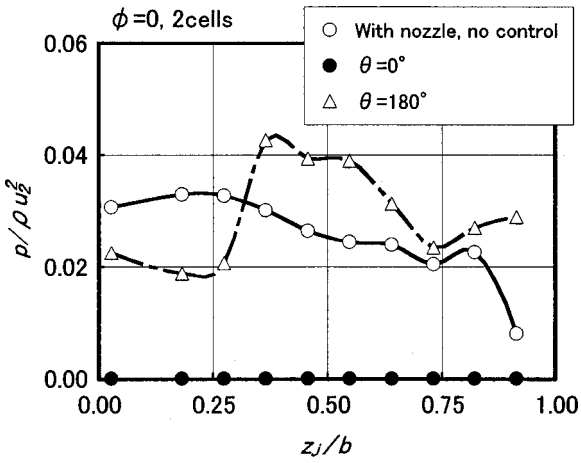

Fig. 8 Dependence of control effect on jet position. Uncertainty of data: z_j/b: ±0.03, $p/\rho u_2^2$: ±6%.

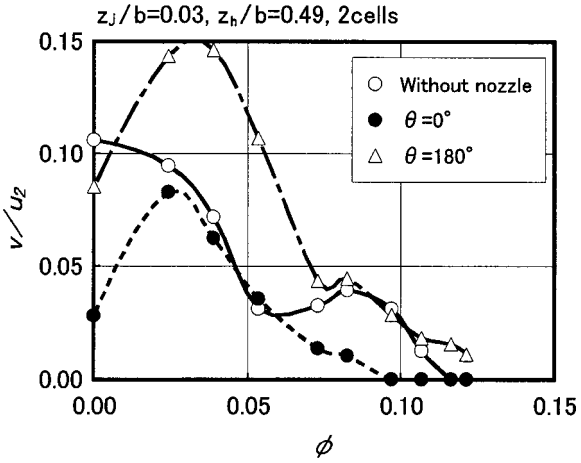

Fig. 10 Dependence of control effect on flow coefficient (velocity fluctuation). Uncertainty of data: ϕ: ±0.001, v/u_2 : ±6%.

neighborhood of the diffuser wall. This shows that the flow near the wall (backflow) is not the only factor contributing to the occurrence of rotating stall. The instability of the main flow may have also caused rotating stall.

Dependence of Control Effect on Flow Rate. The jet was introduced at $z_j/b=0.03$, and pressure and velocity fluctuations were measured at several flow coefficients. Figures 9(*a*) and 9(*b*) show the results for 2- and 3-cell components. Open circles represent the case where the jet nozzle is not inserted into the diffuser, and solid circles and triangles represent the cases of $\theta=0$ and 180, respectively. In the case of the jet directed at $\theta=0$, rotating stall was completely suppressed at a comparatively high flow rate, but it was not suppressed by the jet velocity used in this experiment at a low flow rate. In the case of the jet at $\theta=180$, the 3-cell component was amplified at $0.08<\phi<0.12$, but suppressed at $0.03<\phi<0.08$. The 2-cell component was amplified over the range $0.03<\phi<0.08$. This phenomenon was also observed under the conditions without control.

Figure 10 shows the velocity fluctuations for the 2-cell component measured inside the diffuser at $r/r_2=1.52$ by using a hot wire probe whose wire was set in the radial direction. Rotating stall was completely suppressed at a comparatively high flow rate, and amplified at low flow rates except for the zero flow rate case. From this experiment, it is obvious that suppression and amplification of rotating stall occur not only at the inlet but also inside of the diffuser.

Change of the Rotational Speed of Stall Cells Due to Control. Figure 11 shows the variation of the nondimensional rota-

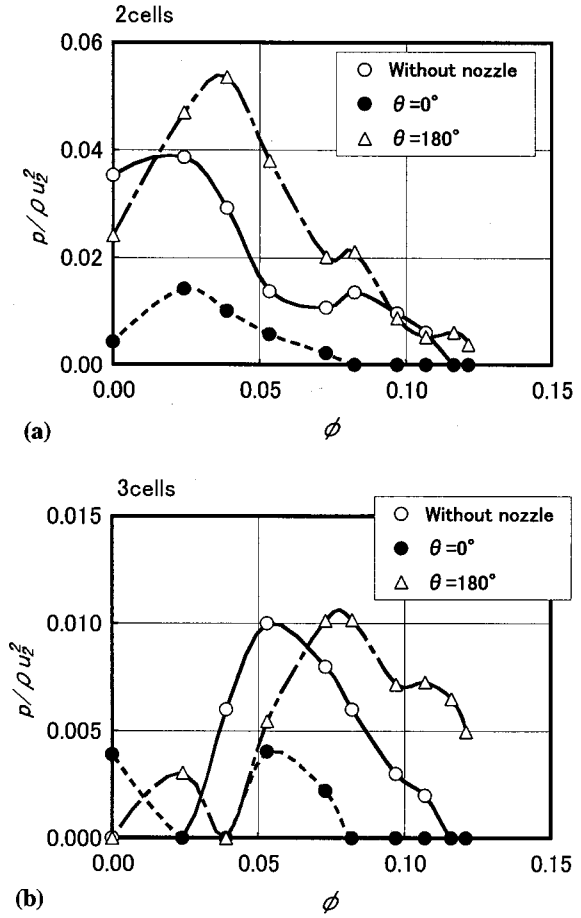

Fig. 9 Dependence of control effect on flow coefficient (pressure fluctuation) (*a*) 2-cell component and (*b*) 3-cell component. Uncertainty of data: ϕ: ±0.001, $p/\rho u_2^2$: ±6%.

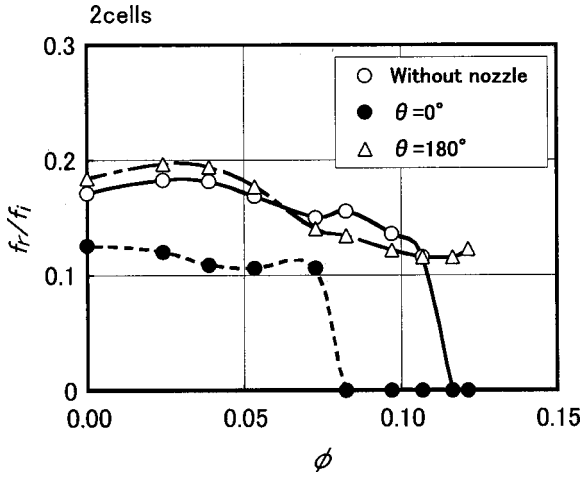

Fig. 11 Dependence of control effect on flow coefficient (rotational speed ratio of cells). Uncertainty of data: ϕ: ±0.001, f_r/f_i: ±0.002.

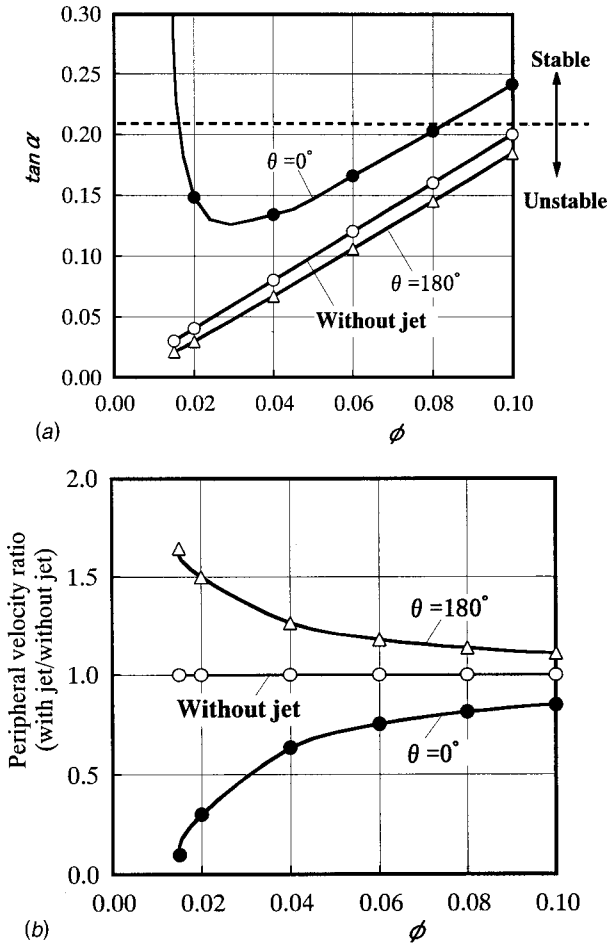

Fig. 12 (*a*) Effect of jet on flow angle of main flow (calculated) and (*b*) effect of jet on peripheral velocity of main flow (calculated, $r/r_2=1.5$)

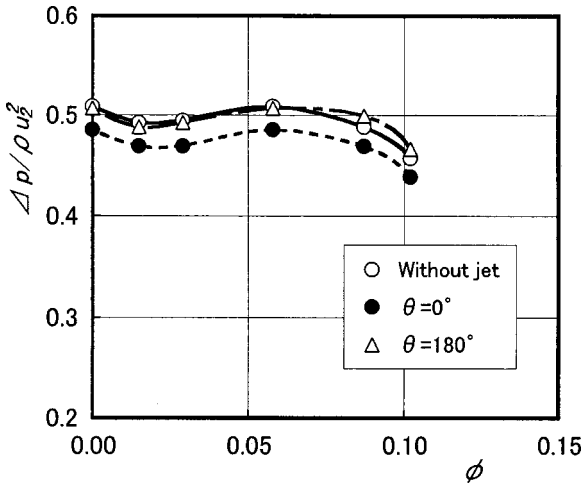

Fig. 13 Effect of jet on performance of tested fan. Uncertainty of data: ϕ: ±0.001, $\Delta p/\rho u_2^2$: ±0.02.

tional speed of the stall cells for the two cases of jet directions, $\theta=0$ and 180, where the jet was set at $z_j/b=0.03$. Open circles represent the case where the nozzles were not inserted. With the jet at $\theta=180$, the rotational speed of the cells was increased slightly at low flow rates compared to the case without the nozzle. This is based on the increment of the time-averaged peripheral velocity of the flow. It is established theoretically (Abdelhamid [8]) and experimentally (Tsurusaki et al. [3]) that the rotational speeds of the cells are proportional to the peripheral velocity of the flow. The rotational speed of the cells was decreased markedly when rotating stall was suppressed by the jet at $\phi=0$. Though the jet velocity was the same for the two cases of $\theta=0$ and 180, the degree of change of the rotational speed of the cells was quite different. This remarkable effect of the jet is discussed in detail in the next section.

Consideration of Effect of Jet. The effect of the jet on the flow stability, that is, suppression/amplification of rotating stall, can be explained based on the conservation law of the moment of momentum. From the equations of the moment of momentum and continuity, the flow angles and the nondimensional peripheral velocities for the two cases of $\theta=180$ and $\theta=0$ are expressed, assuming $r_j=r_2$ for simplicity of calculation, as

$$\tan\alpha=\phi(1+m)^2/\zeta(1\pm m\xi),$$

$$c_u/u_2=\zeta(r_2/r)(1\pm m\xi)/(1+m),$$

where + and − denote the cases of $\theta=180$ and $\theta=0$, respectively, m=flow rate of the jet/flow rate of the impeller, ζ=peripheral velocity of the main flow/peripheral velocity of the impeller at $r=r_2$, and ξ=peripheral velocity of the jet/peripheral velocity of the main flow at $r=r_2$. ζ can be assumed to be a constant value of 0.5 from the previous experiment (Tsurusaki et al. [3]), ξ is equal to 6 in the present experiment, and ''m'' is varied as the flow rate of the impeller changes.

Figure 12(*a*) shows the variation of ''tan α'' according to the flow coefficient. The critical flow coefficient for the onset of rotating stall is 0.105 in the case without nozzle (Fig. 9(*a*)). The dotted line in Fig. 12(*a*) was located so that the flow coefficient in the intersection point of the dotted line with the curve ''without jet'' extended was 0.105. In the case of $\theta=0$, the flow angle becomes large at both large and very small flow coefficients. In the previous studies (Jansen [7], Abdelhamid [8]), it was established that the flow is stable at large flow angles. Therefore, this calculated result shows that the flow becomes stable. In the case of $\theta=180$, the flow angle becomes small, therefore, the flow remains unstable. Although the present consideration is based on the averaged value of the flow angle along the diffuser depth, the result on the flow stability agrees qualitatively with the measured results.

Figure 12(*b*) shows the variation of the peripheral velocity ratios calculated at $r/r_2=1.5$ with the flow coefficient. The increment of the peripheral velocity due to the jet at $\theta=180$ is smaller than the decrement of that due to the jet at $\theta=0$. The changes of the measured rotational speeds of the cells due to the jets (Fig. 11) are qualitatively conformable with the changes of the peripheral velocity calculated over the range $0<\phi<0.05$. The peripheral velocity calculated in the case of $\theta=180$ becomes very large at very low flow coefficients. However, in the case of $\theta=180$, the real peripheral velocity will not be so large at very low flow coefficients, because the pressure fluctuation (Fig. 9(*a*)) and the rotational speed of the cells (Fig. 11) are not so large compared to those measured in the case without jet.

The effect of the jet on the performance of the impeller-diffuser combination is shown in Fig. 13 over the range of ϕ when rotating stall occurred. In the case of $\theta=0$, a five percent decrement of the pressure rise is observed compared to the case without jet. This is due to the decrement of the peripheral velocity of the flow (Fig. 12(*b*)). In the case of $\theta=180$, in spite of the increment of the peripheral velocity, the pressure rise is nearly equal to that in the case without jet. It is believed that kinetic energy given by the jet was almost dissipated in the diffuser due to rotating stall strengthened with the jet.

Uncertainty Estimation

The uncertainties in the measured data were estimated using a formula for propagation of errors given in ASME PTC19.1-1985.

Conclusions

The main results of this study are as follows:

1 It is believed that the instability of the main flow contributes to the occurrence of rotating stall.

2 Rotating stall can be suppressed or amplified by the jet set in the directions of $\theta=0$ or 180, respectively. In particular, rotating stall is completely suppressed at a comparatively high flow rate. However, the performance of the impeller-diffuser combination is reduced with the control jet at $\theta=0$.

3 The control effect of a jet on rotating stall can be explained qualitatively using the conservation law of the moment of momentum.

4 The phenomenon that the alternate amplification/suppression of the 2- and 3-cell components with the flow coefficient was observed (Figs. 9(*a*) and 9(*b*)).

Acknowledgment

The authors wish to thank Mr. T. Yokota, who is a former graduate student of Fukuyama University, for his cooperation in the experiment.

Nomenclature

- b = diffuser width (m)
- c = velocity of the flow (m/s)
- f_i = rotational speed of the impeller (rps)
- f_r = rotational speed of the stall cell (rps)
- p = pressure amplitude of the fundamental component of rotating stall (Pa)
- r = radius (m)
- u = impeller peripheral velocity (m/s)
- v = velocity amplitude of the fundamental component of rotating stall (m/s)
- z = position measured from the upper wall of the diffuser (m)
- α = flow angle measured from the tangent of the diffuser (degree)
- Δp = pressure rise of impeller-diffuser combination (Pa)
- θ = flow angle of the jet (degree)
- ρ = air density (kg/m^3)
- ϕ = flow coefficient (radial velocity/impeller peripheral velocity at impeller outlet)

Subscripts

- 2 = impeller outlet (diffuser inlet)
- h = hot wire probe
- j = jet
- u = peripheral direction

References

[1] Tsurusaki, H., et al., 1984, ''Rotating Stall in a Vaneless Diffuser of a Centrifugal Fan (2nd Report, Instantaneous Flow Condition),'' Turbomachinery, **12**, No. 6, pp. 323–332 (in Japanese).

[2] Kinoshita, Y., and Senoo, Y., 1985, ''Rotating Stall Induced in Vaneless Diffusers of Very Low Specific Speed Centrifugal Blowers,'' ASME J. Eng. Gas Turbines Power, **107**, No. 2, pp. 514–521.

[3] Tsurusaki, H. et al., 1987, ''A Study on the Rotating Stall in Vaneless Diffusers of Centrifugal Fans,'' JSME Int. J., **30**, No. 260, pp. 279–287.

[4] Abdelhamid, A. N., 1987, ''A New Technique for Stabilizing the Flow and Improving the Performance of Vaneless Radial Diffusers,'' ASME J. Turbomach. , **109**, No. 1, pp. 36–40.

[5] Yoshida, Y. et al., 1992, ''Active Control of Vaneless Diffuser Rotating Stalls,'' Trans. JSME , **58**, No. 554, pp. 3067–3073 (in Japanese).

[6] Kurokawa, J., et al., 1997, ''A New Passive Control of Rotating Stall in Vaneless and Vaned Diffusers by Shallow Grooves,'' *Proceedings JSME International Conference on Fluid Engineering*, Vol. 2, pp. 1109–1114.

[7] Jansen, W., 1964, ''Rotating Stall in a Radial Vaneless Diffuser,'' ASME J. Basic Eng., **86**, No. 4, pp. 750–758.

[8] Abdelhamid, A. N., 1980, ''Analysis of Rotating Stall in Vaneless Diffusers of Centrifugal Compressors,'' ASME Paper, 80-GT-184.

[9] Frigne, P., and Van den Braembussche, R., 1985, ''A Theoretical Model for Rotating Stall in the Vaneless Diffuser of a Centrifugal Compressor,'' ASME J. Eng. Gas Turbines Power, **107**, No. 2, pp. 507–513.

[10] Imaichi, K., and Tsurusaki, H., 1979, ''Rotating Stall in a Vaneless Diffuser of a Centrifugal Fan,'' *ASME Proceedings, Flow in Primary, Non-Rotating Passages in Turbomachines*, pp. 23–31.

An Aerodynamic Shroud for Automotive Cooling Fans

Scott C. Morris

John F. Foss

A38 Research Complex Engineering,
Michigan State University,
East Lansing, MI 48823

Results from an experimental investigation of an aerodynamic fan shroud are reported. The device was motivated by the relatively large (2.5 cm) tip clearance required in automotive cooling fans which are mounted to the engine. The shroud consists of a pressurized plenum and a Coanda attachment surface to deliver a jet of high momentum air into the tip clearance region. Both the performance and the efficiency for the initial system design were enhanced at higher flow rates, and degraded at lower flow rates. A small tuft was used to observe qualitative flow features in the near wake and tip clearance region of the fan. This information was used to create a modified design. The new geometry was tested and found to provide improved performance characteristics for a wider range of flow rate conditions. [DOI: 10.1115/1.1359212]

1 Introduction

Automotive cooling fans, which are engine mounted (primarily truck applications), require a large tip clearance between the fan tip and the shroud. The range of typical values for tip clearance is $2<\tau<3$ cm. This distance accommodates the relative motion between the engine and the chassis mounted shroud. As a consequence, the typical operating efficiencies of these fans are less than 20 percent. Considerable effort has been directed toward the understanding of tip clearance effects in more typical turbomachinery applications, e.g., see Adamczyk [1], Laksminarayana [2], and the references within Laksminarayana [3]. The negative effects of large tip clearance in automotive applications has been recognized in, for example, Baranski [4] and Mellin [5]. However, due to the extremely large tip clearances of these applications, little effort has been devoted to the understanding of these flows. Additionally, very few technological suggestions have been made as to how to improve automotive cooling fan efficiencies. Note that this application is also unique in the field of turbomachinery because of the partially shrouded nature of the fan. Specifically, in automotive fan flows, the fan is typically inserted only part way into the shroud as shown in Fig. 1. This allows for a radial outflow pattern which provides enhanced performance through a range of operating conditions.

The present communication is to report on experimental data which characterizes the performance and efficiency of an ''Aerodynamic Shroud'' (see Foss [6], and Foss and Morris [7]) that is to enhance performance in these automotive applications. To the author's knowledge, this was the first study which utilized active flow control in the tip clearance region of an automotive cooling fan. This shroud utilizes a pressurized plenum to deliver a Coanda attachment jet that serves to ''fill'' the gap between the blade tip and the physical surface of the shroud; see Fig. 1. The jet velocity profile shown in Fig. 1 is a schematic representation of that which would exist if the cooling fan were not spinning. The specific design of the convex wall jet shown was derived from data presented in several previous research efforts involving Coanda jets, most notably: Wilson and Goldstein [8], Ameri and Dybbs [9], and Shakouchi et al. [10].

The variables used to describe typical fan investigations are the fan diameter (D_{tip}), tip clearance $\tau=(D_{\text{shr}}/2)-(D_{\text{tip}}/2)$, rotating speed characterized by U_{tip}, fluid viscosity (υ), pressure rise (ΔP_{fan}), and flow rate (Q_{fan}). The aerodynamic shroud introduces the following variables: shroud jet-gap (g), shroud flow rate (Q_{shr}), and shroud plenum pressure ($\Delta P_{\text{shr}}=P_{\text{shroud}}-P_{T\text{-approach}}$). Note that $P_{T\text{-approach}}$ represents the total pressure of the inflow. The use of $P_{T\text{-approach}}$ permits the use of the upstream loss elements (e.g., heat exchangers) to be represented in the measurements. The value used in the present study is that of the undisturbed atmosphere. Note that if loss producing elements were present and sufficiently close to the fan inlet, the $P_{T\text{-approach}}$ value would have to be suitably averaged over the inlet area if the present data were to be used as a predictive guide for the behavior of this new configuration.

The next section presents the experimental equipment and procedure. The third section utilizes the above considerations to extract the dimensionless integral parameters (pressures, flow rates) for the axial fan/aerodynamic-shroud combination. Performance and efficiency results are then presented in which the efficacy of the aerodynamic shroud is demonstrated. Tuft visualizations were used to obtain information about the flow directions in the near wake and tip clearance area for varied fan/shroud conditions. These results motivated geometric modifications which were made to the original design. Performance measurements using the improved geometry were also obtained.

2 Experimental Equipment and Procedure

An Automotive Cooling Fan Research and Development (ACFRD) facility (see Fig. 2 and Morris et al. [11]) has been developed at Michigan State University. Note that capital letters are used to identify specific features of the system. The test fan moved air from the laboratory, and into the upper receiver (*F*) which had dimensions 3 m×3 m×2 m. The air was then reaccelerated through nozzles (*L*) to a lower receiver (*T*), which delivered the air to a secondary blower (*I*). This blower then moved the air past a throttle plate (*H*), and back to the laboratory.

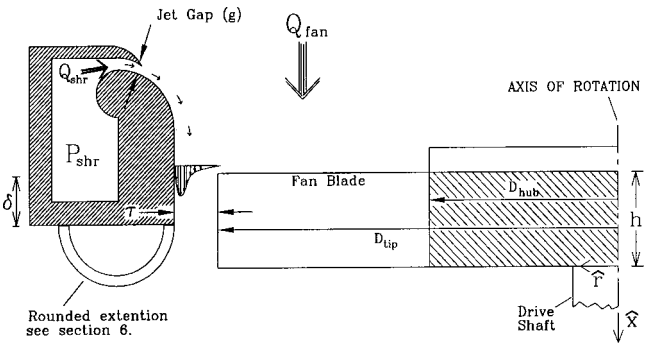

Fig. 1 Schematic of aerodynamic shroud

Contributed by the Fluids Engineering Division for publication in the JOURNAL OF FLUIDS ENGINEERING. Manuscript received by the Fluids Engineering Division June 19, 2000; revised manuscript received December 31, 2000. Associate Editor: Y. Tsujimoto.

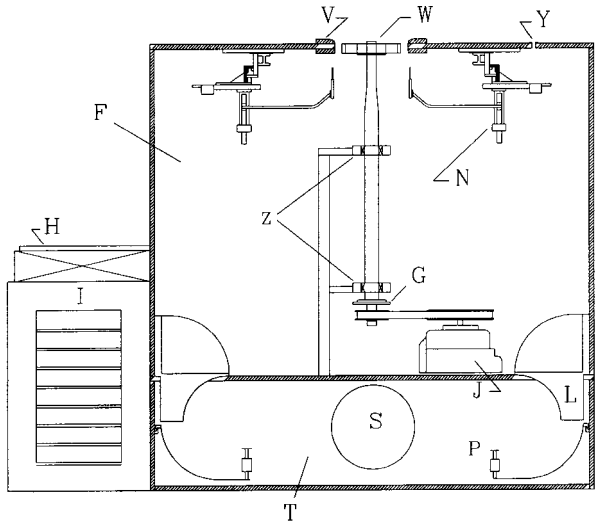

F	UPPER RECEIVER	P	FLOW RATE MEASUREMENT SYSTEM
G	OPTICAL ENCODER	S	INLET TO PRIME MOVER
H	THROTTLE PLATE	T	LOWER RECEIVER
I	PRIME MOVER	V	SHROUD
J	DRIVE MOTOR	W	TEST FAN
L	NOZZLE	Y	PRESSURE TAP
N	TRAVERSE	Z	BEARING SHAFT SUPPORTS

Fig. 2 Schematic of ACFRD facility

A pressure tap (Y) was located at the top of the upper receiver to measure the pressure rise (ΔP_{fan}). A 1-Torr Baratron pressure transducer was used for this measurement; the accuracy of this measurement was ± 1 percent. The agreement of pressure rise measurements between the ACFRD facility and AMCA certified tunnels gives confidence in this measurement. The total flow rate (Q_{total}) was measured by the metering system (P) between the upper and lower receivers. The accuracy of the flow rate measurement was estimated to be less than or equal to ± 1.5 percent, as described in detail in Morris et al. [12]. The value (Q_{shr}) is separately metered using a calibrated elbow meter in the shroud air delivery system. This permitted the approach flow rate $Q_{\text{fan}} = Q_{\text{total}} - Q_{\text{shr}}$ to be evaluated. Electric power measurements (and known losses in the drive system) permitted the input power to the fan ($\wp_{\text{fan}}$) to be known. The relative uncertainty in the power measurement was ± 3 percent of the measured value.

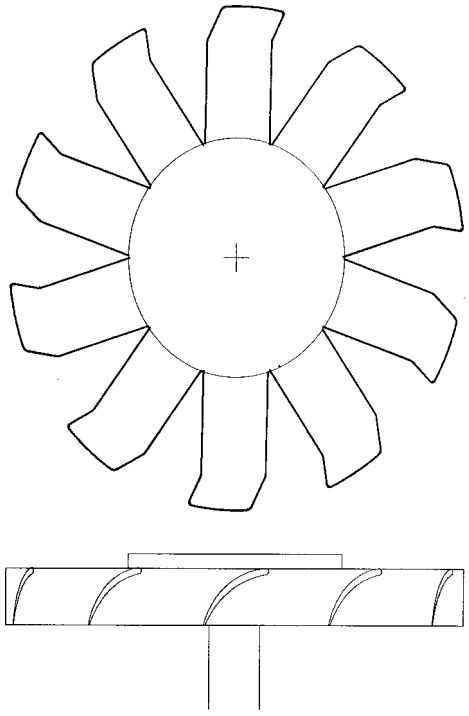

Fig. 3 Schematic of test fan

The test fan selected for the experiments was that of a 1994 Ford Explorer vehicle; see Fig. 3. The fan was manufactured by Usui Corporation (part #F37A-8600-FA). The fan had 10 cambered blades with a tip diameter of 0.453 m ($R = 0.227$ m) and a hub to tip ratio of 0.5. Axial depth of the blades was 56 mm, and nearly constant from hub to tip. The chord angle of the blades was 40 degrees, and constant along the radius. The blade thickness was 3 mm. The outer 30 mm of the blades were ''swept back'' at an angle of 30 degrees. This design is common in automotive cooling fans to assist in the radial outflow around the engine. The shroud was axisymmetric with a tip clearance of $\tau = 2.5$ cm ($= 0.11R$). The blade chord (C) was 5.0 cm; thus $\tau/C = 0.50$. The fan was placed relative to the shroud such that the upstream 50 percent of the blade height was within the shroud; see Fig. 1. This placement of the fan/shroud is typical and often required in automotive applications due to the effect of the engine blockage on fan outflow.

3 Analysis

It is useful to consider the axial fan and the aerodynamic shroud to be the internal elements of a boundary value problem whose upstream boundary is in the laboratory ''atmosphere'' and whose downstream boundary is within the receiver (F). Since the desired information (the appropriately normalized velocity and pressure fields) represents the solution to this boundary value problem, the nondimensional parameters that are present in the governing equations (Navier-Stokes) and the boundary conditions are sufficient to fully characterize the subject problem. The selected velocity and length scales, plus the characterization of the working fluid, are:

(i) the tip speed of the fan blade (U_{tip}) as the velocity reference in the problem,
(ii) the fan diameter (D_{tip}) as the length scale of the problem, and
(iii) the kinematic viscosity (υ) of the working fluid (air).

The boundary value problem described above in general terms for the flow field of Fig. 1 will be made specific by identifying the boundary conditions (i.e., the independent variables). First, the approach flow rate (Q_{fan}) can be expressed as

$$\phi = \frac{Q_{\text{fan}}/A_{\text{flow}}}{U_{\text{tip}}} = \frac{U_0}{U_{\text{tip}}}. \tag{1}$$

where $A_{\text{flow}} = \pi/4(D_{\text{shr}}^2 - D_{\text{hub}}^2)$ represents the annular area between the shroud and fan hub. Note that the use of A_{flow} rather than $D_{\text{tip}}^2 (= A_{\text{flow}} \times 1.29)$ is conventional in fan scaling. Second, the pressure in the shroud plenum referenced to the tip speed as $\Delta P_{\text{shr}}/\rho U_{\text{tip}}^2$ characterizes the ''driving potential'' for the shroud flow.

The height (g) of the jet opening characterizes the shroud (given its basic aerodynamic shape as noted in Fig. 1). Its parametric designation is (g/D_{tip}). The boundary value problem can therefore be specified in terms of these three boundary condition parameters and the Reynolds number ($U_{\text{tip}} D_{\text{tip}}/\upsilon$). It is typical in fan studies (see e.g., Lakshminarayana [3]) to not include the Reynolds number as a significant parameter given the dominance of inertial effects. The insensitivity of the present data to the magnitude of the Reynolds number was confirmed by observations of the data presented in Section 4; hence it will not be considered in the governing parameter set given below.

The dependent variables of interest are: fan pressure rise, shroud volume flow rate, and system efficiency. In dimensionless form, the typical expression for the performance of a conventional fan:

$$\psi \equiv \frac{\Delta P_{\text{fan}}}{\frac{1}{2}\rho U_{\text{tip}}^2} = \psi(\phi), \tag{2}$$

is modified to:

$$\psi = \psi\left(\phi, \Delta P_{\text{shr}}/\rho U_{\text{tip}}^2, \frac{g}{D_{\text{tip}}}\right). \tag{3}$$

The shroud flow rate and system efficiency can be respectively described as

$$\Lambda \equiv \frac{Q_{\text{shr}}}{U_{\text{tip}} A_{\text{flow}}} = \Lambda\left(\phi, \Delta P_{\text{shr}}/\rho U_{\text{tip}}^2, \frac{g}{D_{\text{tip}}}\right). \tag{4}$$

and

$$\eta_{\text{sys}} \equiv \frac{\Delta P_{\text{fan}} Q_{\text{fan}}}{\wp_{\text{fan}} + \wp_{\text{shr}}} = \eta_{\text{sys}}\left(\phi, \Delta P_{\text{shr}}/\rho U_{\text{tip}}^2, \frac{g}{D_{\text{tip}}}\right) \tag{5}$$

where the power required to pressurize the shroud is defined as

$$\wp_{\text{shr}} = \frac{\Delta P_{\text{shr}} Q_{\text{shr}}}{\eta_{\text{shr}}} \tag{6}$$

and η_{shr} is the efficiency of the shroud delivery system. The numerical value of η_{shr} will depend on the design of the shroud delivery system which is specific to an application. For this communication, a single value of $\eta_{\text{shr}} = 0.7$ was selected in order to permit characteristic system efficiencies to be evaluated. This was necessary because a large centrifugal blower was used in to present experiments to provide experimental flexibility of the operating conditions. Because the shroud power levels were typically less than 10 percent of the main fan power, values of η_{shr} other than 0.7 made only small quantitative changes to the results.

Using Eq. (4), Eqs. (3) and (5) can be rewritten in terms of their functional dependence as

$$\psi = \psi(\phi, \Delta P_{\text{shr}}/\rho U_{\text{tip}}^2, \Lambda) \tag{7}$$

and

$$\eta_{\text{sys}} = \eta_{\text{sys}}(\phi, \Delta P_{\text{shr}}/\rho U_{\text{tip}}^2, \Lambda). \tag{8}$$

An examination of the experimental data that will be presented in the Results section has revealed a useful simplification of Eqs. (7) and (8). Specifically, the variables $\Delta P_{\text{shr}}/\rho U_{\text{tip}}^2$ and $Q_{\text{shr}}/A_{\text{flow}} U_{\text{tip}}$ can be combined to a single dimensionless variable:

$$\chi \equiv \left(\frac{\Delta P_{\text{shr}}}{\rho U_{\text{tip}}^2}\right)\left(\frac{Q_{\text{shr}}}{A_{\text{flow}} U_{\text{tip}}}\right) \tag{9}$$

where χ represents a dimensionless ''power level'' of the shroud.

4 Performance Results

The system performance was established as the functional relationship between the pressure rise across the fan and flow rate through the fan. This performance can be expressed in terms of the dimensionless variables defined in the analysis described by Eq. (7). The system efficiency is defined by Eq. (8). Typically 15 points were acquired from $\phi = 0$ (pressure is maximum) to the maximum flow rate ($\psi = 0$) to define this ''characteristic curve.'' These data were acquired for fan speeds of 800, 1000, 1200, 1400, 1600, and 1800 rpm with the shroud gap (g) set to 2 mm. Data were also taken for $g = 1.0$, 1.5, 2.0, 2.5, and 3.0 mm with a fan speed of 1000 rpm. Typically 5 shroud pressure conditions were examined for each of the above jet gap settings and fan speeds; these ranged from 0–800 Pa. This combination of variables led to a total of 50 curves to fully characterize the shroud and fan performance. The above dimensional conditions can be described in nondimensional form as $0.000 < \chi < 0.068$ where χ is defined in Eq. (9).

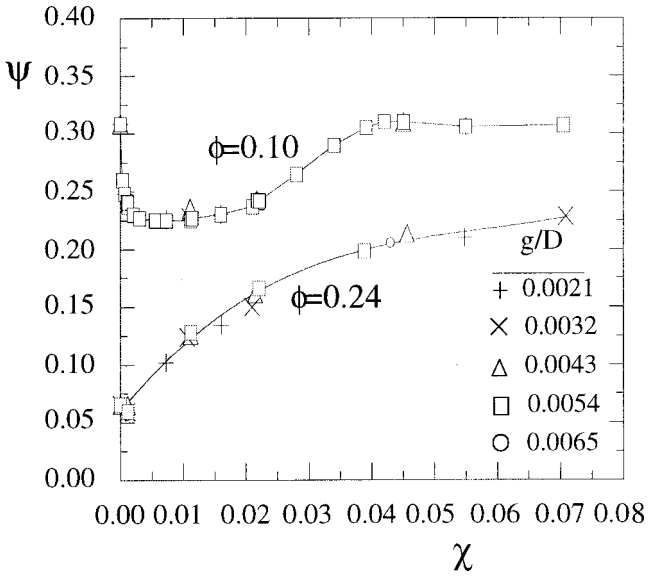

Fig. 4 Fan pressure (ψ) vs. shroud power (χ) for two fan flow rates

An additional ''collapse'' of the data was found that could not be anticipated from the boundary value problem analysis given above. Specifically, the shroud power, represented as χ in Eq. (9), can be used to fully characterize the contribution of the shroud. This observation has allowed the test condition to be specified in terms of two, instead of three, dimensionless variables. Equations (7) and (8) can now be rewritten as:

$$\psi = \psi(\phi, \chi) \tag{10}$$

and

$$\eta_{\text{sys}} = \eta_{\text{sys}}(\phi, \chi) \tag{11}$$

Figure 4 supports the simplified description of Eq. (10). The fan pressure rise as a function of χ for two representative flow rates ($\phi = 0.10, 0.24$) is shown. The ability of the single variable (χ) to represent both g/D and Λ is evident in this figure for the two ϕ values. Similar results represent the data collapse for other ϕ values. Hence, Eq. (10), and by extension (11), is supported by the results presented in Fig. 4.

The performance data are presented in Fig. 5 for selected χ values in the range $0.000 < \chi < 0.068$. For clarity, only 8 of the 50 performance curves tested are shown. The balance of the data is available in Morris [13]. It is evident from these figures that the fan performance (i.e., ψ at a given ϕ value) is strongly dependent on the parameter χ. The contribution of the aerodynamic shroud in terms of the fan performance at higher flow ($\phi > 0.13$) rates is apparent in Fig. 5. Note that the maximum flow rate obtained (i.e., ϕ for the condition $\psi = 0$) is increased significantly as χ is increased. Note again that the abscissa (ϕ) represents the approach flow rate $Q_{\text{fan}} = Q_{\text{total}} - Q_{\text{shr}}$. The additional flow rate is an aerodynamic effect and not simply the addition of flow from the shroud. In contrast, however, lower values of ϕ indicate a decrease in ψ for the tested χ values, albeit the decrease was less for the higher χ values.

The energy efficiency of the system (η_{sys}) is shown in Fig. 6. For values of $0 < \phi < 0.17$, a dramatic decrease in η_{sys} is observed as χ is increased from 0–0.009. The efficiency was relatively insensitive to χ for $0.009 < \chi < 0.068$ for this range of ϕ. Conversely, for $\phi > 0.17$ an increase in efficiency was obtained, which remains relatively constant for $0.021 < \chi < 0.068$, with the maxi-

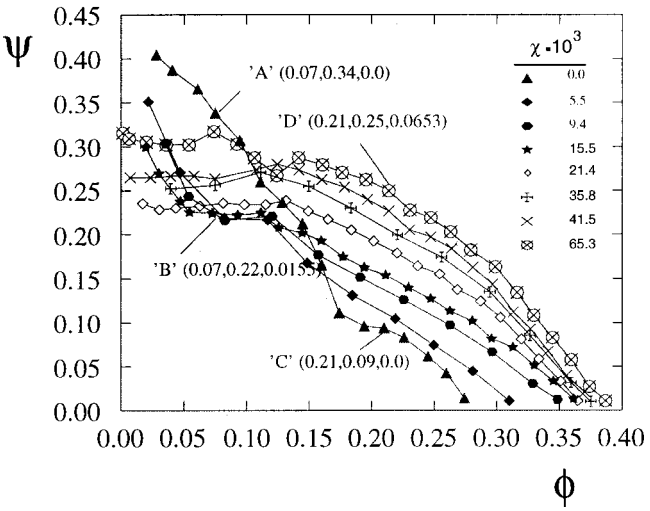

Fig. 5 Performance data for fan and shroud conditions A B C D are labeled with their respective (ϕ,ψ,χ) values

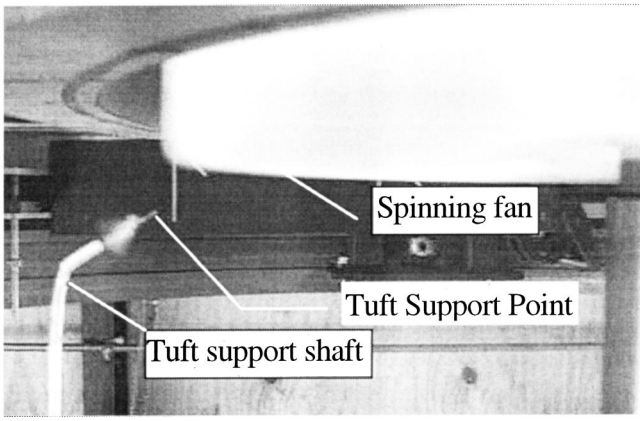

Fig. 7 Representative (x-r) plane digital image of fan and tuft at condition D ($\Delta P_{shr}=0=\chi$)

mum occurring for $\chi\cong 0.041$. It is interesting to note the existence of a single value of $\phi\cong 0.17$ for which $\eta_{sys}>\eta_{sys}(\chi=0)$. This is quite useful when considering an application of the device. Specifically, it is necessary that $\phi>0.17$ to enhance η_{sys} with the aerodynamic shroud as shown in Fig. 1. These observations, continued in the next sections, suggested a modification of the outflow region. The suggested modification was successful in improving the performance of the system for lower ϕ values as described in Section 7.

5 Tuft Observations

A small (15 mm) tuft was used to identify the time mean velocity vector direction in the near flow field of the fan. The purpose of this experiment was to quantify the flow directions in the fan/shroud area to better identify and understand the physical mechanisms that led to the results shown in Figs. 5 and 6. A fine thread was used to support the tuft. Quantitative information about the flow direction was obtained by acquiring orthogonal digital images of the tuft and processing the images. Figure 7 shows an example of a digital image acquired visualization for tuft position $x/R=0.1$, $r/R=1.0$. Results described in Morris et al. [14] wherein a similar tuft was used to align an x-wire probe have shown that this is an accurate method of measuring the time averaged flow direction. A typical uncertainty in the flow angle is ± 7 degrees as defined by the time averaged axial, radial, and tangential velocity components in comparison with the inferred tuft observations.

Four operating conditions were selected for detailed study. These are shown on Fig. 5 with an identification letter (''A,'' ''B,'' ''C,'' and ''D''). The conditions A and B represent χ values of 0 and 0.015, respectively, for a relatively low flow rate ($\phi=0.07$). Note that the performance was degraded by the activated shroud at this flow rate. The conditions C and D represent χ values of 0 and 0.068 at a higher flow rate ($\phi=0.21$) for which the performance was greatly enhanced.

Figure 8 shows the vector directions observed for the conditions A and B, projected onto the x-r plane for several positions in the fan wake and near the fan tip. Condition A (shroud off, low flow rate) clearly shows what is typically referred to as a ''stalled'' fan condition. That is, the flow over the majority of the blade area is separated as shown by the tufts pointing in the *negative axial* direction. Additionally, the flow near the fan tip is highly radial. The high pressure rise created by the fan is clearly a result of the fan's ability to create this radial momentum flux near the tip. It is then noted that condition B (shroud on, low flow rate) that the general characteristics of the flow field are unchanged. Specifically the predominantly radial outflow at the fan tip and negative axial flow below the fan. It can be inferred that the

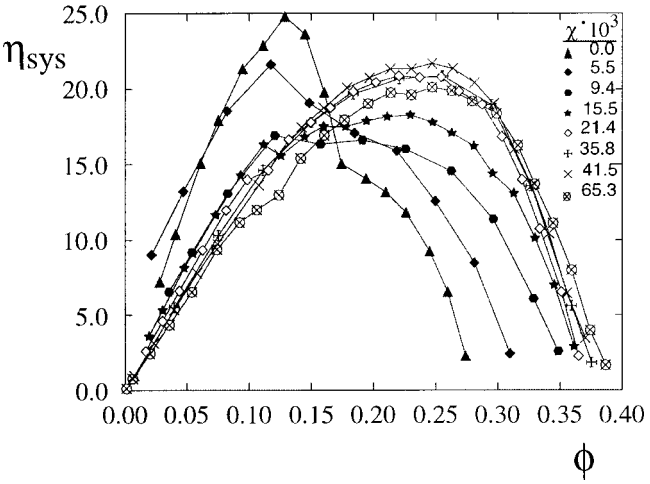

Fig. 6 System efficiency data

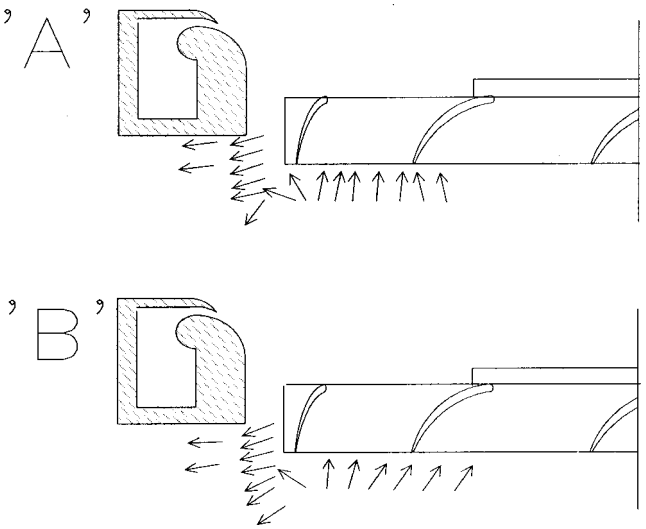

Fig. 8 Tuft obervations in the x-r plane for conditions A and B

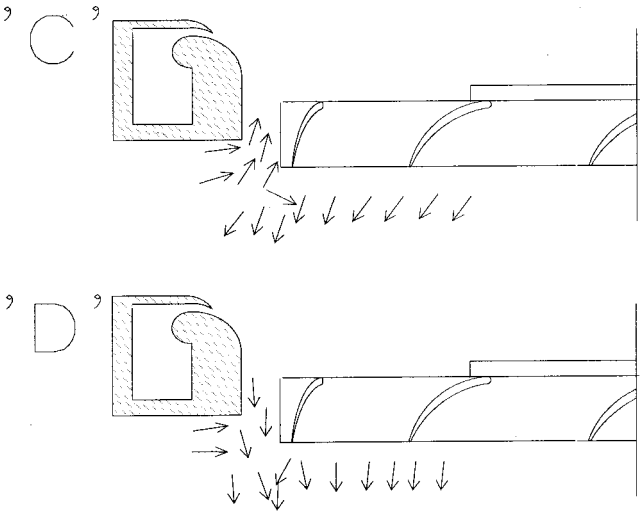

Fig. 9 Tuft observations in the *x-r* plane for conditions C and D

greatly reduced pressure rise of the fan at condition B is due to the presence of the axially directed shroud flow which inhibits the fan's ability to create radial outflow.

Tuft results from conditions C and D are shown in Fig. 9. Condition C (shroud off, high flow rate) shows a predominantly axial flow condition over the blade area, and a *negative axial* flow direction in the entire tip region: $A_{cl}=\pi/4(D_{shr}^2-D_{tip}^2)$. The relatively large ratio of $A_{cl}/A_{flow}=0.31$ indicates that the negative axial velocity through the tip clearance area greatly reduced the effective flow area which contributes to Q_{fan}. Condition D shows the effect of the Coanda jet in maintaining the tip clearance flow in the positive axial direction. It can be inferred that all of the positive axial flow in the fan area contributes to Q_{fan} when the shroud is activated. By allowing the entire blade section to contribute to the net flow rate, the fan/shroud combination can provide a significant increase in flow rate for a given pressure loading condition on the blades.

6 Modified Shroud Geometry Results

The data presented in the previous section motivated a modified shroud geometry. Specifically, the decreased fan pressure rise caused by the aerodynamic shroud at low flow rate conditions suggested that the shroud flow was interfering with the fan aerodynamics for the lower flow rate conditions. The initial aerodynamic shroud design, with it's 90 degree trailing edge, provided a predominately axial component of momentum to the tip clearance area. It is conjectured that this axial momentum ''chokes'' the radial outflow from the fan, thereby decreasing the performance.

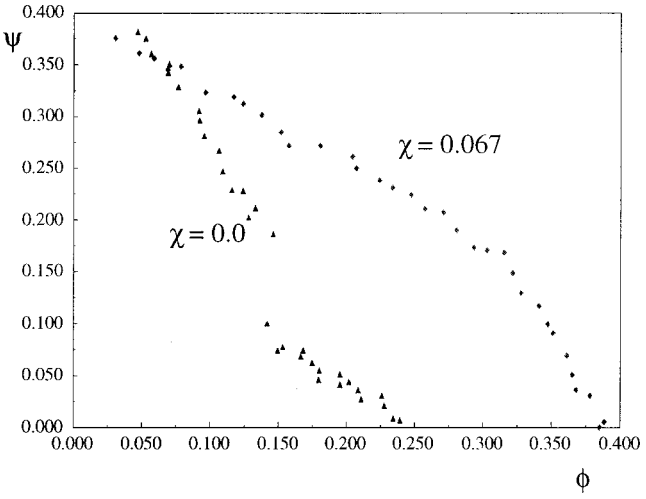

Fig. 10 Fan performance curve for modified shroud geometry

The new geometry included an axisymmetric addition which was attached to the trailing edge of the shroud as shown in Fig. 1. The purpose of this device was to provide the Coanda jet with a radial component of momentum at the exit of the fan plane. The intent was to allow the radial outflow from the fan to be ''assisted''by the Coanda jet. Performance data were taken for $\chi=0.00$ and $\chi=0.067$ for the modified geometry; see Fig. 10. It can be observed that the modified geometry with activated shroud shows equal or better performance for $\phi>0.06$. This is a significant improvement compared to the data shown in Fig. 5 where $\phi>0.12$ was required for $\Delta P_{fan}(\chi=0.068)\geqslant\Delta P_{fan}(\chi=0)$.

7 Conclusions

The relatively low energy efficiency of light truck cooling fans has motivated the design of an aerodynamic fan shroud. The use of an annular air jet to control the aerodynamics of the tip clearance region had proven to be an effective method of changing the performance and efficiency characteristics of the fan. Specifically, the integral performance measurements have established the efficacy of the aerodynamic shroud for mid-to-high flow rates. The addition of the rounded trailing edge has improved the performance for a larger range of flow rates.

The tuft observations discussed in Section 5 have illustrated the physical mechanisms that have led to the change in performance with the Aerodynamic shroud. These results illustrate the sensitivity of the present fan to changes in the boundary conditions near the tip. It is envisioned that future generations of fan and shroud design can be optimized to take full advantage of the interactions between the shroud jet, tip clearance flow, and shroud/blade geometry.

It is clear that the use of the aerodynamic shroud in a vehicle will depend on a variety of factors not considered in this study. These include underhood packaging constraints and the availability of a pressurized air source. The energy efficiency of the device in an automotive application will then depend on the energy supplied to the shroud as described by the variable χ, and the operating point of the system. The latter will depend on both the vehicle speed as well as underhood design.

Acknowledgments

This research was partially supported by a grant from the Ford/University Research Program. Their support, and the technical counsel of Mr. Thomas Veling, is gratefully acknowledged.

Nomenclature

A_{cl} = area bounded by the shroud and fan tip
A_{flow} = area bounded by the shroud and fan hub
D_{tip} = diameter of the fan tip
D_{hub} = diameter of the fan hub
D_{shr} = inside diameter of the shroud ($=D_{tip}+2\tau$)
g = gap thickness of Coanda jet
$\wp_{fan}$ = shaft power input to the fan
$\wp_{shr}$ = power input to the shroud
Q_{fan} = approach flow rate through the fan
Q_{shr} = flow rate through the shroud
Q_{total} = total flow rate measured by the facility
r = radial coordinate measured from the fan axis
U_0 = spatial average flow velocity through the fan (Q_{fan}/A_{flow})
U_{tip} = linear velocity of the fan tip ($\Omega D_{tip}/2$)
x = axial coordinate measured from the trailing edge of the fan blades
χ = dimensionless power input to the shroud

ΔP_{fan} = pressure rise across the fan
ΔP_{shr} = pressure of the shroud plenum (P_{shroud}-$P_{t\text{-approach}}$)
ϕ = dimensionless flow rate through the fan
η_{sys} = efficiency of the fan and shroud system
η_{shr} = efficiency of the shroud delivery system
Λ = dimensionless flow rate through the shroud
τ = tip clearance ($D_{shr}/2$-$D_{tip}/2$)
ψ = dimensionless pressure rise across the fan
Ω = rotational speed of the fan (radians/s)

References

[1] Adamczyk, J. J., Celestina, M. L., and Greitzer, E. M., 1993, ''The Role of Tip Clearance in High Speed Fan Stall,'' ASME J. Turbomach., **115**, pp. 28–31.
[2] Lakshminarayana, B., 1970, ''Methods of Predicting the Tip Clearance Effects in Axial Flow Turbomachinery'' ASME J. Basic Eng., **82**, Sept, pp. 467–482.
[3] Lakshminarayana, B., 1996, *Fluid Dynamics and Heat Transfer of Turbomachinery*, Wiley, New York.
[4] Baranski, B., 1974, ''Designing the Engine Cooling Fan,'' SAE paper No. 740691.
[5] Mellin, 1980, ''Noise and Performance of Automotive Cooling Fans,'' SAE paper No. 800031.
[6] Foss, J. F., 1998, ''Improved Cooling Fan Shroud,'' U.S. Patent No. 5,762,034.
[7] Foss, J. F., and Morris, S. C., 1999, ''Fan Shroud with Integral Air Supply,'' U.S. Patent No. 5,991.685.
[8] Wilson, D. J., and Goldstein, R. J., 1976, ''Turbulent Wall Jets with Cylindrical Streamwise Surface Curvature,'' ASME J. Fluids Eng., **98**, pp. 550–557.
[9] Ameri, M., and Dybbs, A., 1993, ''Theoretical Modeling of Coanda Ejectors,'' Journal of Fluid Machinery, **16**, pp. 43–48.
[10] Shaouchi, T., Onohara, Y., and Kato, S., 1989, ''Analysis of a Two-Dimensional, Turbulent Wall Jet Along a Circular Cylinder,'' JSME Int. J., Ser. II, **32**, No. 3, pp. 332–339.
[11] Morris, S. C., Foss, J. F., and Pakkala, J. E., 1997, ''The Automotive Cooling Fan Research and Development Facility,'' Proceedings of the 3rd Vehicle Thermal Management Systems Conference, Indianapolis IN, USA.
[12] Morris, S. C., Neal, D. R., Foss, J. F., and Cloud, G., 2000, ''A Unique Airflow Measurement Device,'' accepted to Meas. Sci. Technol.
[13] Morris, S. C., 1997, ''Experimental Investigation of an Aerodynamic Shroud for Cooling Fan Applications,'' Masters thesis, Michigan State University, East Lansing, MI.
[14] Morris, S. C., Good, J. J., and Foss, J. F., 1998, ''Velocity Measurements in the Wake of an Automotive Cooling Fan,'' Exp. Therm. Fluid Sci., **17**, pp. 100–106.

Spatially Resolved Temperature Measurements in a Liquid Using Laser Induced Phosphorescence

S. L. Thomson
Research Assistant

D. Maynes[1]
Assistant Professor

Department of Mechanical Engineering,
Brigham Young University,
435 CTB,
Provo, UT 84602

This paper describes recent advances in the development of a temperature measurement methodology based on phosphorescence of a tracer molecule in a liquid. The methodology represents an extension of molecular tagging velocimetry (MTV). MTV is a laser-based technique of obtaining spatially resolved fluid velocity profiles. The methodology has the potential of providing spatially resolved simultaneous measurements of velocity and temperature data over a planar domain. Presently, a method of obtaining temperatures over a range of 30°C with a typical uncertainty of ±1.0–1.5°C has been developed. Recent progress has resulted in a method of generating robust calibration curves for use in subsequent temperature measurements. A discussion of the experimental methodology, calibration curve development, and error analysis is presented. Finally, simultaneous temperature and velocity profile measurements using the method are demonstrated under dynamic conditions. [DOI: 10.1115/1.1365960]

1 Introduction

Quantification of the temperature and velocity fields is critical to understanding the transport of heat in a fluid. Specifically, for turbulent flows, the correlation between the temperature field and velocity field is important, including the correlation of the fluctuating components. Measurements of the correlation terms provide the basis for closure of the Reynolds decomposed transport equations by modeling. Thus, simultaneous measurements of temperature and velocity are of significant advantage.

Many previous investigations that report simultaneous velocity and temperature measurements and their correlations utilized separate and intrusive measurement methodologies to quantify velocity and temperature at a point. For example, studies utilizing combinations of hot-wire and cold-wire probes have been reported in the literature (e.g., Fabris, [1], Yao et al. [2]). Combinations of laser doppler anemometry (LDA) and fast response thermocouples have also been reported (Gould et al. [3]).

Recently, laser-based methods have been utilized to obtain simultaneous measurements of temperature and velocity. Some recent examples include LIF and LDA (Lemoine et al. [4], Nakajima et al. [5]), LIF and particle image velocimetry (PIV) (Sakakibara et al. [6], Sakakibara et al. [7]), liquid crystal thermography (LCT) and PIV (Lattime et al. [8], Doh et al. [9]), and calibrated multichannel electronic interferometry (CMEI) and PIV (Upton and Watt [10]). All of these experiments employed two separate techniques and allow quantification of temperature and velocity.

Using fluorescence to measure temperature is the basis for the established technique of laser-induced fluorescence (LIF). Three recent studies demonstrate the capabilities of LIF in liquid flows. Sakakibara and Adrian [11] presented whole field temperature measurements using LIF with a random error of ±1.4°C over a range of 40°C or more. Coolen et al. [12] investigated convection effects using LIF and demonstrated temperature measurements in the range of 20–60°C with an accuracy of 1.7°C. Additionally, Lemoine et al. [4] demonstrated LIF in conjunction with laser doppler anemometry (LDA) to measure temperature and 2-D velocity measurements in a turbulent heated jet.

It is also possible to utilize the phosphorescence of tracer dyes to quantify fluid temperature fields and the use of such a dye, 1-BrNp·Gβ-CD·ROH, is the focus of this paper. The advantages of using 1-BrNp·Gβ-CD·ROH are that it is the same dye utilized in many studies employing molecular tagging velocimetry (MTV) in liquids (Koochesfahani [13]). Consequently, use of this dye can allow the quantification of velocity and temperature fields using the same optical and equipment setup. In addition, it may be possible to obtain these temperature and velocity field data simultaneously. The primary focus of this paper, however, is to report on the development of a robust calibration procedure and the range and resolution of the temperature measurement method. The following sections describe the background of photoluminescence measurements, the experimental methodology used in quantifying the temperature-intensity relationship, the results of a large number of experiments from which the temperature-intensity relationship is correlated, the development of the calibration relationship, and an analysis detailing both the range and resolution capabilities of the technique. Also, simultaneous temperature and velocity profile measurements using the method under dynamic conditions are demonstrated for horizontal laminar flow with buoyant mixing.

2 Measurements Using Molecular Photoluminescence

Many substances exhibit some sort of photoluminescent behavior; that is, subsequent to excitation of electrons in the molecule to a higher energy level due to exposure of the molecule to incident photons, some of the energy is released in the form of light. Short lived emission, i.e., lifetimes shorter than 10^{-8} seconds is generally termed fluorescence. Conversely, longer emission, milliseconds to minutes, is generally referred to as phosphorescence. Because the emission intensity is a function of the temperature of the molecule, both fluorescence and phosphorescence of a tracer molecule in a fluid enables measurements of temperature fields by quantification of the photoluminescence intensity and this is the basis of LIF.

While fluorescence in liquids and gases is very common, phosphorescence is not due to the rapid quenching that can occur. The ratio of the phosphorescence emission intensity, I_e, to the incident light intensity, I_d, is related to the phosphorescence quantum yield, ϕ_p, as shown in Eq. (1) (Hartmann et al. [14], Ferraudi [15])

$$\frac{I_e}{I_d} = C\varepsilon\phi_p = \frac{k_r}{k_r + k_{nr} + k_q[Q]} C\varepsilon \tag{1}$$

[1]Corresponding Author: maynesrd@et.byu.edu.

Contributed by the Fluids Engineering Division for publication in the JOURNAL OF FLUIDS ENGINEERING. Manuscript received by the Fluids Engineering Division February 9, 2000; revised manuscript received February 8, 2001. Associate Editor: D. R. Williams.

In this expression C is the concentration of the dye solution, ε is the absorption coefficient, k_r and k_{nr} are radiative and nonradiative decay constants (properties of the excited molecule), and k_q is the quenching rate constant due to some quencher molecule Q.

Recent investigations into methods of reducing the quenching of phosphorescence in solutions led to a method of decreasing k_q in aqueous solutions containing the photoluminescent chemical 1-bromonapthalene (1-BrNp) such that phosphorescence could be observed (Ponce et al. [16], Hartmann et al. [14]). In aqueous solutions, the phosphorescence of 1-BrNp is quenched by oxygen. Addition of the cup-shaped molecule mono glucosyl-β-cyclodextrin (Gβ-CD) results in the 1-BrNp binding to its hydrophobic interior. Addition of an appropriate substrate results in the substrate acting as a lid to the cup, thus shielding the 1-BrNp from the quenching effects of oxygen. When both Gβ-CD and the alcohol are present, the phosphorescence intensity is enhanced by a factor of nearly 10^5 (Ponce et al. [16]).

Various substrates can be used, including alcohols, amines, and acids, and Hartmann et al. [14] give a thorough discussion of several that have been utilized. For our work we use three different alcohols: *tert*-butanol (t-BuOH, $(CH_3)_3COH$), cyclohexanol (cycOH, $C_6H_{12}O$), and neopentyl alcohol (NpOH, $(CH_3)_3CCH_2OH$). The time constant of delay of the phosphorescence of 1-BrNp in solution has been measured to be from 0.1 ms–7 ms, depending on the alcohol used (Hartmann et al. [14]). This refers to the time until the phosphorescence emission has decayed to 37 percent of its original intensity, thus the actual imageable lifetime is much longer. Delays up to 30 ms have been used (Koochesfahani et al. [17]). The 1-BrNp absorbs efficiently at 308 nm and the emission wavelength of maximum intensity is about 550 nm. One disadvantage is that the quantum efficiency is low, $\theta_p \approx 0.035$. However, this is offset by the fact that excitation of 1-BrNp produces a reversible transition, thus eliminating the need to periodically replace the working fluid.

2.1 Velocity Measurements Using Phosphorescence. Because phosphorescence is a delayed response, as opposed to the near-instantaneous response of fluorescence, velocity measurements can be easily obtained by tracking a region of fluid that has been ''tagged'' by exciting that region with an external source. This is the basis for molecular tagging velocimetry (MTV), an established method of obtaining spatially resolved velocity profiles over a planar domain of interest using the phosphorescence of a tracer molecule in either liquid- or gas-based flows. For the present experiments the molecular complex 1-BrNp·Gβ-CD·ROH, dissolved in water is used.

For implementation of MTV in aqueous solutions, an ultraviolet (308 nm) laser beam is directed through the solution containing 1-BrNp·Gβ-CD·ROH (where the ROH represents any of the three alcohols listed above). A bright green light is emitted due to the phosphorescence of the 1-BrNp after excitation (''tagging'') by a photon source. This light emission is detected by a gated intensified CCD array positioned normal to the line. By comparing the displacement of the tagged region at two short time intervals, the Lagrangian velocity (1-component) of the fluid can be determined. MTV can thus be thought of as the molecular counterpart to particle image velocimetry (PIV) where the flow is seeded with large particles (large relative to the molecules of MTV) and velocity measurements are obtained by tracking the particles (Koochesfahani [13]). Depending on the excitation pattern one or two velocity components can be measured over a planar domain. Details of these methods have been described in detail previously by Hill and Klewicki [18] and Gendrich et al. [19].

An interesting area of application of MTV is for flow through microscale devices. At small scales (less than 100 μm) deviations from macroscale laminar flow theory have been observed for both momentum and heat transport based on integral measurements. Integral measurements alone are incomplete because they fail to give sufficient insight into the flow field details. Thus velocity and temperature measurements are critical for understanding the physical mechanisms causing these observed behaviors. Laser-based techniques that rely on the photoluminescence of molecules appear to be well suited for micro-scale flows. Recent efforts toward applying MTV to microscale flows have demonstrated velocity resolution of 2 μm/pixel in tubes 750 μm in diameter (Webb and Maynes [20]), with measurements in smaller tubes currently being conducted.

In macroscale flows, MTV has been demonstrated in boundary layer flows in both gases (Thurlow and Klewicki [21]) and liquids (Lee [22], Gendrich [23], Maynes [24]) and in jet flows in gases (Stier and Koochesfahani [25]). MTV has also been successfully employed in turbulent flows (Hill and Klewicki [18]), rotating unsteady flows (Maynes et al. [26]), and in buoyancy-driven convective flow during solidification (Wirtz et al. [27]).

2.2 Temperature Measurements Using Phosphorescence. Three factors significantly affect the phosphorescence emission intensity of the 1-BrNp·Gβ-CD·ROH solution. These are the concentration of the different constituents of the molecular complex, the intensity of the excitation beam, and the temperature of the solution. In a solution of uniform concentration and constant excitation, increasing the solution temperature results in a decrease in the intensity of the emitted light at each point along the excitation path. This is because as the temperature increases, both the phosphorescence lifetime and quantum yield decrease (Adamson and Fleischauer [28], Ferraudi [15]).

Ferraudi [15] suggests that the phosphorescence lifetime temperature dependence is due to the dependence of the phosphorescence radiation decay constant (k_r in Eq. (1)) on temperature. The quantum yield temperature dependence is due to the nonradiative mixing of states, or intersystem crossing (Adamson and Fleischauer [28], Ferraudi [15]). Back intersystem crossing occurs when sufficient thermal energy is acquired and results in the transitioning of molecules from a state from which phosphorescence may occur to a state from which phosphorescence does not occur and the release of energy is nonradiative (k_{nr} in Eq. (1)). Thus as temperature increases, the rate of back intersystem crossing increases, more of the energy release is nonradiative, and the phosphorescence quantum yield decreases; hence the decrease in intensity.

It is this temperature-intensity relationship that enables us to obtain temperature data using phosphorescence. The flow is excited in the same manner as MTV, only the intensity of the tagged region is characterized rather than the deformation. No additional equipment is necessary. When used to measure temperature, we have termed it molecular tagging thermometry (MTT) to reference its relation to MTV. To the authors' knowledge this is the only temperature measurement technique based on photoluminescence that utilizes phosphorescence instead of fluorescence emission.

If MTT is employed with a small time delay, such that the deformation of the line is negligible, it can be utilized accurately as a temperature measurement technique in laminar or turbulent flows and is comparable to LIF in capability; the remainder of the paper focuses on this approach. By using recently available detectors capable of capturing two images separated by a very short time delay, temperature information can be obtained from the initial undeformed image and velocity information by comparison of the two images. In laminar flows or microscale flows longer time delays can be employed using single frame detection such that velocity and temperature can be determined simultaneously, from the same image, using the same equipment. Dependent on the nature of the flow field, simultaneous measurements in turbulent flows may also be possible. The limitations and possibilities for this are discussed further in Section 7.

3 Experimental Methodology

3.1 Equipment Setup. Figure 1 depicts the experimental setup used in correlating the phosphorescence intensity with tem-

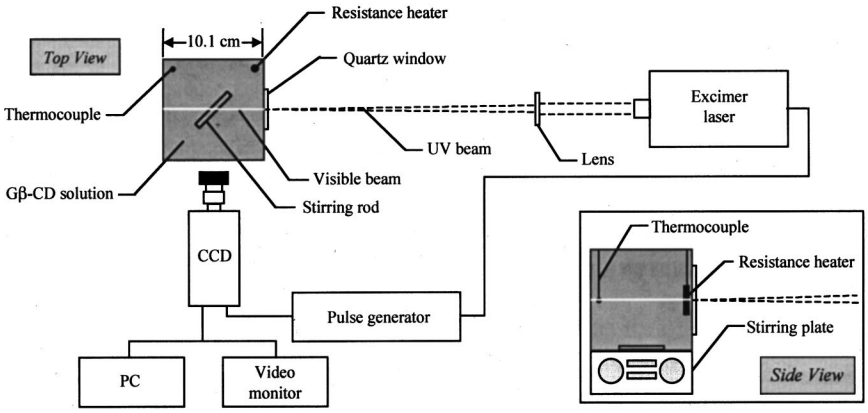

Fig. 1 Temperature measurement setup for calibration curve development

perature. The laser, a Lambda Physik LPX 100 Excimer Laser, emitted pulsed light (308 nm, 16 ns pulsewidth, 60 Hz pulse rate) that was directed and focused into a small cube-shaped apparatus containing an aqueous solution doped with 1-BrNp·Gβ-CD·ROH. The diameter of the beam in the solution was approximately 1 mm and the laser was operated and maintained at constant energy throughout all of our experiments at 120 mJ and the size of the beam at the laser cavity exit was 2 cm^2. The maximum variation in pulse energy from the set value was specified by Lambda Physik as ± 3.5 percent.

The apparatus was constructed of black Plexiglas, sandblasted in the interior to minimize reflected light, with a quartz window in one side through which the UV light could pass. The apparatus also had a glass window on a side adjacent to the quartz window through which the resulting phosphorescence was viewed with a CCD. A small resistance heater was placed in one corner of the apparatus and a thermocouple in another corner. A stirring rod rested in the bottom of the apparatus; the apparatus was then placed on a stirring plate to achieve thermal equilibrium in the test cell. The test cell volume was 720 mL and was completely filled with solution to minimize degradation of the solution due to reaction with oxygen.

The laser was synchronized with an 8-bit Princeton Instruments Video Rate Fiber-Coupled Intensified CCD (640×480 pixels). The CCD acquired images of the phosphorescence shortly after the excitation beam was transmitted through the apparatus; typical delay times were 200–300 μs. The images were subsequently transferred to a PC for analysis. The 8 bits allowed for the intensity signal to be discretized into 256 grayscale values, 0 being black and 255 being white.

3.2 Data Acquisition and Analysis. To acquire temperature data, the fluid was first heated to a predetermined initial temperature. After thermal equilibrium was established, 50 consecutive images were captured at standard video rate (30 frames per second) with the fluid temperature held constant. The solution was then heated to a slightly higher temperature (typically 2°C–3°C at a time) and the image acquisition process was repeated. This continued until the line intensity had decreased to where it was no longer distinguishable from the background. Figure 2 shows three images transferred by the CCD to the PC at three different temperatures.

The images were analyzed to quantify the beam intensity. To accomplish this, first the pixel of maximum intensity at each horizontal (*x*-direction) pixel location along the length of the line profile was determined. A gaussian smoothing routine to reduce spatial noise was then implemented over a small vertical region (approximately 21 pixels) normal to the pixel of maximum intensity. This smoothing algorithm is shown in Eq. (2),

$$I_{y,\text{new}} = 0.5I_{y,\text{old}} + 0.25(I_{y-1} + I_{y+1}) \tag{2}$$

where $I_{y,\text{new}}$ and $I_{y,\text{old}}$ are the pixel values before and after smoothing, respectively, and I_{y-1} and I_{y+1} correspond to the pixel intensities directly above and below $I_{y,\text{old}}$. The effect of smoothing on the line profile is illustrated in Fig. 3. Note that smoothing only occurred normal to the line not parallel to it. The net effect of smoothing is a decrease in the maximum intensity and also a decrease in the intensity rms. For all of our present data five smoothing passes were implemented.

After smoothing, a second order curve fit was applied to the centermost pixels and the maximum value of the curve fit was determined. This curve fit maximum then represented the intensity of the line at that *x* location. This process was repeated along the entire length of the line and for each of the acquired images. At each *x* location, the pixel intensities for the 50 images obtained with the fluid at a given temperature were then averaged.

Shown in Fig. 4 is an example of the data returned for such a procedure. The bottom coordinate gives the *x* location in the test cell parallel to the incoming light, with increasing values of *x* corresponding to increasing beam penetration depth. The left axis is the measured emission intensity of the phosphorescence after smoothing, curve fitting, and averaging. Shown are profiles of intensity versus *x* location for 6 temperatures. Also shown is the variation in intensity with no excitation, labeled background. The width of the test cell was 10.1 cm but the length of the line that was imaged was only 5.6 cm. The spatial resolution was approximately 100 μm/pixel and markers are shown every 30 data points. The decrease in intensity with increase in temperature, as discussed above, is evident in Fig. 4. Also the intensity decreases as *x* increases due to attenuation of the excitation beam as it propagates through the fluid.

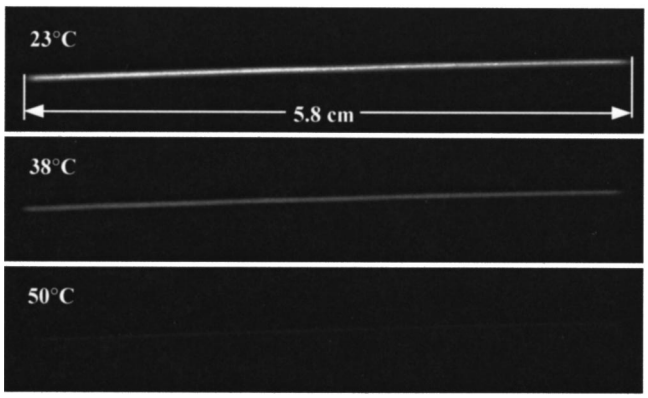

Fig. 2 Phosphorescence of excited lines at increasing temperature

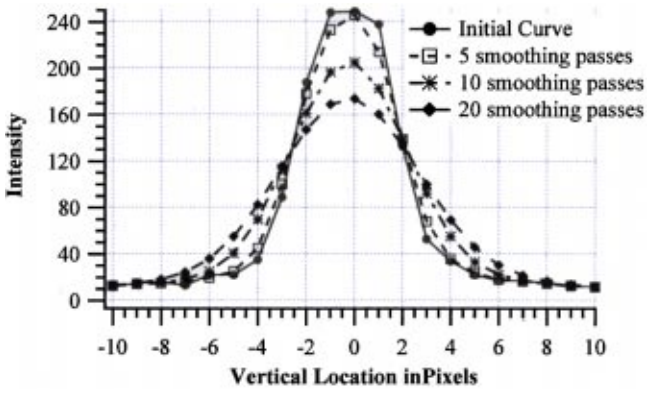

Fig. 3 Effect of smoothing on phosphorescent line profiles

3.3 Experimental Variables. A number of parameters exist which significantly affect the imaged phosphorescence emission intensity, the quality of the acquired images, and the range of temperatures capable of being imaged. These are the equipment settings (i.e., camera gain and offset, laser power, and shutter settings), chemical composition, solution pH, and the initial temperature of the solution. These are each discussed below.

3.3.1 Equipment Settings. Since the phosphorescence emission intensity is excited by a photon source and then detected by a CCD camera, the imaged intensity depends strongly on both the UV beam characteristics and the camera characteristics. Specifically, for constant tracer and alcohol concentrations and constant temperature, the beam width and energy density determine the actual emission during phosphorescence.

Prior to hitting the CCD array, the imaged light passes through an intensifier tube. When photons strike the array a voltage signal is generated for each discrete location on the array. When imaging the phosphorescence, the signal can be intensified by gain controls on the intensifier and the entire image can be amplified with CCD gain controls. In addition to the gain controls, an offset could be applied to the signal. The other primary parameters of importance are: the time delay between excitation of the tagged region and when the camera shutter opens, the length of time (gate width) that the shutter remains open, and the characteristics of the lens and aperture. The intensity of the phosphorescence decays exponentially with time, thus for larger delays the true intensity of the line is decreased and the use of gains are necessary for imaging. For the calibration data presented here the delay time was consistently held at 8 μs between laser pulse and shuttering of the camera. The gate width varied from 200–300 μs, but was held consistent for each set of data.

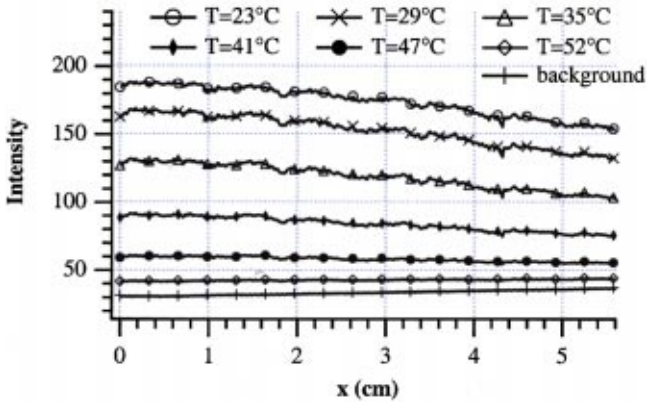

Fig. 4 Average intensity vs. location for six temperatures

3.3.2 Chemical Composition. The alcohol used in the solution significantly affects both the intensity and duration of the phosphorescent emission. The phosphorescence duration is significantly longer when using CycOH and NpOH than when using t-BuOH and the use of NpOH results in the greatest intensity. Also the concentration of both the alcohol and the tracer affect the emission intensity with greater concentrations of each resulting in greater intensities. Following the suggestion of Gendrich et al. [19], we typically use a concentration of 2×10^{-4} M for the G_-CD and a saturated (approximately 1×10^{-5}) solution of 1-BrNp. The alcohol concentrations used were 0.04–0.1 M.

3.3.3 Initial Temperature. For most of the data presented here the initial temperature was 23°C–24°C, although some data was taken with initial temperatures between 51°C and 53°C. As the solution temperature is increased the range of temperature over which intensity can be quantified decreases. At the higher temperatures, imaging was made possible by increasing the initial intensity by increasing either the gain, CCD gate width, or solution concentration.

4 Results

Shown in Figs. 5 and 6 are data relating phosphorescent intensity versus bath temperature for 16 different conditions. The solution temperature was homogeneous at the temperatures indicated in the figures. The shown intensity corresponds to the $x \approx 2.85$ cm location of each line profile (see Fig. 4). The initial temperature, T_i, was 23°C for all cases except three. For these three cases the initial temperature was 24°C, 51°C, and 53°C. The variation in intensity magnitude and behavior between the data sets is now discussed.

For all of the data of Fig. 5 the initial temperature was 23°C and the alcohol for the OH bond was NpOH for five of the cases (labeled Ne1-Ne5) and CycOH for three of the cases (labeled Cy1-Cy3). The concentration of the Gβ-CD was 2×10^{-4} M and the concentration of the NpOH and CycOH were 0.05 M and 0.10 M, respectively. All equipment settings were the same for the first four cases using NpOH. The intensifier and CCD gains and the offset were set to zero values for all cases unless otherwise specified.

The measured intensity is quite different when comparing the first four NpOH cases. The reason for the variation exists because the individual data sets were acquired on separate days and long-term quenching of the 1-BrNp occurred between data acquisition. The Ne5 data set was acquired after the first four cases using NpOH (Ne5 was taken 5 days after Ne1). However, for this data set the intensifier gain control was used and the lens aperture was

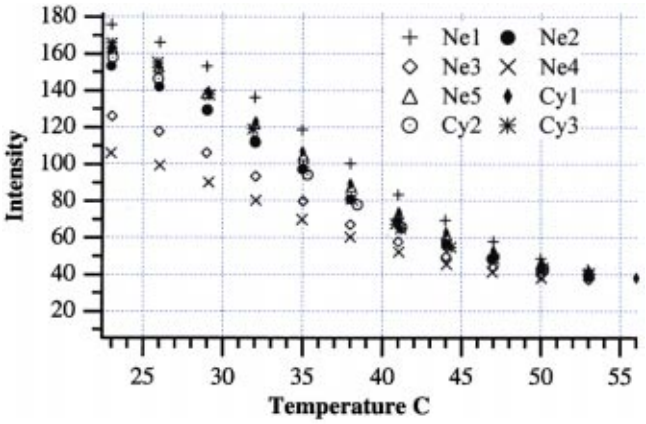

Fig. 5 Variation of intensity with bath temperature at $x \approx 2.85$ cm for an initial temperature of 23°C, eight different initial intensities, cases of CycOH and NpOH as the OH bond alcohol, and similar equipment settings

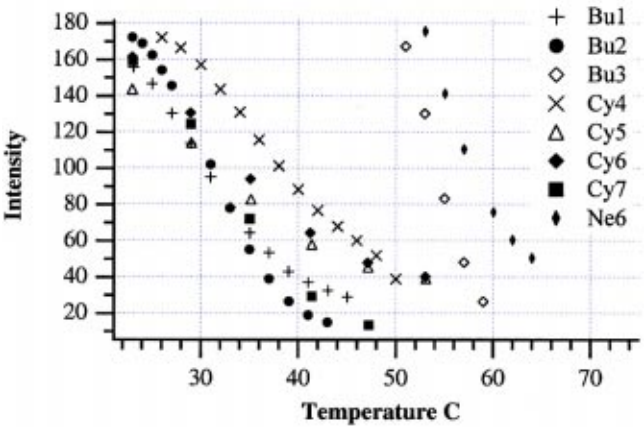

Fig. 6 Variation of intensity with bath temperature at $x \approx 2.85$ cm for four different initial temperatures, eight different initial intensities, cases of BuOH, CycOH, and NpOH as the OH bond alcohol, and different equipment settings

increased resulting in an initial intensity between the Ne1 and Ne2 data sets. The three data sets in Fig. 5 using CycOH all have about the same initial intensity and very similar behavior is exhibited in the intensity versus temperature distribution. Slight differences in the equipment settings did exist.

Note that for all cases in Fig. 5 the quantifiable temperature range is about 30°C. At 53°C the intensity approaches the background level and is nearly the same for every case regardless of alcohol, lens, aperture opening, or gain settings. The primary difference between the sets is the value of the intensity over the entire temperature range. The data of Fig. 6 show significantly more variation between different data sets than the data of Fig. 5 because the equipment settings for these data were much more varied. Shown in Fig. 6 are three cases with t-BuOH as the alcohol, four cases with CycOH and one case with NpOH. The concentration of Gβ-CD for the t-BuOH cases was 1×10^{-4} M and the concentration of the t-BuOH was 0.04 M. Two of the data sets were acquired with initial temperatures at 51°C (Bu3) and 53°C (Ne6). To enable imaging of the beam at the higher temperature, the solution concentration was increased to 0.12 M for Bu3. The camera aperture was increased and gain controls were used for Ne6. These data show that as the initial temperature is increased the intensity of the phosphorescence decreases at a much more rapid rate, and the range of temperatures that can be quantified is much smaller. The resolution is improved, however.

The Cy5, Cy6, and Cy7 data sets were acquired with very little time elapsed between acquisition of each set. Consequently, the amount that the 1-BrNp was quenched between sets was negligibly small. For the Cy5 data the gains and offset were set to zero. The gains were increased while the offset was held at zero for the Cy6 data and the gains were increased even more while the offset was increased from zero for the Cy7 data. Note how this affects the behavior of the intensity. Increasing the gain increases the initial intensity but does not affect the background level. By increasing the offset, the background level is shifted to lower intensity and the quantifiable temperature range is slightly decreased. This is also evident in the Bu1 and Bu2 data where the offset was nonzero for both of these cases. The offset was greater for the Bu2 data. The net result is a much steeper intensity versus temperature curve, similar to the cases where the initial temperature was increased. If measurements over a small temperature range are desired, these adjustments will benefit the measurement resolution. Lastly, for the Cy4 data the initial temperature was 24°C and the gain and offset were both nonzero.

It should be noted that while the CCD intensity range is from 0 to 255 grayscale values, the data in Figs. 5 and 6 are all below 180. This is a result of the smoothing algorithm used in the image analysis as previously discussed.

5 Calibration Curve Formulation

Once a set of intensity versus temperature measurements has been obtained for a given experimental setup, equipment configuration, solution, temperature range of interest, and beam location, it is possible to quantify temperature variations in a fluid at the calibration location. However, if the measurement location in the fluid is changed (i.e. the beam is moved relative to the camera so that there is more or less solution between the beam and the camera thus altering the attenuation of the phosphorescence emission), if the camera settings or optics are adjusted, or if the 1-BrNp has become quenched (i.e., a long period of time has elapsed since calibration), new calibration data will be required. All of these conditions are likely to occur. Thus for this methodology to be of practical utility, it is beneficial if only a small number of calibration measurements are required for minor changes in equipment setup, optics, measurement location, etc.

By normalizing the intensity and temperature using a two-point normalization, it is possible to develop a calibration curve that is very accurate for all of the data we have obtained (more than the 16 data sets presented here). The approach for normalization is suggested by the behavior of the intensity versus temperature profiles and is similar to that used by Coolen et al. [12]. Note from Figs. 5 and 6 that the curves all exhibit a similar trend with two inflectional points. These points are at approximately 29°C and 47°C for the data sets with $T_i=23$°C; for the cases where $T_i=51-53$°C, the inflectional points are less distinct. By normalizing the data sets so that at these inflectional points the data collapse to a single point, all other points also merge onto a single curve. For all of our data the inflectional points occur at about $T=T_i+(T_f-T_i)/5.0$ and $T=T_i+(T_f-T_i)4.0/5.0$, where T_i is the initial temperature and T_f is the temperature where the intensity value levels off (i.e., 53°C for the data of Fig. 5). Thus, normalization of the temperature scale is done as follows

$$T'=\frac{T-T_A}{T_B-T_A} \tag{3}$$

where

$$T_B=T_i+\tfrac{4}{5}(T_f-T_i) \tag{4}$$

and

$$T_A=T_i+\tfrac{1}{5}(T_f-T_i) \tag{5}$$

Normalization of the intensity is similar and is expressed as

$$I'=\frac{I-I_B}{I_A-I_B} \tag{6}$$

where I_A and I_B are the intensities corresponding to T_A and T_B, respectively.

All of the data of Figs. 5 and 6 are normalized in this manner and are shown in Fig. 7(*a*). Also shown on the figure is a fourth-order curve fit representing an average of the 16 data sets shown. The significance of the normalization is that although there were significant differences in camera settings, beam intensity, measurement location, alcohol type, lens characteristics, and initial temperatures, when normalized, all of the data merge onto one representative curve. To utilize this calibration curve the temperature range over which the emission intensity can be detected must be known. Once this is established, measurements of the intensity of T_A and T_B are necessary for calibration at a spatial location in a flow field. Subsequently any temperature can be quantified utilizing I_A, I_B, and the established calibration curve.

Variations between some data sets and the calibration curve are evident in Fig. 7(*a*). These exist because the variations in the equipment settings and values were large. For an appropriate cali-

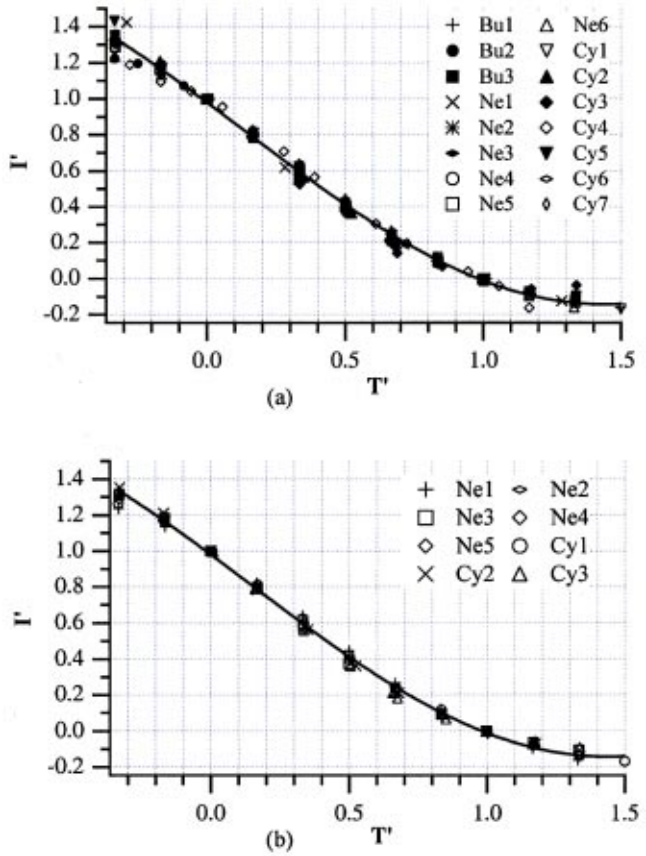

Fig. 7 (*a*) **Normalized intensity versus normalized temperature for 16 different cases.** (*b*) **Normalized intensity versus normalized temperature at $x \approx 2.85$ cm for eight cases with the initial temperature at 23°C and similar equipment settings.**

bration, the control parameters should not deviate so significantly from those that will exist for the test condition. The data of Fig. 5 were all obtained with few variations in these parameters. When plotting I' versus T' for these data, all of the I' values at a given T' are almost identical. This is shown in Fig. 7(*b*).

Because it is intensity that is measured and temperature is determined by correlation, an expression for T' as a function of I' is necessary. T' can be related to I' for the data of Fig. 7 by the expression

$$T' = 1.02 - 2.22I' + 3.171I'^2 - 2.781I'^3 + 0.808I'^4 \qquad (7)$$

Note that the above relationship is valid for the data of Fig. 7 and corresponds to $x \approx 2.85$ cm in the test cell. Because of the spatial variations in the signal (as seen in Fig. 4) due to excitation beam attenuation, optical aberrations, etc., normalization and development of T' versus I' expressions are required at each pixel location along the line. Thus in practice an expression similar to Eq. (7) is required for every pixel location, or at some specified interval, along the laser line. For our present data the maximum change in the coefficients of Eq. (7) when moving along the line is less than 10 percent. Note that for measurements in a different flow facility a complete calibration will be required. Once this is done however, calibration measurements need only be performed at T_A and T_B to utilize the existing calibration data for subsequent measurements. If dramatic changes occur (i.e. significant change in beam position) a complete characterization of the I versus T relation will again be required.

We have presented results for a line similar to what would be used in the multiple line approach of MTV. The same approach could be employed if using the grid technique for 2-D velocity measurements. Alternatively, a sheet of light could be used to quantify temperature over a 2-D domain with high spatial resolution.

6 Uncertainty Analysis

We now discuss the uncertainty associated with our present capability. Although the quantum efficiency of the 1-BrNp phosphorescence is significantly lower than that for dyes typically utilized in LIF temperature experiments, there exists at least one significant advantage. Because the emission wavelength is much longer than that for excitation there is no reabsorption of the emitted light by the dye causing self absorption, or re-emission as is the case with some dyes used for LIF. Also, since the excimer laser is pulsed, with a pulse duration of 18 ns, as opposed to the continuous operation of an Ar-ion laser, the actual time that the dye is exposed to exciting light is very short. This results in minimal photobleaching effects which can introduce uncertainty. We observed no significant short term quenching of the solution due to photon interaction. Long term quenching of the solution does occur due to oxygen reactions necessitating recalibration at T_A and T_B immediately prior to performing measurements.

There exist two primary sources of uncertainty in our present method. These are fluctuations in the excitation beam intensity and the uncertainty in fitting a curve to the calibration data. Shown in Fig. 8 is the ratio of double the rms of the intensity (95 percent confidence) over the actual intensity as a function of temperature. These data correspond to the same location as the data of Fig. 5 and for the five data sets (Ne1-Ne5). As the data indicate, the uncertainty in determining I is about 3.5–4.4 percent for the entire range 23–53°C. This uncertainty is due mostly to fluctuations in the excitation beam which has a fluctuation range of ± 3.5 percent. Also contributing to the rms magnitude are electrical noise and the fact that an 8 bit camera with a range from 0–256 and a least count of one, resulting in a measurement uncertainty of 0.4 percent, was used. For steady conditions, the uncertainty in determining the intensity can be reduced by averaging over several images. Thus for the intensity data presented previously for the calibration curve, since averaging occurred over 50 images, the uncertainty in determining I is reduced from 3.5–4.4 percent to 0.5–0.62 percent. These values are quite typical for all of our data.

If an entire set of calibration measurements were performed prior to investigating the flow field of interest, the uncertainty in determining T would be entirely due to the laser fluctuations, CCD resolution, and electrical noise. However, when using an existing calibration curve by measuring I_A and I_B at T_A and T_B, respectively, error is introduced due to the uncertainty associated with mapping the measured intensity back to the calibration data.

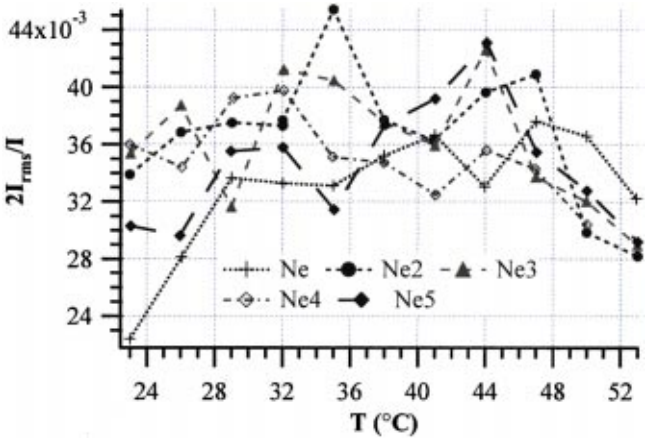

Fig. 8 Fluctuations in intensity signal at $x \approx 2.85$ cm versus temperature for Ne1-Ne5

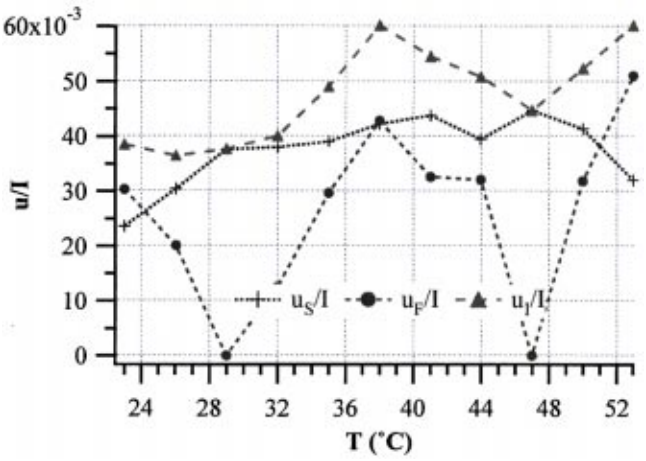

Fig. 9 Uncertainties in u_S, u_F, and u_I versus temperature at $x \approx 2.85$ for the Ne1 data set

The uncertainty in determining temperature, T_e, can be obtained from standard error analysis (e.g., Figliola and Beasley [29]) as

$$T_e = \sqrt{\left(\frac{\partial T}{\partial I}\right)^2 u_I^2} = \left(\frac{\partial T}{\partial I}\right) u_I \tag{8}$$

where u_I is the uncertainty in measuring I. u_I can be divided into two components, u_S and u_F. u_S includes the uncertainty due to laser power fluctuations, electrical noise, and measurement uncertainty using the 8 bit CCD as discussed above and u_F is the uncertainty involved with fitting a curve to the calibration data. u_S can be characterized by measuring fluctuations in the intensity signal for a known constant temperature environment and is simply double the intensity rms for a 95 percent confidence. As noted above, u_S is between 3.5–4.4 percent of the detected intensity for all of our data when considering instantaneous measurements. The magnitude of u_F can be estimated at each temperature by quantifying the difference between the average I values at that temperature, for a given configuration, and the predicted value based on the curve fit of all of the calibration data (the 16 sets of data shown in Fig. 7*a*), $u_F \approx 1/2[I - I_{\text{curvefit}}]$.

Thus the total uncertainty due to intensity fluctuations and curve fitting errors is $u_I = \pm\sqrt{(u_S)^2 + (u_F)^2}$. Figure 9 shows values of u_S, u_F, and u_I all normalized by I for the Ne1 data. The

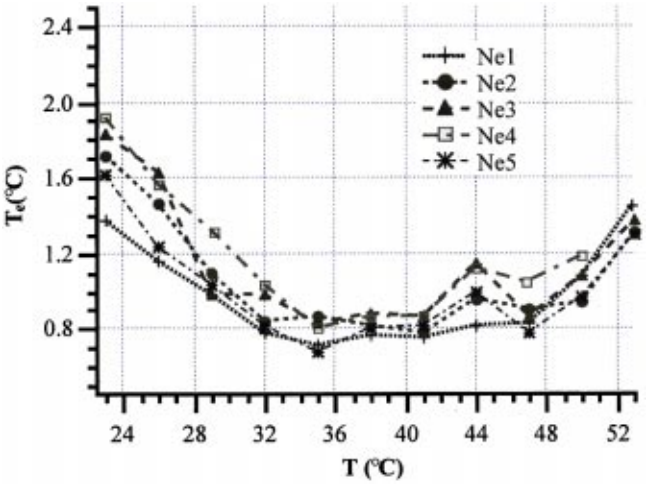

Fig. 10 Total error in determining temperature for Ne1-Ne5

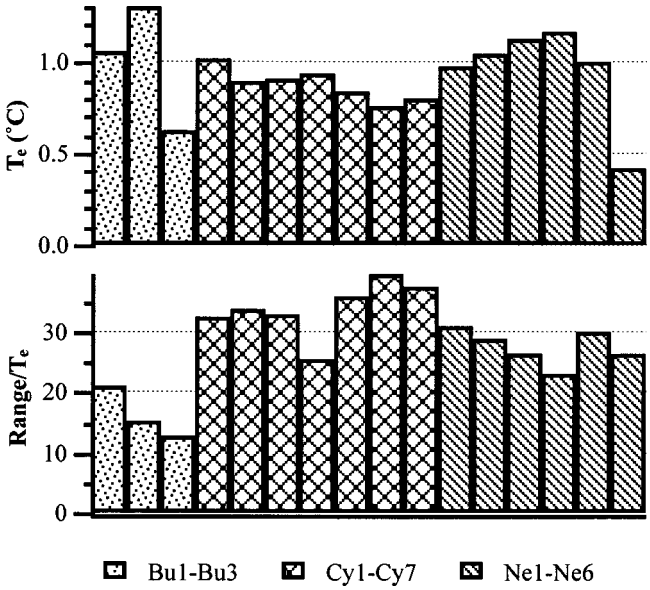

Fig. 11 Ratio of temperature range to averaged error for 16 data sets

total uncertainty in determining I ranges from 4.0–6.0 percent for instantaneous measurements but if averaging over many images the uncertainty approaches the curve of u_F/I. Using the data of Fig. 9 and Eqs. (3), (5), (7), and (8), T_e can be determined for the Ne1 data. In a similar manner T_e has been determined for all of our data. Values for T_e for the cases Ne1-Ne5 are shown in Fig. 10. The uncertainty range for instantaneous measurements is from ± 0.7–1.4°C for Ne1 to ± 0.8–1.9°C for Ne4. The average error over the temperature range shown in Fig. 10 is between ± 1.0–1.2°C for all five cases.

From Fig. 10 it can be seen that the error is greatest at the temperature extremes. This is due to the higher values of u_S and u_F at lower temperatures and higher values of u_F and $\partial T/\partial I$ at higher temperatures (evident in Fig. 7). The uncertainty due to curve fitting can be minimized significantly by making temperature measurements immediately after calibration. In this case no normalization is necessary, temperature can be measured by direct comparison to intensity, and the uncertainty is primarily due to the signal rms. The uncertainty in determining temperature is then about 0.75–1.0°C for instantaneous measurements. Figure 10 also illustrates the repeatability of MTT. Even though differences existed in the equipment settings and some long term quenching had occurred, the uncertainty is close to the same for all cases.

Figure 11 summarizes the uncertainty results by displaying the average value of T_e, and the total temperature range for each case divided by the range (dynamic range) for all 16 sets of previously presented data.

7 Simultaneous Temperature and Velocity Measurements

7.1 Laminar Flow in a Horizontal Tube With Buoyant Mixing. All of the measurements discussed above were performed in a thermally homogeneous medium. We now present MTT measurements in a flow field with temperature variations. Figure 12 shows the flow facility used to demonstrate MTT. A solution of 1-BrNp·Gβ-CD·CycOH originated in a reservoir at room temperature and traveled through a constant-temperature bath, after which it entered a horizontal quartz tube. The quartz tube had an inside diameter of 5 mm and the flow was laminar with a Reynolds number of approximately 200. The flow was allowed to develop hydrodynamically while thermally insulated. It

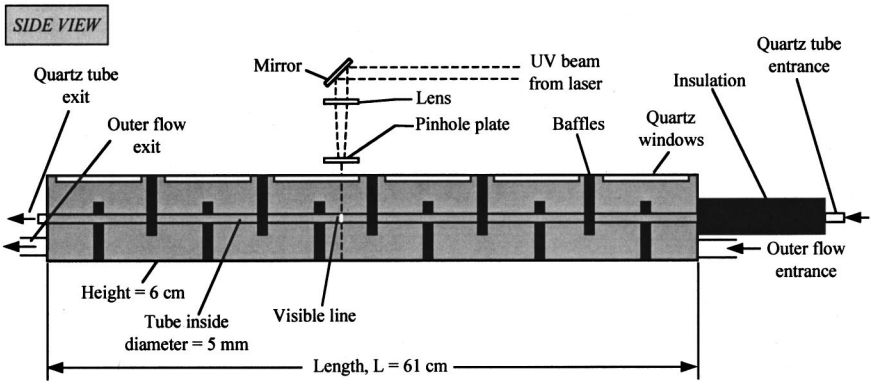

Fig. 12 Side view of flow apparatus used in demonstrating MTT under dynamic conditions

then entered a rectangular heat exchanger section in which the tube was surrounded by a flow of different temperature and much higher flow rate.

A single excitation beam was directed through the tube vertical central axis at various locations along the thermal entrance region of the tube. The diameter of the excitation beam was approximately 300 μm. The CCD acquired images of the beam in the tube with delay and exposure times of 6 ms and 0.6 ms, respectively. Figure 13 shows two such images, one with the inner flow at the inlet of the heat exchanger section at 21°C and the outer flow at 31°C and one with these temperatures reversed. These images were obtained at $x/D=45.1$, with x measured from the heat exchanger entrance. The velocity profile is also quantifiable from these images due to the deformation of the tagged line and the result is simultaneous velocity and temperature profile characterization. The system was calibrated with the inner and outer flows at equal temperatures in a manner similar to that described above for the static case. The result was a calibration curve that is unique to this arrangement but can be utilized for other temperature measurements in this apparatus. The temperature profiles were subsequently obtained from the images by referencing the intensities to the developed calibration curve. Using the error analysis method described above, the uncertainty of the measurements for an average of 190 images was estimated to be ± 1.0°C for the cold inner case and ± 0.75°C for the hot inner case (95 percent confidence; averaged over the temperature range). This uncertainty was due primarily to the uncertainty in calibration curve formulation.

Buoyancy affected the resulting temperature and velocity profiles due to the temperature gradient and relatively low Reynolds number. Consequently, the resulting velocity and temperature profiles are asymmetric. Because of this, an analytical solution for comparison was not available and a numerical simulation was performed using FLUENT. The FLUENT model solution domain included only the flow of the fluid inside of the 5 mm tube but included the entire hydrodynamic and thermal developing regions. The specified boundary condition was an overall heat transfer coefficient (convection due to the flow on the tube outside and conduction through the tube wall), U_f, in addition to the temperature of the outer fluid. The magnitude of this heat transfer coefficient was estimated by measuring the inlet and exit temperatures of both the inner and outer flows in addition to the mass flow rates for each and recognizing that $q=\dot{m}_x C_{Px}\Delta T_x = U_t A \Delta T_{lm}$, where U_t is the total heat transfer coefficient, including convection inside of the tube, and the subscript x denotes the inner flow. With U_t determined, U_f is estimated by noting $U_f = 1/(1/U_t - 1/h_x)$. A correlation of experimental data for buoyant laminar flows was presented by Depew and August and using this correlation we estimate h_x and subsequently solve for $U_f \approx 1000\ \mathrm{W/m^2 \cdot K}$. This is the value we utilized in our FLUENT model.

Figure 14 shows the measured (MTT) and predicted (FLUENT) temperature profiles corresponding to $x/D=45.1$. For Fig. 14(a) the inner flow enters the heat exchanger portion of the tube at a uniform temperature of 21°C and the outer fluid temperature is 31°C. For Fig. 14(b) these temperatures were reversed. At $x/D=0$ the fluid in the tube is hydrodynamically fully developed. Figures 15(a) and 15(b) compare the measured velocity profiles using MTV with the numerical solution for the same two cases. Both the temperature and velocity profiles represent an average over 190 images. The dashed lines on Fig. 15 represent the uncertainty range for instantaneous measurements. With the exception of the wall regions, the average profiles show good agreement, with the numerical solution, with the MTT profiles falling within ± 1.0°C of the predicted profiles. The error at the walls was due to variations in the index of refraction of quartz and water. Note that

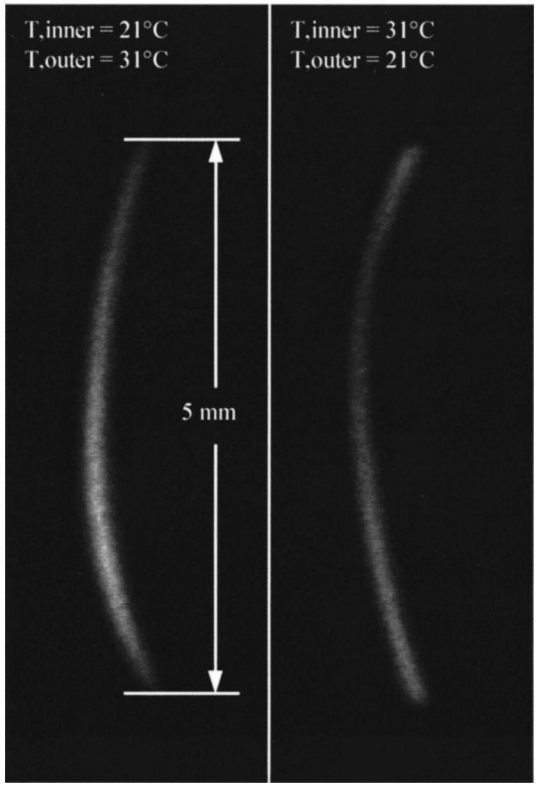

Fig. 13 MTT lines for cold inner flow (left) and hot inner flow (right)

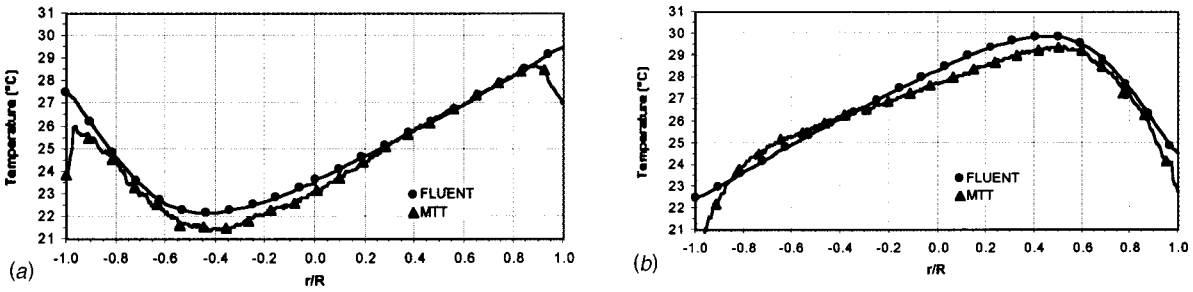

Fig. 14 Measured and predicted temperature profiles for cold inner flow (*a*) and hot inner flow (*b*)

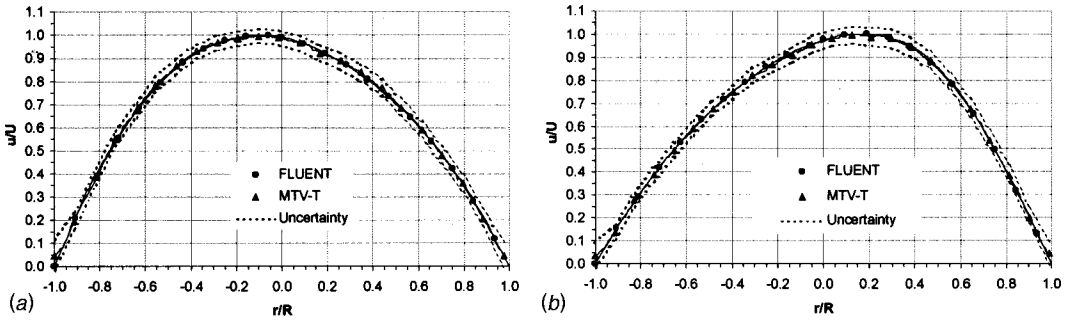

Fig. 15 Measured and predicted velocity profiles for cold inner flow (*a*) and hot inner flow (*b*)

there is also some uncertainty in the FLUENT model since it relies on a specified heat transfer coefficient that was obtained from correlation and inherently has a large uncertainty.

7.2 Discussion of Technique Extension for Turbulent Flows. The above measurements demonstrate the use of MTV for combined velocity and temperature measurements in a laminar flow with buoyant effects where mixing is slow with respect to the time interval between excitation and imaging of the phosphorescence. In flows with rapid mixing (i.e., turbulent flows) the approach needs to be modified. This is because the imaged intensity of the phosphorescence depends on the temperature of the fluid and the concentration of the excited molecules at the point of interest. Thus in a turbulent flow an excited region of fluid may be stretched and reoriented some measurable distance in the time interval between excitation and imaging, resulting in a less intense maximum than would otherwise be measured. Using a CCD camera with the capability of capturing two images separated by a very short time is one method of resolving this issue. This would allow imaging of an undeformed line immediately after excitation, from which phosphorescence intensity and thus temperature information can be quantified, followed by the imaging of a deformed line a short Δt later allowing velocity information to be obtained. The drawbacks to this approach are that the temperature and velocity measurements would not exactly coincide in time being separated by the short delay between acquisition of the two images and so far these cameras are limited to acquiring only a few images per second.

The turbulent mixing issue can also be resolved by relating the fluid temperature to the integral of the imaged intensity, integrated normal to the line instead of the maximum intensity as discussed above. Consider an idealized horizontal flow with an excited line normal to the flow direction where stretching may occur normal to the line but there exist no fluctuations or velocity in the direction parallel to the excited line. For this flow the integral of the intensity along a row of pixels normal to the excited and stretched line must be a constant if the domain includes the entire excited line region regardless of the amount of stretching that occurs because no tagged molecules have left the interrogation region. Difficulties with this approach can arise due to fluid velocity parallel to the line resulting in tagged molecules moving vertically. Due to this motion an interrogated horizontal row of pixels could include molecules that have moved there from above or below during the time delay between excitation and imaging.

As an example consider the tube flow presented above except at $Re \approx 10^4$. For such a flow v', the characteristic velocity fluctuations parallel to the line, will be at the largest 0.1–0.15 percent of the maximum horizontal velocity ($\sim$2 m/s) or about 0.2–0.3 m/s. Since the tube diameter is 5 mm and is imaged to 350 pixels on the screen the time delay between excitation and imaging for velocity measurements will be about 110 μs for a maximum deformation of 15 pixels. The corresponding motion parallel to the line will be at most 1.5–2 pixels. One way to account for the motion parallel to the line then is to integrate the intensity vertically for a small number of pixels (3–4 for the case presented) in addition to the horizontal integration discussed above. The obvious drawback to this approach is the decrease in spatial resolution although the acquisition rate can be much greater than if using a double exposure camera. Efforts focusing on these approaches and their details are currently underway.

8 Conclusion

We have shown that spatially resolved temperature measurements can be obtained using phosphorescence of a tracer molecule, a technique based on molecular tagging velocimetry. These measurements are obtained by imaging and quantifying the intensity of light emitted by the photoluminescent molecule 1-BrNp upon excitation by ultraviolet light. This phosphorescence can only be achieved in the presence of Gβ-CD and a substrate (an alcohol for the present studies) that shields 1-BrNp from the quenching effects of oxygen. The intensity of the emitted light decreases as the fluid temperature increases. The primary advantage of MTT is its potential for use as a tool with MTV to obtain simultaneous measurements of temperature and velocity.

The range and resolution of the measurements depend on experimental variables such as the CCD settings and the initial fluid temperature. With a camera offset of zero and an initial fluid temperature of 23°C, temperature measurements can be made up to 53°C with a typical error of $\pm$1.0°C ($\pm$3.33 percent of the

range). The range can be decreased, resulting in an increase in resolution, by increasing the camera offset or by increasing the initial temperature. Temperature measurements with initial temperatures greater than 50°C have been obtained with a range of approximately 12°C and uncertainties of approximately ±0.4°C to ±0.6°C. At the higher initial temperatures, measurements are possible by increasing the initial intensity by increasing the alcohol concentration, lens aperture, and/or camera gain settings.

We have also shown that when normalized, the data obtained from a number of experiments taken with a wide variety of equipment settings converge to a single curve with a high degree of agreement. This calibration curve provides a basis for subsequent temperature measurements. To obtain measurements using this curve, the range of temperatures capable of being measured using the equipment setup must be known and calibration data must be obtained at two temperatures. These temperatures are 1/5 of the temperature range below the initial temperature and 1/5 of the temperature range above the final temperature.

We demonstrated MTT in a horizontal, laminar pipe flow surrounded by a fluid of different temperature and much higher flow rate. The simultaneously measured temperature and velocity profiles agree well with a FLUENT case study.

Nomenclature

A = surface area of tube (πDL)
C = dye concentration
C_P = specific heat
D = tube diameter (mm)
h_x = convective heat transfer coefficient for inner flow
I = intensity of imaged phosphorescence
I_A = measured intensity at T_A
I_B = measured intensity at T_B
I_e = phosphorescence emission intensity
I_d = incident light intensity
I' = $[I-I_B]/[I_A-I_B]$, normalized intensity
k_{nr} = nonradiative decay coefficient
k_r = radiative decay coefficient
k_q = quenching rate coefficient
L = length of heat exchanger section
$\dot{m}_x$ = mass flow rate of inner flow
q = heat transfer rate
Q = quencher molecule
T = local temperature
T_A = $T_i+\frac{1}{5}[T_f-T_i]$
T_b = $T_i+\frac{4}{5}[T_f-T_i]$
T_e = uncertainty in measuring temperature
T_i = initial fluid temperature
T_f = final fluid temperature
T_{lm} = log-mean temperature difference for tube—heat exchanger flow
T' = $[T-T_A]/[T_B-T_A]$
u_I = total uncertainty in determing I
u_S = uncertainty in determining I due to signal fluctuations
u_F = unertainty in determining I due to fitting a curve to the calibration data
U_t = total heat transfer coefficient for tube flow
U_f = heat transfer coefficient including external convection and conduction
v' = characteristic velocity fluctuations normal to the flow direction
ε = absorption coefficient
ΔT_x = temperature difference between inlet and outlet for tube
ϕ_p = phosphoresence quantum yield

References

[1] Fabris, G., 1978, ''Probe and Method for Simultaneous Measurement of True Instantaneous Temperature and Three Components in Turbulent Flow,'' Rev. Sci. Instrum., **49**, pp. 654–664.

[2] Yao, M., Nakatani, M., Okuda, M., and Suzuki, K., 1994, ''Simultaneous Measurements of Flow and Thermal Fields in a Turbulent Channel Flow with Insertion of a Square Rod,'' Trans. Jpn. Soc. Mech. Eng., Ser. B, **60**, pp. 4192–4199.

[3] Gould, R. D., Stevenson, W. H., and Thompson, H. D., 1994, ''Simultaneous Velocity and Temperature Measurements in a Premixed Dump Combustor,'' J. Propul. Power, **10**, pp. 639–645.

[4] Lemoine, F., Antoine, Y., Wolff, M., and Lebouche, M., 1999, ''Simultaneous Temperature and 2D Velocity Measurements in a Turbulent Heated Jet using Combined Laser-Induced Fluorescence and LDA,'' Exp. Fluids, **26**, pp. 315–323.

[5] Nakajima, T., Ikeda, Y., and Motoyasu, U., 1992, ''Simultaneous Measurement of Velocity and Temperature of Water Using FLDV and Fluorescence,'' Heat Transfer-Jpn. Res., **21**, No. 6, pp. 528–542, English edition Apr. 1993.

[6] Sakakibara, J., Hishida, K., and Masanobu, M., 1997, ''Vortex Structure and Heat Transfer in the Stagnation Region of an Impinging Plane Jet (Simultaneous Measurements of Velocity and Temperature Fields by Digital Particle Image Velocimetry and Laser-Induced Fluorescence,'' Int. J. Heat Mass Transf., **40**, No. 13, pp. 3163–3176.

[7] Sakakibara, J., Hishida, K., and Maeda, M., 1993, ''Measurements of Thermally Stratified Pipe Flow using Image-Processing Techniques,'' Exp. Fluids, **16**, pp. 82–96.

[8] Lattime, S. B., Braun, M. J., and Dzodzo, M., 1995, ''Simultaneous Visualization of Flow and Temperature Patterns in a Shell and Tube Heat Exchanger by TLC,'' *American Society of Mechanical Engineers, Fluids Engineering Division*, Vol. 218, pp. 7–14.

[9] Doh, D., Kobayashi, T., and Tetsuo, S., 1995, ''Experimental Study on Vertical Buoyant Jet using 3D Particle Imaging Thermometry and Velocimetry (PITV),'' *American Society of Mechanical Engineers, Fluids Engineering Division*, Vol. 218, pp. 63–70.

[10] Upton, T. D., and Watt, D. W., 1997, ''Experimental Study of Transient Natural Convection in an Inclined Rectangular Enclosure,'' Int. J. Heat Mass Transf., **40**, pp. 2679–2690.

[11] Sakakibara, J., and Adrian, R. J., 1999, ''Whole Field Measurement of Temperature in Water using Two-Color Laser Induced Fluorescence,'' Exp. Fluids, **26**, pp. 7–15.

[12] Coolen, M. C. J., Kieft, R. N., Rindt, C. C. M., and van Steenhoven, A. A., 1999, ''Application of 2-D LIF Temperature Measurements in Water using a Nd:YAG Laser,'' Exp. Fluids, **27**, pp. 420–426.

[13] Koochesfahani, M. M., 1999, ''Molecular Tagging Velocimetry (MTV): Progress and Applications,'' *30th AIAA Fluid Dynamics Conference*, Norfolk, VA, June 28–July 1, paper no. AIAA 99-3786.

[14] Hartmann, W. K., Gray, M. H. B., Ponce, A. P., Nocera, D. G., and Wong, P. A., 1996, ''Substrate Induced Phosphorescence from Cyclodextrin·Lumophore Host-Guest Complexes,'' Inorganica Chimica Acta, **243**, pp. 239–248.

[15] Ferraudi, G. J., 1988, *Elements of Inorganic Photochemistry*, J. Wiley, New York.

[16] Ponce, A., Wong, P. A., Way, J. J., and Nocera, D. G., 1993, ''Intense Phosphorescence Triggered by Alcohols upon Formation of a Cyclodextrin Ternary Complex,'' J. Phys. Chem., **97**, pp. 11137–11142.

[17] Koochesfahani, M. M., Cohn, R. K., Gendrich, C. P., and Nocera, D. G., 1997, ''Molecular Tagging Diagnostics for the Study of Kinematics and Mixing in Liquid-Phase Flows,'' Chapter 2, Section 1 in *Developments in Laser Techniques and Fluid Mechanics*, Adrian, Durao, Durst, Heitor, Maeda, and Whitelaw, eds., Springer-Verlag.

[18] Hill, R. B., and Klewicki, J. C., 1996, ''Data Reduction Methods for Flow Tagging Velocity Measurements,'' Exp. Fluids, **20**, pp. 142–152.

[19] Gendrich, C. P., Koochesfahani, M. M., and Nocera, D. G., 1997, ''Molecular Tagging Velocimetry and other Novel Applications of a New Phosphorescent Supramolecule,'' Exp. Fluids, **23**, pp. 361–372.

[20] Webb, A. R., and Maynes, D., 1999, ''Velocity Profile Measurements in Microtubes,'' *30th AIAA Fluid Dynamics Conference*, Norfolk, VA, June 28–July 1, AIAA Paper 99–3803.

[21] Thurlow, E. M., and Klewicki, J. C., 1996, ''Mean and Instantaneous Axial Profile Measurements in Turbulent Couette-Poiseuille Flow,'' Bull. Am. Phys. Soc., **41**, p. 1690.

[22] Lee, K. Y., 1994, ''Shear Wake Interactions with a Circular Cylinder,'' Ph.D. dissertation, University of Utah.

[23] Gendrich, C. P., 1999, ''Dynamic Stall of Rapidly Pitching Airfoils: MTV Experiments and Navier-Stokes Simulations,'' Ph.D. thesis, Michigan State University.

[24] Maynes, D., 1997, ''On Rotating Bluff Body Flows,'' Ph.D. dissertation, University of Utah.

[25] Stier, B., and Koochesfahani, M. M., 1997, ''Molecular Tagging Velocimetry in Gas Phase and its Application to Jet Flows,'' ASME *Fluids Engineering Division Summer Meeting*, June 22–26, paper no. FEDSM97–3687.

[26] Maynes, D., Klewicki, J., McMurtry, P., and Robey, H., 1997, ''Hydrodynamic Scalings in the Rapid Growth of Crystals from Solution,'' J. Cryst. Growth, **178**, pp. 545–558.

[27] Wirtz, K., Koochesfahani, M. M., McGrath, J. J., and Bernard, A., 1998, ''Molecular Tagging Velocimetry Applied to Buoyancy-driven Convective Phenomena During Solidification,'' ASME Paper HTD-Vol. 361-4, p. 103.

[28] Adamson, A. W., and Fleischauer, P. D., 1975, *Concepts of Inorganic Chemistry*, J. Wiley, New York.

[29] Figliola, R. S., and Beasley, D. E., 1995, *Theory and Design for Mechanical Measurements*, Second Edition, Wiley, New York.

J. Anagnostopoulos
Department of Mechanical Engineering,
Technological Education Institute of Kozani,
Koila, 50100 Kozani, Greece

G. Bergeles
Laboratory of Aerodynamics,
Department of Mechanical Engineering,
National Technical University of Athens,
9 Heroon Polytechniou ave.,
15700 Zografou, Athens, Greece

B. Epple

P. Stegelitz

ALSTOM Energy Systems GmbH,
Augsburger Str. 712,
D-70329 Stuttgart, Germany

Numerical Simulation of Grinding and Drying Performance of a Fluid-Energy Lignite Mill

A numerical algorithm is developed for a detailed 3D simulation of the two-phase flow field in fluid-energy mills used for pulverization and drying of fossil fuels in large power plants. The gas phase equations are solved using finite differences and the control volume method, whereas a Lagrangian formulation with a stochastic particle dispersion model is adopted for the particulate phase. Fluid-particle interaction is taken into account to calculate the mass, momentum, and heat transfer between phases. Advanced numerical techniques for partially-blocked cells and local grid refinement have been utilized to achieve an accurate representation of the domain geometry and to enhance the accuracy of the results. Particle collisions, fragmentation mechanism, and moisture evaporation are simulated by corresponding models, whereas the special treatment employed for the rotating fan region provides the capability to solve the two-phase flow simultaneously in the entire rotating and nonrotating mill domain. The flow and the operation characteristics of a recently developed lignite mill are measured, and the numerical algorithm is used to predict the mill performance under various inlet profiles of the fuel mass flow rate. The predicted results are reasonable, and in agreement with the available measurements and observations, thus offering a deeper insight into the complex dynamic and thermal behavior of the two-phase flow in the mill. [DOI: 10.1115/1.1350820]

Introduction

The most important fuel preparation process in coal power plants is the grinding of the precrushed fuel, during which the raw coal particles with sizes up to several cm are pulverized to form fine particles of an average diameter below 100 μm. Fluid-energy mills are commonly used to accomplish the above process, as in all the Greek Public Power Corporation (PPC) power stations. Grinding is achieved by the impact action of the blades of a fast rotating fan, which acts also as a suction pump conveying the fuel to the burners. Flue gas extracted from the furnace is led to the mill in order to increase the gas inlet temperature and perform the drying of the coal fragments during their path through the mill volute.

A typical fluid-energy mill of PPC has a rotation speed of 400–450 rpm and pulverizes about 100 tons of lignite per hour. The mill efficiency is affected by the condition of the impact plates surfaces, which are subjected to severe wear, due to the eroding propensity of the abrasive mineral species contained in the impinging lignite particles. Moreover, uncontrollable variations of the feed rate, size distribution, and composition of the fuel cause corresponding variations at the mill outlet, thus affecting drastically the combustion characteristics in the furnace. Therefore, the capability of simulating the mill performance under various operation conditions could provide quite useful guidelines to optimize the mill efficiency. In addition, modeling and solution of the complex two-phase flow in the mill can lead to suggestions for an improved design of some parts of the mill.

A first such attempt to model a fluid-energy mill along with its classifier was made by the authors in a previous two-dimensional study (Anagnostopoulos and Bergeles [1]). A Lagrangian stochastic approach was used for the calculation of particle trajectories, whereas a new model was developed and used to simulate the fragmentation mechanism of the particles impinging on the rotating plates. Moisture evaporation, particle rebound characteristics, and erosion wear were also modeled in this study, and the various model coefficients were optimized for the Greek lignite, on the basis of available measurements. However, the gas flow filed in the mill was not solved, and a global estimation for the fluid velocities was adopted instead.

A fully 3D calculation of the two-phase flow in the mill, using the control volume method and polar Cartesian meshes, was the next target of the modeling effort, the basic features and the results of which are given in the present paper. Several difficulties associated with the construction of the control volumes into the mill volute arose, due either to the deviation of the grid lines from the domain boundaries (spiral or oblique walls), or the need for fine mesh at certain regions of the mill to preserve a satisfactory accuracy. thus, newly developed numerical techniques for the treatment of partially-blocked grid cells and the capability of using local grid refinements (Anagnostopoulos and Bergeles [2]) were incorporated. On the other hand, the unsteadiness of the flow in the rotating fan due to the limited number of plates, imposed a serious computational problem if a simultaneous simulation of the entire mill domain is requested. This problem was solved by a new proposed technique, as described later in the paper.

The complete numerical algorithm was applied to simulate the performance of a conventional EVT/ASLTOM mill. The values of the model coefficients optimized in the previous 2D study (Anagnostopoulos and Bergeles [1]) were kept the same, since both the mill arrangement and the operation conditions are similar and the same lignite type is used. Indicative graphs for the two-phase flow field in the mill are presented, along with the results of a parametric study of the effects of the entering fuel profile on the mill efficiency.

Gas Phase Model

Transport Equations. The general form of the time-averaged transport equations for a viscous, particle-laden, dilute flow is written in 3D-polar coordinates:

$$\frac{\partial}{\partial x}(\rho u\Phi)+\frac{1}{r}\frac{\partial}{\partial r}(r\rho v\Phi)+\frac{1}{r}\frac{\partial}{\partial\theta}(\rho w\Phi)=\frac{\partial}{\partial x}\left(\Gamma_\Phi\frac{\partial\Phi}{\partial x}\right)+\frac{1}{r}\frac{\partial}{\partial r}\left(r\Gamma_\Phi\frac{\partial\Phi}{\partial r}\right)+\frac{1}{r}\frac{\partial}{\partial\theta}\left(\Gamma_\Phi\frac{1}{r}\frac{\partial\Phi}{\partial x}\right)+S_\Phi+S_{p,\Phi} \quad (1)$$

Contributed by the Fluids Engineering Division for publication in the JOURNAL OF FLUIDS ENGINEERING. Manuscript received by the Fluids Engineering Division August 25, 1999; revised manuscript received October 18, 2000. Associate Editor: B. Schiavello.

where ρ is the gas density; u, v, and w the gas velocity components along the axial, x, radial, r, and angular, θ, coordinates, respectively; Γ_Φ is the turbulent exchange coefficient and $S_\Phi, S_{P,\Phi}$ the gas and the particulate-phase source terms. A system of the above equations is constructed to solve for the mass continuity ($\Phi=1$), the velocity components ($\Phi=u,v,w$), the quantities of the k-ε turbulence model (Launder and Spalding [3]), the gas mixture enthalpy ($\Phi=h$), and the water-vapor concentration ($\Phi=m_w$), using the control volume method. The mathematical expressions for the gas source terms, S_Φ, can be found in the literature (e.g., Lixing et al. [4]), whereas the particle source terms, $S_{p,\Phi}$, are given by Shuen et al. [5], except of the enthalpy equation term, which reads:

$$S_{p,h}=-\sum\ (m_{\text{in}}-m_{\text{out}})L_w+\sum\ (m_{\text{in}}T_{p,\text{in}}-m_{\text{out}}T_{p,\text{out}})C_p \qquad (2)$$

where $m_{\text{in}}, m_{\text{out}}$ is the mass of a particle when it enters or exits from a control volume, T_{in} and T_{out} its corresponding temperatures, L_w the latent heat of moisture evaporation, and C_p the particle specific heat. The gas mixture density can be obtained from the equation of state, whereas its temperature is calculated with the relation:

$$T=h/\sum_j\ (m_j\overline{C_{p,j}}) \qquad (3)$$

where $\overline{C}_{p,j}$ is the mean specific heat of species j ($j=O_2$, N_2, H_2O, and CO_2), at a temperature T, which is obtained by third order polynomial functions of temperature (Tribus [6]).

The transport equations are discretized using the hybrid differencing scheme, and a polar, collocated grid (Rhie and Chow [7]), in which all the dependent variables are stored at the center of the grid-cells. After discretization, all equations are cast into the same general form:

$$(A_P-S^P)\Phi_P=\sum_i\ A_i\Phi_i+S^U,\quad A_P=\sum_i\ A_i$$

$$\Phi=1,u,v,w,k,\varepsilon,m_w$$

$$i=\text{East, West, North, South, Up, Down} \qquad (4)$$

where A_i are the coefficients linking a dependent variable Φ_p with its neighbors on the adjacent grid volumes, and S^U, S^P the linearized source terms.

Although convenient for the impeller geometry, the application of a polar coordinate system grid faces some difficulties: As can be seen from the sketch of a typical mill arrangement in Fig. 1, the gridlines do not coincide with the spiral case boundary. The same is valid for the last convergent section of the mill, which in addition, requires an extension of the grid toward the radial direction throughout the entire domain, and hence a large number of nonsolvable, but computer memory consuming, grid cells must be used. In order to overcome these problems, two recently developed numerical techniques were included in the model, the partially-blocked cells and the local grid refinement (Anagnostopoulos and Bergeles [2]), which are briefly presented below.

Partially-Blocked Cells. This numerical technique makes possible the solution of the control volumes that are partially blocked (crossed by the domain boundaries), thus achieving a quite accurate representation of an oblique or curved boundary. A partially-blocked cell can have either less (A-type) or more (B-type) than half of its volume outside the flow field (Fig. 2). The A-type cells can be solved normally, providing that the blocked portion of their faces and volume is taken into account. This is achieved by multiplying the coefficients A_i in Eq. (4) by proper geometric coefficients γ_i expressing the free portion of the corresponding cell-faces i. The volume of the cell is also multiplied by a similar factor γ_v, equal to the free volume portion. Using these new coefficients, Eq. (4) now reads:

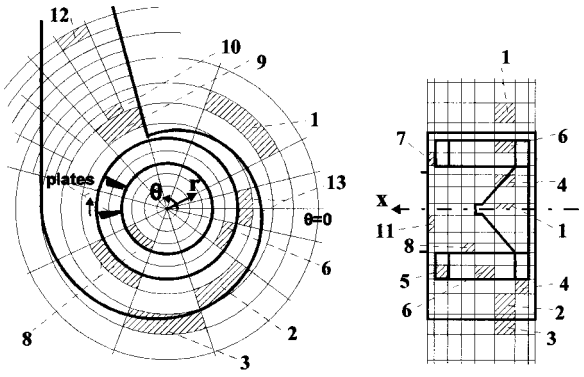

Fig. 1 Polar grid lines and control volumes in a typical mill arrangement

$$(A_P-\gamma_v S^P)\Phi_P=\sum_i\ \gamma_i A_i\Phi_i+\gamma_v S^U$$

$$A_P=\sum_i\ \gamma_i A_i \quad i=E,\ W,\ N,\ S,\ U,\ D \qquad (5)$$

The velocities at the center of a B-type cell are zero, however the fluid is allowed to pass through its partially blocked faces. Thus the fluxes and the pressure are computed as in the A-type cells, in order to satisfy continuity over the free part of the cell.

Local Grid Refinement. Finer meshes can be constructed at selected regions of the flow by dividing the cells of the main grid into any desirable number of smaller volumes. The so formed individual grids are solved separately and successively, together with the main grid, at every iteration of the algorithm, thus achieving fully domain decomposition.

The method ensures global conservation and allows for a smooth and accurate transfer of information between the nonoverlapping grids. At the grids interface, the boundary conditions for the variables of the refined grid are obtained by an interpolation method between the corresponding values of the main grid (Fig. 3). The latter is not solved in the refined regions, and the values of its variables are calculated by a volume-weighted integration of the corresponding variables of the refined grid, whereas the fluxes through the interface are area-weighted.

Simulation of the Rotating Wheel. The flow through a centrifugal rotating impeller is unsteady, due to the finite number of plates. However, the mean flow through the impeller and the spiral casing is influenced very little by this unsteadiness, since the

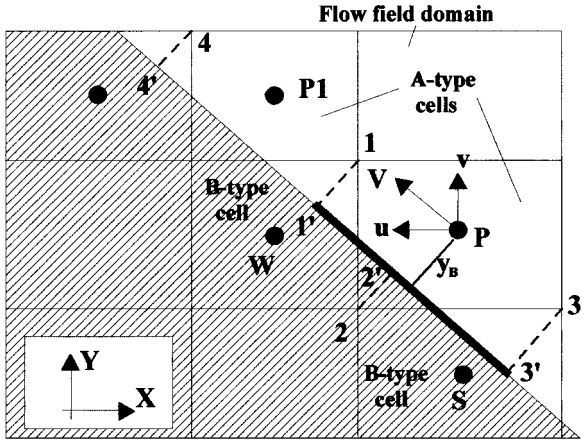

Fig. 2 Treatment of partially-blocked cells

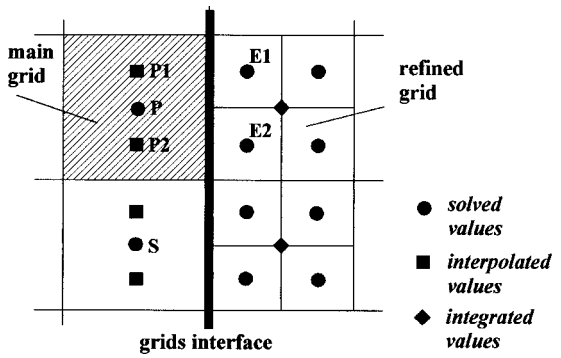

Fig. 3 Information transfer between the main and a locally refined grid

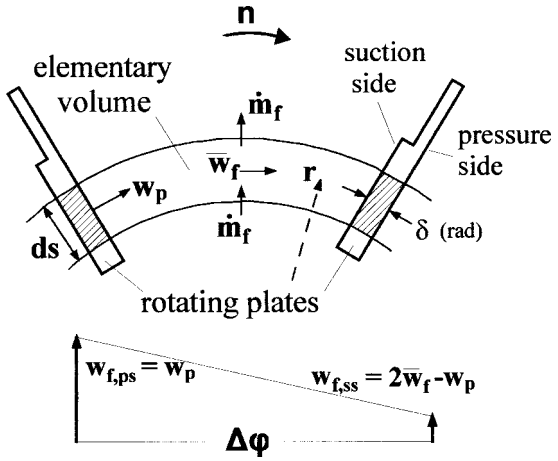

Fig. 4 Elementary fluid volume between two neighboring plates

frequency of the flow field fluctuations is high. Thus, when only the mean flow is of interest, a commonly used simulation strategy solves first for the steady 3D flow between the blades by a blade-to-blade method (e.g., Papantonis and Bergeles [8]), and then averages the obtained profile at the outer periphery of the impeller, to be used as input profile for the spiral casing. However, this method requires the linking of different algorithms, which is a difficult task when a particulate phase is also present. Moreover, the effects of the flow in the spiral case on the exiting from the impeller profile are not considered, and thus, phenomena like the re-entrainment of the flow back into the impeller are ignored. On the other hand, a detailed simulation of the gas flow field between the plates would not be useful for the present case, because the particle trajectories are practically unaffected by the gas, since before the collision the lignite fuel has high inertia (big particles with high response time), and after collision, the bulk mass of the produced fragments is spread radially (Uemois and Kleis [9]), and slides along the plate surface up to the trailing edge.

For these reasons, an alternative technique was developed and applied to simulate the mill wheel section. Assuming that in the elementary volume shown in Fig. 4 the gas tangential speed at a given radius r is constant ($w_f = \bar{w}_f$) and different from the wheel speed w_p, the moving plate exerts a force on the gas volume, which per unit passing mass of the fluid equals ($w_p - \bar{w}_f$). If a more realistic behavior of w_f is adopted, in which the latter varies linearly between the plates, from a maximum value of $w_{f,ps} = w_p$ on the pressure side of the plate to a minimum value of $w_{f,ss} = (2\bar{w}_f - w_p)$ on the suction side in order to give again an averaged value of $\bar{w}_f$ (Fig. 4), then an integration of the plate force over the gas volume produces the same result. Due to its rotation, each plate sweeps per unit time and unit blade span a gas volume $V = w_p \cdot ds$, therefore the cumulative force exerted by N plates on the unit volume of the entire gas circular ring would be:

$$\bar{F} = \frac{(w_p - \bar{w}_f) \cdot w_p \cdot ds \cdot N}{r \cdot (2\pi - N \cdot \delta) \cdot ds} = \frac{(w_p - \bar{w}_f) \cdot 2\pi \cdot n \cdot N}{(2\pi - N \cdot \delta)} \qquad (6)$$

where δ is the blade tangential thickness (rad) at the radial location r, n the wheel rotational speed (rps) and the term $(2\pi - N \cdot \delta) \cdot r \cdot ds$ represents the total volume per unit of blade span of the gas circular ring.

Considering now a grid-cell that lays within the wheel section, it can be assumed that the force exerted on it by the blade is given by the previous Eq. (6) after replacing $\bar{w}_f$ by the calculated tangential velocity at the center of the cell, so the cumulative force on all the grid-cells belonging to the same circular ring equals to that of Eq. (6).

The above force constitutes an extra source term which is introduced in the tangential momentum equation, for all the grid-cells laying within the wheel section. Thus, the latter can be varied along a peripheral line, taking into account the effects of the flow conditions at the impeller inner and outer edges.

Finally, the volume and the parallel to the w-velocity faces of the above grid-cells are multiplied by a factor $(1 - N \cdot \delta/2\pi)$, to account for the tangential blockage effect of the plates, due to their finite thickness.

Boundary Conditions. The commonly used ''wall functions'' boundary conditions are applied only to A-type cells, since the velocity at the center of a B-type cell is zero. However, the actual wall area is considered, e.g., in the plane view of Fig. 2, the area 1′-2′-3′ is taken into account for the node P, the 1′-4′ for the node P1, etc. On the other hand, the wall shear stress is calculated on the basis of the velocity component parallel to the wall (V, Fig. 2), and the resulting source term is then shared out among the three velocity components (u, v, and w). Also, the actual normal distance of the node P from the wall (y_B) is considered.

The various grid-cell types where boundary or other specific conditions must be implemented, are highlighted in the sketch of Fig. 1: Type-1 cells are outside the flow domain and they are not solved. Cells of type 2 and 3 correspond to A- and B-partially blocked cells and are modeled as described above. A free or partially blocked cell of type 4 adjoins a moving (rotating) wall, thus the expressions of the wall functions conditions are properly modified. Type-5 cells are totally blocked inside the calculated domain, and they are solved setting the terms S^U and S^P of Eq. (5) to a zero and a great value, respectively. The treatment of type-6 cells, laying into the impeller section is analyzed in the previous chapter. If the gap of the rotating wheel and the case wall is very small, as in the present case, control volumes of type 7 are not formed. The blockage due to the plates is considered in the adjacent to the wheel faces of the type-8 cells. The boundary conditions at the interface of the main and a refined grid (type-9 and 10 cells) are treated as described previously using interpolation techniques. Dirichlet inlet conditions are imposed at the faces of all type-11 cells which are on the inlet section of the mill. Free rotating flow conditions are set in type-12 cells adjacent to the mill exit, whereas a mass balance produces the outlet flow velocity. Cyclic boundary conditions are applied to type-13 cells, at both sides of the grid-line $\theta = 0$. Finally, the heat losses due to convection through the mill walls are also modeled.

Particulate Phase Model

The methodology followed for the particulate phase simulation is described in detail in the previous 2D study of a similar mill arrangement (Anagnostopoulos and Bergeles [1]), hence only the basic features will be briefly given below:

A Lagrangian approach is used to calculate the trajectories of a statistically sufficient number of representative lignite particles.

The equations of particle motion are integrated using small time-steps, considering the effects of the drag and gravity forces, whereas a stochastic particle dispersion model accounts for the interaction of the gas turbulence with the particles (particle-eddy interaction).

When a particle enters the rotating wheel, its relative distance from the nearest approaching plate is randomly selected, and its trajectory is tracked until it impinges on the fast rotating plate. At this point, the particle is crushed and a range of smaller fragments are produced, the size distribution of which depends on the impact energy and on the materials type. Fragmentation is simulated by a series of successive ''crushing events,'' or breakage steps (Austin et al. [10], Pauw [11]). At each such step all the top-size class fragments are rebroken, producing smaller fragments that obey the $\sqrt{2}$ size interval rule (Austin et al. [10], Tasserie et al. [12]). Hence, the cumulative product size distribution after a particle fragmentation can be calculated if the number of breakage steps is known. The developed model correlates this number with the particle impact energy and introduces additional parameters for the maximum possible normal impact velocity, V_{max}, which results in a maximum number of breakage steps, N_{max}, as well as for the lower limit of this velocity, V_{min}, below which no breakage occurs. The above parameters will be used in the present study as they have been optimized for the Greek lignite (Anagnostopoulos and Bergeles [1]). The value of V_{max} is changed from 50 m/s–60 m/s, to account for the higher tangential speed the leading edge of the rotating plates has in the present mill arrangement (impeller inner radius 1.4 m and rotation speed 420 rpm).

The produced fragments are spread radially and parallel to the surface of the plate. The magnitude of the initial spreading velocity is calculated as the sum of the particle parallel velocity component at the impact point plus a portion of the impact energy transported after the impact to a tangential (parallel to the plate surface) velocity, which was adjusted to 40 percent of the impact speed (40–50 percent, according to Uemois and Kleis [9]) and has a randomly selected direction. The trajectory of a representative fragment of each of the produced size-classes is then tracked up to the mill exit. Until the exit of the wheel, the fragments slide on the plate surface, and the friction due to Coriolis force is taken into account in the equations of their motion. Any further impingement of a fragment on an internal mill wall does not result in breakage.

Evaporation of the fuel moisture is allowed after fragmentation and only if the particle temperature exceeds 100°C. The latter is continuously calculated, by integrating the particle energy balance equation, taking into account both the evaporation and the heating from the gas due to convection. The moisture release rate is computed with the aid of an exponential formula (Mcintosh [13]), and it is a function of the particle size, the fuel type, and the temperature. The latter two parameters were accounted for by the use of an adjustable coefficient, C_v, taken here as optimized in the previous 2D study (Anagnostopoulos and Bergeles [1]), since the fuel is the same and the temperature levels in the mill are similar.

All particle collisions with any other internal surface of the mill (e.g., distribution damper, spiral case, etc.) are simulated, to enhance the accuracy of the results. For example, even the possibility of a particle to impinge on the leading or the trailing edge of a rotating plate at the inner or the outer periphery of the wheel, is considered. The particle rebound velocities after an impingement are calculated using empirical restitution functions (Beacher et al. [14]).

Solution Procedure

A special preprocessing algorithm reads the geometrical data of the mill arrangement, and the dimensions of the grid-volumes, in order to characterize the type of each computational cell, as well as to calculate all the geometrical quantities involved in the main algorithm calculations. Then, the system of Eqs. (5) is solved iteratively, with the SIMPLE algorithm, and the TDMA solver (Patankar and Spalding [15], Patankar [16]). After a certain number of iterations (usually $20 \div 50$), the representative particles of the solid phase are launched into the current flow field and their trajectories are calculated throughout the mill. The produced particle source terms are then re-introduced into the corresponding gas-phase equations to perform a new set of iterations. This coupled solution is repeated until both the gas and the solid-phase results converge.

Table 1 Geometrical data and inlet conditions of the lignite mill

Impeller inner/outer radius	1.4 / 2.05 m
Plate span	1.14 m
Plate inlet / outlet width	100 / 70 mm
Number of impact plates	14
Rotation speed	420 rpm
Gas mass flow rate	65.765 kg/s
Gas temperature	586 °C
Gas density	0.3797 kg/m^3
Gas mean inlet velocity	34.724 m/s
Gas composition (by mass)	17.84 % H_2O, 9.41 % O_2, 11.39 % CO_2, 61.36 % N_2
Lignite mass flow rate	26.224 kg/s
Lignite moisture content	46.8 % by mass (wet basis)
Lignite inlet velocity	10 m/s, inclined 20 deg. downwards
Lignite inlet temperature	50 °C
Size distribution	5 % of mass > 10 mm.

Model Application and Results

Test Cases and Computational Details. The developed numerical model was applied to simulate the performance of a lignite mill designed and constructed by EVT/ALSTOM, and recently installed in the 5th unit (375 MWe) of PPC Aghios Dimitrios power station. The flow, key geometrical, and operation data of the mill are summarized in Table 1. The thermodynamic properties of the gas at the mill inlet were calculated from the measured composition and temperature of the various entering streams: flue-gas, hot air, parasitic air, recycling gas from the classifier, and water vapor due to the earlier evaporation of the coal surface moisture (moisture content of the raw lignite 52 percent). All the measured data used in this work constitute averaged values obtained after several operation hours of the mill, and their experimental uncertainty is estimated low (within 5 percent), providing that the lignite type and preparation, and the combustion conditions in the boiler remain the same.

The simulated mill geometry is sketched on true scale in Fig. 5. After the mill exit, the flow passes through a classification chamber (not shown). A main polar grid of $31\times34\times28$ nodes covers the entire flow domain, whereas two refined meshes of $31\times27\times27$, and $27\times29\times26$ nodes, respectively, are also placed to enhance the accuracy of the simulation, one over the last part of the mill (vertical duct) and the other at the inlet region, covering the vertical distribution dampers. The need for finer grids arises at the first region due to the diversity of the grid lines from the duct walls (Fig. 5) and the flow streamlines, and at the second region because of the expected complexity of the flow field there.

A uniform profile was taken for the gas-phase inlet velocity, whereas several possible cases for the mass distribution of the fuel at the mill inlet section were examined, as shown in Table 2. For all these cases, a number of 30 size-classes of $\sqrt{2}$ rule were used to

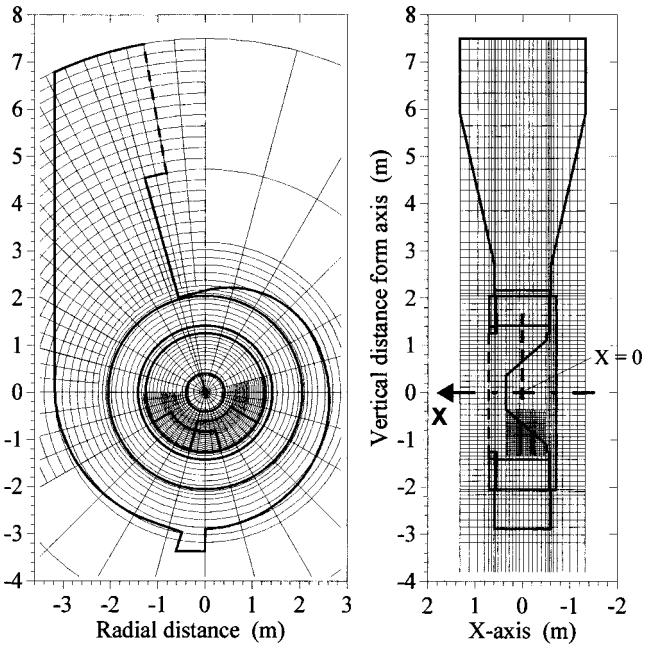

Fig. 5 Simulated mill geometry and grid-lines arrangement

represent the particulate phase, and the mass distribution was obtained by a Rosin-Rammler function, adjusted so as the sizes above 10 mm constitute 5 percent of the total entering mass, to agree with the measurements. A representative particle of each size-class is launched from each of 110 points uniformly distributed at the inlet section, thus the trajectories of about 3300 particles are tracked up to the wheel section, and about ten times more fragments from there to the mill exit. After convergence of the coupled two-phase flow solution, about 135,000 particles are launched, producing more than 10^6 fragments, in order to obtain statistically accurate results for the particulate phase. The total CPU-time for the complete simulation of each case was about 2 days on the average, on a Pentium-2 200 MHz computer.

The Gas Flow Field. Flow velocity vectors are plotted in Figs. 6 and 7 for a selected case (Case-9, Table 2); the basic features discussed below, are similar for all the other cases, since only the particle mass distribution profile is varied.

The gas enters the mill with an axial velocity component and acquires radial momentum flowing round the conical part, before its entrance to the wheel region (Figs. 6 and 7). The tangential velocity in this first part of the mill is small, and there is a trend of moving toward the lower pressure region at the mill contraction duct (Fig. 6).

Table 2 List of the numerically examined cases

CASE	Fuel inlet mass flux
0	uniform mass flux profile
1	70% of mass below A-A′
2	80 % below A-A′
3	90 % below A-A′
4	70 % below B-B′
5	80 % below B-B′
6	90 % below B-B′
7	70 % below C-C′
8	80 % below C-C′
9	90 % below C-C′

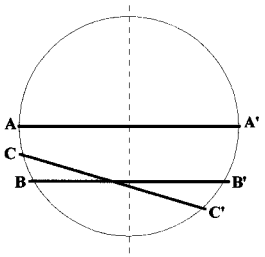

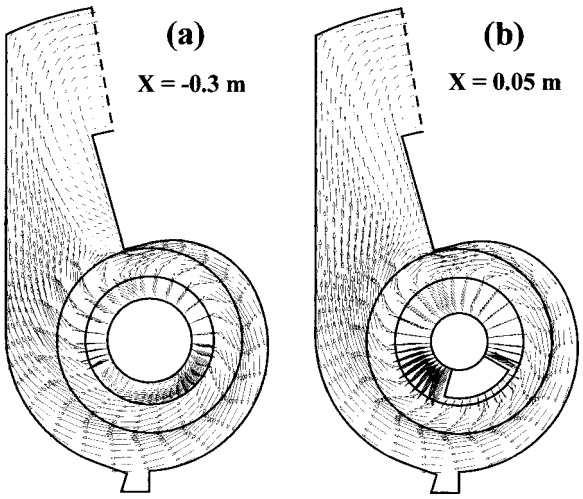

Fig. 6 Gas velocity vectors at two vertical sections of the mill

Several small vortices are formed behind the vertical distribution dampers (Figs. 6(*a*) and 7(*b*)), which are of minor importance, since few particles reach there. However, as can be observed comparing Figs. 7(*a*) and 7(*b*), the dampers produce a more uniform velocity profile along the plates, and consequently, a more even distribution of the coal particles there.

After the entrance to the plates section, the gas exhibits a delay in following the wheel rotational speed, due to inertia effects. Thus, the averaged tangential velocity component is initially small, and increases progressively toward the outward periphery of the wheel (Fig. 6). On the other hand, the cross sections in Fig. 7, reveal a rather complex 3D flow field between the plates, and a trend to form reverse flow near the front part of the wheel (mill inlet). An internal recirculation back into the rotating plates is evident at the upper end of the spiral case, starting from the stagnation area near the lower edge of the right oblique wall (Fig. 6), which causes the reentrainment into the wheel of some of the smaller particle fragments that reach there.

A ring-type vortex formed in the radial section of the case and progressively established along the spiral (Fig. 7), is responsible for the numerically observed trend of the smaller fragments to flow upwards parallel to the front mill wall. As can be observed in

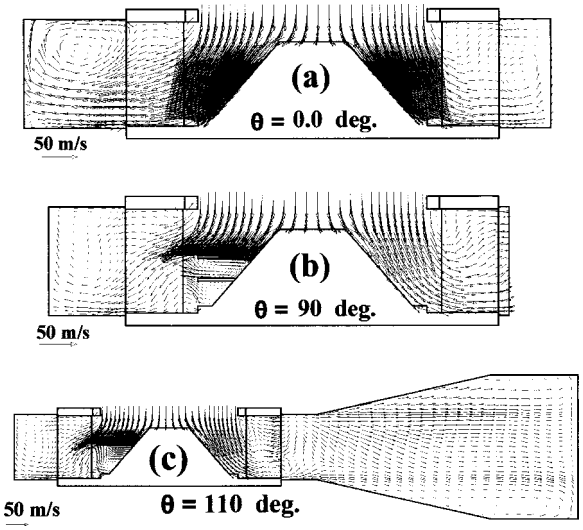

Fig. 7 Gas velocity vectors in the mill, at various r-θ planes

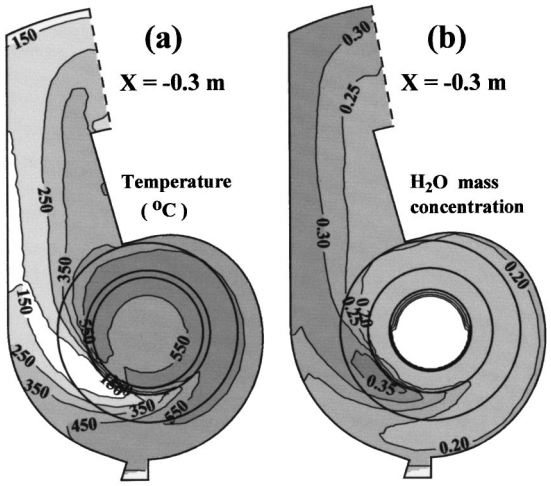

Fig. 8 Contours of temperature distribution (*a*), and water vapor concentration (*b*), at a vertical cross-section of the mill (x = −0.3 m)

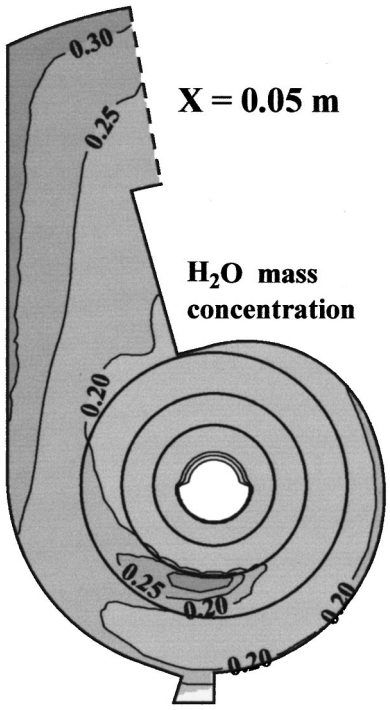

Fig. 9 Water vapor concentration at a vertical cross-section (x=0.05 m)

Fig. 7(*c*), the internal recirculation is more pronounced at this side, thus the above vortex results also in an increased particle reentrainment into the wheel.

The flow stream-wise velocity is reduced in the last mill part, downstream of the spiral volute, where the diverging angle of the front and back walls is relatively high (Fig. 7(*c*)).

Gas Temperature and H_2O Concentration. A significant portion of the gas thermal energy is consumed for the particle moisture evaporation, thus the gas temperatures are inversely proportional to H_2O concentration values and the corresponding distributions are similar (Figs. 8 and 11).

Temperature and water vapor concentration remain constant inside the inlet mill part, because no evaporation is allowed before fragmentation. A substantial portion of the moisture of the produced fragments is evaporated early inside the wheel (e.g., about 70 percent for 100 μm and 95 percent for 50 μm fragments), resulting in an abrupt reduction of gas temperature there (Figs. 8 and 9).

At the upper half of the wheel the particles can travel up to the back mill wall before entering the plates, thus the H_2O concentration is increased at this region (Fig. 10(*b*)). On the other hand, a different behavior can be observed at the lower half, where the particles impinge on the vertical distribution dampers and directed radially to the plates. Hence, higher H_2O concentration is now formed in different regions inside the wheel (Figs. 8(*a*) and 9), depending on the angular and axial location of the corresponding damper. The maximum values are observed into the small recirculation zones behind the dampers (Figs. 10 and 11(*b*)).

This behavior was found to be similar in all the examined cases, however the maximum H_2O concentration increases in the upper half and decrease in the lower half of the wheel as the inlet profile of lignite mass flux becomes more uniform (e.g., cases 3–0, Table 2).

The ring-type vortex formed in the spiral case facilitates the diffusion of the water vapor in the bulk gas, resulting in a more uniform H_2O concentration and temperature profile between the back and the front walls in the last part of the mill (Fig. 11). However, due to the centrifugal action of the plates, the corresponding profiles in the vertical cross section remain nonuniform up to the mill exit (Figs. 8 and 9).

Particle Trajectories. The lignite particles path throughout the mill is demonstrated in the indicative plots of Fig. 12. A raw particle launching from the lower part of the mill inlet section (Fig. 12(*a*)) meets a vertical distribution damper, and is directed radially, toward the fan. The particle impinges on a plate just after its entrance there, due to the high rotational speed of the fan, and fragmentation occurs. The produced fragments are then centrifuged following different paths, depending on their size and rebound velocity. Hence, the bigger fragments leave earlier the plate and, moving along straight lines, exhibit several collisions with

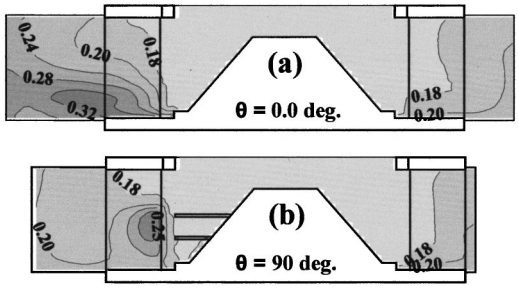

Fig. 10 Water vapor concentration in the mill, at various r-θ planes

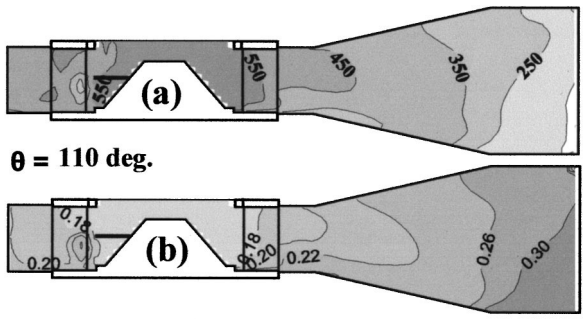

Fig. 11 Contours of temperature distribution (*a*, °C), and H_2O mass concentration (*b*), at an r-θ plane (θ=110 deg)

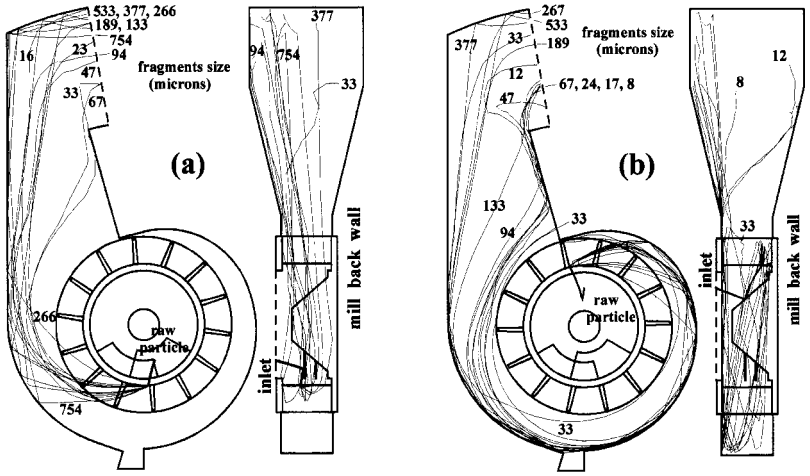

Fig. 12 Indicative particle trajectories of the produced fragments (size in μm) of 12 mm raw lignite particles, launched from: lower part (*a*), and upper part (*b*)

the internal mill walls before they reach the exit. On the contrary, the smaller and low inertial fragments follow closely the gas streamlines (Fig. 6), and does not impinge on the case.

Completely different is the behavior of the particles entering from the upper half of the inlet section (Fig. 12(*b*)). Their path is not obstructed by the dampers, and thus they can penetrate deep into the mill before being centrifuged to the fan. All the produced fragments arrive soon at the casing, where they exhibit repeated collisions, and almost slide along the spiral walls. During this motion, they are captured by the ring-type vortex reported above, which leads them gradually toward the front mill wall and finally causes the reentrainment of some of the smaller fragments into the bulk flow. The latter then reach the oblique wall of the convergent section, and some of them recirculate back into the fan. Such a recirculation is useless, since these fragments are already quite small and completely dried, and in addition, it causes a small reduction of the mill suction and transport efficiency. On the other hand, the bigger fragments keep sliding up to the end of the spiral, and at this point they again enter into the upward flow due to the abrupt change of the wall slope.

Mill Performance. The calculated size distribution of the produced fragments is well compared with the measured values, as shown in Fig. 13. The dotted line represents the expected distribution at the exit of the classifier, assuming that all particles larger than 2 mm will recycle to the mill. The above distribution is, as expected, almost the same for all Cases 0–10, since the grinding efficiency of the mill, which express the degree of size reduction of the raw lignite particles achieved in the mill, depends primarily on the wheel rotation speed, which was constant.

On the other hand, the drying efficiency, namely the portion of the raw fuel moisture that is released in the mill, exhibits some differences, since the final moisture of the particles is closely related to their residence time into the mill. This behavior is illustrated in Fig. 14, where the average moisture content of the fuel at the mill exit increases as more fuel mass enters through the lower half of the mill inlet section (cases 3, 6, and 9). Consequently, any gain in fuel transport efficiency, that could be achieved by reducing the fuel residence time in the mill, will be obtained at the expense of its drying efficiency. Nevertheless, the variation is rather low (max. 3 percent), since the majority of the produced fragments are small and release their moisture rapidly, so as at the mill exit all particles smaller than 100 μm are completely dried. The final fuel moisture content for all the examined cases is quite close to the measured value of 10 percent (wet basis).

The above results confirm that the values for the coefficients of the evaporation and the size reduction models have been well optimized in the previous 2D study (Anagnostopoulos and Bergeles [1]), and can be used also for the fully 3D simulation. Therefore the numerical accuracy of the above models is considered satisfactory, at least for the present fuel type. On the other hand, although a detailed results independence study was not carried out, since this work aims mainly to present the features and capabilities of the developed numerical methodology to simulate this engineering problem, some preliminary tests showed minor

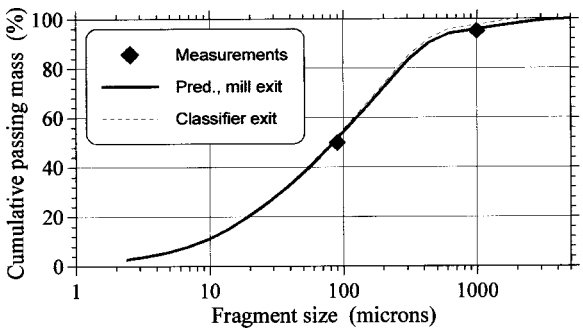

Fig. 13 Size distribution of the produced lignite fragments

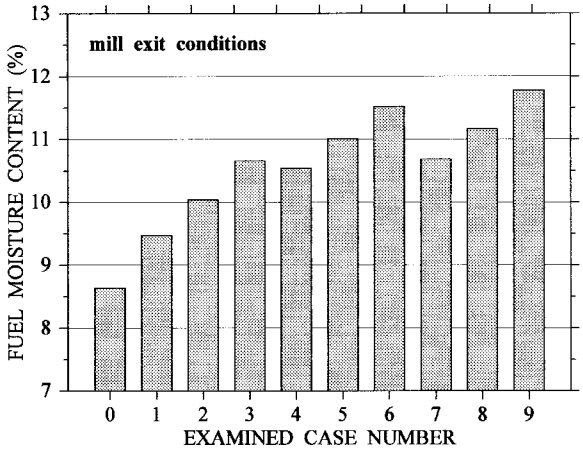

Fig. 14 Calculated fuel moisture content at the mill exit (percent, wet basis)

changes in the predicted global mill grinding and drying efficiency when the local grid refinements were not used, as also when the number of the launched representative particles was reduced from 3300–1500.

Conclusions

A number of advanced numerical techniques, along with a particle fragmentation model and a novel approach for a simultaneous solution of the entire mill domain, including the rotating wheel section, were combined in order to develop an efficient 3D numerical algorithm for the simulation of fluid-energy mills. The algorithm was found capable of not only reproducing the global performance characteristic correctly as measured in a lignite mill of a PPC power plant, but also to provide important details for the complicated two-phase flow developed throughout its volute, which cannot be obtained from measurements or observations in the real unit, thus offering a better understanding of the gas and fuel interaction and dynamic behavior in the mill.

The drying of the smaller lignite fragments, below 100 μm, was found to be completed early into the wheel section, whereas only a minor portion of the moisture content of the large fragments is evolved during their travel throughout the mill. The contribution of the vertical dampers, placed against the mill inlet, to a better distribution of the entering fuel along the impact plates surface is elucidated. The produced fragments exhibit different path-lines, depending on their size and rebound characteristics, as well as on the peripheral location where the raw particle impinges on the rotating plates. The larger fragments are strongly centrifuged and slide along the spiral peripheral wall, whereas the smaller ones closely follow the gas flow and do not collide with the mill internal walls. The establishment of a ring-type vortex along the spiral case was identified, and associated with the trend of the particles to gradually approach the front mill wall, where the inner flow formed between the fan and the spiral is stronger and causes an undesirable internal recirculation of some small fragments. Separation and reverse flow is observed at the last mill section. Detailed results for the temperature distribution and the water vapor concentration in the mill were obtained, and the regions of maximum and minimum values are depicted and explained.

A parametric study was carried out in order to investigate the influence of the fuel inlet mass profile on the grinding and drying efficiency of the specific lignite mill. The produced size distribution showed minor dependence, whereas the final fuel moisture content was found to increase as the center of weight of the fuel entering mass moves downwards, because of a consequent reduction of the average residence time of the particles into the mill. This study constitutes an example of the capabilities of the developed algorithm to examine the influence of several other critical operation, flow, and geometrical parameters affecting the mill efficiency, such as the wheel rotation speed, the impeller and casing geometry, the fuel composition and feed rate, the drying gas temperature. Moreover, since the detailed dynamic path of both raw particles and fragments in the mill is given by the algorithm, the extension of the model to assess the erosion wear of the mill internal walls and impact plates can be a subsequent research step.

Acknowledgments

This work was funded by ALSTOM Energy Systems GmbH, and the authors would like to acknowledge the contribution and support of Dr. Gehrke, director of the research project.

Nomenclature

A_i = transport equation coefficient for the cell-face i
C_p = particle specific heat
$C_{p,j}$ = specific heat of gas species j
F = force acting on the gas-phase
h = gas mixture enthalpy
k = turbulence kinetic energy
L_w = latent heat of moisture evaporation
m_j = mass concentration of gas species j
n = wheel rotation speed (rps)
N = number of impact plates
r = radial coordinate
S_Φ = gas-phase source term
$S_{p,\Phi}$ = particle-phase source term
S^U, S^P = linearized source terms of the transport equation
T = temperature
u,v,w = axial, radial and tangential velocity component
w_f = gas tangential velocity in an elementary volume
$\overline{w_f}$ = mean gas tangential velocity in an elementary volume
$w_{f,ps}$ = gas tangential velocity on the pressure side of the plate
$w_{f,ss}$ = gas tangential velocity on the suction side of the plate
w_p = wheel tangential speed
x = axial coordinate
γ_i = free portion of partially blocked cell-face i
γ_v = free portion of partially blocked cell volume
Γ_Φ = turbulent exchange coefficient
δ = blade tangential thickness
ε = turbulence kinetic energy dissipation rate
θ = angular coordinate
ρ = gas density
Φ = dependent variable

References

[1] Anagnostopoulos, J., and Bergeles, G., 1997, ''Numerical Investigation of the Grinding Process in a Beater Wheel Mill with Classifier,'' ASME J. Eng. Gas Turbines Power, **119,** pp, 723–733.
[2] Anagnostopoulos, J., and Bergeles, G., 1999, ''3-D Modeling of the Flow and the Interface Surface in a Continuous Casting Mold Model,'' Metall. Mater. Trans. B, (in press).
[3] Launder, B. E., and Spalding, D. B., 1974, ''The Numerical Computation of Turbulent Flows,'' Comput. Methods Appl. Mech. Eng., **3**, pp. 269–289.
[4] Lixing, Z., Wenyi, L., Jian, Z., and Zuolan, W., 1986, ''Numerical Modeling of Three-dimensional Flow Field and Two-dimensional Coal Combustion in a Cylindrical Combustor of Co-flow Jets with Large Velocity Difference,'' *21st Symposium (Intl.) on Combustion*, the Combustion Institute, pp. 257–264.
[5] Shuen, J. S., Chen, L. D., and Faeth, G. M., 1983, ''Evaluation of a Stochastic Model of Particle Dispersion in a Turbulent Round Jet,'' AIChE J., **29**, pp. 167–170.
[6] Tribus, M., 1961, *Thermostatics and Thermodynamics*, Van Nostrand, London.
[7] Rhie, C. M., and Chow, W. L., 1983, ''Numerical Study of the Turbulent Flow Past an Airfoil with Trailing Edge Separation,'' AIAA J., **21**, pp. 1525–1532.
[8] Papantonis, D., and Bergeles, G., 1986, ''A Numerical Solution of the Blade-to-blade Flow in Turbomachines by the Application of a Transformation on the S1 Stream Surface,'' Acta Mech., **14**, pp. 141–153.
[9] Uemois, H., and Kleis, I., 1975, ''A Critical Analysis of Erosion Problems which have been Little Studied,'' Wear, **31**, pp. 359–371.
[10] Austin, L. G., Klimpel, R. R., and Luckie, P. T., 1984, *Process Engineering of Size Reduction: Ball Milling*, Society of Mining Engineers, New York.
[11] Pauw, O. G., 1988, ''The Minimization of Overbreakage During Repetitive Impact Breakage of Single Ore Particles,'' Powder Technol., **56**, pp. 251–257.
[12] Tasserie, M., Bideau, D., Troadec, J. P., Dodds, J., Laurent, Y., and Vernier, P., 1992, ''Experimental Results on Fragmentation of Brittle Material,'' Powder Technol., **73**, pp. 61–66.
[13] Mcintosh, M. J., 1976, ''Prediction of Performance of a Browncoal Mill System,'' Braunkohle, **12**, pp. 433–448.
[14] Beacher, B., Tabakoff, W., and Hamed, A., 1982, ''Improved Particle Trajectory Calculations Through Turbomachinery Affected by Coal Ash Particles,'' ASME J. Eng. Power, **104**, pp. 64–68.
[15] Patankar, S. V., and Spalding, D. B., 1972, ''A Calculation Procedure for Heat, Mass and Momentum Transfer in Three-Dimensional Parabolic Flows,'' Int. J. Heat Mass Transf., **15**, pp. 1787–1806.
[16] Patankar, S. V., 1980, *Numerical Heat Transfer and Fluid Flow*, Hemisphere, Washington, DC.

Yin L. Young
Doctoral Graduate Student

Spyros A. Kinnas
Associate Professor

Ocean Engineering Group,
The University of Texas at Austin,
Austin, TX 78712

A BEM for the Prediction of Unsteady Midchord Face and/or Back Propeller Cavitation

A boundary element method (BEM) is used for the numerical analysis of sheet cavitation on a propeller subjected to the non-axisymmetric wakes of marine vehicles. This method is extended in order to treat mixed partial and supercavity patterns on both the face and back of the blades with searched cavity detachment. The convergence of the method is studied. The predicted cavity shapes and forces by the present method agree well with experiments and with those predicted by another numerical method.
[DOI: 10.1115/1.1363611]

Introduction

Accurate predictions of the extent of sheet cavitation and the pressure distribution on the blade are crucial in the design and assessment of marine propulsors. Recent advancements in the propulsor design industry require numerical tools that are able to model more extreme geometries with mixed (partial and supercavity) cavity patterns on both the face and the back of the blades. The ultimate objective of this research is to develop and validate a three-dimensional BEM code, PROPCAV, for the prediction of general cavity patterns and loading on propellers subjected to non-axisymmetric wakes of marine vehicles.

PROPCAV models the three-dimensional unsteady cavitating propeller flow via a low-order boundary element (panel) method (Fine [1]) (Kinnas and Fine [2]). The shape and extent of the cavity are determined in the framework of a boundary-value problem: for a given cavitation number and inflow, the position of the cavity surface is determined in an iterative manner until both a prescribed pressure condition and a zero normal velocity condition are satisfied on the cavity surface. The method was first developed for unsteady partial cavitation with prescribed cavity detachment on the back of propeller blades (Kinnas and Fine [3], Kinnas and Fine [2], Fine [1]). It was then extended to predict leading edge and mid-chord partial cavitation on either the face or the back of the blades by Mueller and Kinnas [4], Mueller [5], and Mueller and Kinnas [6]. In the present work, PROPCAV is further extended to predict leading edge and mid-chord cavitation on both the face and the back of the blades simultaneously.

To validate the panel code, results are compared to those observed in experiments and to those obtained from the latest version of an existing vortex-lattice method, MPUF-3A (Kosal [7], Lee and Kinnas [8]). In the vortex-lattice method, the vortex and source lattice are placed on the mean camber surface of the blade and a linearized cavity model is used. A leading edge correction through linearized dynamic boundary condition on the cavity is used in MPUF-3A to model the effect of blade thickness on the cavity (Kinnas [9], Kinnas [10]). The latest version of MPUF-3A also includes nonlinear thickness-loading coupling (Kinnas [11]) for propellers subjected to fully wetted flow.

MPUF-3A has the advantage of less computational time and memory requirements than PROPCAV. However, the flow details at the propeller leading edge cannot be captured accurately via the vortex-lattice method. Furthermore, the current version of MPUF-3A only considers the effect of nonlinear thickness-loading coupling in fully wetted flow. For cavitating flow, the effect of cavity sources should also be included in the thickness-loading coupling to correctly model the effect of cavity. PROPCAV, on the other hand, captures the geometry of the blades by discretizing the blade surfaces with panels. Thus, PROPCAV inherently includes the effect of nonlinear thickness-loading coupling and offers a more accurate modeling of the flow details at the propeller leading edge. Moreover, the panel code also provides a better foundation for concurrent research efforts in the modeling of developed tip-vortex cavitation and surface-piercing propellers.

In this paper, convergence studies of PROPCAV are presented. Predictions from PROPCAV are also compared with experimental observations and with predictions from MPUF-3A.

Formulation

This section summarizes the formulation of the cavitating flow around a propeller given by Kinnas and Fine [2] and Fine [1].

Consider a cavitating propeller subject to a general inflow wake, $\vec{q}_{\text{wake}}(x_s, y_s, z_s)$, as shown in Fig. 1. The inflow wake is expressed in terms of the absolute (ship fixed) system of cylindrical coordinates (x_s, y_s, z_s). The inflow velocity, $\vec{q}_{in}$, with respect to the propeller fixed coordinates (x, y, z), can be expressed as the sum of the inflow wake velocity, $\vec{q}_{\text{wake}}$, and the propeller's angular velocity $\vec{\omega}$, at a given location $\vec{x}$:

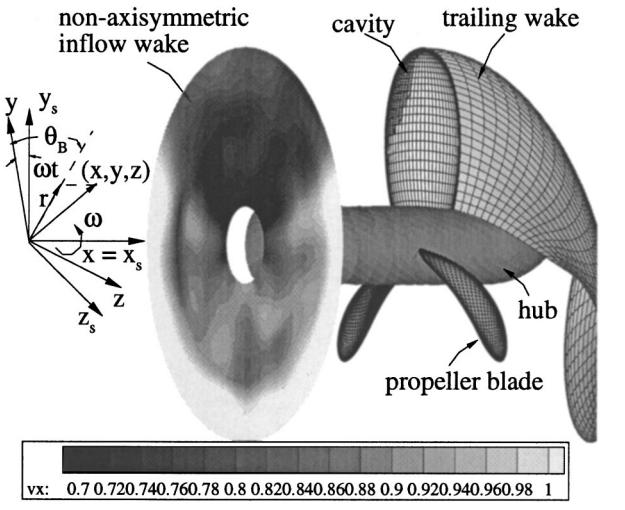

Fig. 1 Propeller subjected to a general inflow wake. The propeller fixed (x,y,z) and ship fixed (x_s, y_s, z_s) coordinate systems are shown.

Contributed by the Fluids Engineering Division for publication in the JOURNAL OF FLUIDS ENGINEERING. Manuscript received by the Fluids Engineering Division November 3, 1999; revised manuscript received January 31, 2001. Associate Editor: J. Katz.

$$\vec{q}_{in}(x,y,z,t)=\vec{q}_{\text{wake}}(x,r,\theta_B-\omega t)+\vec{\omega}\times\vec{x} \tag{1}$$

where $r=\sqrt{y^2+z^2}$, $\theta_B=\arctan(z/y)$ and $\vec{x}=(x,y,z)$.

The inflow, $\vec{q}_{\text{wake}}$, is assumed to be the effective wake, i.e., it includes the interaction between the vorticity in the inflow and the propeller (Kinnas et al. [12], Choi [13]). The resulting flow is assumed to be incompressible and inviscid. The total velocity field, $\vec{q}$, can be expressed in terms of $\vec{q}_{in}$ and the perturbation potential, ϕ, as follows:

$$\vec{q}(x,y,z,t)=\vec{q}_{in}(x,y,z,t)+\nabla\phi(x,y,z,t) \tag{2}$$

where ϕ satisfies the Laplace's equation in the fluid domain (i.e., $\nabla^2\phi=0$). Note that in analyzing the flow around the propeller, the propeller fixed coordinates system is used.

The Green's Formula. The perturbation potential, ϕ, at every point p on the combined wetted blade and cavity surface, $S_{WB}(t)\cup S_C(t)$, must satisfy Green's third identity:

$$2\pi\phi_p(t)=\int\int_{S_{WB(t)\cup S_C(t)}}\left[\phi_q(t)\frac{\partial G(p;q)}{\partial n_q(t)}-G(p;q)\frac{\partial\phi_q(t)}{\partial n_q(t)}\right]dS+\int\int_{S_W(t)}\Delta\phi(r_q,\theta_q,t)\frac{\partial G(p;q)}{\partial n_q(t)}dS;$$

$$p\in(S_{WB}(t)\cup S_C(t)) \tag{3}$$

where the subscript q corresponds to the variable point in the integration. $G(p;q)=1/R(p;q)$ is the Green's function with $R(p;q)$ being the distance between points p and q. $\vec{n}_q$ is the unit vector normal to the integration surface. $\Delta\phi$ is the potential jump across the wake surface, $S_W(t)$. The definitions of S_{WB}, S_C, and S_W are depicted in Fig. 2.

Equation (3) should be applied on the ''exact'' cavity surface S_C, as shown in the drawing at the top of Fig. 2. However, the cavity surface is not known and has to be determined as part of the solution. In this work, an approximated cavity surface, shown in the drawing at the bottom of Fig. 2, is used. The approximated cavity surface is comprised of the blade surface underneath the cavity on the blade, S_{CB}, and the portion of the wake surface which is overlapped by the cavity, S_{CW}. The justification for making this approximation, as well as a measure of its effect on the cavity solution can be found in Kinnas and Fine [3] and Fine [1].

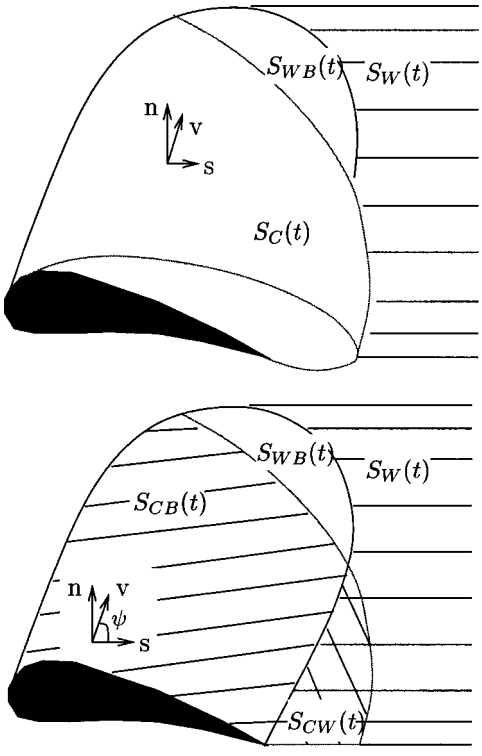

Fig. 2 Top: definition of the exact surface; Bottom: definition of the approximated cavity surface.

Using the approximated cavity surface, Eq. (3) may be decomposed into a summation of integrals over the blade surface, S_B ($\equiv S_{CB}+S_{WB}$), and the portion of the wake surface which is overlapped by the cavity, S_{CW}.

Field Points on S_B. For field points on S_B, Eq. (3) becomes:

$$2\pi\phi_p(t)=\int\int_{S_B}\left[\phi_q(t)\frac{\partial G(p;q)}{\partial n_q}-G(p;q)\frac{\partial\phi_q(t)}{\partial n_q}\right]dS-\int\int_{S_{CW}(t)}q_w(t)G(p;q)dS+\int\int_{S_{CW}(t)\cup S_W(t)}\Delta\phi(r_q,\theta_q,t)\frac{\partial G(p;q)}{\partial n_q}dS;$$

$$p\in S_B \tag{4}$$

where q_w is the cavity source distribution in the wake, defined as:

$$q_w(t)\equiv\frac{\partial\phi^+}{\partial n}(t)-\frac{\partial\phi^-}{\partial n}(t) \tag{5}$$

The superscripts ''+'' and ''−'' denote the upper and lower wake surface, respectively.

The geometry of the trailing wake is assumed to be invariant with time and taken to be the same as that corresponding to the circumferentially averaged flow (Kinnas and Hsin [14]). The dipole strength $\Delta\phi(r,\theta,t)$ in the wake is convected along the assumed wake model with angular speed ω:

$$\Delta\phi(r,\theta,t)=\Delta\phi_T\left(r_T,t-\frac{\theta-\theta_T}{\omega}\right);\quad t\geq\frac{\theta-\theta_T}{\omega}$$

$$\Delta\phi(r,\theta,t)=\Delta\phi^S(r_T);\quad t<\frac{\theta-\theta_T}{\omega} \tag{6}$$

where r, θ are the cylindrical coordinates at any point in the trailing wake surface, S_W, and (r_T,θ_T) are the coordinates of the trailing edge at a point on the same streamline with (r,θ). $\Delta\phi^S$ is the steady flow potential jump in the wake when the propeller is subject to the circumferentially averaged flow.

The value of the dipole strength, $\Delta\phi_T(r_T,t)$, at the trailing edge of the blade at radius r_T and time t, will be given from the Morino's Kutta condition (Morino and Kuo [15]):

$$\Delta\phi_T(r_T,t)=\phi_T^+(r_T,t)-\phi_T^-(r_T,t) \tag{7}$$

where $\phi_T^+(r_T,t)$ and $\phi_T^-(r_T,t)$ are the values of the potential at the upper (suction side) and lower (pressure side) blade trailing edge, respectively, at time t.

Recently, an iterative pressure Kutta condition (Kinnas and Hsin [14]) is applied for the analysis of unsteady fully wetted and cavitating propellers. The iterative pressure Kutta condition modifies $\Delta\phi_T(r_T,t)$ from that of Morino to achieve equality of pressure at both sides of the trailing edge everywhere on the blade (Young et al. [16]).

Field Points on S_{CW}. For field points on S_{CW}, the left-hand side of Eq. (3) reduces to $2\pi[\phi_p^+(t)+\phi_p^-(t)]$, which can be expressed as $4\pi\phi_p^\pm(t)\mp 2\pi\Delta\phi_p(t)$ depending on if the equation is applied on the upper ''+'' or the lower ''−'' surface of the supercavitating region. This will render the following expression for $\phi_p^\pm$:

$$4\pi\phi_p^{\pm}(t) = \pm 2\pi\Delta\phi_p(t) + \int\int_{S_B}\left[\phi_q(t)\frac{\partial G(p;q)}{\partial n_q} - G(p;q)\frac{\partial\phi_q(t)}{\partial n_q}\right]dS - \int\int_{S_{CW}(t)} q_w(t)G(p;q)dS + \int\int_{S_{CW}(t)\cup S_W(t)}\Delta\phi(r_q,\theta_q,t)\frac{\partial G(p;q)}{\partial n_q}dS; \quad p\in S_{CW} \tag{8}$$

Kinematic Boundary Condition on Wetted Part of the Blade. The kinematic boundary condition on the wetted portion of the blade defines the source strengths in terms of the known inflow velocity, $\vec{q}_{in}$:

$$\frac{\partial\phi_q}{\partial n_q} = -\vec{q}_{in}(x_q,y_q,z_q,t)\cdot\vec{n}_q \tag{9}$$

Dynamic Boundary Condition on Cavitating Surfaces. The dynamic boundary condition on the cavitating blade and wake surfaces requires the pressure everywhere on the cavity to be constant and equal to the vapor pressure, P_v. By applying Bernoulli's equation, the total velocity on the cavity, $\vec{q}_c$, can be expressed as follows:

$$\vec{q}_c^2 = n^2D^2\sigma_n + |\vec{q}_{\text{wake}}|^2 + \omega^2r^2 - 2gy_s - 2\frac{\partial\phi}{\partial t} \tag{10}$$

where $\sigma_n \equiv (P_o - P_v)/(0.5\rho n^2D^2)$ is the cavitation number; ρ is the fluid density and r is the distance from the axis of rotation. P_o is the pressure far upstream on the shaft axis; g is the acceleration of gravity and y_s is the ship fixed coordinate, shown in Fig. 1. $n = \omega/2\pi$ and D are the propeller rotational frequency and diameter, respectively.

On the cavitating blade surface, the magnitude of the cavity velocity may also be written in terms of its projections along $\vec{s}$ (the chordwise) and $\vec{v}$ (the spanwise) grid directions on the blade surface:

$$|\vec{q}_c|\sin\psi = \sqrt{V_s^2 + V_v^2 - 2V_sV_v\cos\psi} \tag{11}$$

with:

$$V_s \equiv \frac{\partial\phi}{\partial s} + \vec{q}_{in}\cdot\vec{s} \quad \text{and} \quad V_v \equiv \frac{\partial\phi}{\partial v} + \vec{q}_{in}\cdot\vec{v} \tag{12}$$

where ψ is the angle between s and v directions, as shown in Fig. 2.

Combining Eqs. (10) and (11) renders the following expression for $\partial\phi/\partial s$.

$$\frac{\partial\phi}{\partial s} = -\vec{q}_{in}\cdot\vec{s} + V_v\cos\psi + \sin\psi\sqrt{|\vec{q}_c|^2 - V_v^2} \tag{13}$$

which can then be integrated to form a Dirichlet type boundary condition for ϕ. The unknown terms $\partial\phi/\partial t$ and $\partial\phi/\partial v$ on the right-hand side of Eq. (13) are determined in an iterative manner.

On the cavitating wake surface, the coordinate $\vec{s}$ is assumed to follow the streamline.[1] Thus, the total crossflow velocity is assumed to be small, which renders the following expression for $\partial\phi/\partial s$:

$$\frac{\partial\phi}{\partial s} = -\vec{q}_{in}\cdot\vec{s} + |\vec{q}_c| \tag{14}$$

Kinematic Boundary Condition on Cavitating Surfaces. The kinematic boundary condition on the cavity requires the total velocity normal to the cavity to be zero. As shown in (Kinnas and Fine [2]), the kinematic boundary condition renders the following equation for the cavity thickness (h) on the blade:

$$\frac{\partial h}{\partial s}[V_c - \cos\psi V_v] + \frac{\partial h}{\partial v}[V_v - \cos\psi V_s] = \sin^2\psi\left(V_n - \frac{\partial h}{\partial t}\right) \tag{15}$$

where $V_n \equiv \partial\phi/\partial n + \vec{q}_{in}\cdot\vec{n}$ is the total normal velocity.

Assuming again that the spanwise crossflow velocity on the wake surface is small, the kinematic boundary condition reduces to the following equation for the cavity thickness (h_w) on the wake:

$$q_w(t) - \frac{\partial h_w}{\partial t} = |\vec{q}_c|\frac{\partial h_w}{\partial s} \tag{16}$$

where q_w is the cavity source distribution, defined by Eq. (5).

The definitions of h and h_w are depicted in Fig. 3. The quantity h_w at the blade trailing edge is determined by interpolating the upper cavity surface over the blade and computing its normal offset from the wake sheet.

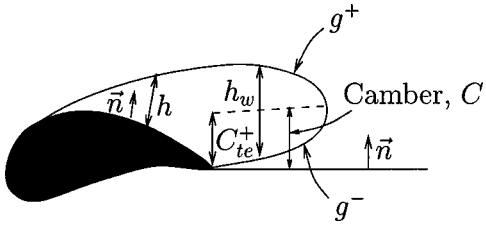

Fig. 3 Definition of the cavity height on the blade and on the supercavitating wake

Cavity Closure Condition. The extent of the unsteady cavity is unknown and has to be determined as part of the solution. The cavity length at each radius r is given by the function $l(r,t)$. For a given cavitation number, σ_n, the cavity planform $l(r,t)$ must satisfy the following requirement:

$$\delta(l(r,t),r;\sigma_n) \equiv h(l(r,t),r,t) = 0 \tag{17}$$

where δ is the cavity height at the trailing edge of the cavity. Equation (17) requires that the cavity closes at its trailing edge. This requirement is the basis of an iterative solution method that is used to find the cavity planform.

Solution Method. The unsteady cavity problem is solved by inverting Eqs. (4) and (8) subjected to conditions (6), (7), (9), (13), (14), and (17). The numerical implementation is described in detail in Kinnas and Fine [2], Fine [1], and Kinnas and Fine [3]. In brief, for a given cavity planform, Green's formula is solved with respect to the unknown ϕ on the wetted blade surface and the unknown $\partial\phi/\partial n$ on the cavity surface. The cavity heights are then determined by integrating Eqs. (15) and (16). The correct cavity planform is obtained in an iterative manner by satisfying the cavity closure condition, Eq. (17). The split-panel technique (Fine and Kinnas [18], Kinnas and Fine [3]) is used to treat blade and wake panels that are intersected by the cavity trailing edge.

Convergence Studies

Convergence studies with varying number of propeller revolutions, panel discretization, and time step size for PROPCAV are presented. Comparisons of predicted cavity volumes and propeller loadings for propeller DTMB4148, of which the paneled geometry and inflow wake are shown in Fig. 4, are studied. The inflow wake corresponds to the wake in Mishima et al. [19] with the effects of the tunnel walls and vortical inflow/propeller interactions (nonaxisymmetric ''effective'' wake) accounted by using the method of Kinnas et al., [12], Choi [13]. It should be noted that the ''unusual'' double peak shown in the cavity volume plots is due to the two slow regions in the inflow wake about the top position. The same behavior was also observed in the experiment.

[1]It has been found by (Fine [1]) (Fine and Kinnas [17]) that the effect of the crossflow term in the cavitating wake region has very small effect on the solution.

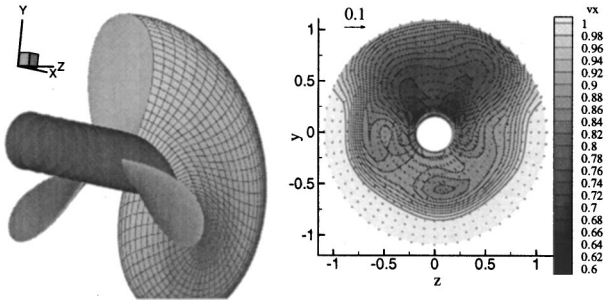

Fig. 4 Geometry and inflow wake of propeller DTMB4148

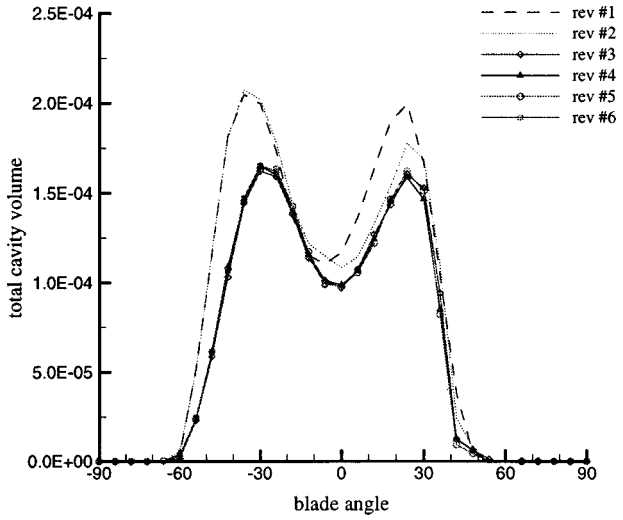

Fig. 5 Convergence of cavity volume with number of propeller revolutions for propeller DTMB4148. 60×20 panels. $\Delta\theta$=6 deg, σ_n=2.576, J_s=0.954, F_r=9.159.

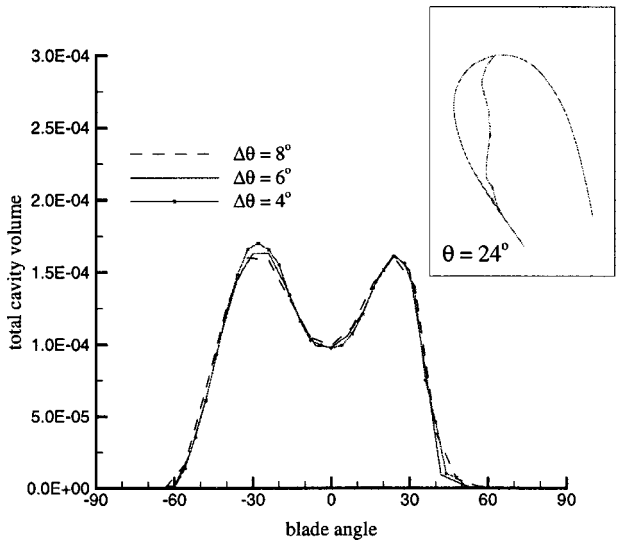

Fig. 6 Convergence of cavity volume with blade angle increments for propeller DTMB4148. 60×20 panels. σ_n=2.576, J_s=0.954, F_r=9.159.

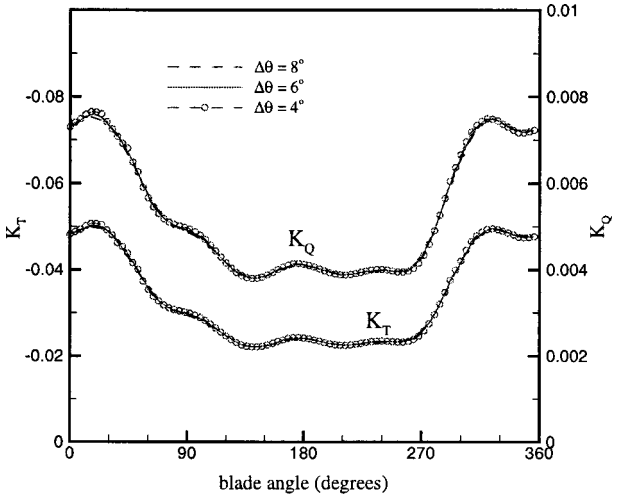

Fig. 7 Convergence of cavitating blade force coefficients with blade angle increments for propeller DTMB4148. 60×20 panels. σ_n=2.576, J_s=0.954, F_r=9.159.

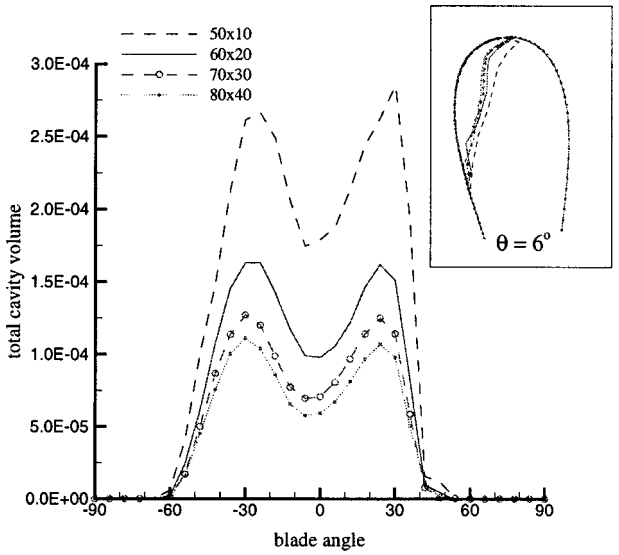

Fig. 8 Convergence of cavity volume with panel discretization for propeller DTMB4148. $\Delta\theta$=6 deg, σ_n=2.576, J_s=0.954, F_r=9.159.

Convergence With Number of Revolutions. PROPCAV accounts for the effect of other blades on the key blade in a progressive manner. At each key blade position, the effects of each of the other blades are accounted for by using the solution (dipole and source strengths) at an earlier time step when the key blade was in the position of that blade. Thus, the solution obtained by PROPCAV depends on the number of revolutions. Figure 5 shows the effect of number of revolutions on cavity volume. As shown on the figure, the solution converged at the fourth revolution for this particular case.

Convergence With Blade Angle Increment. Since the problem is unsteady, the numerical solution depends on the time step size, which is expressed in terms of blade angle increment, $\Delta\theta$, in PROPCAV. Three blade angle increments are used: 4, 6, and 8 deg. The effect of different blade angle increments on the predicted cavity volume and propeller loading are shown in Figs. 6 and 7, respectively. As shown in the figures, the results are not very sensitive to blade angle increments for this particular case.

Convergence With Mesh Size. In addition to the number of propeller revolutions and blade angle increments, panel discreti-

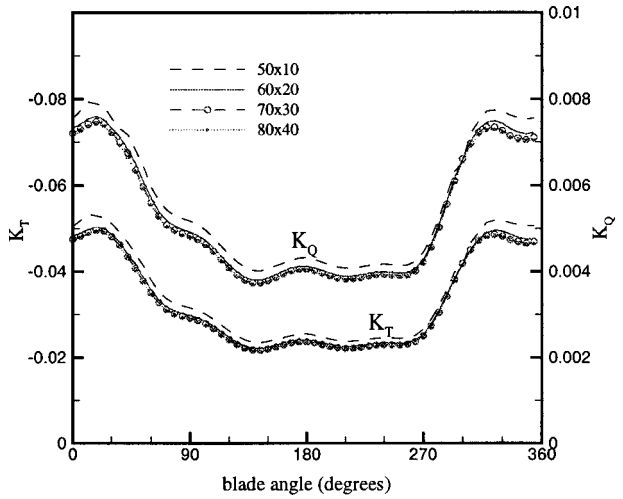

Fig. 9 Convergence of cavitating blade force coefficients with panel discretization for propeller DTMB4148. $\Delta\theta$=6 deg, σ_n =2.576, J_s=0.954, F_r=9.159.

zation is also important in the convergence of the solution. Figures 8 and 9 show the dependence of cavity volume and propeller loading on panel discretization, respectively. As shown in the figures, the results are more sensitive to mesh size than blade angle increment, especially in terms of cavity volume.

Validation With Experiments

In order to thoroughly validate PROPCAV, results from four different sets of experiments are presented.

Propeller DTMB5168—Five Bladed, Highly-Skewed Propeller. Comparisons of measured thrust and torque coefficients in an experiment with predictions from PROPCAV and MPUF-3A for propeller DTMB5168 in fully wetted, uniform inflow are shown in Fig. 10. The geometry of the propeller is also shown in Fig. 10. Notice that PROPCAV yields more accurate force predictions, especially K_Q, than MPUF-3A for all advance coefficients shown.

Propeller DTMB4119—Three Bladed, Zero-Skew and Zero-Rake Propeller. Figure 11 shows the comparison of unsteady thrust and torque coefficients obtained from experiment,

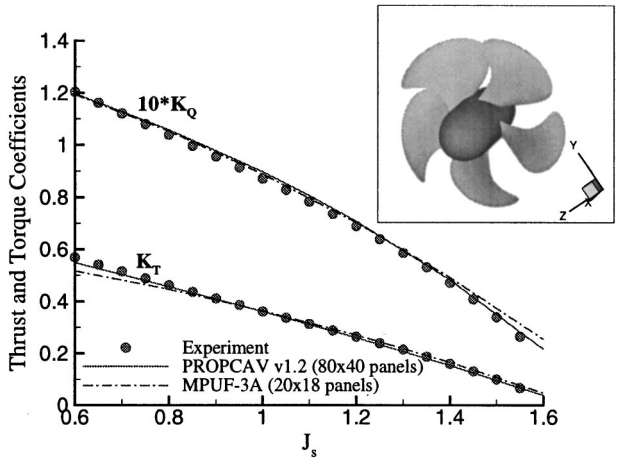

Fig. 10 Geometry of propeller DTMB5168. Also shown are the predicted and measured K_T and K_Q for different advance coefficients. PROPCAV v1.2: 80×40 Panels. MPUF-3A v1.2: 20×18 panels.

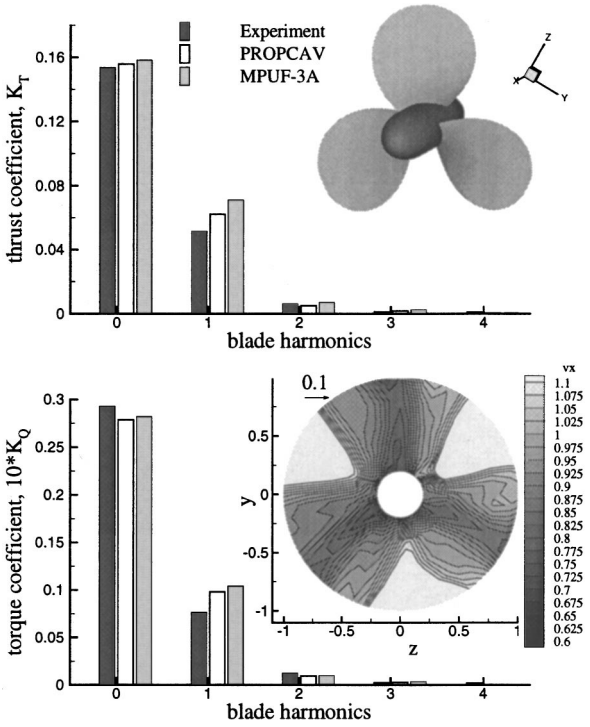

Fig. 11 Geometry and inflow wake of propeller DTMB4119. Also shown are the predicted and measured K_T and K_Q for different blade harmonics. PROPCAV v1.2: 80×50 Panels. MPUF-3A v1.2: 40×24 panels.

PROPCAV, and MPUF-3A for propeller DTMB4119. The propeller was subjected to a non-axisymmetric 3-cycle wake (Jessup [20]) (also shown in Fig. 11) in fully wetted flow. As shown in Fig. 11, both numerical codes did well in predicting the unsteady blade force harmonics, with PROPCAV predicting forces which are somewhat closer to the measured values.

Propeller DTMB4148—Three Bladed, Zero-Skew and Zero-Rake Propeller. In the third set of experiments, PROPCAV is used to predict the cavity shape for propeller DTMB4148 in a screen generated non-axisymmetric inflow inside a cavitation tunnel (Mishima et al. [19]). The predicted cavity shapes from PROPCAV are shown in Fig. 12 together with photographs taken during the experiment. The flow conditions were as follows: J_s =0.9087, F_r=9.159, and σ_n=2.576. The equivalent J_s, 0.957, for unbounded flow is obtained by matching the fully wetted thrust coefficient, K_T, with the measured K_T, 0.0993, from experiment. The inflow wake used in PROPCAV, which is shown in Fig. 4, corresponds to the wake in Mishima et al. [19] with the effects of the tunnel walls and vortical inflow/propeller interactions (nonaxisymmetric ''effective'' wake) accounted by using the method of Kinnas et al. [12] and Choi [13].

As shown in Fig. 12, the numerical results agree fairly well with experimental observations except for the area near the blade tip. Note that PROPCAV's prediction in the blade tip region is unreliable because the current version of PROPCAV does not include a tip-vortex cavity model. Furthermore, the current version of PROPCAV does not require cavity lengths at $r/R>0.95$ to converge due to numerical difficulties very near the tip.

Propeller SRI—Three Bladed, Non-Zero Skew and Rake Propeller. To validate the supercavitation scheme in PROPCAV, predicted force coefficients are compared with experimental measurements (Matsuda et al. [21]) for a supercavitating propeller. The test geometry is M.P.No.345(SRI), which is designed using SSPA charts under the following conditions: J_s =1.10, σ_v

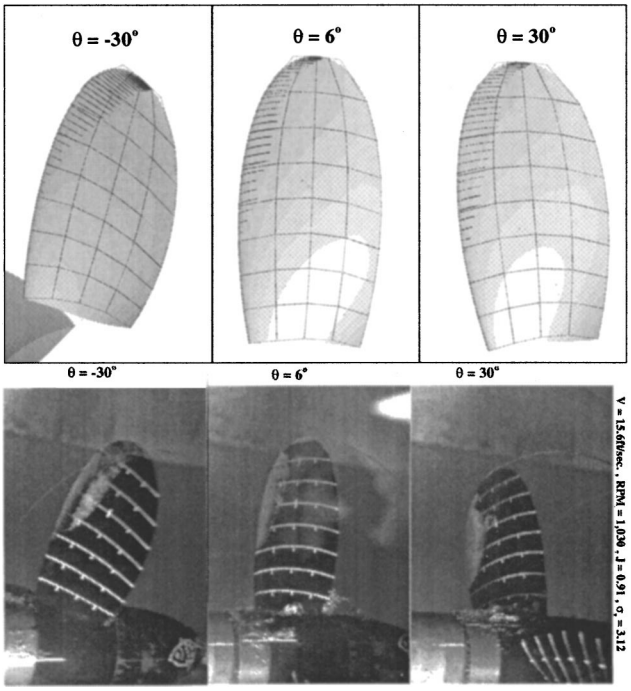

Fig. 12 Comparison OF PROPCAV's prediction (top) to experimental observations (bottom) for propeller DTMB4148. $J_s=0.954$, $\sigma_n=2.576$, $Fr=9.159$, 70×25 panels, $\Delta\theta=6$ deg.

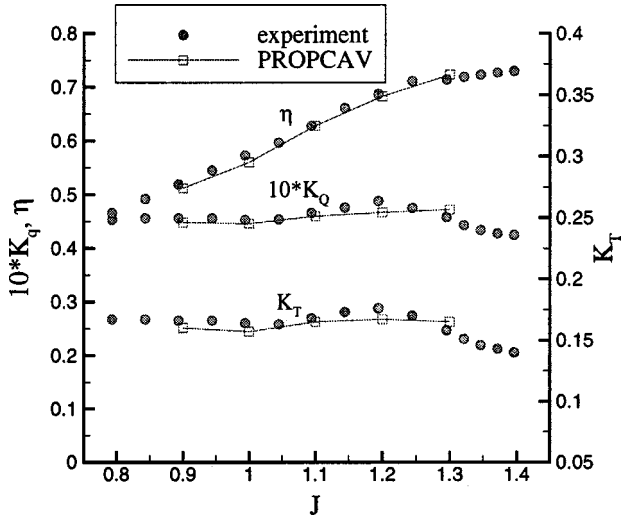

Fig. 13 Comparison of the predicted and versus measured K_T, K_Q, and η for different advance coefficients. Propeller SRI. $\sigma_v=0.4$, $\sigma_n=\sigma_v\times J_s^2$.

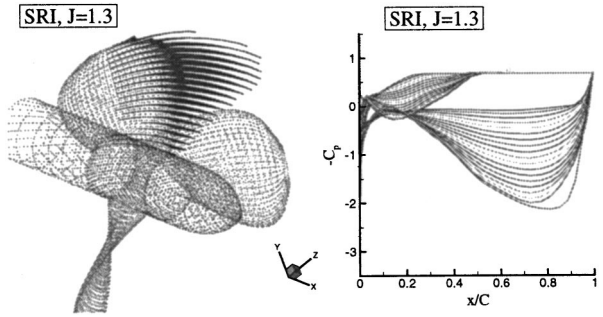

Fig. 14 Geometry, cavitation pattern, and cavitating pressures for propeller SRI at $J_s=1.3$, $\sigma_v=0.4$, $\sigma_n=\sigma_v\times J_s^2$.

$=0.40$, and $K_T=0.160$. It should be noted that the current version of PROPCAV modifies the suction side of the blade section aft of the midchord to render zero thickness at the trailing edge. This modification should not affect the results as long as the blade sections aft of the midchord are within the cavitation bubble.

The comparisons of the predicted versus measured thrust (K_T), torque (K_Q), and efficiency (η) are shown in Fig. 13. The propeller geometry with the predicted cavities at $J_s=1.3$ are shown in Fig. 14. Also shown in Fig. 14 are the predicted cavitating pressures along each radial strip at $J_s=1.3$. It is worth noting that at this particular combination, there is substantial midchord detachment. Figure 14 indicates that the detachment search criterion in PROPCAV, which will be explained later, is satisfied since the cavity thickness is non-negative and the pressures everywhere on the wetted blade surfaces are above the vapor pressure. The comparisons shown on Fig. 13 indicate that the predictions by PROPCAV agree very well with experimental data for values of $J_s \leqslant 1.2$. For $J_s>1.2$, the comparisons are not as good because the cavities begin to detach aft of the midchord, where the suction side geometry was modified.

Mid-Chord Detachment

The latest version of PROPCAV allows the cavity to detach from both the face (pressure side) and the back (suction side) of the blade. The initial detachment lines are obtained based on the fully wetted pressures. The detachment locations at each strip are then adjusted in the next revolution[2] according to the following criterion:

1 If the cavity at the strip has negative thickness, then the detachment location is moved towards the trailing edge of the blade.
2 If the pressure at a point upstream of the cavity is below the vapor pressure, then the detachment location is moved towards the leading edge of the blade.

It can be shown that the above criterion is equivalent to the Villat-Brillouin smooth detachment condition. Details of the formulation and convergence study for mid-chord detachment can be found in Mueller [5] and Mueller and Kinnas [6]. An example of mid-chord cavitation for propeller MW1[3] subjected to uniform inflow

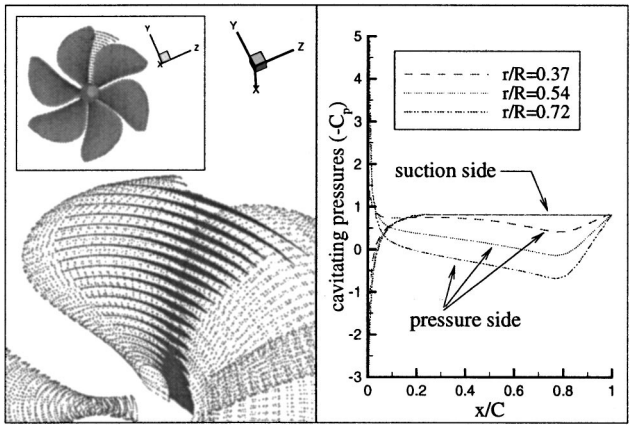

Fig. 15 Cavity shape and pressures for propeller MW1. Midchord cavitation. The propeller is based on a design by Michigan Wheel Corporation, USA. $J_s=1.224$, $\sigma_n=0.8116$, $F_r=26.6$, 60×20 panels. Uniform inflow.

[2]The solution is carried out over several complete revolutions of one blade, the ''key'' blade, with the effects of the other blades being accounted for in an iterative manner.

[3]The propeller geometry, which is listed in Table 1, is based on a design by Michigan Wheel Corporation, USA.

($J_s=1.224$, $\sigma_n=0.8116$, $F_r=26.6$) is shown in Fig. 15. Also shown in Fig. 15 are the corresponding cavitating pressures at three different strips along the span of the blade. It is worth noting that the predicted pressures on the suction side in front of the cavity detachment are higher than the vapor pressure. This indicates that the employed smooth detachment criterion works properly. However, the face side cavitating pressures near the leading edge are below the vapor pressure. This is because PROPCAV was only allowed to search for back cavitation. Had the option to search for face and back cavitation simultaneously (as explained in the next section) been on, PROPCAV would have also detected the expected face cavitation as shown in Fig. 18.

Face and Back Cavitation

The latest version of PROPCAV allows the cavity to grow on both sides of the blade simultaneously. In this case, the dynamic boundary condition is applied on both cavity surfaces, and the kinematic boundary condition is applied on the wetted blade surfaces. PROPCAV also has the ability to search for cavity detachments on both sides of the blade simultaneously.

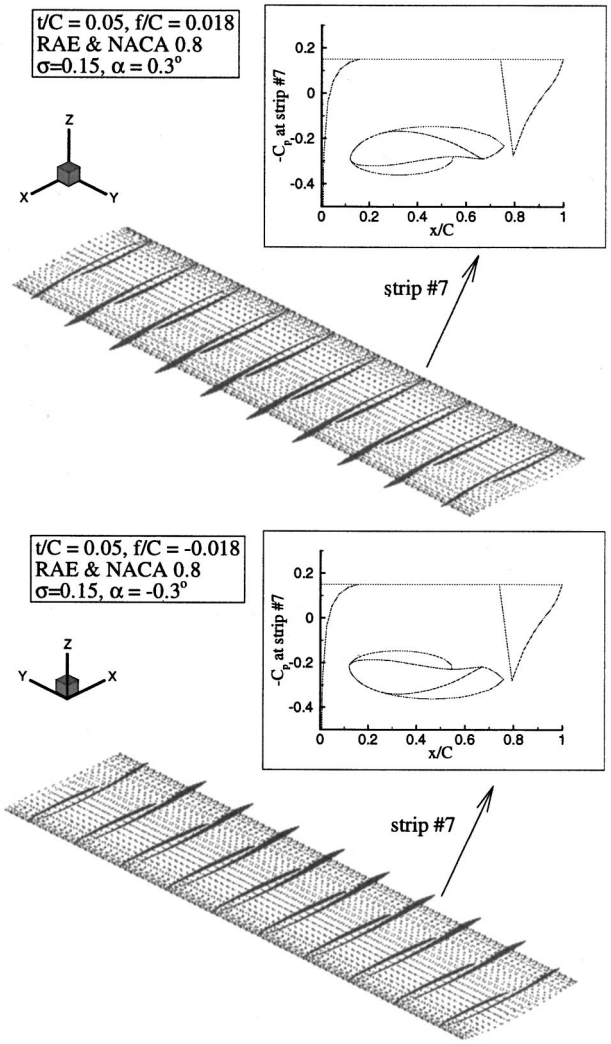

Fig. 16 Validation of simultaneous face and back cavitation on an asymmetric rectangular hydrofoil. 50×10 panels. $\alpha=\pm 0.3$ deg. $fo/C=\pm 0.018$(NACA0.8), $to/C=0.05$(RAE), $\sigma_v=0.15$.

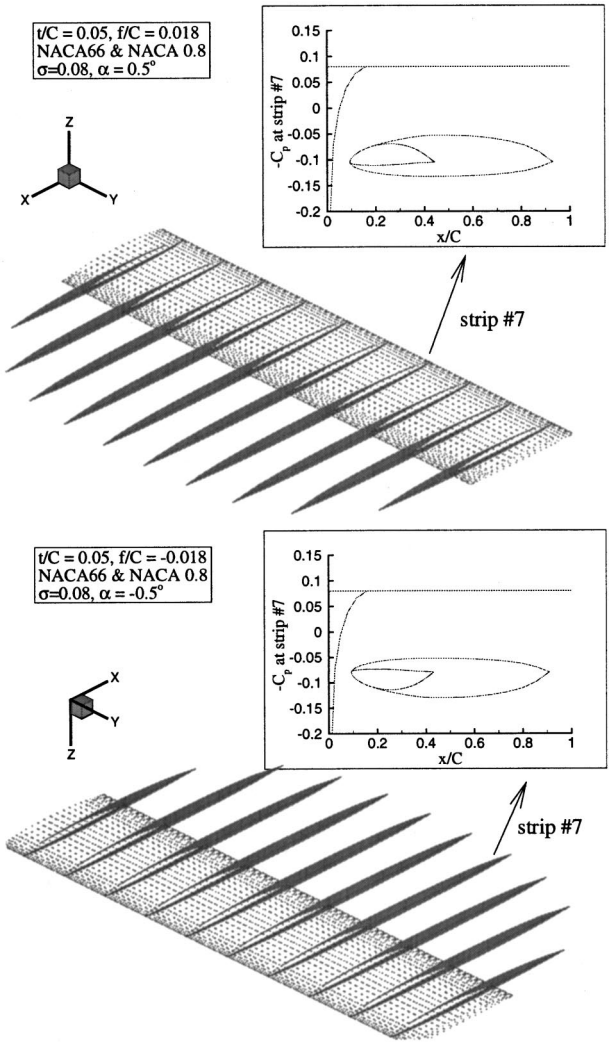

Fig. 17 Validation of simultaneous face and back cavitation on an asymmetric rectangular hydrofoil. 50×10 panels. $\alpha=\pm 0.5$ deg. $fo/C=\pm 0.018$(NACA0.8), $to/C=0.05$(NACA66), $\sigma_v=0.08$.

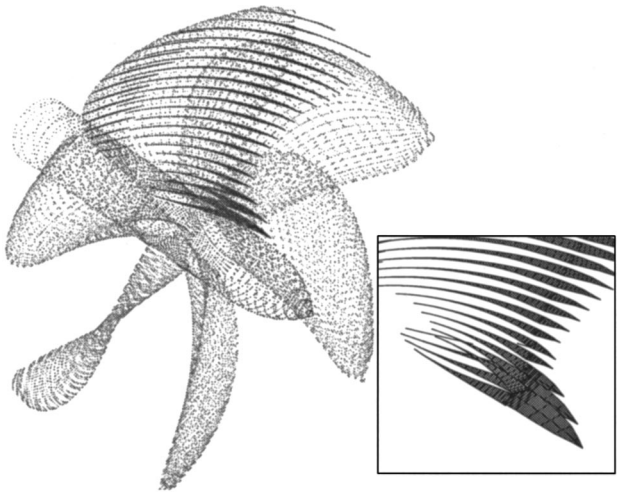

Fig. 18 Predicted 3-D cavity shape for propeller MW1. The propeller is based on a design by Michigan Wheel Corporation, USA. 60×20 panels. $J_s=1.224$, $\sigma_n=0.8116$, $F_r=25.6$. Uniform inflow.

[4]For validation studies, PROPCAV has an option where the numerical method is applied on a 3-D hydrofoil.

Table 1 Geometry of Propeller MW1. 6 blades. NACA66 thickness distribution. NACA 0.8 camber distribution. $J_s=1.244$, $F_r=25.6$, $\sigma_n=0.81160$, r/R=nondimensional radius, P/D=pitch/diameter, RK/D=rake/diameter, SK=skew in degrees, C/D=chord/diameter, f_o/C=maximum camber/chord, τ_o/D=maximum thickness/diameter.

r/R	P/D	RK/D	SK	C/D	f_o/C	τ_o/D
0.1305	1.4000	0.0002	-0.4639	0.1793	0.0146	0.0336
0.1848	1.4125	-0.0011	-0.6288	0.2004	0.0162	0.0316
0.2392	1.4250	-0.0031	-1.0026	0.2216	0.0177	0.0296
0.3479	1.4500	-0.0061	-1.5722	0.2668	0.0229	0.0256
0.4566	1.4750	-0.0051	-1.3064	0.3109	0.0284	0.0218
0.5652	1.5000	0.0016	0.2692	0.3499	0.0336	0.0179
0.6739	1.5250	0.0156	3.5069	0.3706	0.0374	0.0139
0.7826	1.5500	0.0381	8.7053	0.3525	0.0382	0.0099
0.8913	1.5750	0.0693	16.1214	0.2602	0.0344	0.0061
0.9456	1.5875	0.0857	20.7336	0.1641	0.0312	0.0040
1.0000	1.6000	0.1063	25.9848	0.0162	0.0484	0.0000

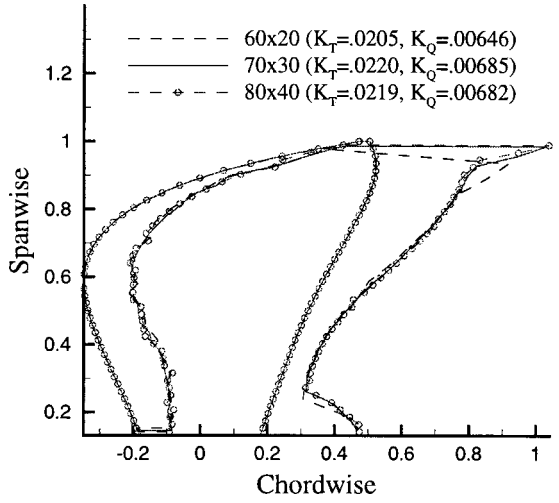

Fig. 19 The convergence of predicted cavities (expanded view) and forces with respect to number of panels for propeller MW1. The propeller is based on a design by Michigan Wheel Corporation, USA. $J_s=1.224$. $\sigma_n=0.8116$, $F_r=25.6$. Uniform inflow.

Validation test for an asymmetric 3-D hydrofoil[4] with ± 1.8 percent camber (f/C) and $\sigma_v=0.15$ at an angle of attack of ± 0.3 deg is shown in Fig. 16. As expected, the predicted cavity shapes are identical mirror images of each other. The same validation test was performed for another asymmetric 3-D hydrofoil at an angle of attack of ± 0.5 deg with ± 1.8 percent camber and $\sigma_v=0.08$. The results are shown in Fig. 17. Note that for both cases, the smooth detachment criterion are satisfied on both sides of the 3-D hydrofoil.

An example of simultaneous face and back cavitation for propeller MW1 is shown in Fig. 18. The propeller geometry, which is listed in Table 1, is based on a design by Michigan Wheel Corporation, USA. The flow conditions were as follows: $J_s=1.224$, $\sigma_n=0.8116$, uniform inflow. Notice that for this propeller, there is midchord supercavitation on the suction side of the blade, and leading partial cavitation as well as midchord supercavitation on the pressure side of the blade. To validate the solution, the convergence of the predicted cavities (on the back side of the blade) and forces with respect to the number of panels are shown in Fig. 19.

Conclusions

The results from the convergence study show that the cavity volume converged relatively quickly with number of revolutions for the tested propeller. It was also shown that the time discretization (in terms of blade angle increments) has a smaller impact on the predicted cavity volume and propeller loading than the panel discretization.

The results from validation tests with experiments show that in general, the predicted propeller loadings and cavity shapes agree well with experimental observations and measurements.

The performance of PROPCAV in mid-chord face and/or back cavitation has been shown and validated numerically. The current version of PROPCAV is able to predict leading edge and mid-chord mixed cavity patterns on both sides of the blade simultaneously.

Future efforts in PROPCAV include the following:

1 Modeling of sections with nonzero trailing edge thickness,
2 Modeling of a developed tip-vortex cavity,
3 Modeling of surface-piercing propellers, and
4 More systematic comparisons with experiments and MPUF-3A.

Acknowledgment

Support for this research was provided by Phase II of the ''Consortium on Cavitation Performance of High Speed Propulsors'' with the following members: American Bureau of Shipping, David Taylor Model Basin, Daewoo Shipbuilding & Heavy Machinery, El Pardo Model Basin, Hyundai Maritime Research Institute, Michigan Wheel, Rolla SP Propellers SA, Sulzer-Hydro GMBH, Ulstein Propeller AS, Volvo-Penta of the Americas, and Wärtsilä Propulsion. The authors wish to thank Mr. Kevin Mitchell and Dr. Brant Savander of Michigan Wheel for making available to them the geometry of a supercavitating propeller.

Nomenclature

α = angle of attack for 3-D hydrofoil
C_p = pressure coefficient, $C_p=(P-P_o)/(0.5\rho n^2D^2)$
D = propeller diameter
η = propeller efficiency, $\eta=(K_T/K_Q)\,(J_s/2\pi)$
$\mathrm{F_r}$ = Froude number, $\mathrm{F_r}=n^2D/g$
g = gravitational acceleration
Γ = blade section circulation, nondimensional form$=\Gamma \times 10^2/\pi D V_R$
h = cavity thickness over the blade surface
h_w = cavity thickness over the wake surface
J_s = advance ratio, $J_s=V_s/nD$
K_Q = torque coefficient, $K_Q=Q/\rho n^2D^5$
K_T = thrust coefficient, $K_T=T/\rho n^2D^4$
l = cavity length
n = propeller rotational frequency (rev/s)
$\vec{n}$ = unit normal vector
ϕ = perturbation potential
P = pressure
P_o = pressure far upstream, at the propeller axis
P_v = vapor pressure of water
$\vec{q}$ = total velocity
$\vec{q}_{in}$ = local inflow velocity (in the propeller fixed system)
$\vec{q}_{\mathrm{wake}}$ = effective wake inflow velocity (in the ship fixed system)
Q = propeller torque
ρ = fluid density
σ_n = cavitation number based on n, $\sigma_n=(P_o-P_v)/(0.5\rho n^2D^2)$
σ_v = cavitation number based on V_s, $\sigma_u=(P_o-P_v)/(0.5\rho V_s^2)$
t = time
T = propeller thrust
V_s = ship speed for propeller, or inflow speed for 3-D hydrofoil
V_R = reference velocity, $V_R=\sqrt{V_s^2+(0.7n\pi D)^2}$

References

[1] Fine, N. E., 1992, ''Nonlinear analysis of cavitating propellers in nonuniform flow,'' Doctoral dissertation, Department of Ocean Engineering, MIT.

[2] Kinnas, S., and Fine, N., 1992, ''A nonlinear boundary element method for the analysis of unsteady propeller sheet cavitation,'' *Proceedings*, Nineteenth Symposium on Naval Hydrodynamics, Aug., pp. 717–737.

[3] Kinnas, S., and Fine, N., 1993, ''A numerical nonlinear analysis of the flow around two- and three-dimensional partially cavitating hydrofoils,'' J. Fluid Mech., **254**, Sept., pp. 151–181.

[4] Mueller, A., and Kinnas, S., 1997, ''Cavitation predictions using a panel method,'' *Proceedings*, ASME Symposium on Marine Hydrodynamics and Ocean Engineering, Vol. 14. Nov. 16–21, pp. 127–137.

[5] Mueller, A., 1998, ''Development of face and mid-chord cavitation models for the prediction of unsteady cavitation on a propeller,'' Masters thesis, UT Austin, Dept. of Civil Engineering, May.

[6] Mueller, A., and Kinnas, S., 1999, ''Propeller sheet cavitation predictions using a panel method,'' ASME J. Fluids Eng., **121**, June, pp. 282–288.

[7] Kosal, E., 1999, ''Improvements and enhancements in the numerical analysis and design of cavitating propeller blades,'' Masters thesis, UT Austin, Dept. of Civil Engineering. May; Also, UT Ocean Eng. Report 99–1.

[8] Lee, H., and Kinnas, S., 2001, ''MPUF-3A (version 1.2) user's manual and documentation,'' Technical Report No. 01–2, Ocean Engineering Group, UT Austin, Jan.

[9] Kinnas, S., 1991, ''Leading-edge corrections to the linear theory of partially cavitating hydrofoils,'' J. Ship Res., **35**, No. 1, Mar., pp. 15–27.

[10] Kinnas, S., 1992, ''Leading edge correction to the linear theory of cavitating hydrofoils and propellers,'' *Proceedings*, Second International Symposium on Propeller and Cavitation. Sept.

[11] Kinnas, S., 1992, ''A general theory for the coupling between thickness and loading for wings and propellers,'' J. Ship Res., **36**, No. 1, Mar., pp. 59–68.

[12] Kinnas, S., Choi, J., Lee, H., and Young, J., 2000, ''Numerical cavitation tunnel,'' *Proceedings*, NCT50, International Conference on Propeller Cavitation, Apr. 3–5.

[13] Choi, J., 2000, ''Vortical inflow—propeller interaction using unsteady three-dimensional euler solver,'' Doctoral dissertation, Department of Civil Engineering, The University of Texas at Austin, Aug.

[14] Kinnas, S., and Hsin, C.-Y., 1992, ''A boundary element method for the analysis of the unsteady flow around extreme propeller geometries,'' AIAA J., **30**, No. 3, Mar., pp. 688–696.

[15] Morino, L., and Kuo, C.-C., 1974, ''Subsonic Potential Aerodynamic for Complex Configurations: A General Theory,'' AIAA J., **12**, No. 2, Feb., pp. 191–197.

[16] Young, Y., Lee, H., and Kinnas, S., 2001, ''PROPCAV (version 1.2) user's manual and documentation,'' Technical Report No. 01–4, Ocean Engineering Group, UT Austin. Jan.

[17] Fine, N., and Kinnas, S., 1993, ''The nonlinear prediction of unsteady sheet cavitation for propellers of extreme geometry,'' *Proceedings*: Sixth International Conference on Numerical Ship Hydrodynamics, Aug., pp. 531–544.

[18] Fine, N., and Kinnas, S., 1993, ''A boundary element method for the analysis of the flow around 3-d cavitating hydrofoils,'' J. Ship Res., **37**, Sept., 213–224.

[19] Mishima, S., Kinnas, S., and Egnor, D., 1995, ''The CAvitating PRopeller EXperiment (CAPREX), Phases I & II,'' Technical Report, Department of Ocean Engineering, MIT, Aug.

[20] Jessup, S., 1990, ''Measurement of multiple blade rate unsteady propeller forces,'' Technical Report, DTRC-90/015, David Taylor Research Center, May.

[21] Matsuda, N., Kurobe, Y., Ukon, Y., and Kudo, T., 1994, ''Experimental investigation into the performance of supercavitating propellers,'' Papers of Ship Res. Inst., **31**, pp. 5.

Z. Zhang
Center for Environmental Medicine
and Lung Biology,
The University of North Carolina,
Chapel Hill, NC 27599

C. Kleinstreuer[2]
Department of Mechanical
and Aerospace Engineering,
North Carolina State University,
Raleigh, NC 27695-7910

C. S. Kim
Human Studies Division,
National Health and Environmental Effects
Research Laboratory, U.S. EPA,
Research Triangle Park, NC 27711

Flow Structure and Particle Transport in a Triple Bifurcation Airway Model[1]

Considering steady laminar incompressible flow in a triple bifurcation, which represents generations three to six of the human respiratory system, air flow fields and micron-particle transport have been simulated for several combinations of relatively high and low inlet Reynolds and Stokes numbers. While the upstream bifurcations are hardly affected by the third bifurcation, complex air and particle flow fields occur in the daughter tubes leading to the third dividers. Variations in Reynolds number, $500 \leqslant Re \leqslant 2000$, and Stokes number, $0.04 \leqslant St \leqslant 0.12$, cause locally changing vortical air flows as well as irregular particle motions. Preferential concentration of particles can be induced by the secondary vortical flow in the tubes when the inlet Reynolds number is high enough. The air and particle velocity profiles in the third daughter tubes are still quite different from those in the upstream tubes, which indicates that additional downstream effects are possible. This work may contribute to respiratory dose estimation in health risk assessment studies, as well as the analyses of drug aerosol delivery. [DOI: 10.1115/1.1359525]

1 Introduction

The respiratory airways can be approximated as a network of repeatedly bifurcating tubes with progressively decreasing dimensions [1,2]. As a result, airflow passages are very tortuous and flow characteristics are difficult to assess. Hence, the measurement and simulation of aerosol transport are quite challenging problems. Inhaled particles, considering a 1–10 μm diameter range, deposit primarily by inertial impaction particularly in the large trachebronchial airways where flow velocities are relatively high [3]. The detailed understanding of air flow structures and particle transport, including wall deposition, is of great importance for estimating the health risk of particulate pollutants, on the one hand, and for delivering drug aerosols to target sites in the lung on the other hand. Thus, of interest here is the air flow and transport of non-interacting monodisperse spherical particles under steady inspiration in a representative triple bifurcation model. Although there are a few experimental and numerical studies which have addressed certain aspects of these problems, they tend to oversimplify the realism and further investigations are needed to contribute to an accurate system assessment.

For example, Balásházy [4] discussed the numerical implementation for computing trajectories for a wide range of submicron- and micron-size particles in bifurcating tubes. Gatlin et al. [5] simulated the fluid flow and particle deposition patterns in an asymmetric single bifurcation based on physiological observations. The transition region for this model consisted of an elliptic region where the cross-sectional area was equal to the parent tubes, followed by a region where the daughter tubes split apart forming the carina ridge. These geometries are supposed to suppress any flow separation during inspiratory (i.e., diverging) flow. However, more recently, Farag et al. [6,7], using a similar geometric configuration, experimentally observed flow separation in the bifurcation region under similar flow conditions. Airway geometries (i.e., branching patterns) result in disturbed flow which affects the flow patterns and particle deposition in subsequent bifurcations. Thus single bifurcation models mentioned previously may not provide a realistic picture of deposition in respiratory airways. Wilquem and Degrez [8] numerically investigated the 2-D steady inspiratory airflow through a double bifurcation model representing three generations of the human central airways. Velocity profiles downstream of the first junction were shown to be highly skewed, thus leading to an important imbalance in flow distribution downstream of the second junction. However, their simulation was based on a 2-D model and particle transport and deposition in such a model were not simulated. Lee et al. [9] computed the velocity field, particle trajectories, and deposition efficiency for 2-D and 3-D single and double bifurcations. They found that the flow field and particle trajectories were altered by the presence of the second bifurcation and that the deposition efficiency in the second bifurcation was almost always less than that in the first bifurcation. However, their geometry utilized constant diameter tubes (i.e., $D_1 = D_2 = D_3$) and sharp outer wall of the junctions, which are not in physiological agreement with the human respiratory airways. Comer et al. [10] and Kleinstreuer et al. [11], who employed double bifurcation geometries of Weibel's lung airway models [12,13], showed numerically that aerosol transport and wall deposition depend strongly on vortical flow fields created by the particular upstream geometric configurations and inlet flow conditions.

In this paper, the validated computer simulation model of Comer et al. [10] is extended to a triple bifurcation respiratory tract segment in order to analyze the complex air flow fields and particle motions, especially in the upper and lower third bifurcations. The resulting particle deposition patterns and wall particle concentrations are discussed in a companion paper [14].

2 Theory and Numerical Solution

2.1 Bifurcation Geometry, Assumptions, and Transport Equations. Steady laminar, constant property air flow, i.e., $500 \leqslant \mathrm{Re} \leqslant 2000$, with dilute suspensions of micron-sized particles, i.e., $3 \leqslant d_p \leqslant 7$ μm, is assumed to enter a rigid, anatomically relevant triple bifurcation tube model with a symmetric in-plane configuration (cf. Fig. 1 and Table 1).

The realistic tube model represents the third–sixth generation of human respiratory airways according to Weibel's lung Model A [1]. While Weibel's lung Model A contains realistic tube diameters and lengths, it bifurcates symmetrically and hence may not

[1]Presented in part at the First Joint Meeting of BMES & EMBS, 13–16 October 1999, Atlanta, GA.

[2]Corresponding author (ck@eos.ncsu.edu).

Contributed by the Fluids Engineering Division for publication in the JOURNAL OF FLUIDS ENGINEERING. Manuscript received by the Fluids Engineering Division January 9, 2000; revised manuscript received December 27, 2000. Associate Editor: J. K. Eaton.

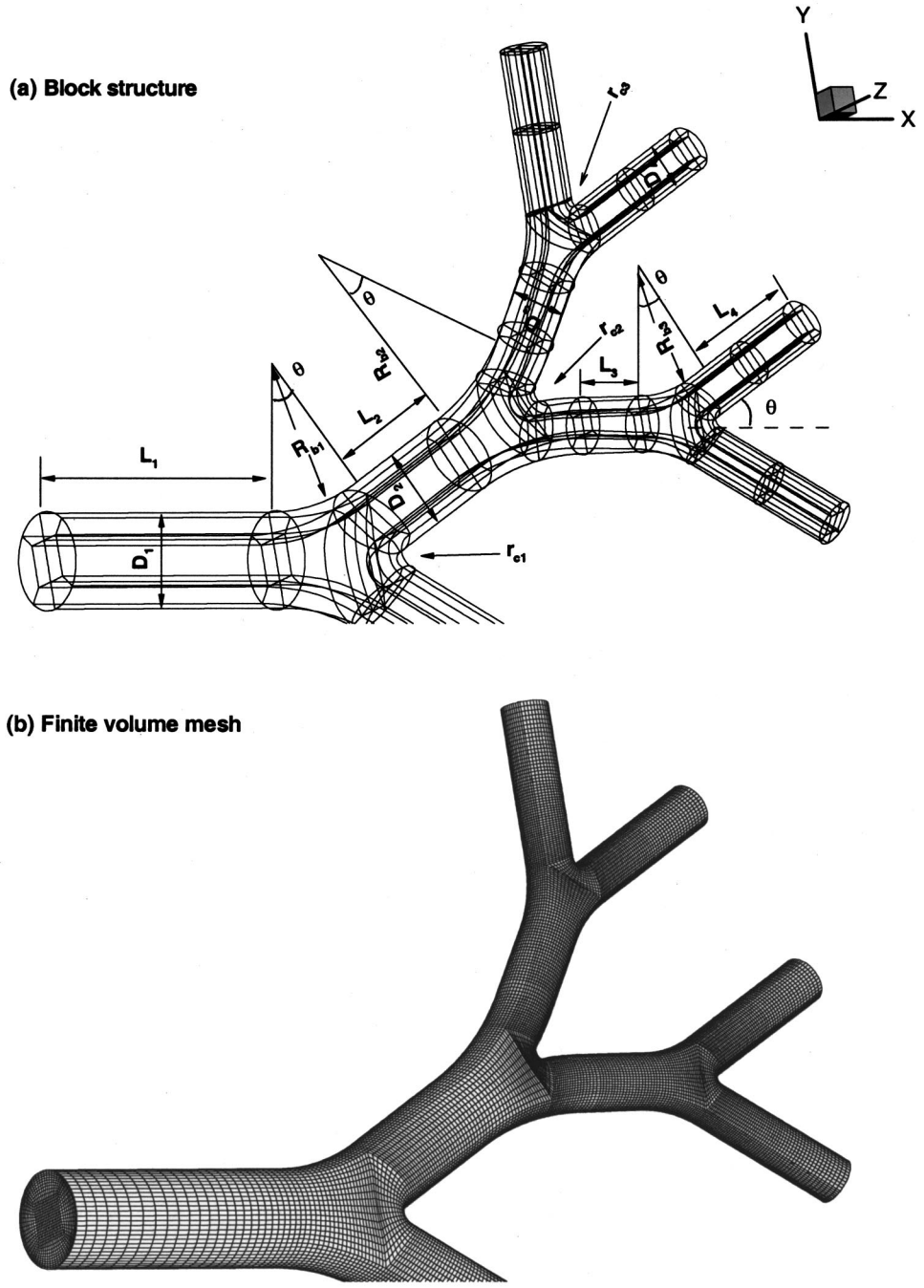

Fig. 1 Schematic of symmetric in-plane triple bifurcation geometry: (*a*) block structure and (*b*) finite volume mesh

be fully representative of actual lung casts. Nevertheless, the model has been and is being used by the vast majority of aerosol researchers for ease-of-use and direct comparison of experimental and theoretical results. Although most bronchial bifurcations are somewhat asymmetric and some cases generation G5 or G6 is out-of-plane [10,15,16], studies have shown that steady inspiratory flow in an asymmetric bifurcation exhibits the main features of the symmetric case [10,17–19]. The reasons for choosing generations G3-G6 are: (i) to simulate air flow structures and particle trajectories in a most representative part of the upper bronchial tree; (ii) to avoid turbulent flow which may occur in the larynx plus G0-G2 under elevated breathing conditions; and (iii) to reduce the effect of cartilaginous rings which are pronounced in the larynx, trachea (G0), and main bronchi (G1) [20]. The rings may become less protruded and are insignificant starting from G3. Hence, the present airway models assume that the tube wall is smooth.

Steady inhalation is one key assumption for the present computational study. The restriction to steady flow requires some explanation in light of the fact that breathing patterns are pulsatile by nature. Specifically, the quasi-steady flow assumption can be justified with the Womersley number, $\alpha = r_0\sqrt{\omega/\vartheta}$ and the frequency parameter $\varepsilon = \omega l/U$. If $\alpha < 1$ and $\varepsilon < 1$, laminar airway flow can be considered to be quasi-steady [21]. These conditions are summarized in Table 2 for the present geometry and two Reynolds numbers, considering several breathing patterns [22]. Indeed, except for extreme conditions, α and ε are consistently less than one.

Table 1 Geometric parameters for triple bifurcation model (dimensions in centimeter)

Bifurcation	First		Second		Third	
Parent duct diameter	D_1	0.6	D_2	0.5	D_3	0.35
Daughter duct diameter	D_2	0.5	D_3	0.35	D_4	0.29
Length of ducts	L_1 L_2	2.4 0.836	L_3	0.437	L_4	0.928
Bifurcation radius of curvature	R_{b1}	$2.7D_2$	R_{b2}	$4.7D_3$	R_{b3}	$2.7D_4$
Carinal radius of curvature	r_{c1}	$0.1D_2$	r_{c2}	$0.1D_3$	r_{c3}	$0.1D_4$
Bifurcation half angle	θ			30 deg		

Table 2 Quasi-steady airflow conditions for different breathing patterns

Mean inspiratory Reynolds number		Re=500	Re=2000
Mean inspiratory flow rate (mouth) Q (l/min)		17.8	71.0
Physical state		Sedentary $Q=16.7$ l/min	Light activity $Q=47.7$ l/min Heavy activity $Q=143$ l/min
Frequency (breath min^{-1})	Sedentary: 14.0	$\alpha=0.92$, $\varepsilon=0.02$	$\alpha=0.92$, $\varepsilon=0.01$
	Light activity: 15.5	$\alpha=0.96$, $\varepsilon=0.02$	$\alpha=0.96$, $\varepsilon=0.01$
	Heavy activity: 24.5	$\alpha=1.21$, $\varepsilon=0.04$	$\alpha=1.21$, $\varepsilon=0.01$
	Panting: 180	$\alpha=3.30$, $\varepsilon=0.14$	$\alpha=3.30$, $\varepsilon=0.04$

Due to the complexity of generating a representative bifurcation model, especially in the cardinal region, the CAD package Pro/Engineer was used to generate a 3-D surface model. A structured mesh was then generated based on the surface information. The effects of variations in geometric characteristics, such as bifurcation angle and wall curvature, are evaluated elsewhere [23]. The appropriate transport equations are [24]:

(continuity)

$$\nabla \cdot \vec{v} = 0 \tag{1}$$

(momentum)

$$(\vec{v} \cdot \nabla)\vec{v} = -\frac{1}{\rho}\nabla p + \nabla \cdot [\nu(\nabla \vec{v} + (\nabla \vec{v})^{\mathrm{tr}})] \tag{2}$$

(particle trajectory)

$$m_p \frac{d^2 \vec{x}_p}{dt^2} = \frac{1}{8}\pi \rho d_p^2 C_{Dp}(\vec{v} - \vec{v}_p)|\vec{v} - \vec{v}_p| \tag{3}$$

where

$$C_{Dp} = C_D / C_{\mathrm{slip}} \tag{4a}$$

$$C_D = \begin{cases} 24/\mathrm{Re}_p & \text{for } 0.0 < \mathrm{Re}_p \leqslant 1.0 \\ 24/\mathrm{Re}_p^{0.646} & \text{for } 1.0 < \mathrm{Re}_p \leqslant 400 \end{cases} \tag{4b}$$

and

$$\mathrm{Re}_p = \rho|\vec{v} - \vec{v}_p| d_p / \mu \tag{4c}$$

A correlation for the Cunningham correction (i.e., slip) factor, C_{slip}, in Eq. (4*a*) can be found in Clift et al. [25]. The largest influence of the slip coefficient was a two percent change in particle deposition efficiency at St=0.24 [23]. With particle Reynolds numbers $\mathrm{Re}_p \leqslant O(1)$ and small Stokes numbers, St<0.25, particle motion is basically a first-order correction to fluid-element motion (cf. Eq. (3)).

For the steady inhalation phase, a parabolic fluid velocity profile, with an associated monodispersed spherical particle distribution, was specified at the inlet. Zhang and Kleinstreuer [26] showed that these conditions are reasonable and most suitable for direct comparison purposes. Nevertheless, the type of inlet velocity profile and particle release condition may have a significant effect on the flow field and particle motion [26], which is another reason why we developed triple bifurcation models instead of the previous single bifurcation models [4] and double bifurcation models [9,10]. A triple bifurcation also allows studying the impact of a skewed flow field induced by the airway geometry on fluid-particle dynamics in the downstream second and even third daughter tubes. In that context, the type of inlet velocity profile should not change the general statements made in the present study.

A uniform pressure boundary condition is used for the outlets, which results in symmetric flow about the first carina (i.e., $y=0$). In a complementary paper [27], this condition has been modified to measure the effects of various causes and levels of flow asymmetry in double bifurcation models. The initial particle velocities were set equal to that of the fluid and one-way coupling was assumed between the air and particle flow fields because the maximum mass loading ratio (mass of particles/mass of fluid) is below 1×10^{-4}. The boundary conditions for the governing equations include symmetry with respect to the mid-plane of the bifurcation (i.e., $z=0$), and no fluid slip at the rigid impermeable walls. The boundary conditions at the symmetric plane are:

$$u = v = 0 \tag{5a}$$

and

$$\partial w / \partial z = 0 \tag{5b}$$

2.2 Numerical Method. The numerical solution of the fluid flow equations (Eqs. (1),(2)) was carried out using a user-enhanced commercial finite-volume based program CFX4.2 [28]. The numerical program uses a structured, multiblock, body-fitted coordinate discretization scheme. In the present simulation using the CFX program, the SIMPLEC algorithm [29] with under-relaxation was employed to solve the flow equations. The relaxation factor for the velocity is 0.65. All variables, including velocity components and pressure, are located at the centroids of the control volumes. An improved Rhie-Chow interpolation method was employed to obtain the velocity components and pressure on the control volume faces from those at the control volume centers. A Higher-Order Upwind (HUW) differencing scheme, which is second-order accurate in space, was used to model the advective terms of the transport equations. The sets of linearized and discretized equations for all variables were solved using an algebraic multi-grid method [30].

The particle transport equation (Eq. (3)) was also solved using the same commercial program in combination with user-specified drag relations and detailed particle tracking. In CFX, the equations for particle trajectories are solved numerically using Gear's

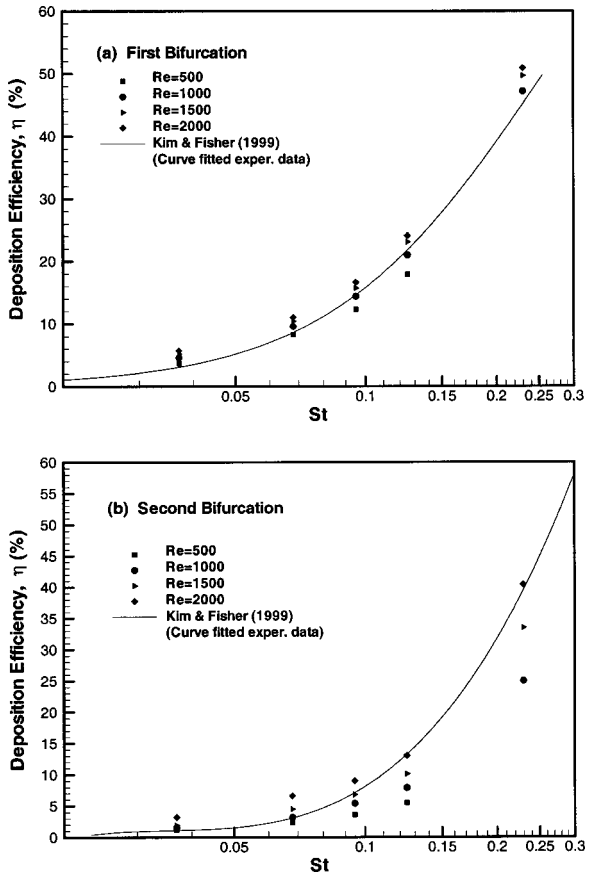

Fig. 2 Comparison between computed data set and measured η(St) correlation for: (*a*) first bifurcation and (*b*) second bifurcation of a symmetric planar bifurcation

BDF method [31]. After each iteration for each particle, the information about position, time, and three components of the velocity, as well as the speed with which the particles cross the control volume boundaries, was obtained. The user-specified near-wall particle tracking program was used to calculate the distances from the center of particles to the wall and then determine if the particles deposit. Based on the symmetry assumptions and the parabolic inlet profile, the particles simulated in this analysis had a parabolic distribution across 1/4 of the model inlet. A parabolic distribution implies that the probability density function for the inlet particle coordinate or the inlet particle concentration is in a parabolic formation [26]. Such a type of inlet particle distribution was verified to be suitable for experimental analyses and data comparisons [26]. The effect of flow symmetry on particle motion was also tested. No particles moved across the symmetric plane in the test run due to the flow symmetry. In the current model the number of particles, 1839, was determined by increasing the inlet particle concentration until the deposition efficiency became independent of the number of particles simulated. The deposition efficiency is defined as the ratio of the number of particles deposited in a given region to the total number entering the region.

As previously stated, the mesh was generated based on the surface information obtained from the CAD models of the experimental glass tube bifurcation models. Utilizing the assumed symmetry condition about the first bifurcation plane, the flow field simulation involved only the upper half of the bifurcation model (i.e., $z \geq 0$). The inlet and outlet locations, and the mesh topology, were determined by refining the mesh until grid independence of the flow field solution was achieved. Grids consisting of 179026, 358052, 716104 cells were tested. Little variation in the parameters of interest, i.e., particle deposition efficiency and the general velocity field, was observed between the two highest grid density solutions (i.e., the maximum relative error was 4.2 percent). The final mesh size of the in-plane configuration we used was 358,052 cells. The computations were performed on a Sun Ultra 60 work-

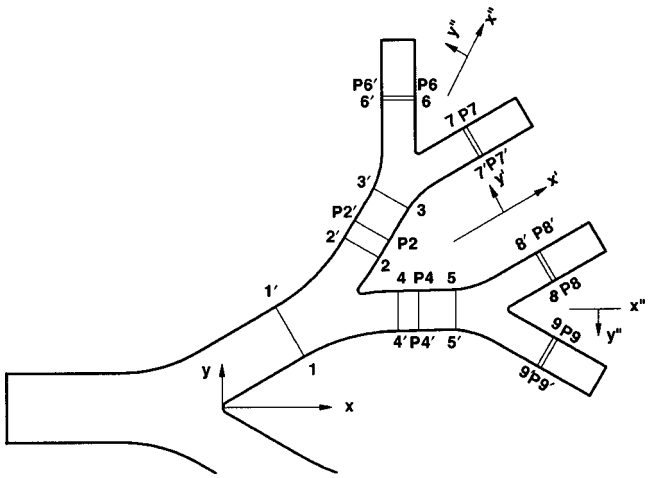

Fig. 3 Coordinate systems and locations of various cross sections used for visualization of air flow and particle transport in a triple bifurcation model

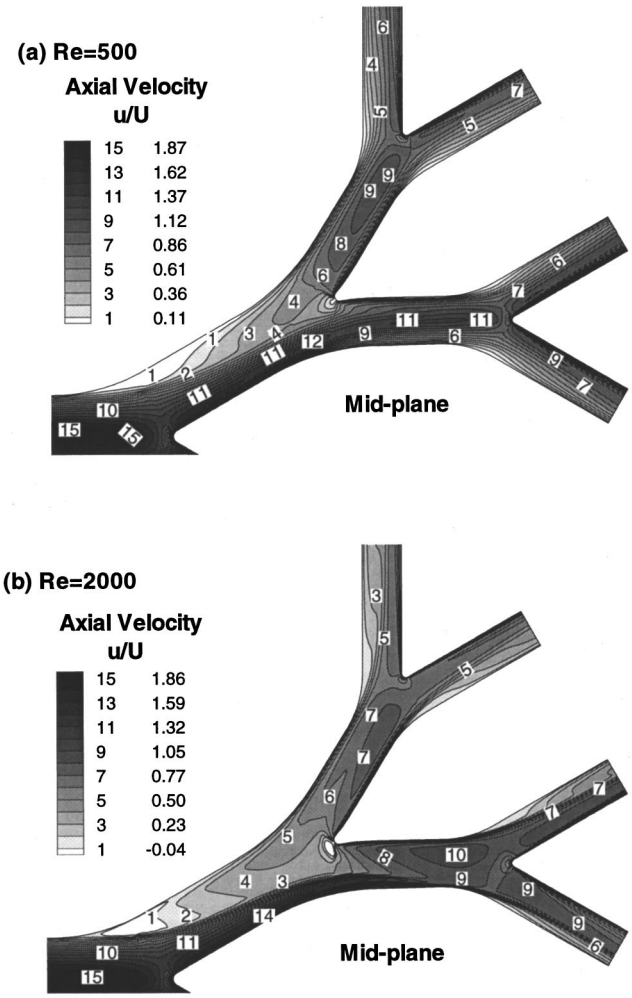

Fig. 4 Mid-plane axial flow patterns of the triple bifurcation model: (*a*) Re=500 and (*b*) Re=2000

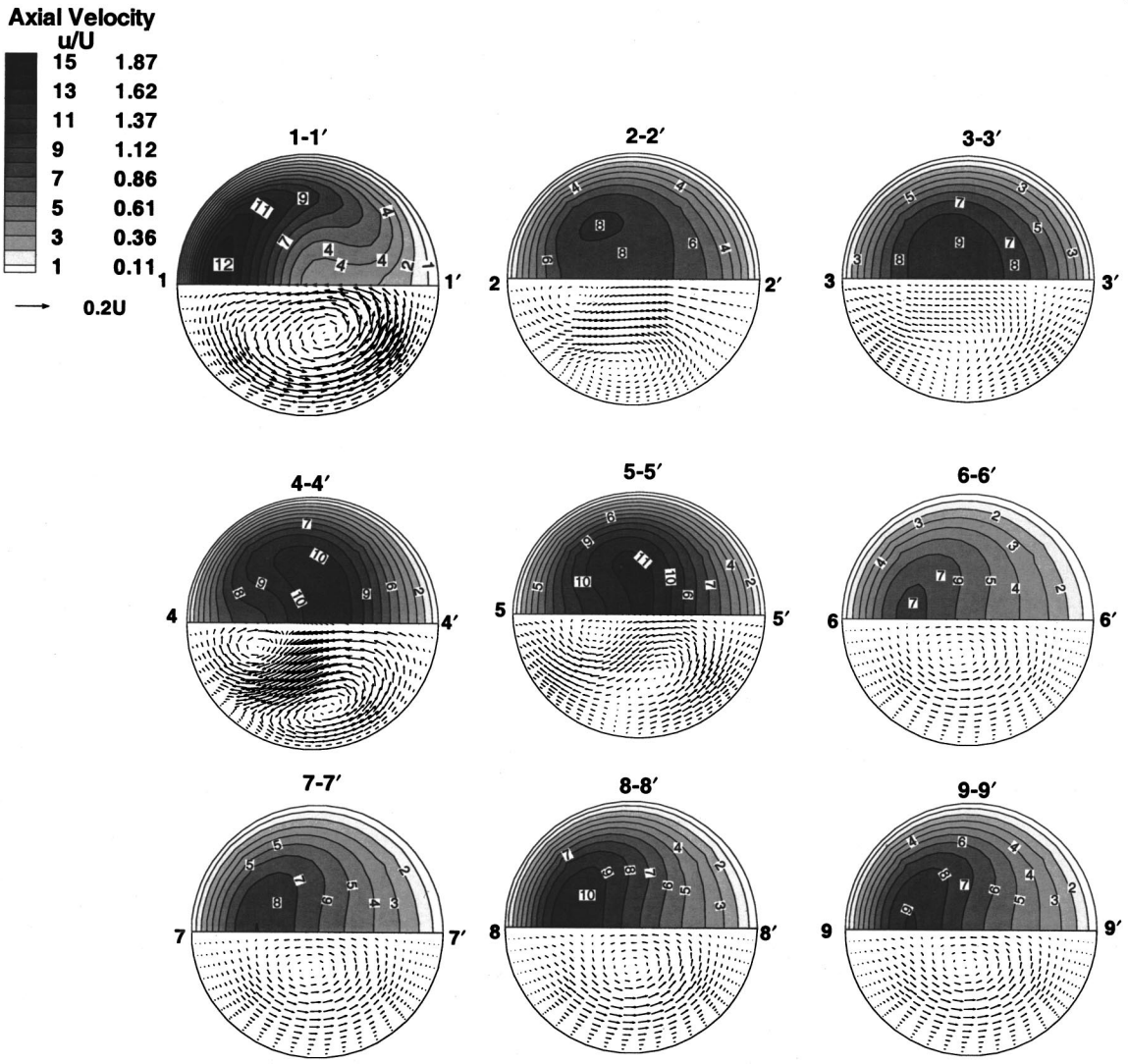

Fig. 5 Axial velocity contours and secondary velocity plots at different cross sections in the triple bifurcation model for Re=500

station with 512 MB of RAM with two 300 MHz CPUs. The steady-state solution of the flow field was assumed converged when the dimensionless mass residual (Total Mass Residual)/(Mass Flow Rate) $<10^{-3}$. Typical run times for the fluid flow simulations on a single processor were approximately 7.2 hours. Utilizing the converged flow field solution, the particle trajectory simulations required approximately 26 minutes for each Stokes number considered.

2.3 Model Validation. For a Stokes number range of $0.02 \leqslant \mathrm{St} \leqslant 0.3$, the measured percentage of particle deposition in a single bifurcation [3,12,32] and double bifurcation [13] has been compared with computer predictions [10,11,33]. The present simulation results in the first two generations were also very close to the deposition correlation of Kim et al. [34] as well as Kim and Fisher [13] for a double bifurcation (cf. Fig. 2). For a given Stokes number, variations in fluid Reynolds number and particle diameter produced only slightly different efficiencies. However, parametric sensitivity analyses revealed that the particle inlet concentration profile and wall curvature, especially around the carinal ridge, had measurable effects on the deposition efficiency as discussed by Comer [23].

3 Results and Discussion

The schematic of Fig. 3 indicates the nine locations of cross-sectional views for the axial and secondary velocity fields as well as the six locations of slices to show cross-sectional particle distributions and directions of particle motion. After the air flow fields at two representative Reynolds numbers, i.e., Re=500 and 2000, are displayed, the particle motions and local concentrations are shown for combinations of two Reynolds numbers (i.e., Re =500, 2000) and two Stokes numbers (i.e., St=0.04, 0.12). Here, both Re and St are based on the inlet of the triple bifurcation models. Local values will vary depending on the local flow conditions.

3.1 Air Flow Structures. The velocity fields in the first and second bifurcation (cf. Figs. 4(*a*,*b*) and slice 1-1′ in Figs. 5 and 6) are quite the same as in a double bifurcation [35] at the respective Reynolds numbers, i.e., Re=500 and 2000. At large Reynolds numbers (cf. Fig. 4(*b*)), a recirculation zone may appear in the first daughter tube and a highly skewed velocity profile approaches the second bifurcation. For any inlet Reynolds number, the *lower* third bifurcation experiences a higher air flow rate, and

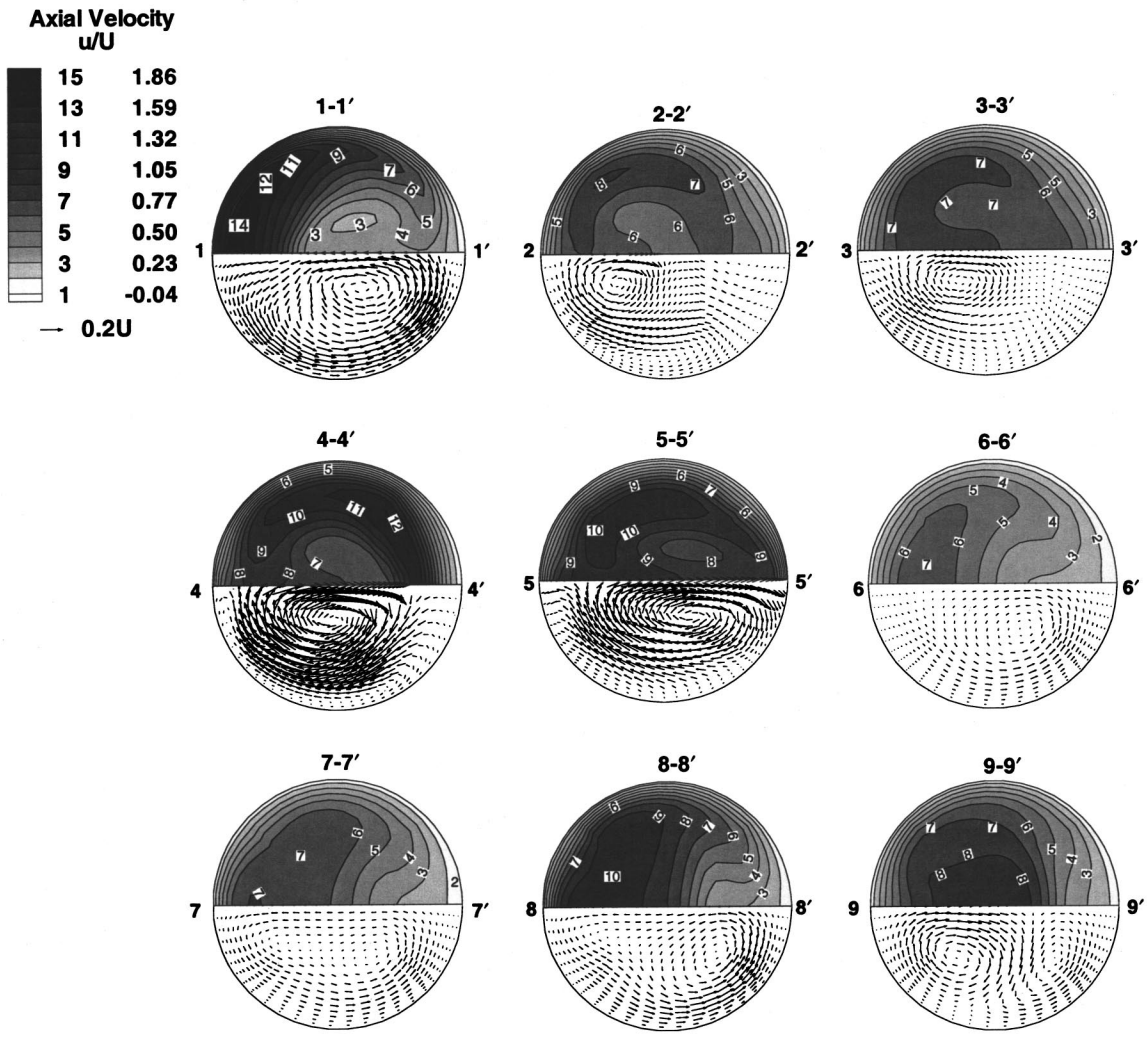

Fig. 6 Axial velocity contours and secondary velocity plots at different cross sections in the triple bifurcation model for Re=2000

both the upper and lower third bifurcations encounter ''more regular'' axial velocity profiles than the second bifurcations.

The velocity fields in cross sections 2-2′ and 3-3′ (cf. Figs. 5, 6) show the development of flow in the upper daughter tube leading to the third bifurcation. The flow fields are still quite similar to those in the exit tube of the double bifurcation model [35]. In cross section 2-2′, i.e., after the second junction, the maximum velocity region has shifted back toward the center of the tube due to the secondary motion at Re=500 (cf. Fig. 5). At Re=2000, the highest axial velocity rotates around the top of the tube, lifting off from the symmetry plane (cf. Fig. 6). For the low-Reynolds-number case, in cross section 3-3′, i.e., the beginning of the third bifurcation curvature, the maximum velocity region is near the center of the tube, while secondary rotation is very weak compared to that in the second bifurcation (cf. Fig. 5). The highest axial velocity region for the high-Reynolds-number case has continued to rotate around until it is located at the inside of the tube (cf. Fig. 6). The situation in the daughter tube before the *lower* third bifurcation is somewhat different. Due to the effects of the skewed flow field upstream, a large portion of high speed fluid enters the lower third bifurcation and the magnitude of the axial velocity and secondary flow is stronger than that in the upper branch (cf. Figs. 5,6). At the beginning of the lower second daughter tube shown in cross section 4-4′, the maximum velocity also shifts back toward the center of the tube for the low-Reynolds-number case (cf. Fig. 5). For the high-Reynolds-number case, the air has continued to rotate around the top of the daughter tube toward the tube inside wall. Like the flow in the upper third bifurcation, the highest velocity region is essentially in the center of the tube for Re=500 and rotates around until it is located on the inside of the tube for Re=2000, as shown in velocity fields of cross section 5-5′ (cf. Figs. 5,6). The existence of the highest axial velocity region being in the tube center in the low-Reynolds-number case will cause a relatively high particle deposition on the third carinal ridge due to inertial impaction (cf. [14]).

Cross sections 6-6′, 7-7′, 8-8′, and 9-9′ are located in the middle of the four exit tubes, i.e., the daughter tubes of the upper and lower third bifurcations (cf. Figs. 5,6). As expected, the secondary flow in the third daughter tube is very weak for both high and low-Reynolds-number cases, although the mean axial vorticity of the secondary flow for Re=2000 is a little higher than that for Re=500. The maximum axial velocity region shifts back toward the inside of the daughter tube at low Reynolds numbers. In the case of large Reynolds numbers, the highest axial velocity is still near the inside of the tube, e.g., cross sections 6-6′, 7-7′ and 8-8′, while in cross section 9-9′, the highest axial velocity is somewhat near the center of the tube. The flow asymmetry in the two daughter tubes of the same third bifurcation is lower when compared to that in the second bifurcation.

Finally, comparing the flow fields in the triple bifurcation

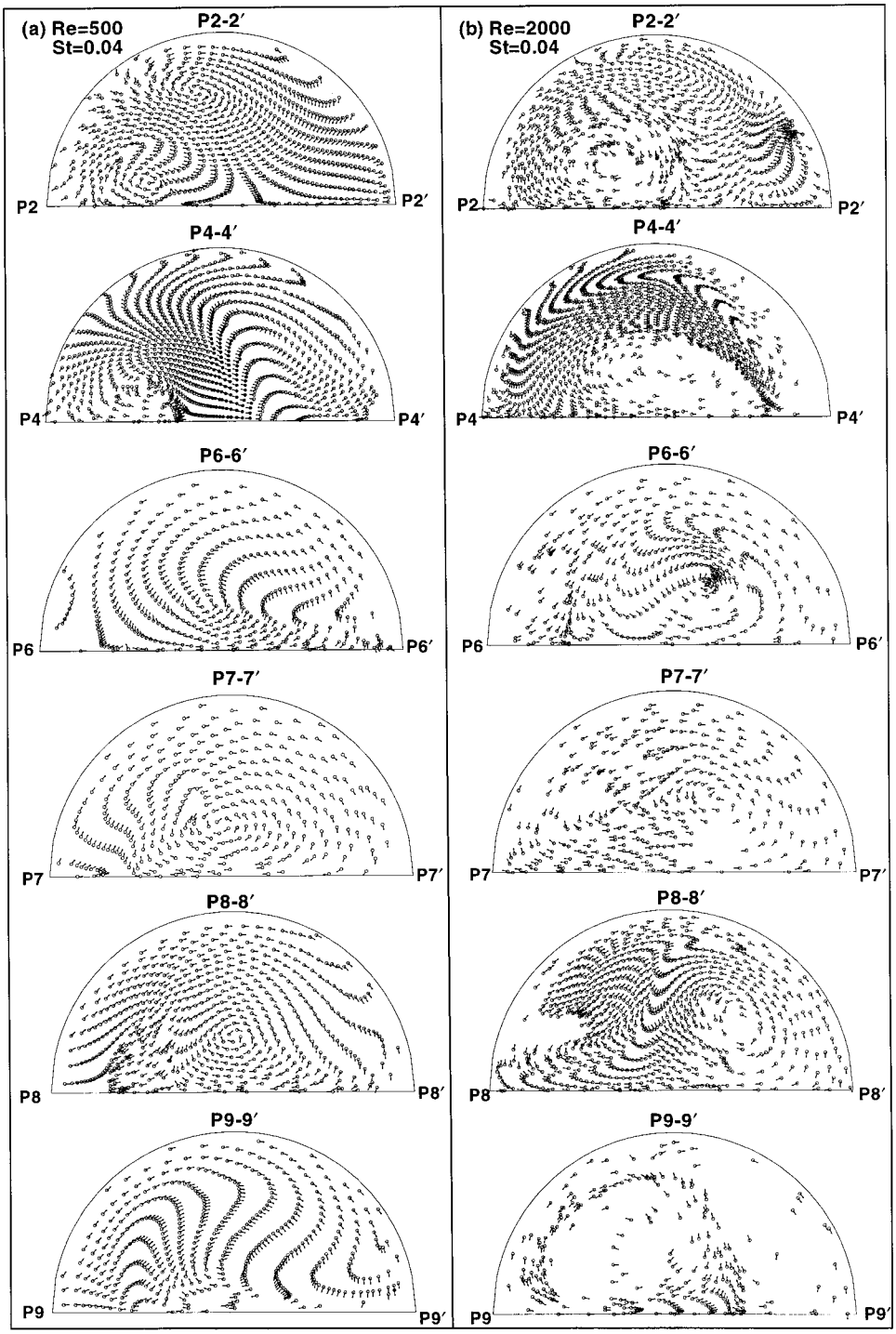

Fig. 7 Particle distributions and flow directions in the triple bifurcation at different cross sections: (*a*) Re=500, St=0.04 and (*b*) Re=2000, St=0.04. (Note: ● indicates impacting particles and the arrow only indicates the direction of particle motion.)

model at the low Reynolds number (Re=500) with those at the high Reynolds number (Re=2000), we can see that the velocity profiles in the first daughter tube (cf. Figs. 4–6) exhibit similar features for these two Reynolds number cases. However, the flow fields in the second and third daughter tubes are much different when the Reynolds number increases from 500–2000. This indicates that the air flow in the second daughter tube leading to the third bifurcation is more sensitive to inlet Reynolds number variations than those in the first daughter tube.

3.2 Particle Transport. Because of the lack of upstream effects of the third bifurcation (cf. Sect. 3.1), cross-sectional particle distributions and motion indicators are only provided for locations P2-2′, P4-4′ and P6-6′ to P9-9′ (cf. Figs. 7,8). The particles shown as black dots will deposit in the third bifurcation area. Cross sections P2-2′ and P4-4′ are, correspondingly, just downstream of the cross sections 2-2′, 4-4′ (cf. Fig. 3). Cross sections P6-6′ to P9-9′ are located in the four exit tubes down-

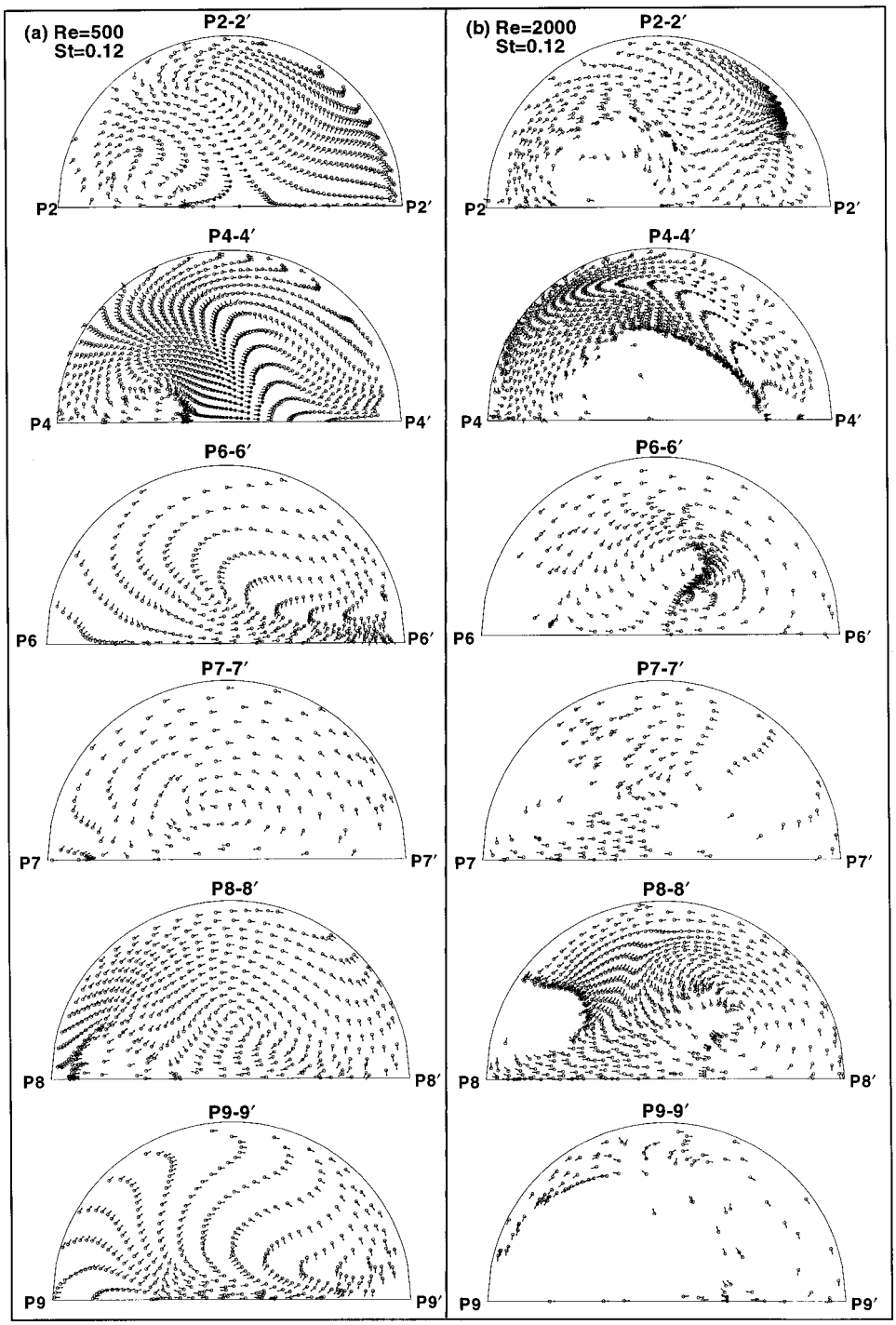

Fig. 8 Particle distributions and flow directions in the triple bifurcation at different cross sections: (*a*) Re=500, St=0.12 and (*b*) Re=2000, St=0.12. (Note: ● indicates impacting particles and the arrow only indicates the direction of particle motion.)

stream of cross sections 6-6′ to 9-9′, respectively. For different inlet Reynolds and Stokes number combinations, such as Re =500 and St=0.04, Re=500 and St=0.12, Re=2000 and St =0.04, and Re=2000 and St=0.12, the particle positions and motion indicators are shown in Figs. 7 and 8. It should be noted that the arrow only indicates the direction of particle motion.

At cross section P2-2′, the particle field indicates two distinct vortical regions for the low Reynolds number (cf. Figs. 7*a* and 8*a*). This may be due to the effect of secondary flow. Two distinct vortexes are exhibited in cross section 2-2′ (cf. Fig. 5). Although these secondary flows are relatively weak, the smaller centrifugal forces acting over a longer time period at low axial velocities have similar effects as larger forces over a shorter time interval. In this case, the particle concentration appears to be somewhat uniform with a low concentration in the region immediately adjacent to the inside wall. The reason is that the upstream carinal ridge initially forced the flow away from the inside wall and toward the outside wall. When compared with the low-Stokes-number case, such a carinal effect on the particle distributions is more apparent for higher Stokes numbers (e.g., St=0.12). In contrast to the high-

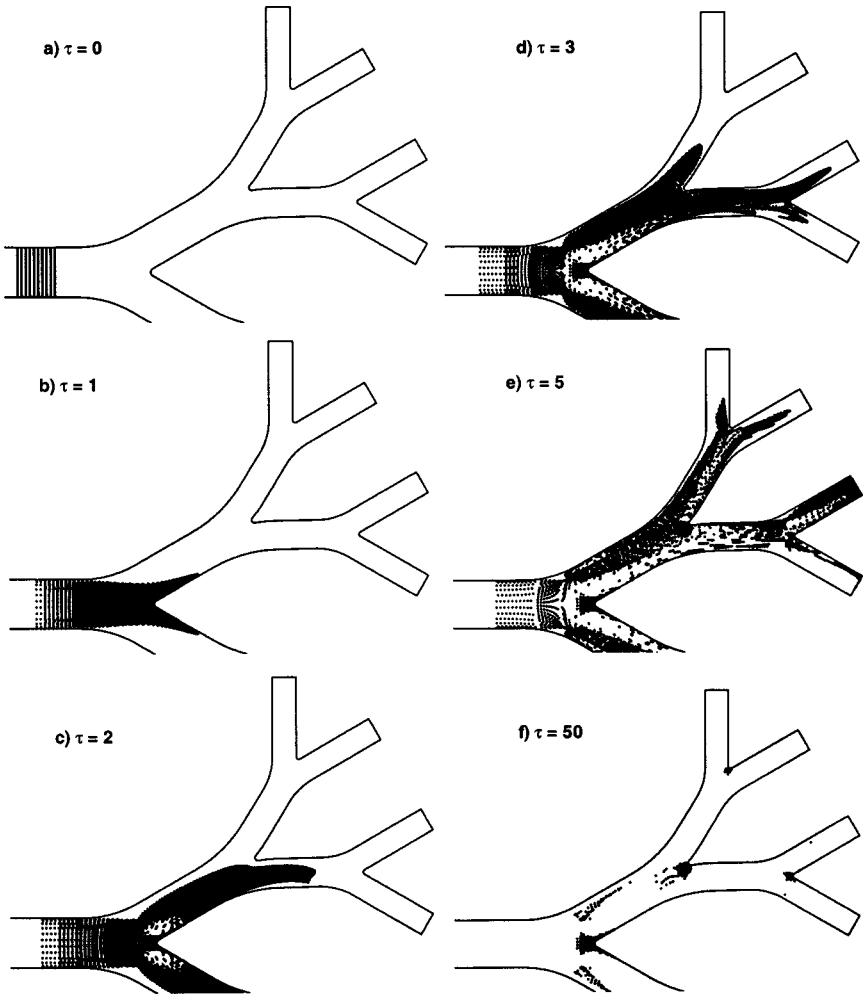

Fig. 9 Time evolution for a volumetric particle pulse in the triple bifurcation for St =0.12 and Re=2000

Reynolds-number case, we can see that more particles in the center of the tube will impact the carina for the low-Reynolds-number case, because the maximum axial velocity zone is located at the center (cf. Fig. 5). For Re=2000, centrifugal forces pull the particles away from the vortex center, generating a distinct particle-free zone. As expected, the higher the Stokes number, the higher the centrifugal force and the larger the void region. In addition, Figs. 7 and 8 show a region of particle concentration along the outside wall of the bifurcation, corresponding to the small secondary vortex in combination with a stronger ''secondary separation'' region at the outside of the tube (cf. Fig. 7). Comparing Fig. 7 with Fig. 8, we can see the Stokes number effect. With an increase in Stokes number, the centrifugal force increases and the particle void regions and high concentration regions become larger. At the same time, because of the higher inertia force with the increasing Stokes number, more particles may impact at the carinal ridge.

For the low-Reynolds-number case at cross section P4-4′ (cf. Figs. 7(*a*) and 8(*a*)), we can see that the axial flow field is a good indicator for the resulting particle concentrations. In the region where two counter-rotating vortices meet, a higher local particle concentration is generated due to the combined centrifugal force effects. For the Re=2000 case, a large void region in the tube center is again present due to the strong vortex (cf. Figs 7(*b*) and 8(*b*)). The highest particle concentration is generally along the outside of the vortex. The Stokes number effect is almost the same as in cross section P2-2′. With an increase in Stokes number, for the high-Reynolds-number case, the void region becomes larger. At low Reynolds numbers, the higher concentration region becomes more pronounced and more particles will impact the carina.

In cross section P6-6′, the axial flow field is still a good indicator for the particle motion, and the particle concentration appears to be almost uniform at Re=500. However, for the high-Reynolds-number case, a particle-free zone does not appear because the secondary flow is rather weak. The particles can generally follow the axial flow, and a high local particle concentration zone is generated in the region where two counter-rotating vortices meet. The higher the Stokes number, the higher the particle concentration.

The particle fields for the low Reynolds number case in cross section P7-7′ indicate the existence of a distinct vortex region; but from the flow field plots it can be observed that the secondary flow effect is very weak. Unlike the situation at cross section P6-6′, the flow rate here does not provide an indicator of the particle concentration. For Re=2000, a particle-free zone appears again in the secondary vortex region. It can be seen that for the high-Stokes-number case, fewer particles will enter this particular tube due to the upstream velocity distribution.

At cross section P8-8′, which coincides with the 8-8′ slice, higher axial flow transports more particles into this daughter tube. For Re=500, the particle can not follow the axial flow as well, and a particle swirl region is generated near the tube center. For the Re=2000 case, two particle-void regions in the tube are

present. One is located near the tube center and the other near the inside wall. This may be attributed to the two secondary vortices indicated in slice 8-8′ of Fig. 6.

The relationship between velocity and particle flow fields in cross section P9-9′ is essentially the same as that discussed for the previous cross section P6-6′ for the low-Reynolds-number case. For Re=2000, very few particles will enter this tube, and a very large particle-free zone appears. The effect of Stokes number on particle motion at this location is not very pronounced, although more particles will deposit for the high-Stokes-number case.

The preferential concentration of particles caused by the coherent vortical structures was also demonstrated in experiment and numerical studies for turbulent flow, as reviewed by Eaton and Fessler [36]. The mechanisms which drive preferential particle concentrations in both vortical turbulent flow and secondary vortical flow of the present laminar case are the same, i.e., the centrifuging of particles away from the vortex cores and accumulation of particles in convergence zones. If the secondary vortical flow is strong enough (e.g., in the high Reynolds number case, Re=2000), the dense particles cannot follow the instantaneous fluid flow streamlines and may be pulled away from the vortex center due to the centrifugal force. The vortex cores would be the regions of low particle concentrations or even distinct particle-free zones.

In order to depict the Lagrangian time evolution of particle transport and ultimately wall depositions, a volumetric particle pulse ($d_p=5\ \mu$m, $n_p=73{,}560$) has been released at $\tau=0$, where $\tau \equiv tU/D_1$, in the parent tube (cf. Fig. 9(*a*)) for Re=2000 and St=0.12, Convected by the parabolic air velocity profile, the particle cloud splits axisymmetrically at the first junction (Fig. 9(*b*)), and follows the skewed flow field into the second bifurcation (Fig. 9(*c*)). At time level $\tau=3$ (Fig. 9(*d*)), the lower third bifurcation has been reached, and at $\tau=5$ (Fig. 9(*e*)) the initial particle volume is distributed throughout the triple bifurcation airway with slowly moving particles still in the parent tube near the wall. After $\tau=50$ (this is equivalent to about 0.057 second) (Fig. 9(*f*)), ''steady state'' has been reached and the particle deposition patterns for this particular case appear. It is of interest to note that the initial particle distribution, e.g., finite particle volume in the parent tube versus uniformly seeded particles throughout the system, has no bearing on the final wall particle deposition patterns [33].

4 Conclusions

Considering steady laminar inhalation of a dilute micron-size aerosol suspension into a representative triple bifurcation lung airway model, air flow structures and particle transport have been numerically investigated. The validated computer simulation results for various inlet Reynolds- and Stokes-number combinations are of interest to researchers studying toxicologic effects of air pollutants or therapeutic effects of drug aerosols.

The air flow and particle motion in the first and second bifurcations are essentially not affected by the third bifurcations. The air flow and particle concentration fields in the second daughter tube leading to the third bifurcation are more sensitive to the variations of inlet Reynolds and Stokes numbers than those in the first daughter tube. Specifically, the subtle and irregular changes in particle distributions in the second daughter tubes due to complex, vortical air flows and triggered by variations in inlet conditions explain subsequent particle deposition patterns [14].

Although the strength of the secondary flow in the second and third daughter tubes become relatively weak compared with that in the first daughter tube, the particle motions and preferential concentrations are still directly related to the corresponding secondary vortical flows in these tubes. This is because the smaller centrifugal forces acting over a longer time period at low axial velocities have a similar effect as larger forces have over a shorter time interval. At lower Reynolds numbers, the strength of secondary flow or vortical flow is low, so the particles can generally follow the axial air flow in a Stokes number range of $0.02 \leqslant \mathrm{St} \leqslant 0.12$. However, with an increase in Reynolds number, the stronger secondary flow, or vortical flow, and the centrifugal force may pull the particles away from the vortex, which generates a particle-free zone with a higher particle concentration along its periphery. With an increase in Stokes number, the particle-free zone may become larger.

The axial and secondary flows as well as the resulting particle motion in the four third daughter tubes are still quite different from those in the upstream daughter tubes. This implies that particle depositions in a fourth generation should be somewhat different from those in the third generation.

Acknowledgments

The use of CFX software from AEA Technology (Bethel Park, PA) and U.S. EPA financial support are gratefully acknowledged.

Disclaimer

Although the research described in this article has been supported by the U.S. Environmental Protection Agency, it has not been subjected to Agency review and, therefore, does not necessarily reflect the views of the Agency, and no official endorsement should be inferred. Mention of tradenames or commercial products does not constitute endorsement or recommendation for use.

Nomenclature

C_{DP} = particle drag coefficient, defined in Eq. 4(a)
D_1 = the diameter of the parent tube
D_2 = the diameter of the first daughter tube
D_3 = the diameter of the second daughter tube
D_4 = the diameter of the third daughter tube
d_p = particle diameter
DE = particle deposition efficiency
l = tube length
m_p = the mass of a single particle
n_p = the amount of particles
p = static pressure
r_0 = tube radius
Re = Reynolds number, UD_1/ϑ
Re_p = particle Reynolds number, $\mathrm{Re}_P=\rho|\vec{v}-\vec{v}_p|d_p/\mu$
St = Stokes number $P_p d_p^2 U/(18\mu D_1)$
t = time
U = averaged inlet axial velocity
u, v, w = velocity component
$\vec{v}$ = fluid velocity vector
$\vec{v}_p$ = particle velocity vector
$\vec{x}_p$ = particle displacement vector
x, y, z = coordinate axis
α = Womersley number, $\alpha=r_0\sqrt{\omega/\nu}$
ε = frequency parameter, $\varepsilon=\omega l/U$
μ = fluid dynamics viscosity
ρ = fluid density
ρ_p = particle density
τ = Lagrangian time, $\tau=tU/D_1$
ν = fluid kinematic viscosity
ω = angular frequency

Special symbols

$\nabla(\ )$ = gradient of ( )
$\nabla\cdot(\ )$ = divergence of ( )
$()^{\mathrm{tr}}$ = transpose of ( )

Superscript

$\rightarrow$ = vector

Subscript

p = particle

References

[1] Weibel, E. R., 1963, *Morphometry of the Human Lung*, Academic Press, New York.

[2] Horsfield, K., and Cumming, G., 1968, ''Morphology of the Bronchial Tree in man,'' J. Appl. Physiol., **24**, pp. 373–383.

[3] Kim, C. S., Lee, B. K., Lewars, G. G., and Sackner, M. A., 1983, ''Deposition of Aerosol Particles and Flow Resistance in Mathematical and Experimental Airway Models,'' J. Appl. Physiol., **55**, pp. 154–163.

[4] Balásházy, I., 1994, ''Simulation of Particle Trajectories in Bifurcating Tubes,'' J. Comput. Phys., **110**, pp. 11–22.

[5] Gatlin, B., Cuicchi, C., Hammersley, J., Olson, D., Reddy, R., and Burnside, G., 1997, ''Particle Path and Wall Deposition Patterns in Laminar Flow Through a Bifurcation,'' *ASME Vol. FEDSM97*, Vancouver, British Columbia, Canada, pp. 1–6.

[6] Farag, A., Hammersley, J., Olson, D., and Ng, T., 1998, ''Fluid Mechanics of a Symmetric Bifurcation Model of the Human Pulmonary System,'' *ASME Vol. FEDSM98*, Washington, DC, pp. 1–8.

[7] Farag, A., Ng, T., Hammersley, J., and Olson, J., 1998, ''Fluid Mechanics of An Asymmetric Bifurcation Model of Human Pulmonary System,'' *ASME Vol. FEDSM98*, Washington, DC, pp. 1–8.

[8] Wilquem, F., and Degrez, G., 1997, ''Numerical Modeling of Steady Inspiratory Airflow Through a Three-Generation Model of the Human Central Airways,'' ASME J. Biomech. Eng., **119**, pp. 59–65.

[9] Lee, J. W., Goo, J. H., and Chung, M. K., 1996, ''Characteristics of Inertial Deposition in a Double Bifurcation,'' J. Aerosol Sci., **27**, pp. 119–138.

[10] Comer, J. K., Kleinstreuer, C., Hyun, S., and Kim, C. S., 2000, ''Aerosol Transport and Deposition in Sequentially Bifurcating Airways,'' ASME J. Biomech. Eng., **122**, pp. 152–158.

[11] Kleinstreuer, C., Comer, J. K., Zhang, Z., and Kim, C. S., 1999, ''Computer Simulation of Aerosol Transport and Deposition in Multi-generation Airway Models,'' *First Joint Meeting of BMES & EMBS*, Atlanta, GA, October 13–16; Conference Proceedings, Fouke, J. M., Nerem, R. M., eds.

[12] Kim, C. S., and Iglesias, A. J., 1989, ''Deposition of Inhaled Particles in Bifurcating Airway Models: I. Inspiratory Deposition,'' Journal of Aerosol Medicine, **2**, pp. 1–14.

[13] Kim, C. S., and Fisher, D. M., 1999, ''Deposition Characteristics of Aerosol Particles in Successively Bifurcating Airway Models,'' Aerosol. Sci. Technol., **31**, pp. 198–220.

[14] Zhang, Z., Kleinstreuer, C., and Kim, C. S., 2001, ''Computational Analysis of Micron-Particle Deposition in a Human Triple Bifurcation Airway Model,'' Computer Methods in Biomechanics and Biomedical Engineering (in press).

[15] Horsfield, K., Dart, G., Olson, D. E., Filley, G. F., and Cumming, G., 1971, ''Models of the Human Bronchial Tree,'' J. Appl. Physiol., **31**, pp. 207–217.

[16] Philips, C. G., and Kaye, S. R., 1997, ''On the Asymmetry of Bifurcation in the Bronchial Tree,'' Respir. Physiol., **107**, pp. 85–98.

[17] Chang, H. K., and El Masry, O. A., 1982, ''A Model Study of Flow Dynamics in Human Central Airways. Part I: Axial Velocity Profiles,'' Respir. Physiol., **49**, pp. 75–95.

[18] Isabey, D., and Chang, H. K., 1982, ''A Model Study of Flow Dynamics in Human Central Airways. Part II: Secondary Flow Velocities,'' Respir. Physiol., **49**, pp. 97–113.

[19] Chang, H. K., and Menon, A. S., 1985, ''Air Flow Dynamics in the Human Airways,'' *Aerosols in Medicine. Principles, Diagnosis and Therapy*, F. Moren, M. T. Newhouse, and M. B. Dolovich, eds., Elsevier Science, Amsterdam, pp. 77–122.

[20] Oho, K., and Amemiya, R., 1980, *Practical Fiberoptic Bronchoscopy*, Igaku-Shoin, Tokyo.

[21] Pedley, T. J., Schroter, R. C., and Sudlow, M. F., 1977, ''Gas Flow and Mixing in The Airways,'' *Bioengineering Aspects of the Lung*, West, J. B., ed., Marcel Dekker, New York.

[22] Martonen, T. B., Yang, Y., and Xue, Z. Q., 1994, ''Influences of Cartilaginous Rings on Tracheobronchial Fluid Dynamics,'' Inhalation Toxicol., **6**, pp. 185–203.

[23] Comer, J. K., 1998, ''Computational Two-Phase Flow Analyses and Applications to Gas-Liquid and Gas-Solid Flows,'' PhD thesis, Mechanical and Aerospace Engineering Department, North Carolina State University, Raleigh, NC.

[24] Kleinstreuer, C., 1997, *Engineering Fluid Dynamics—An Interdisciplinary Systems Approach*, Cambridge University Press, NY.

[25] Clift, R., Grace, J. R., and Weber, M. E., 1978, *Bubbles Drops and Particles*, Academic Press, NY.

[26] Zhang, Z., and Kleinstreuer, C., 2001, ''Effect of Particle Inlet Distribution on Deposition in A Triple Bifurcation Lung Airway Model,'' Journal of Aerosol Medicine, **14**, pp. 13–29.

[27] Zhang, Z., Kleinstreuer, C., and Kim, C. S., 2000, ''Effects of Asymmetric Branch Flow Rates on Aerosol Deposition in Bifurcating Airways,'' J. Med. Eng. Technol. **24**, pp. 192–202.

[28] AEA Technology, 1997, CFX-4.2: Solver, CFX International, Oxfordshire, UK.

[29] Patankar, S. V., 1983, *Numerical Heat Transfer and Fluid Flow*, Hemisphere, NY.

[30] Lonsdale, R. D., 1993, ''An algebraic multi-grid solver for the Navier Stokes equations on unstructured meshes,'' Int. J. Numer. Methods Heat Fluid Flow, **3**, pp. 3–14.

[31] Gear, C. W., 1971, *Numerical Initial Value Problems in Ordinary Differential Equations*, Prentice-Hall, Englewood Cliffs, NJ.

[32] Johnston, J. R., Isles, K. D., and Muir, D. C. F., 1977, ''Inertial Deposition of Particles in Human Branching Airways,'' *Inhaled Particles IV*, Walton, W. H., ed., Pergamon Press, Oxford, pp. 61–72.

[33] Comer, J. K., Kleinstreuer, C., Longest, P. W., Kim, C. S., and Kinsey, J. S., 1998, ''Computational Aerosol Transport and Deposition Analyses for Human Exposure Chambers and Model Respiratory Airways,'' *ASME Vol. FEDSM98*, Washington, DC, pp. 1–6.

[34] Kim, C. S., Fisher, D. M., Lutz, D. J., and Gerrity, T. R., 1994, ''Particle Deposition in Bifurcating Airway Models with Varying Airway Geometry,'' J. Aerosol Sci., **25**, pp. 567–581.

[35] Comer, J. K., Kleinstreuer, C., and Zhang, Z., 2001, ''Flow Structures and Particle Deposition Patterns in Double Bifurcation Airway Models. Part 1. Air Flow Fields,'' J. Fluid Mech., in press.

[36] Eaton, J. K., and Fessler, J. R., 1994, ''Preferential Concentration of Particles by Turbulence,'' Int. J. Multiphase Flow, **20**, Suppl., pp. 169–209.

Simulations of Cavitating Flows Using Hybrid Unstructured Meshes

Vineet Ahuja
Research Scientist

Ashvin Hosangadi
Principal Scientist

Srinivasan Arunajatesan
Research Scientist

Combustion Research and
Flow Technology,
Inc. (CRAFT Tech),
P.O. Box 1150, Dublin, PA 18917

A new multi-phase model for low speed gas/liquid mixtures is presented; it does not require ad-hoc closure models for the variation of mixture density with pressure and yields thermodynamically correct acoustic propagation for multi-phase mixtures. The solution procedure has an interface-capturing scheme that incorporates an additional scalar transport equation for the gas void fraction. Cavitation is modeled via a finite rate source term that initiates phase change when liquid pressure drops below its saturation value. The numerical procedure has been implemented within a multi-element unstructured framework CRUNCH that permits the grid to be locally refined in the interface region. The solution technique incorporates a parallel, domain decomposition strategy for efficient 3D computations. Detailed results are presented for sheet cavitation over a cylindrical head form and a NACA 66 hydrofoil. [DOI: 10.1115/1.1362671]

Introduction

Numerical simulations of cavitating flows are very challenging since localized, large variations of density are present at the gas/liquid interface while the remainder of the flow is generally incompressible. Furthermore, the cavitation zone can detach due to the influence of a re-entrant jet and convect downstream. This detachment/collapse of the cavity in the pressure recovery region can lead to strong acoustic disturbances. These disturbances can manifest themselves as high frequency noise that has the potential to considerably alter the acoustic signal/signature and degrade performance. In general, current cavitation models, which have originated from incompressible formulations, deal with these issues by defining ad-hoc closure models relating density and pressure which are not very general. In our paper, we describe a compressible, cavitation formulation which yields the correct acoustical and thermodynamic behavior for multi-phase systems. The importance of being thermodynamically consistent is that the same cavitation model can be used for simulations from marine propellers to cryogenic pumps. In particular, the system does not require user defined closure models for capturing the gas/liquid interface and is designed to perform efficiently in the nearly incompressible liquid regime. We give a brief review of the literature below and highlight the differences with our formulation.

Cavitation models in the literature may broadly be classified into two categories; interface fitting and interface capturing procedures. Interface fitting procedures explicitly track and fit a distinct gas/liquid interface which is an internal boundary. While this procedure gets around the numerical difficulties of integrating through the interface, its applications are limited to simpler problems where the cavity can be described as a well-defined closed volume of pure gas. Interface capturing schemes, where the gas/liquid interface is obtained as part of the solution procedure, are more general in their applications and may be applied to both sheet cavitation as well as bubbly cavitation. Here, the thermodynamic issues of integrating through gas/liquid mixtures with density and acoustic speed variations have to be dealt with in order to provide closure to the equation system.

Closure models reported in the literature are generally tailored for specific problem classes and do not address the multi-phase physics in a fundamental fashion. For instance, bubbly cavitation has been tackled by providing pseudo-density relations derived from various modified forms of the Rayleigh-Plesset equation (Kubota et al. [1] and Chen and Heister [2]). Here, no additional equation for the convection of gas species is specified and the formulations make assumptions about the bubble number density in the fluid. On the other hand, for sheet cavitation an ad-hoc pseudo-density relationship based on the local pressure is provided to close the system (Delaunay and Kueny [3] and Janssens et al. [4]) which can be quite restrictive since it is decoupled completely from the local phase composition.

More generalized cavitation formulations have been presented in recent papers by Merkle et al. [5] and Kunz et al. [6]. Here, an additional equation for the gas void fraction is solved for and the local mixture density is obtained from the local phase composition. The equations are cast in a compressible-like time marching format with preconditioning to overcome numerical stiffness problems. However, in both cases, the authors implicitly specified a pressure-density relation which leads to an erroneous acoustic speed in the mixture, particularly in the interface region. The non-physical acoustic speeds are clearly not appropriate for unsteady simulations. However, even for steady calculations, this may pose numerical difficulties at the gas/liquid interface since the physical acoustic speed behaves in a nonlinear fashion (as we shall discuss later) and has a very small magnitude; the local Mach number at the interface can be large leading to very different numerical characteristics.

The formulation presented in this paper is an acoustically accurate form of the compressible multi-phase equations (Ahuja et al. [7]) and is an extension of our earlier work in high pressure gas/liquid systems (Hosangadi et al. [8]). The numerical algorithm follows a similar time-marching philosophy (as that in Merkle et al. [5] and Kunz et al. [6]). However, here the local speed of sound in the two-phase mixture is a function of the local void fraction and mimics the two-phase acoustic speed relationship from classical analytic theory. We note that the system presented here is closed and does not require additional equations to resolve the gas/liquid interface. The model is general and may be applied to both sheet and bubbly cavitation by providing appropriate source terms for gas generation/reabsorption in cavitating regions.

The numerical formulation has been implemented on a hybrid unstructured framework which permits tetrahedral/prismatic cells. An unstructured framework is particularly suitable for geometrically complex systems like marine propellers where the blades are

Contributed by the Fluids Engineering Division for publication in the JOURNAL OF FLUIDS ENGINEERING. Manuscript received by the Fluids Engineering Division April 5, 2000; revised manuscript received January 29, 2001. Associate Editor: Y. Matsumoto.

skewed strongly. In addition, the ability for local grid refinement in a complex flow field provided a strong motivation for using unstructured grids here. For instance, in cavitation simulations, the region near the gas/liquid interface exhibits strong gradients in flow properties and requires high local grid resolution which can be achieved most economically with a grid adaption procedure. For efficient computations of large 3D problems, a parallel framework for distributed memory systems has been implemented. Details of the numerical formulation are provided in the following section followed by details of the unstructured framework. In the Results section, we discuss details of our simulation for a cylindrical headform and a NACA 66 hydrofoil. The details of the flowfield in the closing region of the cavity and the turbulence characteristics of the wake are examined in depth. Surface pressure comparisons with experimental data are shown for a range of cavitation numbers to validate the numerics.

Multi-Phase Equation System

The multiphase equation system is written in vector form as:

$$\frac{\partial Q}{\partial t}+\frac{\partial E}{\partial x}+\frac{\partial F}{\partial y}+\frac{\partial G}{\partial z}=S+D_v \tag{1}$$

Here Q is the vector of dependent variables, E, F, and G are the flux vectors, S the source terms and D_v represents the viscous fluxes. The viscous fluxes are given by the standard full compressible form of Navier Stokes equations (see Hosangadi et al. [9] for details). The vectors Q, E, and S are given below with a detailed discussion on the details of the cavitation source terms to follow later:

$$Q=\begin{pmatrix}\rho_m\\ \rho_m u\\ \rho_m v\\ \rho_m w\\ \rho_g\phi_g\\ \rho_m k\\ \rho_m\varepsilon\end{pmatrix}\quad E=\begin{pmatrix}\rho_m u\\ \rho_m u^2+P\\ \rho_m uv\\ \rho_m uw\\ \rho_g\phi_g u\\ \rho_m ku\\ \rho_m\varepsilon u\end{pmatrix}\quad S=\begin{pmatrix}0\\ 0\\ 0\\ 0\\ S_g\\ S_k\\ S_\varepsilon\end{pmatrix} \tag{2}$$

Here, ρ_m is the mixture density, and ϕ_g is the volume fraction or porosity for the gas phase. Note that in Eq. (2) the energy equation is dropped since each phase is assumed to be nearly incompressible thereby decoupling the pressure work term. An additional scalar equation for mixture enthalpy may be solved coupled to this equation set if the temperature effects become important. The mixture density and gas porosity are related by the following relations locally in a given cell volume:

$$\rho_m=\rho_g\phi_g+\rho_L\phi_L \tag{3}$$

$$1=\phi_g+\phi_L \tag{4}$$

where ρ_g,ρ_L are the physical material densities of the gas and liquid phase respectively.

To modify the system in Eq. (1) to a well-conditioned form in the incompressible regime requires a two-step process; an acoustically accurate two-phase form of Eq. (1) is first derived, followed by a second step of time-scaling or preconditioning to obtain a well-conditioned system. We begin by defining the acoustic form of density differential for the individual gas and liquid phase as follows:

$$d\rho_g=\frac{1}{c_g^2}dP,\quad d\rho_l=\frac{1}{c_L^2}dP \tag{5}$$

Here c_g is the isothermal speed of sound $(\partial P/\partial\rho_g)_T$ in the pure gas phase, and c_L is the corresponding isothermal speed of sound in the liquid phase, which is a finite-value. The differential form of the mixture density ρ_m is obtained by differentiating Eq. (3), and using the relationship given in Eq. (5) to obtain,

$$d\rho_m=(\rho_g-\rho_L)d\phi_g+\frac{1}{c_\phi^2}dP$$

$$\left(\frac{1}{c_\phi^2}=\frac{\phi_g}{c_g^2}+\frac{\phi_L}{c_L^2}\right) \tag{6}$$

Here, c_ϕ is a variable defined for convenience and is not the acoustic speed, c_m, in the mixture which will be defined later. Using Eq. (6), Eq. (1) may be rewritten as:

$$\Gamma\frac{\partial Q_v}{\partial t}+\frac{\partial E}{\partial x}+\frac{\partial F}{\partial y}+\frac{\partial G}{\partial z}=S+D_v \tag{7}$$

where

$$\Gamma=\begin{pmatrix}\frac{1}{c_\phi^2} & 0 & 0 & 0 & (\rho_g-\rho_L) & 0 & 0\\ \frac{u}{c_\phi^2} & \rho_m & 0 & 0 & (\rho_g-\rho_L)u & 0 & 0\\ \frac{v}{c_\phi^2} & 0 & \rho_m & 0 & (\rho_g-\rho_L)v & 0 & 0\\ \frac{w}{c_\phi^2} & 0 & 0 & \rho_m & (\rho_g-\rho_L)w & 0 & 0\\ \frac{\phi_g}{c_g^2} & 0 & 0 & 0 & \rho_g & 0 & 0\\ \frac{k}{c_\phi^2} & 0 & 0 & 0 & (\rho_g-\rho_L)k & \rho_m & 0\\ \frac{\varepsilon}{c_\phi^2} & 0 & 0 & 0 & (\rho_g-\rho_L)\varepsilon & 0 & \rho_m\end{pmatrix} \tag{8}$$

and,

$$Q_v=[p,u,v,w,\phi_g,k,\varepsilon]^T \tag{9}$$

The numerical characteristics of the Eq. (7) are studied by obtaining the eigenvalues of the matrix, $[\Gamma^{-1}(\partial E/\partial Q_v)]$. The flux Jacobian $\partial E/\partial Q_v$ is given as:

$$A=\begin{pmatrix} \frac{u}{c_\phi^2} & \rho_m & 0 & 0 & (\rho_g-\rho_l)u & 0 & 0 \\ \frac{u^2}{c_\phi^2}+1 & \rho_m 2u & 0 & 0 & (\rho_g-\rho_l)u^2 & 0 & 0 \\ \frac{vu}{c_\phi^2} & \rho_m v & \rho_m u & 0 & (\rho_g-\rho_l)vu & 0 & 0 \\ \frac{wu}{c_\phi^2} & \rho_m w & 0 & \rho_m u & (\rho_g-\rho_l)wu & 0 & 0 \\ \frac{\phi_g u}{c_\phi^2} & \rho_g\phi_g & 0 & 0 & \rho_g u & 0 & 0 \\ \frac{ku}{c_\phi^2} & \rho_m k & 0 & 0 & (\rho_g-\rho_L)ku & \rho_m u & 0 \\ \frac{\varepsilon u}{c_\phi^2} & \rho_m \varepsilon & 0 & 0 & (\rho_g-\rho_L)\varepsilon u & 0 & \rho_m u \end{pmatrix} \tag{10}$$

The eigenvalues of the system are derived to be:

$$\Lambda=(u+c_m,u-c_m,u,u,u,u,u) \tag{11}$$

where c_m turns out to be the well-known, harmonic expression for the speed of sound in a two-phase mixture and is given as:

$$\frac{1}{c_m^2}=\rho_m\left[\frac{\phi_g}{\rho_g c_g^2}+\frac{\phi_L}{\rho_L c_L^2}\right] \tag{12}$$

The behavior of the two-phase speed of sound is plotted in Fig. 1 as a function of the gas porosity; at either limit the pure single-phase acoustic speed is recovered. However, away from the single-phase limits, the acoustic speed rapidly drops below either limit value and remains at the low-level in most of the mixture regime. As a consequence, the local Mach number in the interface region can be large even in low speed flows.

We re-emphasize a critical observation at this point: the equation system (7)–(9) is completely defined and does not require ad-hoc closure models for the variation of mixture density with pressure. In that respect alone this represents a significant advancement over most other cavitation models in the literature. The acoustic speeds for individual phases are well-defined physical quantities, which may be specified, and so is the case with physical material densities (ρ_g,ρ_L) for each individual phase. For low pressure incompressible regimes, the material densities may be assumed to be constant without significant error in the solutions.

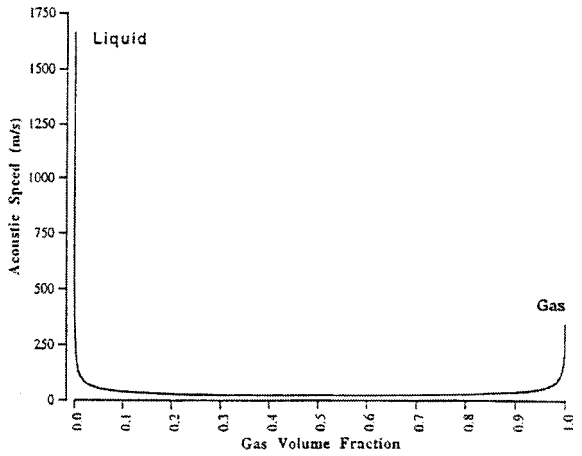

Fig. 1 Speed-of-sound in a two-phase gas-liquid mixture

However, in its most general form the material densities for each phase may be obtained from the pressure using their respective physical equations of state (e.g., ideal gas law for gases, etc.) if that is so desired. If temperature variations were significant, this would involve solving an additional equation for the mixture energy (this formulation is to be presented in a future paper).

To obtain an efficient time-marching numerical scheme, preconditioning is now applied to the system in Eq. (7), in order to rescale the eigenvalues of the system so that the acoustic speeds are of the same order of magnitude as the local convective velocities. This is achieved by replacing Γ in Eq. (7) by Γ_p.

$$\Gamma_p\frac{\partial Q_v}{\partial t}+\frac{\partial E}{\partial x}+\frac{\partial F}{\partial y}+\frac{\partial G}{\partial z}=S+D_v \tag{13}$$

where

$$\Gamma_p=\begin{bmatrix} \frac{\beta}{c_\phi^2} & 0 & 0 & 0 & (\rho_g-\rho_L) & 0 & 0 \\ \frac{\beta u}{c_\phi^2} & \rho_m & 0 & 0 & (\rho_g-\rho_L)u & 0 & 0 \\ \frac{\beta v}{c_\phi^2} & 0 & \rho_m & 0 & (\rho_g-\rho_L)v & 0 & 0 \\ \frac{\beta w}{c_\phi^2} & 0 & 0 & \rho_m & (\rho_g-\rho_L)w & 0 & 0 \\ \frac{\beta\phi_g}{c_g^2} & 0 & 0 & 0 & \rho_g & 0 & 0 \\ \frac{\beta k}{c_\phi^2} & 0 & 0 & 0 & (\rho_g-\rho_L)k & \rho_m & 0 \\ \frac{\beta\varepsilon}{c_\phi^2} & 0 & 0 & 0 & (\rho_g-\rho_L)\varepsilon & 0 & \rho_m \end{bmatrix}$$

Here the parameter β has been introduced to precondition the eigenvalues. The modified eigenvalues of the preconditioned system are given as:

$$\Lambda_P=\left(\frac{u}{2}\left(1+\frac{1}{\beta}\right)+c_m',\frac{u}{2}\left(1+\frac{1}{\beta}\right)-c_m',u,u,u,u,u\right) \quad (14)$$

where

$$c_m'=\frac{1}{2}\sqrt{u^2\left(1-\frac{1}{\beta}\right)^2+4\frac{c_m^2}{\beta}} \quad (15)$$

Equation (15) indicates that by setting $\beta=(c_m^2/u_p^2)$ where $u_p=\max(u,0.01c_m)$ the pseudo-acoustic speed is of the order of u at all mixture composition values. We note that, a rigorous definition of the physical two-phase acoustic speed c_m (as has been done here) is critical to obtaining noise-free propagation of pressure waves across interfaces where the density and acoustic speed are varying rapidly.

Cavitation Source Terms

In the present effort, the cavitation source term is simplified via a simplified nonequilibrium, finite rate form as follows:

$$S_g=K_f\rho_L\phi_L+K_b\rho_g\phi_g \quad (16)$$

where the constant K_f is the rate constant for vapor being generated from liquid in a region where the local pressure is less than the vapor pressure. Conversely, K_b is the rate constant for reconversion of vapor back to liquid in regions where the pressure exceeds the vapor pressure. Here, the rate constants are specified using the form (given by Merkle et al. [5]) as follows:

$$K_b=\begin{vmatrix} 0 & p<p_v \\ \frac{1}{\tau_b}\left(\frac{Q_\infty}{L_\infty}\right) & \left[\frac{p-p_v}{\frac{1}{2}\rho_\infty Q_\infty^2}\right] \quad p>p_v \end{vmatrix}$$

$$K_f=\begin{bmatrix} 0 & p>p_v \\ \frac{1}{\tau_f}\left(\frac{Q_\infty}{L_\infty}\right) & \left[\frac{p-p_v}{\frac{1}{2}\rho_\infty Q_\infty^2}\right] \quad p<p_v \end{bmatrix} \quad (17)$$

$$p_v=p_\infty-\frac{1}{2}\rho_\infty Q_\infty^2 * \quad \text{Cav. No.}$$

$\tau_f=$ time constant for vapor formation

$\tau_b=$ time constant for liquid reconversion

$$\text{Cav. No.}=\frac{p_\infty-p_v}{\frac{1}{2}\rho_\infty Q_\infty^2}$$

We note that the nonequilibrium time scales have not been correlated with experimental data. For steady attached cavitation this simplified form may be adequate since the cavitation time scales do not interact with the fluid time scales if the cavitation rate constants are fast enough. This point has been demonstrated by repeating a calculation for a given cavitation number at three different rates (see Results section). For unsteady cavitation, however, the details of how the nonequilibrium source term is specified could be crucial since it may couple with transient pressure waves. The development of a more rigorous nonequilibrium source term model is a topic of ongoing research.

Turbulence Models

The standard high Reynolds number form of the k-ε equations form the basis for all turbulence modeling in CRUNCH. Transport equations for the turbulent kinetic energy and its dissipation rate are solved along with the basic momentum and energy equations. These equations, with supplemental low Re terms, are as follows,

$$\frac{\partial\rho k}{\partial t}+\frac{\partial}{\partial x_i}\left(\rho u_i k-\left(\mu+\frac{\mu_T}{\sigma_k}\right)\frac{\partial k}{\partial x_i}\right)=P_k-\rho\varepsilon+S_k$$

$$\frac{\partial\rho\varepsilon}{\partial t}+\frac{\partial}{\partial x_i}\left(\rho u_i\varepsilon-\left(\mu+\frac{\mu_T}{\sigma_\varepsilon}\right)\frac{\partial\varepsilon}{\partial x_i}\right)=c_1f_1P_k-C_2f_2\rho\varepsilon+S_\varepsilon \quad (18)$$

$$P_k=\tau_{ij}\frac{\partial u_i}{\partial x_j},\quad \tau_{ij}=-\frac{2}{3}\rho k+2\mu_T^*\left(S_{ij}-\frac{1}{3}\frac{\partial u_k}{\partial x_k}\delta_{ij}\right),$$

$$\mu_T=C_\mu f_\mu\rho\frac{k^2}{\varepsilon}$$

where, σ_k, σ_ε, C_1, and C_2 are the modeling constants, and f_1, f_2, f_μ are empirical modeling functions to account for low Reynolds number (near wall). (They equal unity in the high Reynolds number form.)

Low Reynolds number effects in the near wall are accounted for by using an extension of the near wall model of So et al. [10]. This model has been shown to reproduce the near wall asymptotic relations for the Reynolds stress and kinetic energy accurately. In this model, the damping functions, f_1, f_2, f_μ, are defined as follows,

$$f_1=1.0-\exp\left[-\left(\frac{\mathrm{Re}_t}{40}\right)^2\right]$$

$$f_2=1-\frac{2}{9}\exp\left[-\left(\frac{\mathrm{Re}_t}{6}\right)^2\right]$$

$$S_\varepsilon=\frac{1}{4}c_3\mu_L\left[\left(\frac{\partial k^{1/2}}{\partial x}\right)^2+\left(\frac{\partial k^{1/2}}{\partial y}\right)^2+\left(\frac{\partial k^{1/2}}{\partial z}\right)^2\right] \quad (19)$$

where

$$\mathrm{Re}_t=\frac{\rho k^2}{\mu_L\varepsilon}$$

$$f_\mu=(1+4\,\mathrm{Re}_t^{-3/4})\tanh\left(\frac{\mathrm{Re}_k}{125}\right)$$

where

$$\mathrm{Re}_k=\frac{\rho\sqrt{k}y}{\mu}$$

The constants for this model are given as follows.

$$c_\mu=0.09,\quad \sigma_k=1.4,\quad \sigma_\varepsilon=1.4,$$
$$c_1=1.44,\quad c_2=1.92,\quad c_3=2.9556 \quad (20)$$

This model has been tested for a number of standard turbulence test cases to verify that it gives correct boundary layer growth and reattachment length for recirculating flows. For cavitating flows, where large density gradients are present due to multi-fluid composition, the rigorous validation of the turbulence model will require further study; however, this is beyond the scope of the present paper.

Unstructured Crunch Code Overview

The multi-phase formulation derived in the previous section has been implemented within a three-dimensional unstructured code CRUNCH; a brief overview of the numerics is given here and we refer the reader to Hosangadi et al., [9,11] and Barth [12,13] for additional details. The CRUNCH code has a hybrid, multi-element unstructured framework which allows for a combination of tetrahedral, prismatic, and hexahedral cells. The grid connectivity is stored as an edge-based, cell-vertex data structure where a dual volume is obtained for each vertex by defining surfaces, which cut across edges coming to a node. An edge-based framework is attractive in dealing with multi-elements since dual sur-

face areas for each edge can include contributions from different element types making the inviscid flux calculation ''grid transparent.''

The integral form of the conservation equations are written for a dual control-volume around each node as follows:

$$\Gamma_p \frac{\Delta Q_v V}{\Delta t} + \int_{\partial\Omega_i} F(Q_v, n)ds = \int_{\Omega_i} SdV + \int_{\partial\Omega_i} D(Q_v, n)ds \tag{21}$$

The inviscid flux procedure involves looping over the edge list and computing the flux at the dual face area bisecting each edge. A Riemann problem is solved for using higher order reconstructed values of primitive variables at the dual face. Presently, a second-order linear reconstruction procedure (following Barth [13]) is employed to obtain a higher-order scheme. For flows with strong gradients, the reconstructed higher variables need to be limited to obtain a stable TVD scheme. We note that the inviscid flux as outlined above is grid-transparent since no details of the element type are required in the flux calculation.

The Riemann problem at the dual face is computed with a Roe-averaged, flux-differenced solver which defines the flux, F_m, as:

$$F_m = \frac{1}{2}\left[\begin{array}{c} F(Q_m^-, \vec{n}_{oi}) + F(Q_m^+, \vec{n}_{oi}) + \\ \Delta F^-(Q_{Roe}^m, \vec{n}_{oi}) + \Delta F^+(Q_{Roe}^m, \vec{n}_{oi}) \end{array}\right] \tag{22}$$

where $\vec{n}_{oi}$ is the vector area of the dual face crossing edge $\vec{e}_{oi}$, and the subscript ''Roe'' denotes Roe-averaged variables. The flux differences ΔF^- and ΔF^+ are given as

$$\Delta F^+(Q_{Roe}^m, \vec{n}_{oi}) = \tfrac{1}{2}(R_{Roe}^m(\Lambda + |\Lambda|)_{Roe} L_{Roe}^m)(Q_m^+ - Q_m^-) \tag{23}$$

$$\Delta F^-(Q_{Roe}^m, \vec{n}_{oi}) = \tfrac{1}{2}(R_{Roe}^m(\Lambda - |\Lambda|)_{Roe} L_{Roe}^m)(Q_m^+ - Q_m^-) \tag{24}$$

Here, R and L are, respectively, the right and left eigenvector matrices, while L is the diagonal eigenvalue matrix. The Roe averaged velocities and scalars are defined as

$$y_{Roe} = \frac{y^+\sqrt{\rho^+} + y^-\sqrt{\rho^-}}{\sqrt{\rho^+} + \sqrt{\rho^-}}, \quad \{y \in (u, v, w, k, \varepsilon)\} \tag{25}$$

while, the volume fraction, ϕ_g, is defined by doing a simple arithmetic average:

$$\phi_{g,Roe} = \tfrac{1}{2}(\phi_g^+ + \phi_g^-) \tag{26}$$

This average value of the ϕ_g is used to define the speed of sound of the mixture at the dual face.

For efficient computation of large 3D problems a parallel framework for distributed memory systems has been implemented, along with a time-marching implicit solution procedure. The sparse implicit matrix is derived by doing a Euler explicit linearization of the first-order flux, and a variety of iterative sparse matrix solvers, e.g., GMRES, Gauss-Seidel procedure, are available in the code (see Hosangadi et al. [9] for details). The parallel framework is implemented by partitioning the grid into subdomains with each subdomain residing on an independent processor. The message passing between processors has been implemented using MPI to provide portability across platforms.

Results and Discussion

The multi-phase system described in the previous sections has been applied extensively to both cavitating and non-cavitating problems. Since the single-phase incompressible formulation is a subset of the more general multi-phase system, the code was first validated for standard incompressible test cases in the literature (see Ahuja et al. [7], for results). In the present section, we will focus on the following sheet-cavitation problems which have been studied extensively in the literature: 1) cylindrical headform; and 2) the NACA 66 hydrofoil.

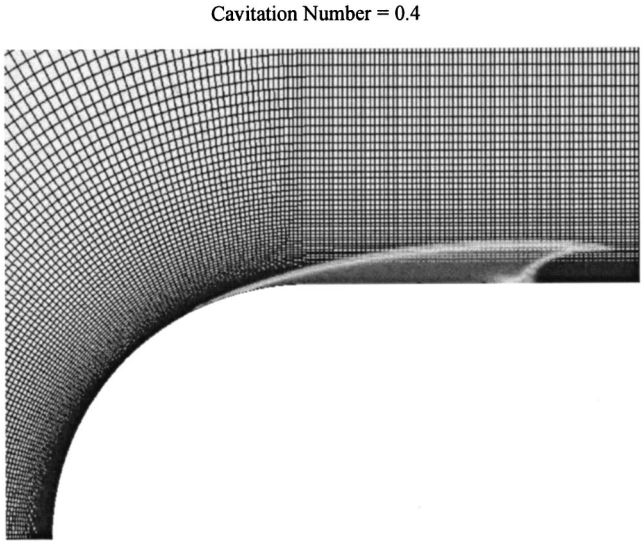

Fig. 2 Resolution of the cavitation zone interface on the numerical grid

All the simulations presented here have been computed as steady-state calculations, using the two-equation (k-e) turbulence model with near-wall damping described earlier. The liquid to gas density ratio was specified to be 100. The baseline forward and backward cavitation rate terms τ_f, τ_b, are specified to be 0.001 s unless otherwise specified. Furthermore, the calculations were performed on parallel distributed memory platforms using 8 processors. We note that although the flowfields simulated here are essentially two-dimensional in character, the CRUNCH code is three-dimensional; the simulations performed here were three-dimensional with minimal resolution in the z coordinate. Hence, we do not anticipate any serious issues in computing a truly three-dimensional flowfield apart from the increased numerical cost.

Cylindrical Headform Simulations. Simulations of the Rouse and McNown [14] experiments for water flowing over a hemisphere/cylinder geometry are presented. The Reynolds number per inch for this configuration is 1.36×10^5. A hexahedral grid with dimensions of 221×113 was used for all the cavitation numbers reported. The grid was clustered both radially near the surface as well as axially at the bend where sphere meets with the cylinder. Simulations for three cavitation numbers of 0.4, 0.3, and 0.2 are presented. The grid is best suited for the highest cavitation number of 0.4 since the cavity zone is completely contained within the zone of high clustering. Hence the results for the 0.4 case will be analyzed in-depth to study the flow features in the cavity closure region, as well as other sensitivity studies such as the effect of the rate constant.

The cavitation zone for a cavitation number of 0.4 is shown in Fig. 2 for the baseline source term rates given earlier. We note that the gas/liquid interface is sharp and captured within a couple of cells is most of the flow except at the tip on the top corner of the back end where a marginal ''pulling'' or extension of the cavitation zone is observed. This is attributed to the strong shear at this location as the flow turns around the cavitation zone to enclose it. The details of the recirculation zone in the cavitation closure region are illustrated in Fig. 3 by plotting the streamlines of the flow. A sharp recirculation zone originating from the tip of the cavitation zone is observed where a re-entrant jet is observed to transport fluid back into the cavity. As we shall see from the surface pressure distribution, the re-entrant jet generates a local pressure peak at the rear of the cavity thereby keeping this cavity shape stable.

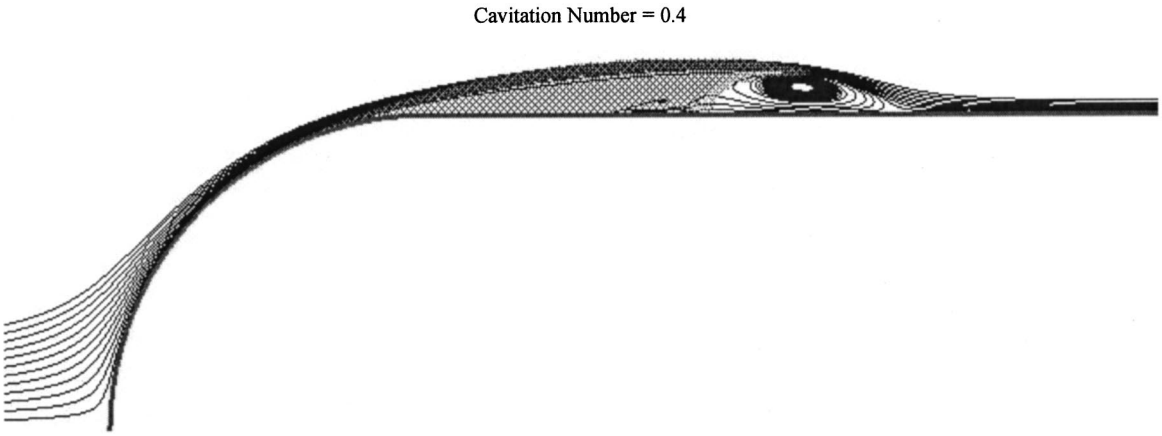

Fig. 3 Flow streamlines depicting recirculation zone/re-entrant jet in the cavity closure region

The turbulent viscosity levels (nondimensionalized by the laminar viscosity) generated in the flowfield are shown in Figs. 4(*a*) and 4(*b*). In Fig. 4(*a*) we plot the overall global characteristics of the turbulent wake while Fig. 4(*b*) gives a close-up view of the cavitation zone itself. From Fig. 4(*a*) we observe the incoming boundary layer lifting off as the flow turns and jumps over the cavitation zone. The cavitation zone itself is observed to be very ''quiet'' with turbulence present mainly in the interface region and the shear layer above it. The plot depicts increasing turbulence intensity levels near the cavity closure/re-entrant jet region, and a fully turbulent wake ensues. We note that since the calculation was performed with a steady RANS turbulence model, the wake simulated corresponds to the time-averaged solution which reproduces the mean mixing rate. If the calculation were performed with an unsteady LES model, an unsteady wake would result with vortices being shed off the cavity tip.

The characteristics of the flowfield at cavitation numbers 0f 0.4, 0.3, and 0.2 are compared in Fig. 5 by plotting both the cavitation zone as well as the surface pressure distribution. Overall the surface pressure profiles compare very well with experimental data. In particular, the cavity closure region appears to be captured well; the location, the pressure gradient, and the overpressurization magnitude in the wake are very close to the data for the two higher cavitation numbers of 0.4 and 0.3. For the 0.2 case, the cavity zone is very large and extends into the region where the grid is not as finely clustered, and we attribute the slight under

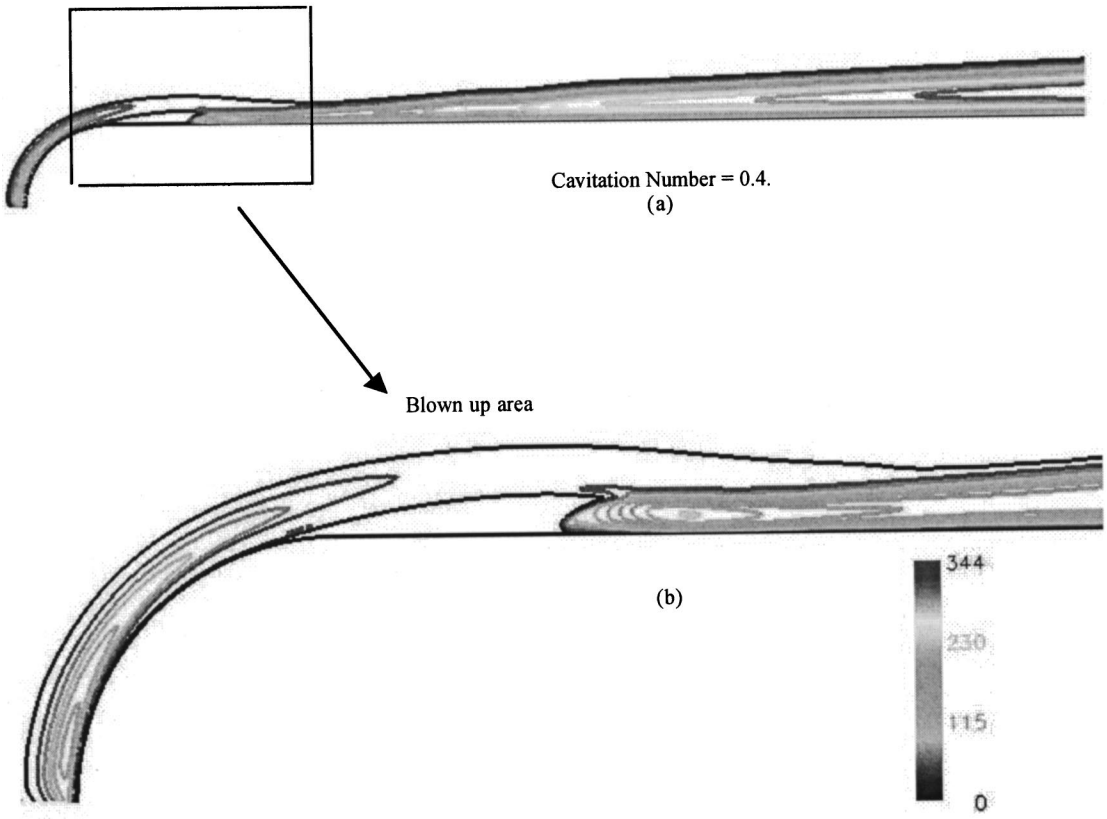

Fig. 4 Turbulent viscosities (μ_t/μ_L) contours in the headform cavity flowfield

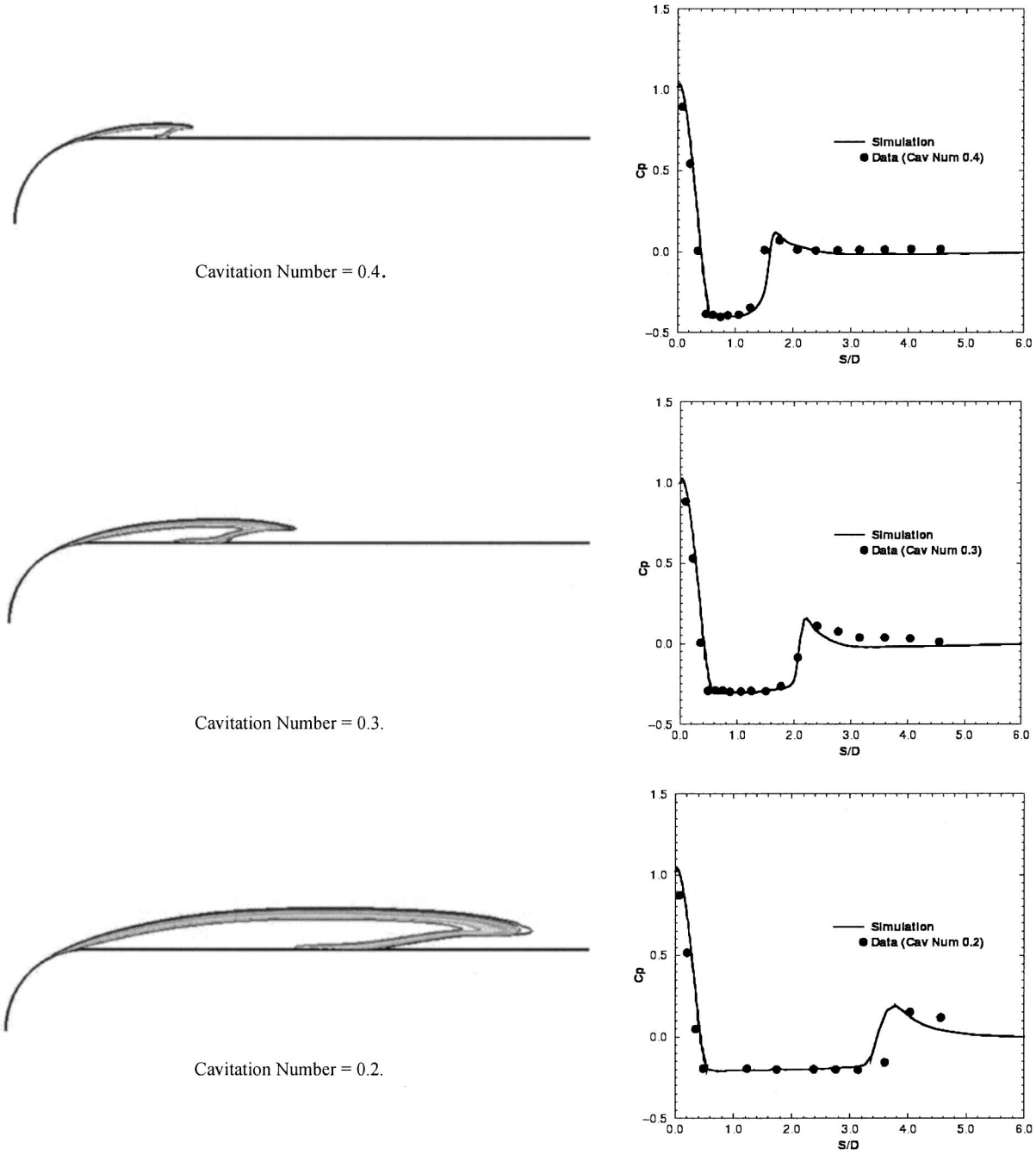

Fig. 5 Cavitation zone and surface pressure profiles at various cavitation numbers for hemisphere/cylinder headform

prediction of the cavity length to grid quality. The coarser grid in the interface region is also reflected in the broader interface zone. It should be noted that all three cases were computed with the baseline source term rates.

To evaluate the impact of the source term rates τ_f and τ_b, we computed the 0.4 cavitation case using the following three different rates: 1) the baseline rate ($\tau_f = 0.001$ s, $\tau_b = 0.001$ s); 2) a faster rate (baseline$\times 10$); and, 3) a slower rate (baseline$\times 0.1$). The surface pressure comparisons are shown in Fig. 6 for the three different rates. The results for the baseline rate and the faster rate are very close; however, as expected, the faster rate gives slightly better results in the wake with the cavity closure being sharper. The slower rate (baseline$\times 0.1$) gives a more diffused cavity particularly in the rear with the time scale for the nonequilibrium source term coupling with the convective time scale. As the cavity closure region gets more diffuse, the strength of the re-entrant jet weakens, and consequently, the pressure does not exhibit the pattern of over-pressurization and relaxation which is observed in the data as well as the other two faster rate cases. We note that the baseline rates have been used to compute all the results reported here including the hydrofoil case. At least for steady-state problems, the nonequilibrium source terms perform adequately and the precise value of the rate appears to be problem/grid independent as long as the time scale is sufficiently fast enough (as defined by our baseline rate) in comparison to the characteristic convective time scales.

NACA 66 Hydrofoil Simulations. In this section, we present results for sheet cavitation on a NACA 66 hydrofoil (Shen and Dimotakis [15]). The freestream flow is at a 4 degree angle-of-

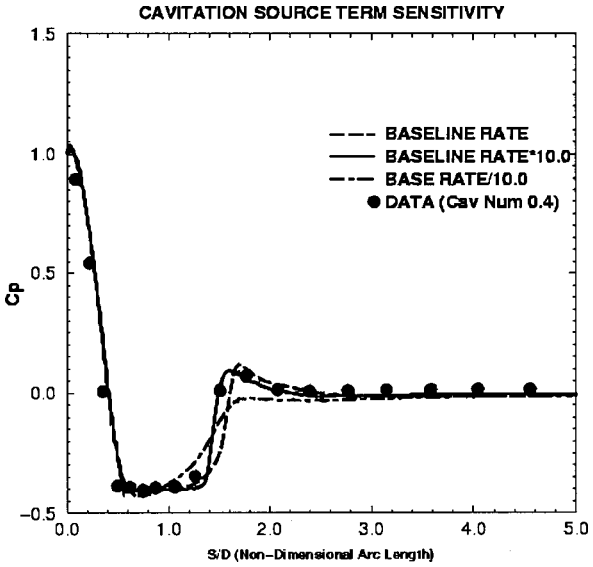

Fig. 6 Sensitivity of cavitation solution to the cavitation source term rate

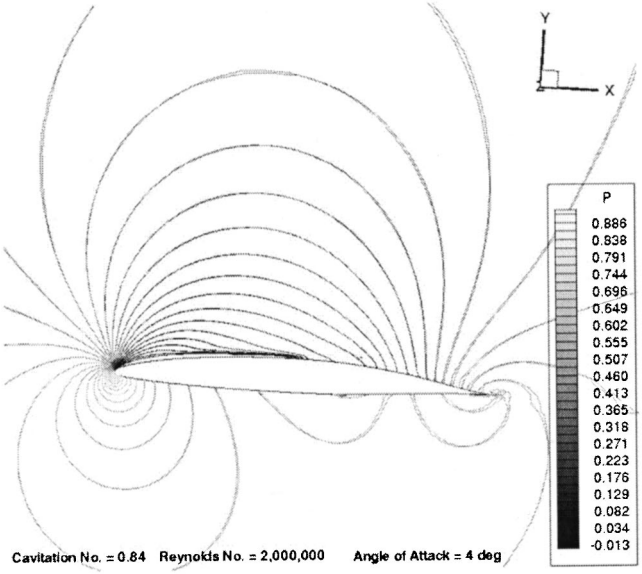

Fig. 8 A representative pressure distribution on the NACA 66 hydrofoil at 4 degrees angle of attack and cavitation number of 0.84

attack, with a Reynolds number of 2×10^6 based on chord length. The hybrid grid used for the calculations is shown in Fig. 7; it has a combination of approximately 200,000 tetrahedral and prismatic cells with clustering around the surface of the hydrofoil. Calculations for two different cavitation numbers of 0.84 and 0.91 are discussed in the following paragraphs. Note that the calculations shown here were computed with a wall function procedure.

The pressure contours for the flowfield at a cavitation number of 0.84 are plotted in Fig. 8. We observe that the pressure contours cluster around the cavitation boundary where the density gradient is very large and the flow turns around the cavitation bubble. The gas void fraction contours at the two cavitation numbers are shown in Fig. 9. At the lower cavitation number of 0.84, the cavity extends up to 50 percent of chord. As the cavitation number increases the gas bubble region decreases in length and comes closer to the surface; the void fraction contours at a cavitation number of 0.91 (Fig. 9(*b*)), indicate that the bubble extends to only 30 percent of chord. The thin confinement region of the gas bubble highlights the potential for using local grid adaption within our unstructured framework.

The surface pressure profiles at the two cavitation numbers are plotted in Figs. 10(*a*) and 10(*b*) for comparison the experimental

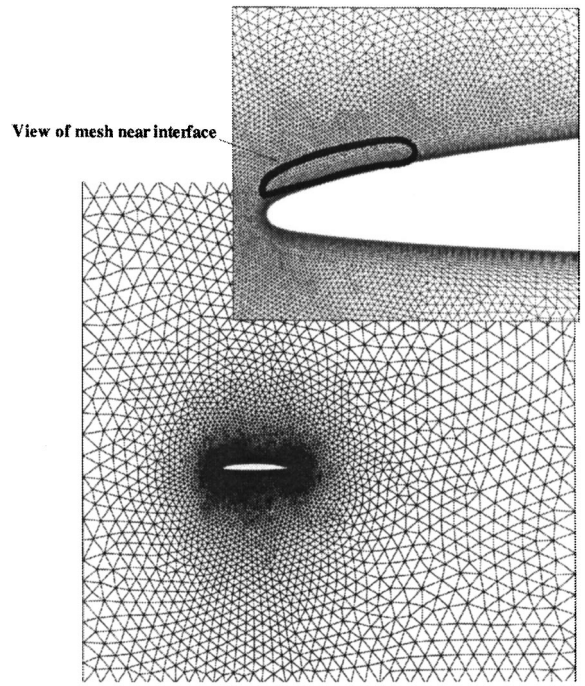

Fig. 7 The prismatic/tetrahedral grid used to capture cavitation on the NACA 66 modified hydrofoil

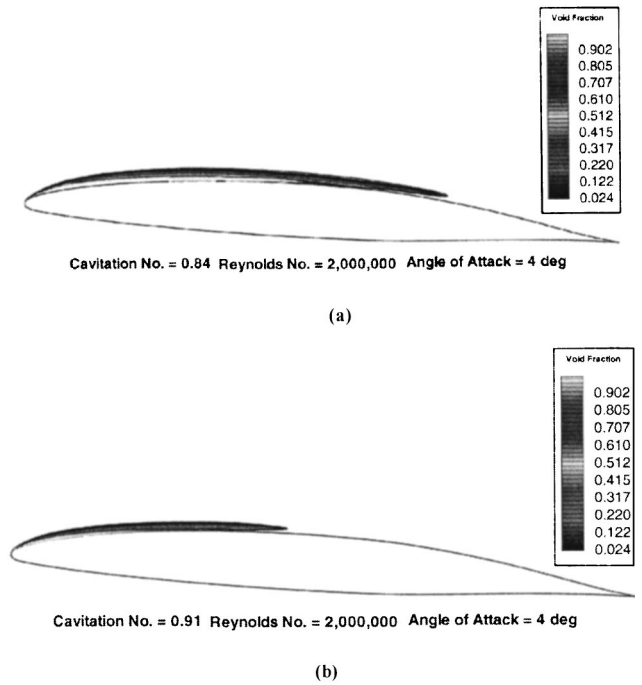

Fig. 9 Cavitation bubbles indicated by void fraction contours on the NACA 66 modified hydrofoil at cavitation numbers of (a) 0.91 and (b) 0.84

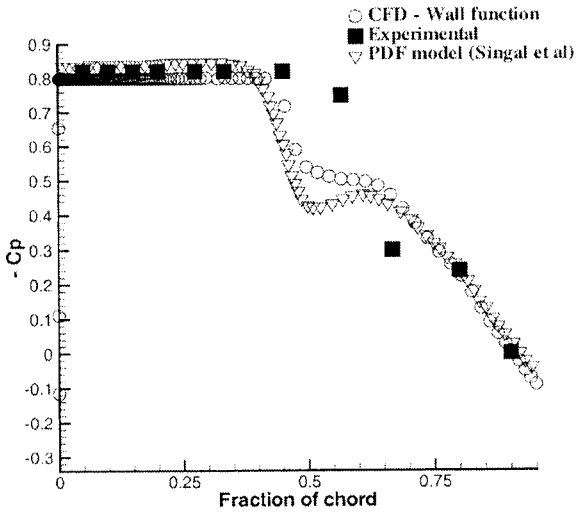

(a) Cavitation number = 0.89.

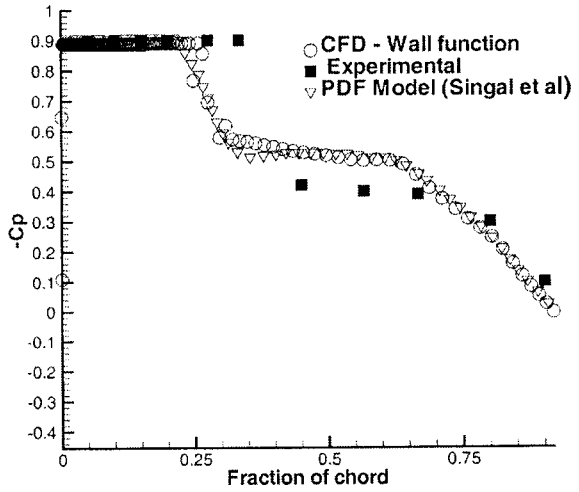

(b) Cavitation number = 0.91.

Fig. 10 Surface pressure distribution on the NACA 66 hydrofoil using wall-function procedure

data points as well as results from the numerical study by Singal et al. [16] are also shown. We note that the simulation by Singal et al. [16] was computed on a structured hexahedral grid using a user specified equation of state, and had a pdf based model for cavitation. We make the following observations; 1) Both the numerical simulations are very similar to each other despite the differences in the numerics and the formulation. The good comparison between the two numerical results is an important validation of the more fundamental formulation presented here which did not require a user specified closure model for the equation of state; 2) While the comparisons with the experimental data are reasonably good, the numerical results underpredict the length of the cavity and overpredict the aft recovery pressure. A preliminary investigation indicates that this may be related to a combination of local grid resolution in the interface region, as well as the details of the near wall turbulence model. However, for the purposes of illustrating the applicability of the new formulation the current results were deemed to be acceptable.

Conclusions

A multi-phase model for low speed gas-liquid mixtures has been developed by reducing the compressible system of equations to an acoustically accurate form that performs efficiently in the incompressible regime. In particular, the equation system does not require ad-hoc density-pressure relations to close the system and yields the correct acoustic speed as a function of local mixture composition. For efficient steady-state solutions, the physical mixture acoustic speed is preconditioned to obtain good convergence. The solution procedure has been implemented within a hybrid, multi-element unstructured framework which operates in a parallel, domain-decomposed environment for distributed memory systems.

Detailed results are presented for steady-state sheet cavitation in an hemisphere/cylinder geometry as well as a NACA 66 hydrofoil at various cavitation numbers. Good comparison is obtained with experimental data, and in particular the details of the cavity closure, and the re-entrant jet are captured well in the simulation. Examination of the turbulence characteristics indicates that turbulent kinetic energy associated with the upstream boundary layer jumps over the cavity, and the interior of the cavity itself is nearly laminar. However, the recirculation zone in the re-entrant jet region generates a fully turbulent wake which stabilizes the cavity zone and generates a pressure pattern of over-pressurization and gradual relaxation in the wake. Sensitivity of the cavitation zone to the finite rate source terms was examined. The solution was found to be relatively insensitive to the source term rate as long as the rate was high enough. As the source term rate dropped by an order of magnitude, coupling between the convective time scale and the source term was observed leading to a more diffuse cavity in the closure region and poorer pressure predictions. Clearly, for unsteady detached cavitation problems, the modeling of the source term needs to be examined carefully and this is an area of ongoing work.

References

[1] Kubota, A., Kato, H., and Yamaguchi, H., 1992, ''Cavity Flow Predictions Based on the Euler Equations,'' J. Fluid Mech., **240**, pp. 59–96.
[2] Chen, Y., and Heister, S. D., 1996, ''Modeling Hydrodynamic Nonequilibrium in Cavitating Flows,'' ASME J. Fluids Eng., **118**, pp. 172–178.
[3] Delaunay, Y., and Kueny, J. L., 1990, ''Cavity Flow Predictions based on the Euler Equations,'' *ASME Cavitation and Multi-Phase Flow Forum*, Vol. 109, pp. 153–158.
[4] Janssens, M. E., Hulshoff, S. J., and Hoeijmakers, H. W. M., 1997, ''Calculation of Unsteady Attached Cavitation,'' AIAA-97-1936, 13th AIAA CFD Conferences, Snowmass, CO, June 29–July 2.
[5] Merkle, C. L., Feng, J. Z. and Buelow, P. E. O., 1998, ''Computational Modeling of the Dynamics of Sheet Cavitation,'' *Proceedings of the 3rd International Symposium on Cavitation*, Grenoble.
[6] Kunz, R. F., et al., 1999, ''A Preconditioned Navier-Stokes Method for Two-Phase Flows with Application to Cavitation Prediction,'' 14th AIAA CFD Conference, Norfolk, VA, June 28–July 1.
[7] Ahuja, V., Hosangadi, A., Ungewitter, R., and Dash, S. M., 1999, ''A Hybrid Unstructured Mesh Solver for Multi-Fluid Mixtures,'' AIAA-99-3330, 14th AIAA CFD Conference, Norfolk, VA, June 28–July 1.
[8] Hosangadi, A., Sinha, N., and Dash, S. M., 1997, ''A Unified Hyperbolic Interface Capturing Scheme for Gas/Liquid Flows,'' AIAA-97-2081, 13th AIAA CFD Conferences, Snowmass, CO, June 29–July 2.
[9] Hosangadi, A., Lee, R. A., Cavallo, P. A., Sinha, N., and York, B. J., 1998, ''Hybrid, Viscous, Unstructured Mesh Solver for Propulsive Applications,'' AIAA-98-3153, AIAA 34th JPC, Cleveland, OH, July 13–15.
[10] So, R. M. C., Sarkar, A., Gerodimos, G., and Zhang, J., 1997, ''A Dissipation Rate Equation for Low Reynolds Number and Near-Wall Technique,'' Theor. Comput. Fluid Dyn., **9**, pp. 47–63.
[11] Hosangadi, A., Lee, R. A., York, B. J., Sinha, N., and Dash, S. M., 1996, ''Upwind Unstructured Scheme for Three-Dimensional Combusting Flows,'' J. Propul. Power, **12**, No. 3, May–June, pp. 494–503.
[12] Barth, T. J., 1991, ''A 3-D Upwind Euler Solver for Unstructured Meshes,'' AIAA-91-1548, 10th AIAA CFD Conference, Honolulu, HI, June.
[13] Barth, T. J., and Linton, S. W., 1995, ''An Unstructured Mesh Newton Solu-

tion for Compressible Fluid Flow and Its Parallel Implementation,'' AIAA-95-0221, 33th AIAA Aerospace Sciences Meeting at Reno, NV, Jan 9–14.
[14] Rouse, H., and McNown, J. S., 1948, ''Cavitation and Pressure Distribution: Head Forms at a Zero Angle of Yaw,'' Technical Report: State University of Iowa Engineering Bulletin No. 32.
[15] Shen, Y. T., and Dimotakis, P., 1989, ''The Influence of Surface Cavitation on Hydrodynamic Forces,'' 22nd American Towing Tank Conference, St Johns, NF, August 8–11.
[16] Singal, A. K., Vaidya, N., and Leonard, A. D., 1997, ''Multi-Dimensional Simulation of Cavitating Flows Using a PDF Model for Phase Change,'' FEDSM97-3272, 1997 ASME Fluids Engineering Division Summer Meeting, Vancouver, British Columbia, Canada, June 22–26.

Mixing Models for Large-Eddy Simulation of Nonpremixed Turbulent Combustion

S. M. deBruynKops
Lecturer

J. J. Riley
Professor

Department of Mechanical Engineering,
University of Washington,
Box 352600,
Seattle, WA 98195-2600

The application of mixture fraction based models to large-eddy simulations (LES) of nonpremixed turbulent combustion requires information about mixing at length scales not resolved on the LES grid. For instance, the large-eddy laminar flamelet model (LELFM) takes the subgrid-scale variance and the filtered dissipation rate of the mixture fraction as inputs. Since chemical reaction rates in nonpremixed turbulence are largely governed by the mixing rate, accurate mixing models are required if mixture fraction methods are to be successfully used to predict species concentrations in large-eddy simulations. In this paper, several models for the SGS scalar variance and the filtered scalar dissipation rate are systematically evaluated a priori using benchmark data from a DNS in homogeneous, isotropic, isothermal turbulence. The mixing models are also evaluated a posteriori by applying them to actual LES data of the same flow. Predictions from the models that depend on an assumed form for the scalar energy spectrum are very good for the flow considered, and are better than those from models that rely on other assumptions.
[DOI: 10.1115/1.1366679]

1 Introduction

In large-eddy simulations of nonreacting flows, the models for the unresolved terms in the momentum and conserved scalar equations rely on the fact that most of the kinetic and scalar energy resides in the largest scales. It is sometimes reasoned that a subgrid model need only extract the correct amount of energy from the large scales to be adequate for many applications. The same argument cannot be applied to the modeling of reacting scalars because, for moderate to high reaction rates, the scale of the entire flame lies below the grid scale. Hence, the chemistry model must be capable of approximating the physical interaction between the species within each LES grid cell. One strategy for accounting for subgrid-scale (SGS) mixing is to employ an assumed form for the probability density function (PDF) of a conserved scalar within a grid volume [1]. Gao and O'Brien [2] refer to this type of PDF as a large-eddy probability density function (LEPDF) while Colucci et al. [3] refer to it as the filtered density function. Bilger [4] and Lentini [5] found that errors in assumed PDFs are greatly reduced upon integration, a common operation which is required in order to obtain, e.g., average concentrations. Frankel et al. [6] and Cook and Riley [7] demonstrated the assumed LEPDF approach to be both practical and accurate for LES with equilibrium chemistry.

To treat nonequilibrium chemistry, information in addition to the amount of SGS mixing is required. One approach is to employ a joint PDF for the SGS species mass fractions [6]. Specification of the joint LEPDF requires modeling of the subgrid-scale species covariance, a quantity that is very difficult to obtain accurately. An alternative method of accounting for non-equilibrium chemistry is to invoke the quasi-steady version of the flamelet approximation of Peters [8], Cook, Riley, Kosály, and de Bruyn Kops [9–12] have used flamelet theory, in conjunction with an assumed LEPDF, to derive a model for predicting the filtered species concentrations in LESs. The model, termed the large-eddy laminar flamelet model (LELFM), requires information about the amount and the rate of SGS mixing in the form of the subgrid-scale scalar variance and the filtered scalar dissipation rate. Those four papers show LELFM to be promising, but do not adequately address the problem of modeling the SGS mixing.

The purpose of this paper is to systematically evaluate several SGS mixing models required for mixture fraction based LES models. The models are tested *a priori* and *a posteriori* using data from high resolution direct numerical simulations and lower resolution large-eddy simulations of the classic experiment in decaying, homogeneous, isotropic, isothermal turbulence of Comte-Bellot and Corrsin [13]. Although the theory behind the mixing models is more general, this canonical flow is studied in order to identify the characteristics of the models, to eliminate questions about the accuracy of the simulation, and thus the mixing process, and because a mixing model should presumably be accurate for the simpler case if it is to be reliably accurate for more complex flows.

2 LES Models

Large-eddy simulation involves the numerical solution of the equations for momentum and scalar transport to which a filter of characteristic width Δ has been applied to remove length scales too small to be resolved on the numerical grid. The filtering operation, denoted by an overbar and defined as the convolution integral of the field with a filter kernel, results in flux terms which must be modeled. In this work, the Smagorinsky [14] model is used to relate each subgrid-scale flux to the corresponding gradient of the resolved-scale velocity component (or scalar) via a dynamically computed SGS viscosity (diffusivity). The dynamic aspect was first proposed by Germano et al. [15], with further development by, e.g., Germano [16], Lilly [17], Carati et al. [18] and Piomelli and Liu [19]. The resulting LES transport equations are:

$$\frac{\partial \overline{u}_i}{\partial t} + \frac{\partial \overline{u}_i \overline{u}_j}{\partial x_j} = -\frac{\partial \overline{p}}{\partial x_i} + 2\frac{\partial}{\partial x_j}[(\nu+\nu_T)\overline{S}_{ij}], \tag{1}$$

$$\frac{\partial \overline{\xi}}{\partial t} + \overline{u}_j \frac{\partial \overline{\xi}}{\partial x_j} = \frac{\partial}{\partial x_j}\left[(D+D_T)\frac{\partial \overline{\xi}}{\partial x_j}\right], \tag{2}$$

where $\overline{S}_{ij}$ is the resolved strain-rate tensor, ν and D are the kinematic viscosity and molecular diffusivity, and ν_T and D_T are their SGS counterparts defined in terms of the magnitude of the filtered

Contributed by the Fluids Engineering Division for publication in the JOURNAL OF FLUIDS ENGINEERING. Manuscript received by the Fluids Engineering Division September 13, 1999; revised manuscript received February 20, 2000. Associate Editor: P. E. Raad.

strain rate tensor as $\nu_T = C\Delta^2|\overline{S}|$ and $D_T = C_\xi \Delta^2 |\overline{S}|$. Both the velocity field and the scalar field, ξ, are statistically homogeneous and isotropic, so that the coefficients C and C_ξ can be considered as constant in space but as functions of time. The scalar, ξ, can be any conserved scalar, but is taken to be the mixture fraction as defined by Bilger [4], with the assumption of equal diffusivities of all species.

2.1 Subgrid-scale Chemistry Model. Our particular motivation for the current research is to develop mixing models for use with the LELFM [9–12], which we use here as a specific example of how SGS mixing models can incorporated into LES chemistry models. While the LELFM is only one approach to modeling species interactions in an LES, mixture fraction based methods in general require information about the amount of mixing at the subgrid scale if equilibrium chemistry is assumed, and information about the amount and rate of mixing for non-equilibrium analysis. For the LELFM and other mixture fraction based models, the mixing statistics required are the filtered mixture fraction, $\overline{\xi}$, the SGS scalar variance, ξ_v^2, and the filtered scalar dissipation rate, $\overline{\chi} = 2D\overline{(\partial\xi/\partial x_i)^2}$. Here, $\xi_v^2 = \overline{\xi^2} - \overline{\xi}^2$, which corresponds to the variance of the filtered probability density function as defined by Gao and O'Brien [2]; an alternative definition $(\xi - \overline{\xi})^2$ is incorrect in general since it cannot correspond to any one point PDF [7,20]. The filtered mixture fraction is computed directly in an LES from (2). Models for ξ_v^2 and $\overline{\chi}$ are discussed in the following sections.

2.1.1 Subgrid-Scale Variance. The SGS variance can be modeled directly or it can be computed from $\overline{\xi}^2$ and $\overline{\xi^2}$, the latter of which must be modeled. Schmidt and Schumann [21] compute $\overline{\xi^2}$ by integrating its governing equation. One difficulty with this method is in developing the initial $\overline{\xi^2}$ field. Another is that it requires an additional model to account for the SGS flux of the scalar variance.

Two models have been proposed for directly modeling ξ_v^2; one relates it to the magnitude of the resolved scale gradient [22,23], the other relates it to a test scale variance [7]. The first is denoted ξ_{m1}^2 and defined $\xi_{m1}^2 \equiv \gamma\Delta^2|\nabla\overline{\xi}|^2$. The derivation starts by defining a test-scale filter of characteristic width $\hat{\Delta}$ and denoted by $(\hat{\ })$, where $\hat{\Delta} > \Delta$, and assuming that the scalar variance below the test scale can be modeled in a manner analogous to ξ_{m1}^2. Then

$$\widehat{\overline{\xi}^2} - \hat{\overline{\xi}}^2 = \gamma\hat{\Delta}^2|\nabla\hat{\overline{\xi}}|^2 - \widehat{\gamma\Delta^2|\nabla\overline{\xi}|^2}, \tag{3}$$

and

$$\gamma = \frac{\widehat{\overline{\xi}^2} - \hat{\overline{\xi}}^2}{\hat{\Delta}^2|\nabla\hat{\overline{\xi}}|^2 - \Delta^2|\hat{\nabla}\overline{\xi}|^2}, \tag{4}$$

assuming that γ varies slowly enough in space so that it can be taken outside the test filter. Unlike the formulations for C and C_ξ, (4) does not involve averages in the homogeneous directions, so γ is a function of space.

In the second model for ξ_v^2, denoted ξ_{m2}^2, the subgrid-scale variance is estimated by assuming similarity between the subgrid-scales and the smallest resolved scales. A test filter-scale variance is defined $Z_v^2 \equiv \widehat{\overline{\xi}^2} - \hat{\overline{\xi}}^2$, which is simply the variance of $\overline{\xi}$ within subvolumes defined by the test filter width. The model assumes scale similarity between Z_v^2 and ξ_v^2, i.e.,

$$\xi_v^2 \approx \xi_{m2}^2 \equiv c_{\xi 2}(\widehat{\overline{\xi}^2} - \hat{\overline{\xi}}^2). \tag{5}$$

The quantity $c_{\xi 2}$ is computed by assuming a form for the SGS scalar energy spectrum and adding it to the resolved-scale spectrum (from the LES) to form the complete scalar energy spectrum, $E_\xi(k)$. Here k is the magnitude of the three-dimensional wave number vector. By assuming homogeneous, isotropic turbulence, Cook [24] shows that

$$c_{\xi 2} = \frac{\int_0^\infty [1 - \tilde{g}^2(k;\Delta)]E(k)dk}{\int_0^\infty [1 - \tilde{h}^2(k;\hat{\Delta})][1 - \tilde{g}^2(k;\Delta)]E(k)dk}, \tag{6}$$

where $\tilde{g}$ and $\tilde{h}$ are the Fourier transformed grid and test filters, respectively. With $c_{\xi 2}$ computed from (6), the average SGS variance from (5) will exactly equal the average SGS variance implicit in $E_\xi(k)$ if the turbulence is homogeneous and isotropic [24].

In a high Reynolds number LES, the inertial range will extend to wavenumbers which make an insignificant contribution to the SGS variance. If the grid filter is in the inertial range, it is reasonable to assume $E_\xi(k) \propto k^{-5/3}$ for all SGS k, and to ignore details of the spectrum in the dissipation range. In moderate Reynolds number flows, such as that presented in this work, the dissipation range accounts for a significant amount of the SGS variance and cannot be ignored. Instead, a form for the high wavenumber spectrum derived by Corrsin [25] and Pao [26] is used:

$$E_\xi(k) = Ak^\alpha \exp\left(-\frac{3}{2}nD\varepsilon_T^{-1/3}k^{4/3}\right). \tag{7}$$

In model ξ_{m2}^2, $\alpha = -5/3$ and $n = 0.59$, which are the values used by Pao [26]. The constant of proportionality in (7) is determined by matching $E_\xi(k)$ to the actual LES spectrum near the highest resolved wave number. The kinetic energy flux supplied by the large eddies, ε_T, can be estimated from the LES by assuming that it is equal to the energy removed from the resolved scales by the LES SGS model. Pao points out that the ε_T used for the theoretical deduction of (7) (which assumes infinite Reynolds number) will always be greater than that measured in a laboratory experiment; presumably, this is also the case for the LES of a flow with finite Reynolds number. Therefore, (7) is expected to underestimate the true SGS spectrum. While the effect that the error in E_ξ will have on ξ_{m2}^2 is not clear due to the application of the grid and test filters in (5), it is expected that $\langle\xi_{m2}^2\rangle \to \langle\xi_v^2\rangle$ as the Reynolds number increases, where $\langle\ \rangle$ denotes a spatial average.

Two additional models for ξ_v^2 are defined which improve on ξ_{m1}^2 and ξ_{m2}^2. The first, ξ_{m3}^2, is identical to ξ_{m2}^2 except that α and n are chosen so that the assumed spectrum more closely matches the spectrum of the flow being studied. This is important for moderate Reynolds number flows in which no true inertial range exists. Formally, $\xi_{m3}^2 \equiv c_{\xi 3}(\widehat{\overline{\xi}^2} - \hat{\overline{\xi}}^2)$. The second is a hybrid of models ξ_{m1}^2 and ξ_{m3}^2: $\xi_{m4}^2 \equiv c_{\xi 4}\Delta^2|\nabla\overline{\xi}|^2$. Analogous to $c_{\xi 3}$, $c_{\xi 4}$ is computed so that $\langle\xi_{m4}^2\rangle$ equals the average SGS variance computed from the assumed spectrum. Values of α and n are tailored for the flow being studied.

It is worthwhile to note that an assumed form for the three-dimensional scalar energy spectrum is utilized in this work because the scalar field in the numerical simulations is homogeneous and isotropic. The assumed spectrum technique works equally well when the scalar field is not isotropic but is homogeneous in at least one direction, so that a form for the one-dimensional energy spectrum can be assumed. For these results, see [27]. The assumed spectrum methods may also work well when the scalar field is locally isotropic on the LES grid.

2.1.2 Filtered Dissipation Rate. The filtered dissipation rate, $\overline{\chi}$, can be decomposed into three terms which represent (1) the cointeractions between the resolved scales, (2) the cointeractions between the unresolved scales, and (3) the interactions between the resolved and unresolved scales. The first of these can be computed directly from the resolved scales of an LES. Girimaji and Zhou [28] develop models for the second and third terms, and note that the backscatter (third) term must be accounted for if $\overline{\chi}$ is to be used to close the transport equation for the filtered scalar

energy. Here, two somewhat simpler classes of models are developed. In the first, denoted $\overline{\chi}_{m1}$, $\overline{\xi}$ is related to the resolved scale dissipation rate via the total diffusivity, $D+D_T$. In the second ($\overline{\chi}_{m2}$,$\overline{\chi}_{m3}$), scale similarity arguments are used to estimate $\overline{\chi}$.

To develop the first model, consider the equation for $\overline{\xi}$-energy obtained by multiplying (2) by $\overline{\xi}$ and simplifying. The resulting term for the dissipation rate of $\overline{\xi}^2$ due to molecular effects and to transfer of $\overline{\xi}$ energy to the subgrid-scales is $2(D+D_T)\times(\partial\overline{\xi}/\partial x_j)^2$. At the larger scales, $\overline{\xi^2}$ is approximately equal to $\overline{\xi}^2$, the difference between the two being due to the filtering of ξ at the smaller scales. This implies, in particular, that the transfer rate of both quantities to the subgrid scales is nearly identical. Assuming in addition that the transfer rate of ξ to the subgrid scales is equal to its dissipation rate at those scales leads to a model for $\overline{\chi}$:

$$\overline{\chi}_{m1} \equiv 2(D+D_T)\,\frac{\overline{\frac{\partial\xi}{\partial x_i}\frac{\partial\xi}{\partial x_i}}}{\frac{\partial\overline{\xi}}{\partial x_i}\frac{\partial\overline{\xi}}{\partial x_i}}. \tag{8}$$

This is similar to a term in a model for $\overline{\chi}$ proposed by Girimaji and Zhou [28].

The second model for $\overline{\chi}$ is defined as

$$\overline{\chi}_{m2} \equiv c_{\chi 2} D\,\frac{\overline{\frac{\partial\xi}{\partial x_i}\frac{\partial\xi}{\partial x_i}}}{\frac{\partial\overline{\xi}}{\partial x_i}\frac{\partial\overline{\xi}}{\partial x_i}}, \tag{9}$$

where the constant $c_{\chi 2}$ is determined by assuming a form for the high wavenumber portion of the ξ energy spectrum, e.g., (7). The derivation is similar to that of $c_{\xi 2}$. In essence, $c_{\chi 2}$ is set so that $\langle\overline{\chi}_{m2}\rangle$ is equal to the dissipation rate computed using the SGS portion of the assumed spectrum. It was argued in the previous section that the assumed SGS $E_\xi(k)$ from (7) will always underestimate the true SGS spectrum because (7) was deduced for the case of infinite Reynolds number. While the effect of the error in $E_\xi(k)$ on ξ^2_{m2} is not obvious, it is clear that underpredicting $E_\xi(k)$ at high wavenumbers will result in $\langle\overline{\chi}_{m2}\rangle<\langle\overline{\chi}\rangle$. It is expected that $\langle\overline{\chi}_{m2}\rangle\approx\langle\overline{\chi}\rangle$ for large enough Reynolds number. Analogous to ξ^2_{m2} is a third model for $\overline{\chi}$, denoted $\overline{\chi}_{m3}$, in which the coefficient $c_{\chi 2}$ is replaced by $c_{\chi 3}$ computed by assuming a form for $E_\xi(k)$ which is tailored to the flow being studied.

3 Numerical Simulations

Data from DNS are used for *a priori* testing of the LELFM and the submodels. The velocity field simulated is that of the laboratory experiment of Comte-Bellot and Corrsin [13] in which nearly isotropic, incompressible turbulence decays downstream of a grid of spacing M oriented normal to a uniform, steady flow. Statistical data were collected in the laboratory at downstream locations $x/M=42$, 98, and 171. The Reynolds number at the first station, based on the Taylor length scale and the rms velocity, is 71.6. The DNS are performed with a pseudo-spectral code using a 512^3-point periodic domain considered to be moving with the mean flow. Taylor's hypothesis is invoked to relate simulated time to laboratory coordinates. The DNS velocity field is initialized to match the laboratory kinetic energy spectrum at $x/M=42$. In the computer code, Fourier pseudo-spectral methods are used to approximate spatial derivatives, and a second-order Adams-Bashforth scheme with pressure-projection is used for time-stepping.

To test the LELFM *a posteriori*, large-eddy simulations were run on numerical grids having 64^3 and 128^3 points. In the simulations, the same pseudo-spectral code that was used for the DNS is employed, with the addition of models for the SGS fluxes, to solve (1) and (2). The LES are initialized with filtered DNS fields at $x/M=42$.

3.1 Spatial and Temporal Accuracy. The direct numerical simulations are among the largest that can be run on presently existing super-computers, and standard spatial resolution tests such as comparing results computed with different numerical grid resolutions are not possible. Nevertheless, several attributes of the simulations indicate that they are extremely accurate. First, the pseudospectral method used has the advantages that phase errors are very small, rates of convergence are very high, and the truncation error decreases faster than algebraically as the number of Fourier modes becomes large [29]. The method has been found to be twice as accurate as finite-difference schemes using the same resolution [30]. Second, spatial resolution tests typically performed for spectral simulations, including observing the evolution of the kinetic and scalar energy dissipation rate spectra and energy transfer spectra show that the largest and smallest dynamically relevant length scales are resolved on the numerical grid. Third, the simulations match the data from the highly respected wind tunnel experiments of Comte-Bellot and Corrsin [13]. The simulation results agree with the laboratory data not just for gross statistics such as average kinetic energy and integral length scale at a single downstream location but, in addition to other higher-order statistics, for the entire three-dimensional kinetic energy spectra from $x/M=42$ to $x/M=171$. For additional discussion of the simulations, see [27,31].

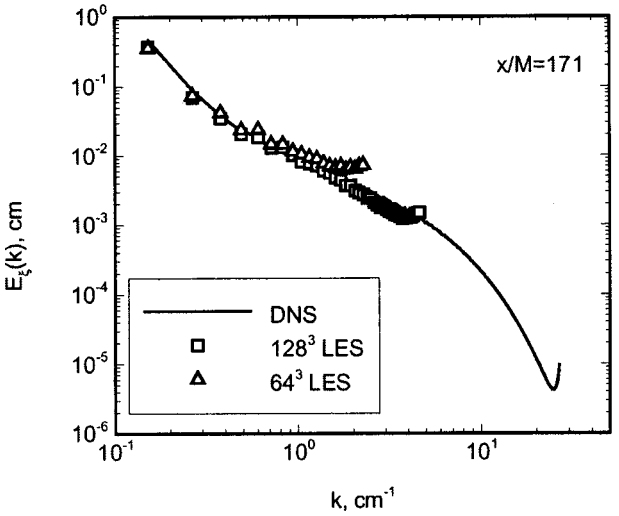

Fig. 1 Three dimensional scalar energy spectra from DNS and LES.

In LESs, the simulation results will change when the grid resolution is increased unless the closure models for the transport equations are perfect. The question becomes what grid resolution is required to accurately predict the length scales of interest. In the current simulations, it was found that about 48^3 grid points are required to accurately predict the growth rate of the integral length scale and the decay rate of the turbulence kinetic energy. These results are consistent with those of Carati et al. [18] for large-eddy simulations of the same flow. In this work, 64^3-point simulations are the lowest resolution reported, since the performances of the SGS mixing models deteriorate markedly when applied to grids coarser than this. The three dimensional scalar energy spectra at $x/M=171$ from 64^3-point and 128^3-point simulations are compared with the corresponding spectrum from the DNS in Fig. 1. There are inaccuracies in the results from both LESs near the smallest resolved scale, but the large scales and the scalar energies are accurate throughout the simulations. Additional details concerning the large eddy simulations can be found in [12,27].

The temporal accuracy of all the simulations was verified by running portions of the simulations with time step sizes differing by a factor of two and noting no measurable difference in the resulting velocity and scalar fields. Using a third order Adams-Bashforth scheme for portions of the simulations also had no effect on the results.

Table 1 Correlation coefficient between the exact filtered dissipation rate, $\overline{\chi}_e$, and related quantities

Grid	x/M	$\overline{\nabla\xi\cdot\nabla\xi}$	$\overline{\chi}_{m1}$	$\overline{\chi}_{m2}$	$\overline{\chi}_{m3}$
32^3	98	0.84	0.76	0.84	0.84
	181	0.79	0.74	0.79	0.79
64^3	98	0.83	0.79	0.83	0.83
	181	0.83	0.81	0.83	0.83

Table 3 Correlation coefficient between the SGS-variance and related quantities

Grid	x/M	$\overline{\nabla\xi\cdot\nabla\xi}$	ξ^2_{m1}	ξ^2_{m2}	ξ^2_{m3}	ξ^2_{m4}
32^3	98	0.93	0.79	0.87	0.87	0.93
	181	0.91	0.74	0.82	0.82	0.91
64^3	98	0.92	0.78	0.84	0.84	0.92
	181	0.91	0.76	0.82	0.82	0.91

4 Results

4.1 A Priori Evaluation of the Models for $\overline{\chi}$. The models for $\overline{\chi}$ are evaluated *a priori* by filtering the 512^3 DNS data onto coarser grids to simulate LES data. The modeled quantities are computed from these filtered fields and compared with the exact filtered dissipation rate, $\overline{\chi}_e$, determined by filtering χ from the DNS. Two filter widths are used, which result in simulated LES fields having 32^3 and 64^3 points.

A good model for $\overline{\chi}$ will be well correlated with $\overline{\chi}_e$ and also will have approximately the same volume average. The correlation between $\overline{\chi}_e$ and related quantities is given in Table 1, and the corresponding mean values, as fractions of $\langle\overline{\chi}_e\rangle$, in Table 2. The factor $\overline{\nabla\xi\cdot\nabla\xi}$ is common to $\overline{\chi}_{m1}$, $\overline{\chi}_{m2}$, and $\overline{\chi}_{m3}$, and there is good correlation between it and the exact filtered dissipation rate. This fact is encouraging because it implies that a model for $\overline{\chi}$ might be based upon $\overline{\nabla\xi\cdot\nabla\xi}$, provided that a method can be found to adjust the mean value of the model appropriately.

In model $\overline{\chi}_{m1}$, the SGS diffusivity, D_T, is used to scale $\overline{\nabla\xi\cdot\nabla\xi}$, and, since D_T is neither constant in space nor well correlated with $\overline{\chi}_e$, this approach adversely affects the correlation between the exact and modeled dissipation rates, but not by a great amount. Of greater concern is that $\langle\overline{\chi}_{m1}\rangle$ is about a quarter of $\langle\overline{\chi}_e\rangle$ in the 32^3 domain and about half $\langle\overline{\chi}_e\rangle$ in the 64^3 domain. In the model, it is assumed that the sum of the molecular and SGS dissipation rates of ξ-energy from the resolved scales, $\langle\chi_{gs}\rangle$, is approximately equal to the dissipation rate from all scales, $\langle\overline{\chi}_e\rangle$. The ratio $\langle\chi_{gs}\rangle/\langle\overline{\chi}_e\rangle$ is only about 0.3 to 0.4 in the 64^3 LES, and an LES grid larger than 128^3 would be required to make the ratio 0.8. The scalar fields depend strongly on the initial conditions, so that it is probable that $\langle\chi_{gs}\rangle$ is a better approximation of $\langle\overline{\chi}_e\rangle$ in some configurations than others. Since the velocity field is driving the transfer of scalar energy from large to small scales, however, it is useful to examine the corresponding relationship for the velocity field; in the 64^3 LES, only about 70% of the kinetic energy dissipation is due to transfer and dissipation from the large scales, and the fraction drops to about 50% for the 32^3 fields. The conclusion is that $\langle\overline{\chi}_{m1}\rangle$ will underestimate $\langle\overline{\chi}_e\rangle$ by 30–75%, depending on the resolution of the LES and the flow configuration.

In model $\overline{\chi}_{m2}$, $\overline{\nabla\xi\cdot\nabla\xi}$ is scaled by a coefficient which has a value such that $\langle\overline{\chi}_{m2}\rangle$ will equal the average dissipation rate computed from a composite dissipation rate spectrum made up of the known resolved scale spectrum and an assumed form for the unresolved scales. The coefficients in the assumed spectrum (7) are those given by Pao [26]. In the present flow, the slope of $E_\xi(\kappa)$ is flatter than $-5/3$ at the highest resolved wave number, especially in the 32^3 LES, so the peak of the assumed $D_\xi(\kappa)$ is lower than the true peak in the dissipation rate spectrum and $\langle\overline{\chi}_{m2}\rangle$ underpredicts $\langle\overline{\chi}_e\rangle$. In model $\overline{\chi}_{m3}$, the coefficients of (7) are adjusted to $\alpha=-1$ and $n=1.2$. From Table 2, it is clear that the model accurately predicts the filtered dissipation rate, provided that the shape of the ξ-energy spectrum is reasonably well known. The strength of the model is that it is based on the transfer of kinetic energy out of the resolved scales, which the LES predicts very accurately. If the LES cannot accurately predict the resolved-scale dissipation rate, the evolution of the velocity and scalar fields will be incorrect and the modeling of $\overline{\chi}$ is moot.

4.2 A Priori Evaluation of the Models for ξ^2_v. Like the models for $\overline{\chi}$, the approximations for ξ^2_v are based on quantities that can be computed locally in the LES and scaled so that the mean SGS variance is approximately correct. In model ξ^2_{m1}, $\overline{\nabla\xi\cdot\nabla\xi}$, is multiplied by a dynamically computed coefficient, γ, which is a function of space and time. From Table 3, it is clear that $\overline{\nabla\xi\cdot\nabla\xi}$ is a good quantity on which to base a model because it is highly correlated with ξ^2_e over the full range of x/M and LES resolution. In the computation of γ, however, it is assumed that the SGS-variance can be predicted from a test-scale variance, which is a poor assumption for the present flow. Even if the flow were such that γ were approximately the correct factor with which to relate $\overline{\nabla\xi\cdot\nabla\xi}$, with ξ^2_e, it is poorly correlated with ξ^2_e and significantly degrades the correlation between ξ^2_{m1} and ξ^2_e.

In models ξ^2_{m2} and ξ^2_{m3}, it is again postulated that the SGS variance can be related to a test-scale variance, but this time the relationship is through the correlation and not the mean. The distinction between ξ^2_{m2} and ξ^2_{m3} is the same as that between $\overline{\chi}_{m2}$ and $\overline{\chi}_{m3}$, namely that ξ^2_{m2} is based on a generic assumed spectrum and ξ^2_{m3} is based on a spectrum tailored for the current flow configuration. Both $\langle\xi^2_{m2}\rangle$ and $\langle\xi^2_{m3}\rangle$ are excellent estimates of $\langle\xi^2_e\rangle$ (Table 4), but the correlation is only moderately good in view of the excellent correlation between ξ^2_e and $\overline{\nabla\xi\cdot\nabla\xi}$. In model ξ^2_{m4}, the concept of relating the SGS variance to a test-scale variance is discarded and $\overline{\nabla\xi\cdot\nabla\xi}$ is scaled the same way $(\widehat{\xi^2}-\hat{\xi}^2)$ is scaled in model ξ^2_{m3}. The result is a model that almost exactly matches $\langle\xi^2_e\rangle$ with excellent correlation.

4.3 A Posteriori Tests. It is the accuracies of $\overline{\chi}$ and ξ^2_v when computed from an LES which are of prime interest, although the models cannot be validated on a point-wise basis as they can be when applied to filtered DNS data. In the current simulations, the scalar dissipation rate from the smallest resolved-scales is slightly too high, and the resolved-scale scalar variance is correspondingly low (Fig. 1). This causes $\overline{\chi}_{m1}$ to perform better than expected from the *a priori* tests, but still significantly worse than $\overline{\chi}_{m3}$ at most downstream locations, as shown in Fig. 2(*a*). *A*

Table 2 Mean values of various quantities as fractions of $\langle\overline{\chi}_e\rangle$

Grid	x/M	$\overline{\nabla\xi\cdot\nabla\xi}$	$\overline{\chi}_{m1}$	$\overline{\chi}_{m2}$	$\overline{\chi}_{m3}$
32^3	98	0.026	0.19	0.55	0.89
	181	0.049	0.24	0.74	0.96
64^3	98	0.067	0.34	0.65	0.89
	181	0.13	0.45	0.83	0.96

Table 4 Mean values of various quantities as fractions of $\langle\xi^2_e\rangle$

Grid	x/M	ξ^2_{m1}	ξ^2_{m2}	ξ^2_{m3}	ξ^2_{m4}
32^3	98	0.57	0.93	0.98	0.98
	181	0.62	0.94	0.97	0.97
64^3	98	0.71	0.98	0.99	0.99
	181	0.75	0.99	0.99	0.99

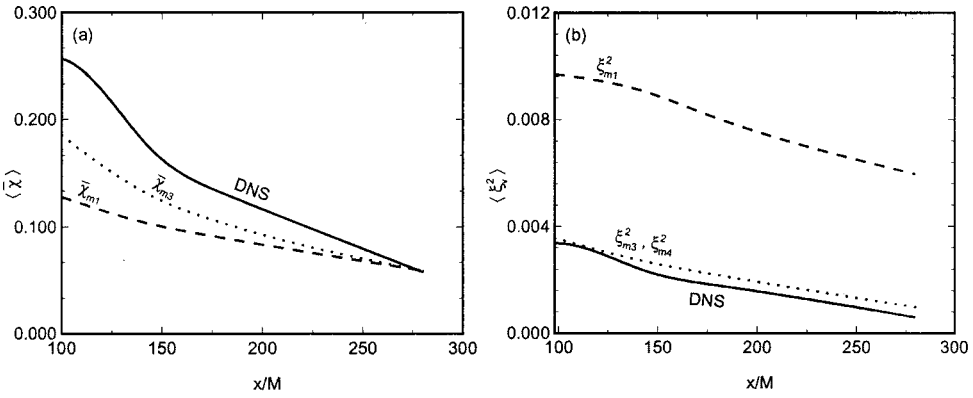

Fig. 2 LES predictions for $\bar{\chi}$ (*a*) and ξ_v^2 (*b*), compared to DNS values, from 64^3 LES

priori tests of ξ_{m1}^2 show that it underpredicts ξ_e^2, whereas it significantly overpredicts the exact value in an actual LES (Fig. 2*b*). Both ξ_{m2}^2 and ξ_{m3}^2 are very good, but not nearly perfect as suggested by the tests with DNS data.

When the resolution of the LES is increased to 128^3-points (not shown), the models that depend on an assumed spectrum improve dramatically [27]. This is in part due to the fact that more of the spectrum is computed directly in a higher resolution LES, and so less must be estimated. The principal problem, however, in estimating the spectra for the current (moderate Reynolds number) flow is that there is no inertial range, which makes the parameter α in (7) difficult to estimate. The spectra for flows with higher Reynolds number may be easier to estimate from 64^3-point LES data.

5 Conclusions

Information about mixing at scales smaller than those resolved on an LES numerical grid is needed if mixture fraction based models are to be used for predicting species concentrations in LESs of non-premixed, turbulent reacting flows. For example, the large-eddy laminar flamelet model requires submodels for the SGS scalar variance and the filtered scalar dissipation rate to provide information about SGS mixing. Several formulations for each submodel are presented and tested using filtered DNS data and LES results. Predictions from the models that depend on an assumed form for the scalar energy spectrum are very good for the flow considered, and are better than those from models that rely on other assumptions. Additionally, the spectrum-based models perform consistently when tested *a priori* and *a posteriori* at several different LES resolutions, which encourages the thought that the models are robust. In contrast, several of the other models tested behave differently in *a priori* and *a posteriori* tests, and the accuracy of the model predictions varies widely as the scalar field develops with downstream distance. Since the spectrum-based models are applicable to flows for which a form for the one-dimensional scalar energy can be estimated [12], these models show promise for a variety of flow configurations.

Acknowledgments

This work is supported by the National Science Foundation (grant no. CTS9810103) and the Air Force Office of Scientific Research (grant no. F49620-97-1-0092), and by grants of high performance computing (HPC) time from the Arctic Region Supercomputing Center and the Pittsburgh Supercomputing Center.

References

[1] Givi, P., 1989, ''Model free simulations of turbulent reactive flows,'' Prog. Energy Combust. Sci., **15**, pp. 1–107.
[2] Gao, F., and O'Brien, E. E., 1993, ''A large-eddy simulation scheme for turbulent reacting flows,'' Phys. Fluids A, **5**, pp. 1282–1284.
[3] Colucci, P. J., Jaberi, F. A., Givi, P., and Pope, S. B., 1998, ''Filtered density function for large eddy simulation of turbulent reacting flows,'' Phys. Fluids, **10**, No. 2, pp. 499–515.
[4] Bilger, R. W., 1980, ''Turbulent flows with nonpremixed reactants,'' P. A. Libby and F. A. Williams, editors, *Topics in Applied Physics Number 44: Turbulent Reacting Flows*, chapter 3, Springer, New York, pp. 65–113.
[5] Lentini, D., 1994, ''Assessment of the stretched laminar flamelet approach for non-premixed turbulent combustion,'' Combust. Sci. Technol., **100**, pp. 95–122.
[6] Frankel, S. H., Adumitroaie, V. Madnia, C. K., and Givi, P. 1993, ''Large-eddy simulation of turbulent reacting flows by assumed PDF methods.'' *Engineering Applications of Large Eddy Simulations*, New York, ASME, pp 81–101.
[7] Cook, A. W. and Riley, J. J., 1994, ''A subgrid model for equilibrium chemistry in turbulent flows.'' Phys. Fluids, **6**, No. 8, pp. 2868–2870.
[8] Peters, N., 1984, ''Laminar diffusion flamelet models in non-premixed turbulent combustion,'' Prog. Energy Combust. Sci., **10**, pp. 319–339.
[9] Cook, A. W., Riley, J. J., and Kosály, G., 1997, ''A laminar flamelet approach to subgrid-scale chemistry in turbulent flows,'' Combust. Flame, **109**, pp. 332–341.
[10] Cook, A. W., and Riley, J. J., 1997, ''Subgrid-scale modeling for turbulent, reacting flows,'' Combust. Flame, **112**, pp. 593–606.
[11] de Bruyn Kops, S. M., Riley, J. J., Kosály, G., and Cook, A. W., 1998, ''Investigation of modeling for non-premixed turbulent combustion,'' Flow, Turbul. Combust., **60**, No. 1, pp. 105–122.
[12] de Bruyn Kops, S. M., and Riley, J. J., ''Large-eddy simulation of non-premixed reacting flows with realistic chemistry,'' Comput. Math. Appl., to appear.
[13] Comte-Bellot, G. and Corrsin, S., 1971, ''Simple Eulerian time correlation of full and narrow-band velocity signals in grid-generated, 'isotropic' turbulence,'' J. Fluid Mech., **48**, pp. 273–337.
[14] Smagorinsky, J., 1963, ''General circulation experiments with the primitive equations. I. The basic experiment,'' Mon. Weather Rev., **91**, pp. 99–164.
[15] Germano, M., Piomelli, U., Moin, P., and Cabot, W. H., 1991, ''A dynamic subgrid-scale eddy viscosity model,'' Phys. Fluids A, **3**, pp. 1760–1765.
[16] Germano, M., 1992, ''Turbulence: the filtering approach,'' J. Fluid Mech., **238**, pp. 325–336.
[17] Lilly, D. K., 1992, ''A proposed modification of the Germano subgrid-scale closure method,'' Phys. Fluids A, **4**, pp. 633–635.
[18] Carati, D., Ghosal, S., and Moin, P., 1995, ''On the representation of backscatter in dynamic localization models,'' Phys. Fluids, **7**, No. 3, pp. 606–616.
[19] Piomelli, U., and Liu, J., 1995, ''Large-eddy simulation of rotating channel flows using a localized dynamic model,'' Phys. Fluids A, **7**, pp. 839–848.
[20] Jiménez, C. F. Ducros, and B. Cuenot, 2000, ''Subgrid scale variance and dissipation of a scalar field in large eddy simulation combustion models,'' 8th European Turbulence Conference, Barcelona, Spain.
[21] Schmidt, H., and Schumann, U., 1999, ''Coherent structure of the convective boundary layer derived from large-eddy simulations,'' J. Fluid Mech., **200**, pp. 511–562.
[22] Yoshizawa, A., 1986, ''Statistical theory for compressible turbulent shear flows, with the application to subgrid modeling,'' Phys. Fluids A, **29**, pp. 2152–2164.
[23] Mathey, F., and J. P. Chollet, 1996, ''Sub-grid model of scalar mixing for large eddy simulations of turbulent flows,'' The Second ERCOFTAC Workshop on Direct and Large Eddy Simulations, Grenoble, France.
[24] Cook, A. W., 1997, ''Determination of the constant coefficient in scale similarity models of turbulence,'' Phys. Fluids, **9**, No. 5, pp. 1485–1487.
[25] Corrsin, S., 1964, ''Further generalizations of Onsager's cascade model for turbulent spectra,'' Phys. Fluids, **7**, pp. 1156.
[26] Pao, Yih Ho, 1965, ''Structure of turbulent velocity and scalar fields at large wavenumbers,'' Phys. Fluids, **8**, No. 6, pp. 1063–1075.

[27] de Bruyn Kops, S. M., 1999, ''*Numerical Simulation of Non-premixed Turbulent Combustion*'' PhD thesis, University of Washington.
[28] Girimaji, S. S., and Zhou, Y., 1996, ''Analysis and modeling of subgrid scalar mixing using numerical data,'' Phys. Fluids A, **8**, No. 5, pp. 1224–1236.
[29] Gottlieb, D., and S. A. Orszag, 1977, ''*Numerical Analysis of Spectral Methods: Theory and Applications*,'' Vol. 26, *NSF-CBMS, Regional Conference Series in Applied Mathematics*. Society of Industrial and Applied Mathematics, Philadelphia.
[30] Peyret, P., and T. D. Taylor, 1993, *Computational Methods for Fluid Flows*, Springer, New York.
[31] de Bruyn Kops, S. M., Riley, J. J., 1998, ''Direct numerical simulation of laboratory experiments in isotropic turbulence,'' Phys. Fluids, **10**, No. 9, pp. 2125–2127.

Direct Numerical Simulation of Flow and Heat Transfer From a Sphere in a Uniform Cross-Flow

P. Bagchi
Department of Theoretical & Applied Mechanics,
University of Illinois,
Urbana, IL 61801-2935

M. Y. Ha
School of Mechanical Engineering,
Pusan National University,
South Korea

S. Balachandar
Department of Theoretical & Applied Mechanics,
University of Illinois,
Urbana, IL 61801-2935

Direct numerical solution for flow and heat transfer past a sphere in a uniform flow is obtained using an accurate and efficient Fourier-Chebyshev spectral collocation method for Reynolds numbers up to 500. We investigate the flow and temperature fields over a range of Reynolds numbers, showing steady and axisymmetric flow when the Reynolds number is less than 210, steady and nonaxisymmetric flow without vortex shedding when the Reynolds number is between 210 and 270, and unsteady three-dimensional flow with vortex shedding when the Reynolds number is above 270. Results from three-dimensional simulation are compared with the corresponding axisymmetric simulations for Re>210 in order to see the effect of unsteadiness and three-dimensionality on heat transfer past a sphere. The local Nusselt number distribution obtained from the 3D simulation shows big differences in the wake region compared with axisymmetric one, when there exists strong vortex shedding in the wake. But the differences in surface-average Nusselt number between axisymmetric and three-dimensional simulations are small owing to the smaller surface area associated with the base region. The shedding process is observed to be dominantly one-sided and as a result axisymmetry of the surface heat transfer is broken even after a time-average. The one-sided shedding also results in a time-averaged mean lift force on the sphere. [DOI: 10.1115/1.1358844]

Introduction

There are many examples in nature and technology where the movement of solid particles and liquid droplets play an important role (Clift et al. [1], Faeth [2], Law [3]). Understanding the particle behavior is very important in the performance prediction and enhancement of many industrial equipment. In many applications, the particulate matter is not passively advected by the surrounding fluid flow; but they actively participate in defining the surrounding flow through heat transfer, evaporation, and burning.

Even dilute systems typically consist of millions of particles that in any numerical simulation it is virtually impossible to consider the details of flow and heat transfer from each of these particles. A popular computational approach to these particulate flows has been Eulerian-Lagrangian in nature; where the continuous phase (fluid flow) is treated in an Eulerian fashion, while the distributed phase (particles) is treated Lagrangian. In applications where the particles are active, it is not sufficient to track only their position and velocity; their mass, temperature, and concentration need to be evolved in time as well. An expression for drag and lift coefficients on the particle is required to describe its motion. Additional heat transfer and mass transfer correlations are required to predict heat and mass exchange with the surrounding flow.

The force and heat transfer coefficients clearly depend on the nature of the surrounding flow, which are generally parametrized in terms of Reynolds number based on particle diameter and relative velocity, nondimensional temperature difference between the particle and the surrounding, etc. In the low Reynolds number limit analytical expression for drag coefficient dates back to Stokes. However, as Reynolds number increases flow over the sphere becomes increasingly complex, especially as Re increases above 270, the flow is three-dimensional and time-dependent with periodic vortex shedding (Natarajan and Acrivos [4], Tomboulides et al. [5]). Heat transfer around the sphere is significantly affected by this time-dependence and three-dimensionality of flow field. At these Reynolds numbers (Re$\sim$O(1)) the only possible approach to obtaining accurate parametrization of force and heat transfer coefficients is through either careful experiments or detailed three-dimensional numerical simulations of flow around an isolated particle.

Recent explosion in computing capability has enabled detailed three-dimensional time-dependent simulation of flow past spherical particles at moderate Reynolds numbers. These simulations have allowed investigation of the resulting wake structure and drag and lift forces in both uniform and nonuniform flows (Johnson and Patel [6], Kurose and Komori [7], Mittal [8], Bagchi and Balachandar [9]). However, most effort to calculate the heat and mass transfer around drops and particles at finite Reynolds number have been limited to two-dimensional simulations, where the flow and temperature fields surrounding the sphere have been assumed to be steady and axisymmetric. Sayegu and Gauvin [10] carried out the numerical analysis for the fluid flow and heat transfer around a sphere using finite difference techniques for Reynolds numbers up to 50. Average Nusselt number correlation was obtained which compared well with the experimental data of Ranz and Marshall [11] and Whitaker [12]. This study also considered the effect of variable properties on the fluid flow and heat transfer around a sphere. Renksizbulu and Yuen [13] numerically studied droplet evaporation in a high-temperature stream for Re in the range 10–100. The effects of variable properties and mass transfer (mass efflux from the droplet surface) on the fluid flow and heat transfer around a sphere were investigated. Momentum, energy, and species continuity equations were solved in a coupled manner assuming steady axisymmetric conditions. Wong et al. [14] studied the flow and heat transfer characteristics of laminar combined convection from an isothermal sphere in the range of Reynolds number of 5–100 and Grashof number of 0–80,000. The average Nusselt number correlation for the case without natural convection was compared with Yuge's experimental correlation (Yuge [15]). In addition to heat transfer calculation from a spherical particle or droplet, Chiang et al. [16] and Xin and Megaridis [17] considered the effects of variable thermo-physical properties, transient heating, internal circulation of liquid, and droplet rotation on heat and mass transfer from a spherical droplet, under the axisym-

Contributed by the Fluids Engineering Division for publication in the JOURNAL OF FLUIDS ENGINEERING. Manuscript received by the Fluids Engineering Division January 10, 2000; revised manuscript received November 17, 2000. Associate Editor: D. R. Williams.

metric condition. Dandy and Dewyer [18] obtained three-dimensional numerical solutions for steady and linear shear flow past a fixed spherical particle over a wide range of Reynolds number of 0.1–100 and dimensionless shear rates of 0.005–0.4. They studied the effects of shear rate on the drag and lift coefficients and Nusselt number.

The assumption of steady state and axisymmetric flow for a uniform flow past a spherical particle is well justified at lower Reynolds numbers considered in the above investigations. As Reynolds number increases above 210, it has been well established that the axisymmetry of the wake is broken with a *double threaded* wake; however, the flow remains steady. At Reynolds numbers greater than 270, periodic shedding of vortices is observed; as a result the flow is time-dependent and three-dimensional. To our knowledge, there is little study on the time-dependent and three-dimensional nature of heat transfer around a sphere at Reynolds numbers greater than 270. Thus, the purpose of the present study is to investigate the effects of time-dependence and three-dimensionality on the prediction of heat transfer around a sphere. Time-dependent and three-dimensional results are compared with those based on steady and axisymmetric flow approximation.

Numerical Methodology

Here we consider the problem of flow of heat transfer from an isothermal sphere of temperature, T_S, subjected to a uniform cross-flow of relative velocity, U_∞, and constant farfield temperature of T_∞. The particle is assumed to be stationary (or at most moving at constant velocity without acceleration) and without any spin. We solve the continuity, Navier-Stokes and energy equations in their nondimensional form in a frame of reference fixed on the spherical particle

$$\nabla \cdot \mathbf{u} = \mathbf{0}$$

$$\frac{\partial \mathbf{u}}{\partial t} + \mathbf{u} \cdot \nabla \mathbf{u} = -\nabla p + \frac{1}{\mathrm{Re}} \nabla^2 \mathbf{u} \tag{1}$$

$$\frac{\partial T}{\partial t} + \mathbf{u} \cdot \nabla T = \frac{1}{\mathrm{Pr\,Re}} \nabla^2 T.$$

In the above equations, diameter of the spherical particle, d, is the length scale, the freestream velocity in the frame of reference fixed on the particle, U_∞, is the velocity scale. The nondimensional temperature is defined as $T=(T^*-T_\infty)/(T_S-T_\infty)$, where T^* is the dimensional temperature and $\mathbf{u}$ and p are the nondimensional velocity and pressure of the fluid flow. The above nondimensionalization results in two dimensionless parameters: $\mathrm{Re}=dU_\infty/\nu$ and $\mathrm{Pr}=\nu/\kappa$, where ν and κ are the kinematic viscosity and thermal diffusivity of the fluid. In the simulations to be reported here the Prandtl number, Pr, has been taken to be 0.72 corresponding to that of air.

The governing equations are solved in spherical coordinates (r,θ,ϕ) where $r_p \leqslant r \leqslant r_d$, $0 \leqslant \theta \leqslant \pi$ and $0 \leqslant \phi \leqslant 2\pi$. Here r_p represents the particle radius and r_d represents the boundary of the computational domain. θ and ϕ are the tangential and azimuthal directions, respectively. In the nonperiodic radial direction a Chebyshev collection scheme is used. In order to resolve the shear layer near the sphere surface, a radial grid stretching is used to cluster more points. The azimuthal direction is periodic over 2π and a Fourier expansion is used with a uniform distribution of collocation points in ϕ. In the θ direction, variables are defined only over π and therefore a sine or cosine expansion is used in θ as appropriate. A grid stretching is also used in θ to cluster points in the wake region of the sphere.

A two-step time-split scheme is used to advance the flow field. First, the velocity field is advanced from time level ''n'' to an intermediate level by solving the advection-diffusion equation. In the advection-diffusion step, the nonlinear terms and the θ-diffusion terms are treated explicitly using second-order Adams-Bashforth scheme. The radial and azimuthal diffusion terms are treated implicitly using Crank-Nicholson scheme. Then a Poisson equation for pressure is solved fully implicitly. The final divergence-free velocity field at ''$n+1$'' is obtained with a pressure-correction step. The temperature field is advanced in a similar manner with second-order Adams-Bashforth for the advection term and Crank-Nicholson scheme for the diffusion term. Once the velocity and temperature fields are obtained, force acting on the particle is computed by

$$F_i = \int_S [-p\mathbf{e}_r + \tau_{r\theta}\mathbf{e}_\theta + \tau_{r\phi}\mathbf{e}_\phi] \cdot \mathbf{e}_i dS \tag{2}$$

where the integration is over the surface of the sphere. The first term on the right corresponds to the pressure force, and the next two terms correspond to the viscous force. A nondimensional force coefficient is defined using the scaling parameters mentioned above as

$$C_F = \frac{\mathbf{F^*}}{\frac{1}{2}\rho U_\infty^2 \pi (d/2)^2}, \tag{3}$$

where $\mathbf{F^*}$ is net force on the particle in dimensional terms. In terms of corresponding nondimensional force given in Eq. (2), the force coefficient becomes $C_F = 8\mathbf{F}/\pi$. The component of C_F along the direction of relative velocity is then the drag coefficient, C_D, and the component perpendicular to drag will be the lift coefficient, C_L. Local heat transfer from the sphere is calculated as

$$h(\theta,\phi) = \nabla T \cdot \mathbf{e}_r \tag{4}$$

From the above nondimensional form the local heat transfer coefficient is the same as local Nusselt number. Surface-averaged Nusselt number is then defined as

$$\overline{\mathrm{Nu}} = \frac{1}{\pi}\int_S \mathrm{Nu}(\theta,\phi) dS \tag{5}$$

where the integral is over the surface of the sphere, whose nondimensional radius is 1/2.

A uniform flow is specified at the inlet to the computational domain. At the outflow, a nonreflecting boundary condition is used (Mittal and Balachandar [19]). Here the governing equations are smoothly parabolized by multiplying the radial diffusion terms by a filter function. On the surface of the sphere, the no-slip and no-penetration conditions are imposed.

In a spherical coordinate system, the azimuthal resolution near the poles is much higher than what is necessary to resolve the flow. The viscous stability constraint is avoided by the implicit treatment of the diffusion terms. However, a severe convective (CFL) stability constraint still exists. In order to avoid such restriction, high frequency azimuthal components are filtered out near the poles. The axisymmetric mode $k_\phi = 0$ does not lead to convective instability and need not be filtered. Also the $k_\phi = \pm 1$ modes should be retained in the entire computational domain as these modes are the source of asymmetry and unsteadiness in the sphere wake. For the higher order Fourier modes along the azimuthal (ϕ) direction, we apply a smooth filter in both r and θ. The filtering is localized to a small region near the poles and the size of the region increases with the azimuthal mode. The details of numerical methodology can be seen in (Bagchi and Balachandar [9]).

Results and Discussion

First, we shall consider the structure of the wake in the steady flow regime. Figure 1 shows the streamline, azimuthal vorticity, and dimensionless temperature distribution past a sphere for $\mathrm{Re}=200$. When Reynolds number is less than 210, it is known that the sphere wake in a uniform flow remains symmetric and steady, giving rise to the observed symmetric flow and dimensionless

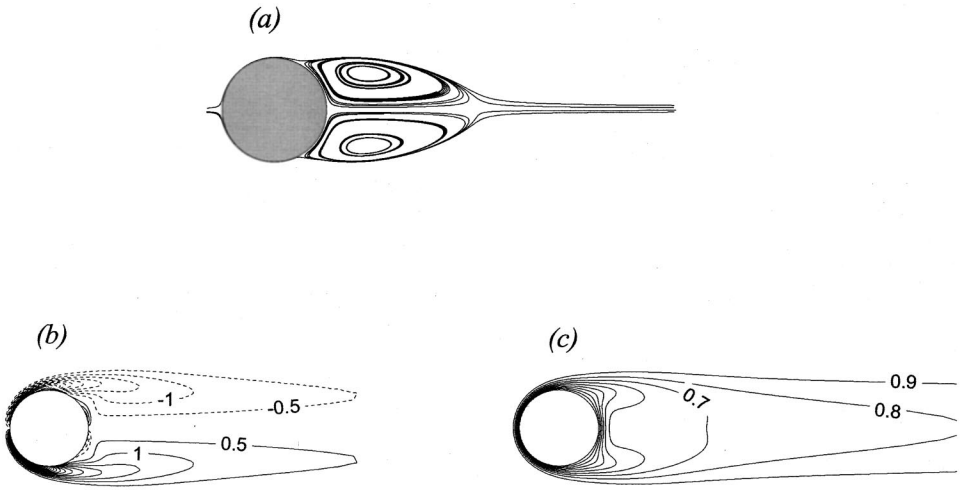

Fig. 1 Axisymmetric flow at Re=200. (*a*) Streamlines; (*b*) azimuthal vorticity (ω_ϕ) contours at an interval of 0.5; dashed lines indicate negative values; (*c*) dimensionless temperature at an interval of 0.1.

temperature fields past a sphere for Re=200. The gradient of dimensionless temperature is the largest at the front stagnation point ($\theta=\pi$) and decreases with increasing thermal boundary layer thickness along the streamwise direction. The maximum thermal boundary layer appears to be close to the point of flow separation. In the wake region, the flow is recirculating and the gradient of dimensionless temperature decreases again reaching a local minimum at the rear stagnation point. This behavior qualitatively remains the same over the range of Reynolds number from about 10–210, when the flow is steady and axisymmetric, and the size of the wake recirculation region progressively increases with increasing Reynolds number.

Figure 2 shows the variation of local Nusselt number over the sphere as a function of θ for different Reynolds numbers of 50, 100, and 200. In the present coordinate system $\theta=0$ corresponds to the rear stagnation point and $\theta=\pi$ corresponds to the front stagnation point and $\theta=\pi/2$ corresponds to the equatorial plane dividing the leeward ($\theta<\pi/2$) and windward ($\theta>\pi/2$) sides of the sphere. When the Reynolds number is small, at Re=50, the local Nusselt number has a maximum at the front stagnation point and decreases monotonically along the streamwise direction with increasing thermal boundary layer thickness, reaching a plateau in the wake region. When Re is increased, the local Nusselt number is the wake region increases due to increasing strength of the recirculating flow. The local Nusselt number increases with increasing Re owing to increasing effect of forced convection. At Re=200, the local minimum in Nu can be observed to coincide with the location of flow separation and the thicker thermal boundary layer. Figure 3 shows contours of local Nusselt number on the surface of the spherical particle for Re=200. The view is along the negative *x*-axis looking upstream from the wake region. Thus the region observed is the rear half of the sphere from $\theta=0$ to $\pi/2$. Thus, Nusselt number has a larger value at $\theta=\pi/2$, decreases along the streamwise direction up to about the point of separation ($\theta\approx0.8$) and increases again as the rear stagnation point is approached. The contours in Fig. 3 are concentric, representing that the flow and thermal fields past a sphere at Re=200 are axisymmetric.

When Re increases, it is known that the flow undergoes a regular bifurcation at around 210, resulting in the development of a nonaxisymmetric wake. However, the wake still remains steady

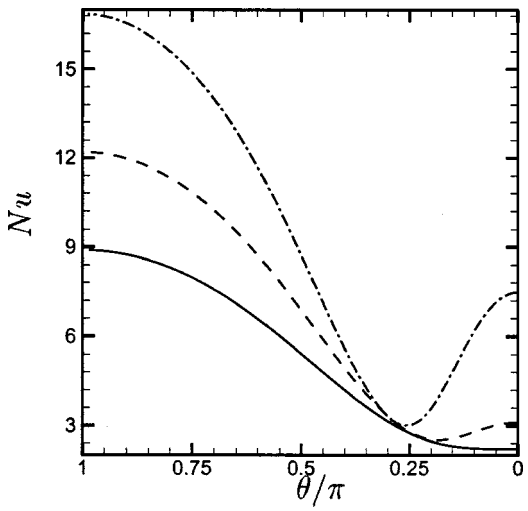

Fig. 2 Variation of Nusselt number for axisymmetric flow over the sphere: ——, Re=50; – – –, Re=100, —·—·—, Re=200.

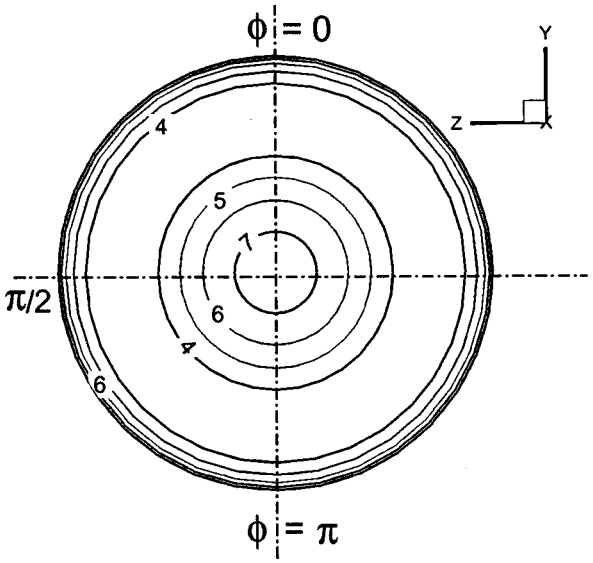

Fig. 3 Contours of Nusselt number on the sphere surface for Re=200.

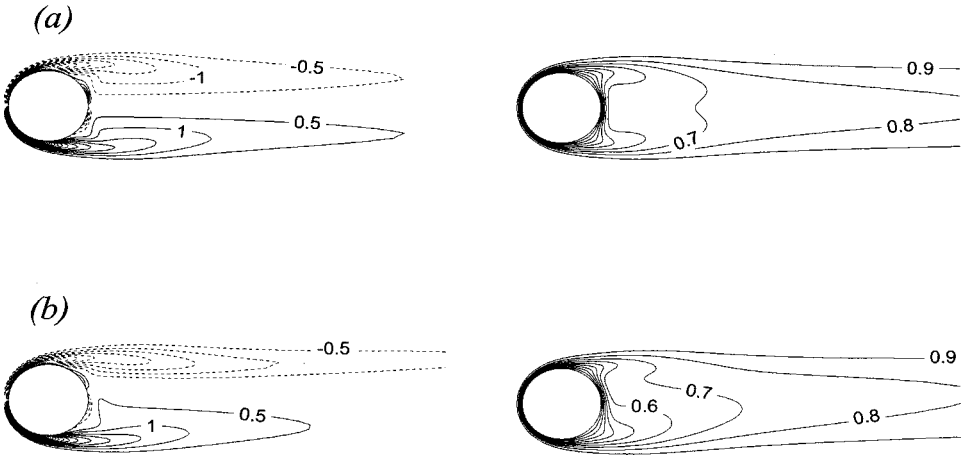

Fig. 4 Contours of azimuthal vorticity (ω_ϕ) (left panel) and dimensionless temperature (right panel) at Re=250. ω_ϕ contours are plotted at an interval of 0.5 while temperature contours are plotted at an interval of 0.1. Dashed lines indicate negative values. (*a*) Results from axisymmetric simulation; (*b*) results from 3-D simulation.

without vortex shedding. While the steady axisymmetric wake is *single threaded*, the steady nonaxisymmetric wake is *double threaded* (Nataragan and Acrivos [4] and Wu and Faeth [20]). Figure 4 shows contours of azimuthal vorticity and dimensionless temperature at Re=250. Figures 4(*a*) and (*b*) represent the results obtained from two different simulations, in order to compare them; (*a*) from an axisymmetric simulation where the flow is forced to be axisymmetric and (*b*) from a three-dimensional simulation. When axisymmetry is broken, there exists a plane passing through the streamwise (x)-axis about which the flow is symmetric (Mittal [8]). The exact orientation of this plane of symmetry is arbitrary and in the present three-dimensional simulation without loss of generality the x-y plane is chosen to be the plane of symmetry. The nonaxisymmetric nature of the wake is most clear on this plane of symmetry. The azimuthal vorticity and dimensionless temperature obtained from the three-dimensional calculation plotted on the plane of symmetry display nonsymmetric nature of the wake and are different from those obtained from the axisymmetric simulation. For example, in Fig. 4(*b*) the rear stagnation point can be seen to shift upwards to $\theta \approx 18°$, with corresponding asymmetric thinning of the thermal boundary layer. However, the impact of three-dimensionality in azimuthal vorticity and dimensionless temperature is not large.

Figure 5 shows variation of Nusselt number as a function of θ for Re=250. Here the 3D local Nusselt number (Nu) are shown at three different ϕ locations of 0, $\pi/2$, and π. The ϕ-averaged Nusselt number, defined as $\langle \mathrm{Nu} \rangle = 1/2\pi \int_0^{2\pi} \mathrm{Nu}\, d\phi$, is represented by the thick solid line and is compared with that obtained from the axisymmetric simulation. The effect of nonaxisymmetry can be seen only in the wake in terms of the large variation in the Nusselt number for the three different ϕ values, especially for $\theta < 0.3\pi$. Contours of local Nusselt number on the sphere surface for Re =250 obtained from the axisymmetric and 3D simulations are shown in Figs. 6(*a*) and (*b*) (again the view is from the wake and only the rear half of the sphere is shown). In the front half of the sphere the thermal field is nearly axisymmetric. The effect of three-dimensionality can be seen in Fig. 6 as the upward shift in the rear stagnation point with increased heat transfer above and decreased heat transfer below the x-z plane.

Above Re≈270 the solution undergoes Hopf bifurcation resulting in a periodic shedding of vortices in the wake. Figure 7 shows contours of azimuthal vorticity and dimensionless temperature for Re=350. Figure 7(*a*) shows the result of axisymmetric simulation and Figs. 7(*b*)–(*e*) show results of the corresponding 3D simulation at four different time instants. At this Re the flow is not

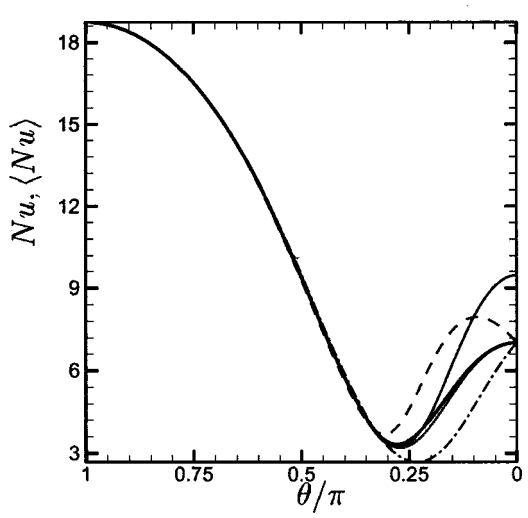

Fig. 5 Variation of Nusselt number for Re=250. ——, Nu obtained from axisymmetric simulation. Nu obtained from 3-D simulations are shown at three different ϕ locations: – – –, $\phi=0$; —·—·—, $\phi=\pi$; · · · ·, $\phi=\pi/2$. The thick line represents ϕ-averaged Nusselt number ⟨Nu⟩ obtained from 3-D simulation.

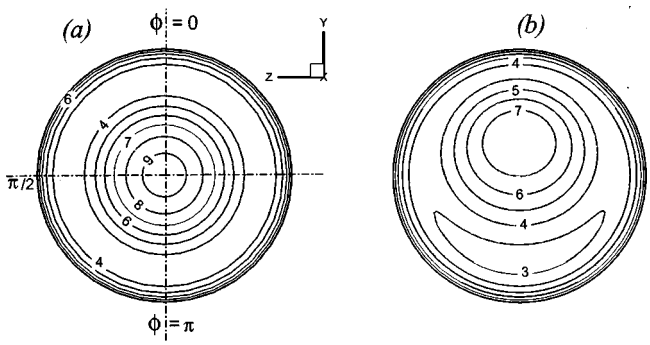

Fig. 6 Contours of local Nusselt number on the surface of the sphere for Re=250. (*a*) Results from axisymmetric simulation; (*b*) results from 3-D simulation.

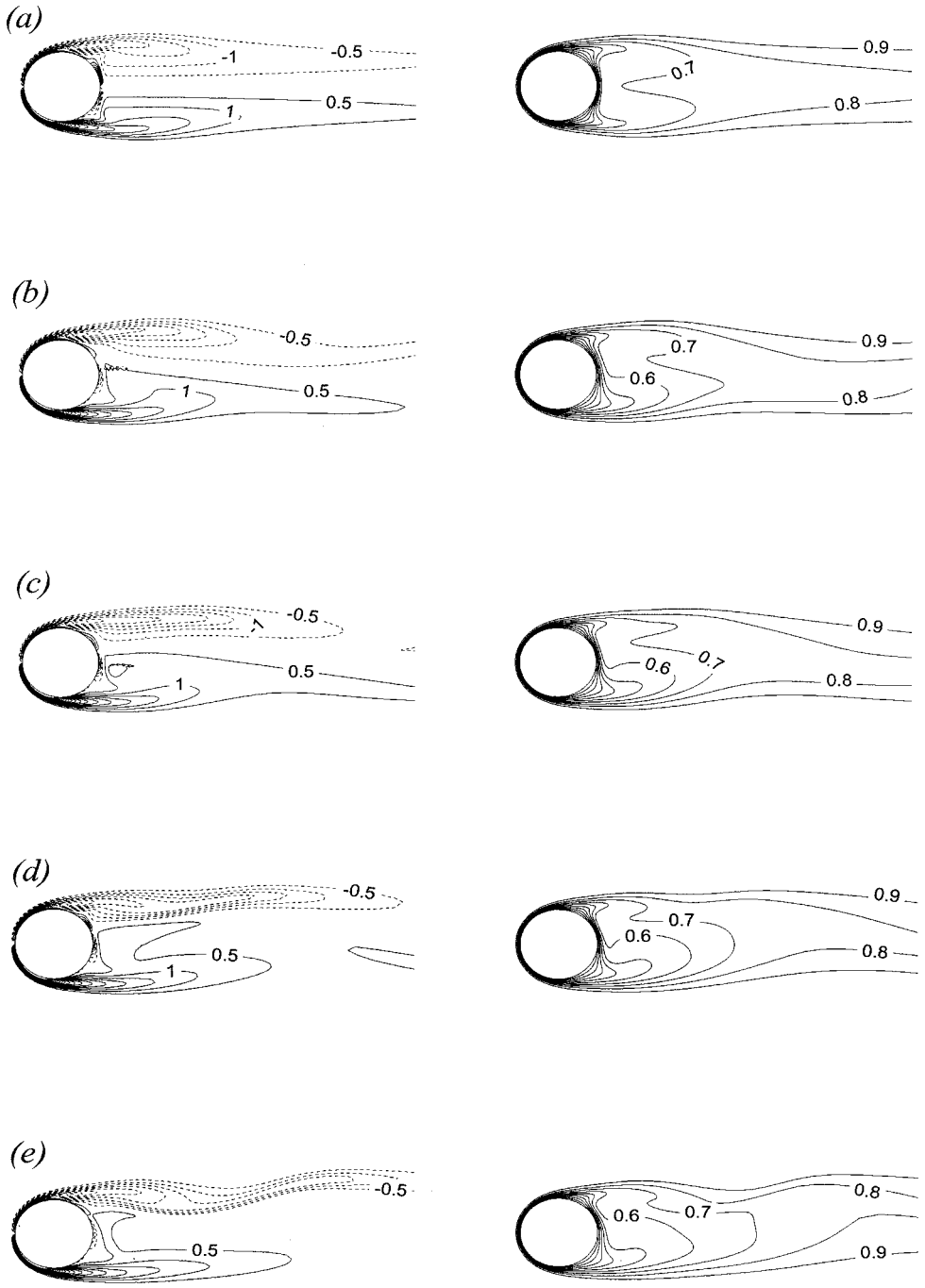

Fig. 7 Contours of azimuthal vorticity (ω_ϕ) (left panel) and dimensionless temperature (right panel) at Re=350. ω_ϕ contours are plotted at an interval of 0.5 while temperature contours are plotted at an interval of 0.1. Dashed lines indicate negative values. (*a*) Results from axisymmetric simulation. Results of 3-D simulation are presented in (*b*), (*c*), (*d*), and (*e*) at four different time instants approximately at equal interval in a shedding cycle.

precisely periodic (see Fig. 11); nevertheless, an approximate period of shedding T_p can be established. Figures 7(*b*)–(*e*) are (1/3)rd shedding period apart. At Re=350 the vortex shedding process is one-sided (Mittal [8]); in the present simulation vortices are shed only from the top of the sphere and not from the bottom. In this respect vortex shedding from a sphere is distinctly different from that of a circular cylinder. The one-sided shedding has its roots in the existence of the steady nonaxisymmetric wake prior to the on-set of shedding. The manifestation of the one-sided shedding process can be seen in Fig. 7, where the asymmetric contours are not seen to clearly oscillate up and down the wake centerline as they would in the case of flow over a circular cylinder. For example, the thinning of the thermal boundary layer near the rear stagnation point remains above the centerline over the entire shedding cycle, although oscillatory behavior can be observed.

Figure 8 shows variation of Nusselt number for Re=350 as a function of θ at the four different time instants shown in Fig. 7. The local Nusselt numbers at three different ϕ locations of 0, $\pi/2$, and π obtained from the 3D simulation are compared with the ϕ-averaged Nusselt number represented by the thick solid line and the axisymmetric Nusselt number. Contours of local Nusselt number on the sphere surface obtained from the axisymmetric and 3D

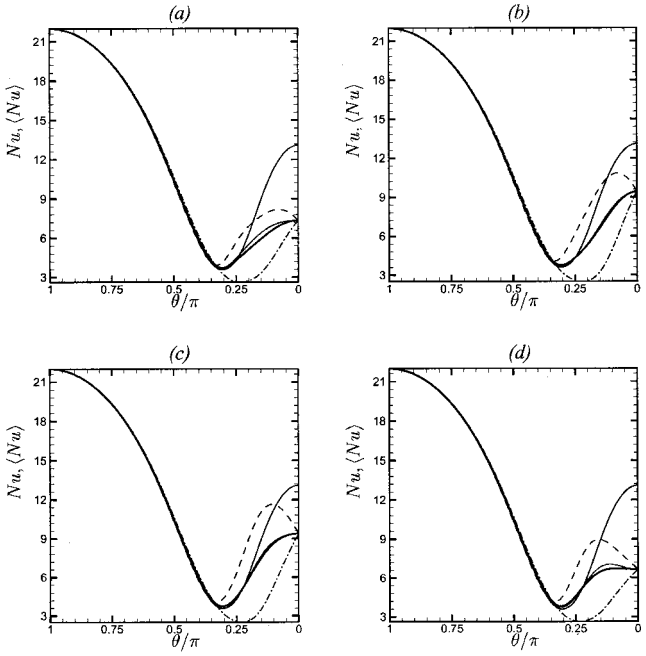

Fig. 8 Variation of Nusselt number for Re=350. (*a*), (*b*), (*c*), and (*d*) represent four different time instants in the shedding cycle corresponding to Fig. 7. ——, Nu obtained from axisymmetric simulation. Local Nu obtained from 3-D simulations are shown at three different ϕ locations: – – –, $\phi=0$; —·—·—, $\phi=\pi$; · · · ·, $\phi=\pi/2$. The thick line represents ϕ-averaged Nusselt number ⟨Nu⟩ obtained from 3-D simulation.

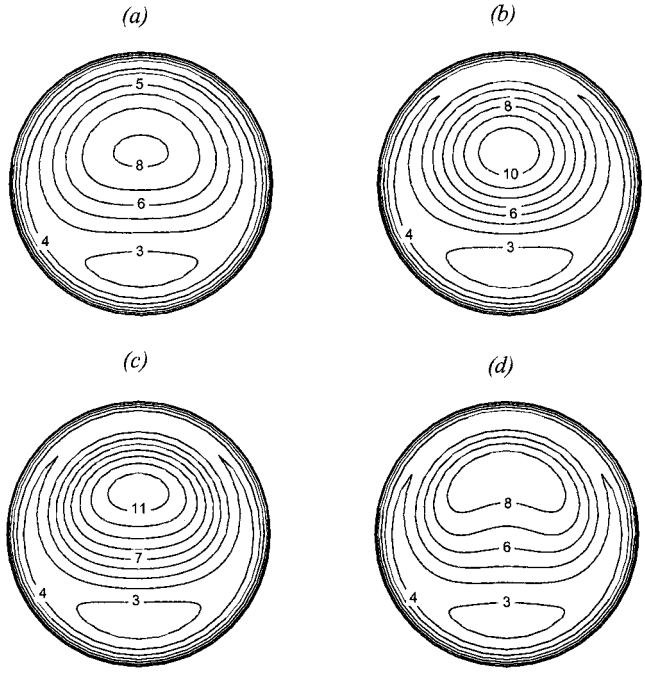

Fig. 9 Contours of Nusselt number on the surface of the sphere for Re=350 from the 3D simulations. Four different time instants are shown and they are the same as in Figs. 7 and 8.

simulations for Re=350 are shown in Fig. 9. Similar to the case of Re=250, the local Nusselt number distribution on the windward side of the sphere is not influenced much by the nonaxisymmetric nature of the wake. However, in the wake region, the local Nusselt number obtained from the three-dimensional simulation shows large variation for different azimuthal (ϕ) locations and time instances. Local variation in ϕ can be in excess of 100%; for example, in Fig. 8(*d*) at $\theta\approx 0.25\pi$, Nu varies from 3–9. When results for Re=350 are compared with those for Re=250, the extent of three-dimensionality in local Nusselt number can be seen to increase with increasing Re. Significant difference exists between the axisymmetric result and the ϕ-averaged three-dimensional Nu distribution. The maximum difference is at the geometric pole on the leeward side ($\theta=0$). The axisymmetric approximation tends to overpredict the local heat transfer and the level of overprediction increases with Reynolds number. For example, at Re=250 the actual local Nu at $\theta=0$ is 7.03 while the corresponding axisymmetric approximation estimates local Nu to be 9.48—a 35% overprediction. At Re=350 the actual local Nu (averaged over time) predicted by the three-dimensional simulation is 8.2, while the estimate of the corresponding axisymmetric approximation is 13.1—a 60% overprediction.

Figure 9 shows significant deviation in the Nu contours away

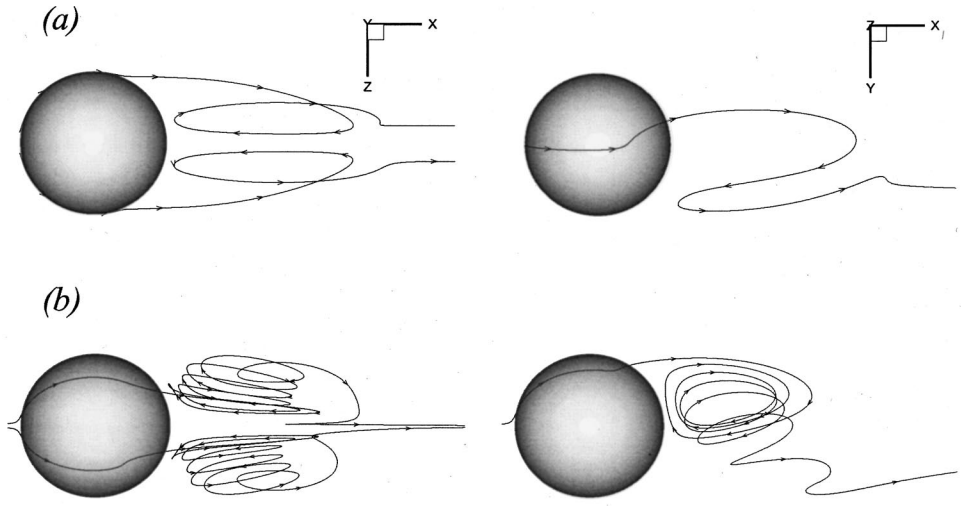

Fig. 10 Instantaneous pathlines for Reynolds number (a) 250 and (b) 350. Figures in the left panel show the pathlines that originate on two sides of the *x-y* plane. In the right panel, the *x-y* view, two particle paths coincide.

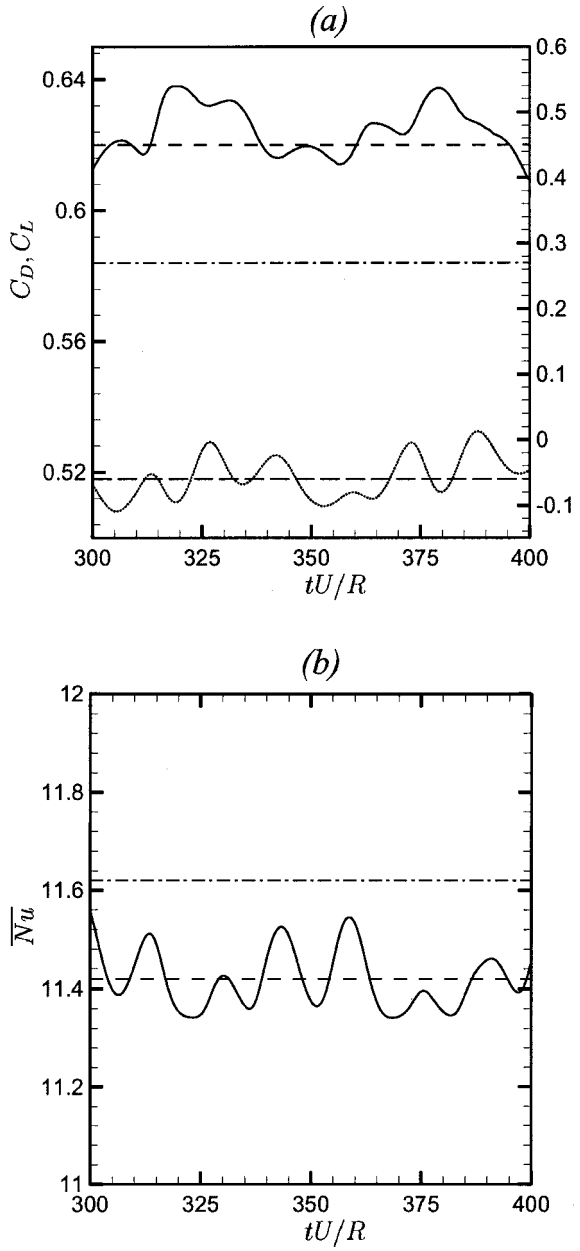

Fig. 11 Time evolution of drag and lift coefficients and surface-averaged Nusselt number $\overline{\text{Nu}}$ for Re=350. (*a*) Vertical axis on the left is for C_D and that on the right is for C_L. ——, C_D obtained from 3-D simulation; – – –, mean (time-averaged) drag coefficient; —·—·—, C_D obtained from axisymmetric simulation; · · · ·, C_L obtained from 3-D simulation; – – –, mean (time-averaged) lift coefficient. (*b*) ——, $\overline{\text{Nu}}$ obtained from 3-D simulation; – – –, mean (time-averaged) $\overline{\text{Nu}}$; —·—·—, Nu obtained from axisymmetric simulation.

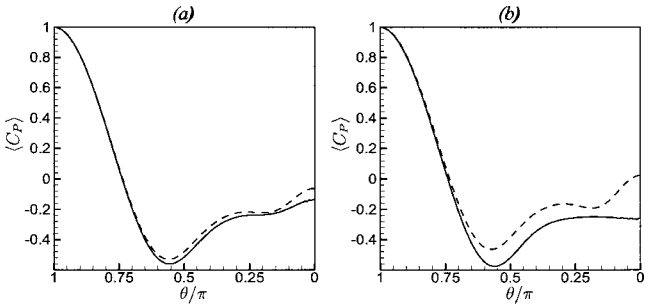

Fig. 12 ϕ-averaged surface pressure coefficient $\langle C_P \rangle$ for (*a*) Re=350 and (*b*) Re=500. Dashed line is the result from axisymmetric simulations and solid line is the result from 3-D simulations.

from axisymmetry. Over the entire cycle the local Nusselt number maxima corresponding to the rear stagnation point is located on the upper side of the sphere, consistent with the observations of Fig. 7. The location of the local Nu peak seems to oscillate between 12 to about 40 deg, which can also be seen in Fig. 8 in the movement of the peak in the Nu distribution for $\phi=0$.

In the 3D simulation the nonaxisymmetric and time-dependent nature of the flow contributes to enhanced mixing in the wake. This can be seen in Fig. 10, where two sample instantaneous pathlines in the wake of the sphere are plotted for Re=250 and 350. The left panel shows the trajectory projected on the x-z plane and the right panel shows the projection on the x-y plane. The starting position of the two pathlines are symmetrically placed on either side of the x-y plane, thus the two pathlines coincide on the right panels. At Re=200, when the flow is steady and axisymmetric, the wake bubble is closed and the streamlines are the same as pathlines. From Fig. 1(*a*) it can be seen that pathlines that originate upstream of the cylinder go around the closed bubble, suggesting that there is no mixing in the wake. At Re=250, axisymmetry is broken and results in certain amount of mixing between the wake fluid and the oncoming freestream fluid. At even higher Reynolds number (Re=350) the wake is unsteady and as a result of the vortex shedding process a wake bubble exists only in the mean; significant mixing between the wake and the freestream fluid can be observed. Based on this enhanced mixing one might expect higher heat transfer in the wake when the assumption of axisymmetry is relaxed. On the other hand, in the case of axisymmetric flow, a focused recirculation region exists and one can expect a strong stagnation point flow directed toward the wake region in this case. From Fig. 8 it is clear that at Re=350, the strength and the influence of the recirculation eddy far outweighs any potential benefits of enhanced mixing due to three-dimensionality, as far as heat transfer is concerned.

Figure 11 shows time evolution of drag and lift coefficients and surface-averaged Nusselt number (Nu) for Re=350. The results obtained from the 3D simulation are compared with those obtained from the axisymmetric simulation. Also shown are the time averaged results for the 3D simulation (the axisymmetric results are steady state). The signature of vortex shedding is evident in the time-dependent oscillatory nature of C_D, C_L, and $\overline{\text{Nu}}$. As indicted earlier, the shedding process appears to be irregular at Re=350 and therefore a perfect periodic variation is not observed. The approximate shedding period, based on average time between adjacent peaks in the lift coefficient is $T_p=14.8$, corresponding to a nondimensional Strouhal number ($\text{St}=d/U_\infty T_p$) of 0.135. As expected the oscillation in drag coefficient is at about twice the shedding frequency. The time averaged drag coefficient obtained from the 3D simulation is 0.62 and the corresponding axisymmetric approximation underpredicts drag coefficient by about 5% with a C_D of 0.58. This underprediction of drag when three-dimensionality is ignored is contrary to the case of two-dimensional cylinders, where drag is overpredicted when the effect of three-dimensionality in the wake is ignored (Mittal and Balachandar [21]).

The difference in behavior is significant and can be explained as follows. In the case of a cylinder, vortex shedding is possible even when restricted to 2D simulation and in fact the shed vortices are stronger and remain more coherent in the absence of three-dimensionality. As a result, the Reynolds stress distribution in the wake is higher in 2D simulation. The enhanced Reynolds stress leads to higher suction pressure and overprediction of drag. In the case of a sphere, the assumption of axisymmetry precludes vortex

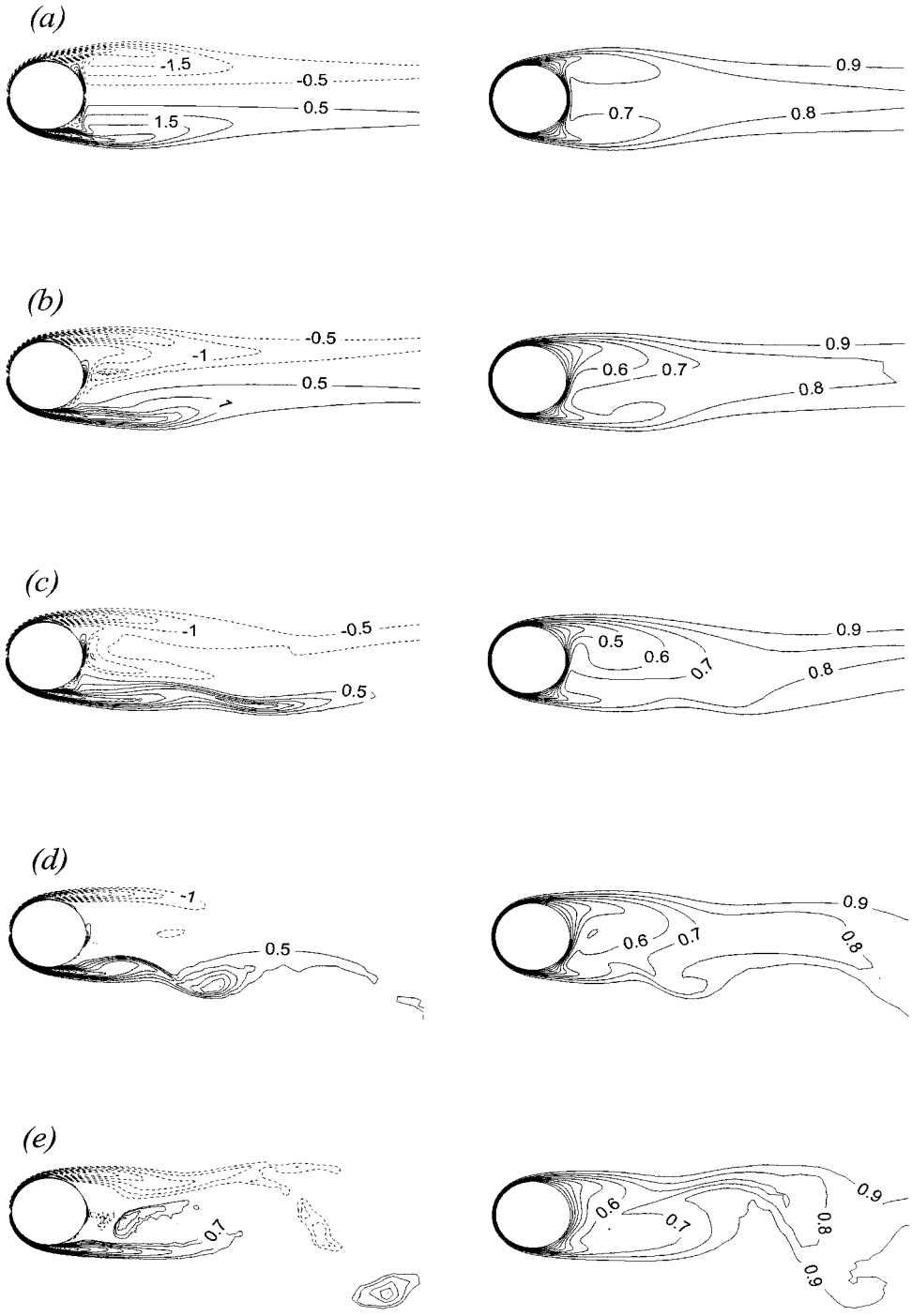

Fig. 13 Same as Fig. 7 but for Re=500. Time instants for the unsteady simulations (*b*, *c*, *d* and *e*) are at approximately equal interval in a shedding cycle.

shedding and time dependence; thus Reynolds stress is zero. The pressure distribution around the surface of the sphere with and without the assumption of axisymmetry is shown in Fig. 12. In the case of three-dimensional simulations ϕ-averaged surface pressure is plotted. Pressure distribution over the windward side is not significantly influenced by differences in the wake structure; however, substantial differences exist in the wake region and, in particular, the effect of three-dimensionality is to decrease the base pressure, thus explaining the higher drag.

Furthermore, unlike the case of a circular cylinder, for the sphere the time-averaged lift is nonzero. The mean C_L is observed to be -0.06 and is consistent with the one-sided shedding of the wake vortices. The plane of symmetry that was observed at Re $=250$ persists even at Re$=350$, which can be seen in the x-z projection of pathline in Fig. 10.

Figure 13 shows contours of azimuthal vorticity and dimensionless temperature at a even higher Reynolds number of Re$=500$, obtained with an axisymmetric assumption (Fig. 13(*a*)) and from the three-dimensional time-dependent simulation (Figs. 13(*b*)–(*e*)). In the case of time-dependent simulation four different time instances are shown, which are separated by approximately (1/3)rd shedding period. At this Re, the wake oscillation can be seen to have increased with a more chaotic shedding pattern with larger and stronger vortices than that for Re$=350$. As a result, deviation

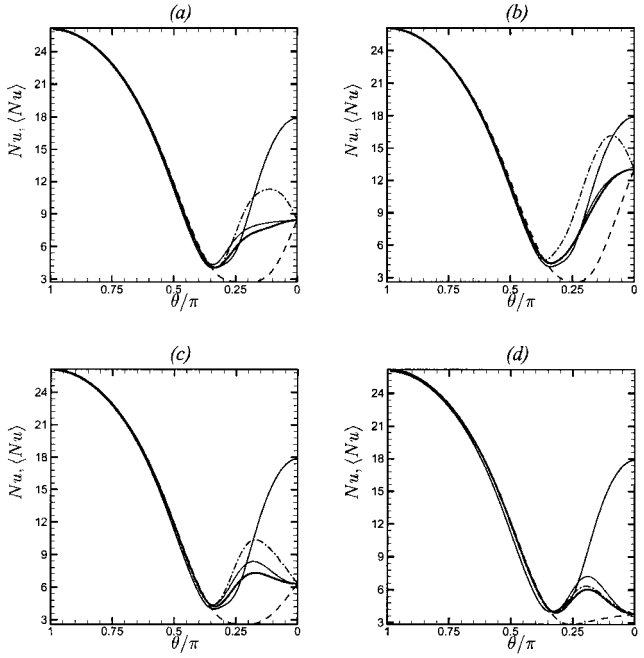

Fig. 14 Variation of Nusselt number for Re=500 at four different time instants: *a*, *b*, *c* and *d* represent same time instants as in Fig. 13 corresponding to the unsteady simulation. Symbols used here are same as in Fig. 8.

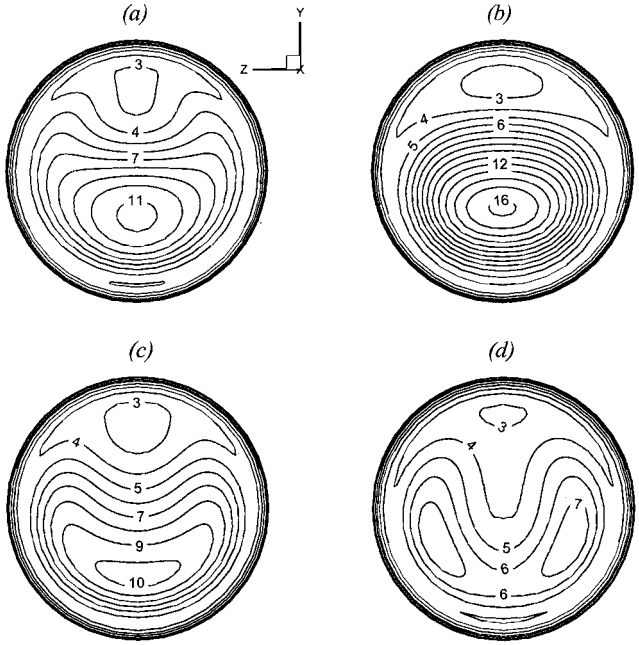

Fig. 15 Same as Fig. 9 but for Re=500. Results from 3D simulations are shown at four different time instants that are same as in Fig. 14.

in both azimuthal vorticity and temperature fields from the axisymmetric case is enhanced. Figure 14 shows the θ-variation in local and ϕ-averaged Nusselt number at the four different time instances shown in Fig. 13 obtained from the 3D simulation. Also shown for comparison are the local Nusselt number obtained from the axisymmetric simulation. The impact of strong vortex shedding at this Reynolds number can be seen in the large temporal-variation in the Nusselt number in the wake region. For example, the local Nu at $\theta=0$ can be seen to vary between 3.6–13.0 over a shedding cycle. As a result the axisymmetric prediction can grossly overestimate local heat transfer in the wake region over most of the shedding cycle. The time-averaged local Nu at $\theta=0$ is about 7.9, while the corresponding prediction by the axisymmetric simulation is about 18, resulting in a overprediction of 130%. Of course, the overprediction in terms of instantaneous local heat transfer can be even higher.

The location and the motion of the separation and the rear stagnation points can be further investigated in the contours of local Nusselt number on the sphere surface shown in Fig. 15. The 3D results are shown corresponding to the four time instances shown in Fig. 13. Due to the strong vortex shedding in the wake region, contours of local Nusselt numbers on the sphere surface in the wake have a nonconcentric shape. Strong time-dependence is also observed. When compared to Fig. 9 the extent of deviation from axisymmetry is observed to increase with increasing Reynolds number. Especially in Fig. 15(*d*) the contours can be observed to symmetrically split into two with local peaks located on either side of the *x*-*y* plane, whereas the local minima still remains on the *x*-*y* plane. As a result, at this time a local peak is observed in the ϕ-averaged Nusselt number as well at about $\phi=45$ deg.

Figure 16 shows time evolution of drag and lift coefficients and surface-averaged Nusselt number for Re=500. At this Reynolds number the shedding process appears to be more chaotic than at Re=350 and the approximate nondimensional shedding frequency increases to 0.175. The time averaged drag coefficient obtained from the 3D simulation is 0.555 and the corresponding axisymmetric approximation underpredicts drag coefficient by about 10% with a C_D of 0.487. Thus the importance of three-dimensionality in accurately predicting drag increases with Re. The mean C_L is observed to be -0.048.

At Re=500 the plane of symmetry that was observed at lower Reynolds numbers is somewhat broken. The chaotic shedding process is now seen to slightly oscillate—vortices are now shed over a range of azimuthal angles. Yet the transition from one-sided to all-around shedding is not complete at this Re. As a result, there is a mean negative lift. However, compared to Re =350 the mean negative lift is smaller in magnitude, in spite of the stronger shedding process. It can be conjectured that at even higher Re, when the near wake behavior is turbulent, vortex shedding may precess over the entire range of azimuthal angles. Correspondingly, the direction of lift force may drift in direction over time, thus resulting in a zero net lift force over long time average. However, in the present simulations up to Re=500, we observe the lift force to be persistent in direction over more than 15 shedding cycles. The mean lift coefficients presented here are obtained through long time average over several shedding cycles—18 shedding cycles in case of Re=350 and 15 shedding cycles in case of Re=500.

From Fig. 12 substantial influence of three-dimensionality on pressure distribution in the wake region can be observed. Although surface pressure distributions for Re=350 and Re=500 cases are qualitatively the same, increasing importance of three-dimensionality on C_D with increasing Re is clear. Mean drag is evaluated by integrating the surface pressure around the sphere with a weighting factor of sin (2θ) (see Eq. (2)). Thus large difference in base pressure at $\theta=0$ makes little contribution to drag coefficient. The underprediction of drag coefficient is mainly due to differences in surface pressure distribution in the wake around $\theta=\pi/4$.

In Figs. 11 and 16 the time-averaged Nu in the case of 3D simulations is observed to be 11.42 and 13.27 at Re=350 and 500, respectively. With the assumption of axisymmetry the overall heat transfer is overpredicted by about 2% in both cases with $\overline{\mathrm{Nu}}$ =11.62 and 13.54. Thus the impact of three-dimensionality on overall heat transfer seems to be minimal and independent of Reynolds number. However, the effect of three-dimensionality cannot

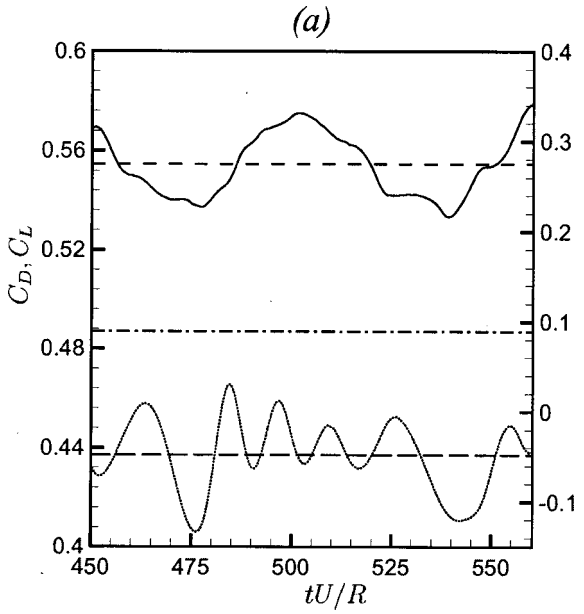

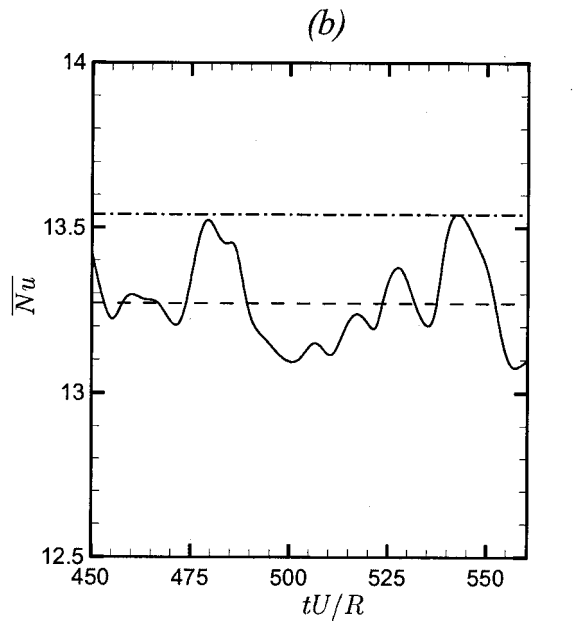

Fig. 16 Same as Fig. 11 but for Re=500

be ignored when it comes to local heat transfer behavior. Three-dimensionality has a strong influence on local heat transfer. As indicated in Figs. 8 and 14, local Nu near the base of the sphere can be overpredicted by several hundred percent if the flow is constrained to be axisymmetric. The difference in the local and surface-averaged behavior can be seen from the definition of $\overline{\mathrm{Nu}}$ (Eq. (5)), where local Nusselt number is integrated with the geometric weighting factor of $\sin(\theta)$. Most contribution to $\overline{\mathrm{Nu}}$ is from the equatorial region, with very little contribution from region near the poles. Thus the impact of vortex shedding on local heat transfer is much stronger than on overall heat transfer. Accurate computation of local heat transfer is important in the prediction of processes, such as evaporation, surface reaction, and surface tension, which are nonlinearly (often exponentially) dependent on temperature.

Figures 17 and 18 summarize the results of the three-dimensional simulations. C_D, C_L, and Nu obtained from the

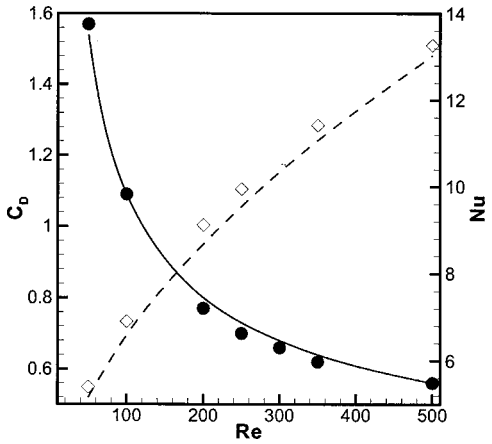

Fig. 17 Comparison of computational C_D and Nu with experimental correlations. Symbols are computational results ranging from Re=50–500. Correlation for drag is from Clift et al. [1] and the Nu correlation is from Ranz and Marshall [11].

simulations over the Reynolds number range of 50–500 are compared with popular correlations for drag and heat transfer from a sphere given as

$$C_D=\frac{24}{\mathrm{Re}}(1+0.15\ \mathrm{Re}^{0.687}) \quad \text{Clift et al. [1]}$$

$$\overline{\mathrm{Nu}}=2+(0.4\ \mathrm{Re}^{1/2}+0.06\ \mathrm{Re}^{2/3})\mathrm{Pr}^{0.4} \quad \text{Whitaker [12]}$$

$$\overline{\mathrm{Nu}}=2+0.6\ \mathrm{Re}^{1/2}\,\mathrm{Pr}^{1/3} \quad \text{Ranz and Marshall [11]}$$

The lift coefficient is zero for Re<210, as the flow is axisymmetric. Above Re=210 the lift coefficient is non-zero reaching a peak value of about −0.07 at Re=300. At higher Reynolds numbers the mean lift coefficient somewhat decreases, but remains non-zero, at least up to Re=500. At very large Reynolds number long time-averaged lift coefficient can be expected to approach zero owing to the turbulent nature of the wake; however, over shorter periods persistent lift force is possible. Also included in Fig. 18 are mean lift coefficient data from Johnson and Patel [6] for 210 <Re<300. Good agreement with the present data can be observed. The correlations shown above are based on several experimental measurements over a range of Reynolds number and therefore comparison with individual experimental measurement

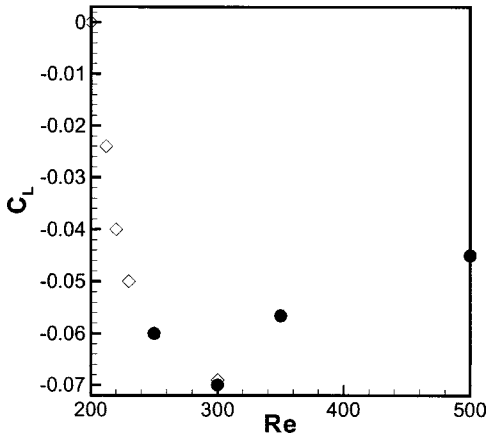

Fig. 18 The mean (time-averaged) lift coefficient versus Reynolds number for flow past a sphere. ● symbols are the results from present simulations. ◇ symbols correspond to simulation results of Johnson and Patel [6].

Table 1 Comparison of present simulations with previous experimental and numerical results

	Present simulations					Previous results				
Re	C_D	θ_s	L_e/D	St	Nu	C_D	θ_s	L_e/D	St	$Nu^{\ddagger}$
50	1.57	40.8	0.41		5.4	1.57*	40.0†	0.44*		5.16, 5.77
100	1.09	53.2	0.87		6.91	1.09*	53.6†	0.87*		6.59, 7.32
200	0.77	63.7	1.43		9.12	0.78*	65.0†	1.29†		8.68, 9.53
250	0.70				9.95	0.70*				9.55, 10.42
350	0.62			0.135	11.42	0.62*			0.13–0.14¶	11.07, 11.97
500	0.56			0.175	13.27	0.55*			0.17–0.18¶	13.03, 13.91

*Clift et al. [1];
†Magnaudet et al. [23];
¶Sakamoto & Haniu [22];
‡First Nu is obtained from Ranz and Marshal [11]; and the second value is from Whitaker [12]. For Re≥250, mean properties are listed.

is not attempted. Good agreement between these correlations and the simulation results is observed over the entire range of Reynolds numbers considered. For further validation of the present simulation; Table 1 shows a comparison of present results for separation angle (θ_s), dimensionless wake length (L_e), Strouhal number (St) for different Reynolds numbers with previous experimental and numerical results. The results for Re≥210 are surface-averaged mean values. The present results for θ_s and L_e show excellent agreement with the experimental and numerical ones over the Reynolds number ranges listed in Table 1. The Strouhal numbers for Re=350 and 500 are also in good agreement with experimental results given by Sakamoto and Haniu [22].

Summary and Conclusions

The heat transfer past a sphere in a uniform flow is investigated using direct numerical simulation. The solution is obtained using a highly accurate Fourier-Chebyshev pseudospectral method. When the Reynolds number is less than 210, the flow and temperature fields are axisymmetric. When Reynolds number increases above 210 (at Re=250), the flow and temperature fields become non-axisymmetric but without vortex shedding. But the deviation of 3D results from the axisymmetric ones is small and C_D and Nu from the 3D simulation are almost the same as those from axisymmetric one. When Reynolds number exceeds 270 (Re=350 and 500), the flow and temperature fields become highly three-dimensional with strong vortex shedding. Local Nusselt number distribution on the surface of the sphere significantly deviates from concentric distribution; strong variation in local Nu over time is observed, especially in the wake region.

Vortex shedding and three-dimensionality of the wake has a stronger influence on the mean drag force. Their influence on mean drag increases with Reynolds number; this behavior for the wake of a sphere is consistent with the importance of three-dimensionality in the wake of a circular cylinder. For the sphere, axisymmetric approximation results in underprediction of drag coefficient; this is in contrast to the circular cylinder where two-dimensional approximation results in overprediction of drag. In the case of a sphere, the assumption of flow axisymmetry precludes any vortex shedding (at least up to Re=500) and as a result temporal oscillations in lift and drag forces and surface averaged Nusselt number are features of only the 3D simulation. Vortex shedding off a sphere is predominantly one-sided, which results in a small but finite time-averaged lift coefficient.

Three-dimensionality has its strongest effect on the local heat transfer in the wake region. Heat transfer near the base of the sphere ($\theta \approx 0$) will be overpredicted by several hundred percent if three-dimensionality of the wake is ignored. This is due to the highly enhanced stagnation point flow resulting from the strong coherent recirculation bubble predicted in the case of axisymmetric assumption. In spite of this strong local effect, the impact on surface averaged Nu is not significant, owing to the smaller area associated with the base region. Thus, if the interest is only in surface-averaged heat transfer then a simple axisymmetric simulation itself is sufficient. However, the instantaneous 3D local Nusselt number exhibits significant deviation from the axisymmetric prediction. This difference in local heat transfer can be important when we consider evaporation and combustion of a liquid droplet (or surface reaction of a particle), where the fuel mass fraction on the droplet surface is expressed as an exponential function of droplet surface temperature according to the Clausius-Clapeyron relation. This shows that the mass transfer rate from the droplet is a strong function of local droplet temperature and very sensitive to local heat transfer rate. In such applications, it is important to predict the local behavior of Nusselt number correctly through the 3D calculation.

Acknowledgments

This work was supported by the Center for Simulation of Advance Rockets under a grant from the Department of Energy ASCI program. Prof. Ha wishes to express his appreciation for the financial support provided by LG Yonam Foundation. The computations presented here were performed with computer support from the National Center for Supercomputing Application. PB and SB would like to thank Dr. J. P. Ferry for helping with some of the simulations.

References

[1] Clift, R., Grace. J. R., and Weber, M. E., 1978, *Bubbles, Drops and Particles*, Academic Press, New York.
[2] Faeth, G. M., 1983, ''Evaporation and Combustion of Sprays,'' Prog. Energy Combust. Sci., **9**, pp. 1–76.
[3] Law, C. K., 1982, ''Recent Advances in Droplet Vaporization and Combustion,'' Prog. Energy Combust. Sci., **8**, pp. 171–201.
[4] Natarajan, R., and Acrivos, A., 1993, ''The Instability of the Steady Flow Past Spheres and Disks,'' J. Fluid Mech., **254**, pp. 323–344.
[5] Tomboulides, A. G., Orszag, S. A., and Karniadakis, G. E., 1993, ''Direct and large-eddy simulation of axisymmetric wakes,'' AIAA Paper 93-0546.
[6] Johnson, T. A., and Patel, V. C., 1999, ''Flow past a sphere up to a Reynolds number of 300,'' J. Fluid Mech., **378**, pp. 19–70.
[7] Kurose, R., and Komori, S., 1999, ''Drag and lift forces on a rotating sphere in a linear shear flow,'' J. Fluid Mech., **384**, pp. 183–206.
[8] Mittal, R., 1999, ''A Fourier Chebyshev spectral collocation method for simulation flow past spheres and spheroids,'' to appear in Int. J. Numer. Meths. Fluids.
[9] Bagchi, P., and Balachandar, S., 2000, ''Unsteady motion and forces on a spherical particle in nonuniform flows,'' *Proceedings of FEDSM 2000*, Boston, MA.
[10] Sayegh, N. N., and Gauvin, W. H., 1999, ''Numerical Analysis of Variable Property Heat Transfer to a Single Sphere in High Temperature Surroundings,'' AIChE J., **25**, pp. 522–534.
[11] Ranz, W. E., and Marshall, W. R., 1952, ''Evaporation From Drops,'' Chem. Eng. Prog., **48**, pp. 141—146.
[12] Whitaker, S., 1972, ''Forced Convection Heat Transfer Correlations for Flow in Pipes, Past Flat Plates, Single Spheres, and for Flow in Packed Beds and Tube Bundles,'' AIChE J., **18**, pp. 361–371.
[13] Renksizbulut, M., and Yuen, M. C., 1983, ''Numerical Study of Droplet Evaporation in a High-Temperature Stream,'' ASME J. Heat Transfer, **105**, pp. 389–397.
[14] Wong, K., Lee, S., and Chen, C., 1986, ''Finite Element Solution of Laminar

Combined Convection From a Sphere,'' ASME J. Heat Transfer, **108**, pp. 860–865.
[15] Yuge, T., 1960, ''Experiments on Heat Transfer From Spheres Including Combined Natural and Forced Convection,'' ASME J. Heat Transfer, **82**, pp. 214–220.
[16] Chiang, C. H., Raju, M. S., and Sirignano, W. A., 1992, ''Numerical Analysis of Convecting, Vaporizing Fuel Droplet With Variable Properties,'' Int. J. Heat Mass Transf., **35**, No. 5, pp. 1307–1324.
[17] Xin, J., and Megaridis, C. M., 1996, ''Effects of Rotating Gaseous Flows on Transient Droplet Dynamics and Heating,'' Int. J. Heat Fluid Flow, **17**, pp. 52–62.
[18] Dandy, D. S., and Dewyer, H. A., 1990, ''A Sphere in Shear Flow at Finite Reynolds Number: Effect of Shear on Particle Lift, Drag, and Heat Transfer,'' J. Fluid Mech., **216**, pp. 381–410.
[19] Mittal, R., and Balachandar, S., 1996, ''Direct numerical simulation of flow past elliptic cylinders,'' J. Comp. Phys., **124**, pp. 351–367.
[20] Wu, J-S., and Faeth, G. M., 1993, ''Sphere Wakes in Still Surroundings at Intermediate Reynolds Numbers,'' AIAA J., **254**, pp. 323–344.
[21] Mittal, R., and Balachandar, S., 1995, ''Effect of three-dimensionality on the lift and drag of nominally two-dimensional cylinders,'' Phys. Fluids, **7**, pp. 1841–1865.
[22] Sakamoto, H., and Haniu, H., 1995, ''The formation mechanism and shedding frequency of vortices from a sphere in uniform shear flow,'' J. Fluid Mech., **287**, pp. 151–171.
[23] Magnaudet, J., Rivero, M., and Fabre, J., 1995, ''Accelerated flows past a rigid sphere or a spherical bubble. Part 1. Steady straining flow,'' J. Fluid Mech., **284**, pp. 97–135.

Random Flow Generation Technique for Large Eddy Simulations and Particle-Dynamics Modeling

A. Smirnov
S. Shi
I. Celik

Department of Mechanical and Aerospace Engineering,
West Virginia University,
Morgantown, WV 26506-6106
e-mail: andrei@smirnov.mae.wvu.edu

A random flow generation (RFG) technique is presented, which can be used for initial/inlet boundary generation in LES (Large-Eddy-Simulations) or particle tracking in LES/RANS (Reynolds-Averaged Navier-Stokes) computations of turbulent flows. The technique is based on previous methods of synthesizing divergence-free vector fields from a sample of Fourier harmonics and allows to generate non-homogeneous anisotropic flow field representing turbulent velocity fluctuations. It was validated on the cases of boundary layer and flat plate flows. Applications of the technique to LES and particle tracking are considered. [DOI: 10.1115/1.1369598]

1 Introduction

In a Reynolds Averaged Navier-Stokes (RANS) turbulence modeling approach information about turbulent fluctuations is contained in the time averaged Reynolds stresses of the form $\overline{u_i u_j}$. These are obtained as an outcome of a turbulence model that links Reynolds Stresses to mean flow quantities (e.g., k-ϵ model), or solves modeled transport equations for each Reynolds stress component (e.g., Reynolds stress models). However, this is not the case when the large eddy simulation (LES) methodology is employed since the goal here is to explicitly resolve the turbulent fluctuations. In LES the inlet conditions cannot be derived directly from experimental results, because of the unsteady and pseudo-random nature of the flow being resolved, unless, off course, the turbulent intensity is zero at the inlet, which is rarely the case. This problem becomes more important for spatially developing turbulent flows where, for example, the boundary or shear layer thickness changes rapidly. In such cases periodic boundary conditions cannot be specified as in the case of a fully developed channel flow (Ravikanth and Pletcher [1], Akselvoll and Moin [2]). A similar situation exists when prescribing the initial conditions over the whole calculation domain. This can be of importance when the turbulent flow is not steady in the mean (i.e., nonstationary turbulence) and the transients of the flow are to be resolved. Even for stationary turbulent flows, if realistic initial conditions are not prescribed, the establishment of a fully developed turbulence takes unreasonably long execution time. For these reasons, it is necessary to initialize the flow-field with some form of perturbation to provide the initial turbulent conditions. It is important that the perturbation be spatially correlated, as is the case with the real flow. For external flow problems the turbulent flow field can be initiated simply by appropriately perturbing the inlet flow-field. In this case an accurate representation of temporal correlations of the flow-field can be important. The inlet perturbation propagates throughout the domain and helps trigger the turbulence that is to be captured. Many applications of LES begin with initializing the flow field to that of a previously obtained RANS solution. A higher resolution grid is then used with an appropriate subgrid-scale model. The Reynolds stress terms provided by the RANS solution can be used to construct spatially and temporally correlated perturbed inlet and initial conditions. In principle, it is possible to predict turbulence via LES technique by starting from a quiescent flow or with the mean flow obtained from RANS. Unfortunately, it takes a very long time for a turbulent flow to develop spatially and temporally. This is especially true in the case of decaying turbulence in the absence of strong turbulence generating factors like walls. A reasonably accurate approach to this problem is used in modeling of boundary layer turbulence (Lund [3]). It consists in applying a separate flow solver with periodic boundary conditions to construct the inlet conditions for the LES/DNS solver. It provides well-formed inflow conditions consistent with the solution of the Navier-Stocks equation, which makes it particularly suitable for DNS. However, its implementation may not be straightforward for the problems without well-defined fully developed boundary/shear layers. For some engineering problems it may also be too expensive in the usage of computer resources and programming effort.

To remedy this problem the inlet and initial conditions are often viewed as consisting of a mean component and a randomly fluctuating component with the appropriate statistics. Most of the work done in this direction is based on simplified variants of a spectral method, in which Fourier harmonics are generated with the appropriate statistics and assembled into a random flow-field. Realistic turbulence spectra can be realized in this way. In the work of Lee et al. [4] for example, a very good representation of turbulence spectra was achieved by using Fourier harmonics with a random phase shift. This is a rather efficient method to generate the inflow turbulence with predefined characteristics. However, it does not satisfy the continuity of the flow-field, which may be important in diminishing the nonphysical transition region between the inlet flow-field and the solution provided by the Navier-Stokes solver inside the computational domain.

A considerable amount of work in random flow generation has been performed in the area of particle dispersion modeling using the RANS approach (Zhou and Leschziner [5], Zhou and Leschziner [6], Li et al. [7]). RANS modeling produces smooth flow fields, which do not accurately disperse particles that are embedded in the flow. To correct this turbulent Reynolds stresses are used to generate temporally and spatially correlated fluctuations, such that the resultant instantaneous velocity can be superimposed on the particles to induce a realistic dispersion. A number of approaches found in the literature (Li et al. [7], Bechara et al. [8], Fung et al. [9]) are based on a variant of spectral method of generating an isotropic continuous flow-field proposed earlier by Kraichnan [10]. However, this flow-field does not satisfy the requirement of spatial inhomogeneity and anisotropy of turbulent shear

Contributed by the Fluids Engineering Division for publication in the JOURNAL OF FLUIDS ENGINEERING. Manuscript received by the Fluids Engineering Division March 31, 2000; revised manuscript received February 16, 2001. Associate Editor: G. Karnia Dakis.

stresses, which may be important in realistic flows. The method of Zhou and Leschziner [5] complies with the latter requirement, but the resultant flow field does not satisfy the continuity condition and is spatially uncorrelated. For homogeneous isotropic turbulence, the initial conditions can also be constructed as described by Ferziger [11]. The approach is based on a vector curl operation and forward/backward Fourier transforms, which require a considerable computational effort. The extension of this method to anisotropic inhomogeneous flows is not trivial. At least one study presents a successful application of Kraichnan's method to anisotropic flows (Maxey [12]). The technique is based on filtering and scaling operations applied to the generated isotropic flow-field to filter only the vectors with the prescribed correlations. Again, the filtering operation may be expensive computationally. The method presented in this paper is different in that it is based only on scaling and simple coordinate transformation operations, which are efficient and fast.

It is the objective of this study to formulate a relatively simple random flow generation (RFG) algorithm, which can be used to prescribe inlet conditions as well as initial conditions for spatially developing inhomogeneous, anisotropic turbulent flows. In principle, the same procedure can also be used for initializing direct numerical simulations, but the focus of our study is on LES, and particle tracking applications. The method takes advantage of the previous studies in the area of particle dispersion (Li et al. [7], Maxey [12]). The RFG procedure is developed on the basis of the work of Kraichnan [10], and can be used as an efficient random flow-field generator in LES and in particle tracking (Shi et al. [13]; Smirnov et al. [14]). The technique was validated on the cases of boundary-layer and flat-plate shear layer flows and is further illustrated on the example of bubbly ship-wake flow as one of the most challenging cases for LES and particle dynamics applications. Performing LES of ship wakes is particularly difficult given the fact that the whole ship must be modeled to capture a relatively thin 3D-boundary layer, preferably including the viscous sublayer. The boundary layer is the source of the flow dynamics that sets the initial conditions for the wake. A simulation that includes the whole ship and the wake would require prohibitively large computational resources. It is proposed in this study that the needed computational resources could be substantially reduced if the appropriate time-dependent inlet conditions could be constructed at the beginning of the wake, thus avoiding the need to model the entire ship.

2 Methodology

To generate a realistic flow field we propose a modified version of Kraichnan's technique (Kraichnan [10]). The procedure we call RFG (random flow generation) combines the advantages of the approaches mentioned above and is also computationally efficient. It involves scaling and orthogonal transformation operations applied to a continuous flow-field generated as a superposition of harmonic functions. The procedure consists of the following steps.

1 Given an anisotropic velocity correlation tensor

$$r_{ij} \equiv \overline{\tilde{u}_i \tilde{u}_j} \tag{1}$$

of a turbulent flow field $\{\tilde{u}_i(x_j,t)\}_{i,j=1..3}$, find an orthogonal transformation tensor a_{ij} that would diagonalize r_{ij}[1]

$$a_{mi} a_{nj} r_{ij} = \delta_{mn} c_{(n)}^2 \tag{2}$$

$$a_{ik} a_{kj} = \delta_{ij} \tag{3}$$

As a result of this step both a_{ij} and c_n become known functions of space. Coefficients $c_n = \{c_1, c_2, c_3\}$ play the role of turbulent fluctuating velocities (u', v', w') in the new coordinate system produced by transformation tensor a_{ij}.

2 Generate a transient flow-field in a three-dimensional domain $\{v_i(x_j,t)\}_{i,j=1..3}$ using the modified method of Kraichnan (Kraichnan [10])

$$v_i(\vec{x},t) = \sqrt{\frac{2}{N}} \sum_{n=1}^{N} \left[p_i^n \cos(\tilde{k}_j^n \tilde{x}_j + \omega_n \tilde{t}) + q_i^n \sin(\tilde{k}_j^n \tilde{x}_j + \omega_n \tilde{t}) \right] \tag{4}$$

$$\tilde{x}_j = \frac{x_j}{l},\ \tilde{t} = \frac{t}{\tau},\ c = \frac{l}{\tau},\ \tilde{k}_j^n = k_j^n \frac{c}{c_{(j)}} \tag{5}$$

$$p_i^n = \varepsilon_{ijm} \zeta_j^n k_m^n,\ q_i^n = \varepsilon_{ijm} \xi_j^n k_m^n \tag{6}$$

$$\zeta_i^n,\ \xi_i^n,\ \omega_n \in N(0,1),\quad k_i^n \in N(0,1/2)$$

where l, τ are the length and time-scales of turbulence, ε_{ijk} is the permutation tensor used in vector product operation (Spain [15]), and $N(M,\sigma)$ is a normal distribution with mean M and standard deviation σ. Numbers k_j^n, ω_n represent a sample of n wavenumber vectors and frequencies of the modeled turbulence spectrum

$$E(k) = 16 \left(\frac{2}{\pi} \right)^{1/2} k^4 \exp(-2k^2) \tag{7}$$

3 Apply a scaling and orthogonal transformations to the flow-field v_i generated in the previous step to obtain a new flow-field u_i

$$w_i = c_{(i)} v_{(i)} \tag{8}$$

$$u_i = a_{ik} w_k \tag{9}$$

The procedure above takes as input the correlation tensor of the original flow-filed r_{ij} and information on length- and time-scales of turbulence (l,τ). These quantities can be obtained from a steady-state RANS computations or experimental data. The outcome of the procedure is a time-dependent flow-field $u_i(x_j,t)$ with correlation functions $\overline{u_i u_j}$ equal to r_{ij} and turbulent length/time scales equal to l,τ. As will be shown later this flow-field is also divergence free for a homogeneous turbulence and to a high-degree divergence-free for an inhomogeneous turbulence. By virtue of Eq. (4), spatial and temporal variations of u_i follow Gaussian distribution with characteristic length and time-scales of l, τ. Sampling for a different spectrum instead of Gaussian can also be used in different problems.

Equation (8), provides the scaling, and (9) the orthogonal transformation. Scaling factors c_i obtained in step II represent the scales of turbulent fluctuations along each axis. They do not depend on time, whereas vectors v_i and w_i represent time-dependent velocity fluctuations. Both the scaling factors c_i and the transformation tensor a_{ij} are computed in step II using efficient matrix diagonalization routines that can be found in standard libraries or programmed specifically for a 3D case to boost the performance. By construction, the correlation tensor of the flow-field produced by Eq. (4) is diagonal

$$\overline{v_i v_j} = \delta_{ij} \tag{10}$$

The flow-field w_i produced after the scaling transformation (8) is divergence free for a homogeneous turbulence and nearly divergence free for an inhomogeneous turbulence, as is shown by the following estimate

$$\begin{aligned} w_{i,i} &= c_{i,i} v_i + c_i v_{i,i} \approx c_i v_{i,i} \\ &= \frac{c}{l} \sqrt{\frac{2}{N}} \sum_{n=1}^{N} \left[-p_i^n k_i^n \sin\left(\frac{c}{c_j} k_j^n \frac{x_j}{l} + \omega_n \frac{t}{\tau} \right) \right. \\ &\quad \left. + q_i^n k_i^n \cos\left(\frac{c}{c_j} k_j^n \frac{x_j}{l} + \omega_n \frac{t}{\tau} \right) \right] = 0 \end{aligned} \tag{11}$$

$$\Rightarrow w_{i,i} \approx 0 \tag{12}$$

where we neglected all derivatives of c_i, which are slowly varying functions of $\vec{x}$, and used the relation of orthogonality between k_i^n and p_i^n, q_i^n

$$k_i^n p_i^n = k_i^n q_i^n = 0$$

[1] $f_{,i} \equiv \partial f / \partial x_i$. Repeated subindexes imply summation, parentheses around indexes preclude summation.

which follows from the way vectors p_i^n, q_i^n are constructed in (6). For a homogeneous turbulence the approximate equality in (11) will become a strict equality, leading to a divergence free flow-field. In the case of inhomogeneous turbulence the justification for neglecting the derivatives of c_i comes from the fact that c_i are derived from the correlation tensor r_{ij}, which is produced by the time-averaging operation in (1). As a result of this averaging r_{ij} is independent of time and may be a slowly varying function of space as compared to the fluctuating velocity u_i

$$\|c_{i,j}\| \approx \|r_{ij,k}\|^{1/2} \ll \|u_{i,j}\| \tag{13}$$

where $\|\cdot\|$ denotes an appropriate function norm. Relation (13) justifies the first approximate equality in (11), leading to an approximate satisfaction of continuity.

The orthogonal transformation (9) preserves the solenoidal (divergence-free) property of the flow-field

$$u_{i,i} = a_{ij}a_{ki}w_{j,k} = \delta_{jk}w_{j,k} = w_{j,j} = 0 \tag{14}$$

where we used relation (12) and the rule of transformation of derivatives: $f'_{,i} = a_{ji}f_{,j}$. Thus, the generated flow-filed u_i is divergence-free within the accuracy determined by (13). At the same time the new flow field satisfies the anisotropy of the original flow-field $\vec{u}(\vec{x},t)$, i.e.,

$$\begin{aligned}\overline{u_i u_j} &= \overline{a_{im}w_m\, a_{jn}w_n} \\ &= a_{im}a_{jn}\overline{w_m\, w_n} = a_{im}a_{jn}c_m c_n \overline{v_m\, v_n} \\ &= a_{im}a_{jn}c_m c_n \delta_{mn} = a_{im}a_{jn}\delta_{mn}(c_n)^2 = r_{ij}\end{aligned} \tag{15}$$

where we used relations (3), (8) and the last equality was obtained by solving (2) for r_{ij}. Thus, the obtained flow-field $u_i(\vec{x},t)$ is transient, divergence-free, inhomogeneous, and anisotropic with the pre-defined correlation coefficients.

Considering the flexibility and computational efficiency of the algorithm, we should note that the random spectrum sampling in Eq. (6) can be performed separately from the actual assembly of the vectors in Eq. (4). This leads to a higher computational efficiency, since the spectrum sampling can be done outside of the main time iteration loop of the flow solver with only the assembly of fluctuating velocity components left inside the time loop. This efficiency comes at a price of extra memory requirements for storing the random sample. The size of this sample is equal to $10 \cdot \mathrm{N}$, where N is the number of harmonic functions representing the turbulent spectrum in (4), which is independent of the actual grid size. So, for $N = 1000$ and double precision arithmetics only $80\,KB$ of computer memory will be needed to store the spectrum for any grid size. This offers a flexibility of shifting the priorities between the high-accuracy spectrum generation and speed.

The RFG procedure can be extended to include the anisotropy of turbulence length-scale. In this case instead of using a scalar value for l in (5) one can define a vector l_i. An appropriate re-scaling would be necessary to preserve the continuity of the flow-field. This can be done by introducing another scaling transformation, similar to (8), which will guarantee that the resultant flow-field is divergence-free.

It should be noted that the turbulent flow-field obtained by the RFG procedure does not represent the solution of a complete Navier-Stokes (NS) equation, but rather of a continuity equation only. This is not a severe limitation, since the procedure is used mainly in the context of unsteady 3D computations, like LES, to generate initial or inlet boundary conditions. These conditions are given on three-dimensional subsets of a four-dimensional computational domain: two space and one time dimension for the inlet flow-filed and three space and zero time dimensions for the initial flow-field. As such these flow-fields do not have to satisfy the NS equation, since for an unsteady LES this equation is defined on a four-dimensional, 3-space $\times$ 1-time domain. However, the boundary conditions should be reasonably continuous, so that the NS solver will gracefully adjust the solution to the boundary conditions within the computational domain. This is exactly what the RFG procedure is designed to do. In addition to this, it provides the desired statistical characteristics of turbulence at the boundaries, like anisotropy and inhomogeneity, which is of importance for LES and unsteady particle-dynamics computations.

Naturally, this approach to generate the inlet/initial boundary conditions is an approximation and should be used only when the statistical features of turbulence at the boundaries are of special concern while the solution of a full unsteady NS equation beyond the given boundaries is a practical impossibility.

3 Validation of RFG Procedure

The first test of the procedure was for a homogeneous isotropic flow field. The Fourier space was sampled with 1000 wave-numbers selected according to Eq. (4). Figures 1(a) and 1(b) show the snapshot of a homogeneous isotropic velocity field. Figure 1(a) shows the vorticity field in a cross-section of the computational domain, and in Fig. 1(b) the velocity distribution is presented. Statistical post-processing of velocity correlations was applied to the generated flow-field in order to verify that the velocity field was isotropic. For this purpose a turbulent flow-field with the characteristic time scale of 10^{-3} s was generated from the Fourier spectral sample of 1000 wave-vectors Eq. (4). The fluctuating velocities were sampled at the rate of 10^5 Hz. Correlations of the fluctuating velocity components were computed at one point in space by averaging over time. Figure 4 shows the behavior of the velocity correlations as a function of the averaging time-interval. The figure indicates convergence to the values corresponding to Eq. (10).

The procedure was next applied to a homogeneous anisotropic flow field with c_i selected from typical boundary layer distributions. This type of anisotropy leads to higher amplitudes of the velocity vectors in one direction relative to the other (Fig. 1(c)). The procedure was also used to generate the flow-field with anisotropic length-scales (see comments in Section 2). In this case the length-scale of fluctuations was selected differently in different spatial directions. This produced a flow-field where the structure of the velocity fluctuations seemed stretched in one direction (Fig. 1(d)).

Next we applied the procedure to the case of a nonhomogeneous anisotropic boundary layer. Figure 1(e) shows a snapshot of the velocity magnitude in the three-dimensional boundary layer. An additional empirical factor related to the boundary-layer thickness was introduced in this case to better account for the intermittency effects. Figure 2 shows the random signal produced by the RFG procedure sampled at different locations above the boundary plane. As can be seen from that figure both anisotropy and inhomogeneity are evident in the fluctuating components. Experimental and direct numerical simulation (DNS) data do exist for this flow field, providing both mean and fluctuating velocity profiles, as well as turbulent correlations. The turbulent boundary layer is two-dimensional in the mean, though turbulent fluctuations exist in all three dimensions, i.e., $c_1 = u'$, $c_2 = v'$, and $c_3 = w'$ for the axial, vertical, and tangential directions, respectively. In addition, the correlation involving the axial and vertical velocity fluctuations is significant. The Reynolds stresses were obtained from (Hinze [16]) where the classical experiments of Klebanoff [17] are summarized.

A number of realizations N_T of the boundary layer was computed using the turbulence time scale of $t_{\mathrm{turb}} = 10^{-3}$ s, length-scale of $l_{\mathrm{trub}} = 10^{-3}$, and a sample size of 1000 harmonic functions. The wave-vectors for these functions were taken from a normal distribution with the mean $\sim t_{\mathrm{turb}}^{-1}$. The boundary layer thickness (δ) was allowed to grow according to the following empirical relation:

$$\delta = 0.16 \cdot x \cdot \left(\frac{U_0 x}{\nu}\right)^{-1/7} = 0.16 \cdot x \cdot \mathrm{Re}_x^{-1/7} \tag{16}$$

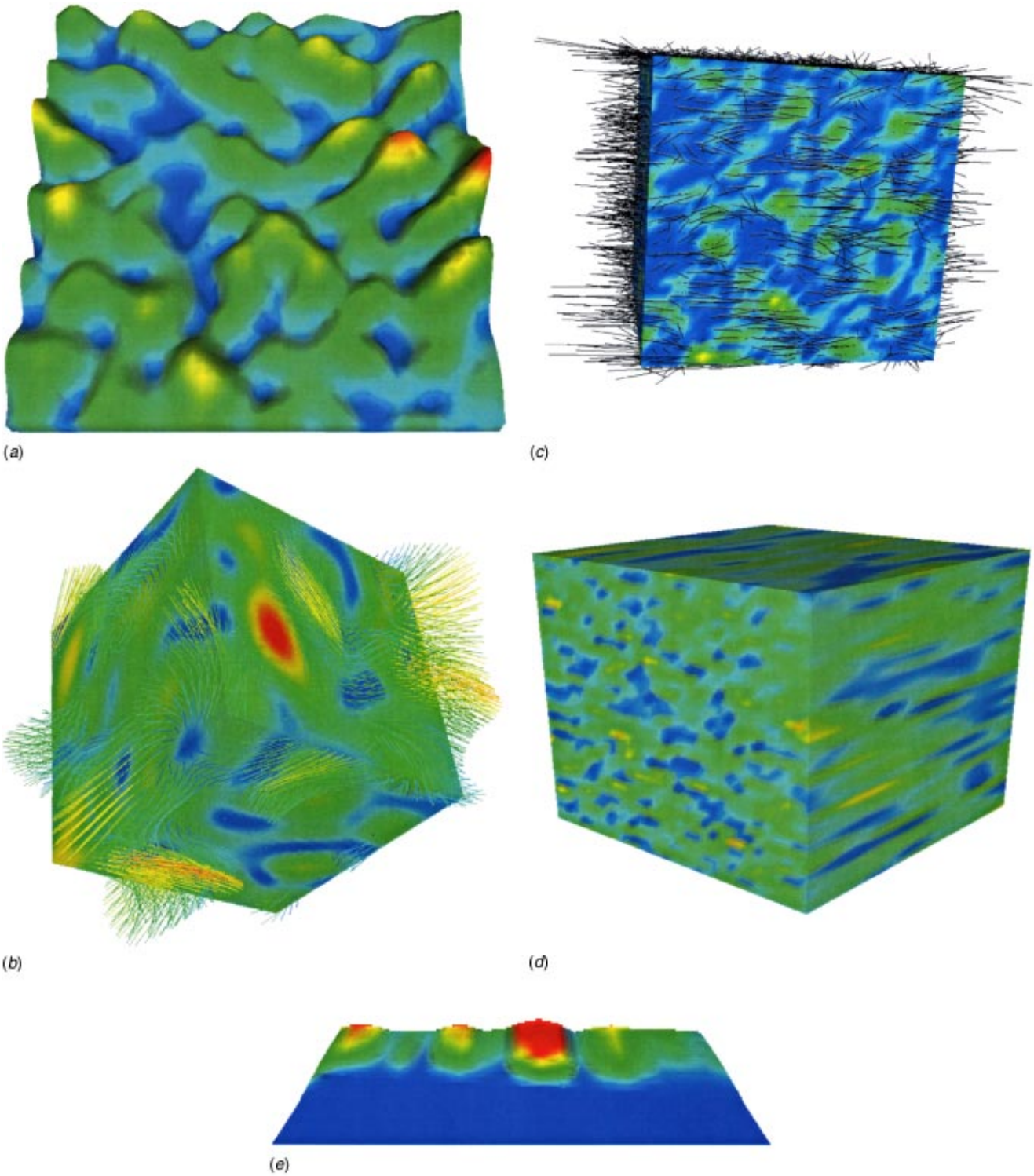

Fig. 1 Simulated flow-field, (*a*) Isotropic vorticity, (*b*) isotropic velocity, (*c*) anisotropic velocity, (*d*) anisotropic length-scale, (*e*) fluctuating velocity in the boundary layer

where x is the axial distance and U_0 is the free-stream velocity, which was set equal to 1.0 m/s. The cross correlation ($\overline{uv}$) was normalized with the friction velocity U_τ, which is itself a function of U_0. The boundary layer thickness was randomly perturbed with a continuous function using the same spectral sampling technique as for the velocity fluctuations to emulate intermittency.

Figure 3 shows the vorticity field of the generated boundary layer flow-field compared with LES data (Speziale [18]). As can be seen from the figure, by choosing the turbulence length-scale correctly, one can achieve a good resemblance in the flow structure simulated with this semi-analytic approach and a LES flow-field.

To compare the simulation results with the experimental data the velocity profile along a vertical line in the center of the axial plane was stored for each simulated realization of the flow-field (Fig. 4). The profiles of the thousand time realizations were then

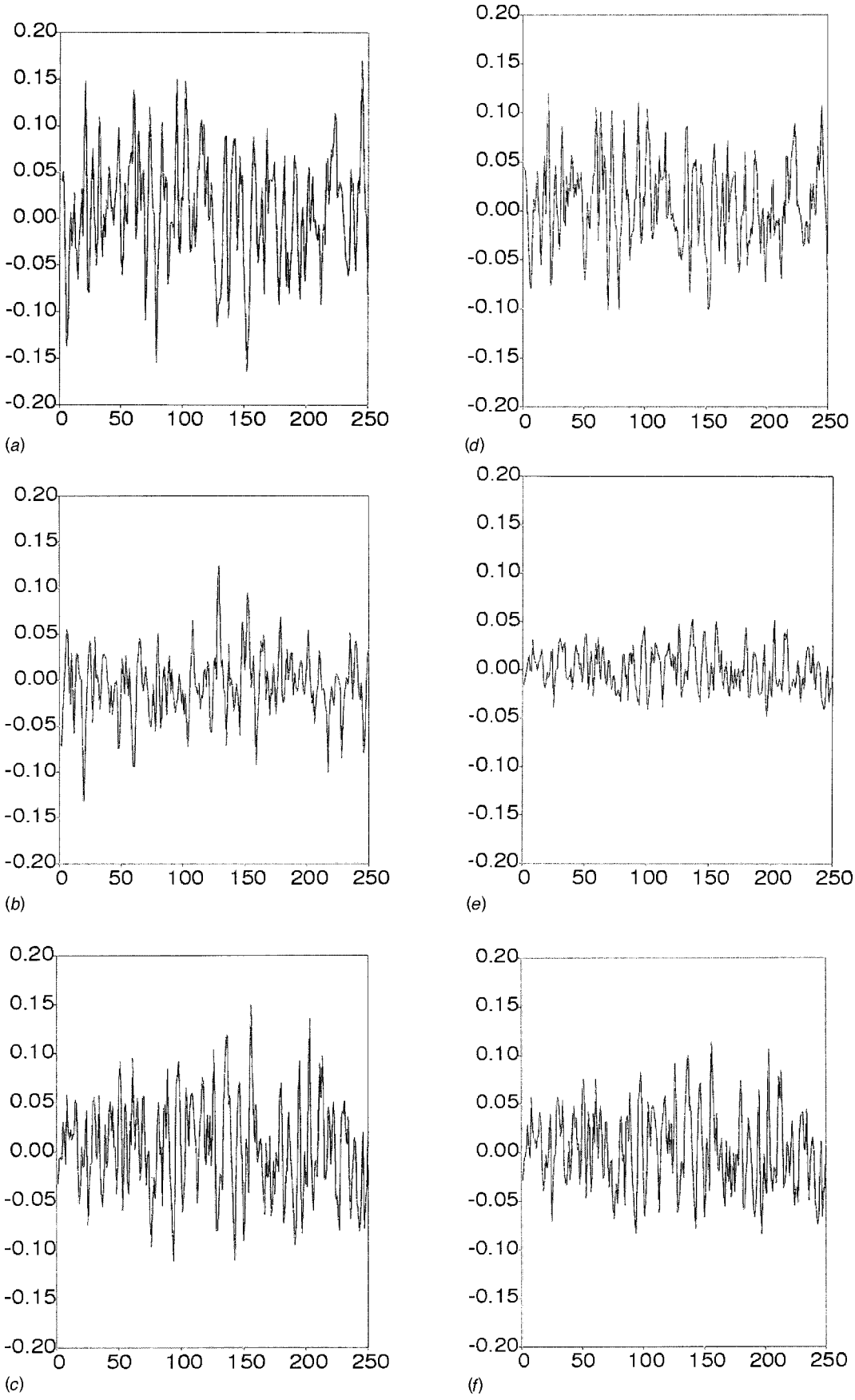

Fig. 2 Instantaneous velocity versus time step at different locations, $y^* = y/\delta$, (*a*) Axial, $y^* = 0.13$, (*b*) vertical, $y^* = 0.13$, (*c*) tangential, $y^* = 0.13$, (*d*) axial, $y^* = 0.46$, (*e*) vertical, $y^* = 0.46$, (*f*) tangential, $y^* = 0.46$, (*g*) axial, $y^* = 0.76$, (*h*) vertical, $y^* = 0.76$, (*i*) tangential, $y^* = 0.76$

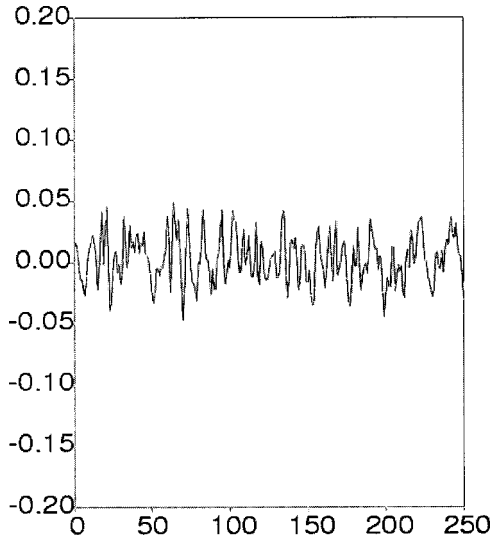

(g)

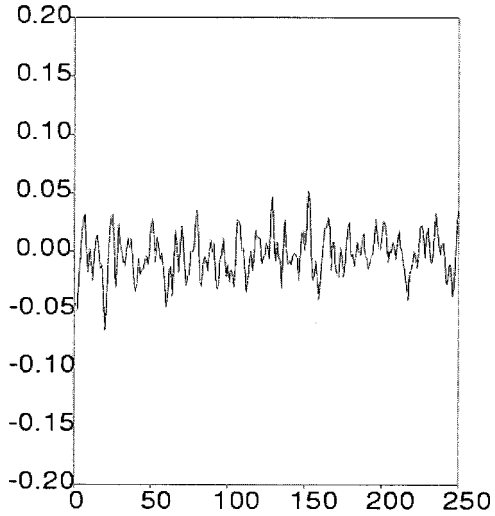

(h)

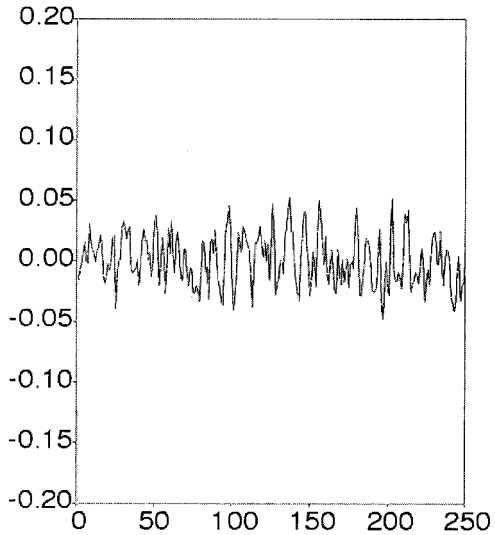

(i)

Fig. 2 (**Continued**)

used to calculate the average fluctuating components in each direction, as well as the corresponding cross correlations. These are compared to the original experimental data in Fig. 5. As can be seen, the experimental data is well reproduced.

The divergence-free property of the generated flow-filed was tested by computing the divergence as a function of turbulence length-scale for three cases: isotropic velocity field, generated according to the original Kraichnan method (Kraichnan [10], Li et al. [7]), anisotropic velocity field, generated according to the modified Kraichnan method, using Eqs. (4)–(5) with $\tilde{k}_j^n \equiv k_j^n$, and anisotropic velocity field generated according to the RFG algorithm based on Eqs. (2)–(9). For this test case the anisotropy of different fluctuating velocity components was selected to be given by a ratio: 0.1:1.4:1 for c_1, c_2, and c_3, respectively.

The divergence test was done on a cubic grid. For each grid-cell the divergence was computed as the sum of fluxes through cell faces. The Fourier space was sampled with 1000 wave-numbers selected according to Eq. (4). Figure 6 depicts the computed divergence as a function of the ratio of turbulence length-scale l to grid cell size. The result represents an average over 10,000 realizations of the flow-field. As can be seen from the figure in all three cases the continuity error decreases with the increase of the turbulence length-scale. This decrease is considerably slower for the anisotropic flow-field generated according to the original Kraichnan method compared with the the cases of isotropic flow field and anisotropic flow generated with RFG procedure. It should be noted that the theoretical continuity error in the isotropic case is zero. The discrepancy between this case and the anisotropic case computed with the Kraichnan method is due to the violation of continuity of that method in the presence of anisotropy. In contrast, the flow-field produced with the new RFG procedure has practically the same as for the isotropic case. This means that the anisotropic flow-field generated by the RFG procedure is essentially divergence free. At the same time it shows the importance of scaling transformation for k_j^n in (5) for the fulfillment of continuity. The upper divergence limit in the figure occurs when the grid cell-size is comparable or greater than turbulence length-scale l. It is due to the integration errors, which in this limit case can be estimated from the relation $\|\overline{u_i u_j}\| \approx 1$.

Another validation of the method was done on a flat-plate wake flow, which is a well-documented case in the literature (Ramaprian et al. [19]). In this case the simulation starts from a plane located behind the plate in the wake region (Fig. 7). The inflow boundary is generated using RFG with an input from the experimental data (Ramaprian et al. [19]), including mean velocity U_m, the turbulence intensities u_{rms}, v_{rms}, w_{rms} and the shear stresses $\overline{uv}$. In this way we can provide realistic inflow boundary conditions including the turbulence characteristics created by the plate, which is an important factor for LES. The length of the plate is $L = 1.829$ m. The inflow boundary is located at 19.5 mm ($x/L = 0.01$) measured from the rear edge of the plate. The computational domain size is $1.0\text{m} \times 0.2\text{m} \times 0.6\text{m}$ in x, y, and z direction, respectively. The corresponding grid sizes are $82 \times 50 \times 50$. Non-uniform grid is used in both x and y directions with stretching not exceeding three percent.[2] The size of the smallest cell is $0.6\text{mm} \times 0.2\text{mm} \times 1.2\text{mm}$ while that of the biggest cell is $50\text{mm} \times 8\text{mm} \times 1.2\text{mm}$ in x, y, z direction, respectively. Neumann boundary condition is applied at the outflow boundary. Symmetry boundaries are used in a vertical direction and periodic boundaries are used in the spanwise direction. Central difference numerical scheme and Smagorinsky model are applied in this study.

Figure 8 presents the comparison of the turbulent characteristics between the simulation and the experimental results at the inlet plane. They agreed very well except the center region. The reason is that the grid is relatively coarse in the center, which leads to the smoothing of very sharp gradients. The overall difference is under

[2]In this study, x represents stream-wise, y-vertical and z-span-wise directions, respectively

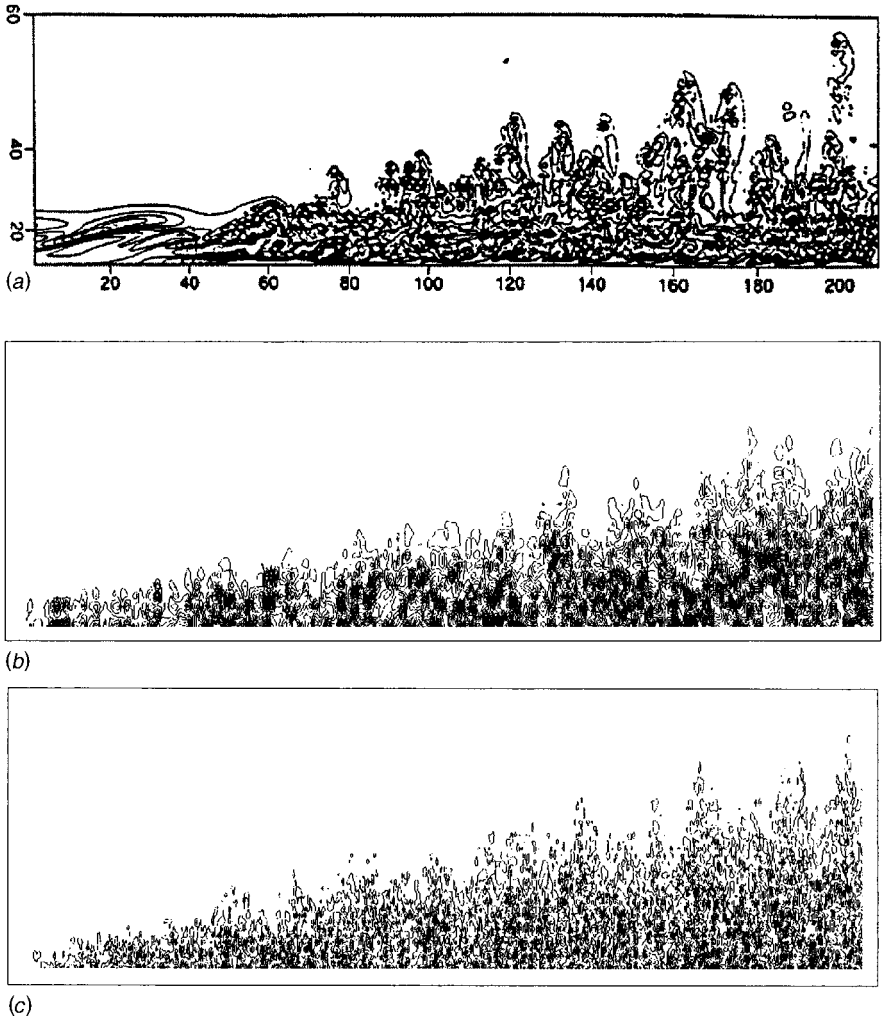

Fig. 3 Vorticity contours in the boundary layer (*a*) LES (Speziale, 1998) (*b*) RFG (large length-scale) (*c*) RFG (small length-scale)

1 percent. It should be noted that the agreement is so good because the comparison is given for the inlet plane where the RFG procedure was designed to reproduce the turbulence quantities exactly.

Figure 9(a) shows the energy spectrum at the inflow boundary. A sharp cut exists at wave length 0.01, which is matching the length scale we selected for RFG. Figures 9(b) and 9(c) show the energy spectrum at $x=0.16$ and $x=0.53$, respectively, which were produced after the application of LES inside the domain. From these figures, one can see that a good portion of the inertial range is captured. With the grid becoming coarser in the wake, only large wave lengths can be resolved.

Next we investigated the turbulence intensities downstream. From Figs. 10–13 the Reynolds stresses computed along y-direction at different x locations are compared with the experimental results. The comparison looks good although more quantitative studies would be appropriate. Near the very beginning of the wake most of the fluctuations can be captured. Later in the flow field, the percentage of the resolved turbulence is becoming small due to the coarser grids. It can be noted that both v' and uv at the second x-station are higher than those at the first one. This effect has been investigated and discussed by Nakayama and Liu [20] where they attribute it to a near wake phenomenon. Figure 14 shows the decay of the turbulent kinetic energy along the center line of the wake. Most parts of the turbulent kinetic energy have been captured. We are confident to make an assumption that with finer grids the turbulent resolution will be much better.

4 Applications

4.1 Boundary Conditions for LES/RANS. As an illustration of the technique we used it first in conjunction with the RANS and LES methods to simulate turbulent fluctuations in a ship wake. The high-Reynolds number character of ship wakes ($R_e \sim 10^7 - 10^8$) makes it rather time-consuming to perform full-scale LES of these flows. In this situation a combination of a RANS and the RFG technique can offer an efficient way to restrict the LES runs to the wake region only.

Figure 15 shows a snapshot of an unsteady turbulent flow-field in the inflow-plane serving as inlet condition for LES of a ship wake. Initially a steady-state RANS solution is obtained (Figs. 15(a), 15(c)), providing turbulent stresses r_{ij} and time-scales ω_i. Next, the RFG procedure is used to generate continuous time-dependent inlet conditions with the given turbulence characteristics (r_{ij}, ω_i, Figs. 15(b), 15(d)).

In another application (Fig. 16) turbulent flow around a ship-hull was produced as a superposition of the mean flow velocity, computed with a RANS method ($k-\epsilon$) (Larreteguy [21]) and the

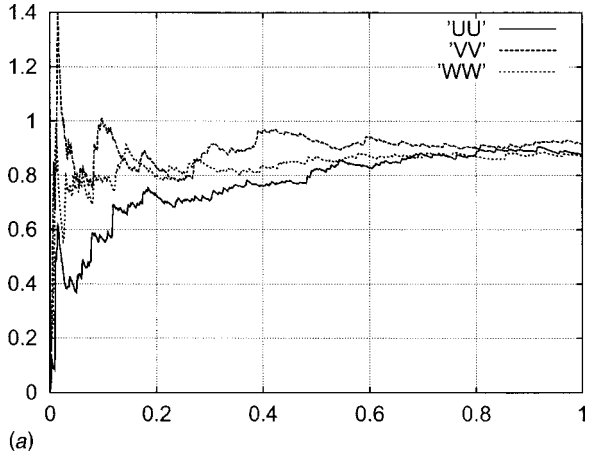

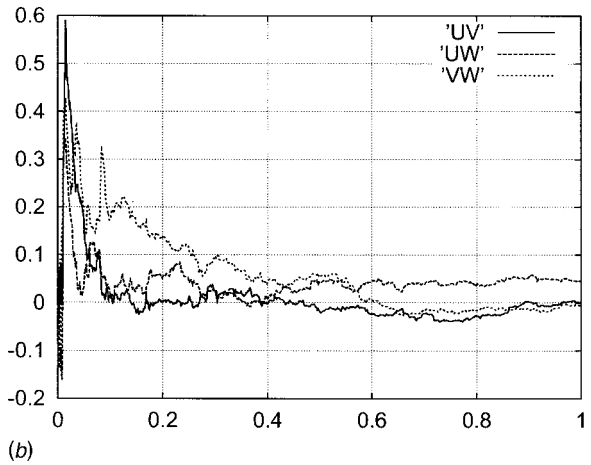

Fig. 4 Convergence of velocity correlations (*a*) Diagonal correlations (*b*) Cross Correlations

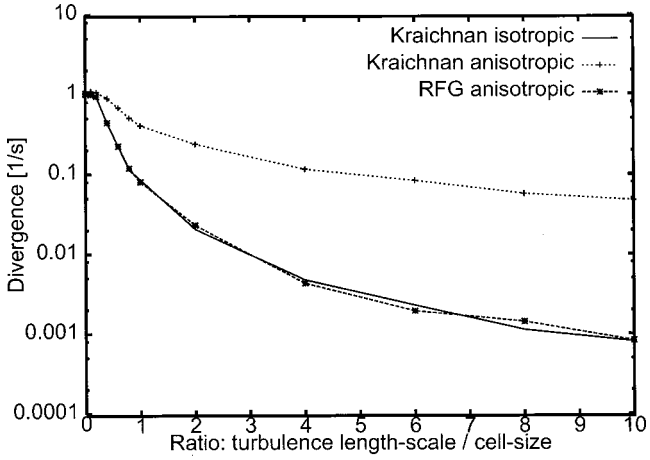

Fig. 6 Normalized divergence of an anisotropic velocity field

fluctuating velocity obtained with the RFG procedure. This flow-field can be used to initialize the unsteady LES and for particle tracking applications (see Section 4.2).

As noted earlier, the flow generated in both cases may not necessarily represent a realistic turbulent vortex dynamics at the respective boundaries, but statistically the flow-field will reproduce the turbulent shear stresses and time/length scales correctly. Furthermore, the statistics of turbulent fluctuations imposed at the space/time boundaries may not necessarily be preserved by the flow-solver inside the domain. That is, there may be a transition region between the boundary and the inside of the domain where the flow-solver will adjust to the boundary conditions. However, if the boundary conditions were generated using continuous functions and realistic turbulence quantities and spectra this transition

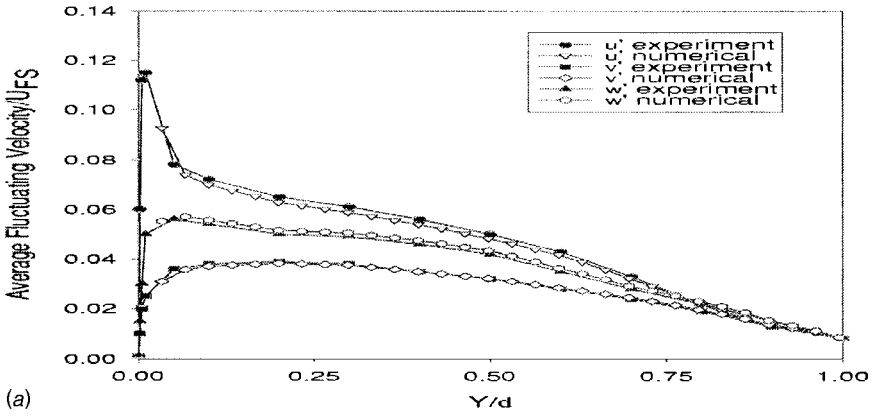

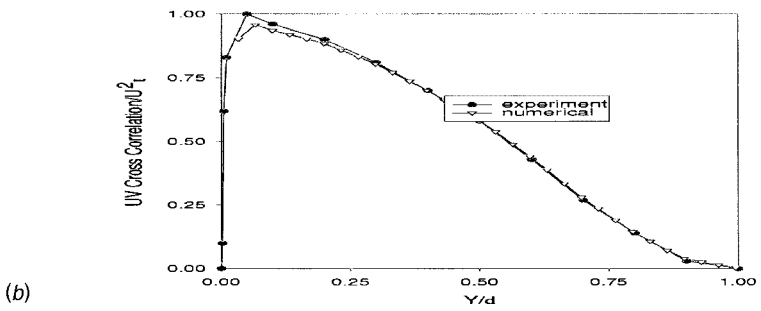

Fig. 5 Comparison with experimental data. (*a*) Fluctuating velocities, (*b*) axial/vertical cross correlations.

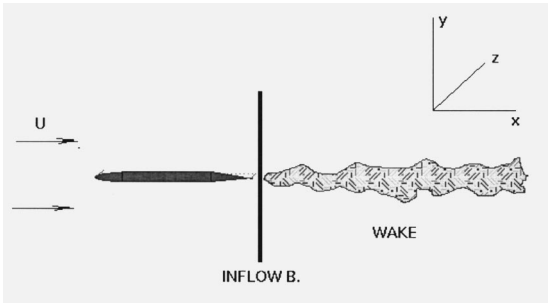

Fig. 7 The schematic of the flat plate wake

region will be small and the technique may still present a good alternative to solving the complete NS equation in a larger computational domain.

4.2 Particle Dynamics Modeling. Particle tracking in transient flows is usually a time-expensive computational procedure. In the situations when the turbulent flow is computed using RANS models it is possible to compute particle dynamics in a steady-state mean flow field and add a fluctuating component to particle velocities. When LES technique is used, particles should follow a time-dependent flow-field and the fluctuating component should still be added to it at smaller turbulence scales. In both cases the fluctuating component is derived from the turbulence intensity and length-scales, provided by the turbulence model.

4.2.1 Bubble-Dynamics in a Turbulent Flow. We shall continue with a ship-wake flow as an illustrative example of particle-tracking application in turbulent high-Reynolds-number flows. Simulations of bubbles in ship wakes requires account of several processes, like drag, lift and buoyancy forces, bubble dissolution in water, bubble interaction with the free-surface (including bubble disappearance at the surface and bubble generation due to air entrainment). In some cases, because of uneven bubble distribution (e.g., local clustering), the coalescence and/or breakup of bubbles may be important. Because of this nonuniformity, sharp gradients in bubble concentration, and low volume fraction of the bubbles Lagrangian approach to model bubble dynamics is often preferred. Compared to the two-fluids method (Elghobashi [22], Crowe [23]) the Lagrangian approach requires less empiricism and is more suitable for parallel implementation. We use a particle dynamics (PD) algorithm based on efficient particle tracking, population dynamics and a novel particle interaction techniques (Smirnov et al. [14]).

To simulate bubbles in a ship-wake we use the combination of RFG and PD algorithms. Fluid velocity at the location of every bubble was approximated as a sum of the mean fluid velocity obtained from the RANS calculations and the fluctuating part computed with the RFG procedure. Since RANS solution is given only at the Eulerian grid-node locations and bubbles follow Lagrangian trajectories, an interpolation is required to approximate the mean velocity at bubble's current location. No such approximation is necessary for the fluctuating part, since the RFG procedure defines a flow-field at every point in space and time. In the simulation the bubbles were injected at a single point close to the

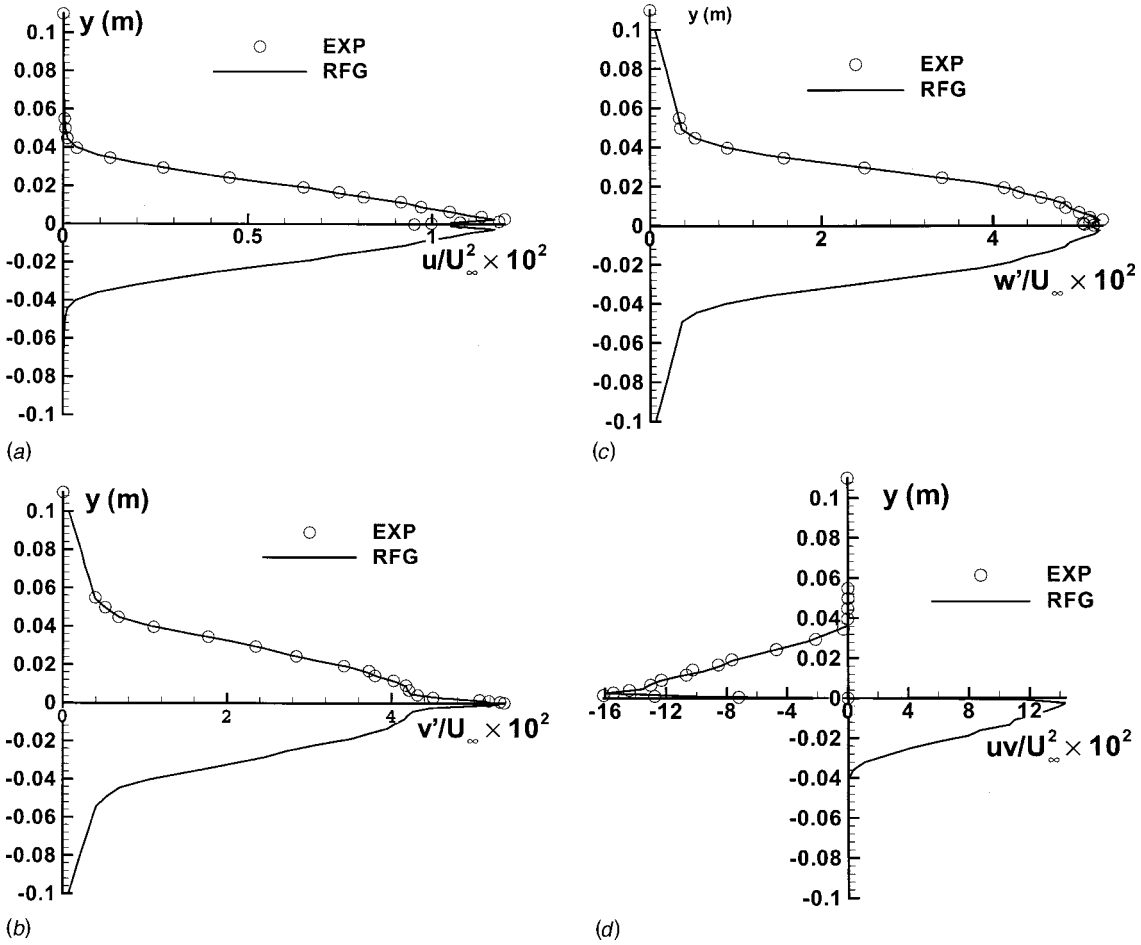

Fig. 8 Turbulence intensities at the inflow boundary, (*a*) Stream-wise, u_{rms}, (*b*) span-wise, v_{rms}, (*c*) vertical, w_{rms}, (*d*) shear Stress, uv_{rms}

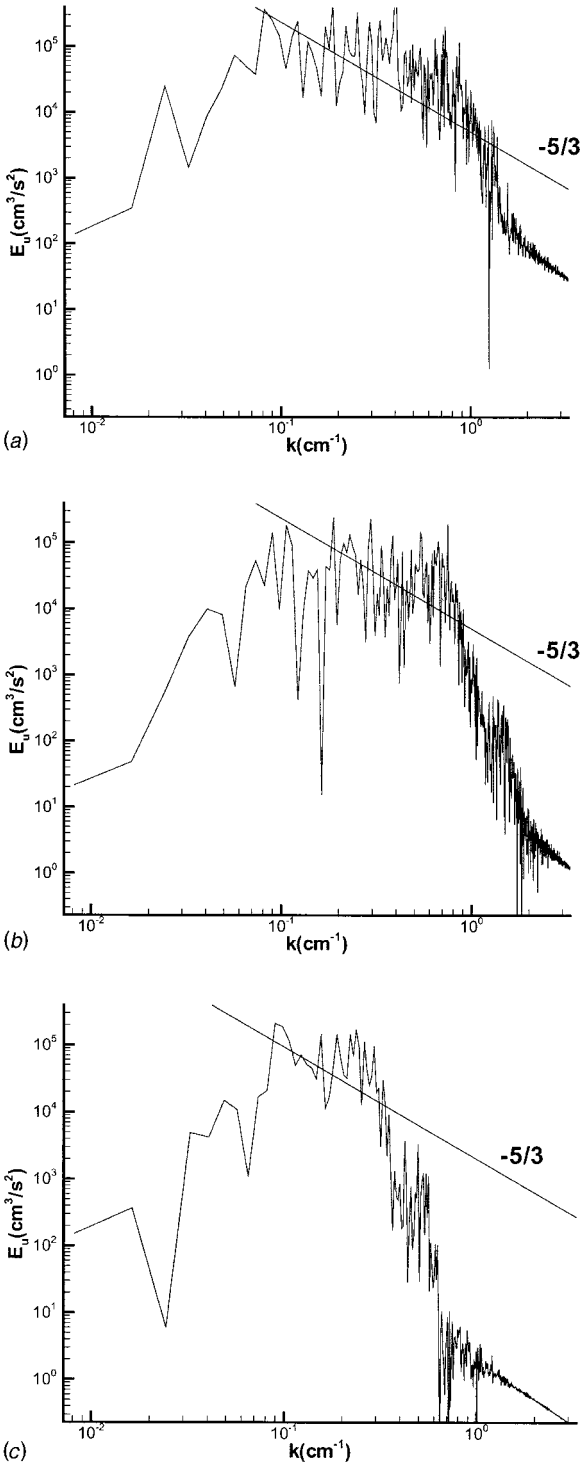

Fig. 9 Energy spectrum at different x locations, (*a*) Energy spectrum at the inflow boundary, (*b*) energy spectrum at $x=0.16$, (*c*) energy spectrum at the $x=0.53$

ship hull where the turbulent kinetic energy was near its maximum (Fig. 17). Drag, buoyancy, and added-mass terms were included (Crowe et al. [24]). A total of 10,000 bubbles of 100 microns in diameter were continuously injected into the domain. Two seconds of real-time were simulated for the ship-length of 6 m traveling with the speed of 3 m/s. The figure shows the tendency of particles to agglomerate in dense groups. The characteristic sizes of these groups are in many instances smaller than the

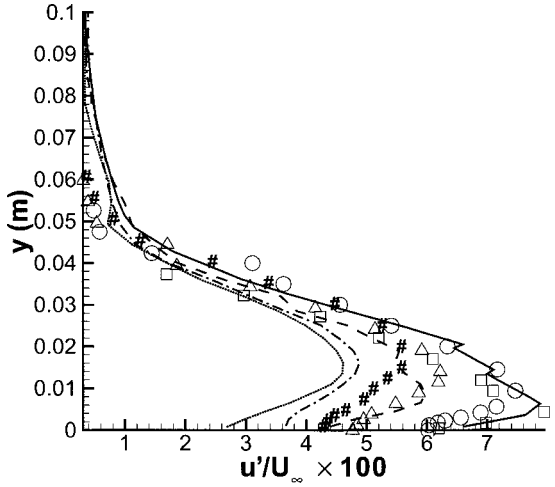

Fig. 10 Comparison between simulation and measured turbulence intensity (u_{rms}). —— Present simulation results at $x=31.75$ mm. — — — Present simulation results at $x=158.75$ mm. —·—·—·— Present simulation results at $x=361.95$ mm. · · · · Present simulation results at $x=590.55$ mm. □ Experimental results (Ramaprian et al.,) at $x=31.75$ mm. ○ Experimental results (Ramaprian et al.,) at $x=158.75$ mm. △ Experimental results (Ramaprian et al.,) at $x=361.95$ mm. # Experimental results (Ramaprian et al.,) at $x=590.55$ mm.

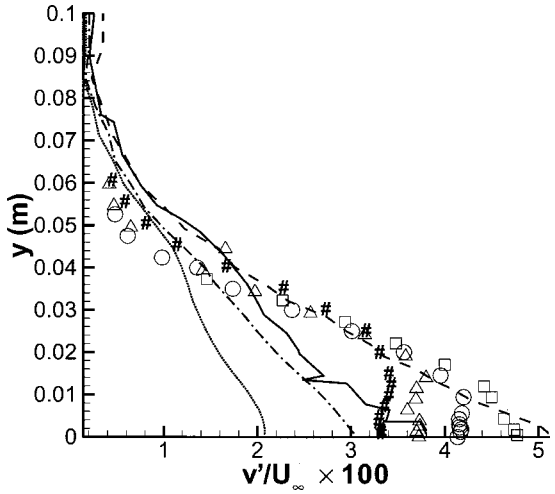

Fig. 11 Comparison between simulation and measured turbulence intensity (v_{rms}). Symbols are the same as Fig. 10.

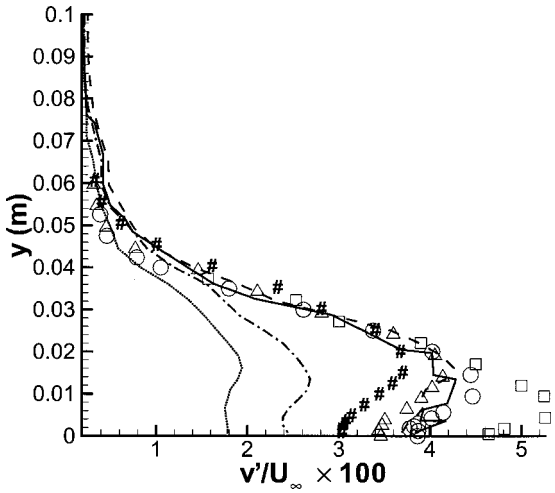

Fig. 12 Comparison between simulation and measured turbulence intensity (w_{rms}). Symbols are the same as Fig. 10.

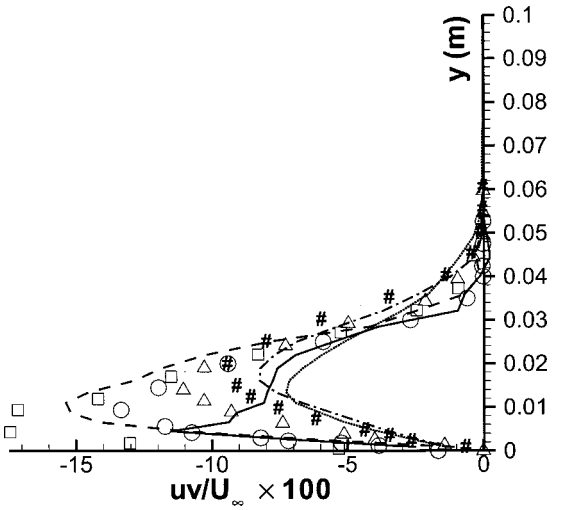

Fig. 13 Comparison between simulation and measured shear stresses. Symbols are the same as Fig. 10.

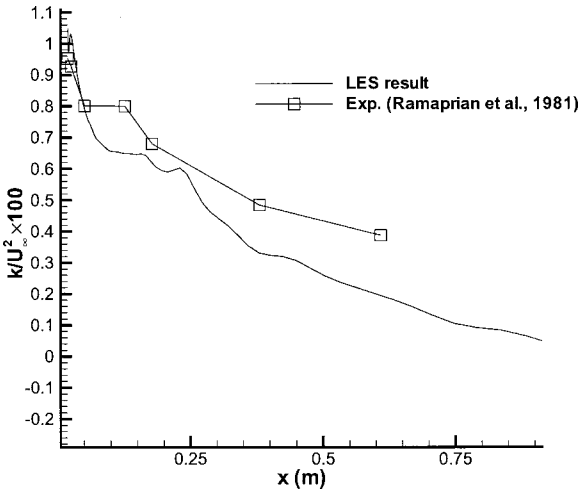

Fig. 14 Kinetic energy profile along the center line in the wake of a flat plate

grid-cell size. This reflects the very subgrid nature of the RFG method, which enables to capture finer details of particle dynamics than can be resolved on an Eulerian grid.

4.3 Large-Eddy Simulations (LES). In Large Eddy Simulations the RFG procedure can be used to generate random inflow-conditions or serve as a subgrid-scale model. There is an extensive literature regarding LES techniques (Piomelli [25]). To reach a state of developed turbulence in LES simulations requires a substantial computational time. Regarding this there are two important problems in LES of a high-Reynolds number turbulence that can be solved with the RFG procedure: (1) assigning initial flow-field distribution and (2) assigning turbulent inflow conditions. Conventionally, the first problem is dealt with by increasing the transition phase of the simulation and the second by extending the size of the computational domain. Consequently, the remedy comes at a price of a longer execution time and higher memory requirements. By using a RFG procedure to generate the initial conditions one can cut down on the execution time considerably. For stationary turbulence the approximate nature of the initial ve-

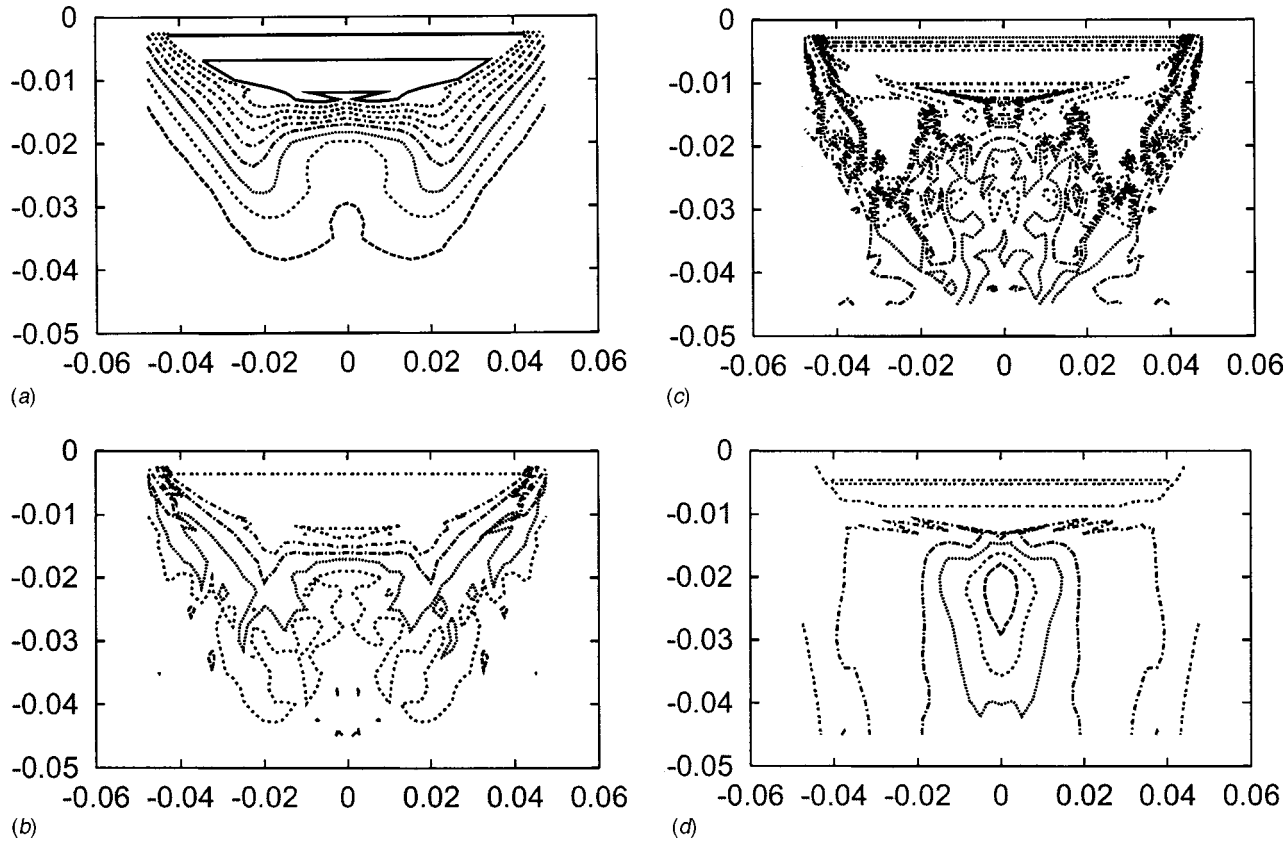

Fig. 15 Unsteady inlet velocity components: inlet conditions for LES of a ship wake. (*a*) Streamwise (RANS), (*b*) streamwise (RANS+RFG), (*c*) vertical (RANS), (*d*) vertical (RANS+RFG).

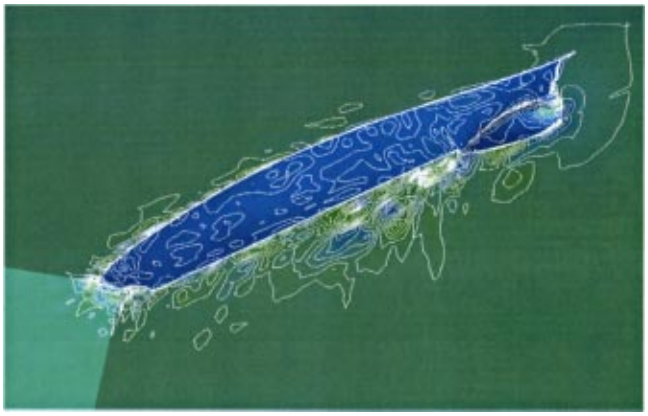

Fig. 16 Turbulent velocity around a ship hull computed with the RFG algorithm, view from below

locity distribution with respect to the solution of the NS-equation is of little significance, since these discrepancies are corrected in the first few iterations of the NS-solver.

The problem of inlet conditions could be even more important, since extending the computational domain will increase both execution time and memory requirements of the simulation. In this case, RFG can provide reasonable inflow conditions with the predetermined anisotropy properties. Here again, we illustrate these advantages on the example of a ship wake. A complete LES simulation of the wake would normally require simulating the unsteady flow around the ship hull and in the wake region. Employing the RFG procedure for the inlet conditions, we can restrict LES run to the wake region only. In this case, the information on turbulence levels and anisotropy at the inlet plane, required by RFG, can be obtained from relatively inexpensive RANS calculations.

After validating this approach on the case of a flat-plate (see Section 3), we applied it to the wake of a model ship (Navy 5415 model (Carrica et al. [26])). As in the flat-plate case the inflow boundary was constructed using the data from RANS calculations (Larreteguy [27]) (Fig. 15). The turbulent normal stresses are based on the kinetic energy. The time scale and length scale which are used in generation of the perturbation at the inlet plane are

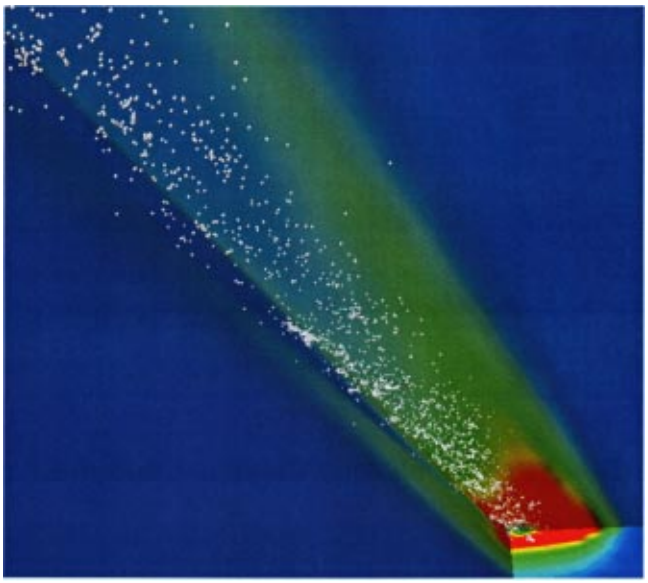

Fig. 17 Bubbles in a ship wake. Background shading is according to the turbulent kinetic energy.

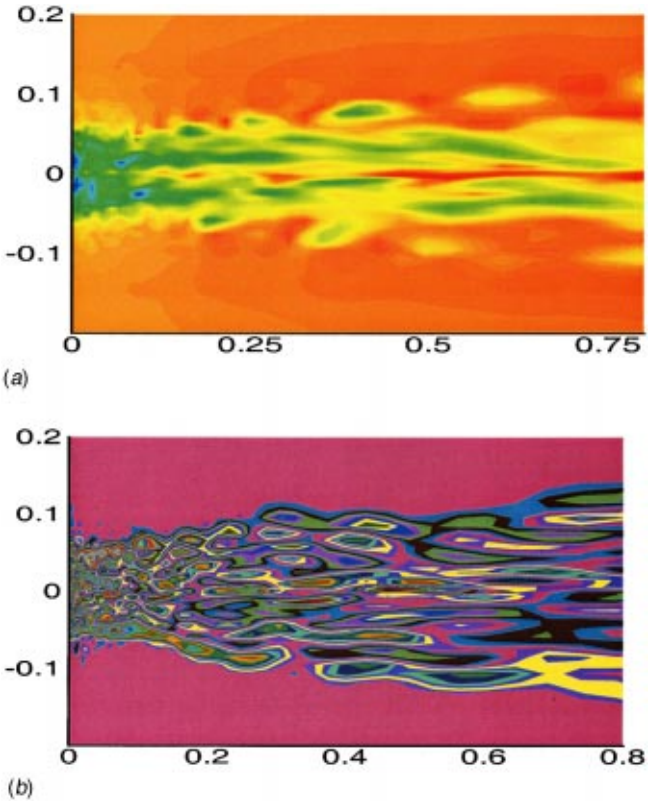

Fig. 18 LES of a ship wake flow, (*a*) stream-wise velocity contours of the simulated wake flow, (*b*) instantaneous vertical vorticity contours

selected from the corresponding relation between the turbulent kinetic energy and its dissipation rate provided by the RANS calculations.

Figure 18 shows the instantaneous stream-wise velocity contours and vertical vorticity contours, respectively, in a plane parallel to the free surface, where some of the the turbulence structures in the wake can be observed. Small-scale turbulent structures can be seen in both figures in the near wake region. These structures tend to increase in the far wake. This can be due to the following two factors: (1) In the very near wake, fine grids are applied so that smaller turbulence structures are captured. (2) Physically, larger turbulence structures include more energy so that they can last longer, while smaller turbulence structures have less energy and die quickly by dissipation. Another phenomenon is the increase of the width of the wake in the downstream direction. The mean velocity profile (not shown here) also supports this result. Capturing of these phenomena testifies to the validity of our approach of computing the inflow boundary.

5 Conclusions and Future Work

The analytical method of Kraichnan [10] was modified to account for the effects of inhomogeneity and anisotropy of turbulent shear stresses. The technique was realized in an efficient random field generation (RFG) algorithm which was tested on the cases of isotropic turbulence, channel flow anisotropic flows, boundary layer inhomogeneous anisotropic turbulence (Celik et al. [27]) and flat-plate wake flow. The simulated flow fields are transient in nature and satisfy the conditions of continuity and anisotropy for homogeneous flows and to a good approximation satisfy these conditions for inhomogeneous flows.

The RFG procedure offers a relatively inexpensive way to generate random velocity fluctuations, representing a turbulent flowfield. Since the generated velocity field satisfies the relations of

continuity and anisotropy it is a far more realistic representation of turbulence than can be obtained with a simple Gaussian velocity distribution using a random-number generator. Because the flow-field produced by RFG may not satisfy the momentum equations it is still an approximation. However, in some applications this approach may offer a simple and reasonably accurate way to model turbulence without solving the complete Navier-Stokes equation, which would require much more memory and execution time.

In practical applications the RFG procedure provides the flexibility of a trade-off between the accuracy of representing a turbulent spectrum and memory/time requirement. By increasing the spectral sample size N in (4) one can increase the accuracy of reproducing the turbulent spectrum at the cost of longer execution time and higher memory utilization. In addition to that, since the velocity field is calculated by analytical functions it is given at any point in space and time, and not just at the grid nodes and at discrete time values. Because of this quality, the method has a potential as a subgrid-scale model for LES or RANS simulations and in modeling turbulent particle-laden flows, although its validity in this respect would require a separate study.

Advancing the realistic LES run to the stage of developed turbulence may require days of computation time.[3] Similarly, to obtain realistic turbulent inflow conditions may require the extension of the computational domain with the corresponding increase in computer time and memory requirements. The RFG technique can reduce the flow initialization time to several hours and can be used to continuously supply the turbulent inlet conditions close to the domain of interest, thereby reducing time and memory requirements of the LES simulations.

This study showed the feasibility of applying a hybrid LES technique in combination with RFG algorithm to high-Reynolds number flows, like those of ship wakes. It is also shown that the technique can be used effectively in conjunction with a Lagrangian particle dynamics approach, is appropriate for bubble tracking in the wake and can be easily incorporated into LES codes.

Acknowledgments

This work has been performed under a DOD EPSCoR project sponsored by the Office of Naval Research (ONR), Grant No. N00014-98-1-0611. The program officer is Dr. Edwin P. Rood. We thank professor Robert Street of Stanford University who kindly provided us with the basic code for LES. We also thank Dr. Calhoun and Mr. Li Ding in Stanford University for their suggestions about using the code.

Nomenclature

DNS = direct numerical simulation
LES = large eddy simulation
NS = Navier Stokes
RANS = Reynolds averaged Navier Stokes equation
RFG = random flow generation
PD = particle dynamics
l = length scale of turbulence
τ = time scale of turbulence

[3]Our benchmarking was performed on the 533 MHz DEC-Alpha processor.

References

[1] Ravikanth, V., and Pletcher, R., 2000, AIAA Paper (2000-0542).
[2] Akselvoll, K., and Moin, P., 1995, Technical Report TF-63, Stanford University.
[3] Lund, T., 1998, ''Generation of Turbulent Inflow Data for Spatially-Developing Boundary Layer Simulations,'' J. Comput. Phys., **140**, p. 233.
[4] Lee, S., Lele, S., and Moin, P., 1992, ''Simulation of Spatially Evolving Turbulence and the Applicability of Taylor's Hypothesis in Compressible Flow,'' Phys. Fluids A **4**, p. 1521.
[5] Zhou, O., and Leschziner, M., Sept. 1991, ''A Time-Correlated Stochastic Model For Particle Dispersion in Anisotropic Turbulence,'' 8-th Turbulent Shear Flows Symp., Munich.
[6] Zhou, Q., and Leschziner, M., 1996, ''Modelling Particle Dispersion in Turbulent Recirculating Flow with an Anisotropy-Resolving Scheme,'' Technical Report TFD/96/07, UMIST.
[7] Li, A., Ahmadi, G., Bayer, R., and Gaynes, M., 1994, ''Aerosol Particle Deposition in an Obstructed Turbulent Duct Flow,'' J. Aerosol. Sci. **25**, No. 1, p. 91.
[8] Bechara, W., Bailly, C., and Lafon, P., 1994, ''Stochastic Approach to Noise Modeling for Free Turbulent Flows,'' AIAA J., **32**, No. 3.
[9] Fung, J., Hunt, J., Malik, N., and Perkins, R., 1992, ''Kinematic Simulation of Homogeneous Turbulence by Unsteady Random Fourier Modes,'' J. Fluid Mech., **236**, p. 281.
[10] Kraichnan, R., 1970, ''Diffusion by a Random Velocity Field,'' Phys. Fluids, **11**, p. 22.
[11] Ferziger, J., 1983, ''Higher-level Simulations of Turbulent Flows,'' J. Essers, ed., *Computational Methods for Turbulent Transsonic and Viscous Flows*, pp. 93–183, Hemisphere, Springer-Verlag.
[12] Maxey, M., 1987, ''The Gravitational Settling of Aerosol Particles in Homogeneous Turbulence and Random Flow Fields,'' J. Fluid Mech., **174**, p. 441.
[13] Shi, S., Smirnov, A., and Celik, I., 2000, ''Large-Eddy Simulations of Turbulent Wake Flows,'' Twenty-Third Symposium on Naval Hydrodynamics, Val de Reuil, France, pp. 203–209.
[14] Smirnov, A., Shi, S., and Celik, I., 2000, ''Random Flow Simulations with a Bubble Dynamics Model,'' in ASME Fluids Engineering Division Summer Meeting, No. 11215 in FEDSM2000, Boston, MA.
[15] Spain, B., 1965, *Tensor Calculus*, Oliver and Boyd.
[16] Hinze, J., 1975, Turbulence, 2nd edition, McGraw-Hill, New York.
[17] Klebanoff, P., 1954, NACA Tech. Notes, p. 3133.
[18] Speziale, C., 1998, ''Turbulence Modeling for Time-Dependent RANS and VLES: a Review,'' AIAA J., **36**, No. 2, p. 173.
[19] Ramaprian, B., Patel, V., and Sastry, M., 1981, ''Turbulent Wake Development Behind Streamlined Bodies,'' Technical Report IIHR Report No. 231, Iowa Institute of Hydraulic Research, The University of Iowa.
[20] Nakayama, A., and Liu, B., 1990, ''The Turbulent Near Wake of a Flat Plate at Low Reynolds Number,'' J. Fluid Mech., **217**, p. 93.
[21] Larreteguy, A., 1999, ''Ship-Wake Simulations,'' Private Communication.
[22] Elghobashi, S., 1994, ''On Predicting Particle-Laden Turbulent Flow,'' Appl. Sci. Res., **52**, p. 309.
[23] Crowe, C.: 1998, ''An Assessment of Multiphase Flow Models for Industrial Applications,'' Proceeding of FEDSM'98, Vol. FEDSM-5093, Washington, DC.
[24] Crowe, C., Sommerfeld, M., and Tsuji, Y., 1998, *Multiphase Flows with Droplets and Particles*, CRC Press.
[25] Piomelli, U., 1999, ''Large-Eddy Simulation: Achievements and Challenges,'' Prog. Aeronaut. Sci., **35**, p. 335.
[26] Carrica, P., Bonetto, D., Drew, D., and Lahey, R., 1998, ''The Interaction of Background Ocean Air Bubble With a Surface Ship,'' Int. J. Numer. Methods Fluids, **28**, p. 571.
[27] Celik, I., Smirnov, A., and Smith, J. 1999, ''Appropriate Initial and Boundary Conditions for LES of a Ship Wake,'' 3rd ASME/JSME Joint Fluids Engineering Conference, Vol. FEDSM99-7851, San Francisco, CA.

Computation of Particle and Scalar Transport for Complex Geometry Turbulent Flows

P. G. Tucker
Lecturer
Fluid Mechanics Research Centre,
The University of Warwick,
Coventry, CV4 7AL,
United Kingdom

The prediction of particle and scalar transport in a complex geometry with turbulent flow driven by fans is considered. The effects of using different turbulence models, anisotropy, flow unsteadiness, fan swirl, and electrostatic forces on particle trajectories are shown. The turbulence models explored include $k-l$, zonal $k-\varepsilon/k-l$, and nonlinear eddy viscosity models. Particle transport is predicted using a stochastic technique. A simple algorithm to compute electrostatic image forces acting on particles, in complex geometries, is presented. Validation cases for the particle transport and fluid flow model are shown. Comparison is made with new smoke flow visualization data and particle deposition data. Turbulence anisotropy, fan swirl, and flow unsteadiness are shown to significantly affect particle paths as does the choice of isotropic turbulence model. For lighter particles, electrostatic forces are found to have less effect. Results suggest, centrifugal forces, arising from regions of strong streamline curvature, play a key particle deposition role. They also indicate that weaknesses in conventional eddy viscosity based turbulence models make the accurate prediction of complex geometry particle deposition a difficult task. Axial fans are found in many fluid systems. The sensitivity of results to their modeling suggests caution should be used when making predictions involving fans and that more numerical characterization studies for them could be carried out (especially when considering particle deposition). Overall, the work suggests that, for many complex-engineering systems, at best (without excessive model calibration time), only qualitative particle deposition information can be gained from numerical predictions.
[DOI: 10.1115/1.1365959]

Introduction

The accurate computation of particle transport and deposition is relevant to a wide range of industrial applications. These include the modeling of fuel droplet trajectories in combustors [1] and the movement of contaminants in [2,3] and around buildings. The latter is considered by Hall and Cowan [4] and Drake et al. [5]. Prediction of particle motion is also important in the design of heat exchangers [6,7] and hydro cyclone and electrostatic [8,9] dust collection systems. Since over five percent of electronic failures are caused by dust build-up, the prediction of particle deposition is also highly relevant to electronic system design. Young and Kallio [10] compute particle transport for turbulent flow in computer disk drives. Tucker [11] considers laminar flow, particle transport in a central processor unit.

The complex geometries and flow physics found in many realistic engineering applications give rise to unsteady oscillatory flows. There has been little attention to the effect of unsteadiness on particle transport. Accurate turbulence intensity predictions are important for the prediction of particle transport. Commonly used turbulence models can give significantly different intensity values for the same flow. This is clearly illustrated by Hunt [12] and also Tucker [13]. Also, many models do not account for anisotropy. Zhou and Leschziner [14] demonstrate the importance of considering this with particle transport. In a number of practical situations (especially in electronics, where interference shielding is required), charged particles are deposited onto earthed surfaces. The charge gives rise to a particle electrostatic image force [15]. This is an inverse square function of distance. Here a simple, complex geometry approach for predicting image forces, based on the wall distance method devised by Spalding [16] is described. Using this, the importance of modeling these forces is explored. Also, the effect of flow unsteadiness, turbulence model choice, fan swirl, and anisotropy on particle transport is assessed for flow in the three-dimensional complex system shown in Fig. 1. This is an idealization of an electronic central processor unit. To explore

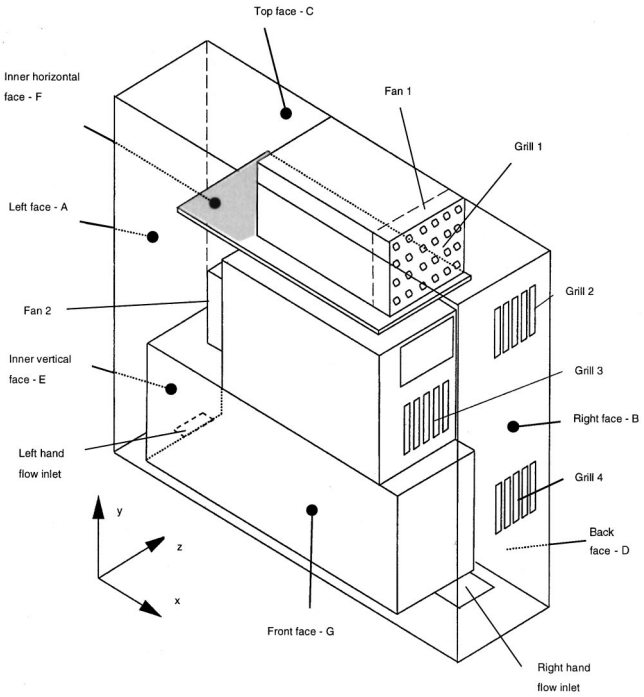

Fig. 1 Schematic of complex system

Contributed by the Fluids Engineering Division for publication in the JOURNAL OF FLUIDS ENGINEERING. Manuscript received by the Fluids Engineering Division November 20, 2000; revised manuscript received February 6, 2001. Associate Editor: L. Mondy.

scalar transport, comparison is made with smoke flow visualization data. Particle deposition data is also compared with an earthed surface Fig. 1 geometry.

Numerical Method

Fluid Flow and Turbulence Equations. For the cyclic-unsteady, turbulent, constant density, ρ, flow of a fixed dynamic viscosity, μ, fluid, the governing equations can be expressed in the following phase-averaged (see Bosch and Rodi [17]) tensor form

$$\frac{\partial\langle U_i\rangle}{\partial t}+\frac{\partial\langle U_i\rangle\langle U_j\rangle}{\partial x_j}=-\frac{1}{\rho}\frac{\partial\langle P\rangle}{\partial x_i}+\frac{\mu}{\rho}\frac{\partial}{\partial x_j}\left(\frac{\partial\langle U_i\rangle}{\partial x_j}+\frac{\partial\langle U_j\rangle}{\partial x_i}\right)+\frac{\partial\langle-\overline{u_i'u_j'}\rangle}{\partial x_j} \tag{1}$$

Equation (1) implies that, along with other variables, the fluid velocity u, at time t and a point x, can be expressed as $u=\overline{U}+u''+u'$, where $\overline{U}$ is a constant time averaged component, u'' temporal fluctuations about this and u' turbulent fluctuations about $\overline{U}+u''$. The phase average velocity resolved by the numerical scheme can then be expressed as $\langle U\rangle=\overline{U}+u''$. The static pressure $\langle P\rangle$, as with other variables below, can be written in a similar averaged manner. The corresponding continuity equation is

$$\frac{\partial\langle U_j\rangle}{\partial x_j}=0 \tag{2}$$

For the successful prediction of the mean flow field and also particle transport the final Eq. (1), $\langle-\overline{u_i'u_j'}\rangle$ phase-averaged Reynolds stress term must be reasonably approximated. The most popular, non-geometry specific, general engineering models characterize this stress in terms of the, here phase-averaged, turbulent kinetic energy, $\langle k\rangle$, and its rate of dissipation, $\langle\varepsilon\rangle$. These two variables must characterize a multiplicity of turbulent length and time scales. Their transport and also that of a general phase-averaged scalar variable, $\langle C\rangle$, are generally expressed using the following convection-diffusion equation

$$\frac{\partial\langle\Phi\rangle}{\partial t}+\frac{\partial\langle U_j\rangle\langle\Phi\rangle}{\partial x_j}=\frac{1}{\rho}\frac{\partial}{\partial x_j}\left(\Gamma_\phi\frac{\partial\langle\Phi\rangle}{\partial x_j}\right)-T_1\langle\overline{u_i'u_j'}\rangle\frac{\partial\langle U_i\rangle}{\partial x_j}-T_2 \tag{3}$$

Especially, for $\langle k\rangle$ and $\langle\varepsilon\rangle$, Eq. (3) arises from many modeling assumptions. These are outlined by Chen and Jaw [18]. Specific Eq. (3) terms are given in Table 1, where σ_Φ is a diffusion Prandtl number, $\langle\mu_t\rangle$ the turbulent viscosity and $C_{\varepsilon1}$ and $C_{\varepsilon2}$ calibration constants.

For attached channel flows, and close to walls, the following algebraic and hence more economical to compute wall distance based $\langle\varepsilon\rangle$ expression is sometimes found effective

$$\langle\varepsilon\rangle=\frac{\langle k\rangle^{3/2}}{\langle l_\varepsilon\rangle} \tag{4}$$

In Eq. (4), the phase-averaged turbulence length scale is $\langle l_\varepsilon\rangle=C_{\varepsilon0}y(1-n_1e^{-A_\varepsilon\langle y^+\rangle/C_\mu^{1/4}})$ and $\langle y^+\rangle=y\rho\langle k\rangle^{1/2}C_\mu^{1/4}/\mu$. Electronic systems consist of many channel regions. On this basis, the $k-l$ model is considered here. When Eq. (4) is used, on the grounds of dimensional arguments, the turbulent viscosity can be expressed as

$$\mu_t=\rho C_\mu\langle l_\mu\rangle\langle k\rangle^{1/2} \tag{5}$$

giving the $k-l$ model of Wolfshtein [19], where $\langle l_\mu\rangle=C_{\mu0}y(1-n_1e^{-A_\mu\langle y^+\rangle/C_\mu^{1/4}})$. When Eq. (3) is used with $\langle\Phi\rangle=\langle\varepsilon\rangle$, the following turbulent viscosity expression is implemented

$$\mu_t=\rho C_\mu\frac{\langle k\rangle^2}{\langle\varepsilon\rangle} \tag{6}$$

Equation (6) completes the standard k-ε model of Launder and Spalding [20]. This, unlike the $k-l$ model presented above, does not contain exponential near wall turbulence damping functions. Therefore, it is only applicable to high turbulence Reynolds number regions away from walls. Hence, with this standard k-ε model, near walls, carefully positioned, logarithmic functions are required (obviously, these can also be used in the $k-l$ model and for one later case this is done). The Reynolds stress related terms, required in Eq. (1), are found using either the linear Boussinesq expression below, arising in an ad-hoc way from the laminar viscous stress equation

$$\langle-\overline{u_i'u_j'}\rangle=-n_0\frac{2}{3}\langle k\rangle\delta_{ij}+\frac{2\mu_t}{\rho}S_{ij} \tag{7}$$

The parameter, δ_{ij} is the Kronecker delta ($\delta_{ij}=1$ if i=j and $\delta_{ij}=0$ if i≠j). A superior alternative to Eq. (7) is the following nonlinear approximation (see Speziale [21])

$$\langle-\overline{u_i'u_j'}\rangle=-\frac{2}{3}\langle k\rangle\delta_{ij}+2\frac{\mu_t}{\rho}S_{ij}+4C_DC_\mu\frac{\mu_t}{\rho}\frac{\langle k\rangle}{\langle\varepsilon\rangle}\left(S_{ik}S_{kj}\frac{1}{3}S_{mn}S_{nm}\delta_{ij}\right)+4C_EC_\mu\frac{\mu_t}{\rho}\frac{\langle k\rangle}{\langle\varepsilon\rangle}\left(\mathring{S}_{ij}-\frac{1}{3}\mathring{S}_{mm}\delta_{ij}\right) \tag{8}$$

The mean strain rate S_{ij} in Eqs. (7) and (8) has the following form

$$S_{ij}=\frac{1}{2}\left(\frac{\partial\langle U_i\rangle}{\partial x_j}+\frac{\partial\langle U_j\rangle}{\partial x_i}\right) \tag{9}$$

Also, the $\mathring{S}_{ij}$ term, in Eq. (8), called the Oldroyd derivative, can be expressed as

$$\mathring{S}=\frac{\partial S_{ij}}{\partial t}+\langle U_k\rangle\frac{\partial S_{ij}}{\partial x_k}-\frac{\partial\langle U_i\rangle}{\partial x_k}S_{kj}-\frac{\partial\langle U_j\rangle}{\partial x_k}S_{ki} \tag{10}$$

Equation (7) is only really satisfactory for simple flows where just one Reynolds stress term has significant influence. Equation (8) is more realistic in allowing the inequality of normal stresses. Numerous variants on Eq. (8) are now available.

Four significantly differing turbulence modeling strategies are compared. These are:

(I) the standard linear k-ε model (Eqs. (3), (6), and (7));
(II) a linear $k-l$ model (Eqs. (3), (5), and (7));
(III) a linear zonal $k-\varepsilon/k-l$ model (Eqs. (3), (5), (6), and (7)) and
(IV) a nonlinear zonal $k-\varepsilon/k-l$ model (Eqs. (3), (5), (6), and (8)).

For models (III) and (IV), when $y^+\geqslant60$ the k-ε model is used and for $y^+<60$ the $k-l$ model is applied. Patching conditions at the $y^+=60$ interface are given by [22]. Model (IV) is essentially the same as (III), except that the nonlinear ''Boussinesq'' approximation (Eq. (10)) is used in place of the linear approximation implemented in models (I)–(III). The following standard con-

Table 1 Equation (3) terms for specific $\langle\Phi\rangle$ values

$\langle\Phi\rangle$	Γ_ϕ	T_1	T_2
$\langle k\rangle$	$\mu+\langle\mu_t\rangle/\sigma_k$	1	$\langle\varepsilon\rangle$
$\langle\varepsilon\rangle$	$\mu+\langle\mu_t\rangle/\sigma_\varepsilon$	$C_{\varepsilon1}\langle\varepsilon\rangle/\langle k\rangle$	$C_{\varepsilon2}\langle\varepsilon\rangle^2/\langle k\rangle$
$\langle C\rangle$	$\mu+\langle\mu_t\rangle/\sigma_C$	0	0

stants are used: $\sigma_k=1$, $\sigma_\varepsilon=1.3$, $\sigma_c\approx 1$, $A_\varepsilon=0.263$, $A_\mu=0.016$, $C_E=C_D=1.68$, $C_{\varepsilon 0}=2.4$, $C_{\varepsilon 1}=1.44$, $C_{\varepsilon 2}=1.92$, $C_{\mu 0}=2.4$, $C_\mu=0.09$.

Boundary Conditions for Fluid Flow. For fluid velocities, at solid surfaces the usual no-slip and impermeability conditions are applied. At inflow boundaries the total pressure is fixed, the normal velocity set to conserve mass and the remaining velocity components made zero. At flow outlets generally the pressure is fixed, the normal velocity again set to conserve mass and the gradients of all other variables set to zero in a second order fashion. The slotted grills 1–4 are treated using quadratic loss coefficients. Fans 1 and 2 are modeled using quadratic momentum sources. When $\langle\Phi\rangle=\langle C\rangle$, in Eq. (3), $\partial\langle C\rangle/\partial n=0$ at solid surfaces and outlets. At the chosen inlet a specified $\langle C\rangle$ value is used. Fuller boundary condition details can be found in Tucker [13].

General Program Features. The flow governing equations are discretized using a standard SIMPLE based structured finite volume technique [23]. Generally, for the Fig. 1 geometry, around 0.5 million-control volumes are used, but to confirm grid independence just over 4 million are implemented. The second-order CONDIF (Runchal [24]) convective term treatment and generally a first-order fully implicit time scheme are used with time steps of $\Delta t=0.001$ s. However, for $k-l$ predictions adaptive time stepping is tried. Step refinement is based on comparison of the first-order fully implicit results with either solutions using smaller steps (step halving), forward Euler results or trapezoidal. All three approaches are found to give useful time savings. Further details of the numerical methods are given by Tucker [13].

Particle Trajectory Equations. Particle movement can be calculated by solving the following Lagrangian particle trajectory and momentum equation pair

$$\frac{d\mathbf{x}}{dt}=\mathbf{U}_p, \quad m\frac{d\mathbf{U}_p}{dt}=\Sigma\mathbf{F} \tag{11}$$

where m is the particle mass, $\mathbf{x}$ its position vector, $\mathbf{U}_p$ the particle velocity and t time. $\Sigma\,\mathbf{F}$ represents the sum of the external particle forces. As usual, the drag force $\mathbf{F}_D=\rho C_D\pi d^2|\Delta\mathbf{U}|\Delta\mathbf{U}/8$ is modeled, where $\Delta\mathbf{U}=\langle\mathbf{U}\rangle-\mathbf{U}_p$ and $\langle\mathbf{U}\rangle$ is the phase averaged fluid velocity, d the particle diameter, and C_D a drag coefficient. The gravitational $\mathbf{F}_g=(\rho_p-\rho)\pi \mathrm{d}^3\mathbf{g}/6$ and electrostatic particle image $\mathbf{F}_i$ forces are also considered. Therefore, $\Sigma\mathbf{F}=\mathbf{F}_D+\mathbf{F}_g+\mathbf{F}_i$. Other well documented forces [25], notably, the Saffman (as in the predictions of [10] are ignored. The particle Reynolds number is defined as $\mathrm{Re}_p=\rho d|\Delta\mathbf{U}|/\mu$. As a drag estimate, for $\mathrm{Re}_p<1$, $C_D=24/\mathrm{Re}_p$. If $1000\geqslant\mathrm{Re}_p>1$, $C_D=24(1+0.15\,\mathrm{Re}_p^{0.687})/\mathrm{Re}_p$ and when $\mathrm{Re}_p>1000$, $C_D=0.44$. Equations (11) are integrated using second-order Crank-Nicolson and fourth-order Runge-Kutta methods, respectively. To illustrate some points to be made here, it is sufficient to stop the integration when particles enter the $y^+<5$ (viscous sublayer) region. For selected deposition predictions, integration is continued up to the wall. For these, the particles are assumed to stick to the wall and not bounce. Due to electrostatic forces (see later) this is the most appropriate boundary condition. Seeded particles are initially assumed to have the same local velocity as the fluid. Either point seeding or random seeding over a specified region is used.

Accounting for the Effect of Turbulence on Particle Transport. The instantaneous velocity field, with which the particle interacts, is expressed as the sum of the phase averaged velocities and a turbulence fluctuation magnitude. Therefore, the following can be written

$$u=\langle U\rangle+N\sigma_1, \quad v=\langle V\rangle+N\sigma_2, \quad w=\langle W\rangle+N\sigma_3 \tag{12}$$

For isotropic turbulence predictions

$$\sigma_1=\sigma_2=\sigma_3=\sqrt{2\langle k\rangle/3} \tag{13}$$

For anisotropic turbulence it is assumed

$$\sigma_1=\sqrt{\langle\overline{u_1u_1}\rangle}, \quad \sigma_2=\sqrt{\langle\overline{u_2u_2}\rangle}, \quad \sigma_3=\sqrt{\langle\overline{u_3u_3}\rangle} \tag{14}$$

where $\langle\overline{u_1u_1}\rangle$ $\langle\overline{u_2u_2}\rangle$ and $\langle\overline{u_3u_3}\rangle$ are given by Eq. (8). N is a Gaussian random number with a standard deviation of unity. It is updated either when an eddy life (t_1) is exceeded or the particle traverses an eddy (this taking the eddy transit time t_t). To evaluate the above two time scales an assumption about the eddy size $\langle l_e\rangle$ is required. Following Gosman and Ioannides [1] it is assumed,

$$\langle l_e\rangle=C_\mu^a\frac{\langle k\rangle^{3/2}}{\langle\varepsilon\rangle} \tag{15}$$

Even when Eqs. (14), to account for anisotropy are implemented, Eq. (15) is still used. Therefore, with regards to size, eddies are always assumed isotropic. In the context of the results, where only relative influences are being assessed, this inconsistency seems reasonable. In the work of others (see Milojevic [26]), to fit experimental data, the exponent a is varied between 0.32 and 0.9. Here $a=0.58$, which is consistent with the predictions of [26]. The eddy life time can be approximated as

$$t_l=\frac{\langle l_e\rangle}{\sigma}, \tag{16}$$

where $\sigma=\sqrt{2\langle k\rangle/3}$. The transit time t_t can be expressed as

$$t_t=\frac{\langle l_e\rangle}{v_d} \tag{17}$$

where v_d is the drift velocity $|\langle\mathbf{U}\rangle-\mathbf{U}_p|$. However, within an eddy v_d is not constant. Therefore, small time steps are implemented and v_d is computed each time step. Values of v_d are used to calculate relative displacements within an eddy. When the total of these is greater than $\langle l_e\rangle$ it is known the particle has left eddy and N is recomputed.

Simple Electrostatic Force Algorithm. There is no electrical field in the Fig. 1 geometry. All surfaces are earthed. Under these conditions, electrostatic particle forces can be expressed as

$$\mathbf{F}_i\approx\frac{q^2}{16m^2\pi\varepsilon_0 m}\mathbf{n} \tag{18}$$

where $\mathbf{F}_i$ is the image force vector (see Kraus [15]), $\varepsilon_0=8.854\times10^{-12}$ F/m the free space permittivity and s the nearest wall to particle distance. Maximum, particle charge, q, data for different particle mass to diameter ratios are given by Blythe and Reddish [27]. They can also be gained from Paschen's law. Where particle charges are considered here, maximum measured values are used.

For complex, cluttered geometries the control volume node to nearest wall distance y can be calculated using a method derived by Spalding [16] (other approaches are possible, see for example Sethian [28]). This involves the solution of a Poisson equation of the following form,

$$\frac{\partial}{\partial x_j}\left(\frac{\partial L}{\partial x_j}\right)=C \tag{19}$$

where $C=-1$ and L is a variable whose gradient is related to the wall distance. At solid walls $L=0$ and at flow boundaries $\partial L/\partial n=0$. Here, y is related to L using the slightly (the absolute values of gradients are taken giving symmetrical wall distances variations for symmetrical geometries) modified expression to Spalding's derived by Tucker [29] and given below

$$y=-\sum_{j=1,3}\left|\frac{\partial L}{\partial x_j}\right|\pm\sqrt{\left(\left(\sum_{j=1,3}\left|\frac{\partial L}{\partial x_j}\right|\right)^2+2L\right)} \tag{20}$$

Derivation of the above requires the assumption that the surface perpendicular to y is infinite. This approximation is reasonable in

Table 2 Gradient arguments for direction cosines of $\hat{n}$

Argument	Direction cosines
$\left\lvert\frac{\partial L}{\partial x}\right\rvert > \max\left[\left\lvert\frac{\partial L}{\partial x}\right\rvert, \left\lvert\frac{\partial L}{\partial y}\right\rvert, \left\lvert\frac{\partial L}{\partial z}\right\rvert\right], \frac{\partial L}{\partial x} > 0$	$n_1=1,\ n_2=0,\ n_3=0$
$\left\lvert\frac{\partial L}{\partial x}\right\rvert > \max\left[\left\lvert\frac{\partial L}{\partial x}\right\rvert, \left\lvert\frac{\partial L}{\partial y}\right\rvert, \left\lvert\frac{\partial L}{\partial z}\right\rvert\right], \frac{\partial L}{\partial x} < 0$	$n_1=-1,\ n_2=0,\ n_3=0$
$\left\lvert\frac{\partial L}{\partial y}\right\rvert > \max\left[\left\lvert\frac{\partial L}{\partial x}\right\rvert, \left\lvert\frac{\partial L}{\partial y}\right\rvert, \left\lvert\frac{\partial L}{\partial z}\right\rvert\right], \frac{\partial L}{\partial y} > 0$	$n_1=0,\ n_2=1,\ n_3=0$
$\left\lvert\frac{\partial L}{\partial y}\right\rvert > \max\left[\left\lvert\frac{\partial L}{\partial x}\right\rvert, \left\lvert\frac{\partial L}{\partial y}\right\rvert, \left\lvert\frac{\partial L}{\partial z}\right\rvert\right], \frac{\partial L}{\partial y} < 0$	$n_1=0,\ n_2=-1,\ n_3=0$
$\left\lvert\frac{\partial L}{\partial z}\right\rvert > \max\left[\left\lvert\frac{\partial L}{\partial x}\right\rvert, \left\lvert\frac{\partial L}{\partial y}\right\rvert, \left\lvert\frac{\partial L}{\partial z}\right\rvert\right], \frac{\partial L}{\partial z} > 0$	$n_1=0,\ n_2=0,\ n_3=1$
$\left\lvert\frac{\partial L}{\partial z}\right\rvert > \max\left[\left\lvert\frac{\partial L}{\partial x}\right\rvert, \left\lvert\frac{\partial L}{\partial y}\right\rvert, \left\lvert\frac{\partial L}{\partial z}\right\rvert\right], \frac{\partial L}{\partial z} < 0$	$n_1=0,\ n_2=0,\ n_3=-1$

the regions of importance, which are close to surfaces. The negative root of Eq. (20) gives the nearest wall distance. This can be expressed as the vector

$$\mathbf{y} = \hat{\mathbf{n}} y \tag{21}$$

The direction cosines of $\hat{\mathbf{n}}$ can, as suggested by Tucker [29], be found using the gradient arguments given in Table 2. The max [ ] construct means that the maximum value inside the brackets is taken. The particle to wall distance vector **s**,

$$\mathbf{s} = \mathbf{x}_p - \mathbf{x}_n + \mathbf{y} \tag{22}$$

is the sum of $\mathbf{x}_p$, the particle position vector, the position vector for the node of the control volume the particle is in $-\mathbf{x}_n$ and **y** (see Fig. 2). For geometries with sloping and curved surfaces, more general expressions for **s** should be derived.

Accounting for Flow Unsteadiness. As part of this work, the particle-tracking procedures were modified so that fluid flow and particle time integrations could be coupled. Predicted unsteadiness amplitudes and frequencies are significantly different to the measured. Therefore, as well as using numerical temporal information, to crudely further gain an idea of the effect of unsteadiness, the measured dominant average normalized resultant unsteadiness $|\mathbf{u}''|/|\overline{\mathbf{U}}| \approx 0.175$ and frequency $f = 0.5$ Hz are superimposed on a predicted instantaneous flow field. A sinusoidal temporal velocity variation is selected. Further, assuming $u''/\overline{U} \approx v''/\overline{V} \approx w''/\overline{W} \approx |\mathbf{u}''|/|\overline{\mathbf{U}}|$ (i.e., isotropy of the measured normalized unsteadiness) gives

$$\langle \mathbf{U} \rangle = \overline{\mathbf{U}}(1 + 0.174 \sin(2\pi f t)), \tag{23}$$

where $t = 0$ just corresponds to the time the first particle is seeded, particles being seeded one after another (sequentially).

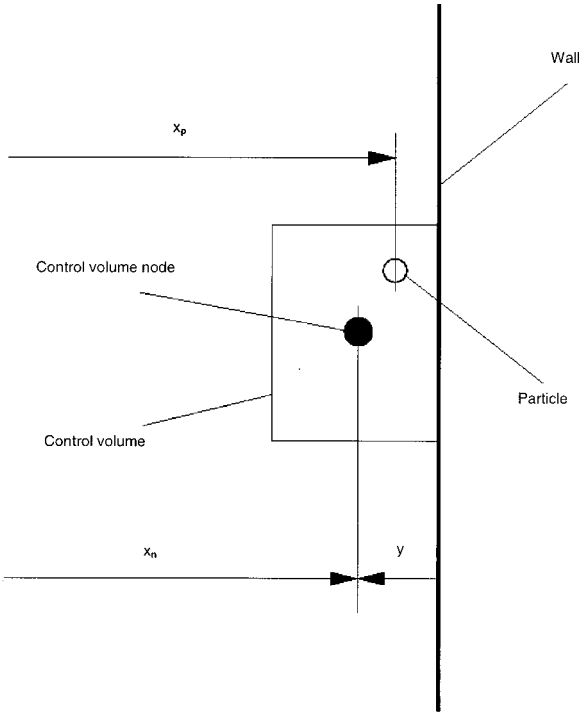

Fig. 2 Schematic showing particle location relative to a right hand wall control volume center

Discussion of Results

Fluid Velocity Validation. Particle trajectories are affected mostly by the predicted velocity or turbulence field. Therefore, it is worth considering errors in these. Figure 3 compares predictions with LDA measurements in the region $0.37 < X < 0.53$ (where the dimensionless x coordinate has the range $0 < X < 1$), for over 100 points. Figure 3(*a*) compares normalized mean velocities. The +, × and ● symbols represent the linear zonal, $k-\varepsilon$ and $k-l$ predictions, respectively. For exact agreement all data would rest on the 45 deg line. As can be seen, predicted velocities are similar and in reasonable agreement with the measurements. Corresponding turbulence intensity comparisons are shown in Fig. 3(*b*). The over prediction of turbulence by the $k-\varepsilon$ approach and considerable discrepancies between models can

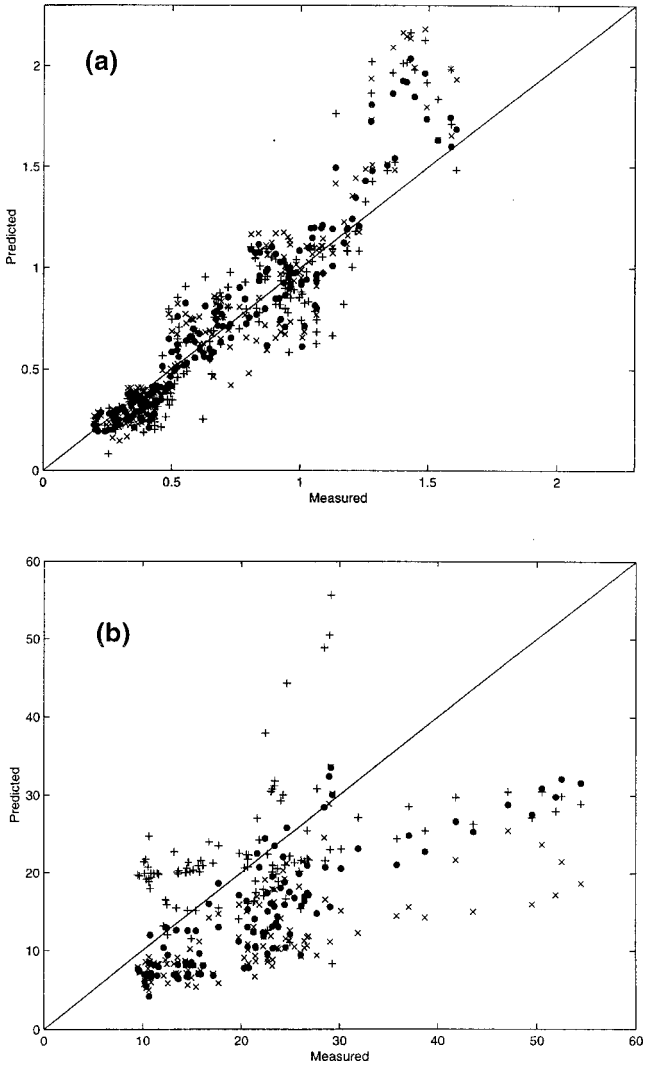

Fig. 3 Comparison of predictions with LDA measurements: (*a*) velocity comparison and (*b*) turbulence intensity comparison (—— line of exact agreement, + $k-\varepsilon$, x $k-l$, ● linear zonal)

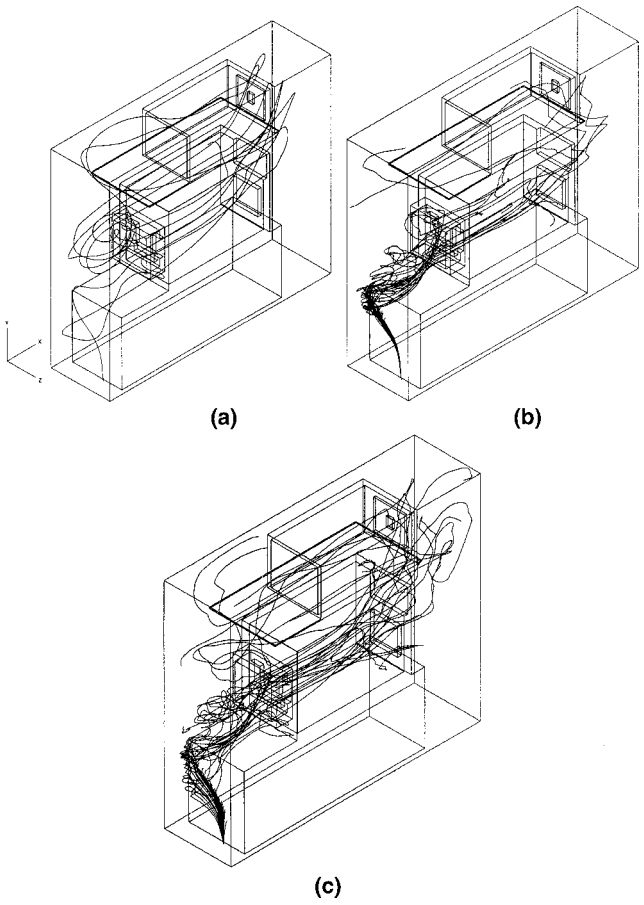

Fig. 4 Particle dispersion for the complex system: (*a*) "laminar" flow; (*b*) isotropic turbulence; and (*c*) anisotropic turbulence

be clearly seen. Overall, the zonal predictions are the most accurate (nonlinear zonal results, not shown here, give a slight turbulence intensity accuracy improvement over the linear). Therefore, these are used as a datum for later comparisons.

Particle Dispersion. Particle dispersion algorithm validation cases for homogenous turbulence are presented in Appendix A. These give confidence in the newly developed particle transport program. Figure 4 shows predicted Fig. 1 geometry particle dispersion. The fans produce a low-pressure area in the left-hand side of the system. This draws fluid in through the left-hand lower hole (flow inlet). Unless otherwise stated 40, $\rho_p \approx 1500\ \mathrm{kg/m^3}$, $d=6\ \mu\mathrm{m}$ particles are seeded at the center of this. So that the effects can be isolated, for all predictions, generally the same datum mean isotropic $k-\varepsilon/k-l$ model velocity field is used. In Fig. 4(*a*), datum velocity field turbulent fluctuations are set to zero. This, in a sense, mimics laminar flow. As expected, there is no dispersion, all particles exactly overlaying. Figure 4(*b*) shows the results when the datum field turbulent fluctuations are nonzero. The significant effect of turbulence on dispersion is clear. Anisotropy can have a major influence on particle and passive scalar transport (see [14]). This is illustrated in Appendix B, where its flow modifying effects can also be seen. In Fig. 4(*c*), using Eqs. (8) and (14), anisotropy is incorporated into the analysis. A significant difference in particle paths is clear. This would be greater if the effect of anisotropy on the fluid velocity field had also been accounted for (i.e. the datum velocity field not used).

Rather than show further plots, illustrating the effects of other modeling aspects, Table 3 is used to quantify particle deviations from (unless otherwise stated) the isotropic $k-\varepsilon/k-l$ solution shown in Fig. 4(*b*). The deviation is defined as a root mean square for the final positions of 1000 particles. For each pair of particle paths under consideration, the deviation is calculated at the point in time when the first particle is captured. Deviations are normalized by the average system dimension $(x_{\max}+y_{\max}+z_{\max})/3 \approx 1/2$ m and expressed as percentages.

Table 3 Summary of particle deviations

Modeling aspect	% Deviation
Anisotropy	19
$k-\varepsilon$ model	20
$k-l$ model	19
Unsteadiness	18
Fan 2 swirl	22
Electrostatic force	10

As can be seen, like anisotropy, both general turbulence model choice and unsteadiness have a significant effect on particle transport. The unsteadiness deviation figure, quoted in the table, is based on Eq. (23). However, other numerically based $k-l$ model evidence also suggests significant temporally related particle path deviations. The clear effect of fan 2 swirl on dispersion is also shown in the table. The swirl component, supplied by the fan manufacturer, is approximately 5.5 m/s. Due to a grill, fan 1 swirl is negligible and so not accounted for. Table 3 shows the electrostatic force effect on particle transport is less but still significant. However, for this estimate, larger ($d=13\ \mu$m) particle (which can hold more charge $-q=1.7\times10^{-15}$ C) predictions are made.

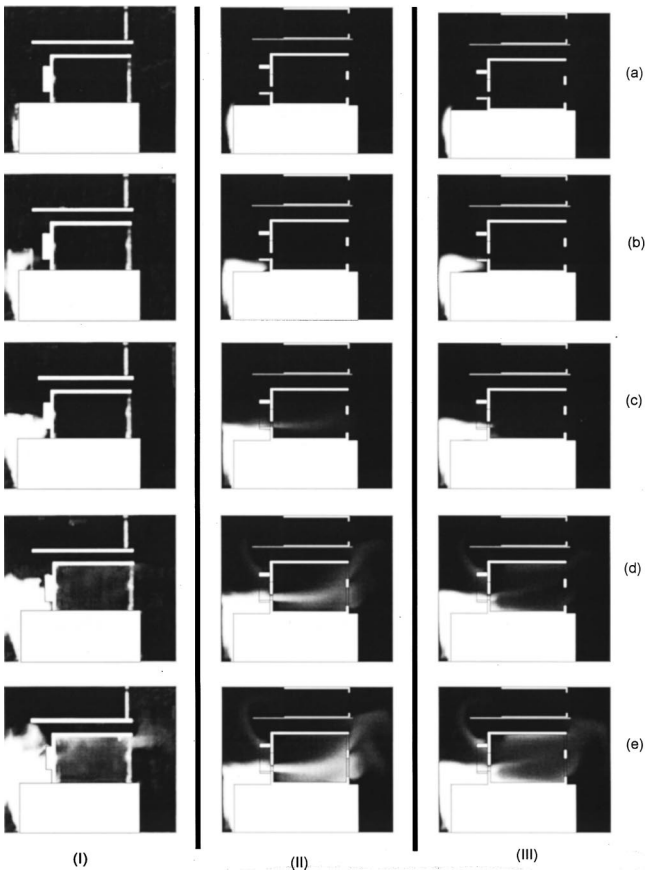

Fig. 5 Comparison of smoke flow visualization evidence with linear zonal predictions at the following dimensionless times: (*a*) t*=1.2; (*b*) t*=2.4; (*c*) t*=3.6; (*d*) t*=4.8 and (*e*) t*=6.0. Columns: (I) experimental flow visualization; (II) predictions with no fan swirl and (III) predictions with fan swirl.

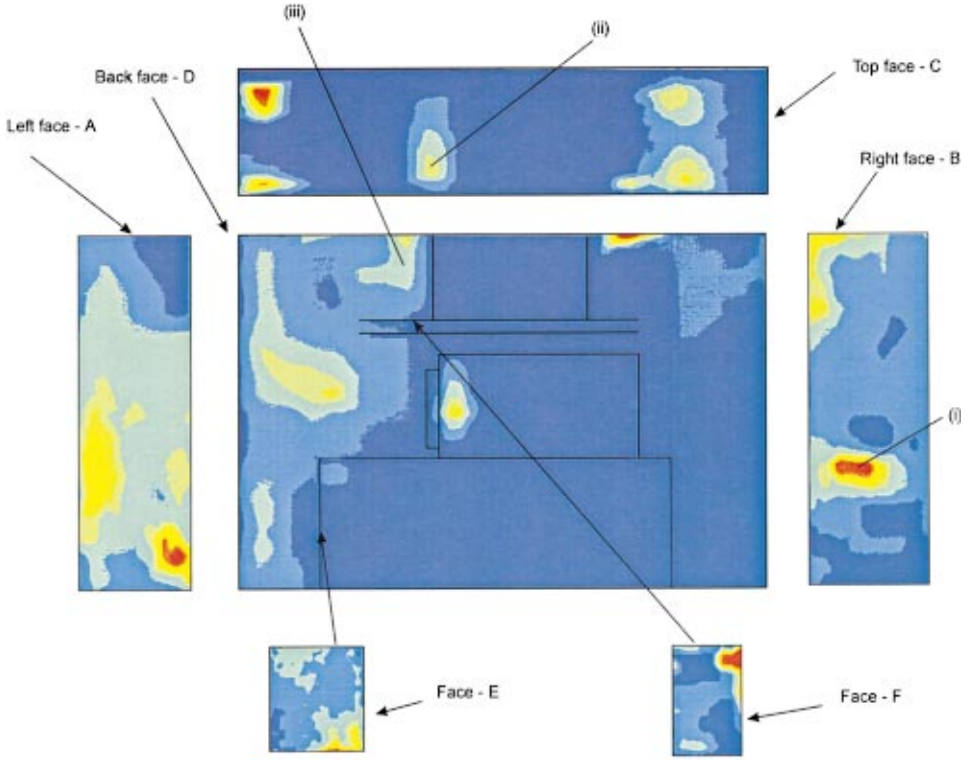

Fig. 6 Measured particle concentration contours for faces A-F

The strong influence of fan 2 swirl is further illustrated along with some basic flow features in Fig. 5. This compares linear zonal model predictions with mid z-axis, x-y plane smoke flow visualization evidence. The left hand column (I) corresponds to the experiment, and (II) and (III) Eq. (3) $\langle\Phi\rangle=\langle C\rangle$ predictions. In column (III) (unlike (II)), fan 2 swirl is modeled.

Frames (a), (b), (c), (d), and (e) correspond to $t^*=tU_0/x_{\max}=1.2$, 2, 4, 3.6, 4.8, and 6, respectively, where U_0 is the characteristic velocity for the fans. White areas correspond to $C>5$ percent of the inlet value regions. This scale is chosen so as to

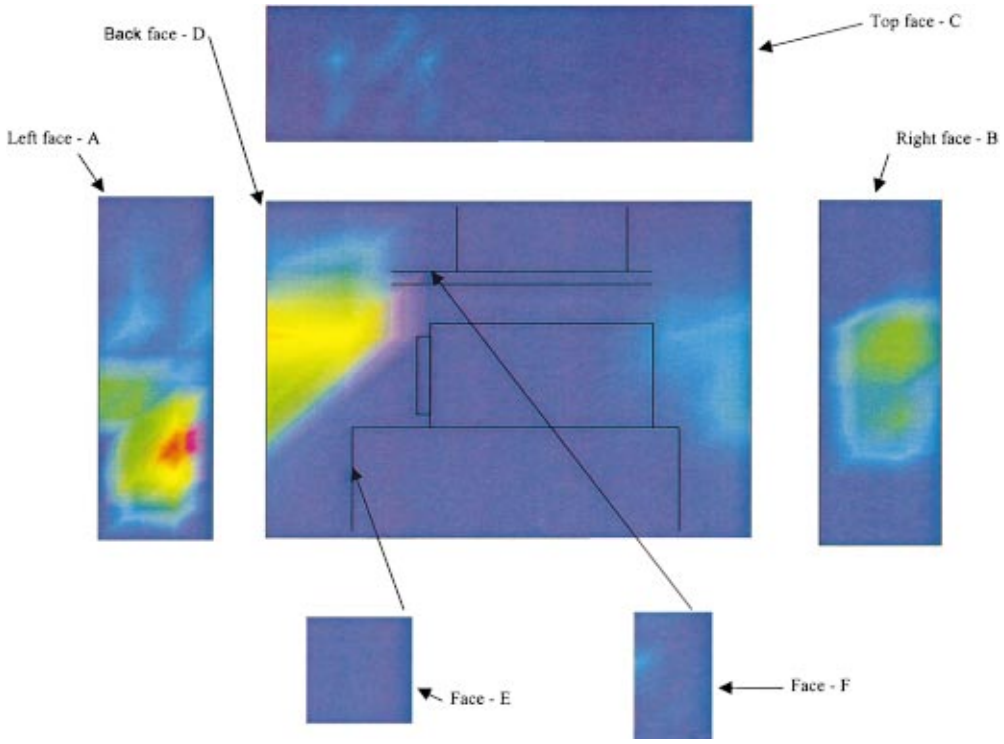

Fig. 7 Predicted particle concentration contours for faces A-F

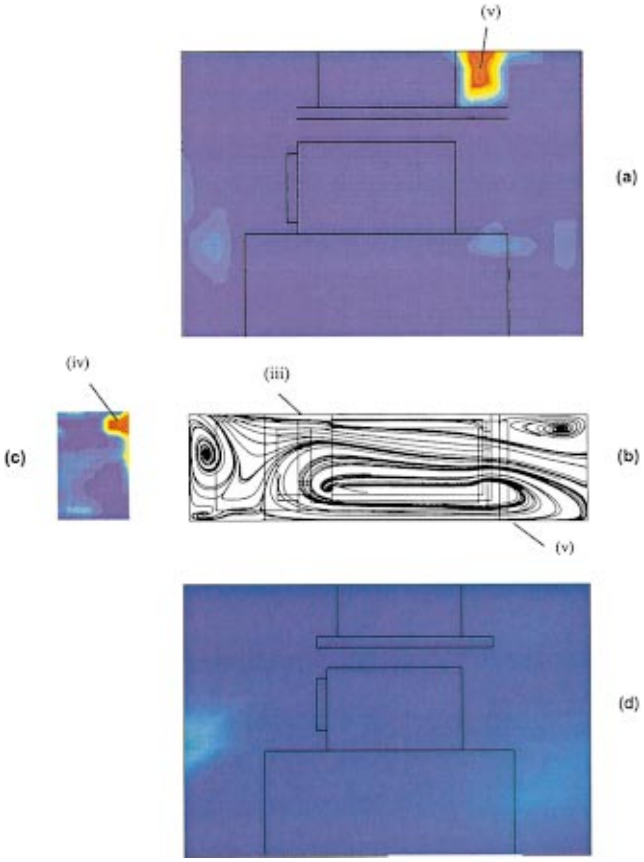

Fig. 8 Particle concentrations and computed flow field: (*a*) face—G measurements; (*b*) x-z plane streamlines; (*c*) face—F measurements and (*d*) face—G predictions.

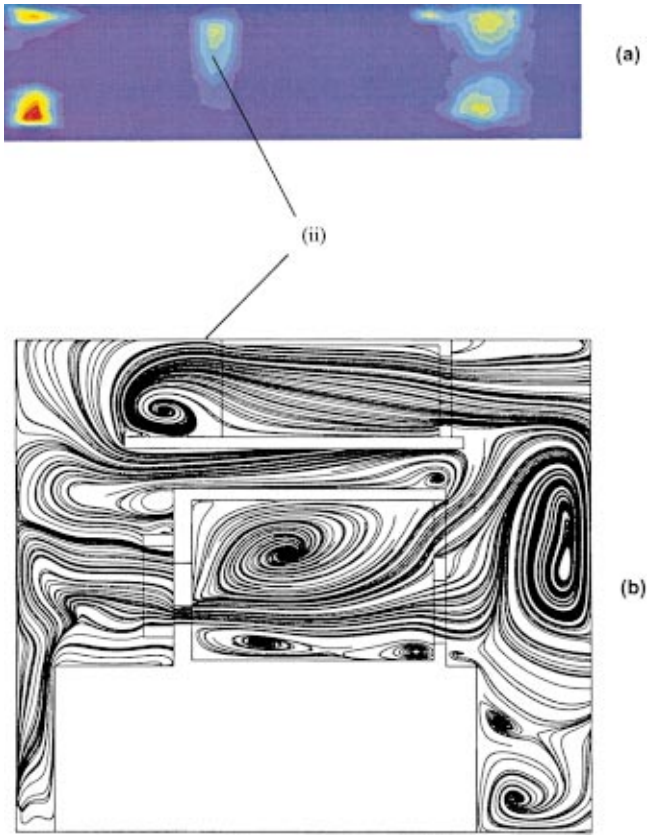

Fig. 9 Measured particle concentrations and predicted flow paths: (*a*) face—C measurements and (*b*) x-y plane predictions

match the measurements at $t^*=0.2$. As can be seen, for $t^*>3.6$ the experiments suggest considerable smoke dispersion downstream of fan 2. For the prediction without swirl (middle column), unlike the experiment, at $t^*=4.8$ a distinct jet of smoke can be seen at the fan 2 exit. The inclusion of swirl (right-hand column) considerably improves agreement in this region, and like the experiment shows less movement of smoke through grill 3. Clearly, for scalar and particle transport the modeling of fan swirl can be important. Fans also induce extra turbulence (Lasance [30]). This has not been adequately accounted for in the fan model used here. Turbulence intensity results are found insensitive to source term enforced increases Gn turbulence energy production in Eq. (3). Further accuracy improvements could probably be made if this matter is resolved. Figure 5 shows that, immediately after entering the system most contaminants are drawn towards the fan 2 area.

Figure 6 shows measured particle concentration contours for the left face-A, right face-B, top face-C, back face-D, vertical face-E and horizontal face-F regions labeled in Fig. 1. Charged particles are randomly seeded at the usual inlet (around 125,000 with an approximate Gaussian size distribution are used for predictions). Deposition images are converted to contours using the UTHSCSA ImageTool software. A seismic color scale is used, red corresponding to higher particle concentration regions. The high region (i), face-B, concentration appears to be caused by impingement downstream of fan 2. Figure 7 gives corresponding linear $k-\varepsilon/k-l$ model deposited particle positions. The agreement with the experimental data is disappointing. Fans and grills are assumed to absorb 50 percent of the particles passing through them. Fan 2 is assumed to produce a 30 percent turbulence increase. Results are found highly sensitive to losses in and downstream of fan 2. However, to a large extent, differences are also attributed to inadequacies in the predicted turbulent intensities. As shown in Fig. 3(*b*) turbulence intensities are generally poorly predicted but dramatically (see Fig. 4) influence particle transport.

Figure 8, frame (a), shows front face-G experimental data. The red, region (v), is most probably due to centrifugal deposition arising from strong *x*-*z* plane (around the fan 1 hub) streamline curvature indicated in Fig. 8(*b*). This figure also possibly partly suggests the horizontal Fig. 8(*c*) (previously presented in Fig. 6) face-F area (iv) deposition. Reasons for this are that, first, strong streamline curvature again appears to cause deposition around region (iii) on face-D (cf. Fig. 6. and 8(*b*)). Heavier particles may then drop out around region (iv). Again, reminiscent of Fig. 7, the predicted face-G deposition distributions, (see frame (d)) are disappointing. However, it is pleasing to note, consistent with measurements, face-G deposition levels are lower than-D. Figure 9(*b*) gives predicted centerline *x*-*y* plane streamlines. These perhaps suggest centrifugal deposition is again a mechanism for the high frame (a) (also shown in Fig. 6) face-C, region (ii) deposition.

Conclusions

Comparisons have been made between velocity and turbulence intensity predictions and measurements for $k-\varepsilon$, $k-l$, and zonal turbulence models. Predicted velocities for the different models were similar. However, they gave significantly different turbulence intensities. The Lagrangian particle trajectory method was validated against both analytical and experimental dispersion data. A simple approach for predicting electrostatic Coulomb forces on particles was presented. Turbulence model choice, anisotropy, unsteadiness, fan swirl and, for larger particles, electrostatic forces

were all shown to have significant effects on particle transport. When fan swirl is included agreement is improved with smoke flow visualization evidence.

Results suggest, centrifugal forces, arising from regions of strong streamline curvature, play a key particle deposition role. They also indicate weaknesses in conventional eddy viscosity based turbulence models make the accurate prediction of complex geometry particle deposition a difficult task. Axial fans are found in many fluid systems. The sensitivity of results to their modeling suggests caution should be used when making predictions involving fans and that more numerical characterization work for them could be carried out. Overall, the work suggests that, for many complex-engineering systems, at best (without excessive model calibration time), only qualitative particle deposition information can be gained from numerical predictions.

Acknowledgments

The author is grateful for the support of the EPSRC (grant number GR/L05600), NCR (Scotland), Hewlett Packard, Digital Equipment and GEC Marconi Avionics. I would like to express my thanks to Mr. M. Mendjeli for his help with some of the computations, and Dr. Z. Pan, Mr S.-T. Kuay, and Ms B. Dummeniel for producing the experimental data.

Nomenclature

A_ε, A_μ = turbulence model constants
a = exponent for C_μ
C = scalar concentration
C_D = particle drag coefficient or turbulence model constant
C_μ, $C_{\mu 0}$, $C_{\varepsilon 0}$, = turbulence model
$C_{\varepsilon 1}$, $C_{\varepsilon 2}$, C_E = constants
d = particle diameter
f = frequency of unsteadiness
$\mathbf{F}$ = force vector
g = earth's acceleration due to gravity
k = turbulent kinetic energy $\overline{u_i' u_i'}/2$
L = Poisson equation wall distance variable
Re_p = particle Reynolds number
l_e, l_μ, l_ε = mixing lengths
m = particle mass
n = direction cosines
N = random number
P = static pressure
q = particle charge
s = distance between particle and wall
$S_{i,j}$ = mean strain rate
$\mathring{S}_{i,j}$ = Oldroyd derivative of $S_{i,j}$
T_1, T_2 = terms in transport equations for C, k, and ε
t = time
$\mathbf{U}$ = velocity vector
U_i = x_i velocity component
u_i' = x_i component of mean turbulence fluctuation velocity
v_d = particle drift velocity $|\langle \mathbf{U} \rangle - \mathbf{U}_p|$.
X_i = dimensionless Cartesian direction coordinates
x_i = Cartesian direction coordinates
y = distance to nearest wall
Γ = diffusion coefficient
Δt = time step
ε = dissipation rate of k
ε_0 = free space permittivity
μ, μ_t = laminar and turbulent viscosities
ρ = density
σ = diffusion Prandtl number or turbulence fluctuation magnitude
Φ = general flow variable

Subscripts

ave = pertaining to an average value
d = pertaining to drag
i = pertaining to an image force
k = pertaining to turbulence kinetic energy
max = pertaining to a maximum value
n = pertaining to a node
p = pertaining to a particle
t = pertaining to a time t
ε = pertaining to the rate of dissipation of k
o = reference value

Superscripts

+ or * = dimensionless variables

Appendix A

Particle Velocity Validation. Hinze [25] gives the following analytically based dispersion expression

$$C(x,y,z) = \frac{S}{4\pi\Gamma|x|} \exp \frac{-U((y-y_0)^2+(z-z_0)^2)}{4\Gamma|x|} \qquad (A1)$$

for fluid particles in homogeneous turbulent flow. S is a source strength and $\Gamma = C_\mu \rho k^2/\varepsilon$. Present computations involving 30,000 particles are compared with Hinze's expression in Fig. 10. To build up a concentration profile from predictions 30 particle bins are used. As can be seen, agreement is reasonable and could be improved with more particles and bins. In Fig. 11, comparison is made with Snyder and Lumley's [31] experiment for dispersion of hollow glass, corn pollen, solid glass and copper particles, in grid generated turbulence. The mean square displacement is estimated as

$$\overline{Y_j^2}(t) = \frac{\Sigma (Y_{jt} - Y_0)^2}{N_t} \qquad (A2)$$

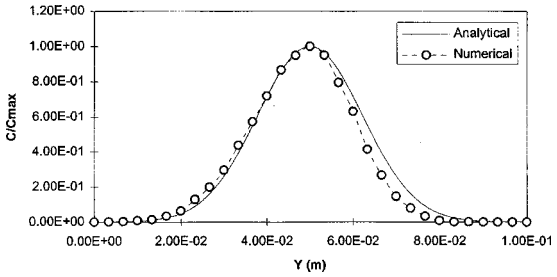

Fig. 10 Comparison of predictions with analytical solution of Hinze

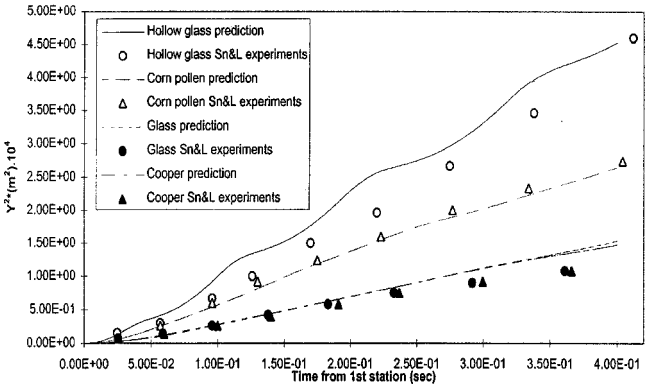

Fig. 11 Comparison with measurements for dispersion in grid generated turbulence

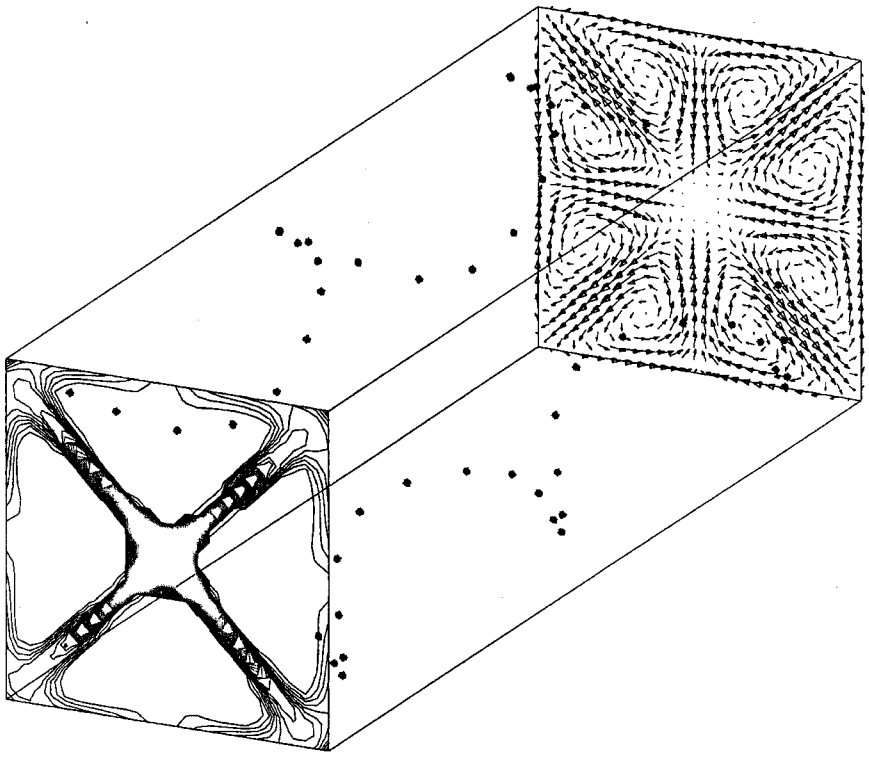

Fig. 12 Predicted velocity vectors, weightless particle paths, and the distribution of a passive scalar

where N_t is the number of particles at time t, Y_{jt} is the y location of any particle j at the same time t and Y_0 the initial y position. Some 1000 trajectories for each kind of particle are calculated and averaged. As can be seen, agreement is reasonable, especially for the corn pollen. This has a density similar to that for which most of the results are presented.

Appendix B

Affect of Anisotropy on Transport Process. For channel flows, unlike nonlinear turbulence models, linear turbulence methods do not predict experimentally observed recirculations (see Speziale [21]) in the plane perpendicular to the streamwise direction. Figure 12 gives predicted velocity vectors, weightless particle paths, and the distribution of a passive scalar seeded upstream around the centreline for a *long* channel. These predictions partly verify the correct implementation the present nonlinear model (Model (IV)).

References

[1] Gosman, A. D., and Ioannides, E., 1983, ''Aspects of computer simulation of liquid fuelled combustors,'' J. Energy, **7**, pp. 482–490.

[2] Awolesi, S. T., and Kokkalis, A., 1991, ''A case study on the application of measurements and computer simulation to the ventilation and airborne contaminants control within a workshop,'' Proc. BEPAC Conf., pp. 1–6.

[3] Killingworth, D., Ong, I. B. S., and Whittle, G. E., 1991, ''The application of computational fluid dynamics (CFD) in the design if clean rooms and process facilities,'' *Proc. Instit. Environ. Sci.*

[4] Hall, R. C., and Cowan, I. R., 1998, ''Modelling atmospheric dispersion near buildings,'' NAFEMS Int. J of CFD Case Studies, **1**, Apr., pp. 7–18.

[5] Drake, S. N., Pericleous, K. A., and Scheiwiller, T., 1991, ''Computational fluid dynamics a mathematical tool to simulate dispersal of airborne pollution,'' *Proc. Int. Conf. Environmental Pollution, Lisbon, Portugal*.

[6] Schuh, M. J., Schuler, C. A., and Humphrey, J. A. C., 1989, ''Numerical calculation of particle laden gas flows past tubes,'' AIChE J., **35**, No. 3, pp. 466–480.

[7] Chan, S. H., and Moussa, B., 1996, ''Trajectories and deposition of silica on cylinders in crossflow with and without a magnetic field,'' ASME J. Heat Transfer, **118**, Nov., pp. 903–910.

[8] Kallio, G. A., and Stock, D. E., 1992, ''Interaction of electrostatic and fluid dynamic fields in wire-plate electrostatic precipitators,'' J. Fluid Mech., **240**, pp. 133–166.

[9] Choi, B. S., and Fletcher, C. A. J., 1997, ''Computation of particle transport in an electrostatic precipitator,'' J. Electrost., **40 and 41**, pp. 413–418.

[10] Young, M. E., and Kallio, G. A., 1991, ''A numerical study of particle motion in an enclosed corotating disk flow,'' *ASME Fluids Engineering Division Publications*, 121, Gas-Solid Flows, D. E. Stock et al., eds., pp. 57–64.

[11] Tucker, P. G., 1996, ''Prediction and measurement of contamination transport in a mechatronic ATM system: a design study,'' *Presented at 11th AT&T Design for Excellence Conf., Florida*.

[12] Hunt, J. C. R., 1995, ''Practical and fundamental developments in the comptuational modelling of fluid flows,'' *Proc. Instn Mech. Engrs-81st Thomas Hawksley Memorial Lecture*, Vol. 209, pp. 297–314.

[13] Tucker, P. G., 2000, ''Prediction of turbulent oscillatory flows in complex systems,'' Int. J. Numer. Methods Fluids, **33**, pp. 869–895.

[14] Zhou, Q., and Leschziner, M. A., 1997, ''Modelling particle dispersion in turbulent recirculating flow with an anisotropy resolving scheme,'' *ASME Fluids Engineering Division Summer Meeting*, FEDSM'97, June 22–26, pp. 1–8.

[15] Kraus, J. D., 1991, *Electromagnetics*, 4th Ed., McGraw-Hill, New York.

[16] Spalding, D. B., 1994, ''Calculation of turbulent heat transfer in cluttered spaces,'' *Proc. 10th Int. Heat Transfer Conf.*, Brighton, UK.

[17] Bosch, G., and Rodi, W., 1998, ''Simulation of vortex shedding past a square cylinder with different turbulence models,'' Int. J. Numer. Methods Fluids, **28**, pp. 601–616.

[18] Chen, C.-J., and Jaw, S.-Y., 1998, *Fundamentals of turbulence modelling*, Taylor&Francis.

[19] Wolfshtein, M., 1969, ''The velocity and temperature distribution in one-dimensional flow with turbulence augmentation and pressure gradient,'' Int. J. Heat Mass Transf., **12**, pp. 301–318.

[20] Launder, B. E., and Spalding, D. B., 1974, ''The numerical computation of turbulent flows,'' Comput. Methods Appl. Mech. Eng., **3**, pp. 269–289.

[21] Speziale, C. G., 1987, ''On non-linear $k-l$ and $k-\varepsilon$ models of turbulence,'' J. Fluid Mech., **178**, pp. 459–475.

[22] Iacovides, H., and Chew, J. W., 1993, ''The computation of convective heat transfer in rotating cavities,'' Int. J. Heat Fluid Flow, **14**, No. 2, pp. 146–154.

[23] Patankar, S. V., 1980, *Numerical heat transfer and fluid flow*, Hemisphere, New York.

[24] Runchal, A. K., 1987, ''CONDIF: A modified central-difference scheme for convective flows,'' Int. J. Numer. Methods Eng., **24**, pp. 1593–1608.

[25] Hinze, J. O., 1975, *Turbulence*, McGraw-Hill, New York.

[26] Milojevic, D., 1990, ''Lagrangian stochastic-deterministic (LSD) predictions of particle dispersion in turbulence,'' Part. Part. Syst. Charact., **7**, pp. 181–190.
[27] Blythe, A. R., and Reddish, E., 1979, ''Charge on powders and bulking effects,'' *Inst. Phys. Conf. Ser.*, No. 48, pp. 107–114.
[28] Sethian, J. A., 1999, ''Fast Marching Methods,'' SIAM Rev., **35**, No. 2, pp. 199–235.
[29] Tucker, P. G., 1998, ''Assessment of geometric multilevel convergence and a wall distance method for flows with multiple internal boundaries,'' Appl. Math. Model., **22**, pp. 293–311.
[30] Lasance, C. M., 2000, Personal communication.
[31] Snyder, W. H., and Lumley, J. L., 1971, ''Some measurements of particle velocity autocorrelation function in turbulent flow,'' J. Fluid Mech., **48**, pp. 41–71.

Direct Numerical Simulation of a Fully Developed Turbulent Channel Flow With Respect to the Reynolds Number Dependence

Hiroyuki Abe

Hiroshi Kawamura

Department of Mechanical Engineering,
Science University of Tokyo,
Noda-shi, Chiba, 278-8510, Japan

Yuichi Matsuo

National Aerospace Laboratory,
Chofu-shi, Tokyo, 182-8522, Japan

Direct numerical simulation (DNS) of a fully developed turbulent channel flow for various Reynolds numbers has been carried out to investigate the Reynolds number dependence. The Reynolds number is set to be $Re_\tau=180$, 395, and 640, where Re_τ is the Reynolds number based on the friction velocity and the channel half width. The computation has been executed with the use of the finite difference method. Various turbulence statistics such as turbulence intensities, vorticity fluctuations, Reynolds stresses, their budget terms, two-point correlation coefficients, and energy spectra are obtained and discussed. The present results are compared with the ones of the DNSs for the turbulent boundary layer and the plane turbulent Poiseuille flow and the experiments for the channel flow. The closure models are also tested using the present results for the dissipation rate of the Reynolds normal stresses. In addition, the instantaneous flow field is visualized in order to examine the Reynolds number dependence for the quasi-coherent structures such as the vortices and streaks. [DOI: 10.1115/1.1366680]

Introduction

With the aid of recent developments in the super and parallel computers, the direct numerical simulation (DNS, hereafter) of turbulence is now being increasingly performed.

The DNS is a time-dependent and three-dimensional numerical solution in which the governing equations are computed as accurately as possible without any turbulence models introduced. The DNS provides various information, such as velocity, pressure, and their derivatives at any time and point in the instantaneous flow field. These are extremely difficult to be measured in experiments. The first attempt of the DNS was made by Orszag and Patterson [1] 25 years ago for a homogeneous turbulence. For the wall turbulence, the DNS of the fully developed turbulent channel flow started more recently. It was, however, more than 10 years ago when Kim et al. [2] (KMM87, hereafter) published their DNS on the turbulent channel flow. Their Reynolds number based on the friction velocity u_τ and the channel half width δ was $Re_\tau=180$. Since then, the DNS of the turbulent channel flow has often been performed because of its simple geometry and fundamental nature to understand the transport mechanism. Kuroda et al. [3] and Kasagi et al. [4] carried out the DNS for a slightly lower Reynolds number of $Re_\tau=150$. Kim et al. [5] (KMM90, hereafter) also performed a DNS with a higher Reynolds number of $Re_\tau=395$. Antonia and Kim [6] analyzed the DNS data by KMM87 [2] and KMM90 [5] and obtained various turbulence quantities in the near-wall region. They found that the Reynolds-number effect on the turbulence quantities was rather significant. However, it is not known yet whether this non-negligible dependence on the Reynolds number could be extrapolated to a higher Reynolds number or not. The authors group (Kawamura et al. [7]; Kawamura et al. [8]) performed the DNS to include the scalar transport with various Prandtl numbers for $Re_\tau=180$ and 395. They carried out the DNS also for a higher Reynolds number of $Re_\tau=640$ and reported preliminary results in Kawamura [9] and Kawamura et al. [10]. Meanwhile the calculation was extended further; the present paper reports the detailed results. Quite recently, Moser et al. [11] published a brief communication on their DNS for a slightly lower Reynolds number of $Re_\tau=590$. Their results are also included in this paper for comparison.

Extensive effort has been devoted to the experimental study of the turbulent channel flow. Laufer [12] first obtained the detailed turbulence statistics in the channel flow at three Reynolds numbers of $Re_c=12{,}300$, 30,800, and 61,600, where Re_c is the Reynolds number based on the centerline velocity u_c and the channel half width. Later, Hussain and Reynolds [13] reported the higher-order turbulence quantities with the use of an extremely long channel for $Re_c=13{,}800-33{,}300$. Kreplin and Eckelmann [14] made their experiments with the hot-film measurement for low Reynolds numbers of $Re_c=2800-4100$. Johansson and Alfredsson [15] carried out the experiment with the hot-film probes in a water channel for $Re_c=6900-24{,}450$, focusing on the Reynolds-number effect. Wei and Willmarth [16] performed an experiment with the laser-Doppler anemometer in a water channel for $Re_c=3000-40{,}000$ to investigate the existence of an inner scaling law. Recently, Antonia et al. [17] made velocity measurement using the *X*-wire for $Re_c=3300-21{,}500$ and also carried out the DNS for $Re_c=3300$, and 7900. They examined the Reynolds number dependence concentrating mainly on the inner region. Although a large amount of knowledge was accumulated through the experiments, there existed always some discrepancies among the existing experimental results, especially in the near-wall region. More recently, Nishino and Kasagi [18,19] carried out the measurement by the three-dimensional particle tracking velocimeter method (PTV, hereafter) at a low Reynolds number of $Re_\tau=205$ ($Re_c=3755$). They obtained a good agreement with the DNS of KMM87 [2] including the near-wall region.

In the present work, the DNS of turbulent channel flow has been carried out with the use of the finite difference method. The Reynolds number is set to be $Re_\tau=180$, 395, and 640. For $Re_\tau=180$ and 395, the obtained results are compared with those of KMM87 [2] and KMM90 [5] to show the reliability of the present numerical method. On the other hand, Moin and Kim [20] carried out a large eddy simulation for $Re_\tau=640$ more than 10 years ago to compare the results with the experiment of Hussain and Reynolds [13]. The present computation is also executed for $Re_\tau=640$ based on that of Kawamura et al. [10], which is, to the authors' knowledge, the highest Reynolds number ever simulated through DNS for this configuration. Various turbulence statistics

Contributed by the Fluids Engineering Division for publication in the JOURNAL OF FLUIDS ENGINEERING. Manuscript received by the Fluids Engineering Division June 19, 2000; revised manuscript received February 16, 2001. Associate Editor: G. Karniadakis.

Table 1 Spatial resolution

Re_τ	180	395	640
Computational volume (x,y,z)	$12.8\delta\times2\delta\times6.4\delta$	$6.4\delta\times2\delta\times3.2\delta$	$6.4\delta\times2\delta\times2\delta$
Computational volume (x^+,y^+,z^+)	2304×360×1152	2528×790×1264	4096×1280×1280
Grid number	256×128×256	256×192×256	512×256×256
Spatial resolution $(\Delta x^+,\Delta z^+)$	9.00, 4.50	9.88, 4.94	8.00, 5.00
Spatial resolution (Δy^+)	0.20~5.90	0.20~9.64	0.15~8.02
Time integration (t^+)	4,320	15,800	24,800

such as turbulence intensities, vorticity fluctuations, Reynolds stresses, their budget terms, two-point correlation coefficients, and energy spectra are examined to investigate the Reynolds-number dependence in detail.

Computational Domain

The DNS must meet the following two requirements to ensure the adequacy of the computation. One is that the computational domain must be chosen to be large enough to contain the largest eddies. The other is that the grid spacing must be fine enough to resolve the smallest eddies. The former is confirmed if the two-point correlation becomes zero within a half of the computational domain. Recently, Jiménez [21] pointed out that the product of the wave number and the one-dimensional spectrum serves also as a good measure of the computational domain. The latter can be satisfied if the one-dimensional energy spectra shows enough drop-offs for the high wave numbers. The present computation takes into account the above requirements, although a rather smaller volume is selected to save the computational storage. The flow is assumed to be fully developed in an infinite two-dimensional channel. The mean flow is in x direction and is driven by a streamwise mean pressure gradient. Note that x (x_1), y (x_2), and z (x_3) imply streamwise, wall-normal and spanwise directions, respectively. The periodic boundary condition is imposed in x and z directions, while nonslip condition is adopted on the top and bottom walls. The uniform meshes are used in the x and z directions. On the other hand, the nonuniform meshes are adopted in the y direction. The transformation is similar to that of Moin and Kim [20] as

$$y_j=\frac{1}{2\alpha}\tanh[\xi_j\tanh^{-1}\alpha]+0.5, \tag{1}$$

with

$$\xi_j=-1+2\frac{j}{N_2}, \tag{2}$$

where α is an adjustable parameter of the transformation ($0<\alpha<1$) and N_2 is the grid number of the y direction. In the case of $Re_\tau=180$ and 395, a constant value of $\alpha=0.967$ and 0.980 are adopted, respectively. On the other hand, in the case of $Re_\tau=640$, a function is employed for the parameter α

$$\alpha(\xi_j)=0.9885-0.5\xi_j^2+0.405\xi_j^3. \tag{3}$$

The computational condition is shown in Table 1. Note that the superscript $+$ indicates the quantities normalized by the wall variables, e.g., $y^+=yu_\tau/\nu$ and $t^+=tu_\tau^2/\nu$. For the highest Reynolds number of $Re_\tau=640$, the computation has been executed on 33, 554, 432 (512×256×256) grid points to resolve the smallest eddies.

Numerical Procedures

The coordinates and flow variables are normalized by the channel half width δ, the kinematic viscosity ν, and the friction velocity $u_\tau=(\tau_w/\rho)^{1/2}$, where τ_w is the statistically averaged wall shear stress and ρ is the density.

The fundamental equations are the continuity equation:

$$\frac{\partial u_i^+}{\partial x_i^*}=0, \tag{4}$$

and the Navier-Stokes equation:

$$\frac{\partial u_i^+}{\partial t^*}+u_j^+\frac{\partial u_i^+}{\partial x_j^*}=-\frac{\partial p^+}{\partial x_i^*}+\frac{1}{\mathrm{Re}_\tau}\frac{\partial^2 u_i^+}{\partial x_j^{*2}}+\frac{\partial\overline{p}^+}{\partial x_1^*}\delta_{il}. \tag{5}$$

Here, $i=1$, 2, and 3 indicate the streamwise, wall-normal, and spanwise directions, respectively. The variables t and p are the time and the pressure. The superscript * indicates that the variables are normalized by δ. Note that the third term for the right-hand side of Eq. (5) is the streamwise mean pressure gradient.

The boundary conditions are

$$u_i^+=0, \quad \text{at } y=0 \quad \text{and} \quad 2\delta. \tag{6}$$

In the present computation, fractional step method proposed by Dukowics and Dvinsky [22] is adopted for the computational algorithm. Time advancement is executed by the semi-implicit scheme: Crank-Nicolson method for the viscous terms (wall-normal direction) and Adams-Bashforth method for the other terms.

For spatial discretization, the finite difference method (FDM, hereafter) is adopted. In the preceding DNSs, the pseudo-spectral method (PSM, hereafter) has been often preferred because a higher-numerical accuracy can be obtained for a given grid size through PSM than through FDM. On the other hand, the FDM has a potential to be applied to more complex geometries and spatially developing flow in future works; thus it is considered to be worthwhile to verify an applicability of the FDM to DNS in comparison with existing PSM results. Several DNSs have been performed with the use of FDM by Rai and Moin [23,24] for turbulent channel and boundary layer and by Gavrilakis [25] for square duct.

In the early stage of the present work, a series of computations, were made in which DNSs of the fully developed turbulent channel flow were performed with various discretization methods including the upwind and the second- and fourth-order central schemes (Kawamura [26]; Suzuki and Kawamura [27]).

As for the transport equation for the turbulent kinetic energy and the Reynolds stresses, the use of the upwind scheme showed an underestimation of the dissipation rate due to the numerical viscosity in the transportation of the turbulent kinetic energy and the Reynolds stresses. Even in the computation with the use of the central scheme, the sum of the all terms in those transport equations never tended to fall to zero. It was noticed that this was due to the inconsistency between the numerical and analytical differential operations employed in solution of the momentum and transport equations.

The obtained conclusions can be summarized as follows. The transport equation of the Reynolds stresses is derived from the momentum equation through a lot of differential operations using the continuity condition. In the calculation of DNS, the momentum equation must be solved with a sufficient accuracy corresponding to the order of applied discretization. Thus, if ever a significant residual remains in the sum of the terms in the Reynolds stress transport equations, it is because the numerical differentiation scheme is not consistent with the analytical one. The inconsistency was pointed out first by Schumann [28] more than

Table 2 Mean flow variables

Re_τ	u_m	u_c	u_c/u_m	Re_m	Re_c	Re_θ	C_f
180	15.72	18.38	1.17	5662	3309	295	8.11×10^{-3}
395	17.70	20.48	1.16	13981	8090	754	6.39×10^{-3}
640	19.00	21.85	1.15	24326	13984	1283	5.50×10^{-3}

twenty years ago. The authors group (Kawamura [26]; Suzuki and Kawamura [27]) extended this idea to apply to DNS. The resultant scheme was called the ''consistent scheme'' because of its consistency between the numerical and analytical difference operations. It was originally with the second-order accuracy. Some more details are given in the Appendix. Later, Kajishima [29] and Morinishi [30] extended it into the fourth-order one. The present computation has been executed with the second-order scheme; while the fourth-order scheme is also tested and compared in the Appendix. As for the computational stencil, the staggered grid is adopted; that is, the pressure is located at the cell center and the velocities at the cell surfaces.

The Poisson equation of pressure is solved using the tridiagonal matrix algorithm in the wall-normal direction and the fast Fourier transform (FFT) in the streamwise and the spanwise directions with the use of the second-order scheme. For the viscous terms, the second-order central scheme is used.

The computer employed is NWT (Numerical Wind Tunnel) located at the National Aerospace Laboratory. It is a vectorized parallel computer with 166 processor elements, connected through the cross bar network of 421 MB/s. The computation speed of each processor is 1.7 GFLOPS, thus the theoretical maximum performance of the whole system is 280 GFLOPS. In case of the highest Reynolds number of Re_τ=640, the computation has been made using of 64 processors with the typical integration time of about 1.4 s for a time step. The calculation has been executed up to 24,800 ν/u_τ^2 in order to obtain a stable statistical average.

Results and Discussion

Mean Flow Variables. Mean flow variables such as the bulk mean velocity u_m, the mean centerline velocity u_c, the Reynolds numbers Re_m, Re_c, and Re_θ and the friction coefficient C_f are given in Table 2 for the three Reynolds numbers. Here, Re_m is the Reynolds number based on the bulk mean velocity and the channel width and Re_c is the one based on the mean centerline velocity and the channel half width. Note that Re_θ is based on the mean centerline velocity and the momentum thickness. In the present case, the momentum thickness θ is defined as

$$\frac{\theta}{\delta} = \int_0^1 \frac{\overline{u}^+}{\overline{u}_c^+}\left(1 - \frac{\overline{u}^+}{\overline{u}_c^+}\right) dy^*. \tag{7}$$

In the case of Re_τ=640, Re_θ is about 10 percent lower than that of the DNS with Re_θ=1410 by Spalart [31] for the turbulent boundary layer; while, u_c for Re_τ=640 is roughly equivalent to u_∞ for Re_θ=1410 by Spalart [31], where u_∞ is the edge velocity. The present results also agree with the correlation between the bulk mean velocity and the mean centerline velocity proposed by Dean [32]:

$$u_c/u_m = 1.28\,Re_m^{-0.0116}. \tag{8}$$

The friction coefficient is defined as

$$C_f = \tau_w / \left(\frac{1}{2}\rho u_m^2\right), \tag{9}$$

where τ_w is the wall shear stress. Figure 1 shows the friction coefficient in comparison with those of DNS by Kuroda et al. [3] and KMM87 [2]. There included are the empirical correlation proposed by Dean [32] for the channel flow and the one by Blasius for the pipe flow. The present results are in good agreement

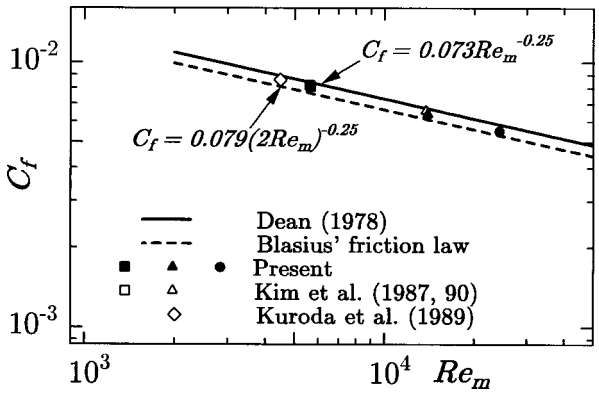

Fig. 1 Friction coefficient

with them. However, there exists a small but discernible difference between the present and the KMM87 [2] and KMM90 [5] results. This is a reflection of the slight difference in the mean velocity distribution in the channel center region.

The mean velocity distribution is given in Fig. 2 and compared with the experiment of Hussain and Reynolds [13]. The DNS of turbulent channel flow by KMM87 [2] and KMM90 [5] and the one of the turbulent boundary layer by Spalart [31] are also included for comparison. The present result for Re_τ=640 is in good agreement with the experiment by Hussain and Reynolds [13]; while a slight deviation from Re_θ=1410 by Spalart [31] is found in the logarithmic region. This is due to a characteristic difference between the channel and the boundary layer flows.

KMM87 [2] pointed out that the logarithmic region exists even in the case of the lowest Reynolds number of 180; while it extends up to a larger y^+ with the increase of Re_τ. Moreover, the wake region is more clearly distinguished from the logarithmic one in the case of the higher Re_τs.

It is well-recognized that the logarithmic region can be expressed as

$$\overline{u}^+ = \frac{1}{\kappa}\ln y^+ + c, \tag{10}$$

where κ is the von Karman constant and c is the additive constant. Note that an overline denotes an average over x, z, and t. In the turbulent boundary layer, Spalart [31] indicated that the result for the higher Reynolds number of Re_θ=1410 gave κ=0.41 and c=5.0. In the case of Re_τ=180, the additive constant c is 5.5, which is in good agreement with that of KMM87 [2]; while in the case of Re_τ=640, the one by the present DNS decreases down to 5.2.

The von Karman constant κ can be obtained from Eq. (10) as

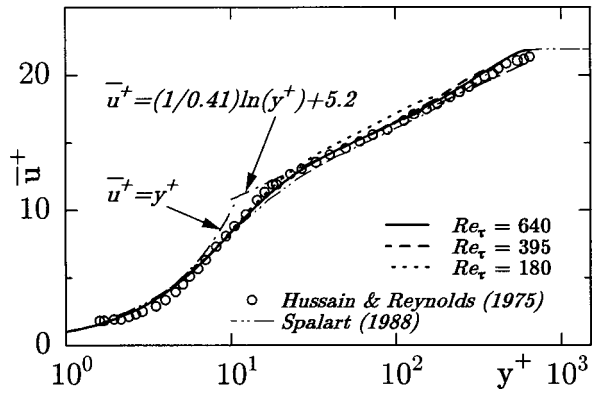

Fig. 2 Mean velocity distribution

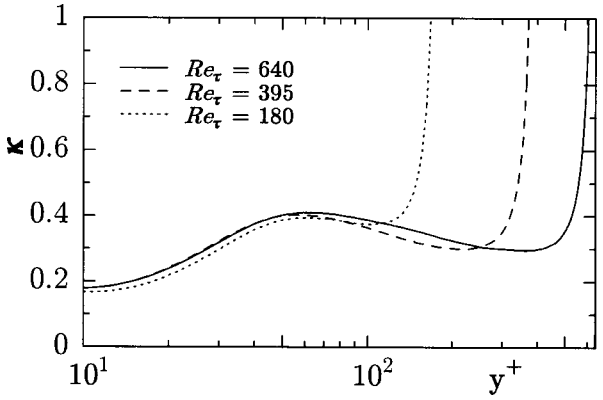

Fig. 3 Von Karman constant

$$\kappa = \left(y^+ \frac{d\overline{u}^+}{dy^+} \right)^{-1} \tag{11}$$

and is plotted in Fig. 3. It is well-known that κ obtained from the experiments ranges from 0.40–0.42. The present calculation indicates that κ is not completely constant but it stays at a roughly constant value of 0.40 around $y^+ = 50-100$. Moreover, the region of the approximate constant tends to expand with the increase of the Reynolds number.

Turbulence Intensities. The root mean square of velocity fluctuations is shown in Fig. 4. Those of Moser et al. [11] and $u'^+_{\rm rms}$ of Hussain and Reynolds [13] are also plotted for comparison. All components increase with the increase of Re_τ. Antonia et al. [17] indicated that the Reynolds number dependence for $w'^+_{\rm rms}$ is significant compared to that for $u'^+_{\rm rms}$ and $v'^+_{\rm rms}$. In the present results, not only $w'^+_{\rm rms}$ but also $v'^+_{\rm rms}$ is enhanced with increasing Reynolds number. Especially, the wall-normal and spanwise components are enhanced. This is because the energy redistribution increases remarkably for $v'^+_{\rm rms}$ and $w'^+_{\rm rms}$ with the increase of the Reynolds number, as will be discussed later. In Fig. 4, the present result shows good agreement with the measurement by Hussain and Reynolds [13] for $u'^+_{\rm rms}$ except for the peak value. This discrepancy may also be caused by the difficulty in the measurement close to the wall. The slight difference between the present (Re_τ=640) and Moser et al. [11] (Re_τ=590) is due to the difference in Re_τ. If they are plotted versus y/δ instead of y^+, the agreement is improved for the central region. In addition, the present results for Re_τ=180 and 395 agree with those of Moser et al. [11].

The root mean square of vorticity fluctuations normalized by the wall variables, i.e., $\omega_i' \nu/u_\tau^2$ are shown in Fig. 5. The near-wall values of streamwise and spanwise vorticity fluctuations $\omega_x'^+$ and $\omega_z'^+$ increase with the increase of the Reynolds number. Especially, $\omega_z'^+$ shows a larger value for a higher Reynolds number. This is caused by the simple shear close to the wall. The wall values of $\omega_x'^+$ and $\omega_z'^+$ correspond to the coefficients b_3 and b_1, respectively, given in Table 3. The wall-normal vorticity fluctuation $\omega_y'^+$, however, tends to become independent of the Reynolds number in the near-wall region as reported by Antonia and Kim [6].

Reynolds Shear Stress. The Reynolds shear stress $-\overline{u'^+ v'^+}$ and the total shear stress $\tau_{\rm total}$ are shown in Fig. 6. As the Reynolds number increases, the peak value of the Reynolds shear stress $-\overline{u'^+ v'^+}$ increases and its position moves away from the wall. When Re_τ is 180, the peak of $-\overline{u'^+ v'^+}$ reaches 0.71 at $y^+ = 30$; while, in the case of Re_τ=640, it becomes 0.87 at y^+ =42. On the other hand, the position of the peak moves closer to the wall with the increase of the Reynolds number if scaled by the channel half width δ.

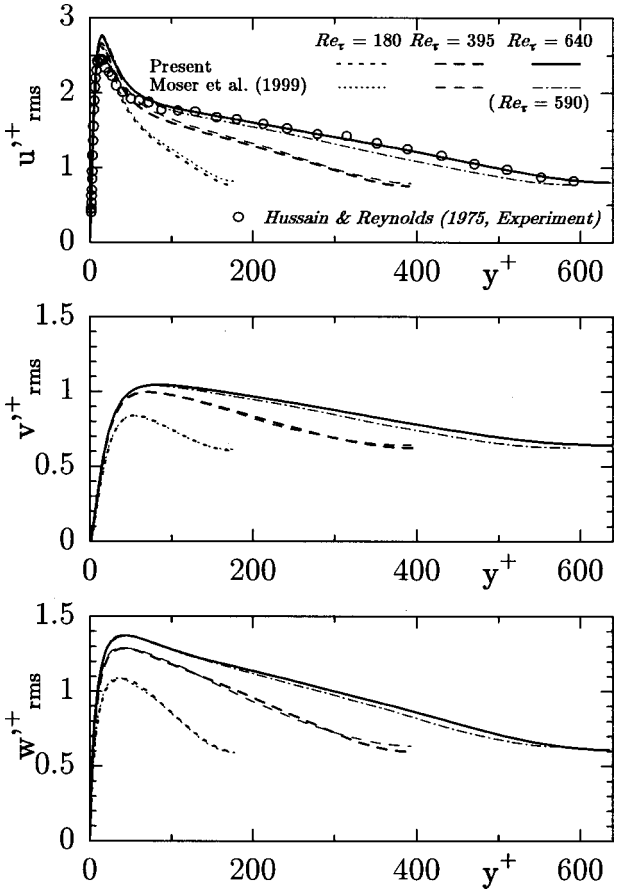

Fig. 4 Rms of velocity fluctuations

The total shear stress is an identification that the calculation reaches a statistically steady state. When the streamwise momentum equation is ensemble averaged, the total shear stress can be obtained as

$$\tau_{\rm total} = 1 - \frac{y^+}{\mathrm{Re}_\tau} = -\overline{u'^+ v'^+} + \frac{\partial \overline{u}^+}{\partial y^+}. \tag{12}$$

Once the statistically steady state is reached, the right and left-

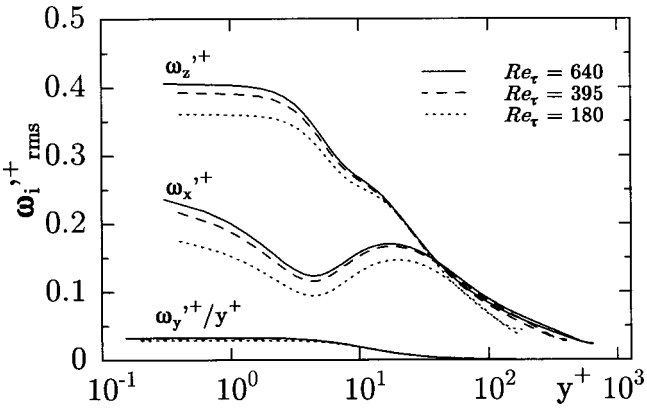

Fig. 5 Rms of vorticity fluctuations

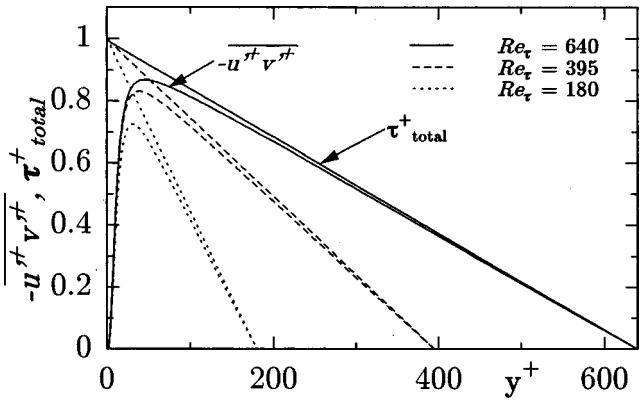

Fig. 6 Reynolds shear stress and total shear stress distributions

hand sides of Eq. (12) must be balanced. In the present DNS, the statistically steady state can be confirmed for all the three Reynolds numbers, as seen in Fig. 6.

Near-Wall Behavior. In the wall vicinity, the velocity fluctuations can be expanded in terms of y^+ as

$$u'^+ = b_1 y^+ + c_1 y^{+2} + \cdots, \tag{13}$$

$$v'^+ = \quad c_2 y^{+2} + \cdots, \tag{14}$$

$$w'^+ = b_3 y^+ + c_3 y^{+3} + \cdots. \tag{15}$$

Considering the expansion of Eqs. (13) and (14), the Reynolds shear stress can be expanded in terms of y^+ as

$$-\overline{u'^+ v'^+} = -\overline{b_1 c_2} y^{+3} + \cdots. \tag{16}$$

The wall-values of b_1, c_2, b_3, and $\overline{b_1 c_2}$ are extrapolated up to the wall and given in Table 3 in comparison with Antonia and Kim [6]. The present results agree well with those of Antonia and Kim [6] in the near-wall region. A discrepancy can be observed for $\overline{b_1 c_2}$. This seems to be caused by the location of the first grid point and the staggered arrangement of the variables in this work. In addition, the present results indicate that the coefficients of b_1, c_2, b_3, and $\overline{b_1 c_2}$ increase with the increase of the Reynolds number. This is because the production rate of the turbulent kinetic energy increases with the increasing Reynolds number as discussed later. Especially, the increase is significant when the Reynolds number goes up from $\mathrm{Re}_\tau = 180-395$. In the case of $\mathrm{Re}_\tau = 640$, however, the increase is rather saturated. This indicates that the low Reynolds-number effect is significant for $\mathrm{Re}_\tau = 180$.

As for the wall-limiting value of b_1 or ω_z', a great deal of effort have been devoted to reaching a consensus through the DNS and experiment. However, there exists long discussion on the quantity because of the experimental difficulties associated with the measurements. Recently, Alfredsson and Johansson [33] carried out the measurements in the air, oil, and water with the hot-film probes and specially designed sensors. They indicated that the rms of the velocity shear stress fluctuation in the streamwise direction is 40 percent of the mean-shear stress for both the channel and the boundary layer flows. This corresponds to $b_1 = 0.40$ in the present definition. Komminaho et al. [34] computed the plane turbulent Couette flow at a Reynolds number of 750 based on half the velocity difference between the walls and half the channel width. They indicated a value of $b_1 = 0.41$ at the wall. This is in good accordance with the present value of $b_1 = 0.409$ for $\mathrm{Re}_\tau = 640$. In the case of the Couette flow, the total shear stress is constant independent upon the Reynolds number. This is equivalent to the Poiseuille flow with an infinite Re_τ (see Eq. (12)). These indicate that the decrease in b_1 with decreasing Re_τ found in Table 3 is due to the reduction of the total shear stress for the smaller Re_τ in the wall vicinity.

Table 3 Near-wall expansion coefficient

Re_τ	b_1	c_2	b_3	$b_1 c_2$
180 (Present)	0.361	9.4×10^{-3}	0.199	7.9×10^{-4}
180 (Antonia and Kim [6])	0.356	8.5×10^{-3}	0.190	7.0×10^{-4}
395 (Present)	0.395	1.1×10^{-2}	0.247	1.0×10^{-3}
395 (Antonia and Kim [6])	0.395	1.1×10^{-2}	0.245	9.5×10^{-4}
640 (Present)	0.409	1.2×10^{-2}	0.261	1.1×10^{-3}

Two-Point Correlations. Streamwise and spanwise two-point correlations of velocity fluctuations $R_{(ii)}$ for $\mathrm{Re}_\tau = 640$ are shown in Fig. 7. No summation rule is applied to the parenthesized indices. In the near-wall region, all of the three components tend to fall off to almost zero within a half width of the computational domain for both the streamwise and spanwise directions. Moving away from the wall, however, the spanwise two-point correlation R_{11} gives a small but noticeable deviation from zero even at the half of the spanwise computational domain. This means that there exist the large scale structures in the center of the channel and that the present computational domain is not enough large to capture some of the largest scale ones. Recently, Jiménez [21] investigated the large scale structures in the center of the channel and indicated that even the computational domain adopted by Moser et al. [11] is too short to contain the large scale ones. The large scale structures were also found by Komminaho et al. [34] in the Couette flow. They observed streamwise structures of the order of 40δ in the center of the channel. The above large structures will be investigated with the use of the energy spectra and be discussed later.

The spanwise two-point correlation R_{11} is given in Fig. 8 and compared with the experiment by Nishino and Kasagi [19]. It is interesting to note that the near-wall negative peak of the spanwise R_{11} becomes less prominent with the increase of Re_τ. This is in accordance with the observation that the streamwise streaks are clustered in higher Reynolds number as discussed later.

Energy Spectra. One-dimensional energy spectra of velocity fluctuations $E_{(ii)}$ in the near-wall region for $\mathrm{Re}_\tau = 640$ compared with that for $\mathrm{Re}_\tau = 180$ are shown in Fig. 9, where k_x and k_z are the wave numbers in the streamwise and spanwise directions, respectively. Note that $E_{(ii)}$ is normalized by the wall units. The energy spectra show acceptable drop-offs in the streamwise and spanwise directions irrespective of the Reynolds number, although a slight pile-up is seen for the highest wave numbers in the spanwise direction. A large difference among three components is observed in the lower wave number region for both the streamwise and spanwise directions. Especially, the difference is significant for the spanwise energy spectra. This indicates that the turbulence structure for the near-wall region becomes more anisotropic in space than the one for the channel center. Moreover, E_{vv} and E_{ww} exhibit noticeable increase in the lower wave number with increasing Reynolds number for both the streamwise and spanwise directions, which is in good accordance with the increase in v'^+_{rms} and w'^+_{rms}.

To investigate whether or not the smallest eddies are resolved, Fig. 10 shows $k_x^2 E_{uu} (\varepsilon^3/\nu)^{-1/4}$ referring to Saddoughi and Veeravalli [35], which represents the energy spectra of the turbulence dissipation rate. In the present result, its peak value occurs at $k_x/k_d = 0.1-0.2$ and falls off for $k_x/k_d > 0.5$ roughly irrespective of the Reynolds number. This corresponds to the well-known fact that the small scale eddies dissipate the energy at a lower wave number than the Kolmogorov scale (Tennekes and Lumley [36]). Although, over $k_x/k_d = 0.2$, some difference is found between the present result and that by PSM (Moser et al. [11]), those higher

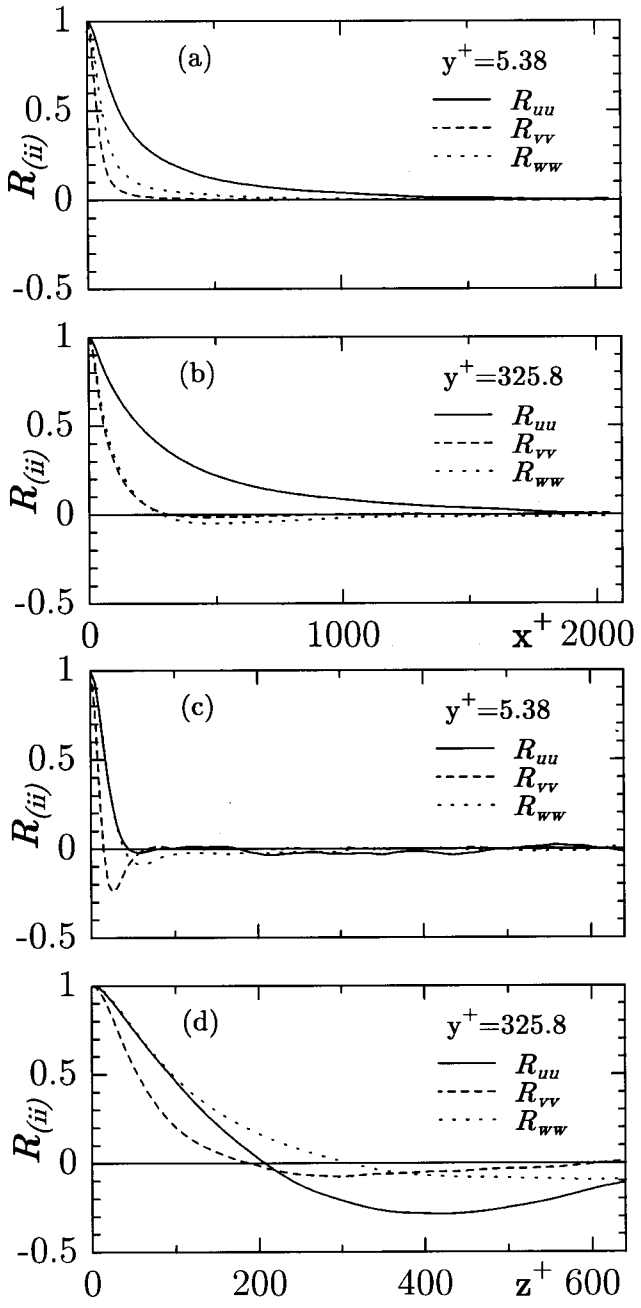

Fig. 7 Two-point correlation coefficients of velocity fluctuations for Re_τ=640: (*a*), (*b*) streamwise, (*c*), (*d*) spanwise correlation coefficients

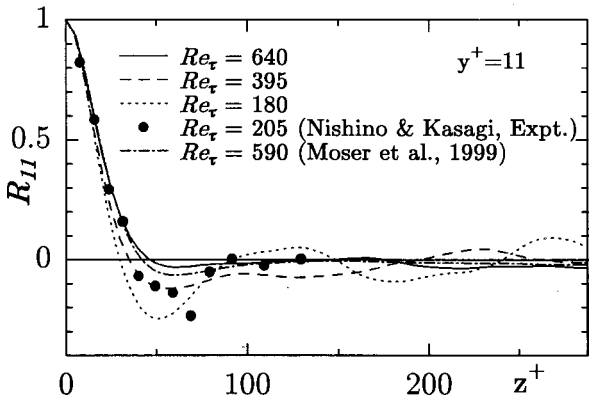

Fig. 8 Spanwise two-point correlation coefficient R_{11} at y^+ =11

wave numbers are less effective for the turbulence statistics. This means that the present spatial resolution is sufficiently small to resolve the energy dissipative eddies.

To show the validity of the adopted computational domain, Figs. 11(*a*) and 11(*b*) show the premultiplied energy spectra $k_xE_{uu}/\overline{u'u'}$ and $k_zE_{uu}/\overline{u'u'}$, respectively, referring to Jiménez [21]. In the near-wall region, the peak of $k_zE_{uu}/\overline{u'u'}$ occurs at $\lambda_z^+ \simeq 100$ independent of the Reynolds number, which agrees with the well-known average spacing of the streamwise streak structures. On the other hand, that of $k_xE_{uu}/\overline{u'u'}$ arises at $\lambda_z^+ \simeq 1000$. These correspond to the formation of the streaks as shown later (see Figs. 16 and 17).

In the center of the channel, however, the peak of $k_zE_{uu}/\overline{u'u'}$ moves toward a larger λ_z^+; i.e., $\lambda_z^+ \simeq 1000$ as indicated by Jiménez [21]. On the other hand, that of $k_xE_{uu}/\overline{u'u'}$ stays at $\lambda_x^+ \simeq 1000$. This means that the spanwise structure is enlarged with the increase of y^+. In the present computation for Re_τ=640, the peak of $k_zE_{uu}/\overline{u'^+u'^+}$ cannot be obtained at the center of the channel. This indicates that the largest scale has not been captured totally at the central region of the channel for Re_τ=640. The present authors are now performing another computation with an extended domain for streamwise and spanwise directions. The preliminary results indicate that its effect on the fundamental turbulent statistics is sufficiently small.

Budget of Reynolds Stress $\overline{u_i'u_j'}$ and Turbulent Kinetic Energy *k*. Budget terms of Reynolds stress $\overline{u_i'u_j'}$ normalized by ν/u_τ^4 are expressed as follows:

$$\text{Production:}\quad P_{ij}=-\left(\overline{u_j'^+u_k'^+}\frac{\partial \overline{u_i}^+}{\partial x_k^+}+\overline{u_i'^+u_k'^+}\frac{\partial \overline{u_j}^+}{\partial x_k^+}\right), \tag{17}$$

$$\text{Turbulent diffusion:}\quad T_{ij}=-\frac{\partial}{\partial x_k^+}(\overline{u_i'^+u_j'^+u_k'^+}), \tag{18}$$

$$\text{Vel. p. -grad. corr.:}\quad \Pi_{ij}=-\left(\overline{u_j'^+\frac{\partial p'^+}{\partial x_i^+}}+\overline{u_i'^+\frac{\partial p'^+}{\partial x_j^+}}\right), \tag{19}$$

$$\text{Molecular diffusion:}\quad D_{ij}=\frac{\partial^2}{\partial x_k^{+2}}(\overline{u_i'^+u_j'^+}), \tag{20}$$

$$\text{Dissipation:}\quad \varepsilon_{ij}=2\overline{\left(\frac{\partial u_i'^+}{\partial x_k^+}\right)\left(\frac{\partial u_j'^+}{\partial x_k^+}\right)}. \tag{21}$$

Figure 12 shows the budget terms of the Reynolds stresses for Re_τ=640 compared with those of Re_τ=180 and 395. For $\overline{u'^+u'^+}$ component, as the Reynolds number becomes higher, the peak value of the production and the wall values of the molecular diffusion and dissipation increase. The production almost balances with the some of the dissipation and the velocity pressure-gradient correlation (v.p.g, hereafter) terms. On the other hand, for $\overline{v'^+v'^+}$ and $\overline{w'^+w'^+}$ components, the v.p.g and dissipation terms are dominant and increase significantly with the increase of the Reynolds number. These indicate that the Reynolds-number effect on $\overline{v'^+v'^+}$ and $\overline{w'^+w'^+}$ components is more enhanced than that of $\overline{u'^+u'^+}$.

Budget terms of turbulent kinetic energy $k(=(\overline{u'^+u'^+}+\overline{v'^+v'^+}+\overline{w'^+w'^+})/2)$ normalized by ν/u_τ^4 are given in Fig. 13 for the three Reynolds numbers calculated. Note that the v.p.g

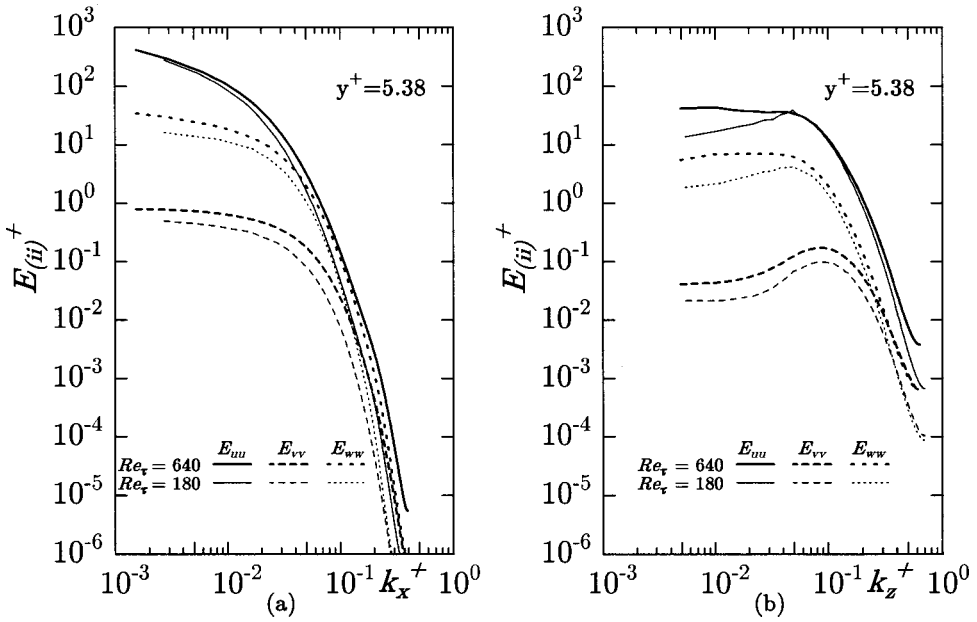

Fig. 9 One-dimensional energy spectra of velocity fluctuations for Re_τ=640 in comparison with Re_τ=180: (*a*) streamwise, (*b*) spanwise

term is reduced to the pressure diffusion one due to the continuity condition. Figure 13 indicates that all terms gradually increase with the increase of Re_τ. Especially, the wall values of the dissipation and molecular diffusion increase appreciably with the increasing Reynolds number. The peak value of the production term $P_{k,\max}$ becomes 0.25 as the Reynolds number goes to the infinity. In the present results, $P_{k,\max}$ is 0.218 for Re_τ=180; while, it reaches 0.239 for Re_τ=640. The increase in $P_{k,\max}$ from Re_τ =180 to 640 is small but significant. This point will be discussed later together with the pressure strain term.

The v.p.g term can be split into the pressure strain and the pressure diffusion terms as follows:

$$\Pi_{ij}=\underbrace{\overline{p'^{+}\left(\frac{\partial u_j'^{+}}{\partial x_i^{+}}+\frac{\partial u_i'^{+}}{\partial x_j^{+}}\right)}}_{\text{Pressure strain}} \underbrace{-\left(\frac{\partial}{\partial x_i^{+}}\overline{u_j'^{+}p'^{+}}+\frac{\partial}{\partial x_j^{+}}\overline{u_i'^{+}p'^{+}}\right)}_{\text{Pressure diffusion}}. \quad (22)$$

It is well-known that the pressure strain term plays a dominant role on the energy redistribution. Figure 12 indicates that all the components for the pressure strain term exhibit a prominent increase with increasing Reynolds number. It is interesting to note that the increase in the pressure strain of $\overline{u'^{+}u'^{+}}$ from Re_τ

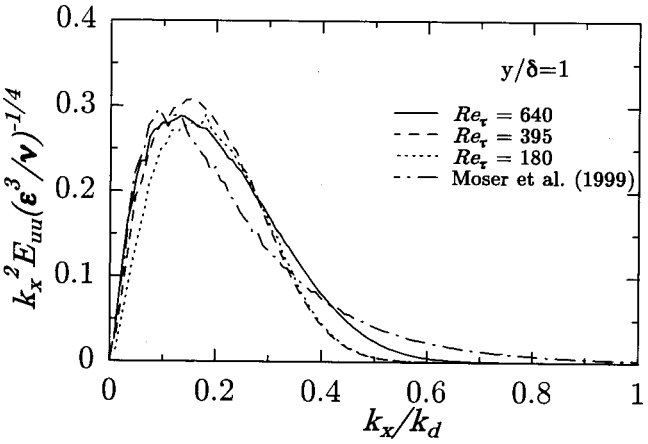

Fig. 10 Streamwise one-dimensional energy dissipation spectra normalized by Kolmogorov scale

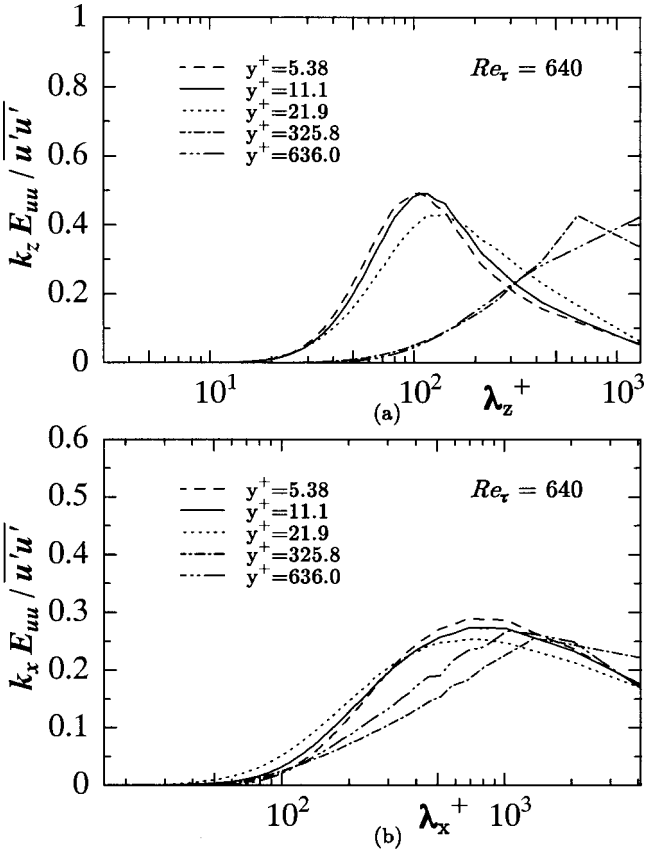

Fig. 11 Premultiplied energy spectra for Re_τ=640 (*a*) $k_zE_{uu}/\overline{u'u'}$, (*b*) $k_xE_{uu}/\overline{u'u'}$

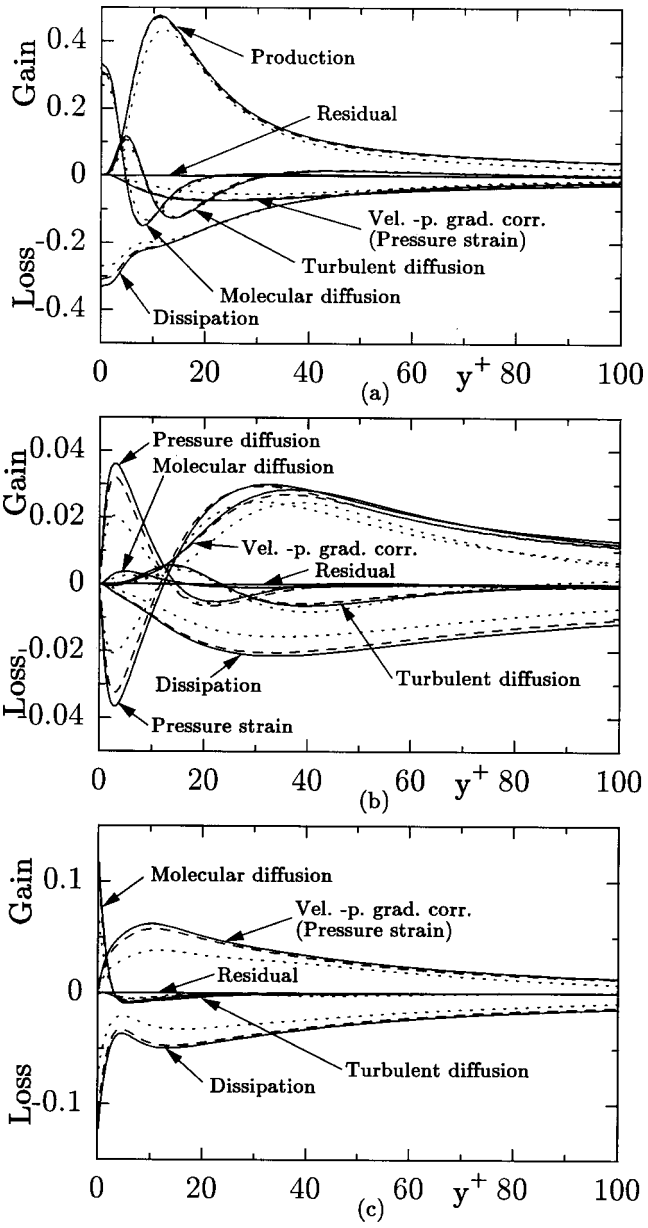

Fig. 12 Budget of Reynolds normal stresses: (*a*) $\overline{u'^+u'^+}$, (*b*) $\overline{v'^+v'^+}$, (*c*) $\overline{w'^+w'^+}$, ——, Re_τ=640; – – –, Re_τ=395; - - -, Re_τ =180

=180−640 is about 0.02 around its peak. This value is roughly equal to the increase in the peak of P_k. Since P_k is a half of the P_{11}, it means that about half of the increase in the production rate of $\overline{u'^+u'^+}$ is consumed by $\overline{u'^+u'^+}$ itself and the rest half is transferred to the other components. This is the reason why $v'^+_{\rm rms}$ and $\omega'^+_{\rm rms}$ increase significantly with the increase of the Reynolds number.

Dissipation Rate of the Reynolds Stresses. The dissipation rate of the Reynolds stresses is the quantity obtained best from DNS. The anisotropy of the dissipation rate for the normal Reynolds stress components is of a great concern in the modeling of turbulence. Mansour et al. [37] examined the DNS data of KMM87 [2] for Re_τ=180 and found that the following expression is a good approximation except for the off-diagonal components:

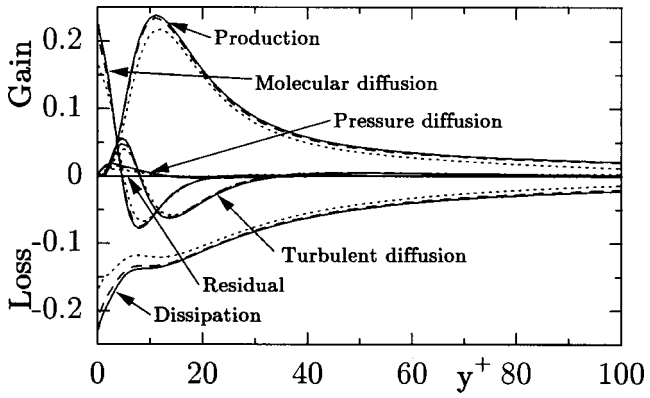

Fig. 13 Budget of turbulent kinetic energy: ——, Re_τ=640; — — —, Re_τ=395; - - -, Re_τ=180

$$\varepsilon_{(ii)}=\frac{\overline{u'^+_{(i)}u'^+_{(i)}}}{2k}2\varepsilon. \tag{23}$$

The present results are compared with the above approximation in Fig. 14. The agreement is generally good for all the normal components. If examined more precisely, however, the agreement is less satisfactory in the central region of $i=1$ and 2 and also in the near-wall region of $i=2$. In the near-wall region, referring to Launder and Reynolds [38], the relation of Eq. (23) is exactly valid for $i=1$ and 3; while, for $i=2$, the wall asymptotic value of ε_{22} becomes

$$\varepsilon_{22}=4c_2^2y^{+2}, \tag{24}$$

where c_2 is the expansion coefficient in Eq. (14). The above relation is shown in Fig. 14 with a dashed straight line; the agreement is good in the close vicinity of the wall. The above Eq. (24) is equivalent to

$$\varepsilon_{22}=4\frac{\overline{v'^+v'^+}}{2k}2\varepsilon, \tag{25}$$

instead of Eq. (23). This is one reason why the agreement of Eq. (23) is not so good for $i=2$ as seen in Fig. 14.

To examine the above approximation further, the anisotropy tensors are defined for the Reynolds stress and its dissipation rate as follows:

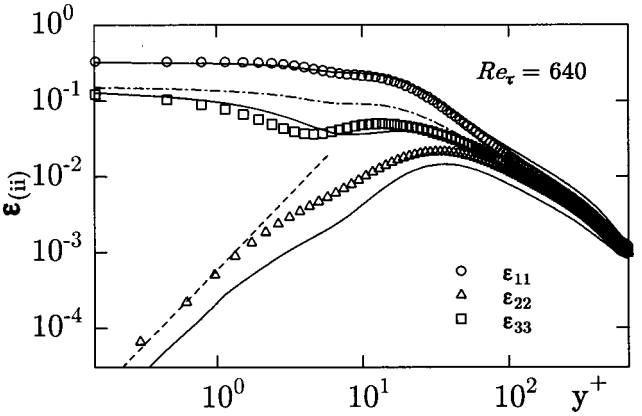

Fig. 14 Dissipation rate of the normal Reynolds stresses for Re_τ=640 symbol, $\varepsilon_{(ii)}$ by Eq. (23); ——, $\overline{u'^+_{(i)}u'^+_{(i)}}(\varepsilon/k)$; —·—·—·—, $(2/3)\varepsilon$; — — —, $4c_2^2y^{+2}$

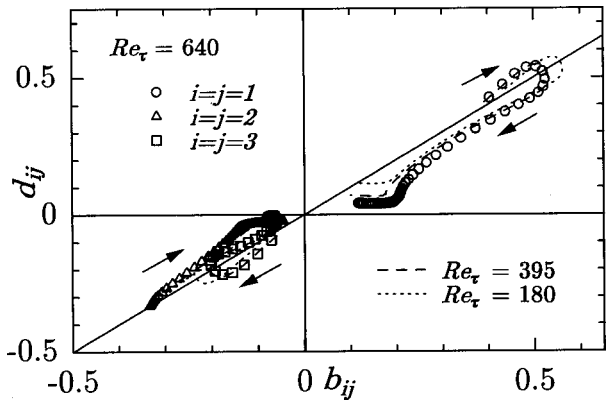

Fig. 15 Relation between anisotropy tensors b_{ij} and d_{ij}

$$b_{ij}=\frac{\overline{u_i'^+ u_j'^+}}{2k}-\frac{\delta_{ij}}{3}, \tag{26}$$

$$d_{ij}=\frac{\varepsilon_{ij}}{2\varepsilon}-\frac{\delta_{ij}}{3}. \tag{27}$$

Antonia et al. [39] compared the relation between b_{ij} and d_{ij} for a turbulent boundary layer. The same kind of comparison is made here for the turbulent channel flow in Fig. 15. For the above approximation of Eq. (23) to be exactly valid, the equality $d_{ij}=b_{ij}$ must hold. The arrows in Fig. 15 indicate the direction from the wall to the channel center. The starting point (wall value) lies on the line of $d_{ij}=b_{ij}$; especially $b_{ij}=d_{ij}=-1/3$ for $i=j=2$. The relation of $d_{ij}=b_{ij}$ holds roughly for the whole region. It is, however, interesting to note that d_{ij} becomes parallel to the horizontal axis where the absolute value of b_{ij} is small. This means that the dissipation becomes nearly isotropic irrespective of the Reynolds stress anisotropy in the central region. This supports the well-known belief that the dissipation must be almost isotropic because it takes place in the microscale, which is more isotropic than the large scale eddies. The isotropic expression

$$\varepsilon_{(ii)}=\frac{2}{3}\varepsilon \tag{28}$$

is plotted with the dot-dashed line in Fig. 14. This is indeed in a better agreement than Eq. (23) in the central region.

Instantaneous Flow Field. A lot of knowledge has been accumulated for the turbulent structures through the experimental observation and the analysis of the DNS data. In the present study, we focus mainly on the Reynolds number dependence for the quasi-coherent structures such as vortices and streaks. Figures 16 and 17 show the high- and low-speed streaks and the second invariant of the deformation tensor ($II'=\partial u_i'/\partial x_j \cdot \partial u_j'/\partial x_i$) for $\mathrm{Re}_\tau=180$ and 640. The visualized domain is set in wall units to be $1152\times180\times576$ for $\mathrm{Re}_\tau=180$ and $2048\times640\times640$ for $\mathrm{Re}_\tau=640$ in x, y and z directions, respectively. Note that fluid flows from the bottom left to the top right.

Chong et al. [40] proposed the identification of the vortex region which exhibits the circular or spiral motion with using the second invariant of the deformation tensor. The low pressure region (p'^+) does not necessarily correspond to the vortex core as indicated by Kim [41] and Robinson [42]. Thus, the second invariant of the deformation tensor is adopted to detect the vortex structure in the present research. When the Reynolds number is low as $\mathrm{Re}_\tau=180$, the well-known vortex structures such as single quasi-streamwise vortices are dominant. On the other hand, as the Reynolds number increases up to $\mathrm{Re}_\tau=640$, many different vortical structures such as the vortical arches are found besides the single streamwise vortices. The vortical arches are rolled up over

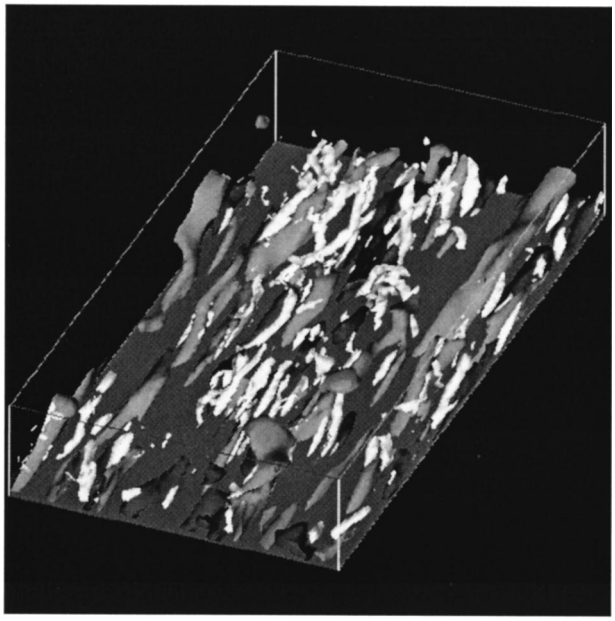

Fig. 16 High- and low-speed streaks and the second invariant of the deformation tensor for $\mathrm{Re}_\tau=180$ ($u'^+<-3.0$; light-gray, $u'^+>3.0$; dark-gray, $II'^+<-0.03$; white)

the low-speed streaks. Other vortices including the single streamwise vortices are also associated closely with the low-speed streaks.

As for the streaks, high- and low-speed streaks are obtained for both Re_τ's. The low-speed streaks are more elongated than the high-speed ones for both of the Reynolds numbers observed. The spanwise two-point correlation R_{11} is generally used to estimate the spacing of the streaks. It is known that the position of the negative peak of R_{11} provides an estimation of the mean separation between the high- and low-speed streaks; that is, the streak spacing becomes twice of the distance to the negative peak. KMM87 [2] obtained the minimum value of R_{11} at $z^+\simeq50$ and

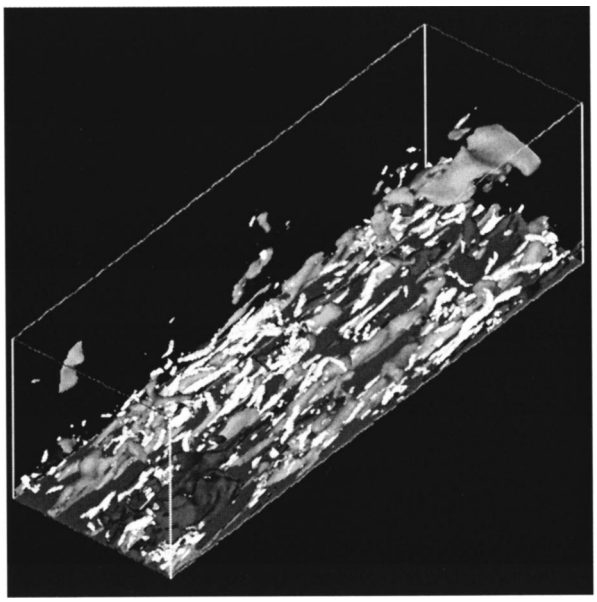

Fig. 17 High- and low-speed streaks and the second invariant of the deformation tensor for $\mathrm{Re}_\tau=640$ ($u'^+<-3.0$; light-gray, $u'^+>3.0$; dark-gray, $II'^+<-0.03$; white)

indicated that the streak spacing was $\Delta z^+ \simeq 100$, with which the present DNS for $\mathrm{Re}_\tau = 180$ gives a good agreement as shown in Fig. 16. Comparison of Figs. 16 and 17 indicates that the separation of the high- and low-speed streaks is more prominent in the lower Reynolds number and less in the higher one. That is, in case of $\mathrm{Re}_\tau = 640$, the shape of the streaks becomes more complicated and the several streaks are clustered with each other. Moreover, several low-speed streaks are often lifted up from the wall and finally broken up (see Fig. 17). This observation is in agreement with the finding that the local minimum of the R_{11} becomes less prominent with the increase of the Reynolds number as seen in Fig. 8.

Conclusions

The direct numerical simulation of a fully developed turbulent channel flow has been carried out. The Reynolds number is set to be $\mathrm{Re}_\tau = 180$, 395, and 640. The computation has been executed with the use of the finite difference method. Various turbulence statistics, such as turbulence intensities, vorticity fluctuations, Reynolds stresses, their budget terms, two-point correlation coefficients and energy spectra, were obtained to investigate the Reynolds number dependence. The conclusions are derived as follows:

1 With the increase of Re_τ, the increase in the wall-normal (v'^+_{rms}) and spanwise (w'^+_{rms}) components is more enhanced than that of the streamwise one (u'^+_{rms}). About half of the increase in the production rate of $\overline{u'^+u'^+}$ is consumed by $\overline{u'^+u'^+}$ and the rest half is transferred to the other components.

2 The near-wall expansion coefficients increase significantly as the Reynolds number goes up from $\mathrm{Re}_\tau = 180-395$, but become rather saturated for $\mathrm{Re}_\tau = 640$. The wall-limiting value of b_1 obtained as 0.409 agrees with the experiment for the channel flow by Alfredsson and Johansson [33] and the DNS for the Couette flow by Komminaho et al. [34].

3 The examination of the spanwise two-point correlation coefficient R_{11} reveals that the negative peak of R_{11} becomes less prominent with the increase of the Reynolds number. This agrees with the more complex streak shapes observed in the instantaneous velocity field for the higher Reynolds number.

4 The dissipation energy spectra $k_x^2 E_{uu}(\varepsilon^3/\nu)^{-1/4}$ in the center of the channel exhibits a peak value at $k_x/k_d = 0.1-0.2$ and falls off for $k_x/k_d > 0.5$ irrespective of the Reynolds numbers calculated as indicated by the local isotropic theory (Tennekes and Lumley [36]).

5 The anisotropy of the dissipation rate for the Reynolds normal stresses is compared with closure models. The anisotropy is pronounced in the wall vicinity; while the well-known isotropic nature is confirmed in the central region for a higher Reynolds number.

6 The second invariant of the deformation tensor represents the vortices such as the single streamwise vortices and the vortical arches for $\mathrm{Re}_\tau = 640$. In addition, different vortical structures are captured with the increase of the Reynolds number. As for the streaks, rather simple and separated streaky structures are observed for the lower Reynolds number of $\mathrm{Re}_\tau = 180$; while, the shape of the streaks becomes more complicated and several streaks are clustered with each other for the higher Reynolds number of $\mathrm{Re}_\tau = 640$.

The present database is open to public access. The detailed information is given at http://muraibm.me.noda.sut.ac.jp/e-pagel.html.

Acknowledgments

This simulation was performed with the use of the Numerical Wind Tunnel (NWT) of the National Aerospace Laboratory. We would like to acknowledge the execution of the computation on NWT. The authors are grateful to Dr. K. Yamamoto of the National Aerospace Laboratory for his great help in the early stage of this computation and to Dr. S. Satake of Toyama University for his helpful comments throughout this work.

Nomenclature

b_i, c_i, d_i = coefficient of series expansion
b_{ij} = anisotropy tensor of Reynolds stress
C_f = friction coefficient
c = additive constant of the logarithmic law
d_{ij} = anisotropy tensor of dissipation rate
E_{ij} = one-dimensional energy spectra of velocity fluctuations
k = turbulent kinetic energy
k_x, k_z = wave number for streamwise and spanwise direction
k_d = Kolmogorov wave number
p = pressure
P_k = production rate for the turbulent kinetic energy
R_{ii} = two-point correlation coefficient of velocity fluctuations
Re_τ = Reynolds number$=u_\tau \delta/\nu$
Re_m = Reynolds number$=u_m 2\delta/\nu$
Re_c = Reynolds number$=u_c \delta/\nu$
Re_θ = Reynolds number$=u_c \theta/\nu$
t = time
u_i, u, v, w = velocity component
u_τ = friction velocity$=\sqrt{\tau_w/\rho}$
u_c = mean centerline velocity
u_m = bulk mean velocity
u_∞ = edge velocity of the turbulent boundary layer
x_1, x = streamwise direction
x_2, y = wall-normal direction
x_3, z = spanwise direction

Greek

δ = channel half width
δ_{ij} = Kroneker symbol
ε = dissipation rate of turbulent kinetic energy
ε_{ii} = dissipation rate of Reynolds stress
κ = von Karman constant
θ = momentum thickness
ν = kinematic viscosity
ω_i = vorticity component
ρ = density
λ_x, λ_z = wavelength for streamwise and spanwise direction
τ_w = statistically averaged wall shear stress
τ_{total} = statistically averaged total shear stress

Superscripts and Subscripts

$(\ )^*$ = normalized by δ
$(\ )^+$ = normalized by u_τ, ν and ρ
$(\ )'$ = fluctuationcomponent
$\overline{(\ )}$ = statistically averaged over x, z, and t
$(\ )_{\mathrm{rms}}$ = root mean square
$(\ )_{\mathrm{max}}$ = maximum value

Appendix

A. Consistent Scheme. The convection terms for u_i can be expressed in either advective (adv.$\equiv u_j \partial u_i/\partial x_j$) or divergence (div.$\equiv \partial/\partial x_j u_i u_j$) forms. Since

$$\frac{\partial}{\partial x_j} u_i u_j = u_j \frac{\partial u_i}{\partial x_j} + u_i \frac{\partial u_j}{\partial x_j}, \tag{29}$$

the advective and divergence forms are analytically equal if the continuity condition is satisfied. Thus, this equality must be satis-

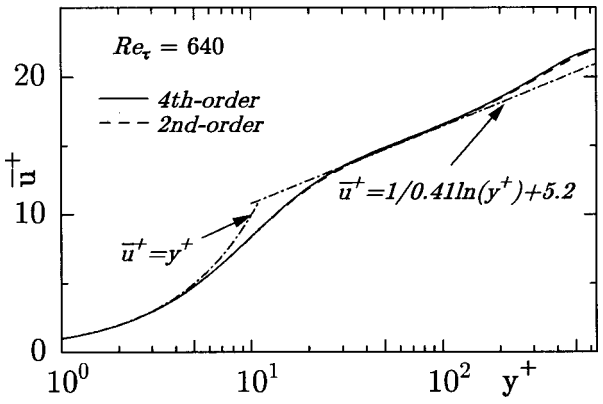

Fig. 18 Mean velocity distribution by fourth-order calculation

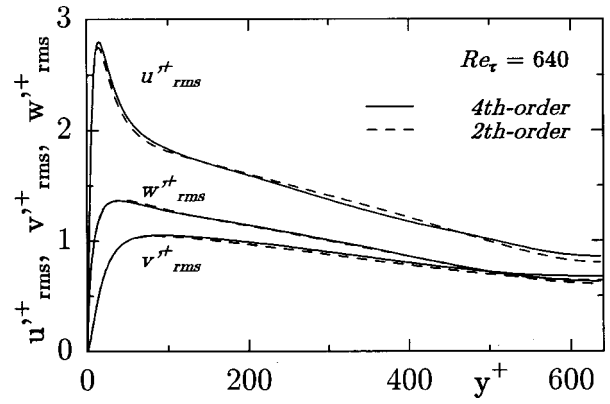

Fig. 19 Rms of velocity fluctuations by fourth-order calculation

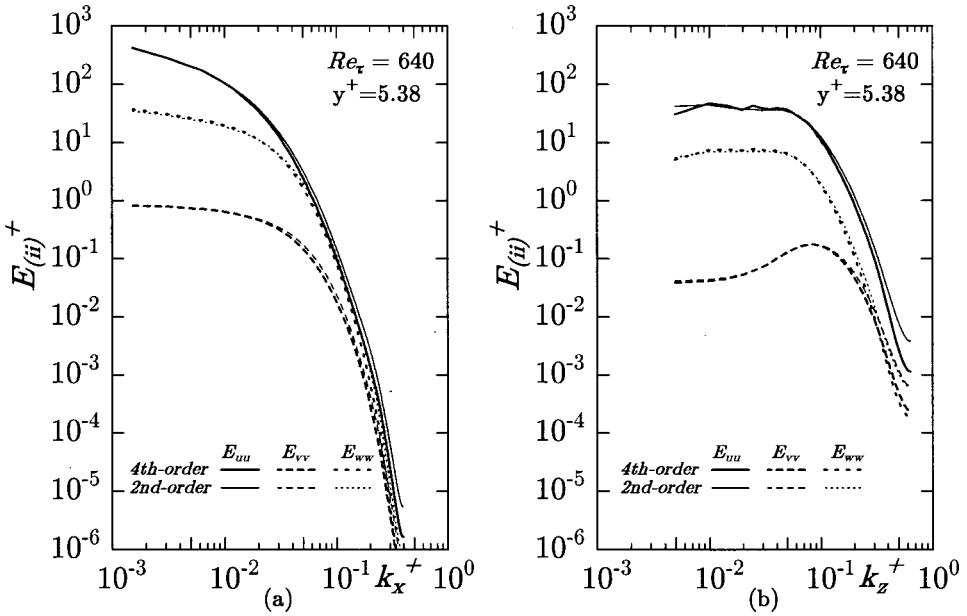

Fig. 20 One-dimensional energy spectra of velocity fluctuations by fourth-order calculation: (*a*) streamwise, (*b*) spanwise

fied in the numerical discretized scheme, too. This is the consistency between the analytical and numerical differential operations.

In the present computational stencil, the staggered grid is adopted; that is, the pressure is located at the cell center and the velocities at the cell surfaces.

The following difference operation is defined referring to Morinishi [30]

$$\frac{\delta\phi}{\delta x_1} = \frac{\phi(x_1+h_1/2,\, x_2,\, x_3) - \phi(x_1-h_1/2,\, x_2,\, x_3)}{h_1}, \quad (30)$$

where ϕ is a variable in the x_1 direction. Interpolation operator is given as

$$\overline{\phi}^{x_1} = \frac{1}{2}(\phi(x_1+h_1/2,\, x_2,\, x_3) + \phi(x_1-h_1/2,\, x_2,\, x_3)). \quad (31)$$

Moreover, a special interpolation of the variables between ϕ and ψ in the x_1 direction is expressed as

$$\overline{\phi\psi}^{x_1} \equiv \frac{1}{2}\phi(x_1+h_1/2,\, x_2,\, x_3)\psi(x_1-h_1/2,\, x_2,\, x_3) + \frac{1}{2}\psi(x_1+h_1/2,\, x_2,\, x_3)\phi(x_1-h_1/2,\, x_2,\, x_3). \quad (32)$$

The present numerical discretization is based on the second accuracy (Kawamura [26]; Suzuki and Kawamura [27]) and defined as follows.

The discretized continuity equation can be expressed as

$$(\text{Cont.}) \equiv \frac{\delta u_i}{\delta x_i} = 0. \quad (33)$$

For the convective terms, the advective and divergence forms are discretized as

$$(\text{Adv.})_i \equiv \overline{u_j}^{x_i} \overline{\frac{\delta u^i}{\delta x_j}}^{x_j}, \quad (34)$$

and

$$(\text{Div.})_i \equiv \frac{\delta \overline{u_j}^{x_i} \overline{u_i}^{x_j}}{\delta x_j}. \tag{35}$$

One can easily confirm that these forms are connected with the following relation:

$$(\text{Adv.})_\alpha = (\text{Div.})_\alpha - u_\alpha \cdot \overline{(\text{Cont.})}^{1x_\alpha}, \tag{36}$$

where the summation convention is not applied to the suffix α. Equation (36) corresponds to the analytical equality of Eq. (29). Therefore, the discretized scheme becomes independent of the above forms within the numerical accuracy of the continuity equation (Eq. (33)). In the present computation, the advective form is adopted for the convective terms. Similar numerical operations have also been devised to calculate the budget terms of the Reynolds stress transport equations with retaining the consistency.

B. Fourth-Order Calculation. To examine the numerical accuracy of the present calculation, the fourth-order scheme proposed by Morinishi [30] is adopted in the x and z directions for spatial discretization. The rest of the calculation method is the same as the one adopted in the text. The Reynolds number is set to be $\mathrm{Re}_\tau = 640$.

The mean velocity distribution and the root mean square of the velocity fluctuations are shown in Figs. 18 and 19, respectively. The results by the fourth-order scheme are in agreement with those by the second-order one in the whole region. The small discrepancy, however, is observed in the channel center region for the turbulence intensities, but it is not significant.

One-dimensional energy spectra of velocity fluctuations $E_{(ii)}$ are given in Fig. 20 in comparison with that of the second-order scheme. In the streamwise energy spectra, no significant difference can be found between the second- and fourth-order schemes. In the spanwise energy spectra, on the other hand, a noticeable difference can be seen in the highest wave numbers. These wave numbers are, however, already beyond the peak of the dissipation spectra; thus the effect is not so significant so long as higher-order correlations and derivatives are not concerned.

For the results, it can be concluded that the mean properties and the second moment correlations can be captured even by the second-order scheme with the present grid resolution. This conclusion, as a matter of course, depends upon the grid resolution. In the case of DNS, however, an enough fine grid is adopted inevitably to capture the finest scale of turbulence. This is the reason why the acceptable results can be obtained even with the second-order scheme.

References

[1] Orszag, S. A., and Patterson, G. S., 1972, ''Numerical simulation of three-dimensional homogeneous isotropic turbulence,'' Phys. Rev. Lett., **28**, pp. 76–79.

[2] Kim, J., Moin, P., and Moser, R., 1987, ''Turbulence statistics in fully developed turbulent channel flow at low Reynolds number,'' J. Fluid Mech., **177**, pp. 133–166.

[3] Kuroda, A., Kasagi, N., and Hirata, M., 1989, ''A direct numerical simulation of the fully developed turbulent channel flow at a very low Reynolds number,'' *Int. Symp. Computational Fluid Dynamics*, Nagoya, pp. 1174–1179.

[4] Kasagi, N., Tomita, Y., and Kuroda, A., 1992, ''Direct numerical simulation of passive scalar field in a turbulent channel flow,'' ASME J. Heat Transfer, **114**, pp. 598–606.

[5] Kim, J., Moin, P., and Moser, R., 1990, *The Diskette of Collaborative Testing of Turbulence Models*, Bradshaw, P., ed., Stanford University.

[6] Antonia, R. A., and Kim, J., 1994, ''Low-Reynolds-number effects on near-wall turbulence,'' J. Fluid Mech., **276**, pp. 61–80.

[7] Kawamura, H., Ohsaka, K., Abe, H., and Yamamoto, K., 1998, ''DNS of turbulent heat transfer in channel flow with low to medium-high Prandtl number fluid,'' Int. J. Heat and Fluid Flow, **19**, pp. 482–491.

[8] Kawamura, H., Abe, H., and Matsuo, Y., 1999, ''DNS of turbulent heat transfer in channel flow with respect to Reynolds and Prandtl number effects,'' Int. J. Heat and Fluid Flow, **20**, pp. 196–207.

[9] Kawamura, H., 1998, ''Direct numerical simulation of turbulence by parallel computation,'' *Proc. 10th Int. Conf. Parallel CFD*, pp. 19–21.

[10] Kawamura, H., Abe, H., and Matsuo, Y., 1999, ''Direct numerical simulation of turbulence by parallel computation,'' *Parallel Computational Fluid Dynamics*, Lin et al., eds., North-Holland, Amsterdam, pp. 3–9.

[11] Moser, R. D., Kim, J., and Mansour, N. N., 1999, ''Direct numerical simulation of turbulent channel flow up to $\mathrm{Re}_\tau = 590$,'' Phys. Fluids, **11**, pp. 943–945.

[12] Laufer, J., 1951, ''Investigation of turbulent flow in a two-dimensional channel,'' NACA Rept., Vol. 1053, pp. 1247–1266.

[13] Hussain, A. K. M. F, and Reynolds, W. C., 1975, ''Measurements in fully developed turbulent channel flow,'' ASME J. Fluids Eng., **97**, pp. 568–580.

[14] Kreplin, H. P., and Eckelmann, H., 1979, ''Behavior of the three fluctuating velocity components in the wall region of a turbulent channel flow,'' Phys. Fluids, **22**, pp. 1233–1239.

[15] Johansson, A. V., and Alfredsson, P. H., 1982, ''On the structure of turbulent channel flow,'' J. Fluid Mech., **122**, pp. 295–314.

[16] Wei, T., and Willmarth, W. W., 1989, ''Reynolds-number effects on the structure of a turbulent channel flow,'' J. Fluid Mech., **204**, pp. 57–95.

[17] Antonia, R. A., Teitel, M., Kim, J., and Browne, L. W., 1992, ''Low-Reynolds-number effects in a fully developed turbulent channel flow,'' J. Fluid Mech., **236**, pp. 579–605.

[18] Nishino, K., and Kasagi, N., 1989, ''Turbulence statistics measurement in a two-dimensional channel flow using a three-dimensional particle tracking velocimeter,'' *Proc. 7th Turbulent Shear Flows*, Vol. 2, pp. 22.1.1–22.1.6.

[19] Nishino, K., and Kasagi, N., 1991, ''On the quasi-coherent turbulence structures in the two-dimensional channel flow,'' *Proc. 8th Turbulent Shear Flows*, Vol. 2, pp. 28.3.1–28.3.6.

[20] Moin, P., and Kim, J., 1982, ''Numerical investigation of turbulent channel flow,'' J. Fluid Mech., **118**, pp. 341–377.

[21] Jiménez, J., 1998, ''The largest scales of turbulent wall flows,'' *Center for Turbulence Research Annual Research Briefs*, pp. 137–154.

[22] Dukowics, J. K., and Dvinsky, A. S., 1992, ''Approximate factorization as a high order splitting for the implicit incompressible flow equations,'' J. Comput. Phys., **102**, pp. 336–347.

[23] Rai, M. M., and Moin, P., 1991, ''Direct simulation of turbulent flow using finite-difference schemes,'' J. Comput. Phys., **96**, pp. 15–53.

[24] Rai, M. M., and Moin, P., 1993, ''Direct numerical simulation of transition and turbulence in a spatially evolving boundary layer,'' J. Comput. Phys., **109**, pp. 169–192.

[25] Gavrilakis, S., 1992, ''Numerical simulation of low-Reynolds-number turbulent flow through a straight square duct,'' J. Fluid Mech., **244**, pp. 101–129.

[26] Kawamura, H., 1994, ''Direct numerical simulation of turbulence by finite difference scheme,'' *The Recent Developments in Turbulence Research*, Z. S. Zhang and Y. Miyake, eds. International Academic Publishers, pp. 54–60.

[27] Suzuki, T., and Kawamura, H., 1994, ''Consistency of finite-difference scheme in direct numerical simulation of turbulence (in Japanese),'' Trans. JSME, **60–578B**, pp. 3280–3286.

[28] Schumann, U., 1975, ''Subgrid scale model for finite difference simulations of turbulent flows in plane channels and annuli,'' J. Comput. Phys., **18**, pp. 376–404.

[29] Kajishima, T., 1994, ''Conservation properties of finite difference method for convection (in Japanese),'' Trans. JSME, **60–574B**, pp. 2058–2063.

[30] Morinishi, Y., 1995, ''Conservative properties of finite difference scheme for incompressible flow,'' *Center for Turbulence Research Annual Research Briefs*, pp. 121–132.

[31] Spalart, P. R., 1988, ''Direct simulation of a turbulent boundary layer up to $R_\theta = 1410$,'' J. Fluid Mech., **187**, pp. 61–98.

[32] Dean, R. B., 1978, ''Reynolds number dependence of skin friction and other bulk flow variables in two-dimensional rectangular duct flow,'' ASME J. Fluids Eng., **100**, pp. 215–222.

[33] Alfredsson, P. H., and Johansson, A. V., 1988, ''The fluctuating wall-shear stress and the velocity field in the viscous sublayer,'' Phys. Fluids, **31**, pp. 1026–1033.

[34] Komminaho, J., Lundbladh, A., and Johansson, A. V., 1996, ''Very large structures in plane turbulent Couette flow,'' J. Fluid Mech., **320**, pp. 259–285.

[35] Saddoughi, S. G., and Veeravalli, S. V., 1994, ''Local isotropy in turbulent boundary layers at high Reynolds number,'' J. Fluid Mech., **268**, pp. 333–372.

[36] Tennekes, H., and Lumley, J. L., 1972, *A First Course in Turbulence*, MIT Press, Cambridge, MA.

[37] Mansour, N. N., Kim, J., and Moin, P., 1988, ''Reynolds-stress and dissipation-rate budgets in a turbulent channel flow,'' J. Fluid Mech., **194**, pp. 15–44.

[38] Launder, B. E., and Reynolds, W. C., 1983, ''Asymptotic near-wall stress dissipation rates in a turbulent flow,'' Phys. Fluids, **26**, p. 1157.

[39] Antonia, R. A., Djenidi, L., and Spalart, P. R., 1994, ''Anisotropy of the dissipation tensor in a turbulent boundary layer,'' Phys. Fluids, **6**, pp. 2475–2479.

[40] Chong, M. S., Perry, A. E., and Cantwell, B. J., 1990, ''A general classification of three-dimensional flow fields,'' Phys. Fluids A, **4**, pp. 765–777.

[41] Kim, J., 1989, ''On the structure of pressure fluctuations in simulated turbulent channel flow,'' J. Fluid Mech., **205**, pp. 421–451.

[42] Robinson, S. K., 1991, ''The kinematics of turbulent boundary layer structure,'' *NASA TM*, 103859.

Ram Balachandar
Professor

D. Blakely
Graduate Student

M. Tachie
Graduate Student

G. Putz
Associate Professor

Department of Civil Engineering,
Fluid Engineering Laboratory,
College of Engineering,
University of Saskatchewan, Saskatoon, Canada

A Study on Turbulent Boundary Layers on a Smooth Flat Plate in an Open Channel

An experimental study was undertaken to investigate the characteristics of turbulent boundary layers developing on smooth flat plate in an open channel flow at moderately high Froude numbers ($0.25<Fr<1.1$) and low momentum thickness Reynolds numbers ($800<\mathrm{Re}_\theta<2900$). The low range of Reynolds numbers and the high Froude number range make the study important, as most other studies of this type have been conducted at high Reynolds numbers and lower Froude numbers (~ 0.1). Velocity measurements were carried out using a laser-Doppler anemometer equipped with a beam expansion device to enable measurements close to the wall region. The shear velocities were computed using the near-wall measurements in the viscous subregion. The variables of interest include the longitudinal mean velocity, the turbulence intensity, and the velocity skewness and flatness distributions across the boundary layer. The applicability of a constant Coles' wake parameter ($\Pi=0.55$) to open channel flows has been discounted. The effect of the Froude number on the above parameters was also examined. [DOI: 10.1115/1.1366321]

1 Introduction

In an extensive review and analysis, George and Castillo [1] report that the turbulent boundary layer is the most investigated aspect of turbulent flows. This is not surprising from a practical viewpoint as turbulent boundary layers are encountered in many industrial and environmental applications. For example, the estimation of mixing of pollutants in water bodies and sediment transport rates in open channels will be directly influenced by the nature of the turbulent boundary layer. The friction characteristics of boundary layers have been studied extensively for the better part of the last ten decades. Our ability to model the various practical flows is limited by our understanding of turbulent boundary layers. In open channel flows, there still remain important questions regarding the structural characteristics of turbulent boundary layers. Many of the previous investigations have centered on either identifying the various regions of the boundary layer or characterizing deviations from a universally accepted standard form. In open channel flows, the development of the laser-Doppler anemometer (LDA) has enabled researchers to overcome the intrusive nature of other measuring devices and assisted a great deal in deciphering some of the structural characteristics. The LDA has especially played a very important role in conducting measurements in the near-wall viscous region.

Previous Studies. One should recall that researchers working in closed conduits and pipe flows have carried out extensive experiments and analysis of turbulent boundary layers. Starting with Keulegan's [2] suggestion, a significant part of this analysis has been essentially borrowed and used in open channel flows, which assumes that there is no Froude number effect. A number of experimental [3–11] and a few analytical [12,13] open channel flow investigations have been carried out. The textbook by Nezu and Nakagawa [14] has come to be accepted as the standard reference for turbulent boundary layers in open channel flow and provides an important collation of data and results. It is presently well understood that the turbulent boundary layer characteristics are a function of the momentum thickness Reynolds number. For example, Nezu and Rodi [6] identified an increasing fullness in the velocity profile with increasing Re_θ and an increasing turbulence intensity with increasing Re_θ. Froude number is generally assumed to have no effect on the friction characteristics of open channel turbulent boundary layers [15]. This agrees with Keulegan's [2] suggestion that pipe flow formulations could probably be adopted in open channel flow.

Table 1, adopted and modified from that presented by Nezu and Nakagawa [14], provides a brief summary of the previous measurements in open channel flow turbulent boundary layers. Some of the above studies have pointed out the deficiencies/limitations in extrapolating information from closed conduit and zero-pressure gradient flows to open channel flows. There has been little work done at the lower range of Reynolds numbers. There has also been little work done to study the effect that Froude number has on the various parameters characterizing turbulent boundary layers in open channel flows [15].

Present Study. Froude number directly relates to the speed of a surface disturbance, and since a Froude number increase causes the surface disturbance to increase [16], the effect of the Froude number on the wake parameter was of interest in this paper. This is particularly important in shallow open channel flows due to the proximity of the boundary layer wake region to the free surface. In this work, the effect of Froude number can be viewed as a perturbation applied to a canonical boundary layer. Recent work [10] has indicated that open channel boundary layers in shallow flows behave somewhat differently from canonical boundary layers. For example, existing literature suggests that the wall normal turbulence fluctuation goes to zero at the free surface and the vertical component of the turbulence kinetic energy is redistributed to the streamwise and spanwise components via the pressure strain.

The present study was carried out using a single component LDA system in open channel flow turbulent boundary layers. Because Froude number increases cause the surface disturbance to increase, measurements were conducted both at subcritical states ($\mathrm{Fr}\sim 0.3,0.8$) and at a supercritical state ($\mathrm{Fr}>1.0$). This is significant, as most measurements in this area have been done at low Froude numbers ($\mathrm{Fr}\sim 0.1$). At each Froude number, the flow Reynolds number based on the boundary layer momentum thickness (Re_θ) varied from 800–2900. The variables of interest include the longitudinal mean velocity, turbulence intensity, skewness and

Contributed by the Fluids Engineering Division for publication in the JOURNAL OF FLUIDS ENGINEERING. Manuscript received by the Fluids Engineering Division March 1, 2000; revised manuscript received January 29, 2001. Associate Editor: D. R. Williams.

Table 1 A summary of turbulence measurements in open-channel flows

Authors	Date	Reference	Technique	Velocity u	v	w	Re ($x10^4$)	Fr
Ippen & Raichlen	1957	ASCE, HY-6 Paper 1392	Total tube	x			5.0	.03-.04
Yokoshi	1967	D.P.R.I., Kyoto Univ., 17. P.1	Propeller	x			350 River	0.25
Raichlen	1967	ASCE, EM-2, p. 73	Hot-film	x			3.0-4.0	0.25-0.4
Richardson & McQuivey	1968	ASCE, HY-2, p. 411	Hot-film	x			0.8-2.0	0.5-1.0
McQuivey & Richardson	1969	ASCE, HY-1, p. 209	Yawed hot-film	x	x		0.7,1.2	0.6,0.4
Smutek	1969	ASCE, HY-1, p. 519	Yawed tube	x	x		0.8-3.7	0.3-1.3
Blinco & Partheniades	1971	J. Hydr. Res., IAHR, 9, p. 43	Hot-film	x			1.0-2.8	0.15-1.2
Grass	1971	J. Fluid Mechanics, 50, p. 233	H_2-bubble	x	x		0.67	0.2
Imamoto	1973	D.P.R.I. Kyoto Univ., 22, p. 153	Hot-film	x			0.4-7.6	0.45-2.0
Kisisel, Rao & Delleur	1973	ASCE, EM-1, p. 31	Hot-film	x	x		<0.7 Shallow	<1.5
McQuivey	1973	USGS, Prof. Paper 802	Hot-film	x			Rivers	
Eckelmann	1974	J. Fluid Mechanics, 65, p. 439	Hot-film	x	x		0.56,0.82	Oil flow
Blinco & Simons	1975	ASCE, EM-3, p. 241	Flush hot-film	Shear Stress			1.0-3.4	0.4-1.4
Nakagawa, Nezu & Ueda	1975	JSCE, No. 241, p. 155	Hot-film	x	x	x	0.9-1.1	0.16
Bayazit	1976	J. Hydr. Res., IAHR, 14, p. 115	Hot-film	x			0.3-15	0.2-0.9
Nezu	1977	JSCE, No. 261, p. 67	Hot-film	x	x	x	0.9-4.6	0.15-3.1
Nakagawa & Nezu	1977	J.Fluid Mechanics, 80, p. 99	Hot-film	x	x		1.0	0.16
Nakagawa & Nezu	1979	JSCE, No. 285, p. 45	Hot-film	x	x	x	1.2	0.17-0.6
Li, Shall & Simons	1980	ASCE, HY-4, p. 575	Hot-film	x	x			
Anwar & Atkins	1980	ASCE, HY-8, p. 1273	Electromag.	x	x	x	7.5	0.75
Griffith & Grimwood	1981	ASCE, HY-3, p. 311	Electromag.	x	x		River	
Nakagawa & Nezu	1981	J. Fluid Mechanics, 104, p. 1	Hot-film	x	x		1.1	0.16
Komori, Ueda & Mizushina	1982	Int. J. Heat Mass Transfer, 25, p. 513	LDA.	x	x	x	0.3	0.11
Imamoto & Ishigaki	1983	Osaka Symp. Flow Meas. 1, p. 17	LDA	x	x		1.1	0.5-1.3
Nezu & Rodi	1986	ASCE, HY-5, Vol. 112, p.335	LDA.	x	x		0.6-11.0	0.7-1.2
Steffler, Rajaratnam & Peterson	1985	ASCE, Vol. 111, HY-1, p. 119	LDA	x	x		2.3-8.5	0.3-0.6
Kirkgoz	1989	ASCE, Vol. 115, No. 11, p. 1543	LDA	x			0.13-43	0.04-0.9
Kirkgoz and Ardichoglu	1997	ASCE, J. Hydraulic Engr., Vol. 123, p. 1099	LDA	x			0.7-34.0	0.3-0.7
Balachandar & Ramachandran	1999	J. Fluids Engineering, ASME Vol. 121, p. 684	LDA	x			0.2-0.5	0.1-0.2
Tachie et al.,	2000	J. Fluids Engineering, ASME Vol. 122, p. 533	LDA	x			< 7	0.4-0.7
Tachie et al.,	2000	Intl. Symp. Turbulence, Heat & Mass Transfer, Nagoya, Japan.	LDA	x			1.5-7.0	0.1-0.2

ASCE – American Society of Civil Engineers, EM – Engineering Mechanics, HY- Hydraulic Division, IAHR- International Association of Hydraulic Research, ASME – American Society of Mechanical Engineers, JSCE – Japanese Society of Civil Engineers

flatness factor of the velocity distribution. The universality of the von-Karman constant (κ) was verified and the applicability of the log-law was also identified.

2 Experimental Arrangement

Open Channel Flume. An open channel flume available at the University of Saskatchewan Hydrotechnical Laboratory was used in the present study. The flume was 10 m in length, 0.8 m wide, and 0.6 m deep. The bottom of the flume was made of brass and the sides were of tempered glass. At the upstream end of the flume, a settling tank, a contraction, and several stilling arrangements were used to reduce the turbulence level in the flow. A downstream gate was used to control the water depth in the flume. In order to ensure that a controlled boundary layer is developed in the test region, all the measurements were conducted on a polished aluminum plate placed on the bottom of the flume. Figure 1 shows a schematic of the flow field. The leading edge of the plate was 5 m from the contraction. The surface of the plate was 63 mm above the bottom of the flume. The flow was free to pass over and below the plate. As is well known, for the present flow configuration, the turbulent boundary layer is expected to be fully developed at a distance of about 50–70 depths from the leading edge. To ensure a developed boundary layer at closer distances, tripping of the boundary layer was necessary. A wire 1.0 mm in diameter was fixed across the plate, 250 mm from the leading edge in order to trip the flow. For the purpose of this study, the coordinate system has its origin situated at the leading edge of the plate along the channel axis. Specifically, the *y*-coordinate was measured through the depth of the flow and the *z*-coordinate was measured in the direction of the flow. Following the procedure outlined in a previous study [3], longitudinal velocity measurements were obtained along the axis of the channel at $z=500$, 600, 700, and 850 mm. The mean velocity profiles were found to converge to an asymptotic state. Based on this observation, $z=850$ mm was chosen as the measurement location. Spanwise measurements were also taken to determine the quality of the flow. The mean velocity profiles and the skewness profiles, at the centerline and 100 mm to the right of the centerline did not show any significant deviations.

Laser-Doppler Anemometer. A laser-Doppler anemometer (Dantec Inc.) was used to conduct the velocity measurements due to its accuracy and nonintrusive nature. The measurement volume of the laser-Doppler anemometer system with the beam expansion device is $0.12\times0.12\times1.4$ mm^3. Further details for the laser-Doppler anemometer and the signal processing system is not included here, but can be found in other reports from this institution (e.g., Balachandar and Ramachandran [3]). Prior to commencing the study, a series of measurements were conducted using the

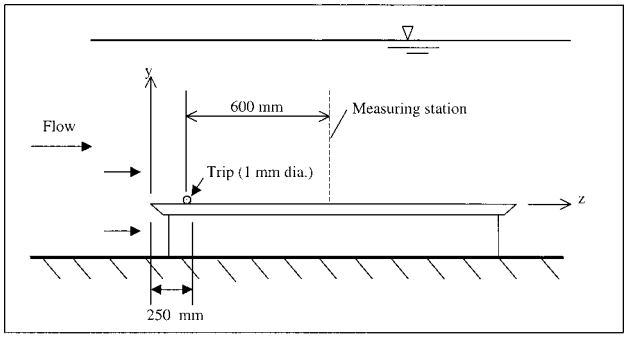

Fig. 1

Table 2 Summary of velocity measurement uncertainty analysis

Distance from wall (mm)	Mean velocity of 30 measurements (m/s)	Standard deviation (m/s) x 10^3	Uncertainty in mean velocity measurements (%)
0.50	0.375	2.38	± 1.3
35.0	0.785	2.79	± 0.73

LDA on a known flow field to confirm the accuracy of the measurements. To this end, velocity measurements were conducted in the potential core of a turbulent water jet at the outlet of a well-designed nozzle. The mean velocity and turbulence measurements conformed to the expected values. Following the work of Schultz and Swain [17], and based on the work of Coleman and Steele [18], the repeatability of the velocity measurements was determined within a 95 percent certainty range. Thirty measurements were taken at three different distances from the channel bottom ($y=0.05$ mm, 0.5 mm, and 35 mm). The depth of the flow was 50 mm for this test. The maximum flow velocity was set to be approximately 0.78 m/s. Measurements were obtained at the centerline of the plate (which coincided with the channel axis), 600 mm downstream from the trip. The $y=0.05$ and 0.5 mm results represent the uncertainty of the laser-Doppler anemometer readings in the inner region, defined as $y/\delta<0.2$ [19]. The $y=35$ mm results will represent the uncertainty of the laser Doppler-anemometer readings in the outer region, defined as $0.2<y/\delta<1.0$. A two-tailed *t*-value of 2.045 was obtained for the thirty velocity measurements (twenty-nine degrees of freedom) at a 95 percent level of confidence. This value was then multiplied by the standard deviation for each of the elevations to determine the uncertainty in the repeatability of the velocity measurement. Table 2 summarizes the results for the mean velocity measurements at $y=0.5$ and 35.0 mm. For the thirty repeated velocity measurements taken at $y=0.05$ mm, a few of them had zero readings. The zero readings were a result of there being no particles passing through the measuring volume in the 300-second interrogation period. In an effort to acquire high quality data, the signal-to-noise ratio was set high (+3 dB). This results in poor quality data to be rejected. The rate of rejection is higher in the near-wall region. It should also be remarked that the flow is naturally seeded. A different method was used to determine the repeatability for the near-wall data. The mean velocity for each set was computed and compared with one another to determine if they were significantly different at a 95 percent level of confidence. The sets were found not to be significantly different. The low number of readings is a problem that plagues the LDA in the very near-wall region. This problem likely could be improved by increasing the sampling period, but then one is also restrained by a reasonable amount of time, so a balance must be found between sample time and acceptable sample accuracy.

Test Conditions. Table 3 indicates the summary of the test conditions used in the present study. A range of momentum thickness Reynolds numbers between 800 and 2900 was obtained at the three different Froude numbers.

3 Important Relations

Turbulent Boundary Layer. Figure 2 shows a typical mean velocity profile in a turbulent open channel flow. The figure also indicates some of the standard definitions used in the study. The boundary layer formed on the bed consists of distinct regions with different characteristics. The region closest to the bed is the called the viscous sublayer. Viscous forces dominate this layer and Newton's law of viscosity dictates the shear stress at the wall. The region well above the viscous sublayer is called the turbulent region. The transitional region between the viscous sublayer and the turbulent region is called the buffer zone. The turbulent region has

Table 3 Summary of test conditions

Test	depth (d - mm)	u_e (m/s)	δ^* (mm)	δ (mm)	Re_θ	u_τ x 10^3 (m/s)
Fr ≈ 0.3	75	0.33	5.53	44	1380	15.5
	75	0.30	4.00	33	905	14.7
	75	0.30	4.28	36	927	14.4
	75	0.39	7.31	65	2160	17.2
	150	0.36	6.50	55	1884	16.0
Fr ≈ 0.8	50	0.53	3.72	24	1612	24.5
	50	0.52	2.58	18	1120	24.5
	75	0.69	4.02	58	2484	31.1
	75	0.66	3.26	26	1775	29.5
	75	0.66	3.60	28	1914	28.8
	100	0.75	3.32	24	1924	34.0
	100	0.74	3.46	35	2186	33.0
	100	0.79	4.34	45	2878	35.5
	100	0.75	3.50	26	2128	40.2
	100	0.78	3.73	30	2353	39.1
	100	0.76	3.76	28	2370	40.1
	100	0.76	3.76	30	2318	33.5
Fr ≈ 1.0	25	0.51	2.26	14	850	25.5
	25	0.53	2.08	14	836	26.5
	25	0.52	2.61	18	1056	23.5
	25	0.49	2.56	18	1010	23.5
	50	0.77	2.76	18	1644	35.0
	50	0.76	2.60	22	1633	35.0
	50	0.73	2.75	24	1646	32.5
	50	0.73	2.97	21	1602	35.0
	75	0.91	1.81	18	1642	40.0
	75	0.90	2.00	20	1788	39.0
	75	0.90	1.75	16	1715	40.0
	75	0.89	2.11	26	2056	40.0

an inner region and an outer region with varying characteristics. In Fig. 2, the parameter δ is the boundary layer thickness, which is taken as the depth at which the velocity is equal to 99 percent of the free stream velocity (u_e).

Inner Coordinates. Equations (1) and (2) describe the dimensionless inner coordinates:

$$u^+=\frac{u}{u_\tau} \tag{1}$$

$$y^+=\frac{u_\tau \cdot y}{\nu} \tag{2}$$

$$u'^+=\frac{u_{\rm rms}}{u_\tau} \tag{3}$$

Here, u_τ is the friction velocity. The velocity distribution in the viscous sublayer is governed by:

$$u^+=y^+ \tag{4}$$

The usefulness of this relation in evaluating u_τ from experimental data is detailed in Balachandar and Ramachandran [3]. For the range of Re_θ used in this study, fortunately a few more points are available for use in the near-wall region to compute the friction velocity using Eq. (4).

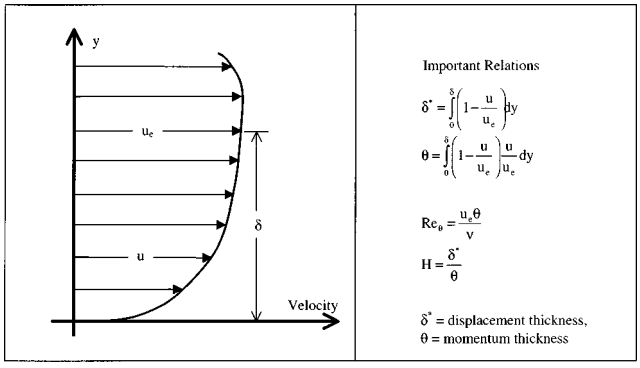

Fig. 2

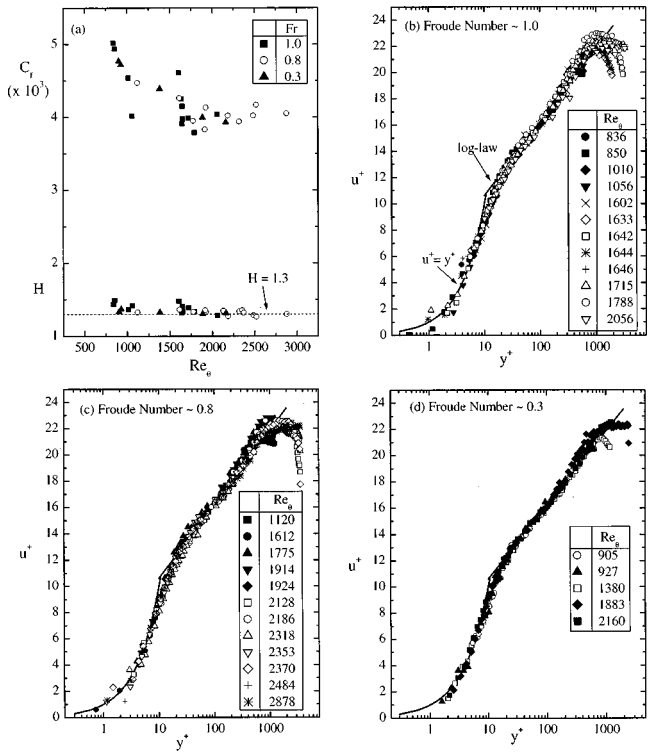

Fig. 3

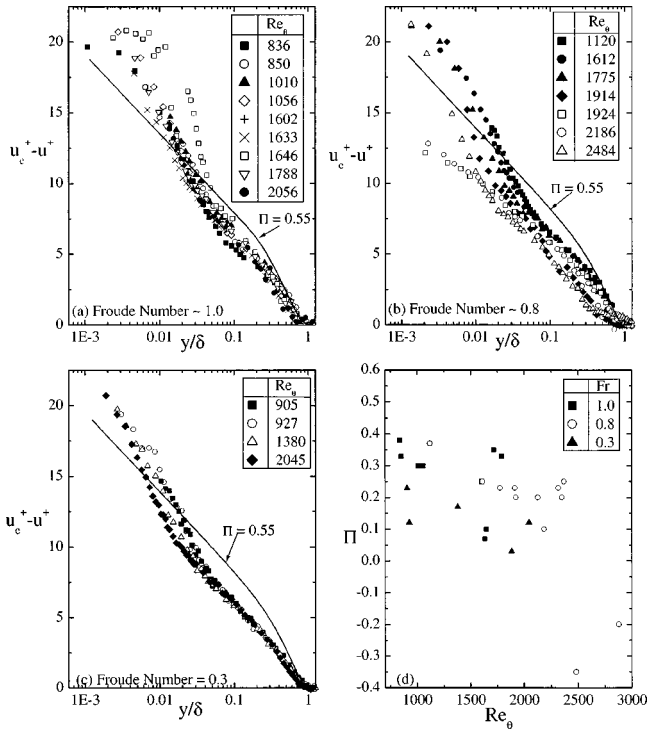

Fig. 4

Log-Law. A commonly used relationship to describe the velocity profile in the turbulent inner region is the log-law:

$$u^+ = \frac{1}{\kappa} \ln y^+ + A \tag{5}$$

Here, $\kappa = 0.41$ is von-Karman constant and $A \approx 5.0$ [14].

Velocity Defect Relation. The velocity defect is the retardation of the flow due to wall effects [20]. The shape of the velocity defect profile is a function of the local pressure gradient. A commonly used equation for the velocity defect, borrowed from smooth plate, zero pressure-gradient flow, is outlined in Eq. (6).

$$u_e^+ - u^+ = \frac{2\Pi}{\kappa}\left[1 - \frac{1}{2\Pi}\left((1+6\Pi)\left(\frac{y}{\delta}\right)^2 - (1+4\Pi)\left(\frac{y}{\delta}\right)^3\right)\right] - \left(\frac{1}{\kappa}\right)\ln\left(\frac{y}{\delta}\right) \tag{6}$$

Here, Π is commonly called the wake parameter.

Higher-Order Moments. The skewness, or third-order moment, gives an indication of how far off the peak of a population is from being symmetrically distributed. If data has a normal probability distribution, the skewness will be equal to zero. The fourth-order moment, flatness factor, gives an indication of homogeneity in the flow. A flatness value of 3 indicates a Gaussian distribution, or a totally random variation of turbulence. It is important to note that skewness and flatness provide valuable statistical information related to the coherent structures in the flow.

4 Results and Discussion

Skin Friction Coefficient and Boundary Layer Shape Parameter. Figure 3(*a*) shows the variation of the skin friction coefficient (C_f) and the boundary layer shape parameter (H) with the momentum thickness Reynolds number. The values for the boundary layer shape parameter are very close to 1.3 and tend to show a slight decreasing trend with increasing Reynolds number. One should recall that the turbulent flat plate boundary layer reported in most previous studies has a shape factor close to 1.3 which indicates that qualitatively the boundary layer in the present study should be similar to boundary layers reported in literature. The skin friction coefficient shows a decreasing trend with momentum thickness Reynolds number and is once again qualitatively similar to the data presented in literature [3,21,22]. The present value of C_f is about 10 percent higher at $\mathrm{Re}_\theta = 1000$ than that noticed in a canonical zero pressure-gradient boundary layer. As one would expect, the present C_f results indicate an absence of Froude number effects.

Longitudinal Mean Velocity Profiles. As indicated earlier, the data in the viscous subregion were used to compute u_τ. This value of u_τ is indirectly validated as the data in the proper normalized form also validate the log-law equation. Figures 3(*b*), 3(*c*), and 3(*d*) show the velocity profiles in inner coordinates for all three Froude numbers. There is no apparent Froude number dependence for the mean velocity at the low range of momentum thickness Reynolds numbers examined in this study. The data points in the turbulent region for each series fit the log-law well (Eq. (5)), confirming that the constants, $\kappa = 0.41$ and $A = 5.0$, are valid. At each one of the Froude numbers, the extent of collapse of the experimental data with the log-law increases with increasing Re_θ.

Velocity Defect Profiles. Figures 4(*a*)–4(*c*) show the velocity defect profiles for each of the Froude numbers. To avoid cluttering of data, the data at some representative Re_θ values are chosen at each Froude number. The velocity defect profile for zero pressure-gradient smooth flat plate flow is also depicted as a line (Eq. (6), with $\Pi = 0.55$ and $\kappa = 0.41$). The data clearly do not agree with the equation. At $\mathrm{Fr} = 0.3$, there is a near collapse of the data at all Re_θ for $y/\delta > 0.05$. For similar range of Re_θ, there is considerably more scatter at the higher Froude numbers and the deviation from Eq. (6) is also higher. This effect is not apparent in the longitudinal mean velocity plots (Fig. 3(*b*)–3(*d*)).

Coles' Wake Parameter. Since the data in Fig. 4(*a*), 4(*b*),

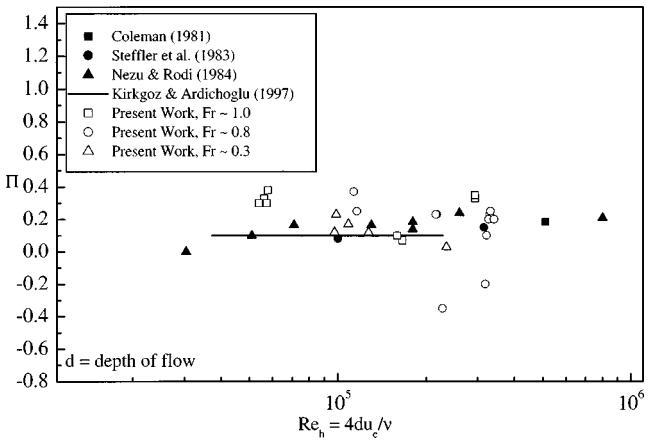

Fig. 5

and 4(*c*) clearly indicate that $\Pi \neq 0.55$, the best value of Π for each data set was sought such that Eq. (6) fit the data in the range from $y/\delta = 0.1$ to 1.0. The resulting Π values are plotted versus Re_θ in Fig. 4(*d*). All values of Π are below the value of 0.55 suggested for zero pressure-gradient smooth plate flow. The Π values were also determined once again by fitting a line to the data in the range of $0.3 < y/\delta < 0.7$, in order to determine if the free surface effects could be eliminated. The resulting Π values increased slightly, but were not close to the zero-pressure gradient smooth plate value of 0.55. The results indicate that the effect of the free surface penetrates through most of the channel depth. The present results also indicate a decreasing trend with increasing Re_θ. To enable comparison with other open channel flow data available in literature, the data in Fig. 4(*d*) are replotted in Fig. 5 as function of Reynolds number based on hydraulic diameter. The present data clearly are within the range indicated by previous studies.

Clauser's Shape Parameter (*G*). Another parameter that is qualitatively useful when comparing the characteristics of turbulent boundary layers is the Clauser's shape parameter, *G*. It should be remarked that *G* is a function of C_f and $H(G=(1-H^{-1})\times(2/C_f)^{1/2})$. The value of *G* for zero pressure-gradient, smooth, flat plate boundary layer, and low turbulence intensity flow, ranges from 6.5–7.5 at high Re_θ [23]. Figure 6 shows the variation of *G* with Re_θ. The equation proposed by Bandyopadhyay and Ahmed [24] based on several experiments is also shown for comparison. The present data in open channel flow are clearly lower than that proposed by the equation. As indicated earlier, the

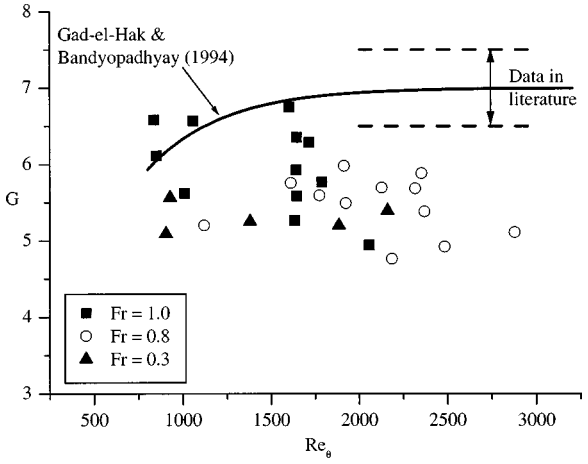

Fig. 6

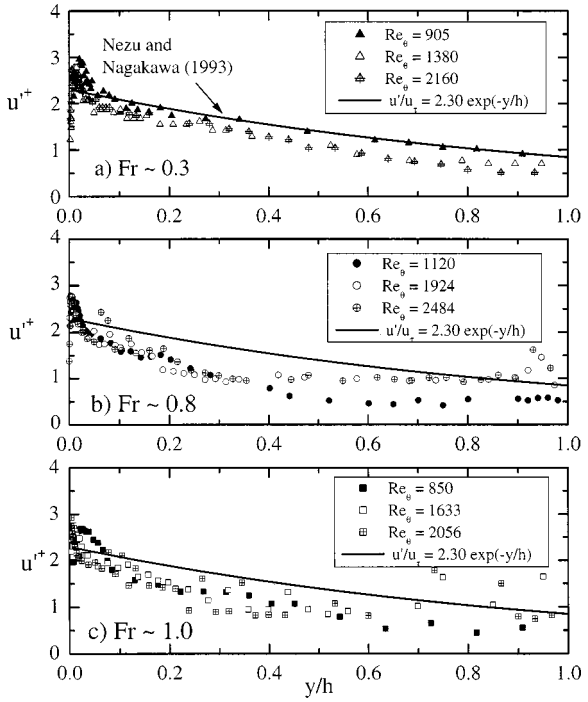

Fig. 7

present C_f values are slightly higher, while the values of Π are slightly lower than that noticed for zero-pressure gradient smooth boundary layers. If Π is forced to be held at a constant value of 0.55 and the corresponding value of u_τ is evaluated to fit the experimental data, the value of u_τ so computed is smaller than that obtained using the data in the viscous subregion. This would then yield lower C_f values. It is important to recognize that one should not decouple the near-wall effects from the outer region effects (or vice-versa) in analyzing boundary layers. The present data are a clear indication to this effect. Since the value of *H* is comparable to most previous studies and the proper value of C_f is higher, the values of *G* are expected to be lower than that noticed in canonical boundary layers. The present data show some weak trends with regard to Froude number albeit with some scatter. On an average, there is a tendency to have a higher value of *G* at higher Fr and no clear Reynolds number dependence can be distinguished from Fig. 6.

Turbulence Intensity Profiles. Figures 7(*a*), 7(*b*), and 7(*c*) show the turbulence intensity profiles at the three Froude numbers over a range of momentum thickness Reynolds numbers. To avoid cluttering of data, only the data at three representative Re_θ values are chosen at each Froude number. In each of these figures, the location of the peak turbulence occurs at approximately $y^+ = 15$. This is where transition occurs within the boundary layer from the viscous region to the turbulent inner region. The intensity of the turbulence drops off as the free surface is approached. Moreover, there is no trend to suggest a significant Reynolds number effect at any given Froude number. It has been suggested by Nezu and Nakagawa [14] that the solid line in Fig. 7 can be used to describe the longitudinal turbulence intensity variation. Nezu and Nakagawa [14] report data at a Reynolds number based on the depth of flow ($\mathrm{Re}_d = u_e d/\nu$) of 3×10^4 and various Fr values. Their data, measured using a hot-film, conforms to the suggested equation. The present experimental data ($1.3 < \mathrm{Re}_d \times 10^{-4} < 7.8$) clearly lie below this expected trend at all values of Fr. Furthermore, the present data also indicate that the deviation from the suggested equation is slightly greater at the higher Froude numbers.

Velocity Skewness Distribution. The distribution of the

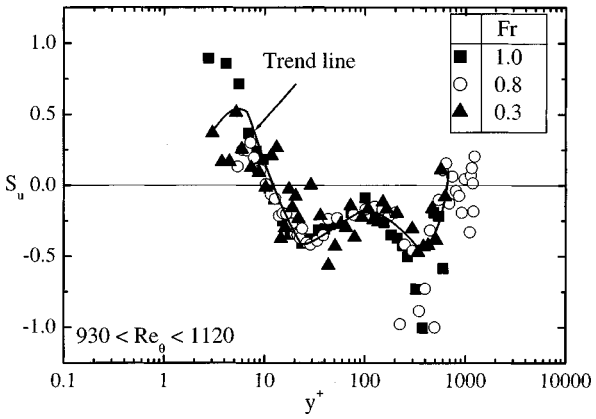

Fig. 8

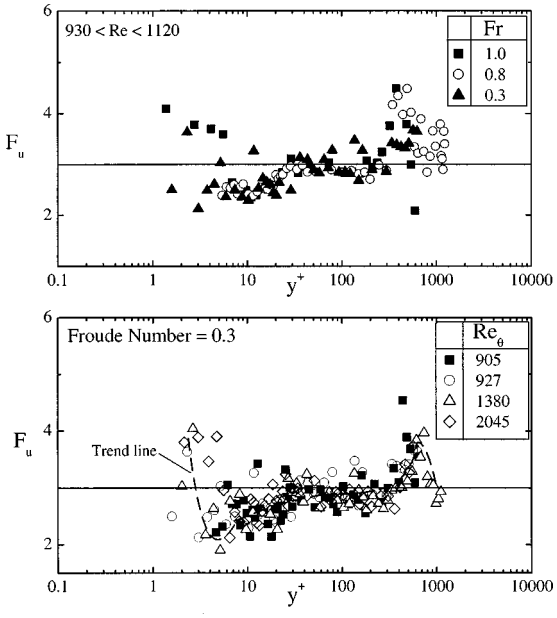

Fig. 9

skewness at the three Froude numbers is shown in Fig. 8. There is no apparent Froude number effect on the skewness distribution. It should be remarked that when the data were plotted at each value of Fr at various Re_θ, there was a fair collapse indicating Reynolds similarity. However, there was an increased amount of scatter at the higher Reynolds numbers. Previous data at higher Re_θ in canonical boundary layers have indicated some Reynolds number effects in the wake region [25]. The dashed line in Fig. 8 indicates the trend in the distribution of S_u. The present data are positively skewed in the near-wall region ($y^+<10$). This is due to the large amplitude fluctuations in the velocity. This is consistent with previous zero-pressure gradient boundary layer studies [26,27]. Simpson et al. [27] reasoned that this should be the case because the in-rush phase of the bursting cycle would bring the high velocity fluid from the outer region causing a positive velocity fluctuation. The arrival of the higher speed fluid from regions away from the wall results in positive values of u to occur more frequently in the viscous sublayer. The skewness factor decreases with further increasing distance from the wall, and becomes zero around $y^+ \sim 10$. Zero skewness would generally indicate Gaussian distributed velocity fluctuations. With increasing y^+, the skewness attains a local minimum in the buffer region. The location of minimum skewness also corresponds to the location where the turbulence intensity attains its maximum value. In the log-law region ($y^+>30$), one would expect the intense mixing and momentum exchange to result in the occurrence of a normally distributed probability density function and S_u should approach zero. In all the tests in the present study, the value of S_u was consistently below zero in the log-law region. This is consistent with the arrival of the low speed fluid from the near-wall region. There is a tendency for the skewness to approach a Gaussian value of zero in the turbulent overlap region and parts of the outer region. In this region the flow approaches shear-free turbulent flow. It should be remarked that in Fig. 3(*b*)–3(*d*), the mean velocity profiles indicate an excellent collapse with the log-law equation. However, in the same y^+ range, the skewness value is not constant and different from zero. The skewness becomes highly negative near $y=\delta$ and approaches a positive values as the free surface is approached ($y^+>500$). The large changes in skewness between the edge of the boundary layer and the free surface is a unique characteristic of open channel flows and is not reported in zero-pressure gradient flat plate flows. Nagano and Tagawa [28] point out that a change in sign in the skewness factor is an indication of the existence of coherent structures. One would thus expect large coherent structures both near the wall and near the edge of the boundary layer.

Velocity Flatness Distribution. Figure 9(*a*) shows a typical set of flatness profiles for a narrow range of Reynolds numbers and various Froude numbers. For the most part, the variation of F_u with y^+ is very similar to that noted in canonical boundary layers [23]. Near the wall, the value of flatness is higher than 3. This indicates that velocity is not normally distributed in the viscous subregion. The value of flatness decreases to a minimum at $y^+ \approx 15$, which corresponds with the region of peak turbulence intensity and a local minimum skewness, which are located in the buffer zone. The flatness approaches the value of 3 in the log-law region, which indicates that the turbulence approaches a Gaussian distribution. In this region, unlike the value of S_u, the flatness factor exhibits a greater tendency to be constant (though slightly below the expected value of 3). Near the outer edge of the boundary layer, the value of flatness increases. At this location, a close examination of the data indicates that the samples contributing to negative fluctuations are many. The flatness factor, by definition, weighs large values of u heavily, and consequently, results in large values of F near the edge of the boundary layer. Close to the free surface, the flatness factor decreases. This aspect is different from that noticed in earlier smooth flat plate canonical boundary layers. As Fig. 9(*a*) indicates, Froude number has no effect on the flatness distribution. Figure 9(*b*) shows the variation of flatness factor at various Reynolds numbers. In the range $10<y^+<500$, the data collapse onto a single line and this is similar to that noted in previous studies at higher Re_θ values. For the range of Re_θ studied, the present set of data do not exhibit any organized Reynolds number effects as noticed in zero pressure-gradient previous studies [25].

Conclusions

The characteristics of turbulent boundary layers on a smooth flat plate in an open channel flow were examined over a range of Froude numbers. The following general conclusions were found:

1 For the range of Re_θ studied, the skin friction coefficient values were higher than that noticed in canonical zero pressure-gradient flows. The skin friction coefficient showed a decreasing trend with increasing momentum thickness Reynolds number. The skin friction coefficient was not dependent on the Froude number.

2 The log-law was also found to be applicable for range of momentum thickness Reynolds numbers and Froude numbers ($800<\mathrm{Re}_\theta<2900$, $0.25<\mathrm{Fr}<1.1$) studied. The extent of the log-law applicability increased with increasing momentum thickness

Reynolds number. The von-Karman constant $\kappa=0.41$ was found to be valid for the open channel flow smooth plate data.

3 Coles' wake parameter of 0.55 obtained from zero pressure-gradient, smooth flat plate flow was found to be inappropriate for the smooth plate open channel flow data, and new wake parameters were determined. The wake parameter was found to decrease with the increasing momentum thickness Reynolds number. The wake parameter, Π, increased with increasing Froude number. The present results indicate that the effect of the free surface penetrates through most of the channel depth.

4 The S_u and F_u distributions across the boundary layer provide useful structural information. The higher-order moments indicate some behavior that is different from that noticed in canonical boundary layers. For example, in the log-law region, the value of skewness is not constant and not equal to zero. Closer to the free surface, both the skewness and flatness distribution show significant deviations from the canonical boundary layer. Further, the higher-order moments, did not exhibit any Reynolds number or Froude number dependence in the range of Re_θ tested in the present study.

5 The turbulence intensity peak increased for increasing Froude number, at the same momentum thickness Reynolds numbers. At the higher Froude number, a Reynolds number trend was visible in the velocity defect profiles, with the higher Re_θ data deviating further from the curve suggested by Nezu and Nagakawa [14].

References

[1] George, W., and Castillo, L., 1997, ''Zero-pressure-gradient turbulent boundary layer,'' Appl. Mech. Rev., **50**, No. 11, pp. 689–729.

[2] Keulegan, G. H., 1938, ''Laws of turbulent flow in open channels,'' J. Res. Natl. Bur. Stand., Sect. A, **21**, Dec., pp. 707–741.

[3] Balachandar, R., and Ramachandran, S., 1999, ''Turbulent boundary layers in low Reynolds number shallow open channel flows,'' ASME J. Fluids Eng., **121**, pp. 684–689.

[4] Bayazit, M., 1976, ''Free surface flow in a channel of large relative roughness,'' J. Hydraul. Res., **14**, No. 2, pp. 115–126.

[5] Kamphius, J. W., 1974, ''Determination of sand roughness for fixed beds,'' J. Hydraul. Res., **12**, No. 2, pp. 193–203.

[6] Nezu, I., and Rodi, W., 1986, ''Open-channel flow measurements with a laser-Doppler anemometer,'' J. Hydraul. Eng., **112**, No. 5, pp. 335–355.

[7] Rajaratnam, N., and Muralidhar, D., 1969, ''Boundary shear stress distribution in rectangular open channels,'' La Houille Blanche, **24**, No. 6, pp. 603–609.

[8] Sarma, K. V. N., Lakshminarayana, P., and Rao, N. S. L., 1983, ''Velocity distribution in smooth rectangular open channels,'' J. Hydraul. Eng., ASCE, **109**, No. 2, pp. 270–289.

[9] Steffler, P. M., Rajaratnam, N., and Peterson, A., 1985, ''LDA measurements in open channel,'' J. Hydraul. Eng., ASCE **111**, No. 1, pp. 119–130.

[10] Tachie, M., Bergstrom, D., and Balachandar, R., 2000, ''Rough wall turbulent boundary layers in shallow open channel flow,'' ASME J. Fluids Eng., **122**, pp. 533–541.

[11] Zippe, H. J., and Graf, W. H., 1983, ''Turbulent boundary-layer flow over permeable and non-permeable rough surfaces,'' J. Hydraul. Res., **21**, No. 1, pp. 51–65.

[12] Vedula, S. and Achanta, R., 1985, ''Bed shear from velocity profiles: a new approach,'' J. Hydraul. Eng., ASCE, **111**, No. 1, pp. 131–143.

[13] Willis, J. C., 1985, ''Near-bed velocity distribution,'' J. Hydraul. Eng., ASCE, **111**, No. 5, pp. 741–753.

[14] Nezu, I., and Nakagawa, H., 1993, *Turbulence in open channel flows*, A. A. Balkema, The Netherlands.

[15] Chow, V. T., 1988, *Open channel hydraulics*, McGraw-Hill, New York.

[16] Henderson, F., 1966, *Open channel flow*, Macmillan, New York.

[17] Schultz, M. P., and Swain, G. W., 1999, ''The effect of biofilms on turbulent boundary layers,'' ASME J. Fluids Eng., **121**, No. 1, pp. 44–51.

[18] Coleman, H. W., and Steele, W. G., 1995, ''Engineering application of experimental uncertainty analysis,'' AIAA J., **33**, No. 10, pp. 1888–1896.

[19] Cardoso, A., and Gust, G., 1989, ''Uniform flow in a smooth open channel,'' J. Hydraul. Res., **27**, No. 5.

[20] White, F. M., 1991, *Viscous fluid flow*, Second Edition, McGraw-Hill, NY.

[21] Purtell, L. P., Klebanoff, P. S., and Buckley, F. T., 1981, ''Turbulent boundary layer at low Reynolds number,'' Phys. Fluids, **24**, No. 5, pp. 802–811.

[22] Spalart, P. R., 1988, ''Direct simulation of a turbulent boundary layer up to $\mathrm{R}_\theta=1410$,'' J. Fluid Mech., **187**, pp. 61–98.

[23] Gad-el-Hak, M., and Bandyopadhyay, P. R., 1994, ''Reynolds number effects in wall-bounded turbulent flows,'' Appl. Mech. Rev., **47**, No. 8, pp. 307–365.

[24] Bandhyopadhyay, P. R., and Ahmed, A., 1993, ''Turbulent boundary layers subjected to multiple curvatures and pressure gradients,'' J. Fluid Mech., **246**, pp. 503–527.

[25] Andreopoulos, J., Durst, F., Zaric, Z., and Javonovic, J., 1984, ''Influence of Reynolds number on characteristics of turbulent wall boundary layers,'' Exp. Fluids, **2**, pp. 7–16.

[26] Ueda, H., and Hinze, J. O., 1975, ''Fine-structure turbulence in the wall region of turbulent boundary layer,'' J. Fluid Mech., **67**, pp. 125–144.

[27] Simpson, R. L., Chew, Y. T., and Shivaprasad, B. G., 1981, ''The structure of a separating turbulent boundary layer,'' Part 2, ''Higher order turbulence results,'' J. Fluid Mech., **113**, pp. 53–73.

[28] Nagano, Y., and Tagawa, M., 1987, ''Statistical characteristics of transfer process in a wall turbulent shear flow,'' *International symposia on transport phenomena*, Hemisphere Publishing, pp. 275–288.

Elgin A. Anderson

Robert E. Spall

Department of Mechanical and
Aerospace Engineering,
Utah State University,
Logan, UT 84322
e-mail: eanderson@mae.usu.edu;
spall@fluids.me.usu.edu

Experimental and Numerical Investigation of Two-Dimensional Parallel Jets

The flowfield of dual, parallel planar turbulent jets is investigated experimentally using an x-type hot-wire probe and numerically by solving the Reynolds-averaged Navier-Stokes equations. The performance of both differential Reynolds stress (RSM) and standard k-ε turbulence models is evaluated. Results show that the numerical models predict the merge and combined point characteristics to good accuracy. However, both turbulence models show a narrower width of the jet envelope than measured by experiment. The predicted profiles of the mean velocity along the symmetry plane agree well with the experimental results. [DOI: 10.1115/1.1363701]

Introduction

Single turbulent plane and offset wall jets are of great engineering importance, and consequently have been studied extensively [1–3]. Applications include burners and boilers, film-cooling of lining walls within gas turbine combustors, fuel-injection systems, and heating and air-conditioning systems. However, far fewer investigations into the behavior of multiple parallel jets appear in the literature. In addition to the applications mentioned above, the study of multiple jets may be particularly important in the design of pollutant exhaust stacks. Specifically, relative to a single exhaust stack, the close grouping of stacks to form parallel jets may be employed as a means to increase the exhaust plume trajectory and consequently decrease the impact of exhaust pollutants.

Flow patterns for two parallel plane jets have previously been reported in the literature [c.f., [4–12]]. The earliest studies were those of Tanaka [4,5] in which the basic flow patterns and entrainment mechanisms of parallel jets were described. In particular, Tanaka identified three relevant regions of the flowfield in the axial direction. The first may be termed the converging region that begins at the nozzle exit and extends to the point where the inside shear layers of the jets merge (denoted the merge point). The merging of the jets is due to the asymmetric nature of the entrainment rates which results in a region of sub-atmospheric pressure between the jets. The jets are consequently deflected toward each other; at their merge point the velocity on the symmetry plane is equal to zero. The intermediate, or merge region is that existing between the merge point and the combined point. The combined point is defined as that point along the symmetry plane at which the velocity is a maximum. This also coincides with the streamwise location where the maximum streamwise mean velocity occurs on the symmetry plane (as opposed to two distinct peaks). Finally, the combined region is that downstream of the combined point where the two jets begin to resemble a self-similar single jet. The general characteristics of the flow field are illustrated in Fig. 1.

The mixing between two parallel jets was experimentally investigated by Elbanna et al. [6]. Their results showed that the mean velocity profile of the parallel jets agreed well with the single jet in the region downstream of the combined point. Also, in that region, the mean velocity decay matched that of a single jet although the magnitude of the velocity was higher for the parallel jets. They report a linear jet spreading rate for the parallel jets at an angle slightly lower than that of the single jet. Self-similarity for the mean flow was attained a short distance from the combined point. However, the turbulent velocity fluctuation became self-similar only for $x/d > 120$

Lin and Sheu [7,8] used hot-wire anemometry to show that the mean velocity approaches self-preservation in both the merging and combined regions, while the Reynolds shear stresses approach self-preservation in the combined region only. The trajectory of the maximum velocity was almost unchanged by variance of nozzle spacing in the converging region. Measurements also indicated that the entrainment and spreading rates in the combined region were greater than those in a single jet flow. This was attributed to significant increases in the values of lateral turbulence intensity and the Reynolds shear stress relative to a single jet.

Nasr and Lai [9] provides a comparison between the parallel planar jets and the offset jet (where a wall replaces the symmetry plane). They suggest that the symmetry plane that exists between two parallel jets may affect the flow in much the same way as the solid wall of the offset jet. A non-dimensional separation distance of 4.25 was examined for the parallel jet and 2.125 for the offset jet. The interaction of the two inner shear layers on both sides of the symmetry plane resulted in a much more turbulent near-field than that of the offset jet. The recirculation region was signifi-

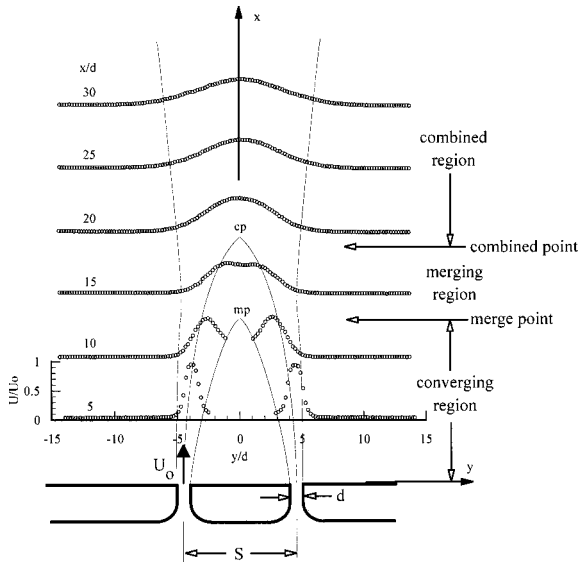

Fig. 1 Description of parallel jet flowfield parameters and coordinates

Contributed by the Fluids Engineering Division for publication in the JOURNAL OF FLUIDS ENGINEERING. Manuscript received by the Fluids Engineering Division September 11, 2000; revised manuscript received February 9, 2001. Associate Editor: K. Zaman.

cantly smaller for the two jets than for the offset jet. Turbulence in the recirculation zone was also significantly stronger for the two parallel jets. The presence of the wall in the offset jet case was shown to produce significant retarding and turbulence suppression effects on the flow development and turbulence field in the recirculation and reattachment regions.

It appears that no numerical studies of plane parallel jets have been published in the literature. However, one may seek guidance from the work of Nasr and Lai [10] in which numerical results were obtained and compared with experimental data for the case of a turbulent plane offset jet. Somewhat surprisingly, their results indicated that the k-ε turbulence model overpredicted the attachment length by 3 percent, whereas a Reynolds stress transport model overpredicted the length by 14 percent.

The purpose of the present work is to evaluate the ability of the standard k-ε model and a Reynolds stress transport model to predict the evolution of twin, plane, parallel jets. Toward that end, numerical and experimental results are compared over a range of jet spacings $9 \leqslant S/d \leqslant 18.25$. For comparative purposes, single jet results are also presented.

Experimental Procedure

The schematic shown in Fig. 1 defines the relevant parameters for the parallel jet configuration. Several characteristic length scale are present in this problem; the width of a single jet, d, the combined width of both jets, $2d$, and the spacing between the jet centerlines, S. It may be argued that the combined jet nozzle width would be most appropriate for the far field (combined region) analysis, while the single jet nozzle width would be most appropriate in the near field where the flow is dominated by individual jet behavior. However, to avoid confusion and to abide by traditional practice, in the current study the single jet width, d is used to non-dimensionalize all length parameters.

A schematic of the jet facility is shown in Fig. 2. Flow was produced by a 1 HP blower controlled by a variable frequency drive. The rotational speed of the blower could be adjusted to within 0.1 Hz over a range of 0–110 Hz. The geometry of the jet nozzles is defined in Fig. 3. The nozzles have a 5:1 contraction with a nozzle width of 2.54 cm. The jet slots are 0.635 cm×20.32 cm which gives an aspect ratio of 32. End plates were positioned perpendicular to the slot direction extending in

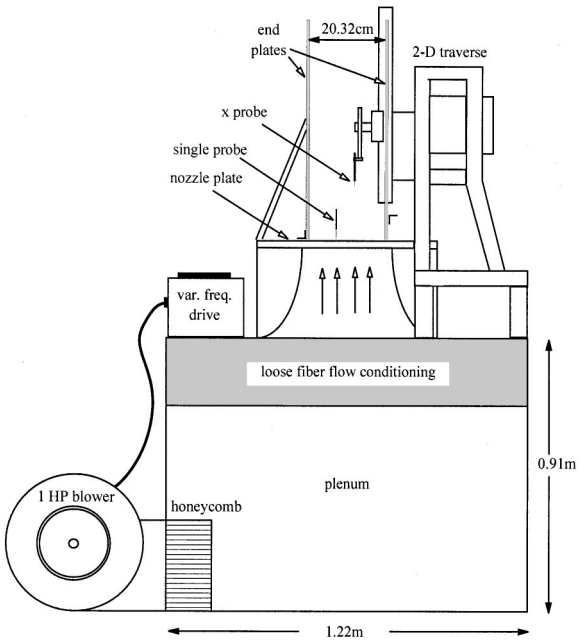

Fig. 2 Schematic of parallel jet experimental facility

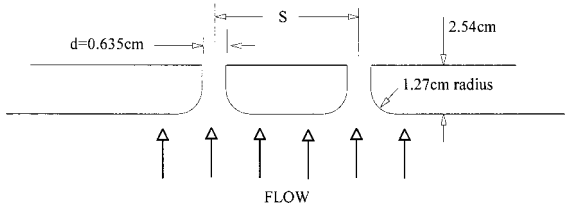

Fig. 3 Jet nozzle geometry definition

the streamwise direction from the jet origin to $x/d=96$ and in the transverse direction to $y/d=\pm 48$ to simulate two-dimensional flow. Two-dimensionality was confirmed by several transverse traverses at different spanwise positions near the center span that indicated negligible changes in the mean profile. Three different spacers were utilized to produce non-dimensional jet separation distances of $S/d=9$, 13, and 18.25. The experiments were performed at a Reynolds number of 6000 based on the single jet width which relates to a initial jet velocity of approximately 18 m/s. The turbulence intensity at the jet exit was 3.6 percent.

A TSI IFA-300 constant temperature anemometer system was used to obtain the hot wire voltage data and TSI ThermalPro software was utilized to calculate velocity parameters from the raw voltages. The parallel jet flow field was surveyed in the streamwise and transverse directions using a two-sensor, x-type hot wire probe. A second, single-sensor probe was positioned along the centerline of one of the jets at the exit plane to measure the jet reference velocity, U_o and the initial turbulence intensity of the jet to be used in the CFD calculations as inlet boundary conditions. The mean velocity along the symmetry plane is denoted by U_m. Symmetry between the jets was verified by experiment and is illustrated by the results shown in Fig. 1. The x-probe was positioned by a computer controlled two-degree-of-freedom traverse with accuracy of ± 0.01 mm in the streamwise and transverse directions. Ambient temperature and pressure were monitored and recorded over the duration of the test runs using electronic sensors.

Numerical Models

The pressure-based finite-volume code Fluent Vers. 4.4 (Fluent, Inc., Lebanon, NH) was utilized to solve the steady, two-dimensional, Reynolds-averaged Navier-Stokes equations. Interpolation to cell faces for the convection terms was performed using a bounded QUICK scheme [13]; second-order central differencing was used for viscous terms. Pressure-velocity coupling was based on the SIMPLEC procedure [14]. Solutions obtained using the segregated solver were considered converged when residuals for each of the equations (based on an L2 norm) were reduced by a minimum of four to five orders of magnitude.

Both differential Reynolds stress (RSM) and standard k-ε models were employed for turbulence closure. The empirical constants in the k-ε model were taken as $C_{1\varepsilon}=1.44$, $C_{2\varepsilon}=1.92$, $C_\mu=0.09$, $\sigma_k=1.0$, and $\sigma_\varepsilon=1.3$. The RSM closure approximations employed are based upon the work of Launder et al. [15] and Gibson and Launder [16]. In particular, the pressure strain term, ϕ_{ij} consisted of the linear return-to-isotropy model for the ''turbulence'' portion as,

$$\phi_{ij1}=-C_1\frac{\varepsilon}{k}\left(\overline{u_i'u_j'}-\frac{2}{3}\delta_{ij}k\right) \tag{1}$$

and the isotropization of production model for the mean-strain part,

$$\phi_{ij2}=-C_2\left(P_{ij}-\frac{1}{3}\delta_{ij}P_{kk}\right) \tag{2}$$

(where $\phi_{ij}=\phi_{ij1}+\phi_{ij2}+\phi_{ij}^w$; P_{ij} is the production term, and ϕ_{ij}^w is the wall reflection term).

The range of C_1 and C_2 employed are those defined by the relation $(1-C_1)/C_2=0.23$, with the most commonly assigned values, which were used in this work, as 1.8 and 0.6, respectively. In addition, the dissipation term was modeled by an isotropic dissipation rate, while diffusion was modeled by a gradient approximation which accounts for directional diffusivity [17].

The computational domain was defined by a rectangular region, which was discretized using a cartesian grid covering one half of the flow field with a symmetry boundary condition representing the plane between the jets. The domain was bounded on the $x=0$ plane by a solid wall along which standard equilibrium wall functions were specified. This eliminated the need to specify an overly fine grid near the wall, which is far removed from the regions of primary interest. An opening of width d in the wall defining the location of the jet inlet boundary condition was also specified. The opening was centered at $y/d=4.5$, 6.5, or 9.125, providing the three jet spacings studied herein. A uniform inlet velocity profile was then set at the opening. Based on experimental results, turbulence intensities at the inlet were set to 3.6 percent, from which the turbulence kinetic energy or (isotropic) Reynolds stress distributions were obtained. The dissipation rate boundary condition was derived from the relationship

$$\varepsilon=\frac{C_\mu^{3/4}k^{3/2}}{0.07L} \tag{3}$$

where L is a characteristic length; in particular, the jet width. A symmetry boundary condition was defined along the $y=0$ plane. Constant pressure boundary conditions were specified on the $y=y_{\max}$ and $x=x_{\max}$ planes. Depending upon the S/d ratio, $x_{\max}$ ranged from 100–120; whereas $y_{\max}$ ranged from 20–30. Note that numerical tests performed by increasing the extent of the domain in each direction by 50 percent did not result in any significant changes in the results.

Experimental Uncertainties

The mean velocity results presented in this study are based on an average of 8192 samples per data point acquired at a sample rate of 600 Hz for a total sample period of 13.65 seconds. Turbulence quantities are based on 65,536 samples acquired at a sample rate of 10,000 Hz for a total sample period of 6.55 seconds. The sample rate for the turbulence quantities was defined by the minimum sample rate beyond which the statistical quantities remain constant and repeatable. Calibration of the hot wire probes was accomplished using a TSI Model 1129 automatic air velocity calibrator using 17 points to cover a velocity range of 0–30 m/s. The maximum velocity measured in the test was approximately 19 m/s. The mean standard errors of the velocity calibration are as follows; <2 percent for velocities between 0–1 m/s, <1 percent for velocities between 1–8 m/s, and <0.5 percent for velocities greater than 8 m/s. Several probe recalibrations were required to maintain the accuracy of the velocity results and occurred at least within 48 hours of any test results reported in this study. The x-type hot wire probe was calibrated over a pitch angle range of ± 30 deg using 5 deg increments. Data in the recirculation region between the jets are not presented due to the inability of the hot wire probes used in this study to detect and measure reverse flow.

The Reynolds number ranged from a value of 5900–6100 over the duration of the complete flow field survey presented in Fig. 9 due to an approximate 10°C change in ambient temperature over the 24 hour time period of the survey. The IFA-300 contains a thermocouple circuit that compensates for temperature drift and therefore the accuracy of the velocity results should not be adversely affected. All other results are based on run times that were of short enough duration that the ambient temperature could be considered constant. For these runs the Reynolds number is calculated to be 6000 ± 50 based on the root-mean-square method and utilize real-time ambient temperature and barometric pressure measurements. All mean velocity data are normalized by the jet exit velocity acquired simultaneous with the local velocity. The mean velocity outside the jet does not decay to zero outside the jet envelope in the surveys shown in Fig. 6 due to both, the transverse entrainment by the jet which produces a cooling velocity for the hot wire at a flow angle that exceeds the resolution capability of the system and, the relatively high uncertainty in the low velocity measurement range. Combined and merge point results are accurate to within $\pm 0.5x/d$ based on repeated tests.

Results

Results are presented from the experimental and numerical analysis of the parallel jet flowfield for three jet spacings and the single jet. Mean velocities and turbulence quantities are nondimensionalized by the jet exit velocity (U_o) and the local mean velocity along the symmetry plane (U_m) respectively. As stated previously, all experimental data was obtained at $5900<\mathrm{Re}<6100$. Consequently, all numerical calculations were performed at $\mathrm{Re}=6000$.

Figures 4(*a*–*e*) show mean streamwise velocity profiles along the symmetry plane for $S/d=0$ (single jet), 9, 13, 18.25, and a summary of experimental results for all configurations, respectively. Data from the experimental measurements and numerical computations using the two turbulence models are compared. In general, Fig. 4(*a*) shows that numerical predictions of the mean velocity decay of a single jet match very well with experiment for both turbulence models. The numerical results are presented for two grid densities to reveal the near grid independence of these solutions.

The parallel jet configurations shown in Figs. 4(*b*–*d*) indicate that the RSM provides slightly greater agreement with experiment for slope of the mean velocity decay than the k-ε model. However, it predicts a velocity magnitude by 3–5 percent higher than experiment. In all cases the streamwise location of the velocity maximum correlates well between experiment and CFD.

A summary of the experimental mean velocity profiles for all tested S/d configurations is shown in Fig. 4(*e*). The results indicate that the mean velocity decay rates for the twin jets tend to the single jet result in the far-field. A curve showing the universal decay rate from Gutmark and Wygnanski [3] for a single, 2-D jet is also presented for comparison. The single jet data match the universal profile quite well.

At this point it is appropriate to introduce the results from a grid convergence study for the twin jet cases. Results using both k-ε and RSM turbulence models are shown in Fig. 5 using three different grid densities at the jet spacing ratio $S/d=13$. The results indicate that solutions obtained on a 139 (spanwise) $\times 394$ (streamwise) grid may be considered grid converged. Consequently, all subsequent (and previous) results displayed have been have been obtained using this (or similar) grid point distributions. Although for purposes of brevity they are not shown, validation tests were also performed by extending the length of the domain by 50 percent in both streamwise and spanwise directions. No significant differences in the results were obtained.

Mean velocity profiles for transverse surveys at select streamwise locations for $S/d=9$ are shown in Fig. 6. These results show the evolution of the flowfield from the near-field, where each jet produces a distinct profile, to the far field or, combined region where the two jets have completely merged to produce a single jet mean velocity profile. Hot wire data are not shown for the recirculation region between the jets where reverse flow is present. Comparison between the experimental and numerical results (using the RSM) show good agreement with respect to peak velocity magnitude and decay rate in the converging and combined region. However, the numerical results predict a more rapid merging of the jets. The k-ε model (not shown) produced a similar trend although the merge rate is slightly accelerated. The largest discrepancy in the location of the velocity peak between experimental and numerical results occurs at approximately $x/d=8.8$. This discrepancy may be partially due to the close proximity of this streamwise location to the merge point of the jet where the rela-

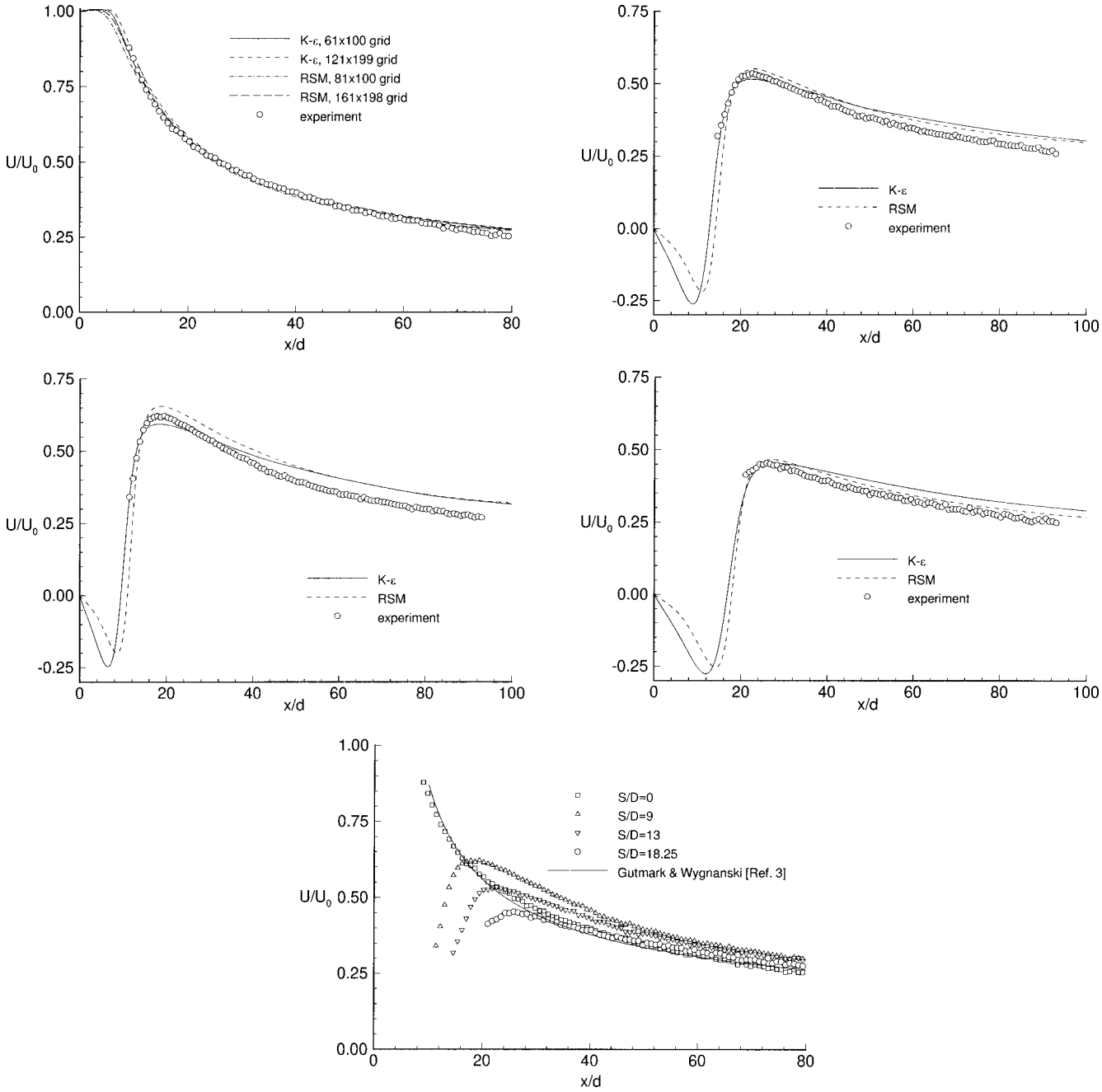

Fig. 4 (*a–e*) Comparison of experimental and numerical mean streamwise velocity profiles along the symmetry plane. (*a*) $S/d=0$ (single jet); (*b*) $S/d=9$; (*c*) $S/d=13$; (*d*) $S/d=18.25$; (*e*) summary of experiment.

tively high mean flow angles approach the limit of the x-sensor's resolution capability. The CFD calculations show that the maximum mean velocity flow angles vary between 27–36° near the merge point for $S/d=9-18.25$, respectively, while the x-sensor calibration is limited to a maximum angle of 30°. It should be added that useful insight of this type is a good example of the mutually beneficial nature of joint experimental/numerical investigations.

Comparisons of combined and merge point results from the current investigations and several other previous investigations are shown in Figs. 7(*a–b*). We note that Tanaka's [4] combined point results are calculated by the current authors from his published jet centerline radius of trajectory results. In this case, the combined point is determined by the intersection of the circular arcs tracing the trajectory of the centerline of each jet based on mean velocity. In all other cases the combined point is defined as the location of the maximum streamwise mean velocity along the symmetry plane. Figure 7(*a*) shows that the current results correlate well with those of previous investigations with respect to the slope of the data trend although, there is scatter in the data between different investigations with respect to location of the combined point. The comparison also shows very good correlation between the current experimental and CFD results. We do note that the predicted merge length of the RSM was slightly greater than that predicted by the k-ε model, a result consistent with the work of Nasr and Lai [10] for the case of an offset jet.

The comparison of merge point results is presented in Fig. 7(*b*). The merge point is the point of zero velocity on the symmetry plane and is easily determined from the CFD calculations. Experimentally, this point is more difficult to determine due to hot wire sensor's lack of reverse flow sensitivity. In the current experimen-

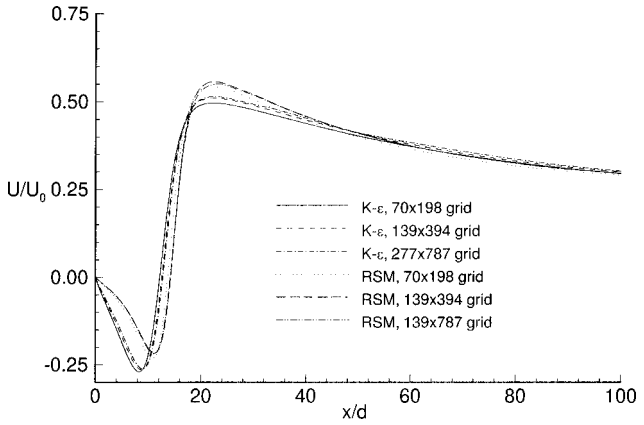

Fig. 5 Sensitivity of mean velocity results to computational grid size

tal results the merge point is estimated by the streamwise location along the symmetry plane where the streamwise normal stress, non-dimensionalized by the local mean velocity rapidly increases toward an asymptote (see Figs. 8(*a*,*b*)). This definition is consistent with findings by Nasr and Lai [9] where LDV measurements show that the maximum normal stress coincides with the point where the local mean velocity equals zero (which defines the merge point). The merge point comparison shows an agreement similar to the combined point results from the different investigations.

Although the slope of the combined or merge point versus S/d relationship agrees well between the various investigations, the absolute location of the combined point for a given S/d varies significantly. This is most likely a facility dependent phenomenon. For example, in his review of mixing layers and jets Thomas [1] finds that although the widening and decay rates of a single turbulent planar jet in the self-similar region correlate well between various studies, the virtual origin is quite sensitive to plenum conditions upstream of the nozzle and published values vary significantly. Hence, the facility dependent influence is one that affects the initial and interaction region of the jet but has little or no influence in the similarity region except to determine its initial width. Therefore, the merge and combined points of parallel jets should demonstrate a similar facility dependent sensitivity since they are determined by the initial spreading rate of each jet upstream of the combined (similarity) region. This effect could also account for the differences in the CFD and experimental merge and combined point results in the current investigation.

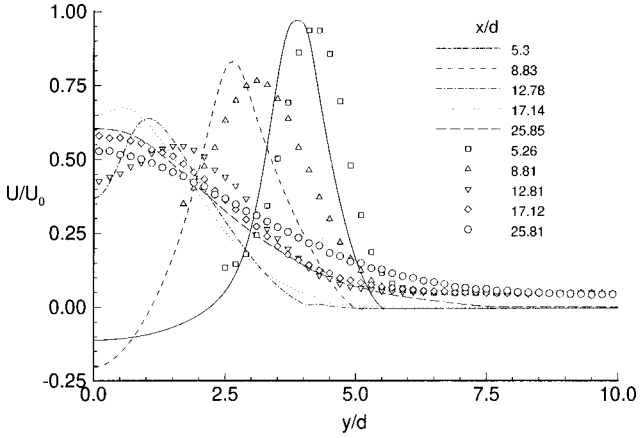

Fig. 6 Comparison of experimental and RSM numerical transverse mean velocity profiles for $S/d=9$

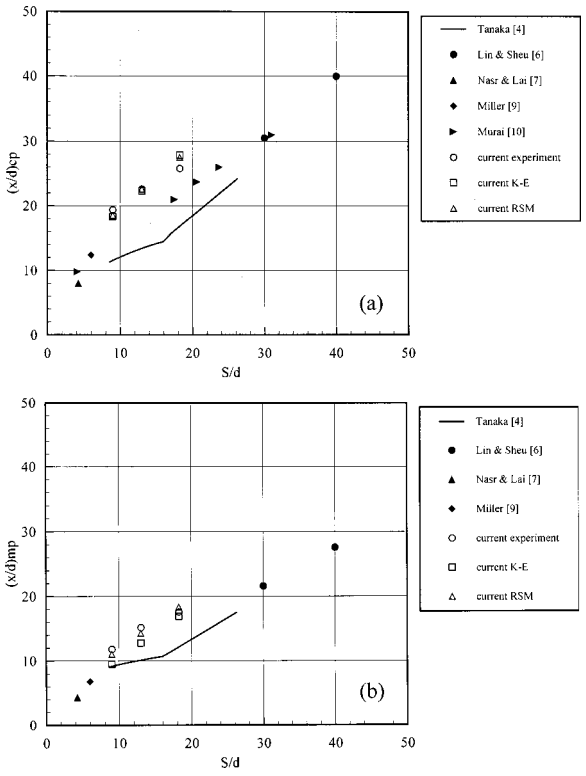

Fig. 7 (*a*–*b*) Comparison of experimental and numerical combined (*a*) and merge (*b*) point results

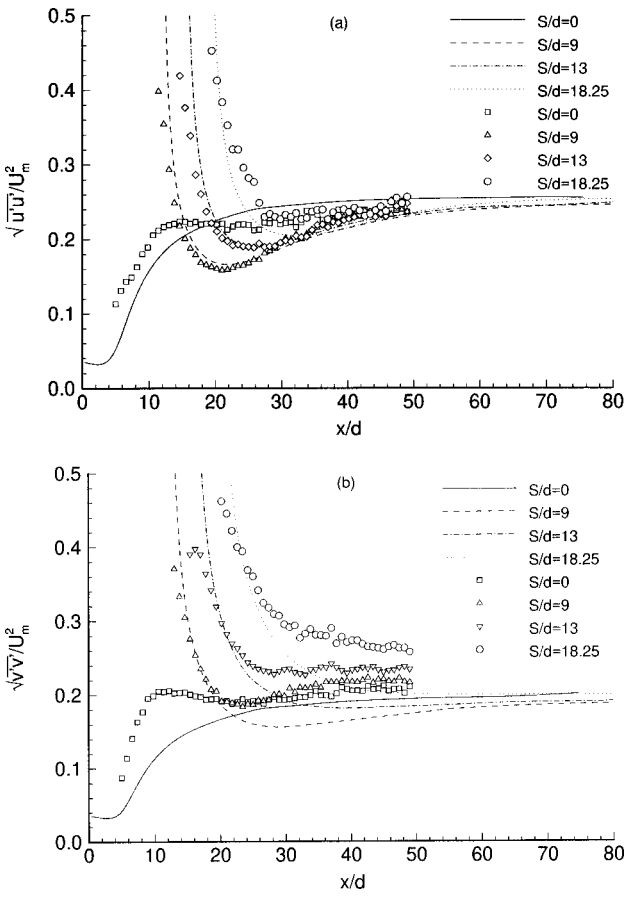

Fig. 8 (*a*–*b*) Comparison of experimental and RSM numerical normal stress profiles along the symmetry plane (*a*) streamwise normal stress; (*b*) transverse normal stress.

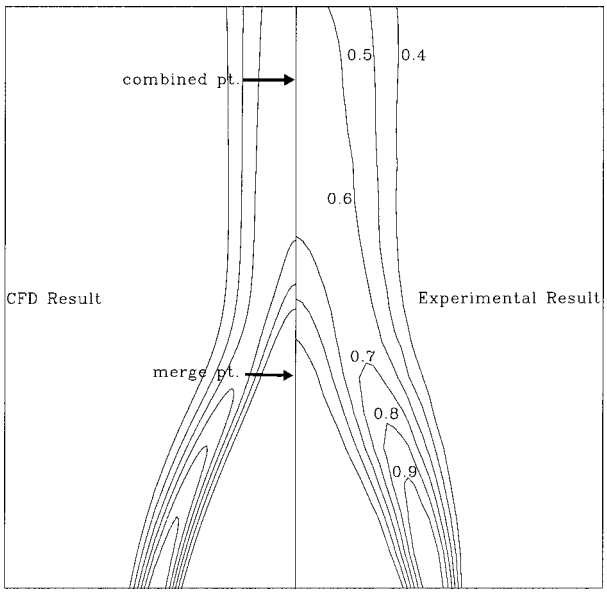

Fig. 9 Comparison of experimental and RSM numerical mean velocity (U/U_o) flowfield contours at $S/d=9$. Experimental contours are presented on the right hand side. Transverse and streamwise scales are $y/d=0$ to 8.2 and $x/d=5$ to 21.5, respectively.

Experimental and RSM computational Reynolds normal stress profiles are shown in Figs. 8(*a*,*b*) for the three jet spacings and the single jet. In these results the streamwise and transverse normal stress is non-dimensionalized by the local mean velocity along the symmetry plane, $u'u'/U_m^2$. As stated previously, the streamwise location of rapid increase in normal stress toward an asymptote is used to define the location of the merge point. The location of the asymptote and the relative changes in normal stress profile due to changes in S/d compare very well. Far downstream both experimental and numerical results reveal that the streamwise normal stress approaches a constant value of approximately 0.25. This matches the value measured by Gutmark and Wygnanski [3] for a single turbulent jet. The transverse normal stress profiles from the experiment progressively increase with S/d, and were found to be greater than the levels predicted by CFD. The experiment and CFD results for the single jet both approach Gutmark and Wygnanski's single jet value of 0.20 for transverse fluctuations at large x/d.

The overall structure of the flow field can be examined in Fig. 9 where the experimental and numerical results using the RSM are compared for the $S/d=9$ configuration. The experimental results are based on traverse increments of $0.2y/d$ and $1.0x/d$ in the transverse and streamwise directions respectively. The contours show good correlation between the experimental and numerical results with respect to the overall topology of the flow. However, the CFD results show a narrower jet width than is revealed by experiment. This result may be caused by differences between the experimental and numerical inlet boundary conditions that may effect the jet entrainment rates in the near field consistent with observations made by Thomas [1] regarding the sensitivity of the virtual origin to plenum conditions.

Conclusions

Comparison between experimental measurements and numerical predictions of the parallel jet flowfield reveal excellent agreement in the location of the merge and combined points. In addition, the CFD methods incorporated are capable of predicting the mean symmetry plane velocity profiles to good accuracy. The measured lateral flow topology shows a slightly wider combined jet envelope than is predicted numerically. The differences may be attributed to the sensitivity of the jet's initial widening rate to exit boundary conditions. The magnitude and decay of the predicted normal stress profiles along the symmetry plane of the flowfield are in close agreement with the experimental results. Future work will consider the fully three-dimensional interaction between round jets and investigate an unsteady phenomena observed in the region between the jets at large *d*.

References

[1] Thomas, F. O., 1991, ''Structure of mixing layers and jets,'' Appl. Mech. Rev., **44**, No. 3, pp. 119–153.
[2] Everitt, K. W., and Robins, A. G., 1978, ''The development and structure of turbulent plane jets,'' J. Fluid Mech., **88**, pp. 563–568.
[3] Gutmark, E., and Wygnanski, I., 1976, ''The planar turbulent jet,'' J. Fluid Mech., **73**, pp. 465–495.
[4] Tanaka, E., 1970, ''The interference of two-dimensional parallel jets (1st report, experiments on dual jet),'' Bull. JSME, **13**, No. 56, pp. 272–280.
[5] Tanaka, E., 1974, ''The interference of two-dimensional parallel jets (2nd report, experiments on the combined flow of dual jet),'' Bull. JSME, **17**, No. 109, July, pp. 920–927.
[6] Elbanna, H., Gahin, S., and Rashed, M. I. I., 1983, ''Investigation of two plane parallel jets,'' AIAA J., **21**, No. 7, pp. 986–990.
[7] Lin, Y. F., and Sheu, M. J., 1990, ''Investigation of two plane parallel unventilated jets,'' Exp. Fluids, **10**, pp. 17–22.
[8] Lin, Y. F., and Sheu, M. J., 1991, ''Interaction of Parallel Turbulent Plane Jets,'' AIAA J., **29**, pp. 1372–1373.
[9] Nasr, A., and Lai, J. C. S., 1997, ''Comparison of flow characteristics in the near field of two parallel plane jets and an offset plane jet,'' Phys. Fluids, **9**, No. 10, Oct, pp. 2919–2931.
[10] Nasr, A., and Lai, J. C. S., 1998, ''A turbulent plane offset jet with small offset ratio,'' Exp. Fluids, **24**, pp. 47–57.
[11] Miller, D. R., and Comings, E. W., 1960, ''Force momentum fields in a dual-jet flow,'' J. Fluid Mech., **7**, p. 237.
[12] Murai, K., Taga, M., and Akagawa, K., 1976, Bull. JSME, **19**, p. 956.
[13] Leonard, B. P., 1979, ''A stable and accurate convective modeling procedure based on quadratic upstream interpolation,'' Comput. Methods Appl. Mech. Eng., **19**, pp. 59–98.
[14] Patankar, S. V., 1980, *Numerical Heat Transfer and Fluid Flow*, Washington D.C., Hemisphere Publishing Corp.
[15] Launder, B. E., Reece, G. J., and Rodi, W., 1975, ''Progress in the development of a Reynolds-stress turbulence closure,'' J. Fluid Mech., **68**, pp. 537–566.
[16] Gibson, M. M., and Launder, B. E., 1978, ''Ground effects on pressure fluctuations in the atmospheric boundary layer,'' J. Fluid Mech., **86**, pp. 491–511.
[17] Lien, F. S., and Leschziner, M. A., 1994, ''Assessment of turbulence transport models including non-linear RNG eddy-viscosity formulation and second moment closure for flow over a backward-facing step,'' Comput. Fluids, **23**, pp. 983–1004.

Junye Wang
Research Associate

Geoffrey H. Priestman
Senior Lecturer

Department of Chemical
and Process Engineering,
The University of Sheffield,
Sheffield, S1 3JD, UK

Dongdi Wu
Professor,
School of Mechanical Engineering,
East China University of
Science and Technology,
Shanghai 200237, P.R. China

An Analytical Solution for Incompressible Flow Through Parallel Multiple Jets

A theoretical model of multiple jet flow is introduced based on the thin shear layer theory. The analytical solution has been obtained by using Prandtl's mixing length hypothesis. The results show that along the streamline direction, the axial velocity decreases gradually like a single jet and in the transverse direction, the velocity distribution changes as a cosinoidal function, in which the velocity amplitude decreases with increasing x, gradually approaching a flat profile. It is also shown that the distance at which the individual jets begin to merge increases with increasing pitch, s. For the special cases when the pitch, s is zero, the row of multiple jets becomes equivalent to a single jet. Finally, the predictive results are found to agree well with experimental data in the fully developed turbulent flow region. [DOI: 10.1115/1.1363612]

Keywords: Multiple jets, Turbulent jet, Jet mixing, Process intensification

1 Introduction

Multiple jets in a row are extensively used for various industrial applications. In chemical engineering the processes of mixing, separation, and transport among species can be intensified by using a series of jets instead of a single jet. In power boilers the mixing between fuel and air is improved with a row of combustor jets. In aerospace engineering for vertical or short distance take off and landing planes, multiple jets are used to give improved propulsion and noise level. Furthermore, multiple jet flow is also a fundamental issue in fluid mechanics.

The early studies of multiple jets were mainly experimental. A seven hole jet series was studied by Corrsin et al. [1] Krothapalli et al. [2,3] studied the development and structure of a rectangular jet in a multiple jet configuration, followed by mixing intensification and jet noise with edge tones [3]. The effect of the geometry of nozzles on jet interaction was studied by Wlezien [4]. Other researchers studied twin jets [5,6] and multiple jets [7–10].

It is mathematically difficult to set up a theoretical model because of interference and interaction between the jets. The first model was developed by Knystautas et al. [7], using Reichardt's inductive hypothesis for the turbulent shear stress in a free jet. The equation of motion for the downstream mean square velocity was linearized. Invoking the superposition principle, the momentum flux at any individual jet was considered as the net summation of the momentum flux contributions from individual axisymmetric jets spaced at a distance. Finally, the square of the mean velocity in the central jet was expressed mathematically as an infinitesimal series, with the other jets extending symmetrically in both transverse directions.

Because Knystautas' solution is based on superposition of a series of individual jets it loses some information of cosinoidal vibration in the transverse direction. Also, it needs another equation in integral form to express an infinitesimal hypothetical slot. Furthermore, there is no explicit relation for the start distance of the fully merged two-dimensional flow. In addition, an infinitesimal series, implicit solution is inconvenient for industrial application.

More recently, a more direct theoretical model of multiple-interfering jet groups was produced by Wang [11], using a different approach. This theoretical model was based not on the superposition principle of individual jets but directly on the Navier-Stokes equations and Prandtl's mixing length hypothesis. The analytical solution was obtained by employing a Taylor's series. Although the approach gave us a possibility of directly solving a multiple-interfering jet system, the approach was rather approximate, the accuracy depending on how many series terms were used. The model was therefore limited for industrial application. In this paper the theoretical model is further developed to overcome this difficulty.

2 Theoretical Model and Analysis

The jet or multiple jet represents free turbulent flows in which there are three related analytical problems to be determined: the growth parameter; the decay of the characteristic velocity, u_c; and the velocity profile, u. It is well known that at some distance downstream of the start of the jet, boundary-layer approximations apply and the velocity profiles become nearly similar in shape when normalized by the local velocity. Turbulent multiple jets from a row of rectangular nozzles are considered as shown in Fig. 1. The analysis assumes two-dimensional incompressible flow, corresponding to nozzles of infinite width. The complete equations of motion consist of continuity and the x-and y-momentum relations [12]:

$$\frac{\partial u}{\partial x}+\frac{\partial \nu}{\partial y}=0 \tag{1}$$

$$\rho\left(u\frac{\partial u}{\partial x}+\nu\frac{\partial u}{\partial y}\right)=-\frac{\partial P}{\partial x}+\mu\left(\frac{\partial^2 u}{\partial x^2}+\frac{\partial^2 u}{\partial y^2}\right) \tag{1a}$$

$$\rho\left(u\frac{\partial \nu}{\partial x}+\nu\frac{\partial \nu}{\partial y}\right)=-\frac{\partial P}{\partial y}+\mu\left(\frac{\partial^2 \nu}{\partial x^2}+\frac{\partial^2 \nu}{\partial y^2}\right) \tag{1b}$$

Except for specific applications, such as the fluidic amplifier, where the jet is confined in a region of varying pressure, the jet flow has little or no pressure gradient associated with it. Such problems in free turbulent flow are of a boundary-layer nature, meaning that the region of space in which a solution is being sought does not extend far in a transverse direction, as compared with the main direction of flow, and that the transverse gradients are large. Thus the following approximations can be justified:

Contributed by the Fluids Engineering Division for publication in the JOURNAL OF FLUIDS ENGINEERING. Manuscript received by the Fluids Engineering Division November 19, 1999; revised manuscript received October 11, 2000. Associate Editors: S. Banerjee and J. Katz.

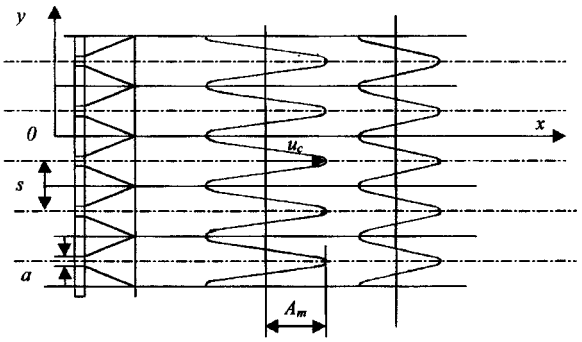

Fig. 1 Flow pattern and coordinates of the row of multiple rectangular jets

$$\nu \ll u$$

$$\frac{\partial}{\partial x} \ll \frac{\partial}{\partial y}$$

$$\frac{\partial P}{\partial x} \approx 0$$

$$\frac{\partial^2 u}{\partial x^2} \ll \frac{\partial^2 u}{\partial y^2}$$

Applying these approximations the *y*-momentum equation can be neglected entirely. The boundary-layer equations for the jet in two-dimensional incompressible flow can then be simplified to:

$$\frac{\partial u}{\partial x} + \frac{\partial \nu}{\partial y} = 0 \tag{2}$$

$$\rho\left(u\frac{\partial u}{\partial x} + \nu\frac{\partial u}{\partial y}\right) = \mu\left(\frac{\partial^2 u}{\partial y^2}\right) \tag{2a}$$

Substituting the turbulent shear stress, $\tau = \mu \partial u/\partial y$, into Eq. (2*a*), gives:

$$u\frac{\partial u}{\partial x} + \nu\frac{\partial u}{\partial y} = \frac{1}{\rho}\frac{\partial \tau}{\partial y} \tag{3}$$

Defining

$$u_1 = u_d - u$$

and

$$u_d = u_c - A_m \tag{4}$$

where u_c is the axial velocity of a single jet and A_m is an amplitude of velocity, *u*. The relationship between *u*, u_d, u_c, u_1, and A_m is shown in Fig. 2.

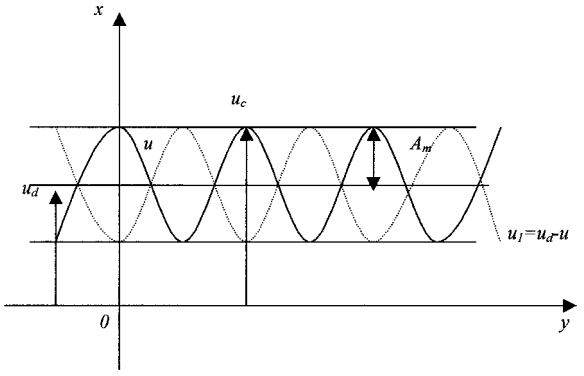

Fig. 2 The relationship among u, u_d, u_c, u_1, and A_m

At a certain distance downstream of the nozzles, x_i, the width of a single jet is equal to the pitch, *s*. u_l is the velocity difference between the *x*-direction mean velocity u_d and local jet velocity, *u*, and is known to be small compared with u_d. Moreover, $\nu\partial u/\partial y$ is less than $u\partial u/\partial x$. Thus, Eq. (3) can be simplified by neglecting higher order terms to

$$-u_d\frac{\partial u_1}{\partial x} = \frac{1}{\rho}\frac{\partial \tau}{\partial y} \tag{5}$$

The momentum equation is greatly simplified by the assumption made above, but the solution cannot be found without an eddy viscosity or some other expression the shear stress in terms of the parameters of the main flow. For this an extension of Prandtl's mixing length hypothesis [13] can be used:

$$\tau = \rho l^2 \frac{\partial u}{\partial y}\sqrt{\left(\frac{\partial u}{\partial y}\right)^2 + l_1^2\left(\frac{\partial^2 u}{\partial y^2}\right)^2} \tag{6}$$

The mixing lengths l and l_1 can be regarded as purely local functions because the turbulence properties develop in proportion to a mean flow length scale and they must be considered appropriately in each particular case.

On the other hand, since the idea of similarity holds well for jets and wakes, or the velocity profiles become nearly similar in shape when normalized by the local velocity and width, velocity difference u_1, decreases in the power function with increasing *x*, i.e.,

$$u_1 \sim x^p f(y)$$

3 Solution of Equations

On putting $u_1 \sim x^p f(y)$, we have:

$$\frac{\partial u_1}{\partial x} \sim x^{p-1} \tag{7}$$

For turbulent jets, the Prandtl's mixing length is constant, being proportional to the jet width. Thus, differentiating Eq. (6), we obtain:

$$\frac{\partial \tau}{\partial y} = \rho l^2 x^{2p} f\sqrt{\left(\frac{\partial f}{\partial y}\right)^2 + l_1^2\left(\frac{\partial^2 f}{\partial y^2}\right)^2}$$

$$\frac{\partial \tau}{\partial y} \sim \left(\frac{\partial u}{\partial y}\right)\left(\frac{\partial^2 u}{\partial y^2}\right) \sim x^{2p} \tag{8}$$

For a two-dimensional rectangular jet, we have:

$$u_d \sim u_c \sim x^{-1/2} \tag{9}$$

Inserting (7), (8), (9) into Eq. (5), and rearranging gives

$$p = -3/2$$

For fully developed flow, the velocity distribution must be expected to be a periodic function in *y*, whose period is equal to the pitch *s*. Thus, we can assume

$$u_1 = u_d A\left(\frac{x}{s}\right)^{-3/2}\cos\left(2\pi\frac{y}{s}\right) \tag{10}$$

where $y = 0$ is located at a concave minimum in the velocity distribution and *A* is an undetermined constant.

Comparing Eqs. (10) and (4) gives A_m as:

$$A_m = u_d A\left(\frac{x}{s}\right)^{-3/2} \tag{11}$$

Inserting Eq. (11) into Eq. (4), gives:

$$u_d = \frac{u_c}{1 + A\left(\frac{x}{s}\right)^{-3/2}} \tag{12}$$

Inserting Eq. (12) into Eq. (10) gives:

$$u_1 = \frac{u_c}{1 + A\left(\frac{x}{s}\right)^{-3/2}} A\left(\frac{x}{s}\right)^{-3/2} \cos\left(2\pi\frac{y}{s}\right) \tag{13}$$

Inserting Eq. (13) into Eq. (4) gives:

$$u = \frac{u_c}{1 + A\left(\frac{x}{s}\right)^{-3/2}} \left[1 - A\left(\frac{x}{s}\right)^{-3/2} \cos\left(2\pi\frac{y}{s}\right)\right] \tag{14}$$

Assuming:

$$A \sim x^n \tag{15}$$

And considering $u_d \sim x^{-1/2}$, Eq. (10) can be differentiated with respect to x to give:

$$\frac{\partial u_1}{\partial x} = -(2-n) u_d A s^{3/2} x^{-5/2} \cos\left(2\pi\frac{y}{s}\right) \tag{16}$$

Because l = constant and assuming that $l_1 = s/2\pi$, which should be permissible, shear stress τ can be expressed by Eq. (6) as follows:

$$\tau = \rho l^2 u_d^2 A^2 \left(\frac{x}{s}\right)^{-3} \left(\frac{2\pi}{s}\right)^2 \sin\left(2\pi\frac{y}{s}\right)$$

The above equation is differentiated with respect to y to give:

$$\frac{1}{\rho}\frac{\partial \tau}{\partial y} = l^2 u_d^2 A^2 \left(\frac{x}{s}\right)^{-3} \left(\frac{2\pi}{s}\right)^3 \cos\left(2\pi\frac{y}{s}\right) \tag{17}$$

Inserting Eq. (16) and Eq. (17) into both sides of Eq. (5), gives:

$$A = \frac{(2-n) s\sqrt{s}}{8\pi^3 l^2} \sqrt{x} \tag{18}$$

Comparison of Eq. (15) and Eq. (18), gives $n = 1/2$. Inserting into Eq. (18) gives:

$$A = \frac{3}{16} \frac{s\sqrt{s}}{l^2\pi^3} \sqrt{x} \tag{19}$$

Substituting Eq. (18) into Eq. (13) and Eq. (14), gives the final solution:

$$u_1 = \frac{3}{16} \frac{u_c}{1 + \frac{3}{16}\frac{s^3 x^{-1}}{l^2\pi^3}} \frac{s^3 x^{-1}}{l^2\pi^3} \cos\left(2\pi\frac{y}{s}\right) \tag{20}$$

$$u = \frac{u_c}{1 + \frac{3}{16}\frac{s^3 x^{-1}}{l^2\pi^3}} \left[1 - \frac{3}{16}\frac{s^3 x^{-1}}{l^2\pi^3} \cos\left(2\pi\frac{y}{s}\right)\right] \tag{21}$$

where ε is defined as:

$$\varepsilon = \left(\frac{u_{\max} - u_{\min}}{u_{\max}}\right)$$

The start of fully merged two-dimensional flow, x_{2D}, can easily be derived from Eq. (21) as:

$$x_{2D} = \frac{3}{16} \frac{s^3}{l^2\pi^3} \frac{1}{\varepsilon} \tag{22}$$

4 Computational Results and Discussion

It is interesting to note how the model behaves at various limiting conditions. First, in the extreme case, when $s = 0$, according to Eq. (20) and Eq. (21), $u_1 = 0$ and $u = u_c$, respectively. This is consistent with the physical situation when $s = 0$, and the row of multiple jets becomes a single jet with centerline x velocity of u_c, nozzle length as per the (individual) jet, and nozzle width equal to that the number of nozzles times the single nozzle width, a. For the other extreme case, when $x = \infty$, then $u_1 = 0$ and $u = u_c$, respectively. That is, at infinite axial distance from the nozzle the amplitude of velocity is zero, and the row of multiple jets can be regarded as a single jet. Equation (20) also shows that when $y = s$, the velocity is equal to the peak velocity, $u = u_c$.

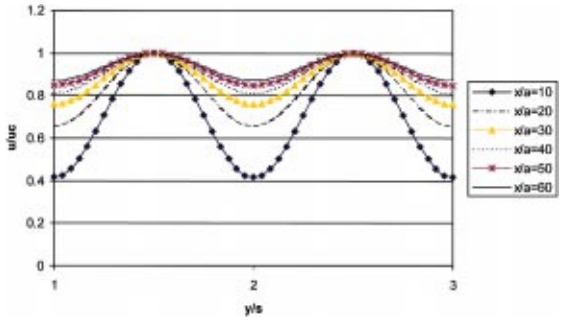

Fig. 3 The velocity profile with various x/a

Figure 3 shows the predicted downstream mean velocity profiles along the center plane $z = 0$ of a two-dimensional jet for $s = 24$ and $l = 4.5$. The velocity amplitude is seen to decrease with increasing x, gradually approaching a flat profile.

Figure 4, Fig. 5, and Fig. 6 plot predicted velocity profiles as a function of nozzle pitch. Obviously, the distance at which the individual jets begin to merge, x_{2D}, decreases with decreasing s. Eq. (22) provides a means of determining the start of fully merged two-dimensional flow for the interfering jets. x_{2D} is seen to be proportional to s^3. Equation (22) is an explicit and simple expression. Beyond x_{2D}, the effectively multiple-interfering jets can be thought of as having originated from a single slot.

Available experimental data on flow fields of multiple jets is very limited. Figure 4 shows data obtained by Krothapalli et al. [2], which corresponds to $s = 24$, $a = 3$, $b = 50$ mm *and* $u_0 = 50$ m/s. The experimental data are shown as points, and the

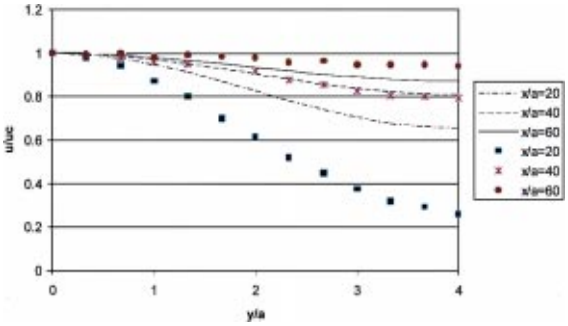

Fig. 4 Shown a comparison between the profile of nondimensional theoretical results from Eq. (21) and measured velocity distribution points

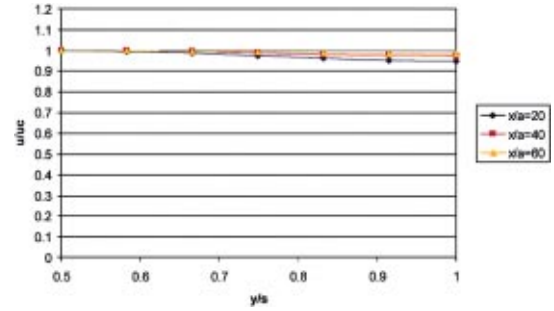

Fig. 5 The velocity profiles at $s = 6$

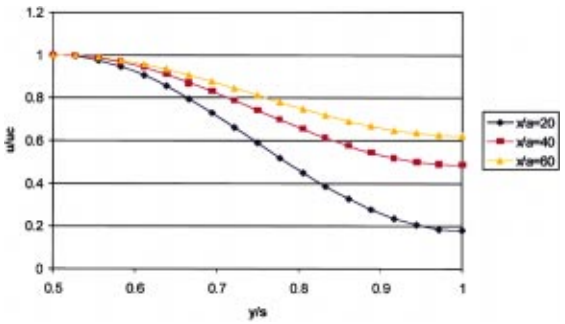

Fig. 6 The velocity profile at $s=36$

lines are theoretical predictions from Eq. (21). It can be seen that for $x/a<40$ the predicted velocities deviate significantly from the experimental data, but for $x/a>40$ the predictions agree well.

The larger deviation between experiment and theory for $x/a<40$ is probably because the model is based on the thin shear theory. For $x/a<40$ multiple jet flow is in the non self-similar region, neglecting higher order terms in the model can result in significant errors. When $x/a>40$, the jets enter a fully developed turbulent flow region, or the self-similar region where the thin shear theory is more appropriate. When $x/a=60$ the experimental results are a little higher than the predicted values. This may be because the theoretical model is based on a row of jets of infinite width, but the experiments used a slot width of 50 mm. The finite slot is affected easily by surrounding fluid, and entrapment mixing makes the velocity profile approach uniformity more rapidly.

For the configuration studied, Krothapalli et al. indicated that a significant region exists where the mean velocity profiles of the individual jets behave quite independently of each other. It was observed that the individual jets do not interact with each other, and in Fig. 6 of Reference [2] the deviation between a single and multiple jet occurred at about $x/a=40$. Thus, it is reasonable that up to $x/a=40$, the theoretical model of a single jet can be employed, and after $x/a=40$, the present model of multiple jets can be used.

Fortunately, when $x/a\geqslant 40$, the present theoretical model agrees well with experimental data. For most engineering cases, the accuracy of the present theory should be sufficient.

5 Conclusion

Groups of multiple-interfering jet have a range of useful industrial applications. The present theoretical model is based on the Navier-Stokes equation and Prandtl's mixing length, and provides some fundamental theory on groups of the multiple-interfering jets. The solution is different from the previous superposition method and is relatively simple and explicit.

The results show that in the streamline direction, the axial velocity decreases gradually as a single jet whilst in the transverse direction, the velocity distribution changes as a cosinoidal function, in which the velocity amplitude decreases with increasing x, gradually approaching a flat profile. Thus at sufficient distance downstream the flowfield appears as if it is emerging from a single two-dimensional slot or nozzle. It is also shown for the special case when the hole pitch, s becomes zero, the model treats a row of multiple jets as equivalent to a single jet, and at infinite axial distance, x, the row of multiple jets also become equivalent to a single jet. Furthermore, the distance at which the individual jets are predicted to merge decreases with decreasing s, the fully merged distance, X_{2D}, being an explicit and simple expression given by Eq. (22).

For the case of an array of rectangular jets having a spacing $8a$, the theoretical predictions agree with available experimental data when $x/a\geqslant 40$. Because the individual jets act quite independently of each other near the nozzle exit when $x/a<40$, the jet velocity profiles can be estimated from data on the growth rate of a single jet. For $x/a\geqslant 40$, in the self-similar flow region, the predictive results are found to agree well with experimental data.

Nomenclature

a = rectangular nozzle width
A = free constant
A_m = amplitude of velocity difference (u_1)
l, l_1 = Prandtl's mixing length
p = power
P = pressure
s = spacing between jets
t = time
u = x axial velocity
u_c = x central axial velocity
u_d = x axial mean velocity ($=u_c-A_m$)
$u_{\min}$ = the valley mean velocity
u_1 = vibration velocity ($=u_d-u$)
$v_{\max}$ = the peak mean velocity
x = x coordinate axes
x_{2D} = the start of the merged two-dim flow
y = y coordinate axes
ε = amplitude undulating mean velocity profile
ρ = density
τ = shear stress
ν = y axial velocity

References

[1] Corrsin, S., 1944, ''Investigation of the Behavior of Parallel Two-Dimensional Air Jets,'' NACA W-90.
[2] Krothapalli, A., Baganoff, D., and Karamcheti, K., 1980, ''Development and Structure of a Rectangular Jet in a Multiple Jet Configuration,'' AIAA J., **18**, No. 8, Aug., pp. 945–950.
[3] Krothapalli, A., Karamcheti, K., Hsia, Y., and Baganoff, D., 1983, ''Edge Tones in High-Speed Flows and Their Application to Multiple-Jet Mixing,'' AIAA J., **21**, No. 7, July, pp. 937–938.
[4] Wlezien, R. W., 1989, ''Nozzle Geometry Effects on Supersonic Jet Interaction,'' AIAA J., **27**, pp. 1361–1367.
[5] Moustafa, G. H., 1994, ''Experimental Investigation of High-Speed Twin Jets,'' AIAA J., **32**, No. 11, Nov pp. 2310–2322.
[6] Okamoto, T., Yagita, M., Watanabe, A., and Kawamura, K., 1985, ''Interaction of Twin Turbulent Circular Jet,'' Bull. JSME, **28**, No. 238, Apr., pp. 617–622.
[7] Knystautas, R., 1964, ''The Turbulent Jet from a Series of Holes in line,'' Aeronaut. Q., **XV**, pp. 1–28.
[8] Raghunarhan, S., and Reid, I. M., 1981, ''A Study of Multiple Jets,'' AIAA J., **19**, No. 1, Jan., pp. 124–127.
[9] Villermaux, E., and Hopfinger, E. J., 1994, ''Periodically Arranged Co-Flowing Jets,'' J. Fluid Mech., **263**, pp. 63–92.
[10] Villermaux, E., Sommeria, J., Gogne, Y., and Hopfinger, E. J., 1991, ''Oscillatory Instability and Genesis of Turbulence Behind a High Solidity Grid,'' Eur. J. Mech. B/Fluids, **10**, pp. 427–439.
[11] Wang, J. Y., Wu, D. D., and Ruan, X. N., 1996, ''An analytical model of multiple jets,'' the 2nd International Symposium on Aeronautical Science & Technology in Indonesia, Jakarta, June 24–27.
[12] White, F. M., 1994, ''Fluid Mechanics,'' 3rd Edition, McGraw-Hill, New York.
[13] Schlichting, H., 1979, ''Boundary-layer theory,'' 7th edition, McGraw-Hill, New York.

Nonlinear Stability Analysis of the Thin Micropolar Liquid Film Flowing Down on a Vertical Cylinder

Po-Jen Cheng
Lecturer,
Department of Mechanical Engineering,
Far-East College, Tainan,
Taiwan, R.O.C.

Cha'o-Kuang Chen
Professor

Hsin-Yi Lai
Professor

Department of Mechanical Engineering,
National Cheng-Kung University, Tainan,
Taiwan, R.O.C.

This paper investigates the weakly nonlinear stability theory of a thin micropolar liquid film flowing down along the outside surface of a vertical cylinder. The long-wave perturbation method is employed to solve for generalized nonlinear kinematic equations with free film interface. The normal mode approach is first used to compute the linear stability solution for the film flow. The method of multiple scales is then used to obtain the weak nonlinear dynamics of the film flow for stability analysis. The modeling results indicate that both subcritical instability and supercritical stability conditions are possible to occur in a micropolar film flow system. The degree of instability in the film flow is further intensified by the lateral curvature of cylinder. This is somewhat different from that of the planar flow. The modeling results also indicate that by increasing the micropolar parameter $K(=\kappa/\mu)$ and increasing the radius of the cylinder the film flow can become relatively more stable traveling down along the vertical cylinder. [DOI: 10.1115/1.1359524]

1 Introduction

The stability of a film flow is a research subject of great importance commonly needed in mechanical, chemical, and nuclear engineering industries for various applications including the process of paint finishing, the process of laser cutting, and heavy casting production processes. It is known that macroscopic instabilities can cause disastrous conditions to fluid flow. It is thus highly desirable to understand the underlying flow characteristics and associated time-dependent properties so that suitable conditions for homogeneous film growth can be developed for various industrial applications.

The problem of the stability of the laminar flow of an ordinary viscous liquid film flowing down an inclined plane under gravity was first formulated and solved numerically by Yih [1]. The transition mechanism from laminar flow to turbulent flow was elegantly explained by the Landau equation (Landau [2]). That shed light for later development on nonlinear film stability. The Landau equation was later rederived by Stuart [3] using the disturbed energy balance equation along with Reynolds stresses. Benjamin [4] and Yih [5] formulated the disturbed wave equation of free flow surface. The flow stability of long disturbed wave was carefully studied and some characteristics of the flow stability on an inclined plane are observed. Benney [6] investigated the nonlinear evolution equation of free surface by using the method of small parameters. The solutions thus obtained can be used to predict nonlinear instability. However, the solutions cannot be used to predict supercritical stability since the influence of surface tension is not considered in the analysis of the small-parameter method. The effect of surface tension was realized by many researchers as one of the necessary conditions that will lead to the solution of supercritical stability. Lin [7], Nakaya [8], and Krishna and Lin [9] considered the significance of surface tension and treated it in terms of zeroth order terms in later studies. Pumir et al. [10] further included the effect of surface tension into the film flow model and solved for the solitary wave solutions. Hwang and Weng [11] showed that the conditions of both supercritical stability and subcritical instability possibly occur for a liquid film flow system. In order to fully understand and characterize the stability conditions for various film flows, detailed flow analysis is of great importance.

Several researchers have already studied the hydrodynamic stability problems regarding the fluid films flowing down a vertical cylinder surface. Lin and Liu [12] compared their analytical solutions with the existing experimental results of falling flow film on a cylinder and creeping annular flow threads in viscous liquid. Krantz and Zollars [13] presented an asymptotic solution and pointed out that the effect of curvature on the stability of the film flow is indeed significant. They also showed that the curvature of the cylinder is indeed one of the important factors that intensify the instability of the film flow. This phenomenon is not found in the planar flow. Rosenau and Oron [14] derived an amplitude equation which describes the evolution of a disturbed free film surface traveling down an infinite vertical cylindrical column. The numerical modeling results indicated that both conditions of supercritical stability and subcritical instability are possible to occur for the film flow. The results also showed that the evolving waves may break at the instant that linearly unstable conditions are satisfied. Davalos-Orozco and Ruiz-Chavarria [15] investigated the linear stability of a fluid layer flowing down inside and outside of a rotating vertical cylinder. They pointed out that the centrifugal force could stabilize the film flow so as to counteract the destabilizing effect of surface tension. In the absence of rotation, the stability can still be found for some critical wave numbers. Hung et al. [16] investigated the weakly nonlinear stability analysis of a condensation film flowing down a vertical cylinder. They also showed that supercritical stability in the linearly unstable region and subcritical instability in the linearly stable region can co-exist. They also indicated that the lateral curvature of the cylinder has the destabilizing effect on the film flow stability.

A vast majority of studies on thin-film flow problems were devoted to the stability analysis of Newtonian fluids. The film flow of non-Newtonian fluids attracted less attention in the past. In recent years, the microstructure of fluid flows has emerged as a research subject of great interest to many researchers. A subclass of these fluids was named micropolar fluids by Eringen [17] who first proposed the theory of micropolar fluids. Micropolar fluids exhibit certain microscopic effects arising from the local structure

Contributed by the Fluids Engineering Division for publication in the JOURNAL OF FLUIDS ENGINEERING. Manuscript received by the Fluids Engineering Division April 24, 2000; revised manuscript received December 27, 2000. Associate Editor: D. R. Williams.

and microrotations of the fluid elements. In application, the micropolar fluids may be used to model some manmade fluids, such as the polymeric fluids, animal blood, fluids with additives, and liquid crystals, etc. The extension of the theory of micropolar fluids to cover the thermal effect was developed by Eringen [18]. Liu [19,20] studied the flow stability of micropolar fluids and found that the initiation of instability was delayed due to the presence of microstructures in the fluid. Datta and Sastry [21] studied the instability of a horizontal micropolar fluid layer which was heated from below. They found that the plot of Rayleigh number versus wave number has two branches separating the zones of stability. Ahmadi [22] studied the same problem by employing a linear theory as well as an energy method. It was observed that the micropolar fluid layer heated from below is more stable as compared with the classical Newtonian fluid, and also found that no subcritical instability region exists. Payne and Straughan [23] investigated the Benard problem for a thermomicropolar fluid by the nonlinear energy stability method. They predicted that subcritical instability may possibly occur, but did not infer the existence of subcritical instabilities from their work. Later, Franchi and Straughan [24] established a nonlinear energy stability analysis for the convection of the thermo-micropolar fluid with temperature dependent viscosity. They showed that the critical Rayleigh number depends strongly on the changes of the interaction coefficient κ, and indicated that the micropolar coefficient γ has very little influence on the convection threshold. Hung et al. [25] employed the method of nonlinear analysis to study the stability of thin micro-polar liquid films flowing down along a vertical plate. The results of their study indicated that the micropolar coefficients, $\Delta(=h_0^{*2}/j)$ and $\Lambda(=\gamma/\mu j)$ have very little effect on the stability of the micropolar film. They also showed that the micropolar parameter $K(=\kappa/\mu)$ plays an important role in stabilizing the film flow. It would be useful for the reader to have the various fluid parameters that are introduced defined, and given an indication of what physical properties they measure.

The stability analysis of the micropolar liquid film flow is indeed an interesting research area in both theoretical development and practical applications. To the best of our knowledge, the weakly nonlinear stability analysis of a thin micropolar liquid film flowing down a vertical cylinder has so far not been seriously investigated. However, since the types of stability problems are of great importance in many practical applications, the behavior of a micropolar liquid film traveling down along a vertical cylinder is carefully studied in this paper by employing both linear and nonlinear stability analysis theories. The influence of both the micropolar property and the cylinder size on finite-amplitude equilibrium is studied and characterized mathematically. The sensitivity analysis of both the micropolar property and cylinder size is also carefully conducted. Several numerical examples are presented to verify the solutions and to demonstrate the effectiveness of the proposed modeling procedure.

2 Generalized Kinematic Equations

Figure 1 shows the configuration of a thin micropolar liquid film flowing down along the outer surface of an infinite vertical cylinder. All physical properties are assumed to be constant. The principles of mass, momentum, and angular momentum conservation for an axisymmetric isothermal incompressible micropolar flow configuration leads one to a set of system governing equations. Let u^* and w^* be the velocity components in r^* and z^* directions, respectively, and N^* is the angular microrotation momentum. The governing equations can be expressed in terms of cylindrical coordinates (r^*,z^*) as (Eringen [18])

$$\frac{1}{r^*}\frac{\partial(r^*u^*)}{\partial r^*}+\frac{\partial w^*}{\partial z^*}=0 \tag{1}$$

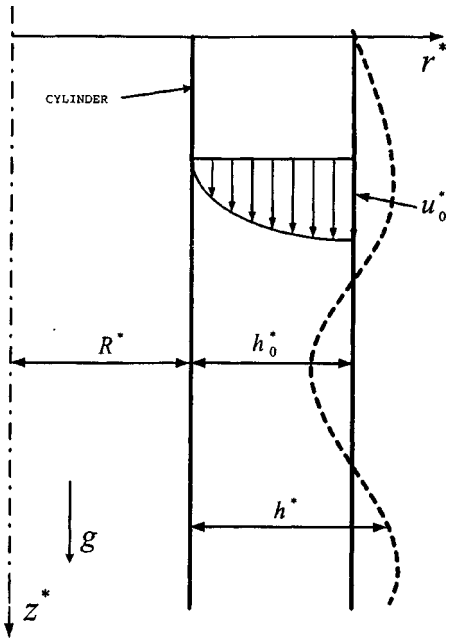

Fig. 1 Schematic diagram of a micropolar thin film flow traveling down along a vertical cylinder

$$\rho\left(\frac{\partial u^*}{\partial t^*}+u^*\frac{\partial u^*}{\partial r^*}+w^*\frac{\partial u^*}{\partial z^*}\right)=-\frac{\partial p^*}{\partial r^*}+(\mu+\kappa)\left(\frac{\partial^2 u^*}{\partial r^{*2}}+\frac{1}{r^*}\frac{\partial u^*}{\partial r^*}+\frac{\partial^2 u^*}{\partial z^{*2}}-\frac{u^*}{r^{*2}}\right)-\kappa\frac{\partial N^*}{\partial z^*} \tag{2}$$

$$\rho\left(\frac{\partial w^*}{\partial t^*}+u^*\frac{\partial w^*}{\partial r^*}+w^*\frac{\partial w^*}{\partial z^*}\right)=-\frac{\partial p^*}{\partial z^*}+(\mu+\kappa)\left(\frac{\partial^2 w^*}{\partial r^{*2}}+\frac{1}{r^*}\frac{\partial w^*}{\partial r^*}+\frac{\partial^2 w^*}{\partial z^{*2}}\right)+\kappa\left(\frac{\partial N^*}{\partial r^*}+\frac{N^*}{r^*}\right)+\rho g \tag{3}$$

$$\rho J\left(\frac{\partial N^*}{\partial t^*}+u^*\frac{\partial N^*}{\partial r^*}+w^*\frac{\partial N^*}{\partial z^*}\right)=\gamma\left(\frac{\partial^2 N^*}{\partial r^{*2}}+\frac{1}{r^*}\frac{\partial N^*}{\partial r^*}+\frac{\partial^2 N^*}{\partial z^{*2}}-\frac{N^*}{r^{*2}}\right)+\kappa\left(\frac{\partial u^*}{\partial z^*}-\frac{\partial w^*}{\partial r^*}-2N^*\right) \tag{4}$$

where ρ is a constant density of the flow, p^* is the flow pressure, μ is the molecule fluid viscosity, J is the micro-inertial density, κ is the vortex viscosity, and γ is the spin-gradient viscosity. The last term on the right-hand side of Eq. (3) is the body force due to gravity.

The fluid motion may assumed to be affected by (1) viscous action, which is measured by μ, (2) the effect of couple stresses, measured by γ, and (3) the direct coupling of the microstructure to the velocity, measured by κ. Stokes [26] showed that each of the constants μ, γ, and κ can have value greater than, or equal to, zero, so that the ratios γ/μ and κ/μ, which are measured, respectively, by the relative strengths of the couple stress to the viscous effect and the microstructure coupling to the viscous effect, can have any value greater than, or equal to, zero. Kolpashchikov

et al. [27] determined the viscosity coefficients of micropolar fluid on the basic of viscometric and thermal measurements. The order of magnitude of the micro-inertial density, J, is comparable to l^2, where l is a material length depending on the size of microstructure. For most suspensions, the order of magnitude of l is about 10^{-3} to 10^{-5} cm (Eringen [28]). The appropriate boundary conditions are:

At the cylinder surface ($r^*=R^*$):

$$u^*=0 \tag{5}$$

$$w^*=0 \tag{6}$$

$$N^*=\frac{1}{2}\left(\frac{\partial u^*}{\partial z^*}-\frac{\partial w^*}{\partial r^*}\right) \tag{7}$$

At free surface ($r^*=R^*+h^*$)

$$2\left(\frac{\partial u^*}{\partial r^*}-\frac{\partial w^*}{\partial z^*}\right)\frac{\partial h^*}{\partial z^*}+\left(\frac{\partial u^*}{\partial z^*}+\frac{\partial w^*}{\partial r^*}\right)\left[1-\left(\frac{\partial h^*}{\partial z^*}\right)^2\right]=0 \tag{8}$$

$$p^*+2\mu\left[1+\left(\frac{\partial h^*}{\partial z^*}\right)^2\right]^{-1}\left[\left(\frac{\partial u^*}{\partial z^*}+\frac{\partial w^*}{\partial r^*}\right)\frac{\partial h^*}{\partial z^*}-\frac{\partial w^*}{\partial z^*}\left(\frac{\partial h^*}{\partial z^*}\right)^2-\frac{\partial u^*}{\partial r^*}\right]+S^*\left\{\frac{\partial^2 h^*}{\partial z^{*2}}\left[1+\left(\frac{\partial h^*}{\partial z^*}\right)^2\right]^{-3/2}-\frac{1}{r^*}\left[1+\left(\frac{\partial h^*}{\partial z^*}\right)^2\right]^{-1/2}\right\}=p_a^* \tag{9}$$

$$N^*=0 \tag{10}$$

$$\frac{\partial h^*}{\partial t^*}+\frac{\partial h^*}{\partial z^*}w^*-u^*=0 \tag{11}$$

where h^* is the local film thickness. The boundary conditions at the interface, Eq. (8) and Eq. (9), are the balance of tangential and normal stresses (Edward et al. [29]). In Eq. (9), p_a^* is the atmosphere pressure, and S^* is the surface tension. The discussion of boundary conditions for the angular microrotation momentum N^* at solid wall and at free surface, shown in Eq. (7) and Eq. (10), can be found in Datta and Sastry [21] and Ahmadi [22]. Equation (11) is the free surface kinetic equation. The variable that is associated with a superscript ''*'' stands for a dimensional quantity. By introducing the stream function, φ^*, into dimensional velocity components, they become

$$u^*=\frac{1}{r^*}\frac{\partial \varphi^*}{\partial z^*}, \quad w^*=\frac{-1}{r^*}\frac{\partial \varphi^*}{\partial r^*} \tag{12}$$

The dimensionless quantities can also be defined and given as

$$r=\frac{r^*}{h_0^*}, \quad z=\frac{\alpha z^*}{h_0^*}, \quad t=\frac{\alpha u_0^* t^*}{h_0^*}, \quad h=\frac{h^*}{h_0^*}, \quad \varphi=\frac{\varphi^*}{u_0^* h_0^{*2}},$$
$$p=\frac{p^*-p_a^*}{\rho u_0^{*2}}, \quad \mathrm{Re}=\frac{u_0^* h_0^*}{\nu}, \quad S=\left(\frac{S^{*3}}{2^4\rho^3\nu^4 g}\right)^{1/3}, \tag{13}$$
$$N=\frac{N^* h_0^*}{u_0^*}, \quad \Lambda=\frac{\gamma}{\mu J}, \quad K=\frac{k}{\mu}, \quad \Delta=\frac{h_0^{*2}}{J}, \quad \alpha=\frac{2\pi h_0^*}{\lambda}$$

where Λ, K, and Δ are the dimensionless micropolar parameters, Re is the Reynolds number, R is the dimensionless radius of the cylinder, λ is the perturbed wave length, and α is the dimensionless wave number. h_0^* is the film thickness of local base flow and u_0^* is the reference velocity which can be expressed as (Hung et al. [16])

$$u_0^*=\frac{g h_0^{*2}}{4\nu\Gamma} \tag{14}$$

where ν is the fluid kinematic viscosity, and

$$\Gamma=\left[2(1+R)^2\ln\left(\frac{1+R}{R}\right)-(1+2R)\right]^{-1} \tag{15}$$

Thus, the nondimensional governing equations and the associated boundary conditions can now be given as

$$p_r=\alpha\,\mathrm{Re}^{-1}[(1+K)(r^{-1}\varphi_{rrz}-r^{-2}\varphi_{rz})-KN_z]+O(\alpha^2) \tag{16}$$

$$(1+K)r^{-1}(r(r^{-1}\varphi_r)_r)_r-Kr^{-1}(rN)_r=4\Gamma+\alpha\,\mathrm{Re}(-p_z+r^{-1}\varphi_{tr}+r^{-2}\varphi_z\varphi_{rr}-r^{-3}\varphi_z\varphi_r-r^{-2}\varphi_r\varphi_{rz})+O(\alpha^2) \tag{17}$$

$$\Lambda(r^{-1}(rN)_r)_r-2K\Delta N+K\Delta(r^{-1}\varphi_r)_r=\alpha\,\mathrm{Re}(N_t+r^{-1}\varphi_z N_r-r^{-1}\varphi_r N_z)+O(\alpha^2) \tag{18}$$

at the cylinder surface ($r=R$)

$$\varphi_r=\varphi_z=0 \tag{19}$$

$$N=2^{-1}(r^{-1}\varphi_r)_r+O(\alpha^2) \tag{20}$$

at free surface ($r=R+h$)

$$(r^{-1}\varphi_r)_r=0+O(\alpha^2) \tag{21}$$

$$p=-2S\cdot\mathrm{Re}^{-5/3}(2\Gamma)^{1/3}(\alpha^2 h_{zz}-r^{-1})+\alpha\{-2\,\mathrm{Re}^{-1}[(r^{-2}\varphi_r-r^{-1}\varphi_{rr})h_z+r^{-2}\varphi_z-r^{-1}\varphi_{rz}]\}+O(\alpha^2) \tag{22}$$

$$N=0 \tag{23}$$

$$h_t-r^{-1}(\varphi_r h_z+\varphi_z)=0 \tag{24}$$

Subscripts of r, z, rr, zz, and rz are used to represent various partial derivatives of associated underlying variables.

Since the long wave length modes (i.e., small wave number α) may introduce flow instability to meet our analysis objectives, the dimensionless stream function φ and pressure p are, therefore, expanded here in terms of some small wave number α as

$$\varphi=\varphi_0+\alpha\varphi_1+O(\alpha^2) \tag{25}$$

$$p=p_0+\alpha p_1+O(\alpha^2) \tag{26}$$

$$N=N_0+\alpha N_1+O(\alpha^2) \tag{27}$$

By plugging the above three equations into Eqs. (16)–(24), the system governing equations can then be collected and solved order by order. In the physical and mathematical justification, the nondimensional surface tension S is a large value, the term $\alpha^2 S$ can be treated as a quantity in zeroth order (Hwang and Weng [11], Hung et al. [25]). Franchi and Straughan [24], and Hung et al. [25] showed that the micropolar parameter $\Lambda(=\gamma/\mu j)$ has very little effect on the stability of the micropolar film. For simplifying the solved equations that gives no spin-gradient viscosity effect, neglecting the Λ term of Eq. (18), one can obtain the solutions for the equations of both the zeroth and the first order (given in Appendix 1). By plugging the zeroth order and the first order solutions into the dimensionless free surface kinematic equation of Eq. (24), the generalized nonlinear kinematic equation is obtained and presented as

$$h_t+A(h)h_z+B(h)h_{zz}+C(h)h_{zzzz}+D(h)h_z^2+E(h)h_z h_{zzz}=0 \tag{28}$$

where $A(h)$, $B(h)$, $C(h)$, $D(h)$, and $E(h)$ are given in Appendix 2. In the case of $K=0$ and $\Delta=\infty$, the fluid flow becomes a typical classical Newtonian film flow. In the case of $R=\infty$, the result agrees exactly with the solution of plane flow.

3 Stability Analysis

The variation of film thickness in the base flow is found to be very small, so it is reasonable to assume that the local dimensionless film thickness is equal to one. The dimensionless film thickness when expressed in perturbed state can be expressed as

$$h(t,z)=1+\eta(t,z), \quad \eta=O(\alpha) \tag{29}$$

where η is a perturbed quantity to the stationary film thickness. By inserting the above equation into Eq. (28) and collecting all terms up to the order of η^3, the evolution equation of η is obtained and given as

$$\begin{aligned}\eta_t+A\eta_z+B\eta_{zz}+C\eta_{zzzz}+D\eta_z^2+E\eta_z\eta_{zzz}&=-\left[\left(A'\eta+\frac{A''}{2}\eta^2\right)\eta_z+\left(B'\eta+\frac{B''}{2}\eta^2\right)\eta_{zz}\right.\\&+\left(C'\eta+\frac{C''}{2}\eta^2\right)\eta_{zzzz}+(D+D'\eta)\eta_z^2\\&\left.+(E+E'\eta)\eta_z\eta_{zzz}\right]+O(\eta^4)\end{aligned} \tag{30}$$

The values of A, B, C, D, E and their derivatives are all evaluated at the dimensionless height, $h=1$, of the film flow.

Linear Stability Analysis. As the nonlinear terms in Eq. (30) are neglected, the linearized equation is obtained and given as

$$\eta_t+A\eta_z+B\eta_{zz}+C\eta_{zzzz}=0 \tag{31}$$

In order to use the normal mode method for analysis, we assume that

$$\eta=a\exp[i(z-dt)]+c.c. \tag{32}$$

where a is the perturbation amplitude, and $c.c.$ is the complex conjugate counterpart. The complex wave celerity, d, is given as

$$d=d_r+id_i=A+i(B-C) \tag{33}$$

where d_r is the linear wave speed, and d_i is the linear growth rate of the amplitudes. For $d_i>0$, the flow is in unstable linearly supercritical condition. For $d_i<0$, the flow is in stable linearly subcritical condition.

Nonlinear Stability Analysis. The method of multiple scales is used to analyze the stability of the nonlinear system. Several associated notions are defined and expressed as

$$\frac{\partial}{\partial t}\rightarrow\frac{\partial}{\partial t}+\varepsilon\frac{\partial}{\partial t_1}+\varepsilon^2\frac{\partial}{\partial t_2} \tag{34}$$

$$\frac{\partial}{\partial z}\rightarrow\frac{\partial}{\partial z}+\varepsilon\frac{\partial}{\partial z_1} \tag{35}$$

$$\eta(\varepsilon,z,z_1,t,t_1,t_2)=\varepsilon\eta_1+\varepsilon^2\eta_2+\varepsilon^3\eta_3 \tag{36}$$

where ε is a small perturbation parameter, $t_1=\varepsilon t$, $t_2=\varepsilon^2 t$, $z_1=\varepsilon z$. After plugging the above expressions into Eq. (30) and performing expansion and rearrangement, the equation can be obtained as

$$(L_0+\varepsilon L_1+\varepsilon^2 L_2)(\varepsilon\eta_1+\varepsilon^2\eta_2+\varepsilon^3\eta_3)=-\varepsilon^2 N_2-\varepsilon^3 N_3 \tag{37}$$

where

$$L_0=\frac{\partial}{\partial t}+A\frac{\partial}{\partial z}+B\frac{\partial^2}{\partial z^2}+C\frac{\partial^4}{\partial z^4} \tag{38}$$

$$L_1=\frac{\partial}{\partial t_1}+A\frac{\partial}{\partial z_1}+2B\frac{\partial}{\partial z}\frac{\partial}{\partial z_1}+4C\frac{\partial^3}{\partial z^3}\frac{\partial}{\partial z_1} \tag{39}$$

$$L_2=\frac{\partial}{\partial t_2}+B\frac{\partial^2}{\partial z_1^2}+6C\frac{\partial^2}{\partial z^2}\frac{\partial^2}{\partial z_1^2} \tag{40}$$

$$N_2=A'\eta_1\eta_{1z}+B'\eta_1\eta_{1zz}+C'\eta_1\eta_{1zzzz}+D\eta_{1z}^2+E\eta_{1z}\eta_{1zzz} \tag{41}$$

$$\begin{aligned}N_3=&A'(\eta_1\eta_{2z}+\eta_{1z}\eta_2+\eta_1\eta_{1z_1})\\&+B'(\eta_1\eta_{2zz}+2\eta_1\eta_{1zz_1}+\eta_{1zz}\eta_2)\\&+C'(\eta_1\eta_{2zzz}+4\eta_1\eta_{1zzz_1}+\eta_{1zzzz}\eta_2)\\&+D(2\eta_{1z}\eta_{2z}+2\eta_{1z}\eta_{1z_1})\\&+E(\eta_{1z}\eta_{2zzz}+3\eta_{1z}\eta_{1zzz_1}+\eta_{1zzz}\eta_{2z}+\eta_{1zzz}\eta_{1z_1})\\&+\tfrac{1}{2}A''\eta_1^2\eta_{1z}+\tfrac{1}{2}B''\eta_1^2\eta_{1zz}+\tfrac{1}{2}C''\eta_1^2\eta_{1zzzz}+D'\eta_1\eta_{1z}^2\\&+E'\eta_1\eta_{1z}\eta_{1zzz}\end{aligned} \tag{42}$$

Equation (37) can now be solved order by order. After collecting the terms of order of $O(\varepsilon)$ and solving for the resulting equation $L_0\eta_1=0$, the solution can be easily obtained as

$$\eta_1=a(z_1,t_1,t_2)\exp[i(z-d_r t)]+c.c. \tag{43}$$

After collecting terms and solving for the secular equation of order $O(\varepsilon^2)$, the solution of η_2 gives

$$\eta_2=ea^2\exp[2i(z-d_r t)]+c.c. \tag{44}$$

By plugging both η_1 and η_2 into the equation of order $O(\varepsilon^3)$, the resulting equation becomes

$$\frac{\partial a}{\partial t_2}+D_1\frac{\partial^2 a}{\partial z_1^2}-\varepsilon^{-2}d_i a+(E_1+iF_1)a^2\bar{a}=0 \tag{45}$$

where

$$e=e_r+ie_i=\frac{(B'-C'+D-E)}{16C-4B}+i\frac{-A'}{16C-4B} \tag{46}$$

$$D_1=B-6C \tag{47}$$

$$\begin{aligned}E_1=&(-5B'+17C'+4D-10E)e_r-A'e_i\\&+(-\tfrac{3}{2}B''+\tfrac{3}{2}C''+D'-E')\end{aligned} \tag{48}$$

$$F_1=(-5B'+17C'+4D-10E)e_i+A'e_r+\tfrac{1}{2}A'' \tag{49}$$

The overhead bar appearing in the above expressions stands for the complex conjugate of the same variable. Here, Eq. (45) is generally referred to as the Ginzburg-Landau equation (Ginzburg and Landau [30]). It can be used to investigate the weak nonlinear behavior of the fluid film flow. The solution of the exponential form is assumed and given as

$$a=a_0\exp[-ib(t_2)t_2] \tag{50}$$

By employing the condition of a filtered wave that gives no spatial modulation, neglecting the diffusion term, and substituting the assumed solution of Eq. (50) into Eq. (45), one can obtain

$$\frac{\partial a_0}{\partial t_2}=(\varepsilon^{-2}d_i-E_1a_0^2)a_0 \tag{51}$$

$$\frac{\partial[b(t_2)t_2]}{\partial t_2}=F_1a_0^2 \tag{52}$$

Of course, if E_1 becomes zero, the Eq. (51) is reduced to a linear equation. The second term on the right-hand side of Eq. (51) is induced by the effect of nonlinearity. It can either decelerate or accelerate the exponential growth of the linear disturbance based

Table 1 Various states of the Landau equation

linearly stable (subcritical region) $d_i < 0$	subcritical instability $E_1 < 0$	$\varepsilon a_0 < (\frac{d_i}{E_1})^{\frac{1}{2}}$	$a_0 \to 0$	conditional stability
		$\varepsilon a_0 > (\frac{d_i}{E_1})^{\frac{1}{2}}$	$a_0 \uparrow$	subcritical explosive state
	subcritical (absolute) stability $E_1 > 0$	$a_0 \to 0$		
linearly unstable (supercritical region) $d_i > 0$	supercritical explosive state $E_1 < 0$	$a_0 \uparrow$		
	supercritical stability $E_1 > 0$	$\varepsilon a_0 \to (\frac{d_i}{E_1})^{\frac{1}{2}}$ $Nc_r \to d_r + d_i \frac{F_1}{E_1}$		

on the signs of d_i and E_1. Equation (52) can be used to modify the perturbed wave speed caused by infinitesimal disturbances appeared in the nonlinear system. In the linear unstable region ($d_i > 0$), the condition for a supercritical stable region to exist is given as $E_1 > 0$. The threshold amplitude, εa_0, is given as

$$\varepsilon a_0 = \sqrt{\frac{d_i}{E_1}} \tag{53}$$

and the nonlinear wave speed is given as

$$Nc_r = d_r + \varepsilon^2 b = d_r + d_i\left(\frac{F_1}{E_1}\right) \tag{54}$$

On the other hand, in the linearly stable region ($d_i < 0$), if $E_1 < 0$, the film flow presents the behavior of subcritical instability, and εa_0 is the threshold amplitude. The condition for a subcritical stable region to exist is given as $E_1 > 0$. Also, the condition for a neutral stability curve to exist is $E_1 = 0$. Based upon the discussion presented above, various characteristic states of the Landau equation can be summarized and presented in Table 1.

4 Numerical Examples

A numerical example is presented here to illustrate the effectiveness of the proposed modeling procedure in dealing with the problem of a thin micropolar fluid film flowing down along a vertical cylinder. In order to validate the result of analytical derivation, a finite-amplitude perturbation generator is employed to disturb the system for both linear and nonlinear stability analyses. Based on the modeling results, the condition for thin-film flow stability can now be expressed as a function of Reynolds number, Re, dimensionless perturbation wave number, α, dimensionless radius of cylinder, R and micropolar parameters, K and Δ. Some important conclusions are made. The modeling results are also used to compare the analytical solutions given in this paper and some other conclusive results appearing in the literature.

Figure 1 shows the schematic diagram of a micropolar liquid film traveling down along a vertical cylinder. Physical parameters that are selected for study include (1) Reynolds numbers ranging from 0–15, (2) the dimensionless perturbation wave numbers ranging from 0–0.12, (3) the values of micropolar parameter K including 0, 0.5, and 1.0, (4) the value of micropolar parameter Δ is 10, and (5) the values of dimensionless radius distance including 10, 20, 50, and ∞. The neutral stability curve was obtained by computing the conditions of linear stability for a linear amplitude growth rate $d_i = 0$. The stability of flow field (α-Re plane) is separated into two different regions by the neutral curve. In the linearly stable subcritical region, the perturbed small waves decay as the perturbation time period increases. However, in the linearly unstable supercritical region, the perturbed small waves grow as the perturbation time period increases. In order to study the influence of the micropolar parameters and radius of cylinder on the stability of the film flow, a constant dimensionless surface tension ($S = 6173.5$) is used throughout for all numerical computations (Hung et al. [25]).

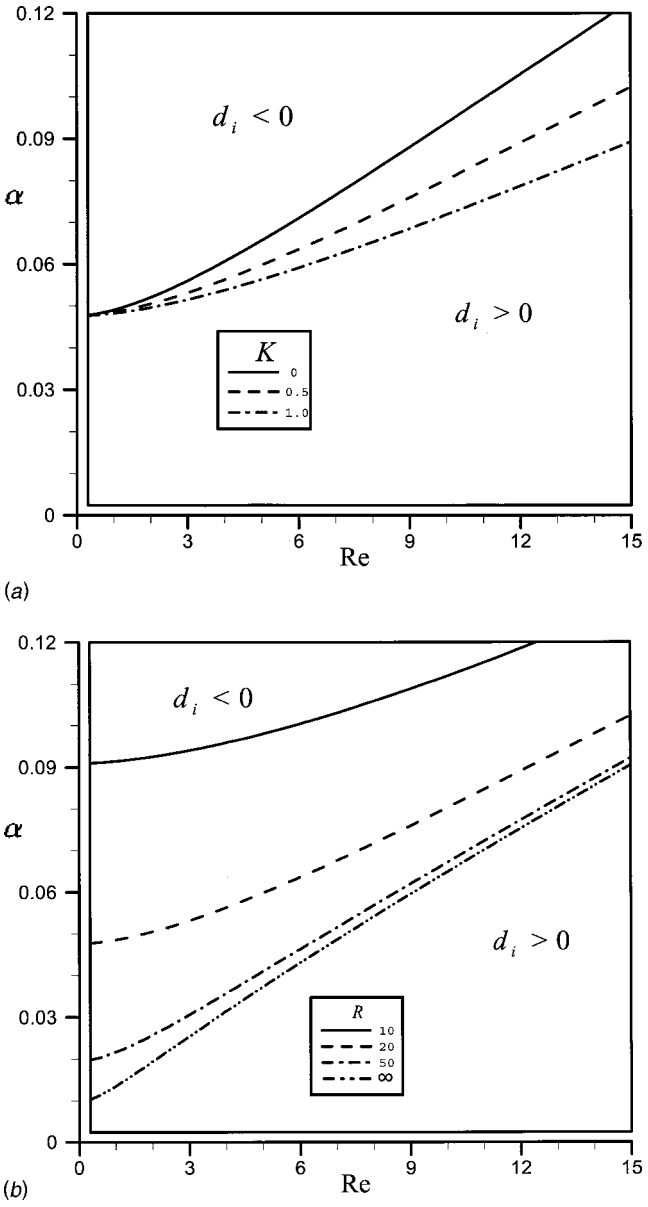

Fig. 2 (*a*) Neutral stability curves for three different *K* values at *R*=20, (*b*) neutral stability curves for four different *R* values at *K*=0.5

Linear Stability Solutions. Figure 2(*a*) shows the neutral stability curves of the micropolar film flow with different values on the micropolar parameter, K. The results indicate that the area of linearly unstable region ($d_i > 0$) becomes larger for a decreasing K. Figure 2(*b*) shows the neutral stability curves of the micropolar film flow with different values on the radius R. The results indicate that the area of linearly unstable region ($d_i > 0$) becomes larger for a decreasing R. Figures 3(*a*)–3(*b*) show the temporal film growth rate of micropolar fluid for $K = 0.5$ and $K = 1.0$. The temporal film growth rate of Newtonian flow (i.e., $K = 0$) is also given in the figure for comparison purpose. It is interesting to note that temporal film growth rate increases as the values of K de-

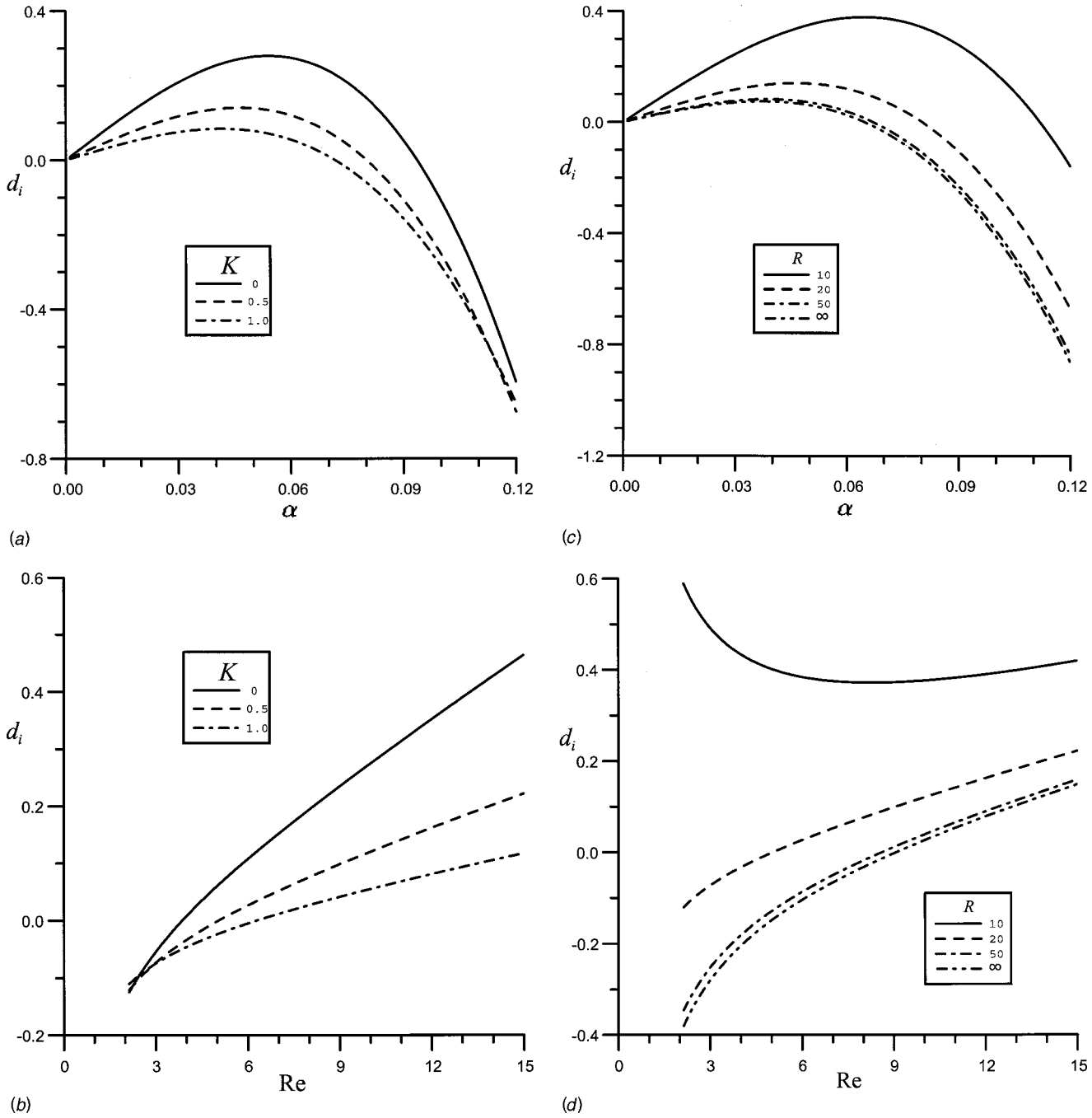

Fig. 3 (*a*) **Amplitude growth rate of disturbed waves in micropolar flows for three different *K* values at Re=10 and *R*=20,** (*b*) **amplitude growth rate of disturbed waves in micropolar flows for three different *K* values at α=0.06 and *R*=20,** (*c*) **amplitude growth rate of disturbed waves in micropolar flows for four different *R* values at Re=10 and *K*=0.5,** (*d*) **amplitude growth rate of disturbed waves in micropolar flows for four different *R* values at α=0.06 and *K*=0.5**

creases and Re increases. Furthermore, it is found that both the wave number of neutral mode and the maximum temporal film growth rate increase as the value of K decreases. In other words, the larger the value of micropolar parameter K is, the higher the stability of a liquid film becomes. Figures 3(c)–3(d) show the temporal film growth rate of micropolar fluid ($K=0.5$) for $R=10$, 20, and 50. The temporal film growth rate of the plane flow (i.e., $R=\infty$) is also given in the figure for comparison purpose. It is noted that temporal film growth rate decreases as the value of R increases. Furthermore, it is found that both the wave number of neutral mode and the maximum temporal film growth rate increase as the value of R decreases. In other words, the larger the value of radius R is, the higher the stability of a liquid film becomes. For $\Delta>10$, the micropolar parameter Δ has very little effect on the stability of film flow.

Nonlinear Stability Solutions. As the perturbed wave grows to finite amplitude, the linear stability theory is no longer valid for accurate prediction of flow behavior. The theory of nonlinear stability should be used to study whether the disturbed wave amplitude in the linear stable region will become stable or unstable. The problem that subsequent nonlinear evolution on disturbance in the linear unstable region will develop to a new equilibrium state (supercritical stability) with a finite amplitude or a unstable situ-

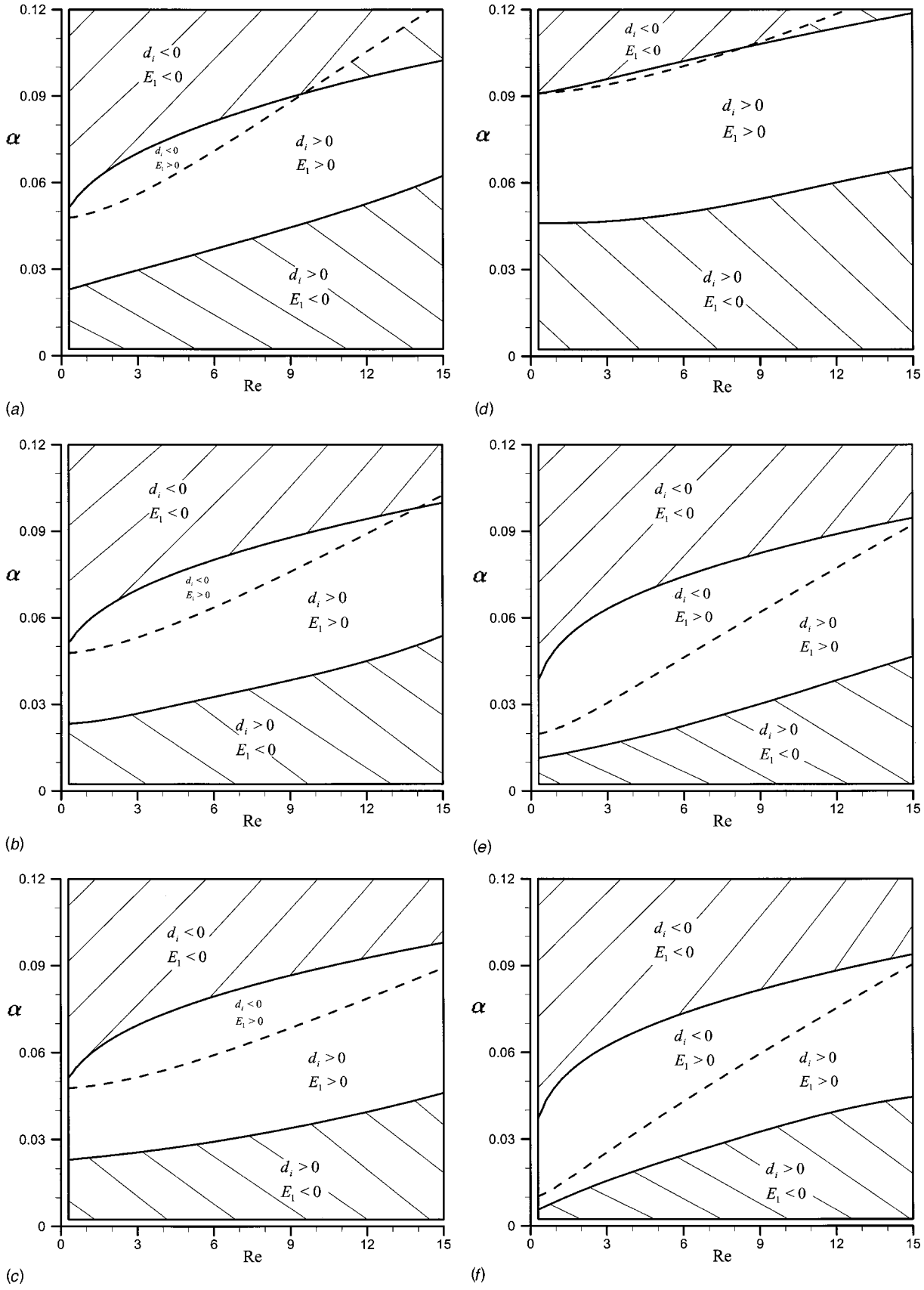

Fig. 4 (*a*) **Neutral stability curve of micropolar film flows for $K=0$ and $R=20$,** (*b*) **neutral stability curve of micropolar film flows for $K=0.5$ and $R=20$,** (*c*) **neutral stability curve of micropolar film flows for $K=1.0$ and $R=20$,** (*d*) **neutral stability curve of micropolar film flows for $K=0.5$ and $R=10$,** (*e*) **neutral stability curve of micropolar film flows for $K=0.5$ and $R=50$,** (*f*) **neutral stability curve of micropolar film flows for $K=0.5$ and $R=\infty$**

ation is also studied. As mentioned before, a negative value of E_1 can cause the system to become unstable. Such a condition in the linear region is referred to as the subcritical instability. In other words, if the amplitude of disturbances is greater than the threshold amplitude, the amplitude of disturbed wave will increase. This is contradictory to the result predicted by using a linear theory. As a matter of fact, such a condition in the subcritical unstable region can, in some cases, cause the system to become explosive.

The hatched areas near the neutral stability curves in Figs. 4(*a*)–4(*f*) reveal that both the subcritical instability condition ($d_i<0$, $E_1<0$) and the explosive supercritical instability condition ($d_i>0$, $E_1<0$) are possible to occur for all values of K and R that are used in this study. Figures 4(*a*)–4(*c*) show that the neutral stability curves of $d_i=0$ and $E_1=0$ are shifted downward as the values of K increase. Therefore, the area of shaded subcritical instability region increases and the area of shaded supercritical instability region decreases as the values of K increase. The area of supercritical stability region ($d_i>0$, $E_1>0$) decreases and the area of subcritical stability region ($d_i<0$, $E_1>0$) increases as the values of K increase. Figures 4(*b*), 4(*d*)–4(*f*) show that the neutral stability curves of $d_i=0$ and $E_1=0$ are shifted upward as the values of R decrease. Therefore, the area of shaded subcritical instability region increases and the area of shaded supercritical instability region decreases as the values of R increase. The area of supercritical stability region ($d_i>0$, $E_1>0$) increases and the area of subcritical stability region ($d_i<0$, $E_1>0$) decreases as the values of R decrease.

Figure 5(*a*) shows the threshold amplitude in subcritical unstable region for various wave numbers with different K values at Re=10 and $R=20$. The results indicate that the threshold amplitude εa_0 becomes smaller as the value of micropolar parameter K decreases. Figure 5(*b*) shows the threshold amplitude in subcritical unstable region for various wave numbers with different values of radius R at Re=10 and $K=0.5$. The results indicate that the threshold amplitude εa_0 becomes smaller as the value of radius R decreases. In such situations, the film flow will become unstable. That is to say, if the initial finite-amplitude disturbance is less than the threshold amplitude, the system will become conditionally stable. On the other hand, if the initial finite-amplitude disturbance is greater than the threshold amplitude, the system will become explosively unstable.

In the linearly unstable region, the linear amplification rate is positive, while the nonlinear amplification rate is negative. Therefore, a linear infinitesimal disturbance in the unstable region, instead of going infinite, will reach finite equilibrium amplitude as given in Eq. (51). Figure 6(*a*) shows the threshold amplitude in the supercritical stable region for various wave numbers under different values of micropolar parameter K at Re=10 and $R=20$. It is found that the increase of K will lower the threshold amplitude, and the flow will become relatively more stable. Figure 6(*b*) shows the threshold amplitude in the supercritical stable region for various wave numbers under different values of radius R at Re=10 and $K=0.5$. It is found that the increase of R will lower the threshold amplitude, and the flow will become relatively more stable.

The wave speed of Eq. (33) predicted by using the linear theory is a constant value for all wave numbers and Reynolds number. However, the nonlinear wave speed, given by Eq. (54), can be influenced by the wave number, Reynolds number, micropolar parameter K, and the radius of cylinder. The nonlinear wave speed is plotted in Fig. 7(*a*) for various wave numbers and K values at Re=10 and $R=20$. It is found that the nonlinear wave speed decreases as the value of K increases. Figure 7(*b*) shows the nonlinear wave speed for various wave numbers and values of R at Re=10 and $K=0.5$. It is found that the nonlinear wave speed increases as the value of R decreases. Similarly, as mentioned in the linear stability analysis, if $\Delta>10$, the micropolar parameter Δ has very little influence on the results and characteristics of the threshold amplitude of subcritical instability or supercritical stability.

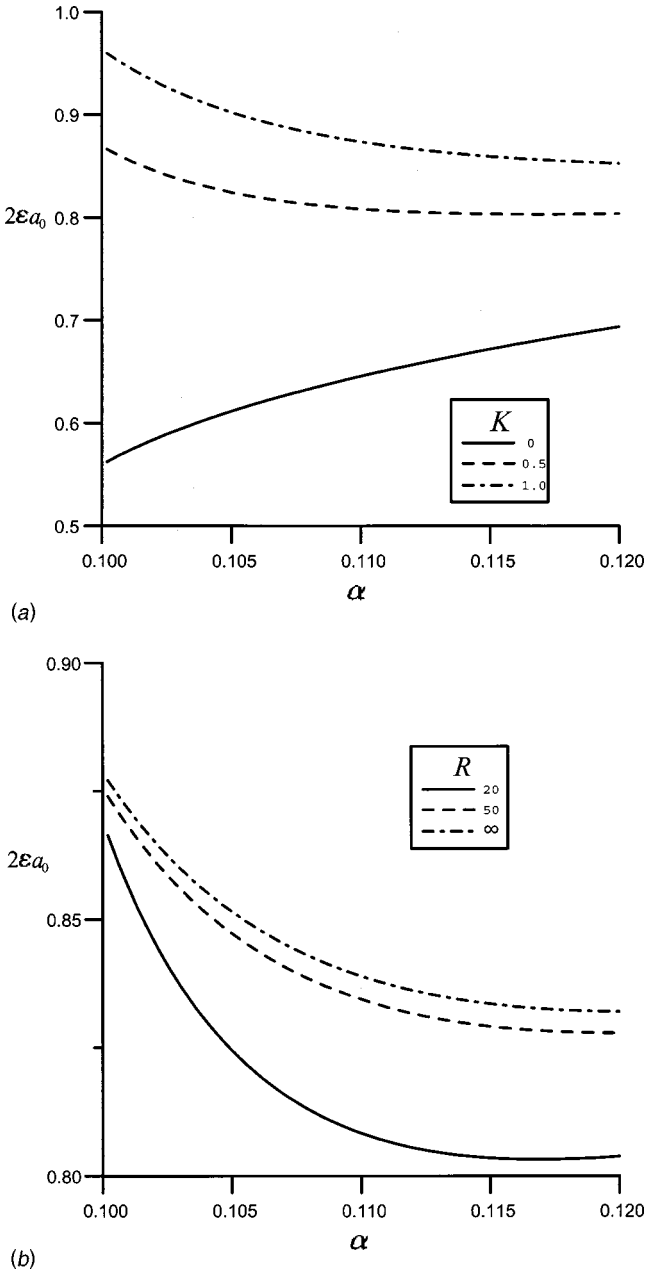

Fig. 5 (*a*) Threshold amplitude in subcritical unstable region for three different K values at Re=10 and $R=20$, (*b*) threshold amplitude in subscritical unstable region for three different R values at Re=10 and $K=0.5$

It is also noted that a cylinder with a smaller radius makes the flow relatively more unstable. This is due to the surface tension of the lateral curvature. In Eq. (22), the streamwise surface tension term, $S\cdot \mathrm{Re}^{-5/3}(2\Gamma)^{1/3}\alpha^2 h_{zz}$, is independent of the value of r. However, the lateral surface tension term, $S\cdot \mathrm{Re}^{-5/3}(2\Gamma)^{1/3}r^{-1}$, is inverse to the value of r. When the film flows down the outer surface of the cylinder with a smaller radius, the surface tension term of the lateral curvature will become larger. Therefore, it has a destabilizing effect. This destabilizing effect occurs because the radius of the trough of waves has a smaller value than that at the crest of the waves, and the surface tension will produce large

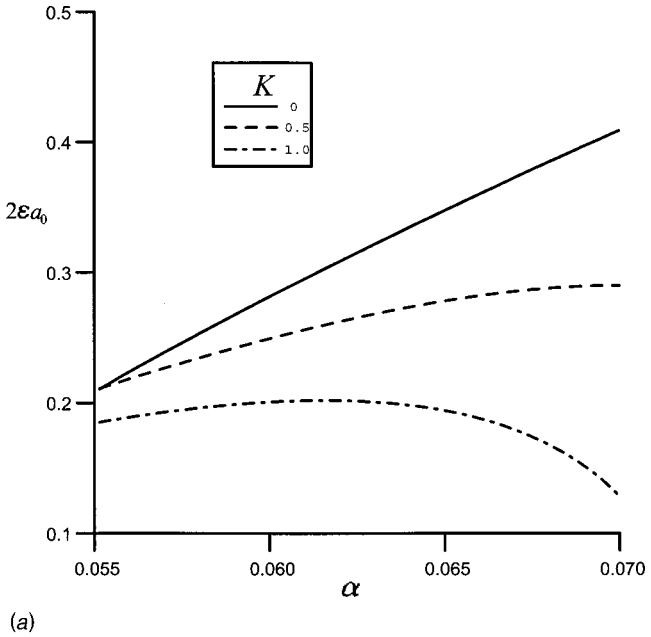

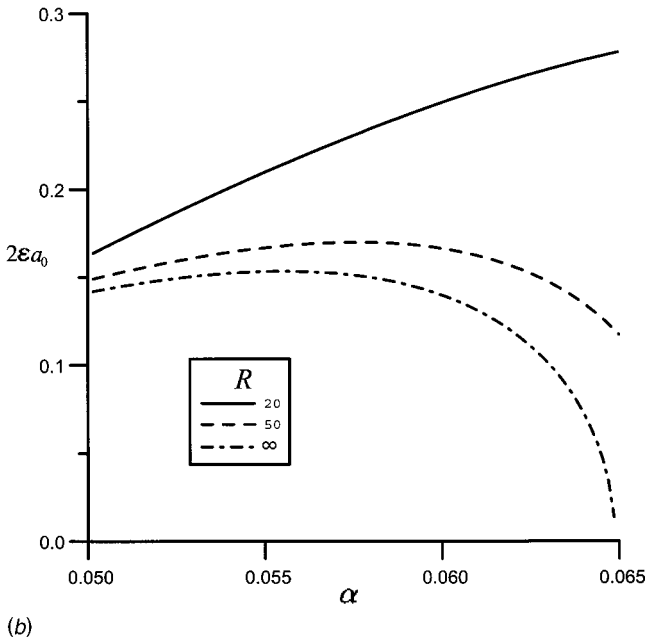

Fig. 6 (*a*) Threshold amplitude in supercritical stable region for three different *K* values at Re=10 and *R*=20, (*b*) threshold amplitude in supercritical stable region for three different *R* values at Re=10 and *K*=0.5

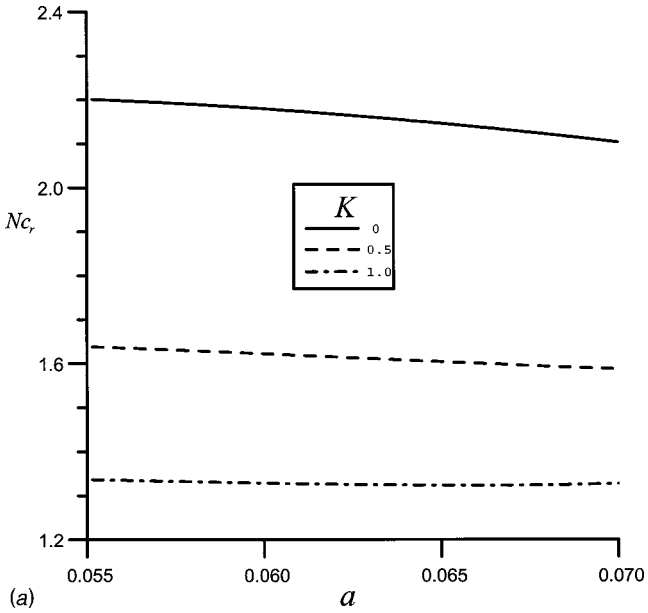

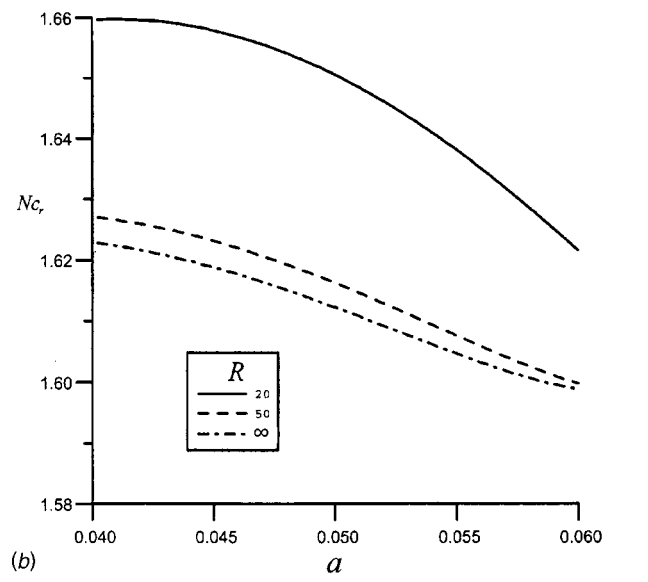

Fig. 7 (*a*) Nonlinear wave speed in supercritical stable region for three different *K* values at Re=10 and *R*=20, (*b*) nonlinear wave speed in supercritical stable region for three different *R* values at Re=10 and *K*=0.5

capillary pressure at a smaller radius of curvature. This will induce the capillary pressure and force the fluid trough to move upward to the crest. Thus, the amplitude of the wave is increased.

As discussed above, it becomes apparent that the stability characteristic of a film flow traveling down along a vertical cylinder is significantly affected by the values of micropolar parameter K and the radius R. That is to say, the degree of stability in a micropolar film flow increases as the values of both K and R increase. By setting $R\rightarrow\infty$, the result becomes a solution for the plane flow problem. In the plane flow solution, it is noted that the flow field becomes relatively stable as the micropolar parameter K increases. This phenomenon agrees well with the conclusion given by Hung et al. [25]. By setting $K=0$, and $\Delta=\infty$, the results of a classical Newtonian flow are obtained. As compared to the modeling results given by Hung et al. [16], it is found that both solutions agree well with each other.

5 Concluding Remarks

The stability of a micropolar thin film flow traveling down along a vertical cylinder is thoroughly investigated in this paper by using the method of long wave perturbation. The generalized nonlinear kinematic equations of the free film surface near the wall is derived and is numerically estimated to study the stability of flow field under different values of micropolar parameters and radius of the cylinder. Based on the modeling results, several conclusions can be made as follows:

1 In the linear stability analysis, the neutral stability curve that separates the flow field into two different regions was first computed for a linear amplitude growth rate of $d_i=0$. The modeling

results indicate that the area of linearly unstable region becomes larger for a decreasing K and a decreasing R. It is also noted that the growth rate of temporal film is reduced with an increasing K and an increasing R. In other words, the degree of stability is increased if the flow is perturbed by waves with a lower Reynolds number, a larger micropolar parameter, and a greater radius of the cylinder.

2 In the nonlinear stability analysis, it is noted that the area of shaded subcritical instability region decreases as the value of K decreases and the value of R decreases. On the other hand, the area of shaded supercritical instability region increases with a decreasing K value and a decreasing R value. It is also shown that the area of supercritical stability region increases as the value of K decreases and the value of R decreases. The area of subcritical stability region decreases as the value of K decreases and the value of R decreases. It is shown that the threshold amplitude εa_0 in the subcritical instability region decreases as the value of micropolar parameter K decreases and the value of radius R decreases. If the initial finite-amplitude disturbance is greater than the threshold amplitude value, the system will become explosively unstable. Both the threshold amplitude and nonlinear wave speed in the supercritical stability region decrease with an increasing K value and an increasing R value.

3 The values of micropolar parameter K and radius R strongly affect the stability characteristic of a flow film. It is generally true that the stability of a micropolar film flow increases as the value of K increases and the value of R increases. The flow field becomes relatively stable for a larger micropolar parameter K and a larger radius R. Because the effect of the microstructure in micropolar fluid will increase the effective viscosity, it can, therefore, reduce the convective motion of flow.

Acknowledgment

The financial support for this work from the National Science Council of Taiwan through grant no. NSC 88-2212-E-006-039 is gratefully acknowledged.

Nomenclature

d = complex wave celerity $= d_r + i d_i$
g = gravitational acceleration
h = film thickness
h_0^* = local base flow film thickness
J = micro-inertial density
K = micropolar parameter $= \kappa/\mu$
N = angular micro-rotation momentum
p = fluid pressure
p_a^* = pressure of the atmosphere
R = radius of cylinder
Re = Reynolds number $= u_0^* h_0^*/\nu$
r, z = coordinates transverse and along to the cylinder surface
S = surface tension of the fluid
t = time
u_0^* = reference velocity $= g h_0^{*2}/4\nu\Gamma$
u, w = velocities along r- and z-directions, respectively

Greek symbols

α = dimensionless wave number
γ = spin-gradient viscosity
κ = vortex viscosity
Δ = micropolar parameter $= h_0^{*2}/J$
ε = infinitesimal parameter
η = dimensionless perturbed film thickness
Λ = micropolar parameter $= \gamma/\mu J$
λ = perturbed wave length
μ = fluid dynamic viscosity
ν = fluid kinematic viscosity
ρ = density of the fluid
φ = stream function of the fluid

Superscripts

$*$ = dimensional quantities
$'$ = differentiation with respect to h

Subscripts

t, r, z = partial differentiation with respect to the subscript
0,1,2.... = expansion order of the long wave

References

[1] Yih, C. S., 1954, ''Stability of parallel laminar flow with a free surface,'' Proceedings of the Second U.S. National Congress of Applied Mechanics, pp. 623–628.
[2] Landau, L. D., 1944, ''On the problem of turbulence,'' C.R. Acad. Sci. U.R.S.S., **44**, pp. 311–314.
[3] Stuart, J. T., 1956, ''On the role of Reynolds stresses in stability theory,'' J. Aeronaut. Sci., **23**, pp. 86–88.
[4] Benjamin, T. B., 1957, ''Wave formation in laminar flow down an inclined plane,'' J. Fluid Mech., **2**, pp. 554–574.
[5] Yih, C. S., 1963, ''Stability of liquid flow down an inclined plane,'' Phys. Fluids, **6**, pp. 321–334.
[6] Benney, D. J., 1966, ''Long waves on liquid film,'' J. Math. Phys., **45**, pp. 150–155.
[7] Lin, S. P., 1974, ''Finite amplitude side-band stability of a viscous film,'' J. Fluid Mech., **63**, pp. 417–429.
[8] Nakaya, C., 1974, ''Equilibrium state of periodic waves on the fluid film down a vertical wall,'' J. Phys. Soc. Jpn., **36**, pp. 921–926.
[9] Krishna, M. V. G., and Lin, S. P., 1977, ''Nonlinear stability of a viscous film with respect to three-dimensional side-band disturbance,'' Phys. Fluids, **20**, pp. 1039–1044.
[10] Pumir, A., Manneville, P., and Pomeau, Y., 1983, ''On solitary waves running down on inclined plane,'' J. Fluid Mech., **135**, pp. 27–50.
[11] Hwang, C. C., and Weng, C. I., 1987, ''Finite-amplitude stability analysis of liquid films down a vertical wall with and without interfacial phase change,'' Int. J. Multiphase Flow, **13**, pp. 803–814.
[12] Lin, S. P., and Liu, W. C., 1975, ''Instability of film coating of wires and tubes,'' AIChE J., **21**, pp. 775–782.
[13] Krantz, W. B., and Zollars, R. L., 1976, ''The linear hydrodynamic stability of film flow down a vertical cylinder,'' AIChE J., **22**, pp. 930–934.
[14] Rosenau, P., and Oron, A., 1989, ''Evolution and breaking of liquid film flowing on a vertical cylinder,'' Phys. Fluids A, **1**, pp. 1763–1766.
[15] Davalos-Orozco, L. A., and Ruiz-Chavarria, G., 1993, ''Hydrodynamic instability of a liquid layer flowing down a rotating cylinder,'' Phys. Fluids A, **5**, pp. 2390–2404.
[16] Hung, C. I., Chen, C. K., and Tsai, J. S., 1996, ''Weakly nonlinear stability analysis of condensate film flow down a vertical cylinder,'' Int. J. Heat Mass Transf., **39**, pp. 2821–2829.
[17] Eringen, A. C., 1964, ''Simple microfluids,'' Int. J. Eng. Sci., **2**, pp. 205–217.
[18] Eringen, A. C., 1967, ''Theory of micropolar fluids,'' J. Math. Mech., **16**, pp. 1–18.
[19] Liu, C. Y., 1970, ''On turbulent flow of micropolar fluids,'' Int. J. Eng. Sci., **8**, pp. 457–466.
[20] Liu, C. Y., 1971, ''Initiation of instability in micropolar fluids,'' Phys. Fluids, **14**, pp. 1808–1809.
[21] Datta, A. B., and Sastry, V. U. K., 1976, ''Thermal instability of a horizontal layer of micropolar fluid heated from below,'' Int. J. Eng. Sci., **14**, pp. 631–637.
[22] Ahmadi, G., 1976, ''Stability of a micropolar fluid layer heated from below,'' Int. J. Eng. Sci., **14**, pp. 81–89.
[23] Payne, L. E., and Straughan, B., 1989, ''Critical Rayleigh numbers for oscillatory and nonlinear convection in an isotropic thermalmicropolar fluid,'' Int. J. Eng. Sci., **27**, pp. 827–836.
[24] Franchi, F., and Straughan, B., 1992, ''Nonlinear stability for thermal convection in a micropolar fluid with temperature dependent viscosity,'' Int. J. Eng. Sci., **30**, pp. 1349–1360.
[25] Hung, C. I., Tsai, J. S., and Chen, C. K., 1996, ''Nonlinear Stability of the thin micropolar liquid film flowing down on a vertical plate,'' ASME J. Fluids Eng., **118**, pp. 498–505.
[26] Stokes, V. K., 1984, *Theories of fluids with microstructures- An introduction*, Chapter 6, Springer-Verlag, Berlin.

[27] Kolpashchikov, V. L., Migun, N. P., and Prokhorenko, P. P., 1983, ''Experimental determination of material micropolar fluid constants,'' Int. J. Eng. Sci., **21**, pp. 405–411.
[28] Eringen, A. C., 1980, ''Theory of Anisotropic micropolar fluids,'' Int. J. Eng. Sci., **18**, pp. 5–17.
[29] Edwards, D. A., Brenner, H., and Wasan, D. T., 1991, *Interfacial transport processes and rheology*, Butterworth-Heinemann, a Division of Reed Publishing (USA) Inc.
[30] Ginzburg, V. L., and Landau, L. D., 1950, ''Theory of superconductivity,'' J. Exp. Theor. Phys., **20**, pp. 1064–1082.

At the Upper Transition of Subcritical Regime of a Circular Cylinder

K. W. Lo[1]

N. W. M. Ko
Professor

Department of Mechanical Engineering,
The University of Hong Kong,
Hong Kong,
People's Republic of China

The present study establishes the transition between the lower and upper subcritical regime of flow over a circular cylinder at $7\times10^3<Re<2\times10^4$. Based on a new sampling technique, it is shown that the small-scale secondary vortices, especially those of high energy, play an important role in the transition. Within a primary vortex shedding period, the secondary vortices appear in groups. In a group, the streamwise velocity of secondary vortices exhibits the increase, peak, and decrease pattern associated with the formation of Strouhal vortices. In the lower subcritical regime, the Group I of singular group occurs most frequently, while in the upper subcritical regime, the Group III of three groups is the most frequent. Pairings of successive secondary vortices are found, and the paired vortices also appear in groups. The present model of transition involves the excitation of the separated shear layer at the most amplified mode by the disturbances associated with the secondary and paired vortices. Due to their mutual interference, the higher-energy small-scale vortices affect the primary vortex sheet, which in turn amplifies the former. These higher-energy vortices have enhanced pairings, which also play a dominant role in the later stage of transition. [DOI: 10.1115/1.1365120]

Introduction

In the subcritical regime of a circular cylinder, $10^3<\mathrm{Re}<2\times10^5$, two subregimes are defined. In the lower subcritical regime, vortex shedding is dominant and is correlated over a large axial distance [1]. The Bloor-Gerrard secondary vortices and the Strouhal vortices induce strong interaction [2]. In the upper subcritical regime, the frequency of the vortex shedding varies with time, and the axial correlation length is smaller [1]. The Bloor-Gerrard secondary vortices amalgamate into the Strouhal vortices [2].

The small-scale Bloor-Gerrard secondary vortices roll up from the Kelvin Helmholtz instability in the formation region of the large-scale primary vortices. The ratio of the frequency of the secondary vortices f_i, to that of the primary vortices, f_v, as recently reviewed by Prasad and Williamson [3], has the relation $f_i/f_v \alpha\ \mathrm{Re}^{0.67}$. With the suppression of the primary vortices by a splitter plate, the frequency of the secondary vortices does not change, indicating the vortices are intrinsically related to the separated shear layer characteristics [2]. At $\mathrm{Re}=5\times10^3$, the secondary vortices appear visually in sequence, consisting of as many as three to five vortices [4]. Their development is not consistent between primary shedding cycles, and an individual vortex can rapidly attain a large circulation. The presence of a secondary vortex with large circulation is observed to result in the delayed formation of the primary vortex at $\mathrm{Re}=2.5\times10^3$. In the lower subcritical regime, these secondary vortices also appear as packets of shear layer fluctuations for parallel shedding at $\mathrm{Re}=2.5\times10^3$ [3]. Wei and Smith [5] observed the rapid distortion of these packets a cellular structure further downstream. A feedback mechanism between the old and new secondary vortices may be responsible for the alignment of the new cells essentially directly downstream of the old ones.

The Bloor-Gerrard vortices generated in the separated shear layer, here referred to as the secondary vortices, resemble those in the plane mixing layer [6], in which pairing of successive vortices occurs further downstream [7,8]. In the near wake of a cylinder, pairing of secondary vortices also occurs [2,9,10,11]. Secondary vortex pairing usually occurs before the roll-up of the large-scale primary vortices, and depends on the Reynolds number [11].

The evolution and strain field of the primary vortices may have a significant effect on the development of the small-scale vortices [4]. The forcing effect of the primary vortices in the region of initial disturbance growth results in more rapid secondary vortex evolution and deformation [5,9,12].

The above studies used flow visualization and spectral analysis to observe the first appearance and behavior of the Bloor-Gerrard secondary vortices. The studies on their mutual effects were based on instantaneous, phase-averaged or averaged flow visualization pictures. There is, however, no systematic and quantitative study of these two types of vortices and their mutual interference in the transition between the lower and upper subcritical regime. As there is not a distinct transition between the two regimes, this study will first establish the Reynolds number range in which transition occurs. It will present the quantitative results of these two types of vortices and their mutual interference using a new conditional sampling technique. The mechanism for the transition will be explored and presented.

Apparatus and Measurement Technique

The experiments were carried out in a low speed wind tunnel of test section $0.4\,\mathrm{m}\times0.4\,\mathrm{m}$. The freestream turbulence intensity was about 0.2 percent at the freestream mean velocity U_0 of 20 m/s. The cylinder diameter d was 50 mm and the blockage ratio of the cylinder was 12.5 percent. The Reynolds number range, based on the diameter, was $4\times10^3<\mathrm{Re}<3\times10^4$, covering the transition between the lower and upper subcritical regime.

The origin of the coordinates is taken at the center of the cylinder. The x axis coincides with the direction of the flow, the z axis with the cylinder axis and the y direction normal to these two. Two rectangular end plates with leading edge of 2.5d and trailing edge of 4.5d, the same as those of Kourta et al. [2], were located at 2d from the tunnel wall. The aspect ratio l/d of the cylinder was

[1]Now at Maunsell Environmental Management Consultants Ltd., Room 1213-1219, Grand Central Plaza, Tower 2, 138 Shatin Rural Committee Road, Shatin, N.T., Hong Kong.

Contributed by the Fluids Engineering Division for publication in the JOURNAL OF FLUIDS ENGINEERING. Manuscript received by the Fluids Engineering Division December 4, 1998; revised manuscript received December 20, 2000. Associate Editor: D. Williams.

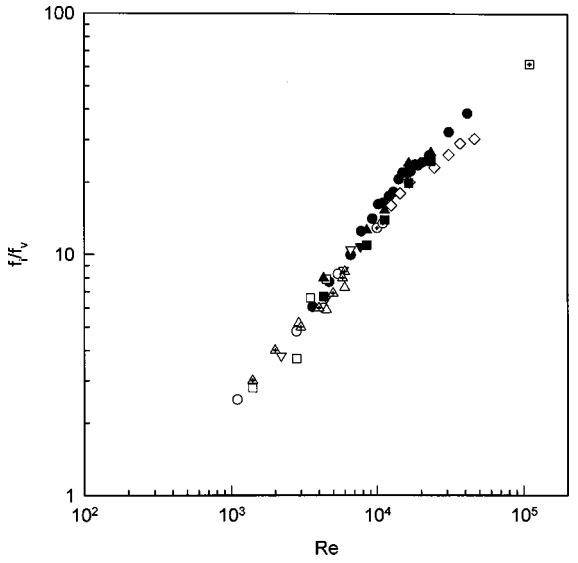

Fig. 1 Frequency ratios of secondary vortices to primary vortices. Present study (hot wire): ■, AR=6; ●, AR=4; ▲, AR =1; Present study (flow visualization): ▼, AR=4. ○, Bloor [18]; Wei and Smith [5]: □, d=2.54 mm; △, d=3.8 mm; ▽, d=4.8 mm; ◇, Norberg [1]; ◊, Kourta et al. [2]; ⊕, Peterka and Richardson [19]; ⊞, Maekawa and Mizuno [42]; ⧋, Prasad and Williamson [3]. Uncertainty: ±5 percent.

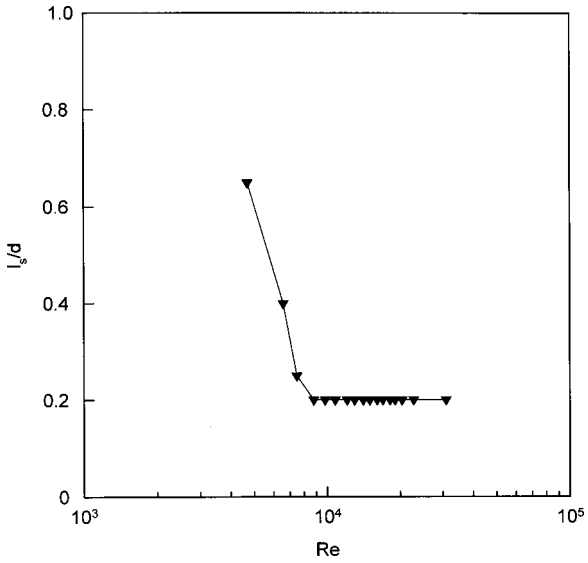

Fig. 2 Variation of formation length of secondary vortices. Uncertainty: ±5 percent.

4. The present aspect ratio (AR), blockage ratio and local turbulence intensity were within the ranges used by past researchers [13,14].

As the free shear layer, the vortex formation length and the separation point are only slightly different at the freestream turbulence intensities of 0.1 percent and 1.4 percent [15–17], one would expect the effect of freestream turbulence to be insignificant in the present investigation. The region of study was mainly at $x/d<1$, and the momentum thickness near the separation of the boundary layer was about 3×10^{-4} m. The cylinder diameter, and thus the blockage ratio, was chosen for reasonable thickness of the separated shear layer. The aspect ratio, as will be shown later in flow visualization, was adopted for two dimensionality of the newly rolled-up secondary vortices. The frequency ratios f_i/f_v obtained with cylinder aspect ratios of 1, 4, and 6 agree with those of Bloor [18], Peterka and Richardson [19], Wei and Smith [5], Norberg [1], Kourta et al. [2], and Prasad and Williamson [3], where higher aspect ratios and smaller blockage ratios were used (Fig. 1). The slightly higher frequency ratios at $AR=4$ and 1 are partly due to the aspect ratio and partly due to the fairly broad spectral peak of f_i. The agreement of the frequency ratio provides further evidence that the present f_i, as determined from the spectrum of the streamwise velocity, is associated with the secondary vortices observed by the previous investigators. The formation length of the primary vortices, based on the maximum streamwise turbulence intensity [1,20], varies from 1.25d–2.5d, depending on Reynolds number. The formation length l_s of the secondary vortices was based on the maximum spectral peak at f_i, and in the present study it depends on Reynolds number [1,9]. It varies from $l_s/d=0.6$ at $\mathrm{Re}=4.7\times10^3$ to 0.2 at $7.5\times10^3\leqslant\mathrm{Re}\leqslant3.1\times10^4$ (Fig. 2). Thus, the main part of the current measurements was carried out in the regime $(0.1<x/d<1)$, just after the roll-up of the secondary vortices but within the formation length of the primary vortices.

The single hot wire measurements were made with a wire diameter of 5 μm and length of 2 mm. Due to the small thickness of the separated shear layer in the formation region, a three-wire probe of wire lateral spacing of 1 mm was used. Among the three signals obtained in the shear layer, only the highest amplitude one was selected. The hot-wire probe was mounted on a computer controlled table for positioning in the x, y, z directions. The signal from the constant temperature anemometer was acquired at a rate of 5000 samples per second through a Data Translation 2821 digital data acquisition board. A sampling time was 500s. The data were then transferred to the Workstation DEC 5000/200 PXG and Pentium II Processor for further analysis.

A new conditional sampling scheme was developed to reveal the interaction of the Bloor-Gerrard secondary vortices and the primary vortex sheet. In this scheme, the velocity trough of the primary vortex sheet time history was located first, then the velocity signal of the secondary vortices in the trough region was sampled according to a threshold level (Fig. 3). Three threshold levels, $1<\sigma_i<2$, $2<\sigma_i<3$ and $\sigma_i>3$ were selected, where σ_i is the threshold level ratio of the instantaneous velocity u_i to the rms value u_i' of the secondary vortices. The primary vortex sheet was also sampled based on the threshold level. Since the formation and presence of the secondary vortices on the primary vortex sheet are not stationary, some cancellation may occur during averaging. Instead of sampling the streamwise velocity u_i of the secondary vortices, their streamwise energy u_i^2 was adopted. The triple decomposition of the fluctuating velocity field yields [21],

$$u=u_v+u_i+u_r,$$

where subscripts v, i, and r denote the primary vortex sheet, secondary vortex and random components, respectively. The triple decomposition of the fluctuating velocity is based on 1/3 octave filtering at the center frequencies of fairly distinct spectral peaks corresponding to the different types of vortices (Fig. 4). Besides the peak at f_v associated with the primary vortices, at $\mathrm{Re}=1.2\times10^4$, $\mathrm{y/d}=0.66$, there are peaks at f_i and $f_i/2$ associated with the secondary and paired vortices at $0.2\leqslant x/d\leqslant0.6$. The signals of the small-scale vortices and their pairings start to appear at $x/d=0.2$. The local random turbulence also starts to build up its energy at this streamwise position.

At the minimum velocity $(u_v)_{\min}$, the time of the jth sample of the primary vortex sheet is $t_v{}^j$ (Fig. 3) The secondary vortices within the time period of the primary vortex sheet were scanned for their maxima in the determination of the threshold level σ_i^j. ΔT_v^j is the period of the successive maximum velocities of the primary vortex sheet. As there are three threshold levels, the function

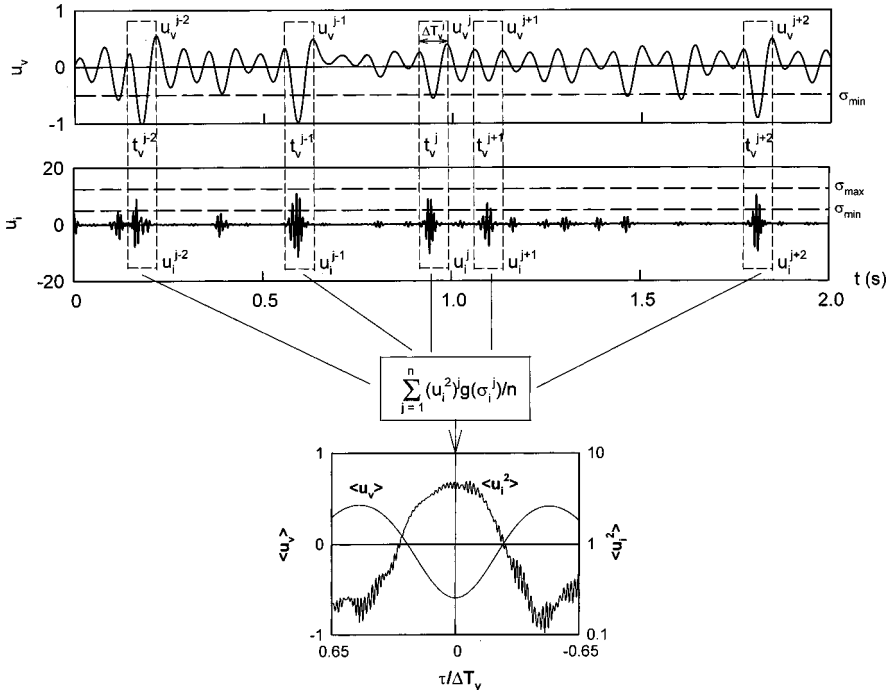

Fig. 3 Scheme of conditional sampling of primary vortex sheet and secondary vortices

$$g(\sigma_i^j)=1 \quad \text{if} \quad \sigma_{\min}<\sigma_i<\sigma_{\max}$$
$$=0 \quad \text{if} \quad \sigma_{\min}>\sigma_i \quad \text{or} \quad \sigma_i>\sigma_{\max}.$$

Thus, the valid samples of the secondary vortices within the time period of $(t_v^j-\Delta T_v^j/2)<t<(t_v^j+\Delta T_v^j/2)$ are acquired. The recovered streamwise energy of secondary vortices of n samples of primary vortex sheet, based on the alignment with t_v^j, is

$$\langle u_i^2\rangle=\sum_{j=n}(u_i^j)^2 g(\sigma_i^j)/n.$$

The recovered streamwise velocity of the primary vortex sheet, based on the alignment with t_v^j, is

$$\langle u_v\rangle=\sum_{j=n} u_v{}^j g(\sigma_i^j)/n.$$

The total number of ensembles of each threshold level was greater than 2000, or about 40–70 percent of total samples.

Some of the patches of secondary vortices within a cycle of the primary vortex sheet may contain up to three groups (Figs. 7(*a-c*)) per Strouhal shedding cycle. A group is defined as a packet of secondary vortices, which produces an increase, a maximum and a decrease in its streamwise velocity. Thus, separate ensemble averaging was carried out.

Pairing of successive secondary vortices also occurs in the near wake [2,12,10,11]. In the recovery of the paired secondary vortices, the same conditional sampling scheme was adopted, except that three threshold levels were based on the $\sigma_{i/2}$ at the subharmonic frequency $f_i/2$. The patches of pairing and paired secondary vortices within a cycle may also contain more than one group (Fig. 7*c*). Thus, the threshold level of the downstream vortex group was used for triggering. The recovered streamwise energy of paired secondary vortices of n samples of primary vortex sheet, based on the alignment with $t_v{}^j$, is

$$\langle u_{i/2}{}^2\rangle=\sum_{j=n}(u_{i/2}{}^j)^2 g(\sigma_{i/2}{}^j)/n.$$

Flow visualization was conducted in another wind tunnel of test section 0.56 m×0.56 m. The diameter of the cylinder was 88 mm, giving a blockage ratio of about 15 percent. The Reynolds number was 7.6×10^3. The aspect ratio was 4.2. The larger cylinder diameter was adopted to produce larger separated shear layers and secondary vortices. The frequency ratio f_i/f_v at $\mathrm{Re}=7.6\times10^3$ from flow visualization agrees with other results (Fig. 1). Tita-

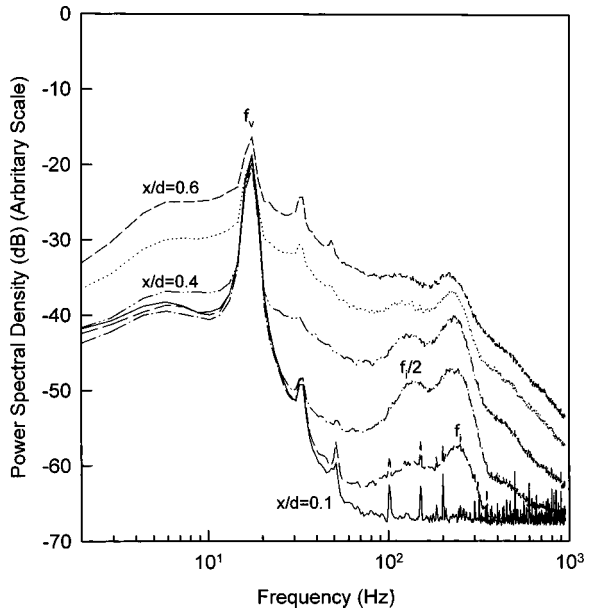

Fig. 4 Spectra of streamwise velocity at different streamwise locations. y/d=0.66. Re=1.2×10⁴. x/d: ——, 0.1; — — —, 0.2; - · - · -, 0.3; - · - · - · -, 0.4; · · · · ·, 0.5; - - - -, 0.6. Uncertainty: ±5 percent.

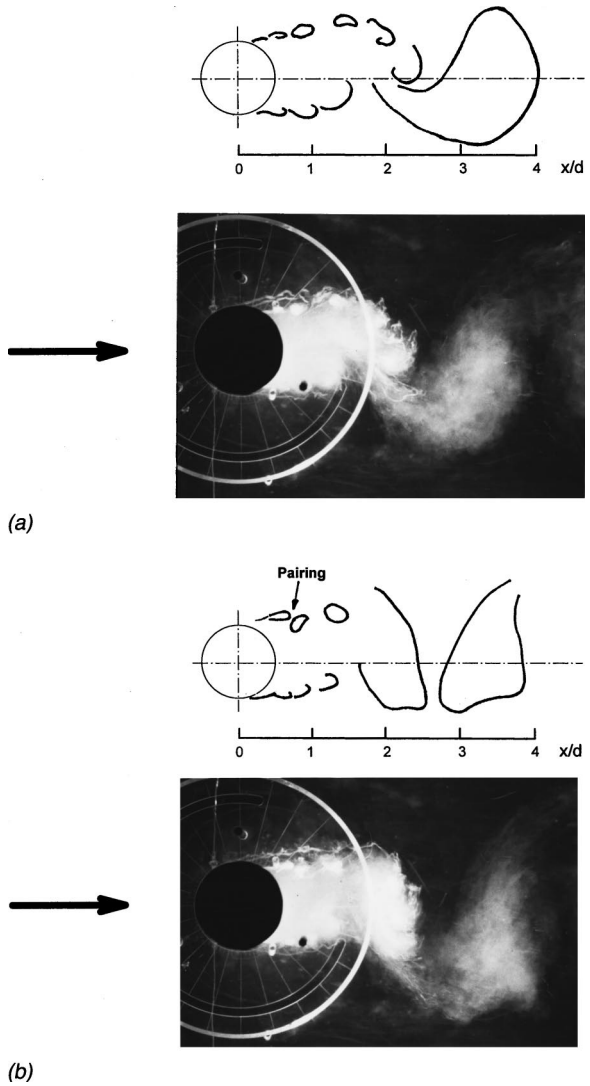

Fig. 5 Flow visualization (streamwise) of near wake. Re=7.6 $\times 10^3$. (*a*) Secondary vortices; (*b*) pairing secondary vortices. Different time instants.

nium tetrachloride ($TiCl_4$) was introduced near the front stagnation point. A 35 mm still camera with a motor drive operating at 3.3 frames per second was used to take the still photographs.

Based on different sets of measurements, the experimental uncertainty of the data was as follows: the mean velocity ± 3 percent, fluctuating velocity ± 5 percent and linear dimensions ± 0.1 mm. The uncertainty of the nondimensional groups, such as frequency ratio and recovered velocity ratios, is ± 5 percent.

Results and Discussion

Flow Visualization. The flow visualization pictures of the developing primary sheet, primary vortices and the secondary vortices at the mid span on the *x-y* plane at $\mathrm{Re}=7.6\times 10^3$ are shown in Figs. 5(*a*) and 5(*b*). T_iCl_4 was introduced at a point downstream of the front stagnation point. Due to parallax, the end of cylinder appears larger. The primary vortex sheet rolls up at $x/d\approx 2$ and 3. The shedding is of parallel mode [3]. In Fig. 5(*a*), there are successive secondary vortices on the upper part of the cylinder. They even appear on the roll of the primary vortex. The frequency ratio f_i/f_v, based on counting the vortices, agrees with the results of hot wires and others (Fig. 1). In Fig. 5(*b*), two successive secondary vortices at $x/d\approx 0.6$ undergo pairing, with the leading one convecting towards the low speed region of the wake. These pairings occur in the formation region and before the roll-up of the primary vortices. The above observation of the small-scale secondary vortices and their pairing in the very near wake agrees with those at nearly the same Reynolds number range of Kourta et al. [2], Unal and Rockwell [12], Braza et al. [10], and Lin et al. [11].

The spanwise flow visualization pictures are shown in Figs. 6(*a*)–6(*c*). In Fig. 6(*a*), the newly rolled-up secondary vortex at $x/d\approx 0.3$ and the three vortices further downstream are basically two dimensional. There are only slight spanwise modulations on the vortices. In Fig. 6(*b*), at another instant, the visualized newly rolled-up secondary vortex appears at $x/d\approx 0.2$. In the upper part of the span, the vortices convect downstream without pairing (Fig. 6(*b*)). In the lower part, the two most downstream vortices undergo pairing, forming a larger and more diffused vortex. At the spanwise locations marked 1, 2, 3, and 4 the succeeding upstream secondary vortices develop earlier. At ''4,'' the earlier development even occurs at $x/d\approx 0.2$. In the lower half, the formation of this part of the primary vortex (at $x/d\approx 1.5$) seems to be delayed. The delayed roll-up of the primary vortex sheet (at $x/d\approx 2$) is more obvious in Fig. 6(*c*), where there is a distinct difference in the positions of these two parts of the developing primary vortices. This illustrates the effect of the secondary vortices and their pairing on the large-scale vortices.

A closer look at another picture, Fig. 6(*d*), shows two secondary vortices pairing into a larger one at $x/d\approx 1$, marked ''1.'' The two succeeding upstream secondary vortices are more intense and larger in size than the adjacent ones. They also show more three dimensionality. The succeeding one farther upstream seems to appear earlier.

The alignment of the new cells of secondary vortices directly behind the older ones has been observed by Wei and Smith [5] and contributes to the feedback mechanism. The instantaneous PIV pictures of vorticity in the near wake of a circular cylinder at $\mathrm{Re}=1\times 10^4$ obtained by Lin et al. [11] show pairing of two secondary vortices at $x/d\approx 0.6$ and the succeeding vortex at $x/d\approx 0.25$ has higher vorticity than other secondary vortices. Thus, Fig. 6 seems to suggest that at $\mathrm{Re}=7.6\times 10^3$, in the early stage of the transition, the two-dimensional newly formed secondary vortices develop spanwise three dimensionality. Local pairing over even more than half the span of the vortices affects the roll-up of the primary vortex sheet. The alignment of the successive secondary vortex cells, at least for some of them, is due to the feedback mechanism associated with the disturbances of the pairing secondary vortices.

Conditional Sampling

Secondary Vortices. Figures 7(*a*)–7(*c*) show the time histories of the overall and filtered streamwise velocities at the center frequency f_v and f_i of the primary vortex sheet and secondary vortices at different Reynolds numbers. The time axes are normalized by the period of the primary vortex sheet ΔT_v at $1<\sigma_i<2$. The measurement locations were at the early state of the developing primary vortex sheet, before its roll-up and just after the formation of the secondary vortices. In the lower subcritical regime of $\mathrm{Re}=4.7\times 10^3$, the overall velocity fluctuations are dominated by the primary vortex sheet with small high frequency components (Fig. 7(*a*)). At $x/d=0.65$, $y/d=0.64$, the secondary vortices occur randomly throughout the time history of the vortex sheet. Further, the vortex sheet has the well-known low frequency modulation.

At $\mathrm{Re}=1.08\times 10^4$, the velocity fluctuations at $x/d=0.2$, $y/d=0.56$ show frequent bursts of intensive activity of the secondary vortices (Fig. 7(*b*)). These bursts of high frequency are clearly shown in the overall fluctuations. They occur near the troughs of the velocity of the vortex sheet, suggesting a coupling between the primary vortex sheet and the secondary vortices. They appear as

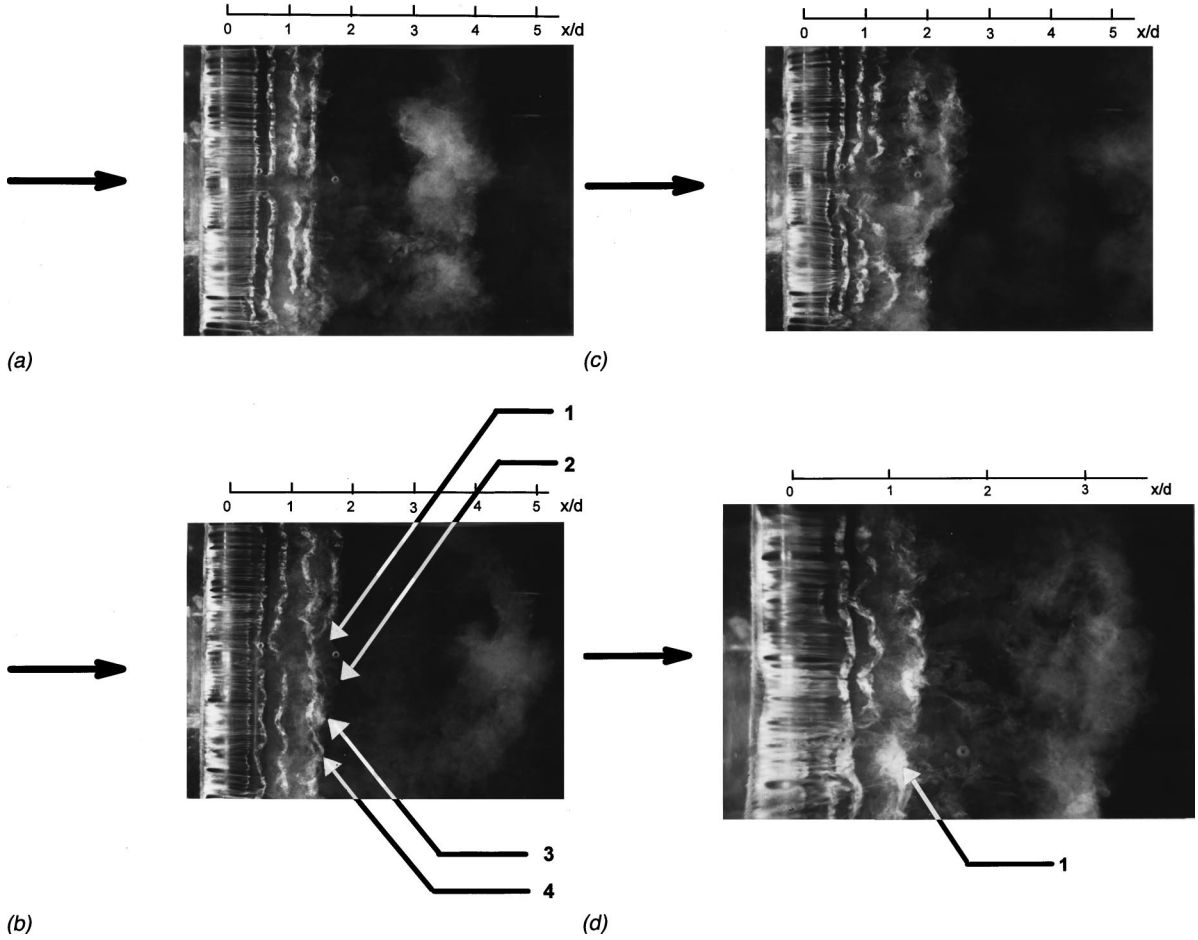

Fig. 6 Flow visualization (spanwise) of near wake. (*a*) Whole span (two dimensional secondary vortices); (*b*) whole span (local pairing on lower part); (*c*) whole span (local pairing on lower part, earlier roll-up of primary vortices); (*d*) close-up (local pairings). Different time instants.

packets of shear layer fluctuations, and are also observed at $x/d=1.0$, $y/d\approx 0.8$, within the formation region of the primary vortex at the Reynolds number range of 2.5×10^3 to 8×10^3 [3]. They are only found for parallel shedding and are more frequent at higher Reynolds number. At this Reynolds number of 1.08×10^4, Fig. 7(*b*) also shows the packets of secondary vortices within a cycle appearing in Group I of singular group and Group II of two groups (marked 1G and 2G, respectively). Further discussion on this issue will be presented later.

In the upper subcritical regime at $\mathrm{Re}=3.1\times10^4$, at $x/d=0.2$, $y/d=0.56$, there are more frequent occurrences of the secondary vortices (Fig. 7*c*). The coupling between the primary vortex sheet and the secondary vortices is still found. The secondary vortices also occur near the troughs of velocity of the vortex sheet. The modulation of the velocity of the vortex sheet seems to occur mainly on the negative side. At this Reynolds number, more secondary vortices appear in Group II (marked 2G), and Group III of three groups (marked 3G) per primary vortex cycle.

The energies of the primary vortex sheet, the secondary vortices, and the random components are shown in Fig. 8. The streamwise position for these measurements is at the end of the secondary vortex formation length. The random component u_r is obtained by subtracting the band-passed signals of u_v, its harmonic, u_i and its subharmonic from the overall u. The secondary vortices contain less than one percent of the overall fluctuating energy, while the random components are about ten percent.

The distributions of the secondary vortices within the three threshold levels are shown in Fig. 9. In the following sections, the high, medium and low-energy secondary vortices are referred to those recovered by the three respective threshold levels of $\sigma_i>3$, $2<\sigma_i<3$ and $1<\sigma_i<2$. The medium-energy vortices constitute only about 20 percent of the total number. The low-energy vortices are more frequent below the crossover Reynolds number of 7.5×10^3, and the high-energy ones are more frequent at higher Reynolds number. This crossover Reynolds number agrees with that of the peak fluctuating velocity $(u_i)_{\max}/u_i'$ (not shown here). At $\mathrm{Re}>2\times10^4$, the number of the high-energy secondary vortices is nearly constant.

In the flow visualization study of Kourta et al. [2], the subdivision of the lower and upper subcritical regimes is suggested to be at $\mathrm{Re}=1.6\times10^4$, below which the formation length of the primary vortices decreases monotonically with increasing Reynolds number. Based on the dramatic changes in the rms lift coefficient and in the primary vortex frequency bandwidth, Norberg [1] suggested the subdivision occurred at about $\mathrm{Re}=5\times10^3$. A closer look at the primary vortex formation length distribution [1,22,23,24] indicates that the end of the monotonic decrease of the formation length occurs near $\mathrm{Re}=7.5\times10^3$. The variation of the mean base pressure coefficient C_{pb} with Reynolds number also indicates a change of the slope at about $\mathrm{Re}=7\times10^3$, and then reaches a nearly constant value at about 1.8×10^4 [1]. The C_{pb} also shows a plateau in the distribution at $7\times10^3<\mathrm{Re}<9\times10^3$ for cylinder aspect ratios greater than 15 [25]. The C_{pb} of the present study (not shown here) also shows a plateau at $6\times10^3<\mathrm{Re}<8\times10^3$ and constant value at $\mathrm{Re}>2\times10^4$, agreeing with those of Norberg

[25]. The intermittency factor of the shear layer fluctuations at $x/d=1.0$ approaches unity at $\mathrm{Re}\approx 7\times 10^3$ [3]. The variation of the relative bandwidth $\Delta f_v/f_v$ of the primary vortex peak of Norberg [1] also indicates a distinct peak at about the same Reynolds number of 7.4×10^3, agreeing with that of the present study (-3 db from the spectral peak) (Fig. 10). The present bandwidth reaches a near constant value at $\mathrm{Re}\approx 2\times 10^4$. The present bandwidths $\Delta f_i/f_i$ of the secondary vortex peak (-3db from the spectral peak) and those of Norberg [1] and Prasad and Williamson [3] are also shown. At $\mathrm{Re}=7.5\times 10^3$, the $\Delta f_i/f_i$ starts to increase sharply.

As shown in Fig. 7, there are up to three groups of secondary vortices within a cycle of the primary vortex sheet. The distributions of the high-energy vortices ($\sigma_i>3$) are shown in Fig. 11. The Group I secondary vortices have the maximum number in the lower subcritical regime, a lower peak at $\mathrm{Re}=7.5\times 10^3$, then decrease rapidly with the increase in Reynolds number. The Group II vortices increase in number, more frequent than the Group I ones at $\mathrm{Re}\approx 1.2\times 10^4$, and reach a maximum at $\mathrm{Re}\approx 1.5\times 10^4$. The Group III vortices increase rapidly from near zero, then reach a local maximum at $\mathrm{Re}\approx 1.5\times 10^4$ and become the most frequent configuration in the upper subcritical regime. Thus, the increasing dominance of the high-energy secondary vortices during the transition is associated with the Group I secondary vortices in the

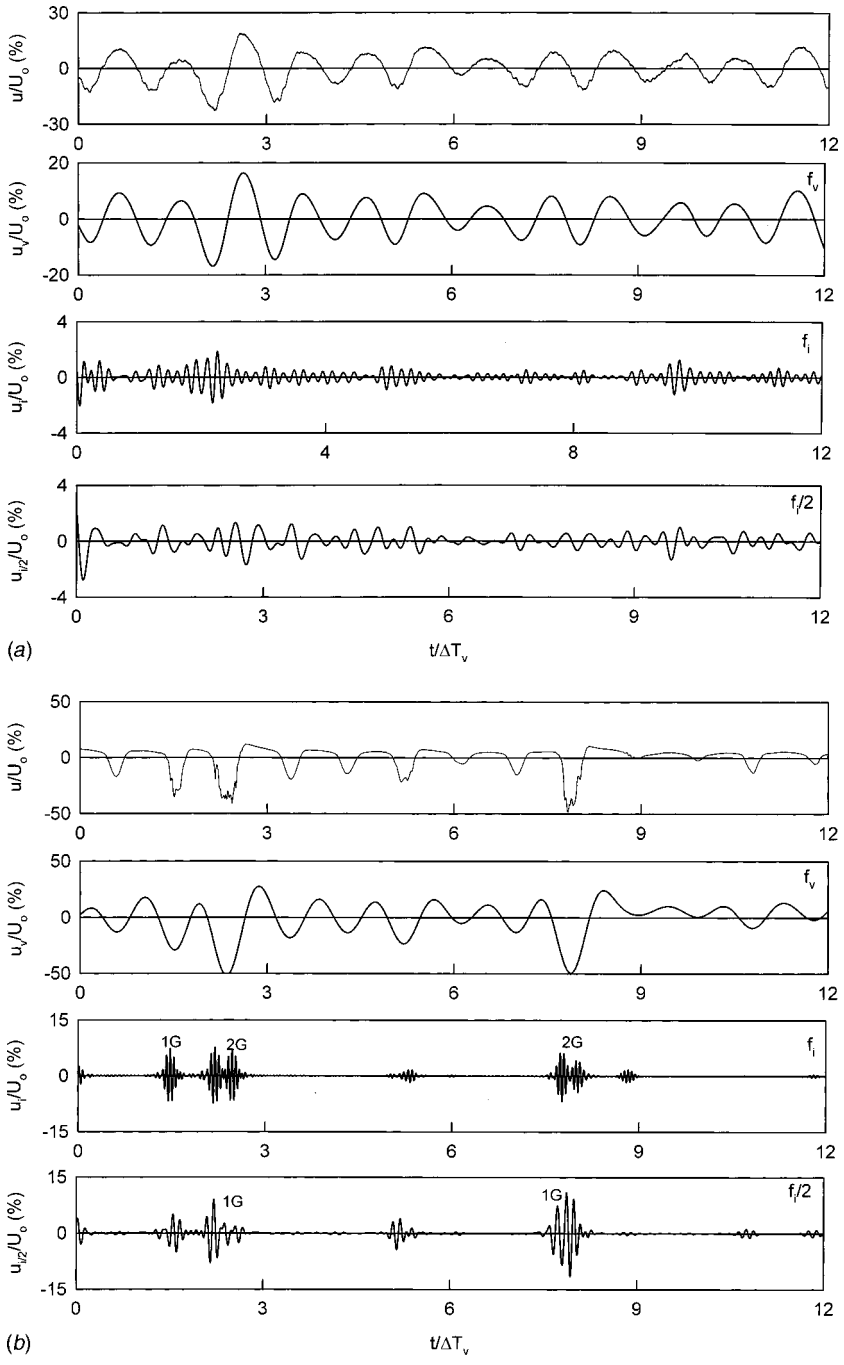

Fig. 7 Time histories of velocity of primary vortex sheet, secondary vortices and paired vortices. (*a*) $\mathrm{Re}=4.7\times 10^3$; (*b*) $\mathrm{Re}=1.08\times 10^4$; (*c*) $\mathrm{Re}=3.1\times 10^4$. 1G: Group I type; 2G: Group II type; 3G: Group III type. Uncertainty: ±5 percent.

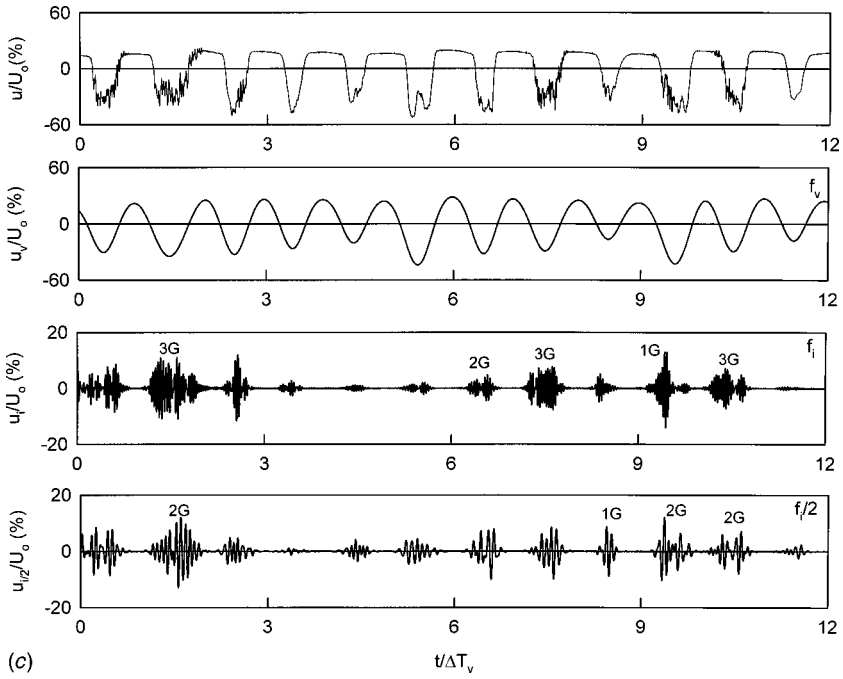

Fig. 7 (*Continued*).

early stage and the Groups II and III vortices in the later stage. Further discussion on the higher number group vortices will be presented later.

The above results suggest that transition starts at $\mathrm{Re}\approx 7\times 10^3$, at which the high-energy secondary vortices, basically of Group I type, increase sharply both in number and energy. At $\mathrm{Re}\approx 1.5\times 10^4$, there also seems to be another transition with the Group II high-energy secondary vortices being the most frequent. This Reynolds number also indicates a local maximum in the $(u_i)_{\max}/u_i$ distribution (not shown here). This explains the two different transition Reynolds numbers of 5×10^3 of Norberg [1] and of 1.6×10^4 of Kourta et al. [2]. This may indicate a subregime in which the low- and high-energy secondary vortices in different groups exchange their role. In this respect, it is named the ''upper transition.''

Based on the time histories of Fig. 7 and others, the ensemble-averaged waveforms of the three threshold levels of the primary vortex sheet and secondary vortices from conditional sampling were obtained. Figure 12 shows the conditionally sampled time series for $\sigma_i>3$ at the Reynolds numbers of 4.7×10^3, 7.5×10^3 and 3.1×10^4. The flow is toward the right, $-\tau$ of the time delay time frame. In the lower subcritical regime at $\mathrm{Re}=4.7\times 10^3$, the recovered $\langle u_v\rangle$ profile of the primary vortex sheet indicates a lower peak level for the downstream one than that of the upstream

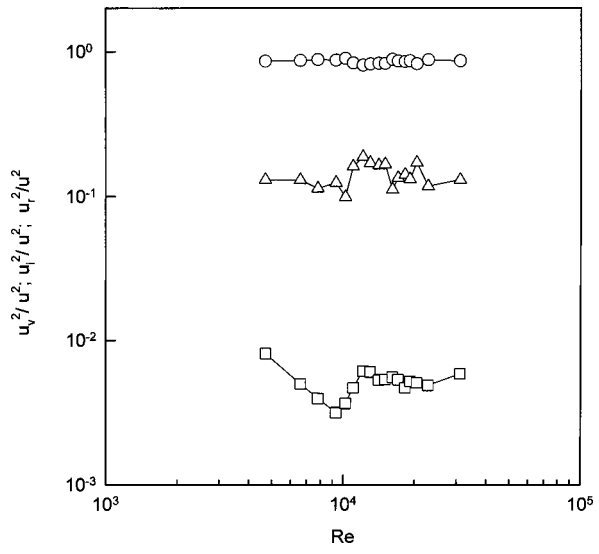

Fig. 8 Distributions of energies of primary vortex sheet, secondary vortices and random components. ○, primary vortex sheet; □, secondary vortices; △, random components. Uncertainty: ±5 percent.

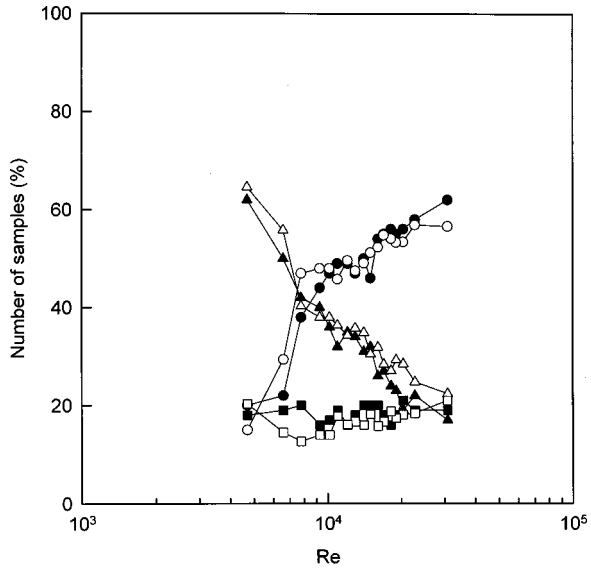

Fig. 9 Variations of numbers of samples of secondary and paired vortices at different threshold levels. △, $1<\sigma_i<2$; □, $2<\sigma_i<3$; ○, $\sigma_i>3$. Open symbol: secondary vortices (f_i); solid: paired vortices ($f_{i/2}$). Uncertainty: ±3 percent.

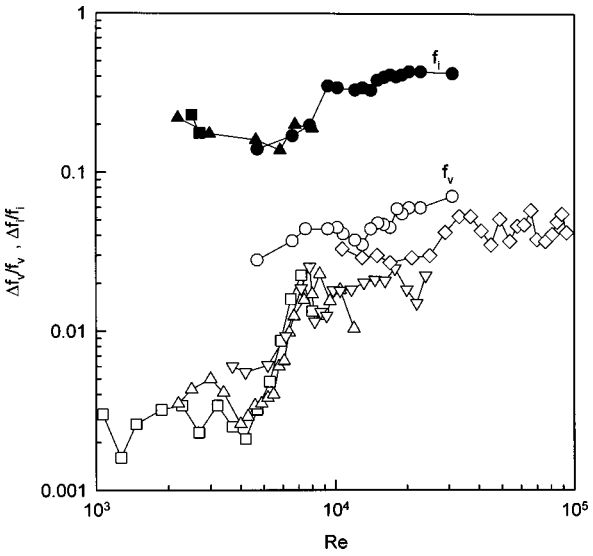

Fig. 10 Variations of bandwidths of primary vortex sheet and secondary vortices. $\Delta f_v/f_v$: ○, present study; Norberg [1]; □, d=3.99 mm; △, d=5.98 mm; ▽, d=9.99 mm; ◇, d=41 mm. $\Delta f_i/f_i$: ●, present study; ▲, Norberg [1]; ■, Prasad and Williamson [3]. Uncertainty: ±5 percent.

one (Fig. 12(*a*)). The recovered secondary vortices spread across the whole primary vortex sheet. The location of the peak recovered $\langle u_i^2 \rangle_{\max}$ depends on the threshold level and is found upstream of the $\langle u_v \rangle_{\min}$ position. At the transition $\mathrm{Re}=7.5\times10^3$, similar phenomena are found, except that the recovered energy of the secondary vortices is more concentrated at or near the trough of the primary vortex sheet (Fig. 12(*b*)), confirming the coupling observed in the time traces. In the upper subcritical regime, at $\mathrm{Re}=3.1\times10^4$, the energy of the secondary vortices is also more concentrated near the trough (Fig. 12(*c*)).

Based on the definitions shown in Fig. 13, the following sections will try to study the interaction between the primary vortex sheet and the secondary vortices. The recovered downstream ve-

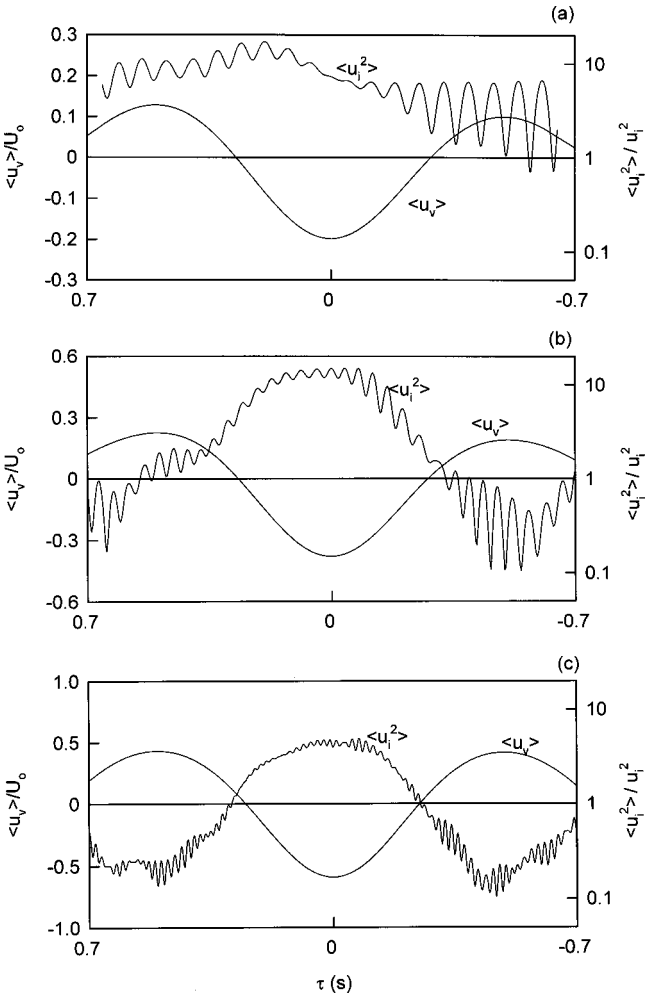

Fig. 12 Recovered time histories of velocity of primary vortex sheet and secondary vortices at different Reynolds numbers ($\sigma_i>3$). (*a*) $\mathrm{Re}=4.7\times10^3$; (*b*) $\mathrm{Re}=7.5\times10^3$; (*c*) $\mathrm{Re}=3.1\times10^4$. Uncertainty: ±5 percent.

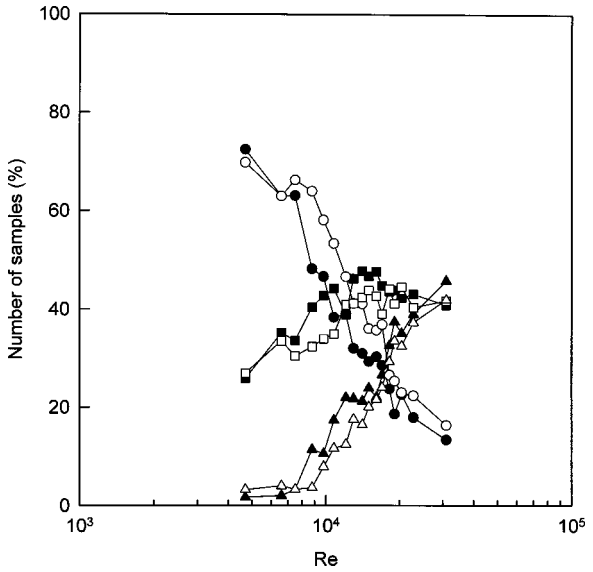

Fig. 11 Variations of numbers of samples of secondary and paired vortices with Reynolds number ($\sigma_i>3$). ○, Group I; □, Group II; △, Group III. Open symbol: secondary vortices (f_i); solid: paired vortices ($f_{i/2}$). Uncertainty: ±3 percent.

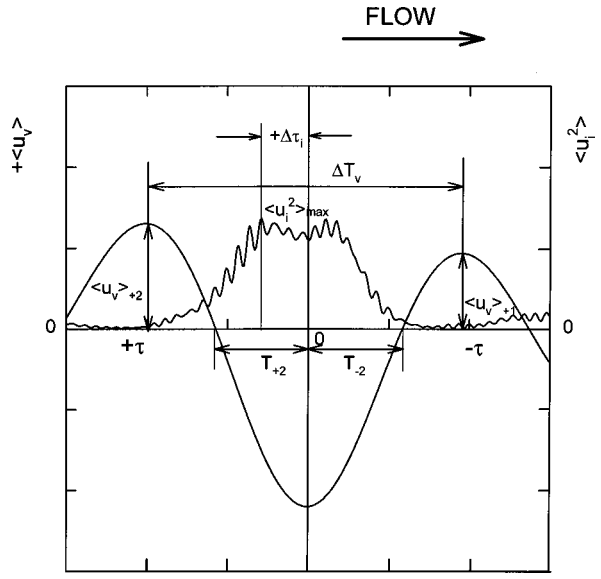

Fig. 13 Definitions of recovered time histories.

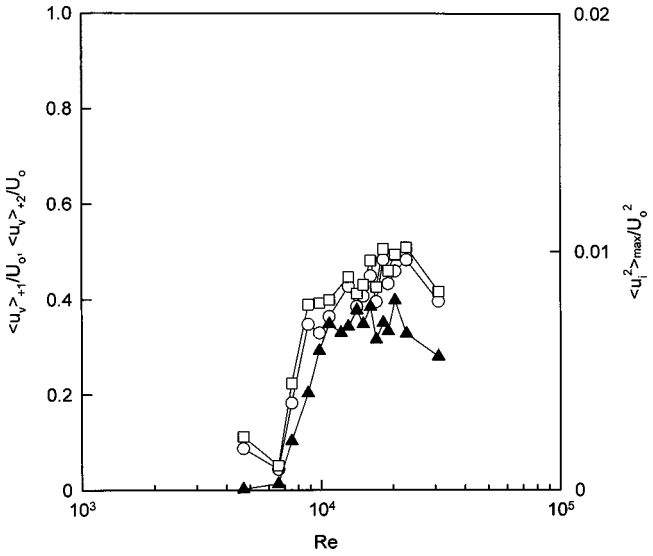

Fig. 14 Variations of recovered velocities of primary vortex sheet and secondary vortices with Reynolds number ($\sigma_i>3$). ○, $\langle u_v\rangle_{+1}$; □, $\langle u_v\rangle_{+2}$; ▲, $\langle u_i^2\rangle$. Uncertainty: ±5 percent.

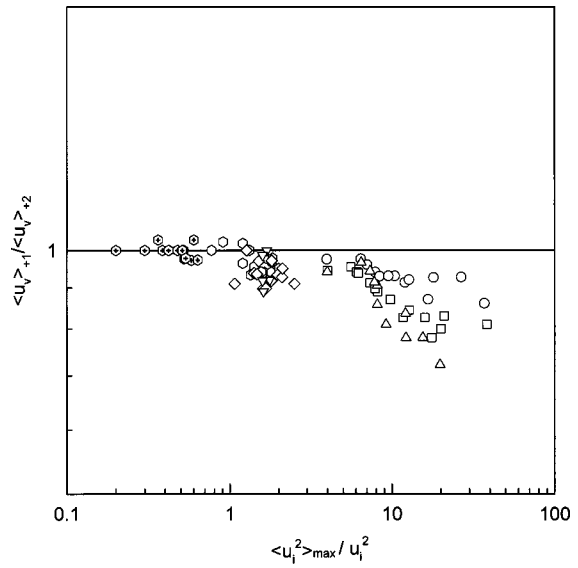

Fig. 16 Variations of recovered velocity ratios of primary vortex sheet. $1<\sigma_i<2$: ⊕, Group I; $2<\sigma_i<3$: ◊, Group I; ◇, Group II; ∇, Group III; $\sigma_i>3$: ○, Group I; □, Group II; △, Group III. Uncertainty: ±5 percent.

locity $\langle u_v\rangle_{+1}/U_o$ and upstream velocity $\langle u_v\rangle_{+2}/U_o$ of the primary vortex sheet and the maximum recovered energy $\langle u_i^2\rangle_{max}/U_o^2$ of the high-energy secondary vortices ($\sigma_i>3$) are shown in Fig. 14. The three distributions show a rapid increase at $Re=7\times10^3$, until the maximum occurs at $Re\approx2\times10^4$, then the distributions decrease with further increase in Reynolds number. Coupled with the results shown above, the transition seems to end at $Re\approx2\times10^4$.

The effect of the threshold level on the maximum recovered energy $\langle u_i^2\rangle_{max}/u_i^2$ of the secondary vortices is shown in Fig. 15. The low- and medium-energy vortices vary only slightly with Reynolds number. The high-energy vortices, which are one order of magnitude higher than those of weaker vortices, increase in energy within the lower subcritical regime until $Re_d=7\times10^3$.

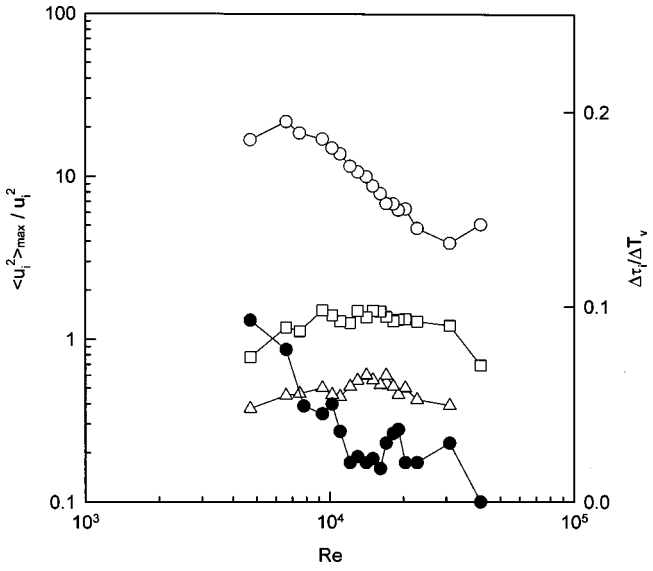

Fig. 15 Variations of maximum recovered energies of secondary vortices at different threshold levels and phase shift. $\langle u_i^2\rangle_{max}/u_i^2$: △, $1<\sigma_i<2$; □, $2<\sigma_i<3$; ○, $\sigma_i>3$; $\Delta\tau_i/\Delta T_v$: ●, $\tau_i>3$. Uncertainty: $\langle u_i^2\rangle_{max}/u_i^2$: ±5 percent; $\Delta\tau_i/\Delta\tau_v$: ±5 percent.

Then the energy decreases with increasing Reynolds number until $Re_d=3\times10^4$ in the upper subcritical regime. This phenomenon confirms the dominant role of these high-energy vortices, especially in the early stage of the transition.

The phase shift $\Delta\tau_i/\Delta T_v$ of the recovered peak of the high-energy secondary vortices is also shown in Fig. 15. The phase shift $\Delta\tau_i$ decreases with increasing Reynolds number in the lower subcritical regime and at transition. In the upper subcritical regime at $Re>2\times10^4$, the phase sift is near zero.

The ratio $\langle u_v\rangle_{+1}/\langle u_v\rangle_{+2}$ may indicate the effect of the secondary vortices on the development of the primary vortex sheet. Figure 16 shows the ratio with the maximum recovered energy of the secondary vortices, including those of the three groups of medium- and high-energy secondary vortices. Because the energy of the low-energy groups ($1<\sigma_i<2$) is two orders of magnitude lower, it is presented as a single group. For others, the peak of the maxima is used. At $\langle u_i^2\rangle_{max}/u_i^2<1$, the waveform of the primary vortex sheet is not affected, meaning that the low-energy secondary vortices do not affect the development of vortex sheet. At $\langle u_i^2\rangle_{max}/u_i^2>1$, the ratio is less than unity. The higher the energy of the secondary vortices, the more significant is the effect on the development of the primary vortex sheet. Further, the higher the number of the group of the vortices, the greater is the effect. Thus, the presence of different groups of small-scale vortices affects the development of the large-scale vortex sheet.

As the primary vortex sheet is not affected by the low-energy vortices, the recovered upstream velocity ratio $[\langle u_v\rangle_{+2}]_{\sigma_i>3}/[\langle u_v\rangle_{+2}]_{1<\sigma_i<2}$ greater than unity at $\langle u_i^2\rangle_{max}/u_i^2>7$ indicates that the high-energy secondary vortices amplify the upstream $[\langle u_v\rangle_{+2}]_{\sigma_i>3}$ of the primary vortex sheet (not shown here). The downstream $[\langle u_v\rangle_{+1}]_{\sigma_i>3}/[\langle u_v\rangle_{+2}]_{1<\sigma_i<2}$ of unity implies the vortex sheet is not affected. In addition, the higher the energy of the secondary vortices, the greater is the amplification. This phenomenon is similar to the findings of Peterka and Richardson [19] for acoustic excitation on the separated shear layer of a smooth cylinder at the initial secondary vortex frequency. The primary vortex is amplified and the formation length is reduced. This increase in the secondary vortex strength increases the fluid entrainment into the primary vortex sheet, and thus, the amplification.

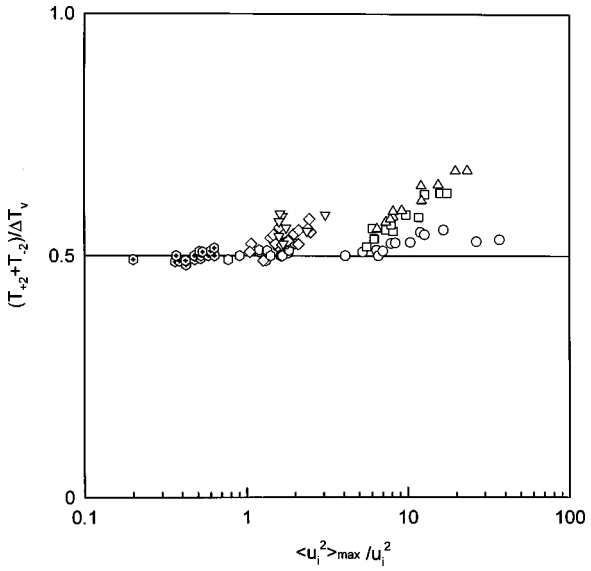

Fig. 17 Variations of recovered periods of primary vortex sheet. Symbols as in Fig. 14. Uncertainty: ±5 percent.

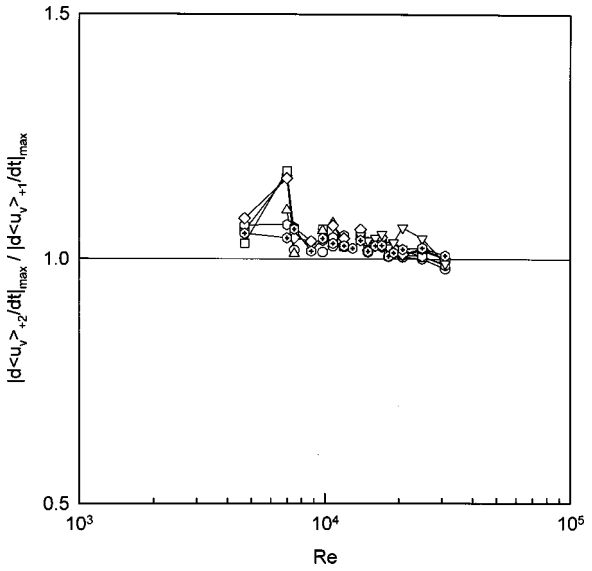

Fig. 18 Variations of linear strain rate ratios with Reynolds number. Symbols as in Fig. 14. Uncertainty: ±5 percent.

The effect of the secondary vortices on the period of the trough $(T_{-2}+T_{+2})/\Delta T_v$ is shown in Fig. 17. The trend indicates that at $\langle u_i^2\rangle_{\max}/u_i^2>1$, the waveform is affected. The higher the energy and number group, the greater is the effect, which also confirms that the development of the primary vortex sheet is affected by the more intense secondary vortices.

The instability associated with the vortex layer between the large-scale transverse vortex structures is unstable to the strain field induced by the transverse vortices [26,27]. The Kelvin-Helmholtz instability of the separated shear layer may then be affected by the strain field associated with the primary vortex sheet. According to Zaman and Hussain [28], $du=U_c dt$ and for a two-dimensional vortex sheet near the separation point with near constant convection velocity U_c, the rate of linear strain in the streamwise direction $\partial u/\partial x$ is proportional to $\partial u/\partial t$ [29]. Thus, the ratios of the upstream and downstream maximum absolute linear strain rates, $|d\langle u_v\rangle_{+2}/dt|_{\max}/|d\langle u_v\rangle_{+1}/dt|_{\max}$, of the primary vortex sheet at the three threshold levels and groups are shown in Fig. 18. The strain rate ratio is greater than unity with the maximum at $\mathrm{Re}\approx 7\times 10^3$, indicating a higher strain rate on the upstream vortex sheet at the start of transition. The maximum is due to the Groups I and II high-energy vortices and Group II medium-energy vortices. This maximum also coincides with the Reynolds number of the recovered maximum energy $\langle u_i^2\rangle_{\max}/u_i^2$ of the high-energy secondary vortices (Fig. 15), indicating their relationship. In the upper subcritical regime, the two strain rates are nearly the same.

The recovered peak energy of the secondary vortices depends also on the linear strain rate of the primary vortex sheet. The variations of $\langle u_i\rangle_{\max}/u_i^2$ of the three groups at $\sigma_i>3$ with the ratio of the maximum absolute linear strain rates $|d\langle u_v\rangle_{+2}/dt|_{\max,\sigma_i>3}/|d\langle u_v\rangle_{+2}/dt|_{\max,1<\sigma_i<2}$ show that the increase in the energy of the secondary vortices is associated with higher strain rate (Fig. 19). Those of Group I have higher energy than those of higher-number groups. In Fig. 20, the phase shifts $\Delta\tau_i/\Delta T_v$ of the three groups of high-energy secondary vortices vary with the ratio of the upstream and downstream maximum absolute linear strain rates, $|d\langle u_v\rangle_{+2}/dt|_{\max,\sigma_i>3}/|d\langle u_v\rangle_{+1}/dt|_{\max,\sigma_i>3}$ of the primary vortex sheet. The results imply that the respective secondary vortices tend to shift more upstream or downstream with higher strain rate.

The above results establish the relationship between the linear strain rate of the primary vortex sheet and the energy of the secondary vortices. As shown by the velocity time trace of each group (Fig. 7), one would expect the development and decay of secondary vortices. Based on Hussain and Hayakawa [30], the fluctuating normal energy production $\langle u_i^2\rangle d\langle u_v\rangle/dt$ of the secondary vortices at the transition $\mathrm{Re}=1.08\times 10^4$ indicates the negative production on the downstream part and positive production on the upstream part of the primary vortex sheet (not shown here). The intense energy is transferred from the primary vortex sheet to the developing high-energy secondary vortices soon after the latter formation. The loss of energy further downstream results in their decay.

The variations of the maximum fluctuating normal energy production of the secondary vortices are shown in Fig. 21. Because the energy of the medium- and low-energy vortices are low compared with those of the high-energy ones, they are not separated

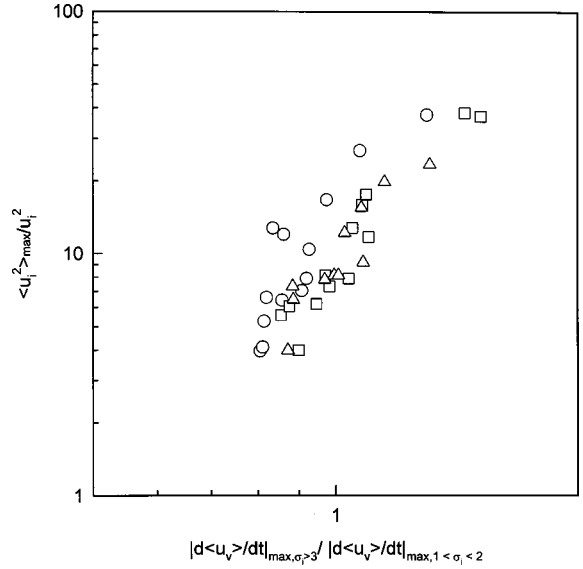

Fig. 19 Variations of maximum recovered energy of secondary vortices with linear strain rate ratio ($\sigma_i>3$). ○, Group I; □, Group II; △, Group III. Uncertainty: ±5 percent.

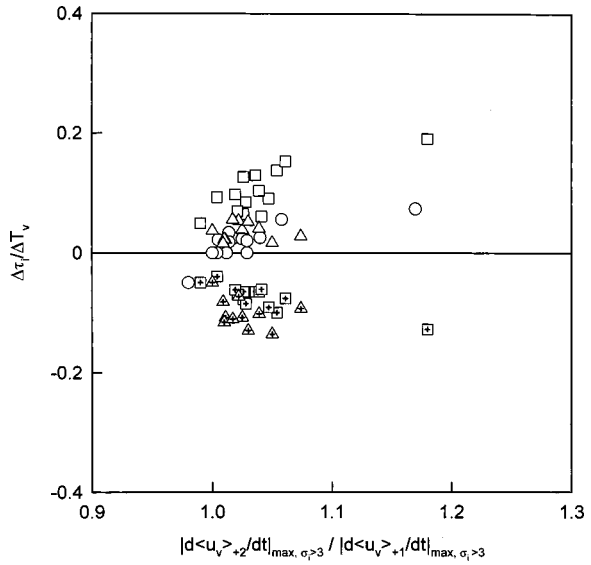

Fig. 20 Variations of phase difference of peaks of secondary vortices with ratio of upstream and downstream linear strain rates ($\sigma_i>3$). Upstream peak: ○, Group I; □, Group II; △, Group III. Downstream peak: ⊞, Group II; ⧋, Group III. Uncertainty: ±5 percent.

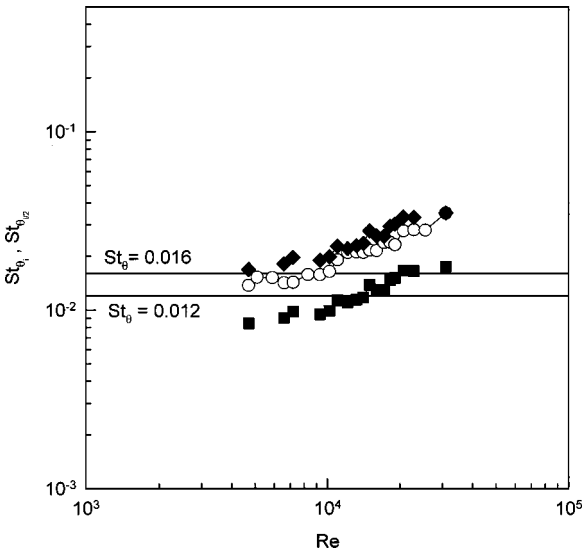

Fig. 22 Strouhal numbers of secondary vortices and paired vortices. ○, Secondary vortices (f_i); ■, paired vortices ($f_{i/2}$); ◆, subharmonic forcing at mode II [41]. Uncertainty: ±5 percent.

into the three groups. The significantly higher energy production of the Groups II and III vortices suggests that higher number group secondary vortices are responsible for the transition.

The above results, in the early part of the formation region of the primary vortices just after the formation of the secondary vortices, establish a transition at $7\times10^3<\mathrm{Re}<2\times10^4$, in which the secondary vortices play an important role. At this transition regime, the primary vortex shedding is of parallel mode [3]. The flow visualization pictures obtained at $\mathrm{Re}=7.6\times10^3$ show the parallel mode (Fig. 6(*a*)). The first secondary vortices at $x/d\approx0.2$ are two dimensional. The present model of the transition mechanism is due mainly to an increasing number of the high-energy secondary vortices of the Group I type and then Group II type in the initial transition. Their rapid build-up to the maximum energy during the earlier stage of transition at $7\times10^3<\mathrm{Re}<1\times10^4$ is associated with a rapid increase in the fluctuating normal energy production of first Group I and then Group II high-energy secondary vortices. This energy production is affected by the high strain rate of the primary vortex sheet. There is significant mutual interference between them, before the latter rolls up into vortices. The interference is due to the influence of the high-energy secondary vortices on the development of the primary vortex sheet and its strain rate. The higher the energy of these small-scale vortices, the higher is the effect. It involves the amplification of the velocity of the upstream primary vortex sheet, which in turn induces rapid energy production of the high-energy secondary vortices. However, the effect of the primary vortex sheet and its associated strain rate on the small-scale secondary vortices seems to be greater. The present observation confirms the effect of weak low-frequency forcing on the formation of higher frequency instability [31,32]. The presence of a heavy forcing effect of the primary vortices on the region of initial disturbance growth results in more rapid secondary vortex evolution and deformation [9]. In the later stage of transition at $1\times10^4<\mathrm{Re}<2\times10^4$, the secondary vortices are first Group II and then of Group III. The latter becomes increasingly dominant until the upper subcritical regime.

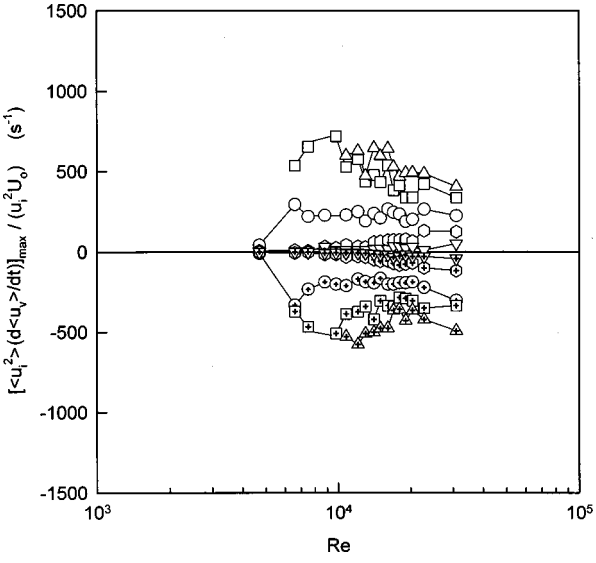

Fig. 21 Variations of maximum recovered fluctuating normal energy production of secondary vortices. Upstream peak: $\sigma_i>3$: ○, Group I; □, Group II; △, Group III; ◊, $2<\sigma_i<3$; ▽, $1<\sigma_i<2$. Downstream peak: $\sigma_i>3$: ⊕, Group I; ⊞, Group II; ⧋, Group III; ⧫, $2<\sigma_i<3$; ⧩, $1<\sigma_i<2$. Uncertainty: ±5 percent.

The above results only present the mutual interference of the high-energy secondary vortices and the primary vortex sheet. The findings do not indicate the reason for the more rapid development of these small-scale vortices in the earlier stage of transition, before the effect of mutual interference becomes significant. The Strouhal numbers $\mathrm{St}_{\theta i}(f_i\theta_i/U_o)$ of the secondary vortices, based on the momentum thickness θ_i of the boundary layer just after separation, are shown in Fig. 22. For a mixing layer, the most amplified wave has a Strouhal number St_θ, based on the average velocity, of 0.032 [33,6]. For the jet instability, the roll-up frequency of an exiting shear layer is $\mathrm{St}_\theta=0.012$ [34,35]. It is lower than the acoustically excited St_θ of 0.016 [36,37]. It is interesting to find that the $\mathrm{St}_{\theta i}$ of the secondary vortices at $\mathrm{Re}<1\times10^4$ lies between the values for these most amplified modes. This means that in the early stage of transition, the disturbances of the secondary vortices themselves excite the Kelvin-Helmholtz instability of the separated shear layer at the most amplified mode. This results in the rapid increase, both in number and energy, of the Group I secondary vortices (Figs. 9, 11, and 15). The disturbances produced by these vortices further excite the shear layer and lead

to the initiation of transition. Coupled with the mutual interference, this may result in the appearance and the increase in the number and maximum recovered fluctuating normal energy production of the Group II secondary vortices at $7.5\times10^3<\mathrm{Re}<1\times10^4$ (Figs. 11 and 16). The energy production of the Group II vortices is about three times higher than that of the Group I vortices. It seems that the mechanism of this model is that Group I secondary vortices at the most amplified mode excite the separated shear layer. The mutual interference with the primary vortex sheet amplifies the secondary vortices, which in turn affects the vortex sheet. For two successive vortices of the same direction of rotation and convection, their self induced velocity and the velocity resulting from mutual induction depend on circulation [38–40]. Thus, with mutual interference, the higher vorticities of the more intense secondary vortices favor pairing. This explains the rapid increase of only the high energy individual and paired secondary vortices ($\sigma_i>3$) at $\mathrm{Re}>7\times10^3$ (Figs. 9 and 15).

Pairing of Secondary Vortices. Local pairings of successive secondary vortices are shown in the flow visualization pictures, (Figs. 5 and 6). The spectra of the streamwise velocity fluctuations indicate a peak associated with the pairing at the subharmonic frequency $f_i/2$ (Fig. 4). The filtered (one third octave) time traces at this frequency are also shown in Figs. 7(*a*)–7(*c*). In the lower subcritical regime at $\mathrm{Re}=4.7\times10^3$, there is no coupling between the subharmonic component with those of f_i and f_v components (Fig. 7(*a*)). At the transition $\mathrm{Re}=1.08\times10^4$, the subharmonic component is coupled with the f_i and f_v components (Fig. 7(*b*)). The secondary vortices of Groups I and II at f_i seem to have phase shift relative to the subharmonic component. In the upper subcritical regime at $\mathrm{Re}=3.1\times10^4$, the subharmonic component also appears in groups, corresponding to those of f_i (Fig. 7*c*). These phenomena occurring at the transition and upper subcritical regime indicate a definite relationship between the subharmonic and f_i components.

Based on the conditional sampling technique, the numbers of the high-energy paired vortices ($\sigma_{i/2}>3$) within the three groups at $\Delta x/d=0.1$, downstream of the formation length of the secondary vortices (Fig. 2), are shown in Fig. 11. At this streamwise position more paired vortices are detected. The numbers of the Group I secondary (at $\Delta x/d=0$) and paired vortices decrease from the maximum in the lower subcritical regime to the lowest in the upper subcritical regime. This trend is the reverse for both types of vortices in Groups II and III. For the paired vortices, the rate of increase is the highest for the Group II ones, while the Group III rate of increase is small. The above phenomena imply that during transition the decrease in the number of Group I high-energy paired vortices is associated with the increase in the number of vortices of Group II type, suggesting that their interchanging role is an important factor for transition.

The maximum recovered energies $\langle u_{i/2}{}^2\rangle_{\max}/u_{i/2}{}^2$ of the three Groups of high-energy paired vortices ($\sigma_{i/2}>3$) at $\Delta x/d=0.1$ are shown in Fig. 23. Those of the secondary vortices in the Group III at $\Delta x/d=0$, just after the roll-up, are also shown. For the higher-number groups, in order to simplify the presentation, the peak of the maxima within the batch is adopted. Because the energies at the lower two threshold levels are much lower, they are not presented. Those of the paired vortices have the same trend as those of the secondary vortices, with the former higher in energy. Both reach the peak energy at $\mathrm{Re}=7\times10^3$.

The induction of the succeeding secondary vortices, as suggested by Wei and Smith [5] and by the present flow visualization pictures (Fig. 6(*b-d*)), may be due to the feedback mechanism of the disturbances associated with the pairing vortices. Based on the momentum thickness of the boundary layer just after separation, the Strouhal numbers $\mathrm{St}_{\theta i/2}$ of the paired vortices are shown in Fig. 22. Based also on the ratio of the response and subharmonic forcing frequencies of mode II [41], the Strouhal numbers $\mathrm{St}_{\theta ip}$ of the succeeding secondary vortices induced by the feedback

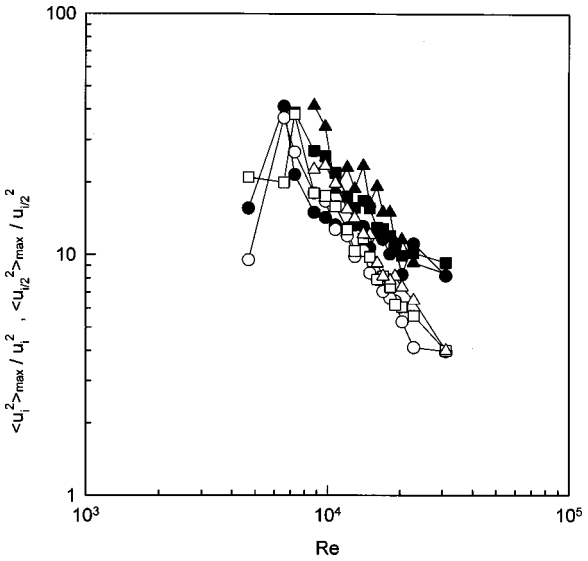

Fig. 23 Variations of maximum recovered energies ($\sigma_i>3$). Secondary vortices $\langle u_i^2\rangle$: ○, Group I; □, Group II; △, Group III. Paired vortices $\langle u_{i/2}{}^2\rangle$: ●, Group I; ■, Group II; ▲, Group III. Uncertainty: ±5 percent.

mechanism are also shown. At $\mathrm{Re}<1\times10^4$, the $\mathrm{St}_{\theta i/2}$ of the paired vortices is different from the St_θ of the most amplified mode. However, the $\mathrm{St}_{\theta ip}$ of subharmonic forcing of mode II is near that of $\mathrm{St}_\theta=0.016$ [36,37]. It suggests the subharmonic forcing of the rapidly increasing high-energy paired vortices (Figs. 9 and 23) also contributes to the excitation of the separated shear layer. In this early stage of transition, the Group I paired vortices are the most frequent. Thus, both the secondary vortices and the Group I paired vortices are responsible for the transition. This confirms the visual observation of intense secondary vortices and intense succeeding secondary vortices, due to the feedback of the disturbances associated with pairing at $\mathrm{Re}=7.6\times10^3$ in Fig. 6 and the visualization of Wei and Smith [5] and Lin et al. [11].

In the later stage of transition and in the upper subcritical regime of $1\times10^4<\mathrm{Re}<3\times10^4$, the $\mathrm{St}_{\theta i}$ of the secondary vortices are above those of the most amplified wave. Coupled with their decreasing number, their contribution to the excitation diminishes. For the paired vortices, however, the $\mathrm{St}_{\theta i/2}$ of the paired vortices are near and within the Strouhal number range of the most amplified mode (Fig. 22). In this regime, the excitation of the separated shear layer is then due to the disturbances associated with the high-energy paired vortices (Figs. 9 and 23). These high-energy paired vortices are mainly of the Group I type (Fig. 11), even though their number decreases with the increase in Reynolds number. In the latter part of the regime, the Group II paired vortices become increasingly more frequent than those of Group I vortices (Fig. 11). In the upper subcritical regime, at $\mathrm{Re}=3\times10^4$ the secondary vortices associated with the Group III paired vortices are the most frequent.

The above observation is based on the peak frequencies of the small-scale vortices. As shown in Fig. 10 of the bandwidth of the secondary vortices and in Figs. 12 and 15 of the broad peak of the recovered secondary vortices, one would also expect the excitation at the transition may be due to these three types of disturbances.

Conclusion

In the present experiment in the formation region of the large-scale primary vortices within the Reynolds number range of $4\times10^3<\mathrm{Re}<3\times10^4$, an upper transition is established at $7\times10^3<\mathrm{Re}<2\times10^4$. Based on a new conditional sampling technique,

the high-energy secondary vortices are shown to play an important role in the transition from the lower to upper subcritical regime. These high-energy vortices appear in packets, or groups, per Strouhal cycle. The Group I vortices are dominant in the lower subcritical regime and are progressively replaced by the Group II vortices in the early stage of transition. In the later stage of transition, the Group III vortices progressively replace the Group II ones. In the upper subcritical regime, the Group III ones are dominant.

In the formation region of the primary vortices, pairings of the secondary vortices are also found. Due to the self and mutual induction, the pairings are related to the more intense secondary vortices. These paired vortices also appear in three groups. The present study observes the feedback mechanism of the disturbances associated with the paired vortices and their excitation of the Kelvin-Helmholtz instability. These disturbances produce the more intense successive secondary vortices.

The present model of the transition mechanism is based on the excitation of the separated shear layer by the disturbances associated with the secondary vortices and their pairings at the most amplified mode. Near the end of the lower subcritical regime and in the early stage of transition, the forcing of the high-energy secondary vortices and the subharmonic forcing of mode II of the increasing number of paired vortices are responsible. In the later stage of transition and in the upper subcritical regime, the paired vortices are responsible. Their frequencies are also at and near those of the most amplified wave.

There is mutual interference between the excited small-scale secondary vortices and the large-scale primary vortex sheet in the early stage of transition. The secondary vortices amplify the upstream part of the vortex sheet. The effect is the most significant for the Group III vortices. The strain field of the amplified vortex sheet, in turn, further amplifies the secondary vortices. In the later stage of transition, the mutual interference between the high-energy paired secondary vortices and the primary vortex sheet plays a similar important role.

Acknowledgment

The first author was supported by a fellowship offered by The University of Hong Kong, Hong Kong.

References

[1] Norberg, C., 1987, ''Effects of Reynolds Number and a Low Intensity Freestream Turbulence on the Flow Around a Circular Cylinder,'' Ph.D. thesis, Chalmers University of Technology, Sweden.
[2] Kourta, A., Boisson, H. C., Chassaing, P., and Ha Minh, H., 1987, ''Nonlinear Interaction and the Transition to Turbulence in the Wake of a Circular Cylinder,'' J. Fluid Mech., **181**, pp. 141–161.
[3] Prasad, A., and Williamson, C. H. K., 1997, ''The Instability of the Shear Layer Separating from a Bluff Body,'' J. Fluid Mech., **333**, pp. 375–402.
[4] Chyu, C., and Rockwell, D., 1996, ''Evolution of Patterns of Streamwise Vorticity in the Turbulent Near Wake of a Circular Cylinder,'' J. Fluid Mech., **320**, pp. 117–137.
[5] Wei, T., and Smith, C. R., 1986, ''Secondary Vortices in the Wake of Circular Cylinder,'' J. Fluid Mech., **169**, pp. 513–533.
[6] Ho, C. M., and Huerre, P., 1984, ''Perturbed Free Shear Layer,'' Annu. Rev. Fluid Mech., **16**, pp. 365–424.
[7] Winant, C. D., and Browand, F. K., 1974, ''Vortex Pairing: the Mechanism of Turbulent Mixing-Layer Growth at Moderate Reynolds Number,'' J. Fluid Mech., **63**, pp. 413–427.
[8] Bernal, L. P., and Roshko, A., 1986, ''Streamwise Vortex Structure in Plane Mixing Layers,'' J. Fluid Mech., **170**, pp. 499–525.
[9] Unal, M. F., and Rockwell, D., 1988a, ''On Vortex Formation from a Cylinder. Part 1: The Initial Instability,'' J. Fluid Mech., **190**, pp. 491–512.
[10] Braza, M., Chassaing, P., and Ha Minh, H., 1990, ''Prediction of Large Scale Transition Features in the Wake of a Circular Cylinder,'' Phys. Fluids A, **2**, pp. 1461–1471.
[11] Lin, S. C., Towfighi, J., and Rockwell, D., 1995, ''Instantaneous Structure of the Near Wake of a Circular Cylinder: On the Effect of Reynolds Number,'' J. Fluids Struct., **9**, pp. 409–418.
[12] Unal, M. F., and Rockwell, D., 1988b, ''On Vortex Formation from a Cylinder. Part 2: Control by Splitter-Plate Interference,'' J. Fluid Mech., **190**, pp. 513–529.
[13] Achenbach, E., 1968, ''Distribution of Local Pressure and Skin Friction Around Circular Cylinder in Cross-Flow Up to $Re=5\times10^6$,'' J. Fluid Mech., **34**, pp. 625–639.
[14] Guven, O., Farell, C., and Patel, V. C., 1980, ''Surface-roughness Effects on the Mean Flow Past Circular Cylinders,'' J. Fluid Mech., **98**, pp. 673–701.
[15] Norberg, C., 1986, ''Interaction between Free Stream Turbulence and Vortex Shedding for a Single Tube in Cross Flow,'' J. Wind. Eng. Ind. Aerodyn., **23**, pp. 501–514.
[16] Norberg, C., and Sunden, B., 1987, ''Turbulence and Reynolds Number Effects on the Flow and Fluid Forces on a Single Cylinder in Cross Flow,'' J. Fluids Struct., **1**, pp. 337–357.
[17] Zdravkovich, M. M., 1990, ''Conceptual Overview of Laminar and Turbulent Flows Past Smooth and Rough Cylinders,'' J. Wind. Eng. Ind. Aerodyn., **33**, pp. 53–62.
[18] Bloor, M. S., 1964, ''The Transition to Turbulence in the Wake of Circular Cylinder,'' J. Fluid Mech., **19**, pp. 290–304.
[19] Peterka, J. A., and Richardson, P. D., 1969, ''Effects of Sound on Separated Flow,'' J. Fluid Mech., **37**, pp. 265–287.
[20] Szepessy, S., and Bearman, P. W., 1992, ''Aspect Ratio and End Plates Effects on Vortex Shedding from a Circular Cylinder,'' J. Fluid Mech., **234**, pp. 191–217.
[21] Hussain, A. K. M. F., 1983, ''Coherent Structures—Reality and Myth,'' Phys. Fluids, **26**, pp. 2816–2850.
[22] Gerrard, J. H., 1978, ''The Wakes of Cylindrical Bluff Body at Low Reynolds Number,'' Philos. Trans. R. Soc. London, Ser. A, **288**, pp. 351–382.
[23] Peltzer, R. D., 1980, ''The Effect of Upstream Shear and Surface Roughness on the Vortex Shedding Patterns and Pressure Distributions around a Circular Cylinder in Transitional Reynolds Number Flows,'' M.S. thesis, VPI & SU.
[24] Woo, H. G. C., Cermak, J. E., and Peterka, J. A., 1981, ''Experiments on Vortex Shedding from Stationary and Oscillating Cables in a Linear Shear Flow,'' Final Rep. on Contract N68305-78-C-0055 for the Naval Civil Flow, Colorado State University.
[25] Norberg, C., 1994, ''An Experimental Investigation of the Flow Around a Circular Cylinder,'' J. Fluid Mech., **258**, pp. 287–316.
[26] Lin, S. J., 1981, ''The Evolution of Spanwise Vorticity in the Free Shear Layer,'' Ph.D. Thesis, University of California, Berkeley.
[27] Lasheras, J. C., Cho, J. S., and Maxworthy, J., 1986, ''On the Origin and Evolution of Streamwise Vortical Structures in a Plane Free Shear Layer,'' J. Fluid Mech., **172**, pp. 231–258.
[28] Zaman, K. B. M. Q., and Hussain, A. K. M. F., 1981, ''Taylor Hypothesis and Large Scale Coherent Structures,'' J. Fluid Mech., **112**, pp. 379–396.
[29] Cebecci, T., and Bradshaw, P., 1977, *Momentum Transfer in Boundary Layers*, McGraw-Hill, New York
[30] Hussain, A. K. M. F., and Hayakawa, M., 1987, ''Education of Large Scale Organized Structures in a Turbulent Plane Wake,'' J. Fluid Mech., **180**, pp. 193–229.
[31] Freymuth, P., 1966, ''On Transition in a Separated Laminar Boundary Layer,'' J. Fluid Mech., **25**, 683–704.
[32] Ho, C. M., and Nosseir, N. S., 1981, ''Dynamics of an Impinging Jet. Part I. The Feedback Phenomenon,'' J. Fluid Mech., **105**, pp. 119–142.
[33] Michalke, A., 1964, ''On the Inviscid Instability of the Hyperbolic Tangent Velocity Profile,'' J. Fluid Mech., **19**, pp. 543–556.
[34] Hussain, A. K. M. F., and Zedan, M. F., 1978, ''Effects of Initial Condition on the Axisymmetric Free Shear Layer: Effects of the Initial Momentum Thickness,'' Phys. Fluids, **21**, pp. 1475–1481.
[35] Zaman, K. B. M. Q., and Hussain, A. K. M. F., 1980, ''Vortex Pairing in a Circular Jet under Controlled Excitation Part 1. General Jet Response,'' J. Fluid Mech., **101**, pp. 449–491.
[36] Zaman, K. B. M. Q., and McKinzie, D. J., 1991, ''Control of Laminar Separation over Airfoils by Acoustic Excitation,'' AIAA J., **29**, pp. 1095–1083.
[37] Zaman, K. B. M. Q., 1992, ''Effect of Acoustic Excitation on Stalled Flows over an Airfoil,'' AIAA J., **30**, pp. 1492–1585.
[38] Lamb, H., 1976, *Hydrodynamics*, Cambridge University Press.
[39] Tang, S. K., and Ko, N. W. M., 1997, ''Sound Generation by Interaction of Two Inviscid Two-dimensional Vortices,'' J. Acoust. Soc. Am., **102**, pp. 1463–1473.
[40] Tang, S. K., and Ko, N. W. M., 1998, ''Effects of a Background Axisymmetrical Potential Flow on Vortex Ring Pairing Sound,'' J. Acoust. Soc. Am., **104**, pp. 3273–3281.
[41] Ho, C. M., and Huang, L. S., 1982, ''Subharmonics and Vortex Merging in Mixing Layer,'' J. Fluid Mech., **119**, pp. 443–473.
[42] Maekawa, T., and Mizuno, S., 1967, ''Flow Around the Separation Point and in the Near Wake of a Circular Cylinder,'' *Physics of Fluids Supplement*, pp. S184–S186.

Journal of Fluids Engineering

Technical Briefs

Simulation and Analysis of a Magnetoelastically Driven Micro-Pump

A. Beskok
Assistant Professor

A. R. Srinivasa
Assistant Professor

Mechanical Engineering Department, Texas A&M University, College Station, TX 77843

The operation of a micro-pump system driven by a magnetoelastic polymeric membrane developed at Texas A&M University is analyzed by numerical simulations. Unsteady, incompressible Navier-Stokes equations in a moving boundary system are solved by a spectral element methodology, employing an Arbitrary Lagrangian Eulerian (ALE) formulation on unstructured meshes. The performance of the micro-pump is evaluated as a function of the Reynolds number and the geometric parameters. The volumetric flowrate is shown to increase as a function of the Reynolds number. The system is simulated by assuming the deformation of the membrane. The required voltage and current are then calculated by a lumped parameter analysis. [DOI: 10.1115/1.1363700]

1 Introduction

Micro-pump systems, delivering volumetric flow rates in the order of $10^{-8} \sim 10^{-12}$ m^3/s, can be used in many bio-fluidic, drug delivery, mixing and flow control applications. Most of the micro-pump systems are actuated by a vibrating membrane in a chamber with hanging-beam-type (Cantilever beam) inlet and exit micro-valves (Van Lintel et al. [1]; Esashi et al. [2]; Smits [3]). These are unidirectional micro-pumps, since the Cantilever-type micro-valves only open in a prefered flow direction. A micro-pump design, based on a rotating cylinder in a micro-channel, was also proposed by Sen et al. [4]. Here, the cylinder is located asymmetrically within the micro-channel, and it propels the fluid due to viscous action, while rotating with a prescribed angular speed. This is a bidirectional micro-pump, as the flow direction can be changed by reversing the angular velocity of the cylinder. This pump works well for low Reynolds number flows. However, the efficiency of the design rapidly diminishes with increased Reynolds number, as the fluid inertia dominates.

In this study, we present a bidirectional (reversible) micro-pump utilizing a vibrating magnetoelastic membrane with magnetic inlet and outlet pinch valves (see Fig. 1). Since the inlet and the exit valves oscillate in between the open and closed positions with a prescribed motion, it is possible to control the performance of the micro-pump with the micro-valves. This design has the advantage of reversibility, yet it maintains its performance for relatively high Reynolds number applications.

The membrane of the pump is built out of a novel magnetoelastic polymer (MAP) developed at Texas A&M University. The material is composed of a tri-plock copolymer that is solidified by a gelling agent and contains a dispersed phase of fine ferritic particles. These particles enhance the permeability of the material, so that the entire membrane acts as a variable inductance whose value depends upon the strain in the material and its proximity to the poles of the electromagnet. The properties of the material with respect to other actuators (such as shape memory alloys (SMA), electroactive polymer (EAP) and piezoelectric crystals (PAC) are shown in Table 1.

2 Geometric Specifications

The micro-pump geometry is presented in terms of the length of the membrane ''*L*,'' in Fig. 1. This allows us to interpret the results using *geometric similarity* in determining the optimum pump dimensions.

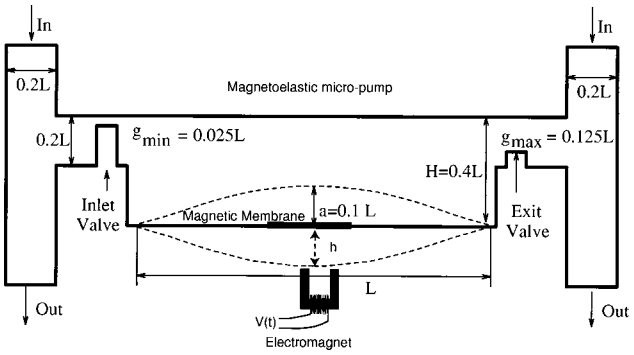

Fig. 1 Sketch of the micro-pump operating between two micro-channel systems

Table 1 The properties of the magnetoelastic polymer (MAP) with respect to the shape memory alloys (SMA), electroactive polymer (EAP) and piezoelectric crystals (PAC)

Property	EAP	PAC	SMA	MAP
Strain	> 10%	0.1 – 0.3%	< 8%	> 10%
Force	0.1-3 Mpa	30-40 Mpa	700 Mpa	2-3 Mpa
Reaction time	microseconds	microseconds	secs to mins	microseconds
Density	1-2.5 g/cc	6-8 g/cc	5-6 g/cc	5-6 g/cc
Voltage	4-7 V	50-100 V	NA	2-12 V
Life	long	long	short(fatigue)	long
Toughness	resilient plastic	brittle ceramic	metallic	soft and tough rubber
Adaptability	Plates, thin, films,	Plates	wires, thin films	moldable to any shape

Contributed by the Fluids Engineering Division of THE AMERICAN SOCIETY OF MECHANICAL ENGINEERS. Manuscript received by the Fluids Engineering Division April 1, 1999; revised manuscript received October 23, 2000. Associate Editor: U. Ghia.

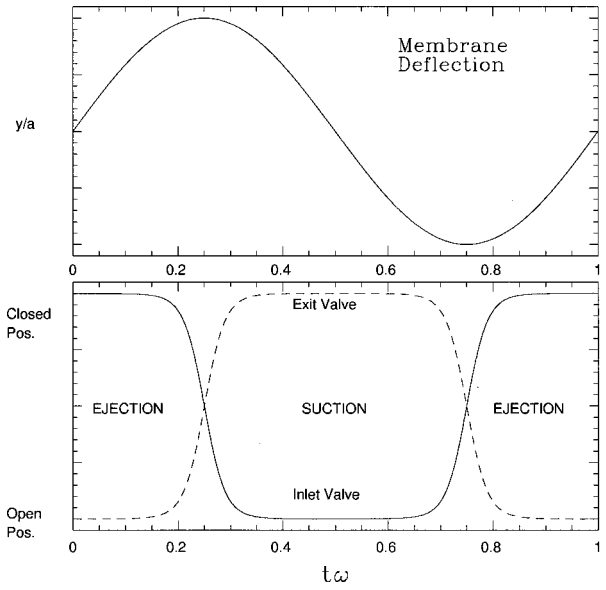

Fig. 2 Top: deflection of the membrane. Bottom: position of the valve tips during a pump cycle.

The micro-pump is ideally placed between two reservoirs. However, numerical simulation of such a system is difficult due to large reservoir size. Any finite size reservoir would require inflow and outflow numerical boundary conditions, and these must be imposed carefully, in order to avoid a preferred flow direction in the micro-pump. This difficulty is overcome by placing the micro-pump in between two symmetric micro-channel flow systems, where equal amount of liquid flow is maintained from top to the bottom direction. Therefore, the flow conditions are symmetric and there is zero net flow from one channel to another, when the pump is not actuated. We verified this by simulations.

Oscillation of the membrane with a specified frequency ω and an amplitude a excites the fluid within the micro-pump cavity. For our simulations we have used $a=L/10$, and $\omega=\pi c/L$, where $c^2=T/M$, T and M are the tension and the mass per unit area of the membrane, respectively. The first-mode of vibration of the membrane is used to determine the position (see Fig. 2, top), velocity and the acceleration as a function of time

$$y(x,t)=a\,\sin(\pi ct/L)\sin(\pi x/L)=A(t)\sin(\pi x/L), \quad (1a)$$

$$v(x,t)=\left(\frac{a\pi c}{L}\right)\cos(\pi ct/L)\sin(\pi x/L)=\dot{A}(t)\sin(\pi x/L), \quad (1b)$$

$$\dot{v}(x,t)=-a\left(\frac{\pi c}{L}\right)^2\sin(\pi ct/L)\sin(\pi x/L). \quad (1c)$$

The pump geometry is symmetric. Therefore, active pumping cannot be achieved solely by the membrane oscillations. The action of the two valves provides the requisite directionality of the flow. In the simulation, the inlet and the exit valves are located at the mean height of $y_0=0.325\,L$ from the membrane, and the position of the valves are specified as a function of time

$$y(t)=y_0\pm 0.05\,L\,\tanh[4\cos(\pi ct/L)]. \quad (2)$$

The valve motion is designed to be close to a step function, oscillating between open and closed positions with finite velocity and acceleration. The positions of the inlet and exit valves during a cycle of the micro-pump is presented in Fig. 2 (bottom). The phase difference between the inlet and the exit valves is π radians.

3 Analysis and Simulation

The performance of our design is based on the following factors: the membrane length L and width W, the pump-cavity height H, the amplitude a and the frequency ω of the membrane motion, the minimum valve clearance (the gap between the closed-valve and the top wall) $g_{\min}$, the time-lapse between the opening and the closing of the valves (see Eq. (2), and Fig. 2, bottom) δ^{-1}, the dynamic viscosity of the fluid μ, and the fluid density ρ. There are nine variables associated with the performance of the micro-pump, with dimensions of length, time, and mass. This corresponds to six nondimensional variables: a/L, W/L, H/L, g/L, δ/ω, and $\rho a^2\omega/\mu$. In this study, we have fixed $\delta=0.15\,\omega$. The geometric length-scales are set as $H=0.4\,L$, $g=0.025\,L$. The parameters W/L and a/L, and $\rho a^2\omega/\mu$ are varied. The magnitude of the membrane velocity $u\simeq\omega a$. Therefore the parameter $\rho a^2\omega/\mu=\rho u a/\mu=a^2\omega/\nu$ is a Reynolds number.

The volumetric flowrate per channel width (W) can be calculated using Eq. (1*b*)

$$\frac{\dot{Q}}{W}=\int_0^L v(x,t)dx=-2ac\,\cos(\pi ct/L). \quad (3)$$

The suction stage of the micro-pump happens while $-L/2c\leqslant t\leqslant L/2c$. Therefore, the average volumetric flow rate for a given period $T=\omega^{-1}$ is

$$\frac{\dot{\bar{Q}}}{\omega}=-2acW\int_{-L/2c}^{L/2c}\cos(\pi ct/L)dt=\frac{4aLW}{\pi}. \quad (4)$$

The average flowrate is

$$\dot{\bar{Q}}=\frac{4aLW\omega}{\pi}=\frac{4}{\pi}\frac{L}{a}W\nu\,\mathrm{Re}. \quad (5)$$

This simple analysis indicates that the volumetric flowrate is proportional to the Reynolds number, the width of the micro-pump membrane W, and the L/a ratio. Our analysis assumes no leaks from the inlet valve during ejection stage, and from the exit valve during the suction stage. Therefore, Eq. (5) gives the maximum theoretical volumetric flowrate of the micro-pump system. This value is used in determining the efficiency of the micro-pump, when leakage effects due to the *imperfect motion* of the inlet and exit valves are considered.

Incompressible Navier-Stokes equations in the micro-pump system is solved by an h/p type spectral element algorithm, employing an Arbitrary Lagrangian Eulerian (ALE) formulation (Beskok and Warburton [5], Karniadakis and Sherwin [6]). The algorithm maintains numerical accuracy and convergence under relatively large mesh stretching conditions. Hence, we can avoid expensive remeshing procedures for most of the times. In fact, full closure of the inlet and exit valves require *annihilation* of the elements trapped in between the valves and the top wall, requiring remeshing of the computational domain. Remeshing is avoided by allowing a gap in between the valves and the top wall. This gap leads to fluid leakage, which affects the micro-pump efficiency.

In Fig. 3, we present instantaneous flowrate variation for two different Reynolds numbers (Re=3 and 30). The volumetric flowrate of fluid entering through the inlet valve is shown as positive and leaving flowrate is indicated as negative. The sum of the two is the rate of change of the control volume due to the oscillation of the membrane

$$dV/dt=\dot{Q}_{\mathrm{in}}-\dot{Q}_{\mathrm{out}}.$$

The membrane's motion is periodic. Therefore, the net amount of fluid displaced by the membrane in a period is zero

$$\oint dV=0=\int_0^\tau\dot{Q}_{\mathrm{in}}dt-\int_0^\tau\dot{Q}_{\mathrm{out}}dt.$$

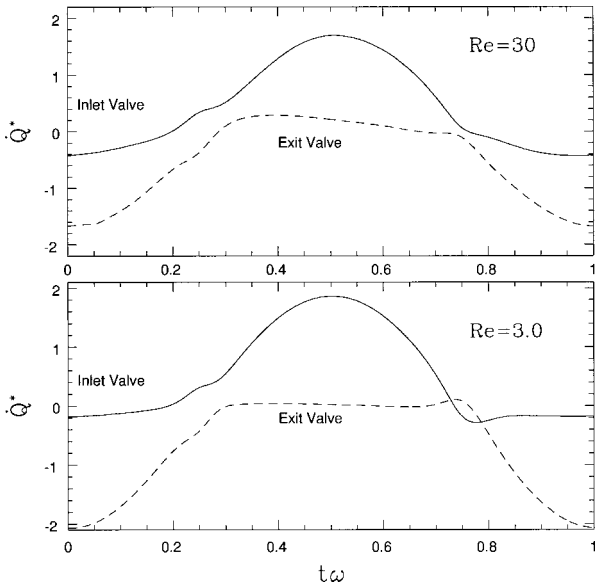

Fig. 3 Nondimensional volumetric flowrate variation with in a period of the micro-pump, as a function of the Reynolds number, Re=$a^2\omega/\nu$ for (a/L=1/10,a/h=1/3)

In other words, $\dot{\bar{Q}}_{in}=\dot{\bar{Q}}_{out}=\dot{\bar{Q}}$. Numerically integrating the curves under inlet and exit valves in Fig. 3, we determined the effective flowrate in our micro-pump for $g_{min}=0.025\,L$. Ratio of the numerical values of the flowrate to the maximum flowrate given by Eq. (5) defines the efficiency (η) of the micro-pump. The results are presented in Table 2. It is clearly seen that the efficiency of the pump decreases with increasing the Reynolds number. The average flowrate of the pump increases with the Reynolds number, as predicted by Eq. (5). This is either due to increase in the size of the pump (increase in a) or increase in the frequency ω, for a given fluid (fixed ν). For fabrication of our conceptual design, the actual dimensions of the micro-pump can be determined by either selecting the admissible amplitude of vibration a or the actuation frequency ω. For example, choosing water and selecting the membrane amplitude to be 10 μm we calculated the frequency of operation and the corresponding mass flowrate in the pump. The results are presented in Table 2. The power required to drive the pump can easily be obtained by integrating the product of the numerically obtained pressure and the velocity on the membrane.

Table 2 The predicted and computed mass flowrate (per unit width), actuation frequency and the efficiency of the micro-pump, as a function of the Reynolds number. The data are obtained for water and a=10 μm

Re	0.3	3	30
$\omega[kHz]$	3	30	300
$\frac{\dot{M}}{W}\left[\frac{kg}{ms}\right]_{Th}$	0.0382	0.382	3.82
$\frac{\dot{M}}{W}\left[\frac{kg}{ms}\right]_{Num}$	0.0351	0.336	2.86
η	92%	88%	75%

4 A Simplified Analysis of the Electromagnetic Drive Mechanism

We analyze the magnetic circuit by using a lumped parameter model. Therefore, the electromagnetic coenergy E (the Legendre transform of the magnetic field energy with respect to the current) of the configuration, shown in Fig. 1, is given by

$$E(\omega,i)=\frac{S\mu_0 N^2 i^2}{2(h-A(t))}, \tag{6}$$

where h is the distance between the equilibrium position of the membrane and the electromagnet, $A(t)$ is the amplitude of the membrane introduced in (1a), S is the cross-sectional area of the electromagnet, N is the number of turns in the coil, μ_0 is the permittivity of free space, and i is the current through the coil. In Eq. (6), the electromagnetic radiation effects and fringing effects are ignored.

The inductance ($\mathcal{L}$) of the circuit as a function of the gap width ($w=h-A(t)$) is given by

$$\mathcal{L}(w)=\frac{S\mu_0 N^2}{2w}. \tag{7}$$

The variations in the inductance of the coil with the gap width enables power transfer to the membrane. Therefore the current i can be calculated from power considerations. Since the electromotive force on the membrane is $-(d\mathcal{L}/dw)i^2$, the total power supplied to the membrane is $-(d\mathcal{L}/dw)\dot{w}i^2$. On the other hand, the fluid power requirement on the membrane is

$$\int_0^L P(x,t)v(x,t)dx=\dot{A}(t)\int_0^L P(x,t)\sin(\pi x/L)dx \tag{8}$$

Since the power requirement can be calculated from the pump simulation, the electric current required is given by

$$i^2=-\dot{A}(t)\int_0^L P(x,t)\sin(\pi x/L)dx \Big/ \left(\frac{d\mathcal{L}}{dw}\dot{\omega}\right). \tag{9}$$

In performing the above simplified analysis, we have neglected the elasticity as well as the inertia of the membrane. A full accounting of these effect will be done in a later work where a complete lumped mass analysis (including the pump, valves and the electromagnetics) will be carried out.

Since the simulation results presented here are obtained by prescribed displacement of the membrane, the voltage required to drive the system can be calculated. For given inductance of the circuit $\mathcal{L}(w)$ and the resistance of the coil windings R, a lumped parameter analysis of the circuit is used to obtain the voltage needed for system activation as

$$V(t)=Ri+\frac{d\mathcal{L}}{dw}\dot{w}i+\mathcal{L}(w)\frac{di}{dt}=\left(R+\frac{d\mathcal{L}}{dw}\dot{w}\right)i+\mathcal{L}(w)\frac{di}{dt}. \tag{10}$$

A seen in the above equation, the influence of the moving membrane is felt as an *additional resistance* that is proportional to the change in inductance due to the motion. Of course, in the current approach, the voltage required is calculated for a particular motion of the membrane and thus the coupling between the response of the pump and the driving circuit is severed. A more complete analysis by modeling the full behavior is being undertaken as a lumped mass system.

5 Discussions

We presented numerical simulation and analysis of a magneto-elastic micro-pump. The piston type inlet and exit valves used in our design could be fabricated as a free floating gate-valve, where thermally generated vapor bubbles enable the valve motion (Papavasiliou et al. [7]). However, such valves typically result in low actuation frequencies, and they are not suitable for many applications. A possible alternative is utilization of pinch valves made

out of the same magnetoelastic material, which has reaction times in the order of a few micro-seconds. The response time of such a design will be primarily limited by the inductance of the magnetic coil.

References

[1] Van Lintel, H. T. G., Van de Pol, F. C. M., and Bouwstra, S., 1988, ''A piezoelectric micropump based on micromachining of silicon,'' Sens. Actuators, **15**, pp. 153–167.
[2] Esashi, M., Shoji, S., and Nakano, A., 1989, ''Normally closed microvalve fabricated on a silicon wafer,'' Sens. Actuators, **20**, pp. 163–169.
[3] Smits, J. G., 1990, ''Piezoelectric micropump with three valves working peristaltically,'' Sens. Actuators A, **21–23**, pp. 203–206.
[4] Sen, M., Wajerski, D., and Gad el Hak, M., 1996, ''A novel pump for MEMS applications,'' ASME J. Fluids Eng., **118**, pp. 624–627.
[5] Beskok A., and Warburton T. C., 2001, ''An unstructured h/p finite element scheme for fluid flow and heat transfer in moving domains,'' Submitted to *Journal of Computational Physics*.
[6] Karniadakis, G. E., and Sherwin, S. J., 1999, *Spectral/hp Element Methods for CFD*, Oxford University Press.
[7] Papavasiliou, A. P., Liepmann D., and Pisano, A. P., 1999, ''Fabrication of a free floating silicon gate valve,'' *Proceedings of ASME IMECE Meeting, MEMS*. Vol. 1, pp. 265–274.

The Problem With Oscillatory Behavior in Grid Convergence Studies

Hugh W. Coleman
Fellow ASME, Propulsion Research Center, Department of Mechanical and Aerospace Engineering, University of Alabama in Huntsville, Huntsville, AL 35899

Fred Stern
Fellow ASME, Iowa Institute for Hydraulic Research, Department of Mechanical Engineering, University of Iowa, Iowa City, IA 52242

Andrea Di Mascio and Emilio Campana
Istituto Nazionale Per Studi Ed Esperienze Di Architettura Navale (INSEAN), Rome, Italy

[DOI: 10.1115/1.1362672]

Discussion of the Problem

The possibility of oscillatory behavior of the value of a computed variable as grid size is refined in a simulation raises questions in the interpretation of grid convergence studies that have, to the authors' knowledge, never been addressed. Such oscillatory behavior has been observed by the authors, for example, in variables such as wave profiles along the hull and wave elevations in the stern flow in simulations of flows about ships with complex geometries. Roache [1], in his comprehensive presentation and critique of work up to that time in the area of verification and validation of simulations, points out that ''behavior far away from asymptotic convergence can be non-monotone'' and ''the additional assumption of monotone truncation error convergence in the mesh spacing . . . may not be valid for coarse grids, or possibly other conditions.''

Contributed by the Fluids Engineering Division of THE AMERICAN SOCIETY OF MECHANICAL ENGINEERS. Manuscript received by the Fluids Engineering Division September 1, 1999; revised manuscript received February 8, 2001. Associate Editor: V. Ghia.

Typically (see Stern, et al. [2], for instance), the behavior of a variable is categorized as monotonically convergent, oscillatory, or divergent based on its behavior as the grid used in a simulation is refined. Consider the values of a computed variable y as a simulation is run using a coarse grid (y_C), a medium grid (y_M), and a fine grid (y_F). The ratio

$$R=\frac{y_M-y_F}{y_C-y_M}=\frac{\Delta y_{M-F}}{\Delta y_{C-M}}$$

has been used to categorize the behavior of y as grid size is decreased as: (1) monotonically convergent when $0<R<1$; (2) oscillatory when $R<0$; and (3) divergent when $R>1$. If the behavior really is monotonically convergent, then (1) holds. If the behavior really is divergent, then (3) holds. The problem that has not been previously recognized and discussed is the ambiguity that arises when the behavior really is oscillatory.

Consider the results from a simulation in which the computed value of variable y is truly an oscillatory function of grid size Δx, as shown in Fig. 1. When a grid size is chosen in a simulation, its value is of course arbitrary relative to the unknown periods of any oscillations of the computed variables, so each of the following cases in this example must be considered equally likely. Three cases are investigated, with a different initial grid size in each. In each case, three simulations are run with grid doubling used twice, resulting in coarse (C), medium (M), and fine (F) grid simulation values of the variable y.

The computed values of y are shown in Table 1 and plotted in Fig. 1. For Case 1, Δy_{C-M} is -1.0 and Δy_{M-F} is $+0.3$, a situation that would be assessed as oscillatory since $R<0$. For Case 2, Δy_{C-M} is $+0.36$ and Δy_{M-F} is $+0.28$, a situation that would be concluded as being monotonically convergent since $0<R<1$. Finally, for Case 3, Δy_{C-M} is $+0.14$ and Δy_{M-F} is $+0.36$, a situation that would be concluded as divergent since $R>1$. Thus, for the same (true) oscillatory behavior any of three conclusions can be supported, depending on the relationship of the chosen grid size to the unknown period(s) of the oscillation(s).

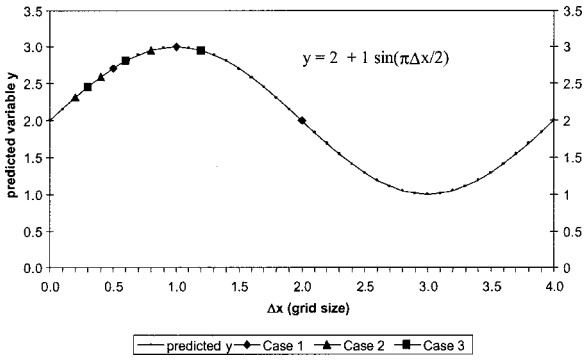

Fig. 1 Illustration of results of grid convergence studies using three grids when the true behavior is oscillatory convergence

Table 1 Results from grid convergence studies

Case	Grid Sizes (Δx's)	y Coarse	y Medium	y Fine	Δy_{C-M}	Δy_{M-F}	Behavior Indication
1	2.0, 1.0, 0.5	2.00	3.00	2.70	-1.00	0.30	R = -0.3 Oscillatory
2	0.8, 0.4, 0.2	2.95	2.59	2.31	0.36	0.28	R = +0.8 Converging
3	1.2, 0.6, 0.3	2.95	2.81	2.45	0.14	0.36	R = +2.6 Diverging

Note that in real cases (with results from three grids, say), the true behavior of y with Δx is unknown, so the only information one has is the three computed values of y. If the true but unknown behavior is oscillatory, then depending on the choices of initial grid size and the grid refinement ratio those three values can produce *any* value of R (including a value indicating asymptotic convergence). Also note that whether the Δx in one's finest grid corresponds to a value of 1, 2, 3, or 100 on a scale such as that shown in Fig. 1 is unknown.

Conclusion

Although the example presented is somewhat contrived, the dilemma one faces in interpreting results of grid convergence studies is not. If there is the possibility of oscillatory behavior of the value of a computed variable as grid size is refined in a simulation, then interpretation of the results of grid convergence studies seems impossible to achieve unambiguously.

Acknowledgment

The authors gratefully acknowledge the sponsorship of this research by the Office of Naval Research under Grants N00014-97-1-0014 and N00014-97-1-0151 under the administration of Dr. E. P. Rood.

References

[1] Roache, P. J., 1998, *Verification and Validation in Computational Science and Engineering*, Hermosa Publishers, Albuquerque, NM.

[2] Stern, F., Wilson, R. V., Coleman, H. W., and Paterson, E. G., 1999, ''Verification and Validation of CFD Simulations,'' Iowa Institute of Hydraulic Research, The University of Iowa, IIHR Report No. 407.

Prediction of Fully Developed Pressure Drops in Regular Polygonal Ducts

SuiFei Nan

Professor, Department of Chemical Engineering, Zhejiang University, HangZhou, 310027, P. R. China

Introduction

Many researchers have investigated the Fanning factors in circular ducts and proposed many correlating equations to calculate the Fanning factors. As to various noncircular ducts, the frictional pressure drops have rarely been investigated. So it has been common practice in the field of fluid mechanics to use the hydraulic or equivalent diameter in the Reynolds number in predicting turbulent pressure drops along duct lengths having noncircular cross section.

But, there is usually large deviation from the circular tube line by using the hydraulic diameter in the Reynolds number. And, therefore, some researchers have proposed various modifying methods to predict friction factors. In the case of rectangular ducts, for example, Jones [1] uses a ''laminar equivalent diameter'' to form the Reynolds number, which is in turn used in any circular tube correlation for friction factors. And in case of annuli, Brighton and Jones [2] modify the constant C in the Blasius equation on the basis of the experimental data. As to triangular ducts, Nan and Dou [3] use an area equivalent round diameter in the Reynolds number.

Contributed by the Fluids Engineering Division of THE AMERICAN SOCIETY OF MECHANICAL ENGINEERS. Manuscript received by the Fluids Engineering Division September 14, 2000; revised manuscript received February 9, 2001. Associate Editor: D. R. Williams.

In the case of regular polygonal ducts, there were no experimental data reported in the literature except equilateral-triangular [4] and square [5] ducts. Therefore, the purpose of the investigation reported here was to obtain friction factors for isothermal, fully developed, laminar, and turbulent flow in smooth equilateral-triangular, square, pentagonal, hexagonal, heptagonal, and octagonal ducts, respectively. Moreover, an area equivalent round diameter is proposed to use in Reynolds number in predicting Fanning factor of turbulent flow in a duct having regular (n-sided) polygonal cross section.

Apparatus

The regular polygonal ducts were made of plate glass. Take a hexagonal duct for example. First cut six slabs of plate glass (width 8.10 mm, thickness 3.0 mm). Then precisely work pattern plates of the hexagonal polygon. Put the slabs of glass into the pattern plates. Finally seal the seams between the adjacent slabs with silica gel, as shown in Fig. 1. The ducts made of plate glass, therefore, are hydraulically smooth.

The sketch of the experimental procedure used to obtain pressure drop data is illustrated in Fig. 2 and Fig. 3. In the setup used, water was pumped from the water pool into the elevated tank that had an overflow pipe to maintain a fixed water level, then flowed through a duct and past an abrupt entrance and into the hydrodynamic entrance section where it became fully developed. It then entered the test section that consisted of four identical test sections in series. These multiple section served to check on the reproducibility of the measurements and to insure that the flow was fully developed. In the test section, the pressure drop readings were

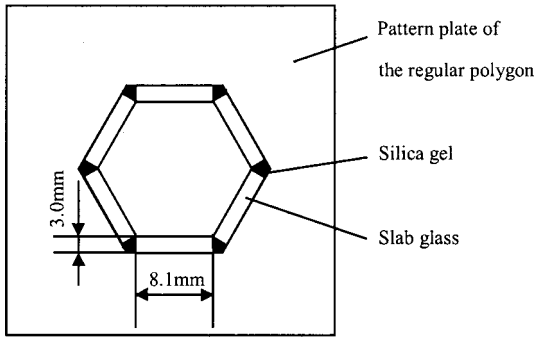

Fig. 1 Structure of the hexagonal polygonal duct

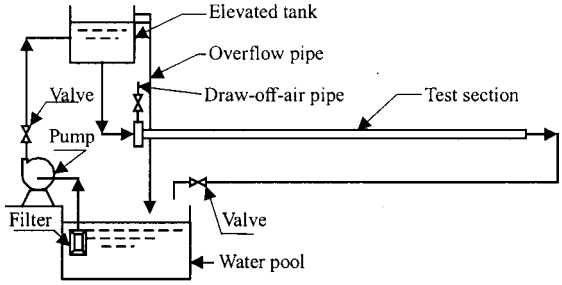

Fig. 2 Sketch of the experimental procedure

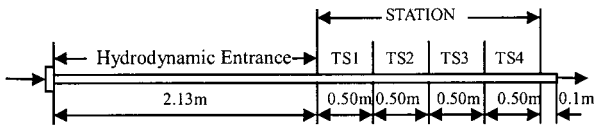

Fig. 3 Sketch of the positions of the pressure holes distributing over the test sections (TS)

Table 1 Dimensions of experimental ducts

Regular polygonal ducts	Side length a, $m\times10^3$	Hydraulic diam., $m\times10^3$	Hydrodynamic entrance length / hydraulic diam.	Overall test section length / hydraulic diam.
n=3	8.10	4.677	455.4	427.6
n=4	8.10	8.10	263.0	246.9
n=5	8.10	11.15	191.0	179.4
n=6	8.10	14.03	151.8	142.3
n=7	8.10	16.82	126.6	118.9
n=8	8.10	19.56	108.9	102.2

made by means of an inclined manometer. The manometer fluid was benzaldehyde (C_7H_6O) with density 1.032 g/cm^3 at 20°C. With an inclined manometer and benzaldehyde as the manometer fluid, the probable error is 0.95 percent of the pressure drop readings.

After leaving the test section, the water flowed through a duct and back to the water pool. The flow rates were determined by measuring the volume of water during a known time interval. The pertinent dimensions of the duct are listed in Table 1 for the various regular polygonal ducts investigated.

In Table 1, the hydraulic diameter d_e is defined as follows

$$d_e=4\times\frac{S}{P_e} \tag{1}$$

where S is the cross-sectional area of fluid flow, and P_e is the wetted perimeter, the length of wall in contact with the flowing fluid at any cross section.

Presentation of Results

The experimental data are presented in the form of Fanning factor against Reynolds number. These two quantities are defined as follows

$$f=\frac{d_e}{2Lu^2}\frac{\Delta P}{\rho} \tag{2}$$

and

$$\mathrm{Re}=\frac{d_e u\rho}{\mu} \tag{3}$$

where P is pressure, ρ is the density of the fluid, f is Fanning factor, L is the pipe length, d_e is the hydraulic diameter, u is the average velocity in flow direction, Re is Reynolds number, μ is the dynamic density of the fluid.

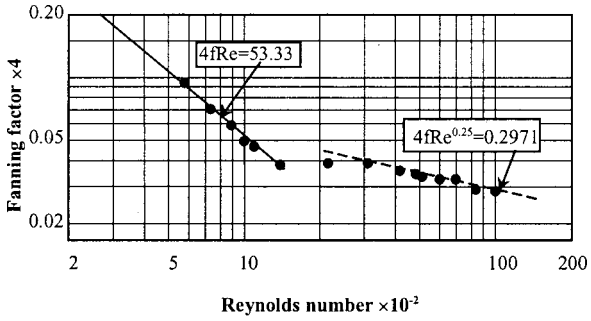

Fig. 4 Fanning factor versus Reynolds number in an equilateral-triangular duct

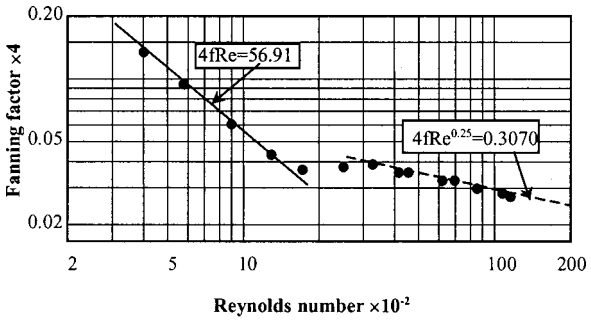

Fig. 5 Fanning factor versus Reynolds number in a square duct

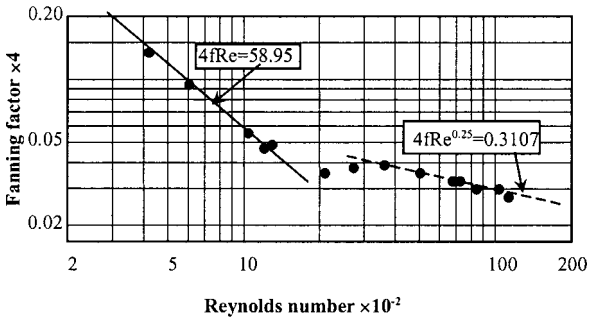

Fig. 6 Fanning factor versus Reynolds number in a pentagonal duct

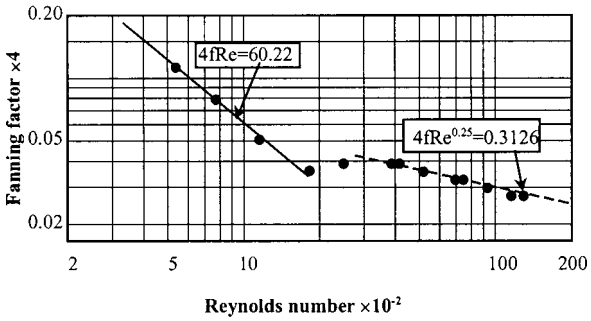

Fig. 7 Fanning factor versus Reynolds number in a hexagonal duct

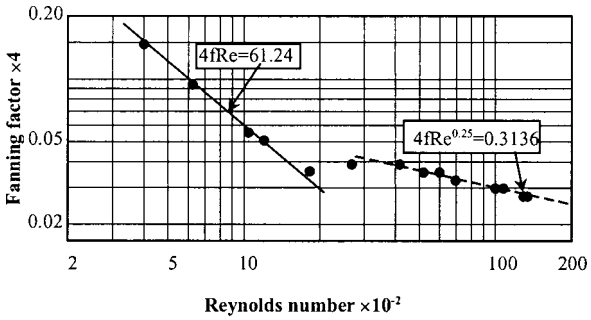

Fig. 8 Fanning factor versus Reynolds number in a heptagonal duct

For each duct, Fanning factors were measured in the laminar, transitional, and turbulent regimes. Figs. 4, 5, 6, 7, 8, and 9 show the relation between Fanning factors and Reynolds numbers for smooth equilateral-triangular, square, pentagonal, hexagonal, heptagonal, and octagonal ducts, respectively. Also shown in the figures, the solid lines are the laminar solutions [6].

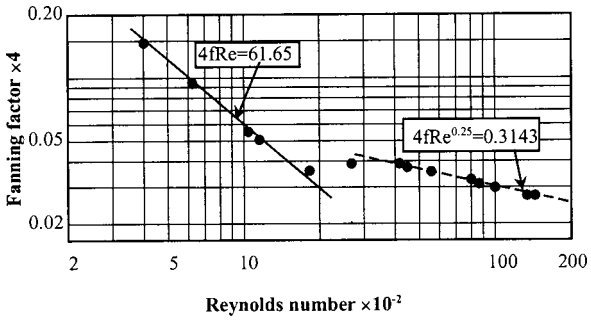

Fig. 9 Fanning factor versus Reynolds number in an octagonal duct

Area Equivalent Round Diameter and Modified Reynolds Number

We suggest an area equivalent round diameter [3] be used in Reynolds number. An area equivalent round diameter may be defined as

$$d_{Se}=\frac{4\times S}{P_S}=\sqrt{\frac{4S}{\pi}} \tag{4}$$

where S is the cross-sectional area of fluid flow, and P_S is the perimeter of a circle whose area is equal to S, $P_S=\pi d_{Se}$.

For the regular (n-sided) polygonal ducts, as shown in Fig. 10, we can calculate their area equivalent round diameters as follows:

According to the geometric relation shown in Fig. 10, the area of the triangle ABC is

$$S_n=\frac{a^2}{4\tan(\beta/2)} \tag{5}$$

where a is the side length of the regular (n-sided) polygon; β is equal to $2\pi/n$.

So, the area of the regular (n-sided) polygon is

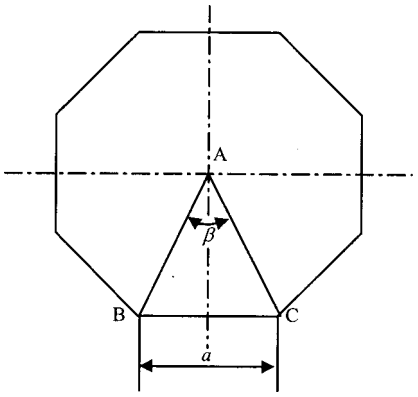

Fig. 10 A regular (n-sided) polygonal duct

$$S=nS_n=\frac{na^2}{4\tan(\pi/n)} \tag{6}$$

Substituting Eq. (6) into Eq. (4), we obtain

$$d_{Se}=a\sqrt{\frac{n}{\pi\tan(\pi/n)}} \tag{7}$$

The modified Reynolds number may be defined as

$$\mathrm{Re}^*=\frac{d_{Se}u\rho}{\mu} \tag{8}$$

The relation between Re* and Re is

$$\mathrm{Re}^*=\frac{d_{Se}u\rho}{\mu}=\frac{d_{Se}}{d_e}\frac{d_eu\rho}{\mu}=k\,\mathrm{Re} \tag{9}$$

where

$$d_e=\frac{4S}{na}=\frac{a}{\tan(\pi/n)}$$

$$k=\frac{d_{Se}}{d_e}=\sqrt{\frac{n\tan(\pi/n)}{\pi}}$$

If Re* is substituted for Re in the Blasius equation, we have

$$4f(\mathrm{Re}^*)^{0.25}=0.3164 \tag{10}$$

or

$$4f\,\mathrm{Re}^{0.25}=0.3164k^{-0.25}=C \tag{11}$$

Table 2 shows a comparison about C between Eq. (11) and the experimental results of Schiller, Hartnett et al., and the smooth equilateral-triangular, square, pentagonal, hexagonal, heptagonal, and octagonal ducts.

Discussion and Conclusion

By experimental data or from Figs. 4–9, the experimental data are fitted to Eq. (11) when Re>3500.

It has been shown in Table 2 that the use of an area equivalent round diameter to calculate a modified Reynolds number yields excellent agreement between Eq. (11) and the experimental data. The maximum deviation from the experimental data is within 1 percent.

If the hydraulic diameter is used in the Reynolds number, the deviation from the experimental data, for equilateral-triangular ducts, is

$$\frac{(0.3164-0.2942)}{0.2942}=7.55\,\text{percent}$$

and, for square ducts, is

$$\frac{(0.3164-0.3045)}{0.3045}=3.91\,\text{percent}$$

Therefore, the area equivalent round diameter is proposed for use in predicting the Fanning factors of the regular (n-sided) polygonal ducts.

Table 2 Comparison about C between Eq. (11) and the experimental results

Regular polygonal ducts	N=3	N=4	N=5	N=6	N=7	N=8
Values C calculated from Eq. 11	0.2971	0.3070	0.3107	0.3126	0.3136	0.3143
Values C_i from experimental data	0.2942	0.3045	0.3100	0.3112	0.3135	0.3143
%error, $(C-C_1)/C_1$	0.99	0.82	0.23	0.45	0.03	0.0
Values C_2 from [4],[5]	0.2970	0.3063	—	—	—	—
%error, $(C-C_2)/C_2$	0.03	0.23	—	—	—	—

References

[1] Jones, Jr., O. C., 1976, ''An Improvement in the Calculation of Turbulent Friction in Rectangular Ducts,'' ASME J. Fluids Eng., **98**, pp. 173–181.

[2] Brighton, J. A. and Jones, J. B., 1964, ''Fully Developed Turbulent Flow in Annuli,'' ASME J. Basic Eng., **86**, pp. 835–844.

[3] Nan, S. F. and Dou, M., 2000, ''A Method of Correlating Fully Developed Turbulent Friction in Triangular Ducts,'' ASME J. Fluids Eng., **122**, pp. 634–636.

[4] Schiller, L., 1923, ''Über den Strömugswiderstand von Rohren verschiedenen Querschnitts und Rauhigkeitsgrades,'' Z. Angew. Math. Mech., **3**, pp. 2–13.

[5] Hartnett, J. P., Koh, J. C. Y., and McComas, S. T., 1962, ''A Comparison of Predicted and Measured Friction Factors for Turbulent Flow Through Rectangular Ducts,'' ASME J. Heat Transfer, **84**, pp. 82–88.

[6] Shah, R. K., and London, A. L., 1978, ''Laminar flow forced convection in ducts,'' Supplement 1, *Advances in Heat Transfer*, T. F. Irvine and J. P. Hartnett, eds., Academic, New York.